Constraining the physical processes of protoplanetary disk evolution

Marion Villenave

▶ To cite this version:

Marion Villenave. Constraining the physical processes of protoplanetary disk evolution. Astrophysics [astro-ph]. Université Grenoble Alpes [2020-..], 2020. English. NNT : 2020GRALY027 . tel-03139885

HAL Id: tel-03139885
https://theses.hal.science/tel-03139885

Submitted on 12 Feb 2021

Université Grenoble Alpes

THÈSE

Pour obtenir le grade de

DOCTEUR DE L'UNIVERSITÉ GRENOBLE ALPES

Spécialité : Astrophysique et Milieux Dilués

Arrêté ministériel : 25 mai 2016

Présentée par

Marion VILLENAVE

Thèse dirigée par **François Ménard**, Directeur de recherche, CNRS
et codirigée par **Myriam Benisty**, Astronome adjointe, CNAP, et par
Bill Dent, Astronome système, ALMA JAO

préparée au sein de **l'Institut de Planétologie et d'Astrophysique de Grenoble**
dans **l'École Doctorale de Physique de Grenoble**

Caractérisation des processus d'évolution des disques protoplanétaires

Constraining the physical processes of protoplanetary disk evolution

Thèse soutenue publiquement le **22 septembre 2020**,
devant le jury composé de :

Dr. Clément Baruteau
Chargé de recherche, IRAP, CNRS, France, Rapporteur
Dr. Carlos Carrasco-Gonzalez
Professeur associé, IRyA, UNAM, Mexique, Examinateur
Dr. Cecilia Ceccarelli
Astronome, Université Grenoble Alpes, France, Présidente
Dr. Anna Miotello
Astronome, ESO, Allemagne, Invitée
Dr. Leonardo Testi
Astronome, ESO, Allemagne
Directeur de recherche, INAF-Arcetri, Italie, Rapporteur

Marion VILLENAVE

Constraining the physical processes of protoplanetary disk evolution

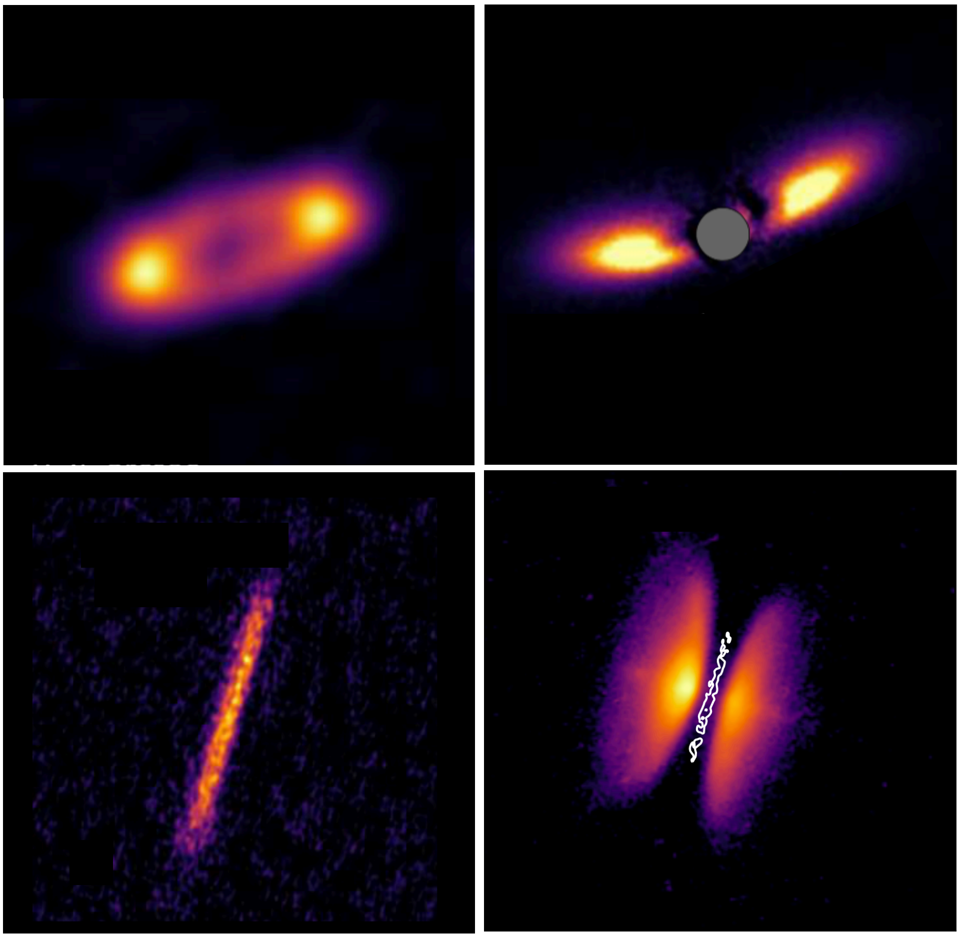

PhD thesis prepared at IPAG, Université Grenoble Alpes
with 2 years at ESO, Santiago de Chile

ABSTRACT

The diversity observed in the exoplanet population likely originates in the variety of physical structures of protoplanetary disks, their progenitors. Considering the timescales for disk dissipation, it is clear that giant planets must form fast, within a few million years. In the standard core accretion model, this implies that micron sized particles have to grow within this short timescale to larger sizes. This PhD thesis is dedicated to adding observational constraints on several aspects of protoplanetary disk evolution in order to understand better the processes of planet formation. In particular, I worked on a statistical study of the dust mass distribution in protoplanetary disks located in the Chamaeleon II star-forming region, on the presence of dust depleted cavities in transition disks and on observational constraints on dust evolution mechanisms such as radial drift and vertical settling. I used mostly ALMA millimeter observations, which I combined with complementary disk tracers such as optical/infrared scattered light images. On several occasions, I modeled these observations with radiative transfer to constrain the structure of these protoplanetary disks.

During this thesis, I have obtained important constraints on the vertical structure of protoplanetary disks, notably by studying a sample of 12 highly inclined disks. I find that the most inclined systems of this survey, where the vertical extent is best seen, are geometrically thin at millimeter wavelengths, all the more so when compared to their vertical extent seen with scattered light observations (probing smaller grains). This indicates that vertical settling is extremely efficient in these disks, which is favorable for fast grain growth in the disk midplane. Additionally, my study of the Chamaeleon II star-forming region showed that the distribution of the disk dust mass statistically decreases with time. This is consistent with predictions from viscous evolution. Finally, with the study of a sample of 22 transition disks, I showed that their cavities can mostly be explained by the presence of planets. These results suggest that planets might already have formed in these disks, implying that planets formation is fast or happens early in the disk lifetime.

A possible mechanism allowing to boost planet formation is vertical settling. Indeed, as detailed previously, my studies showed that the vertical extent of protoplanetary disks is small at millimeter wavelengths, which implies that millimeter sized grains (and larger) are concentrated in a vertically thin midplane where the dust density is increased. Depending on when this vertical settling takes place, this mechanism is a good candidate for enhancing grain growth efficiency. Combined to other processes, vertical settling may contribute to form planets in the earliest stages of disk evolution.

RÉSUMÉ

Au sein des exoplanètes actuellement découvertes, une grande diversité est observée. Or, l'étude des disques protoplanétaires permet d'en apprendre plus sur la formation des planètes. On sait que les disques se dissipent en quelques millions d'années, ce qui implique que les planètes géantes doivent se former très rapidement à partir des petits grains de taille micrométrique présents initialement.

Cette thèse a pour but d'ajouter des contraintes observationnelles à plusieurs théories qui décrivent l'évolution des disques protoplanétaires, et donc la formation des planètes. J'ai travaillé, en particulier, sur une étude statistique de la distribution de la masse de poussière dans des disques situés dans la région de formation stellaire Chamaeleon II, sur la présence de cavités dans les disques de transition, et sur des contraintes observationnelles de quelques mécanismes d'évolution des poussières tels que la dérive radiale et la sédimentation verticale des grains. J'ai utilisé principalement des observations millimétriques ALMA que j'ai comparées avec d'autres traceurs, images aux longueurs d'onde du visible ou de l'infrarouge par exemple. À plusieurs reprises, j'ai modélisé ces observations par transfert radiatif pour déterminer la structure de ces disques protoplanétaires.

J'ai obtenu d'importantes contraintes observationnelles sur la structure verticale des disques protoplanétaires, en étudiant un échantillon de 12 disques très inclinés. Aux longueurs d'onde du millimètre, les disques les plus inclinés de cette étude apparaissent extrêmement minces dans la direction verticale, significativement plus minces que dans les observations en lumière diffusée (grains plus petits). Ceci indique que la sédimentation verticale des poussières est extrêmement efficace dans ces disques, ce qui est favorable à la croissance rapide des grains dans le plan médian. Par ailleurs, en étudiant la région Chamaeleon II, j'ai constaté que la distribution de masse des disques diminue statistiquement avec le temps. Ce résultat est en accord avec les prédictions de l'évolution visqueuse des disques. Enfin, l'étude d'un échantillon de 22 disques de transition a permis de montrer que la plupart de leurs cavités pourraient être causées par des planètes interagissant avec le disque. Ces observations suggèrent donc que des planètes se sont peut-être déjà formées dans ces disques, ce qui implique qu'elles se forment soit rapidement soit précocement.

Le mécanisme de sédimentation verticale des grains semble un bon candidat permettant d'expliquer la formation rapide des planètes. En effet, la faible étendue verticale des grains millimétriques mesurée au cours de cette thèse implique qu'ils sont très concentrés dans le plan médian. Une forte densité de poussière étant favorable à une croissance accélérée des grains, ce mécanisme pourrait expliquer la formation de planètes très tôt dans l'évolution des disques.

Toutes les grandes personnes ont d'abord été des enfants.
Mais peu d'entre elles s'en souviennent.

Le petit prince
Antoine de Saint Exupéry

REMERCIMENTS - ACKNOWLEDGMENTS

Par où commencer lorsqu'il faut remercier tous ceux qui m'ont permis de m'épanouir personnellement et scientifiquement au cours de ces trois années de thèse ? J'ai eu la chance de réaliser une grande partie de cette thèse au Chili et je voudrais commencer par remercier ceux qui ont rendu cette aventure possible. Il s'agit de l'ESO qui a accepté de m'accueillir pendant deux années et évidemment de mes trois directeurs de thèse, François, Myriam et Bill. Je voudrais vous remercier pour votre bienveillance et votre accompagnement tout au long de la thèse malgré la distance et le décalage horaire. J'ai appris énormément grâce à vos expertises complémentaires : parmi tant d'autres choses, sur ALMA et la réduction des données avec Bill et sur SPHERE et le transfert radiatif avec François et Myriam. À chaque fois, vous m'avez demandé de prendre du recul sur les résultats, comment aller plus loin ? Comment conclure ? J'espère que je saurai garder cet esprit critique que vous m'avez appris.

Ces deux années au Chili, à la découverte des grands espaces, m'ont aussi fait découvrir une liberté que je cherchais depuis longtemps. Entre le Nord et le Sud, avec Valentin, Greg ou Célia, nous avons pu admirer le ciel nocturne, contempler le spectacle des volcans et des glaciers, et observer tant d'animaux nouveaux : vicuñas, lobos marinos, manchots de Magellan, peltehue, piqueros, caprintero et bien d'autres. Avec Arroz et Pelao, nous avons aussi survolé le pays, d'abord au nord à Iquique, puis dans la région centrale à Farellones, Piramide y Domos.

Je voudrais aussi remercier mes amis doctorants et fellows de l'ESO et de l'IPAG, dont la présence quotidienne et le soutien m'a été très précieux ; et mes amis de longue date qu'il était bien agréable de retrouver sur le contient américain : Maxence, Florence et Annabelle, et aussi Manon. Pour finir, je voudrais aussi remercier ma famille qui m'a accompagnée tout au long de cette thèse. Tout particulièrement, à mes parents déménagés à Bordeaux, Amélie et Lilian que j'ai réappris à connaitre pendant le confinement et à ma gentille grand-mère, qui a bien voulu m'héberger et m'apprendre le tricot au cours de cette dernière année de thèse : un grand merci !

CONTENTS

LIST OF FIGURES

LIST OF TABLES

1

INTRODUCTION

Contents

While dust and gas are present everywhere in the galaxy, planets likely form in dense environments such as protoplanetary disks, which are located in various star-forming regions. Depending on the disk's properties, a large variety of bodies can form, from tiny dust aggregates to massive giant planets, including terrestrial worlds and asteroids. During my thesis, I aimed to understand the diversity of protoplanetary disks and their evolution to gain insights on the formation of the solar system where we live. In this chapter, I first present protoplanetary disks as a necessary stage of star formation. Then, I describe their structure and the evolutionary mechanisms that I studied during my PhD. Later, I discuss two observational techniques, namely interferometric millimeter observations and scattered light near-infrared imaging, and the radiative transfer code that I used during my PhD. Finally, I end the chapter by presenting the outline of the new work performed during this thesis.

1.1 STARS AND PLANETS FORMATION

1.1.1 *Forming stars from the interstellar medium*

Stars are thought to form from the gravitational collapse of large molecular clouds (see e.g., review by McKee and Ostriker, 2007). Historically, the evolution of young stellar objects (YSO) has been studied through the shape of their spectral energy distribution (SED), the energy received from a source at several wavelengths. Lada (1987) suggested a classification of YSOs into three classes, defined from the sign of their SED slope between 2 and 25 μm (see blue line in Fig. 1.1). The earliest evolutionary stage, called Class 0, has been proposed later on because these objects can generally not be observed at infrared wavelengths (Andre et al., 1993). In this section, I summarize the commonly accepted stages of low-mass star and planet formation.

The first step of star formation is the contraction of dense molecular clouds, composed of gas and sub-micron sized particles. This collapse leads to several over dense regions, where individual protostars will form. The time origin of star formation is generally defined by the start of the collapse of the stellar embryo, the so-called birth line (e.g., Stahler, 1983; Tout et al., 1999). The youngest evolutionary stage of the protostellar phase is the Class 0 stage. At this stage, the protostellar mass is small compared to that of the envelope. The central object is totally obscured by the large amount of cold material in the envelope. Thus, these objects are invisible at optical and near-infrared wavelengths but can be detected through the thermal emission of cold dust in the envelope at larger wavelengths (typically in the millimeter). One characteristic feature of Class 0 and more evolved systems is the apparition of collimated jets and outflows, which is connected with the accretion of material onto the central protostar (conservation of the angular momentum). Then, as a protostar forms, accretion becomes less important, so the jets/outflows become less powerful until they completely disappear.

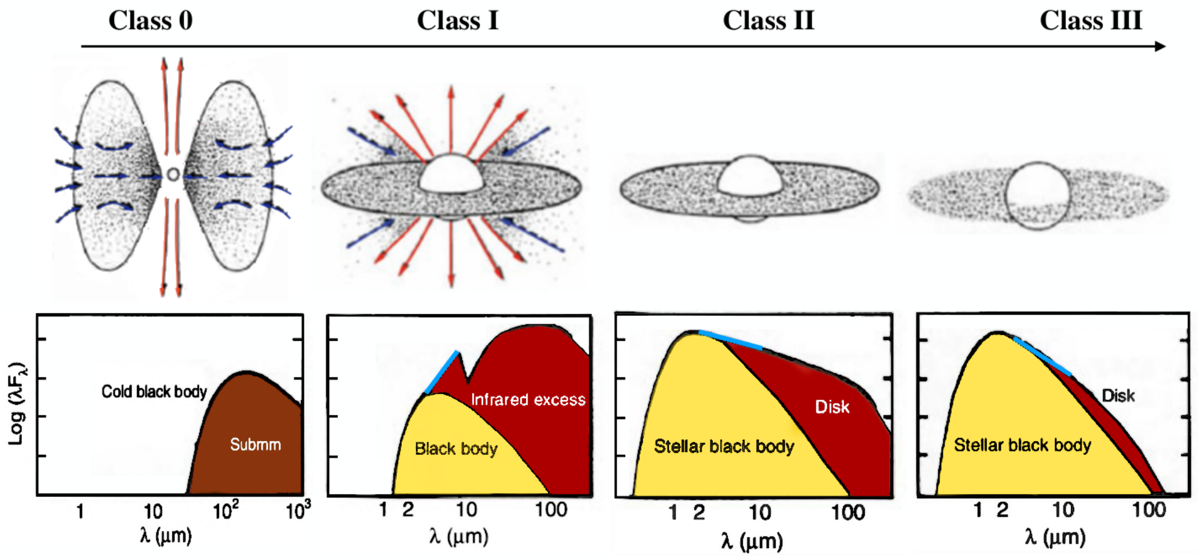

Figure 1.1 – Evolutionary phases of star-formation. The top row shows a schematic view of each stage of star-formation, and the bottom pannels correspond to the typical SED of each phase, decomposed into stellar and disk/envelope emission, respectively in yellow and brown. The blue lines in the Class I to Class III phases correspond to the initial criterium suggested by Lada (1987) to classify young stellar objects. *Adapted from André (2002)*

When the mass of the protostar becomes greater than that contained in the envelope, the system enters in the Class I phase and starts to be detectable at infrared wavelengths. At that stage, the star is warmer than in Class 0 and surrounded by an envelope and an accretion disk. Note that the formation of the disk is required early in the star formation process (e.g., Terebey et al., 1984). Indeed, protostellar cores are not static but rotate with properties inherited from the molecular cloud. Thus, in order to preserve the angular momentum inherited from the parent cloud, particles are predicted to spin up while the system contracts to smaller scales. Due to the centrifugal force, the material rotating too fast in the equatorial plane is not able to fall radially towards the central object, which leads to the accumulation of material in the equatorial plane, forming a circumstellar disk. Although their observation is difficult, circumstellar disks may already be present in the Class 0 stage (e.g., Chandler et al., 1995; Jørgensen et al., 2007; Lee et al., 2017; Maury et al., 2019).

As the central object increases in mass ($M_\star \gtrsim 0.9 \times M_{\star\,\mathrm{final}}$), it changes of evolutionary phase. At that stage, the envelope has dissipated and the central star is surrounded only by the disk, rich in gas and dust. Matter still accretes slowly onto the star, with a rate of about $10^{-8}\,M_\odot/\mathrm{yr}$ (e.g., Manara et al., 2016), which is about two orders of magnitude lower than what is typically observed in the proto-stellar phase (Hartmann et al., 1998; Antoniucci et al., 2014). Objects in this evolutionary stage are classified as Class II, or T Tauris for solar mass stars. Circumstellar disks are thought to allow efficient grain growth and thus to be the stage where planets form.

The further evolution of protoplanetary disks implies the removal of its gas content, which leads to Class III objects. These disks still contain a small amount of dust particles (generated by collision of larger bodies) which are able to reprocess the stellar light and create a small excess in the infrared. Ultimately, a star and its planetary system remain. During my research, I focused on the Class II stage.

1.1.2 *Lifetimes of the evolutionary stages of star formation*

In order to understand the timescale available for planet formation, estimating the ages of young stellar objects is crucial. In this section, I discuss how stellar ages can be estimated from the understanding of protostellar evolution and I report the typical lifetime of each stage of star-formation.

In the Class II phase, the star becomes detectable at optical wavelengths and the accretion luminosity becomes negligible compared to the stellar luminosity (see e.g., Manara et al., 2016). This allows to estimate the stellar luminosity and effective temperature with relatively good precision, which is important to obtain the stellar age and mass. Before discussing the different evolutionary tracks of young stellar objects, let us define the stellar luminosity and effective temperature. The stellar luminosity ($L_\star$) corresponds to the total amount of energy emitted by the central star per unit of time. It can be written as:

$$L_\star = 4\pi R_\star^2 \sigma T_{eff}^4 \tag{1.1}$$

where σ is the Boltzmann constant, $R_\star$ the stellar radius and T_{eff} its effective temperature. By definition, the effective temperature corresponds to the temperature of a blackbody that would emit the same amount of energy as the source. It gives a first order estimate of the surface temperature of the star. The effective temperature can be inferred from the color index of the star at optical wavelengths, while the luminosity is generally estimated from its apparent brightness. To obtain the luminosity, the apparent brightness of the star needs to be rescaled according to its distance to the Earth and also considering the degree of interstellar extinction present around the object. Knowing both the stellar luminosity and the effective temperature of an object allows us to display it on a Hertzsprung-Russell (HR) diagram. Then, comparing its position with theoretical predictions for the evolution of young stars (evolutionary tracks) enables us to estimate its age and mass.

As an example, I present a HR diagram with several evolutionary tracks of low mass stars in Fig. 1.2. When young stars (Class II) first appear in the HR diagram, the star is still too cold to be thermally supported. This leads to a quasi-static contraction phase, where the inner regions of the star heats up. At the same time, the stellar surface keeps an approximately constant temperature. For low mass stars ($\mathrm{M}_\star < 1.5\,\mathrm{M}_\odot$), which are initially partly convective, this contraction phase first leads to a steep decrease in luminosity, which corresponds to vertical lines in Fig. 1.2 (also called Hayashi tracks).

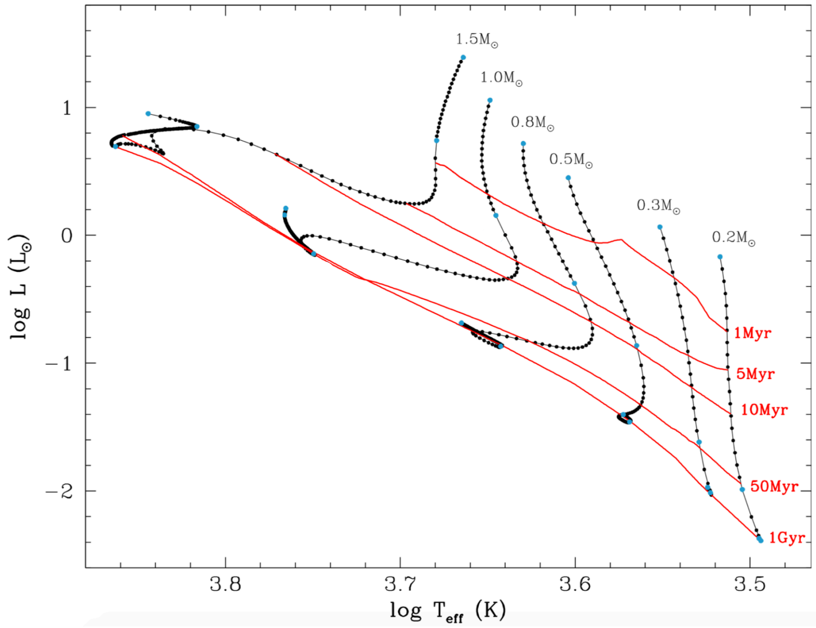

Figure 1.2 – Typical evolutionary tracks for low-mass pre-main sequence stars in an Hertzsprung-Russell diagram. The sequences of black points correspond to evolutionary tracks of young stars with different masses, from 0.2 to 1.5 $M_\odot$. The red lines show different isochrones (bins of age between 1 Myr and 50 Gyr). *Adapted from Amard and Matt (2020)*

Then, the star might turn radiative and continues to increase its temperature with an approximately constant luminosity (horizontal lines for $M_\star \geq 0.5\,M_\odot$ in Fig. 1.2, Henyey tracks). When the inner regions of the star reach $\sim 10^7$ K, thermo-nuclear reactions start, in particular nuclear fusion of hydrogen into helium. This is when the star enters the main sequence.

While all evolutionary models have the same global shape (see for instance Fig. 3 of Amard and Matt, 2020), the exact position of the tracks depends on the physical parameters included in the calculation (e.g., chemical composition, metallicity, nuclear reactions, rotation, atmosphere, etc.). This implies that the estimation of stellar ages and masses remains model dependent. Additionally, stellar ages are particularly difficult to estimate due to uncertainties on determining the zero age (Stahler, 1983; Tout et al., 1999) and also because of observational limitations such as the error on luminosity, the potential multiplicity of a system, and the fact that young stellar objects are variable (Joy, 1945; Bouvier et al., 1993; Herbst et al., 1994). Because of these observational limitations, estimating the average age of a star-forming region is likely more reliable than the age estimate of an individual object. Also, note that very inclined systems suffer particularly from large uncertainties on their luminosity because the disk also participates to the extinction of stellar emission, to a degree which is not known unless dedicated modelling is performed. As an example, no stellar masses and ages could be estimated from a HR diagram for any of the edge-on disks studied in Chapter 4. Still, when available, the relative position of different objects in the HR diagram roughly indicates their relative ages and masses. In Chapter 2, I used a HR diagram and stellar tracks to estimate the stellar masses of a large number of sources in Chamaeleon II and other star-forming regions.

Using evolutionary tracks, several studies estimated the ages of a large number of Class II systems. They showed that they are typically observed from 1 to 10 Myr after the core collapse (Mamajek, 2009; Ribas et al., 2014, see Section 1.3.1). On the other hand, as stellar parameters can not be directly measured for Class 0 and Class I systems, their typical lifetimes were estimated by comparing the number of objects of different classes in numerous star-forming regions. Various studies found that Class 0 and Class I systems are much less numerous than Class II sources and estimated the typical timescale of Class 0 and Class I to be about 10^4 and 10^5 years respectively (e.g., Evans et al., 2009). The Class II stage is thus the longest star-formation phase with a gas-rich disk, which makes it relevant for understanding planet formation.

1.1.3 *Forming planets around young stars*

Planets are likely formed in protoplanetary disks or earlier phases of star formation, from sub-micron-sized particles inherited from the interstellar medium (Mathis et al., 1977). Giant gas planets in particular have to form before the gas has dissipated from the disk, typically in a few million years (see Section 1.3.1). The standard scenario for planet formation is called core accretion (Pollack et al., 1996; Rice and Armitage, 2003). This scenario begins with the accretion of dust particles and planetesimals forming planetary cores (potentially Earth-like planets). If a core becomes massive enough, it attracts more efficiently the surrounding gas and solids which mainly fall into the envelope of the forming planet. When the critical mass is reached (typically about $10\,M_{\oplus}$), the envelope enters in a runaway growth, mainly accreting gas. When this phase is over, either due to disk dissipation or the opening of a gap, a giant planet is formed. This mechanism is attractive because it is able to explain the formation of Jupiter and the other giant planets of the solar system at the location in which they are found. The main caveat however is that the timescale to form a Jupiter like planet (at 5 au from the star) initially found by Pollack et al. (1996) is about 6 Myr, which is longer than the typical disk lifetime (Section 1.3.1). This timescale is expected to be even longer for planets formed at larger radii. However, we note that this issue might be mitigated if different assumptions are considered, for example if planets were migrating during their formation (Alibert et al., 2005) or if the disk had lower opacity than initially assumed (Movshovitz et al., 2010), potentially thanks to grain growth and vertical settling, among other mechanisms. These processes can reduce the growth timescale down to 1 million years. I will come back to this mechanism in Section 1.3.3. In particular, I will detail some remaining issues for forming dust pebbles larger than a few centimeters in size in a short timescale.

An alternative mechanism to form giant planets is gravitational instabilities in the disk (Boss, 1997). This instability appears when the disk gravity becomes stronger than the thermal pressure in the disk. It is thus favored in massive disks and where the disk is cooler (for example at large radius). Contrary to the core accretion mechanism, gravitational instabilities are expected to form planets very quickly: in a few thousands of years! However, it is not clear whether this instability can develop in many disks. Indeed, for gravitational instability to occur in a disk, it needs to be extremely massive and cold, and also to have a short cooling timescale compared to the disk dynamical timescale (Gammie, 2001; Rice et al., 2003).

1.1.4 *Exoplanet population*

Since 51 Peg b, the first exoplanet discovered around a solar type star (Mayor and Queloz, 1995), more than 4330 exoplanets have been discovered (exoplanet.eu, as of August 2020). Recent surveys have shown that most stars should host planets, low mass planets being more numerous than giant ones (Clanton and Gaudi, 2016; Baron et al., 2019; Fernandes et al., 2019). Fig. 1.3 shows a distribution of the masses and orbital distances of known planets, detected using different techniques. In this plot, no planets with both small masses ($< 10\,M_\odot$) and large orbital distances (> 5 au) are detected, due to observational biases. Additionally, the observations revealed several groups of planets which are not present in our solar system: e.g., hot Jupiters and mini-Neptunes for example. The forming mechanisms of these planets are not totally understood.

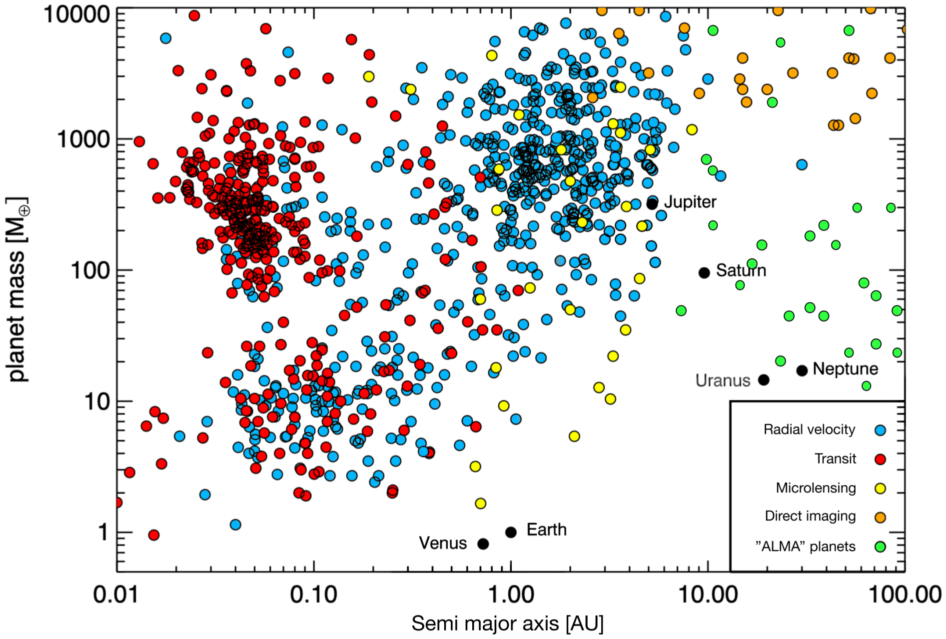

Figure 1.3 – Masses and orbital distances of known exoplanets, detected using different methods. Most ALMA planets reproduced in this plot have however not been confirmed yet. *Adapted from Winn and Fabrycky (2015), including planets inferred from millimeter continuum observations of protoplanetary disks with ALMA (Lodato et al., 2019)*

More recently, high angular resolution studies of protoplanetary disks at submillimeter wavelengths have linked the width of rings with the potential presence of planets and their masses (Zhang et al., 2018; Lodato et al., 2019, see Section 1.3.4). Note that there are other mechanisms able to explain the observed substructures (e.g., magneto- or hydrodynamical effects) but the planetary hypothesis is more relevant for this section. The green points presented in Fig. 1.3 represent some of these ALMA planets, estimated from millimeter continuum emission, as reported in Table 3 and 4 of Lodato et al. (2019). These planets are generally massive (from few Earth masses to few Jupiter masses) and located at large orbital distances ($> 10\,\mathrm{au}$). This opens a new parameter space with planets which is currently not probed by dedicated exoplanet surveys. However, note that the ALMA planets are located around pre-main sequence stars in opposition to most exoplanets probed by dedicated surveys, which are located around main sequence systems. This means that these planets can still be evolving within the disks (undergoing migration, grow in mass, etc.). Understanding protoplanetary disks is important to explain the diversity of exoplanets currently observed.

1.2 STRUCTURE OF PROTOPLANETARY DISKS

As mentioned previously, protoplanetary disks are composed of gas and dust, which orbit around a central star. Using standard assumptions, one can describe the vertical, radial and temperature structure of a protoplanetary disk, which is what I will focus on in this section.

1.2.1 *Vertical structure*

Assuming that the gas is at hydrostatic equilibrium, one can determine the vertical profile of the gas density in a protoplanetary disk. Simplified assumptions are to consider a vertically isothermal disk with negligible mass compared to the stellar mass, supported by gas pressure and with negligible self-gravity. Assuming that the disk is vertically thin ($z/r \ll 1$), the hydrostatic equilibrium in the vertical direction writes as follows:

$$\frac{1}{\rho}\frac{dP}{dz} = -\frac{GM_\star}{r^3}z \tag{1.2}$$

with P the pressure, ρ the density and $\mathrm{M}_\star$ the stellar mass. For an ideal gas (mostly hydrogen in a protoplanetary disk), we can relate the pressure to the density simply with the sound speed (c_S) using the following equation:

$$P = \frac{k_B T}{\mu m_H}\rho = c_S^2\,\rho \tag{1.3}$$

where k_B is the Boltzmann constant, m_H the hydrogen mass and μ the mean molecular weight, with typical value of 2.3.
Additionally, we can define the Keplerian orbital velocity as:

$$\Omega_K(r) = \sqrt{GM_\star/r^3} \tag{1.4}$$

Using these definitions, we can integrate equation 1.2 and obtain the following equation:

$$\rho(r,z) = \rho(r,0) \times e^{-z^2/2H(r)^2} \tag{1.5}$$

We find that the vertical density profile of the gas follows a Gaussian distribution, and so, we can define the pressure scale height as:

$$H(r) = \frac{c_S(r)}{\Omega_K(r)} = \sqrt{\frac{k_B}{G\mu m_H}} \frac{\sqrt{T(r)} \cdot r^{3/2}}{\sqrt{M_\star}} \tag{1.6}$$

Under hydrostatic equilibrium, we find that the scale height depends on the stellar mass, the disk's radial temperature structure, and the distance to the star. Note however that the temperature profile also varies with the radius and altitude (see Section 1.2.3), which affects the scale height. On the other hand, the scale height also affects the temperature profile as it can create shadows on the disk (e.g., Benisty et al., 2018; Muro-Arena et al., 2020), which allow it to cool. Thus, integrating the thermal and hydrostatic equilibrium has to be done iteratively.

Radiative transfer codes generally use the following simplified parametrization to describe the variation of the pressure scale height with radius:

$$H(r) = \mathrm{H}_{100\,\mathrm{au}} \left(\frac{r}{100\,\mathrm{au}}\right)^\beta \tag{1.7}$$

where β is called the flaring exponent, r is the radius and $\mathrm{H}_{100\,\mathrm{au}}$ is the scale height at a radius of 100 au (astronomical units). With the simplifying assumption of a temperature profile varying as $r^{-1/2}$, we find (using equation 1.6) that the flaring exponent is about $\beta \sim 1.25$. However, in the complex environment of a protoplanetary disk, the temperature profile in the midplane can be different from this simple power-law (e.g., Pinte and Laibe, 2014). More generally, the flaring exponent β takes values between 1.1 and 1.25.

Observationally, the first direct estimations of the gas scale height were performed through the modeling of scattered light images of inclined disks, observed at optical/infrared wavelengths[1]. These wavelengths generally probe micron sized dust particles which are expected to be well mixed with the gas (see Sections 1.3.2 and 1.4.1). Thus they are indirect tracers of the gas distribution, which is harder to detect at these wavelengths (faint emission lines). Using radiative transfer modeling on these

---

[1] Indirect constraints on the disks scale height were previously obtained through SED modeling.

observations, several studies estimated the gas scale height of protoplanetary disks to be between 8 and 15 au at a radius of 100 au (Burrows et al., 1996; Stapelfeldt et al., 1998; Stapelfeldt et al., 2003). Finally, note that dust grains larger than those detected by infrared scattered light observations are expected to decouple from the gas and settle down to the midplane. This will be discussed in Section 1.3.2.

1.2.2 *Radial structure*

In the radial direction, a protoplanetary disk is not at hydrostatic equilibrium, because it is still slowly accreting onto the star. Assuming an axisymmetric and vertically flat disk, it is possible to derive the evolution of the disk's radial profile with time. As the vertical structure is decoupled from the radial evolution, we can integrate the equations of mass and angular momentum conservation over the vertical direction. In that case, the evolution of the gas surface density (defined as $\Sigma = \int \rho \, dz$) can be described by:

$$\frac{\partial \Sigma}{\partial t} = \frac{3}{r} \frac{\partial}{\partial r} \left[r^{1/2} \frac{\partial}{\partial r} \left(\nu \Sigma r^{1/2} \right) \right] \tag{1.8}$$

where the standard assumption is to consider a viscous disk, with a viscosity ν.

This equation is a diffusive equation, which implies that the gas expands to larger radius with time. However, the origin of viscosity/turbulence in disk is not well known. In the standard α-disk model (Shakura and Sunyaev, 1973), the disk viscosity ν is related to the pressure scale height H, the sound speed c_S and to a dimensionless parameter α, as of:

$$\nu = \alpha c_S H \tag{1.9}$$

Under the assumption of a constant α throughout the disk, several observational studies constrained the value of α between $10^{-2} - 10^{-4}$ (Hartmann et al., 1998; Pinte et al., 2016; Flaherty et al., 2020). However, further analysis on this parameter are required to better understand the physics involved in protoplanetary disks. For example, it can be noted that, in general, low α values are measured from millimeter studies probing the outer disk (e.g., Pinte et al., 2016; Flaherty et al., 2018; Flaherty et al., 2020), while large values are estimated from infrared observations, surveying the inner disk regions (e.g., Hartmann et al., 1998). This might indicate that α is not constant in the disk.

Historically, the surface density was characterized by a simple power law, truncated at large radius:

$$\Sigma(R) \propto R^{-p}, \quad \text{for } R_{\text{in}} < R < R_{\text{out}} \tag{1.10}$$

Various studies focusing either on dust or gas emission at millimeter wavelengths obtained an exponent p varying between 0.5 and 3/2 (e.g., Dutrey et al., 1998; Wilner et al., 2000; Andrews and Williams, 2007). However, further analysis of several disks showed that the gas (mostly detected through ^{12}CO emission) appears to have a larger outer radius than millimeter dust (Isella et al., 2007; Hughes et al., 2008), which could not be reconciled with a unique truncation radius for dust and gas. To solve this issue, Hughes et al. (2008) suggested to describe the surface density with the alternative tapered-edge profile. This profile, based on similarity solution obtained for a viscously accreting disk subject to stellar gravity (Hartmann et al., 1998), is described by a power law with an exponential taper outside of the critical radius (R_c):

$$\Sigma(R) \propto R^{-p} \times e^{-r/R_c^{2-p}}, \quad \text{for } R_{\text{in}} < R < R_{\text{out}} \tag{1.11}$$

This solution, more physically motivated, appeared to reduce the discrepancy of dust and gas radial extent. Indeed, as ^{12}CO is optically thicker than millimeter dust, it can be detected at lower density, i.e. at larger radius, compared to dust. However, further observations at higher angular resolution and sensitivity showed that optical depth effects are not sufficient to explain the large gas to dust size ratio measured (de Gregorio-Monsalvo et al., 2013; Ansdell et al., 2018; Facchini et al., 2019, chapter 2). Radial drift and grain growth might be needed to reproduce the observations. I detail these mechanisms in Section 1.3.2.

Finally, note that recent high angular observations of protoplanetary disks have revealed that most disks are not smooth as discussed in this section but present a large variety of substructures (Andrews et al., 2018b; Long et al., 2018; Avenhaus et al., 2018). This observation has important implications on disk evolution, which will be described in details in Section 1.3.

1.2.3 *Temperature structure*

The major source of energy in protoplanetary disks is the central star, which emits blackbody emission as well as non-thermal energetic photons. Because dust opacities affect a large range of the electromagnetic spectrum (while the opacity of gas emission lines are concentrated into small fractions of it), dust dominates both the absorption of stellar light and the reprocessed thermal emission: dust controls the disk's temperature. For large enough density, collisions between dust and gas particules allow the disk to reach a thermal equilibrium (called LTE, for Local Thermodynamic Equilibrium), in which dust and gas have the same temperature. Most radiative transfer codes make this assumption. Note that in MCFOST, which I used extensively during my thesis and describe in Section 1.5, the user can chose to assume or not the LTE.

Analytical and numerical computations showed that the disk temperature varies with radius and altitude (e.g., Lynden-Bell and Pringle, 1974; Calvet et al., 1991; D'Alessio et al., 1998). Indeed, stellar irradiation decreases as r^{-2}. This implies that regions close to the star (radially) will be hotter than regions further out. Additionally, the surface layers are directly exposed to stellar emission, while star light can not penetrate far into the disk midplane (because of the disk's opacity). This implies that

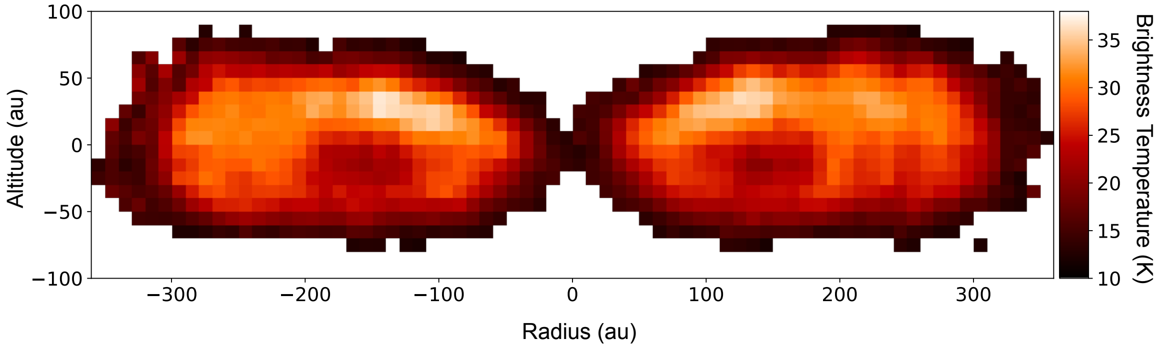

Figure 1.4 – Temperature map of Oph 163131, reconstructed from ^{12}CO observations. *Adapted from Flores et al., in prep.*

the disk's temperature also decreases from the outer upper layers down to the disk midplane. As an order of magnitude, matter heat up to thousands of Kelvins in the inner astronomical units of the disk, while the temperature decreases to a few Kelvin in the outer disk midplane.

Historically, the first observational constraints on the temperature profile were obtained through SED modeling (e.g., Kenyon and Hartmann, 1987). Although such analysis is degenerate, the results were in agreement with predictions for the radial variation of the temperature. More recently, spatially resolved observations of optically thick tracers have been used to constrain the temperature profile of protoplanetary disks. In particular, the modeling of carbon monoxide (CO) millimeter emission lines of several low inclinations disks allowed to estimate their temperature profile at the $\tau = 1$ surface (e.g., Rosenfeld et al., 2013; Pinte et al., 2018). On the other hand, disks close to edge-on inclinations are very favorable for estimating directly both the radial and vertical profile of the temperature (Dutrey et al., 2017; Teague et al., 2020). In Fig. 1.4, I show an example of the temperature structure that we measured in the close to edge-on disk Oph 163131 (Flores et al., in prep.). It shows that the temperature first decreases with radius in the midplane and increases with altitude, as predicted by models (see previous paragraph).

Additionally, in the upper layers of the disk, energetic UV photons from the central object ionize atoms and dissociate gas molecules (e.g., Bergin et al., 2016; Cazzoletti et al., 2018a). Because of the disk's optical depth, such energetic rays do not penetrate deep in the disk, making the disk less ionized close to the midplane compared to the upper layers. The less ionized region in the midplane is generally called a dead zone, because it decouples from the magnetic field, which leads to a low level of turbulence (Gammie, 1996). The ionization structure of protoplanetary disks is important because it is directly related to the coupling efficiency of the magnetic field with the disk and thus to the disk's turbulence, which controls various evolutionary mechanisms (see Section 1.3.2). In the inner few astronomical units, ideal MHD (magnetohydrodynamic) physics apply, while further away or in the disk midplane, the disk is not ionized enough to get an efficient coupling: non ideal effects such as ambipolar diffusion, Hall and Ohmic effects likely take place (e.g., review by Armitage, 2011).

1.3 EVOLUTION OF PROTOPLANETARY DISKS

1.3.1 *Global disk evolution*

As planets are thought to form in the disk phase, the disk dissipation timescale sets a limit on the planet formation timescale. In particular, giant planets have to accrete gas before it disappears from the disk. In general, constraining observationally the gas content is more complex than doing it for the dust (in particular because emission lines are generally fainter than dust continuum emission), so most studies on disk evolution have been performed with dust indicators. For instance, Ribas et al. (2014) gathered a sample of more than 2000 sources in 22 nearby star-forming regions, observed at infrared wavelengths. They compiled the fraction of disks detected in each star-forming region and found that disk lifetimes vary from less than 1 Myr to about 10 Myr. In Fig. 1.5, I report a figure adapted from Ribas et al. (2014) showing that the disk fraction decreases with increasing age: disks disappear/dissipate with time. Fitting an exponential curve to this decay, they obtain a characteristic dissipation timescale of micron-sized particles of about 2.5 ± 0.5 Myr (see also Mamajek, 2009; Currie and Sicilia-Aguilar, 2011). On the other hand, few studies have looked at the dissipation timescale of gas. This was mostly done by estimating the evolution of the fraction of accreting stars with time, as detected through Hα emission. In general, they find a similar timescale for warm gas dissipation and micron-sized dust removal (e.g., Jayawardhana et al., 2006; Fedele et al., 2010).

Some of the dominant processes expected to drive disk dissipation are viscous evolution and photoevaporation (see review by Williams and Cieza, 2011). To the first order, viscous transport, described in Section 1.2.2 (see equation 1.8), dominates the evolution. This mechanism is driven by the accretion of the disk onto the central star. As mentioned previously, this is expected to be a smooth process. As an example, at 30 au, for a disk with a scale height ratio of $H/r \sim 0.05$, the viscous timescale would be between 1 Myr for $\alpha = 10^{-2}$ and up to 100 Myr for $\alpha = 10^{-4}$ (Armitage, 2011). This is long compared to the disk lifetime (see Fig. 1.5) and suggests that another mechanism might happen, leading to rapid disk dissipation.

Photoevaporation is expected to be another important mechanism to remove mass from the disk (Williams and Cieza, 2011). This process consists in the creation of a powerful wind, driven by energetic ultra-violet and/or X-ray photons from the central star, that will remove the disk material from the inside out. Indeed, those photons are thought to warm up gas particles enough so that their thermal velocity can exceed the escape velocity. Then, material is lost in the form of a wind. In general, different

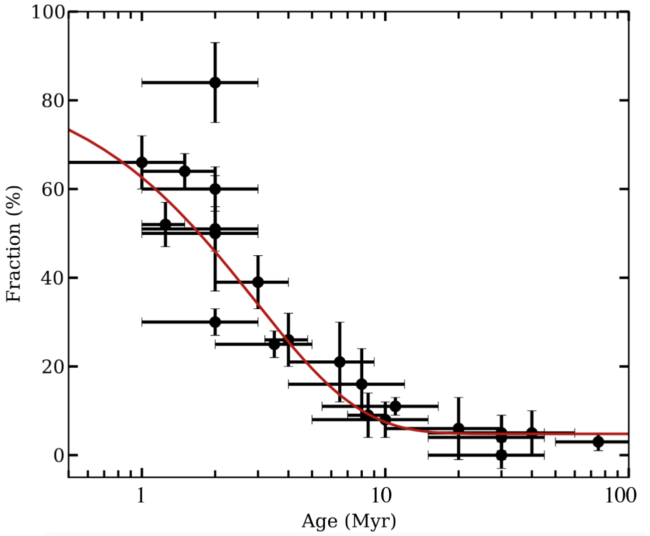

Figure 1.5 – Disk fraction as a function of the age of the star-forming region, based on 8-12 μm detections. *Adapted from Ribas et al. (2014)*

models predict a photoevaporation rate in the range of $10^{-7} - 10^{-10}\,M_\odot/\text{yr}$ (Gorti and Hollenbach, 2009; Owen et al., 2011). This is lower than the typical accretion rate measured in Class II objects (see Section 1.1.1), which implies that the first steps of disk evolution are dominated by viscous dissipation. When the accretion rate becomes low enough, photoevaporation winds open a cavity around the central star. As the hole becomes large enough (about 10 au), energetic photons can heat directly the disk inner rim and dissipate the entire disk very quickly (in significantly less than 1 Myr, Alexander et al., 2006; Owen et al., 2011). Photoevaporation acting like a switch for fast dissipation would thus allow to reproduce the observed disk lifetimes and dissipation timescale. However, note that as it is a fast process, very few disks in the photoevaporation stage were confirmed (e.g., Pascucci and Sterzik, 2009).

Let us come back to the disks lifetime mentioned in the first paragraph of this section. This timescale was primarily estimated from infrared fluxes, which characterize warm micron-sized dust, located close to the central star. These small grains only represent a small fraction of the dust mass, which itself is typically only about 1% of the total disk mass. Thus, constraining the evolutionary timescale of most of the gas and dust mass is still missing to understand the general evolution of disks and the available timescale for giant planet formation.

Several millimeter surveys of star-forming regions have been performed aiming to characterize the bulk of the dust mass. They show that the disk mass decreases with the age of the star-forming region (e.g., Ansdell et al., 2016, Chapter 2), which is consistent with theories. The first project of my PhD focused on such problematics. I compared dust masses in the intermediately aged Chamaeleon II star-forming region (4 ± 2 Myr) with other regions. Additionally, I studied the evolution of gas detection rates for disks with detected dust, as probed by CO emission in the millimeter. This study is presented in Chapter 2.

1.3.2 *Dust and gas interactions, link with radial drift and vertical settling*

While dust particles only feel the stellar gravitational forces and orbit at Keplerian velocity (v_K), the gas also feels pressure forces. In general, due to differences in densities and temperatures between the inner and outer regions of the disk, the pressure gradient decreases towards the outer edge of the disk, generating a force opposite to stellar gravity direction. This additional force slows down the gas, which will rotate at sub-Keplerian velocities. If the disk is static (or evolving slowly), we obtain the following azimuthal velocity for the gas: $v_{\mathrm{g}}^2 = v_K^2 - c_S^2\,|\frac{d\ln P}{d\ln r}|$. Thus, dust and gas orbit around the central object with different speeds. The interaction of dust with the gas leads simultaneously to inward radial drift and vertical settling of dust grains (e.g., Weidenschilling, 1977), which I aimed to constrain during my PhD. In this section, I describe the interaction of dust with gas and some evolutionary mechanisms induced by it.

1.3.2.a. Characterising dust and gas interactions

The drag force between dust and gas that have a relative velocity $\vec{\Delta v} = \vec{v_d} - \vec{v_g}$ can be written as:

$$\vec{F}_{\mathrm{drag}} = -m_d \frac{\vec{\Delta v}}{\tau_s} \tag{1.12}$$

where m_d is the dust particle mass and τ_s is the characteristic friction timescale (also called stopping time). The stopping time allows to determine the coupling intensity between dust and gas. Indeed, from equation 1.12, we identify two regimes depending on the value of τ_s. Particles with a small value of τ_s experience an important drag force: they are well coupled to the gas. On the contrary, particles with a large τ_s feel a small drag force, implying that they decouple from the gas.

The stopping time depends on the size (a) of the particle relative to the mean free path of a gas molecule (l). Dust particles in the regions of interest for my PhD are generally in the so-called Epstein regime, in which the energy transfer between gas and dust is caused by molecular collisions (pressure difference, e. g., Weidenschilling, 1977). In this regime, where dust grains are smaller than the mean free path of gas particles, the stopping time can be written as:

$$\tau_s = \frac{\rho_{dp}}{\rho}\frac{a}{c_s} \tag{1.13}$$

where ρ_{dp} is the dust particle density, ρ the gas density, a the particle size, and c_s the sound speed. This equation indicates that the stopping time increases linearly with the size of the particles (in the Stokes regime, applicable to larger grains: $\tau_s \propto a^2$). Relating this expression to dust and gas coupling efficiency previously described, we find that large grains are increasingly decoupled from the gas. This decoupling is generally parametrised by the Stokes number:

$$St = \Omega_K \tau_s \tag{1.14}$$

where Ω_K is the Keplerian orbital velocity (equation 1.4). Therefore, small particles with $St \ll 1$ are well coupled to the gas, while larger particles will be increasingly decoupled. This decoupling is at the origin of vertical settling and inward radial drift of some relatively large dust grains, which will be described in the following paragraphs.

1.3.2.b. Radial drift

As dust particles feel a head wind from the gas, they loose angular momentum and spiral towards the star. Nakagawa et al. (1986) derived the drift velocity of dust as follows:

$$u_{\mathrm{drift}} = \frac{1}{St + St^{-1}} \frac{c_S^2}{v_K} \frac{\partial \ln P}{\partial \ln r} \tag{1.15}$$

where v_K is the Keplerian velocity and the other quantities have been defined previously. With this equation, one can easily see that grains of Stokes number close to 1 are drifting at the highest velocity towards a pressure maximum: smaller grains remain well coupled with the gas, while larger bodies are not affected at all by the gas. For a smooth disk described by standard equations (see Section 1.2), Brauer et al. (2007) obtained a maximum drift velocity of about $50\,\mathrm{m.s^{-1}}$ at 1 au, which corresponds to a drift timescale of about 100 years. This implies that, due to gas interactions, grains of Stokes number close to 1 (typically 1 mm at 200 au and 1 cm at 50 au, using equation 13 of Riols and Lesur, 2018) rapidly drift towards the star, which is an issue for grain growth. The typical drift timescale of millimeter sized grains is predicted to be much shorter than the disk lifetime which is inconsistent with observations. However, several mechanisms have been suggested in order to maintain grains longer in the disk and allow them to grow. This will be discussed in more details in Section 1.3.3.

In general, radial drift models predict that inward dust migration of single size particles spontaneously produces a sharp edge in the dust density distribution (Birnstiel and Andrews, 2014; Facchini et al., 2017; Powell et al., 2019). The estimation of the sharpness of the outer edge and the dust to gas size ratio are important observational constraints that can improve our understanding of radial drift efficiency.

Several observational studies have aimed to probe dust radial drift. Most of them focused on comparing the radial extent of continuum dust emission with ^{12}CO extent. One of the most extreme example is the disk of CX Tau, where Facchini et al. (2019) found a dust to gas size ratio greater than 5. On a larger sample of 22 disks of the Lupus star-forming region, Ansdell et al. (2016) found a typical dust to gas size ratio of 2. While this difference in size suggests that dust radial drift and dust grain evolution are occurring in the disks, this value is likely affected by differences in opacity between dust and gas (Dutrey et al., 1998; Facchini et al., 2017). Indeed, ^{12}CO emission commonly used to estimate gas sizes is optically thick, which makes it easier to detect at large radius even if dust grains are also present (generally optically thin at millimeter wavelengths). Trapman et al. (2019) used a grid of thermochemical models to predict the gas to dust size ratio needed to observationally discriminate radial drift and opacity effects. They showed that a ratio of $R_{\rm gas}/R_{\rm millimeter\ dust} \gtrsim 4$ can not be due to optical depth only. This means that disks showing this large gas to dust size ratio have to be subject to radial drift and dust grain evolution. Further observational studies of radial extent of protoplanetary disks need to be performed in order to understand more clearly the effect of radial drift on disk evolution and planet formation. In particular, quantifying variations of disk sizes or of the gas to dust size ratio with time would allow to constrain this mechanism.

1.3.2.c. Vertical settling

The interaction of dust particles with gas in the stellar gravity field also leads to vertical settling of dust grains. This mechanism is important because it allows to increase the dust density in the disk midplane, which likely enhances grain growth efficiency (see Section 1.3.3). The settling efficiency depends on the coupling of dust grains with gas, as well as on the degree of turbulence. In general, the turbulence is described by the parameter α of Shakura and Sunyaev (1973, see Section 1.2.2, equation 1.9). The different approaches aiming to understand vertical settling differ mainly in the origin of turbulence and its influence on dust grains.

Weidenschilling (1977) and Nakagawa et al. (1986) conducted some of the first studies of vertical settling. In these models, the turbulence opposes vertical settling by removing dust grains away from the midplane at a turbulent convection velocity. This approach was however recognized as incorrect given that it did not take into account the chaotic nature of turbulence: while some eddies will drive particles away from the midplane, some others might accelerate settling. A better way of handling turbulence consists in averaging the velocities of the eddies. In that case, dust grains are rather diffused by turbulence than advected as assumed previously. With this consideration, Dubrulle et al. (1995) showed that the vertical evolution of the dust density could be described by the following differential equation:

$$\frac{\partial \rho_d}{\partial t} - \frac{\partial}{\partial z}\left(z\Omega_K^2 \tau_s \rho_d\right) = \frac{\partial}{\partial z}\left[D\rho \frac{\partial}{\partial z}\left(\frac{\rho_d}{\rho}\right)\right] \tag{1.16}$$

where ρ_d is the dust density, ρ the gas density, Ω_K the Keplerian orbital velocity, τ_s the stopping time, and D the diffusion coefficient. In the simplifying assumption of a constant diffusion coefficient, equation 1.16 has the following solution (Fromang and Nelson, 2009):

$$\rho_d = \rho_{d,\rm mid} \exp\left[-\frac{(\Omega\tau_s)_{\rm mid}}{\tilde{D}}\left(e^{z^2/2H^2} - 1\right) - \frac{z^2}{2H^2}\right] \tag{1.17}$$

where $\tilde{D} = D/Hc_s = \alpha/Sc$ (with Sc the Schmidt number) and the underscore $_{\rm mid}$ indicates that these values are taken in the disk midplane. To derive these equations,

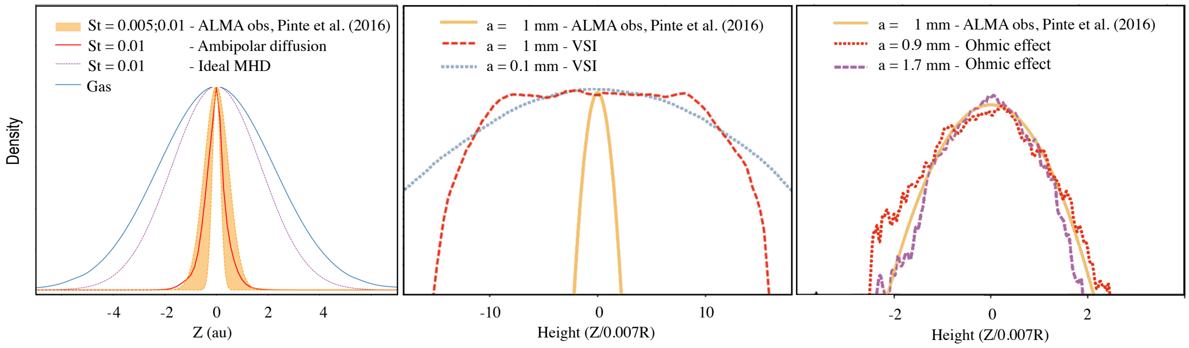

Figure 1.6 – Comparison of settling models present in the literature with the vertical extent of 1 mm grains (equivalent to St=0.005 − 0.01, Riols and Lesur, 2018) obtained by Pinte et al. (2016) modeling the HL Tau disk (orange in each pannel). Ideal MHD or vertical shear instabilities (VSI, see middle panel and purple dashed line in the left panel) do not match the millimeter scale height constrained by observations, while ambipolar diffusion or ohmic effect reproduce it better (see right pannel or red region in left panel). *Adapted from Riols and Lesur (2018) and Flock et al. (2017)*

the gas is assumed at hydrostatic equilibrium and the turbulence is only prescribed by the α parameter, without discussion on its origin. Results from Fromang and Nelson (2009) performing ideal MHD simulations on small grains showed that the assumption of constant dust diffusion coefficient is valid only close to the midplane where the gas density is high enough. As the distance to the midplane increases, the gas becomes less dense and the coupling less efficient so the diffusion coefficient will change. Analytical solutions of equation 1.16 for a varying diffusion coefficient do not exist, numerical simulations have to be performed.

Recent studies by different groups (Fromang and Nelson, 2009; Flock et al., 2017; Riols and Lesur, 2018) investigated the effect of various mechanisms (namely vertical shear instability, ideal and non ideal MHD effects) on vertical settling of dust grains. For large grains, the dust scale height is found to vary with Stokes number as $H_d \propto St^{-1/2}$ (Dubrulle et al., 1995; Riols and Lesur, 2018). Thus, in the Epstein regime, using equations 1.13 and 1.14, this implies that for large grains the scale height varies with the grain size a as: $H_d \propto a^{-1/2}$. However, each model predicts different absolute values for the scale height depending on the physical mechanism that drives the turbulence (see Fig. 1.6). Direct comparisons of vertical settling efficiency measured in observations is important to constrain turbulence in disks and the possible physical mechanisms at its origin.

Before my PhD work, evidence for stratification of dust grains had been shown in several studies, mainly based on optical or infrared observations (e.g., Duchêne et al., 2003; Pinte et al., 2007; Glauser et al., 2008; Duchêne et al., 2010). In all cases, small grains are located at the disk surface while larger grains are found closer to the midplane, consistently with vertical settling predictions. The typical scale height for small grains (expected to be well coupled to the gas) has been inferred of the order of 10 au at 100 au (Burrows et al., 1996; Stapelfeldt et al., 1998). Few studies however were able to estimate the scale height of millimeter grains, expected to be more affected by settling and representing most of the dust mass. This can be explained because the high angular resolution needed for such observations was not available until recently. Additionally, most studies of protoplanetary disks focused on substructures, which led to observations of low inclination systems ($\leq 70°$), where the vertical extent is not directly visible. For the low-inclination disks, the difference in vertical extent between gas and dust grains can only be inferred by detailed modeling of the rings and gaps. For example, Pinte et al. (2016) used the relative brightness of HL Tau rings in the millimeter to model the vertical extent of large grains. For this particular system, they find that the millimeter dust scale height is ~ 1 au at 100 au from the star. It is about 10 times smaller than the gas scale height assumed in their model and implies a low level of turbulence in this disk. In Fig. 1.6, I show recent models aiming to reproduce the millimeter scale height obtained in the HL Tau disk (Riols and Lesur, 2018; Flock et al., 2017). They showed that the turbulence generated by ideal MHD or vertical shear instabilities (VSI) is likely too strong to lead to millimeter scale height of 1 au at 100 au. On the other hand, non ideal effects such as the ohmic effect or ambipolar diffusion lead to lower turbulence and thus to a very thin layer of millimeter sized grains.

During my PhD, I expanded studies on vertical settling by comparing scattered light and millimeter observations of several disks, respectively probing micron-sized or millimeter-sized grains. In Chapter 3, I describe the study of SPHERE and ALMA observations of two transition disks, that I modeled using radiative transfer. In Chapter 4, I present the analysis of the millimeter continuum emission of a survey of 12 edge-on disks, which I compare with their corresponding HST images. These two projects allowed to obtain new constraints on the vertical extent of millimeter sized particles.

1.3.3 *Grain growth in protoplanetary disks*

In Section 1.1.3, I briefly described how the core accretion mechanism allows to form giant gaseous planets. However, I did not mention how ISM micron-sized particles grow to pebbles or planetesimals sizes. This is what I aim to discuss in this section.

While orbiting around the central star, dust and gas particles are also affected, among other mechanisms, by turbulent motions (related to the disk temperature) and differential radial drift (see Section 1.3.2). The relative velocity induced by these effects leads to collisions of dust particles, which can have various outcomes. For collisions at low velocity, numerical simulations and micro-gravity experiments showed that micron-sized particles can grow larger through sticking mechanisms, which are related to electrostatic interactions, and/or through mass transfer (see reviews by Blum and Wurm 2008 and Testi et al. 2014). However, as particles grow, other collision outcomes become possible. In particular, collisions between large grains at large velocity often lead to fragmentation, erosion or bouncing, preventing grains to grow much larger than millimeter/centimeter sizes (Windmark et al., 2012). Additionally, as dust grains grow to larger sizes, their Stokes number increase (see equations 1.13 and 1.14). As detailed in Section 1.3.2, this implies that growing grains progressively decouple from the gas and become increasingly affected by radial drift (until they reach $St = 1$, see equation 1.15). When dust grains are large enough, the rapid inward drift caused by gas drag, acts as a barrier for planet formation. For large grains, the drag becomes so efficient that dust particles drift inward onto the star on short timescales preventing them to grow larger. This is the so-called "radial-drift barrier". One key point for planet formation models is to understand how dust grains can grow larger despite this barrier.

Several possibilities have been studied to solve the radial drift barrier issue. One of them is to consider dust particles as fluffy rather than compact aggregates. In that case, growth can be more efficient because the sticking of fluffy grains can occur at much higher speed, which allows grains to survive collisions at higher relative velocities and grow larger (Wada et al., 2009). Additionally, Garcia and Gonzalez (2020) showed that for fluffy aggregates the transition between the Epstein and Stokes drag regime can happen before reaching a Stokes number of 1 (i.e., before being most affected by radial drift), contrary to compact grains. As mentioned previously, in the Stokes drag regime, the Stokes number increases faster with grain size than in the Epstein regime. This allows porous aggregates to decouple from the gas fast enough for preventing them from falling onto the star. They might be able to grow to larger bodies and form planets.

Dust traps, related to changes in the pressure gradient, can also be a solution to allow grains to grow without falling onto the star. From equation 1.15, one can easily see that the sign of the radial drift speed changes with the sign of the pressure gradient. An inversion of the pressure gradient can thus lead to a change in the drag speed, pushing grains from both sides towards the pressure maxima. If such gradient is stable, it can efficiently trap dust particles. Such configuration will lead to the accumulation of grains in the region of the pressure trap. The resulting enhanced dust density is favorable for gain growth, either through sticking or through streaming instabilities (Youdin and Goodman, 2005). The streaming instability is triggered for sufficiently large dust to gas ratio, in which the back reaction of dust on gas might not be negligible. The large dust to gas ratio impacts the drift speed of dust particles and the instability leads particles to pile up in dense filaments, where they might collapse through dust self-gravity. The streaming instability allows to form $\sim 100\,\mathrm{km}$ sized planetesimals directly from micron-sized dust grains in a very short timescale (of the order of several hundreds of orbital timescales, Johansen et al., 2014).

Finally, note that extremely efficient vertical settling also allows to increase significantly the dust to gas ratio in the disk midplane, which is favorable for the growth mechanisms mentioned. Characterizing vertical settling efficiency is therefore impor-

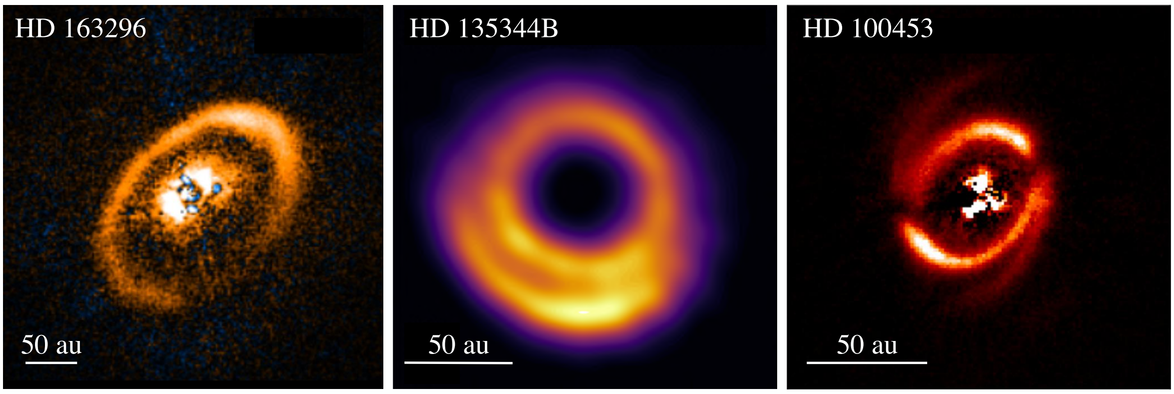

Figure 1.7 – Examples of features observed in protoplanetary disks. The images were taken respectively with SPHERE (HD 163296 and HD 100453) or ALMA (HD 135344B). *Adapted from Muro-Arena et al. (2018), Cazzoletti et al. (2018b), and Benisty et al. (2017)*

tant to understand planet formation.

Interestingly, recent observations of disks at high angular resolution revealed a large variety of features, which can be associated with dust traps. Fig. 1.7 shows some examples of features recently observed with ALMA or SPHERE, namely cavities, rings, lopsided emission and spirals. During my PhD (Villenave et al., 2019), I was particularly interested in transition disks (TD). These disks, which have been historically identified by their lack of IR flux in their SED (Strom et al., 1989), are remarkable from their large inner cavities (at least at millimeter wavelengths).

Proving that grain growth is enhanced in the observed features is however not direct. Some indirect evidence for grain growth can be obtained through the millimeter spectral index, defined as $F_\nu \propto \nu^{\alpha_{mm}}$. Indeed, in the Rayleigh-Jeans regime and for optically thin emission, the millimeter spectral index is directly linked to the dust absorption coefficient $\kappa_\nu \propto \nu^\beta$ (with $\beta \geq 0$) as of $\alpha \approx 2 + \beta$. Small ISM-like grains have a β parameter of $1.5 - 2$ (e.g., Li and Draine, 2001), while grains of millimeter or centimeter sizes are expected to have a β parameter closer to 0 (e.g., Pavlyuchenkov et al., 2019). Low values of spectral index ($\alpha \leq 3$) usually imply either that dust is optically thick or that dust grains have grown from ISM sizes to millimeter or centimeter sizes.

Using resolved spectral index maps, Cazzoletti et al. (2018b) showed that the spectral index decreases in the location of the vortex of HD 135344B. Similarly, Dent et al. (2019) and Huang et al. (2018a) showed that the spectral index decreases at the maximum brightness of the rings of HD 143296 and TW Hya respectively. These studies suggest that the features of these disks (rings or vortex) can be associated with a local increase of grain sizes, which is consistent with them being trapped.

Alternatively, the local decrease of spectral index in the rings can also be related to changes in optical depth, the rings being more optically thick than the gaps.

Complementary analysis of grain growth can now be performed with ALMA dust polarization observations. The polarization fraction observed in a few disks indicates that the maximum grain size is about 100 μm (e. g., Hull et al., 2018; Ohashi et al., 2018; Dent et al., 2019). This is consistent with grain growth from ISM-sizes but is rather low compared to conclusions from spectral index analysis. Several mechanisms might solve this apparent discrepancy. For example fluffy aggregates have different polarization properties than compact grains assumed in the works mentioned previously (Kataoka et al., 2016). Alternatively, it is also possible that millimeter polarization observations trace a different grain population than millimeter total (unpolarized) intensity observations (Yang et al., 2016; Hull et al., 2018).

1.3.4 *Planets and protoplanetary disk structure*

Several mechanisms have been proposed to produce the features currently observed in protoplanetary disks (rings, gaps, spirals, azimuthal asymmetries, see Fig. 1.7). In particular, along with (magneto-)hydrodynamical flows, instabilities and ice lines for example, planets interacting within the disk are able to create a large variety of substructures (see review by Andrews, 2020). In this section, I focus on observational indications for planets in protoplanetary disks.

Theoretical and numerical studies showed that planets can generate various features in protoplanetary disks, depending on their masses and on the disk properties. In this section, I generally associate a planet to 1 gap and 1 ring but note that under specific disk parameters a planet might open several gaps (Dong et al., 2015a; Bae et al., 2018; Weber et al., 2019) and can also launch spiral arms (Dong et al., 2015b; Baruteau et al., 2019). Some important parameters for the outcome of planet-disk interaction are for example viscosity, the temperature structure of the disk, the possibility of heating (and cooling) a forming planet, the grains composition and size distribution, and possibly planet migration. Depending on its relative mass with respect to the disk, the impact of a planet on the gas density structure will vary. Massive planets ($> 1\,M_J$) are able to open deep and wide gaps (e.g., Crida et al., 2006; Tatulli et al., 2011; Dong and Fung, 2017), while planets of ~ 10 Earth masses are just massive enough to have a detectable effect on the gas surface density (e.g., Rosotti et al., 2016). Both massive and low-mass planets are associated to a pressure maximum at larger radius, which implies that they also affect the dust distribution (see Section 1.3.3). As mentioned previously, large particles of Stokes number closest to 1 are expected to concentrate in the pressure maxima, while small dust grains, well coupled to the gas, might flow inwards of the planetary orbit (Zhu et al., 2012; de Juan Ovelar et al., 2013; Dong et al., 2015a). In Villenave et al. (2019), I used the difference in cavity sizes between millimeter and scattered light observations of a sample of 22 transition disks to study the possibility of planets being at the origin of their cavities.

The ubiquity of dust substructures observed in protoplanetary disks (e.g., Andrews et al., 2018b; Long et al., 2018) suggests that planets might form in the earliest stages of disk evolution. A frequent practice to infer the properties of potential planets within disks is to perform dedicated hydrodynamical simulations (including planets) to model the millimeter continuum emission of specific systems with interesting features (e.g., Pohl et al., 2017a; Price et al., 2018a; Baruteau et al., 2019). Several studies also compared continuum gap morphologies (e.g., location, width and depth of the gaps) of various disks with grids of hydrodynamical simulations or analytic prescriptions, aiming to infer the properties of planets potentially carving the gaps (Zhang et al., 2018; Lodato et al., 2019).

However, note that only gaps larger than the angular resolution of the observations (a few au even with the longest ALMA baselines) and at important separations from the central star ($r \gtrsim 10\,\mathrm{au}$) can currently be resolved. Additionally as mentioned previously, massive planets have a stronger impact on the disk morphology than small mass planets. This imply that the detection of planets with ALMA observations are biased towards massive planets, far from their host stars. I represent some planets inferred with ALMA continuum observations by the green points in Fig. 1.3. Interestingly, they probe a parameter space currently unexplored by exoplanets surveys. The current planet formation mechanisms might have to be adjusted to explain the presence of massive planets so far from their central star around young protoplanetary disks.

Additionally, recent works used ALMA CO kinematics in disks, such as deviations from Keplerian motion, to infer the presence of planets (Pinte et al., 2018; Teague et al., 2018; Pinte et al., 2020). In the right panel of Fig. 1.8, I present one of the first indirect detection of planet with such study.

Although substructures are present in most disks, only a few planets have yet been unambiguously detected inside a protoplanetary disk. Young or still-forming planets are expected to be relatively hot because of accretion. They are predicted to be brightest at infrared wavelengths, meaning that these wavelengths are best suited for direct imaging of embedded protoplanets. In the left panel of Fig. 1.8, I show the current most robust direct detection of planet in a protoplanetary disk. The first detection of PDS 70 b was published by Keppler et al. (2018), using scattered light images taken with SPHERE. Since then, this object has been the subject of many studies aiming to characterize it in more details (e.g., Müller et al., 2018; Wagner et al., 2018), and a second protoplanet has been identified in the disk (Haffert et al., 2019). Interestingly, PDS 70 b and c are located in the cavity of this transition disk, which suggests that giant planets might indeed be at the origins of some cavities observed in transition disks. Additionally, note that claims for planetary candidates with direct imaging were also made in various other (transition) disks (Quanz et al., 2015; Sallum et al., 2015; Reggiani et al., 2018), but remain mostly unconfirmed. Large direct imaging surveys also yield low number of detections, even around older

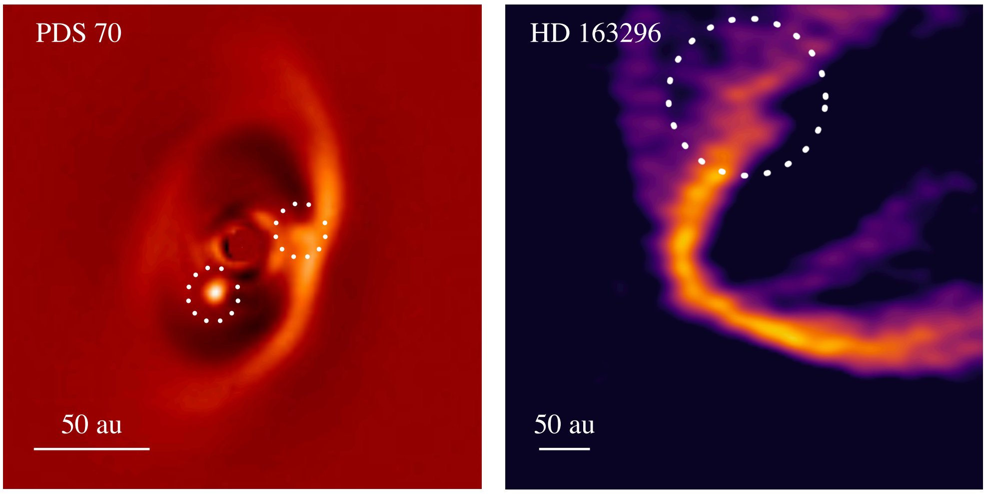

Figure 1.8 – Examples of direct (left panel, SPHERE scattered light image) and indirect detections (right panel, ALMA CO image) of planets in two protoplanetary disks. The dotted circles indicate the position of the planets. *Adapted from Müller et al. (2018) and Pinte et al. (2018)*

systems (Uyama et al., 2017; Nielsen et al., 2019; Vigan et al., 2020). The planets detected by direct imaging surveys are mostly massive (few Jupiter masses) and far from their host star (more than a few au), as can be seen from the orange points in Fig. 1.3.

1.4 DISK OBSERVATIONS

In Section 1.3.2, I showed that the strength of several evolutionary mechanisms, such as radial drift and vertical settling, depend on the size of the particle considered. Observationally, this can be constrained by using multi-wavelength observations. In this section, I first describe why observations at different wavelengths trace different regions and grain sizes. Then, I will discuss two types of observations that I used during my PhD to add constraints on these evolutionary mechanisms. Those are interferometric millimeter observations taken with ALMA, and optical/infrared scattered light observations, either taken with SPHERE at the Very Large Telescope (VLT) or with the Hubble Space Telescope (HST).

1.4.1 *Multi-wavelength observations to probe different disk's regions and grain sizes*

Although gas covers most of the mass of protoplanetary disks, dust dominates the continuum disk's opacities. As mentioned previously, this implies that dust dominates the outcome of the reprocessing of any incident light beam. In particular, dust grains absorb and scatter part of an incident beam. This set of effects is called extinction. At thermal equilibrium, the absorbed energy can be re-emitted by the grains through

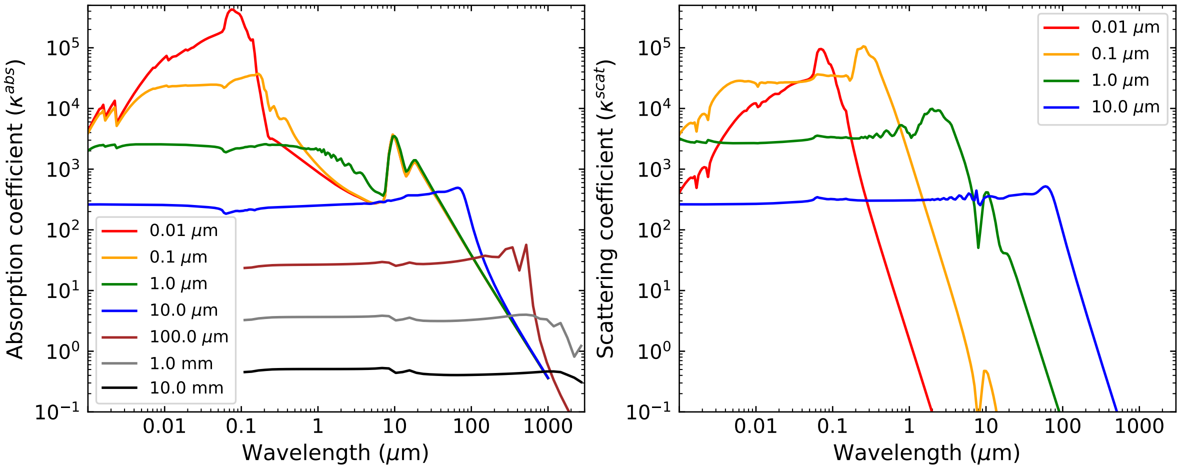

Figure 1.9 – Absorption and scattering coefficient of astronomical silicates for different distributions of grains with mono-sizes between 0.01 μm and 10 mm, expressed in cm^2.g^{-1}. *From tables published in Laor and Draine (1993) and* MCFOST.

thermal emission or may allow chemical reactions on the grain surface. In this section, I discuss some important quantities (opacities and optical depth) which dictate what can be observed in a disk depending on the wavelength of observation.

The absorption properties of dust grains are generally characterized by the opacity coefficient κ_ν, expressed in cm^2.g^{-1}. This coefficient depends, among other parameters, on the grain size (a). In the left panel of Fig. 1.9, I represent the dust opacities for silicate grains of different sizes (7 distributions of mono grain size between 0.01 μm and 10 mm). In this figure, we see that the absorption opacity typically reaches a maximum at wavelengths around $\lambda \sim 2\pi a$. For a given grain size, shorter wavelengths show high opacity values, while the opacity decreases significantly at large wavelengths ($\lambda > 2\pi a$). This implies small grains (e.g., micron sizes) dominate the opacities at short wavelengths (up to the infrared), while large grains (e.g., submillimeter sizes) have an larger impact at larger wavelengths.

An incident light beam can also be scattered by dust grains. In that case, it keeps its original wavelength but changes orientation. The right panel of Fig. 1.9 shows the scattering efficiency of different grain sizes. Note that the scattering efficiencies have similar shapes as the absorption opacities.

At thermal equilibrium, the energy absorbed by dust grains has to be re-emitted. This emission is distributed over the electromagnetic spectrum according to the dust temperature. Assuming that dust emits as a blackbody, we can estimate the wavelength corresponding to the maximum of emission (λ_{peak}) in regions with different temperatures (T, see Section 1.2.3) using the Wien's displacement law: $\lambda_{peak} T = cte$. Following this law, hot particles from the inner regions and the upper layers of the disk, for example at 2000 K, would emit the most at 1.4 μm (H-band). On the other hand, cold particles in the disk midplane, for example at 20 K, will have a peak of

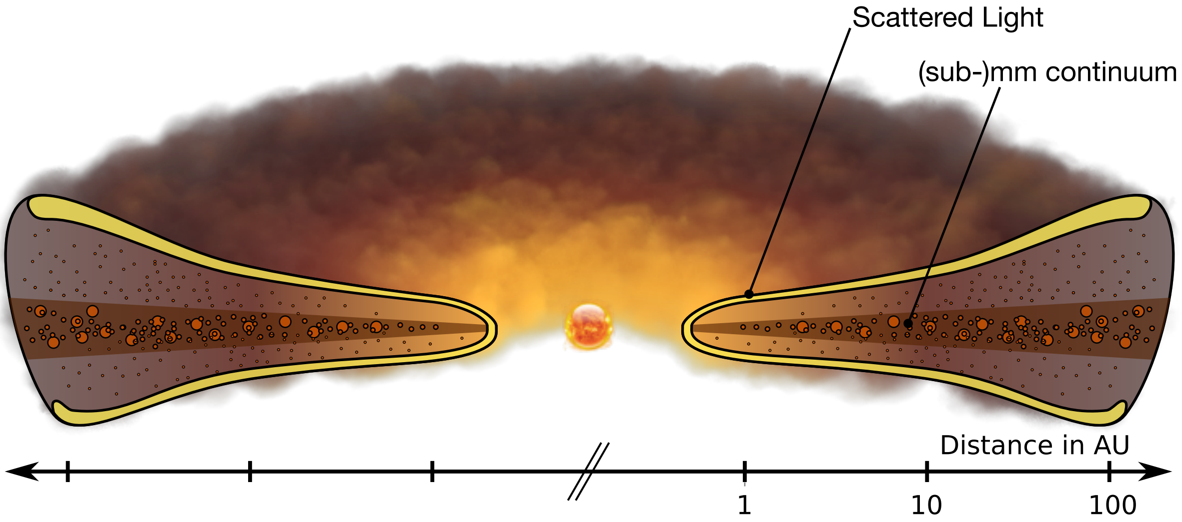

Figure 1.10 – Structure of protoplanetary disks and link with observations. Scattered light observations probe small (μm-sized) grains well mixed with the gas, while millimeter observations probe larger millimeter sized grains, likely settled into the disk midplane and affected by radial drift. *Adapted from Testi et al. (2014)*

emission at larger wavelengths, around 140 μm. This implies that the emission at different wavelengths trace various regions of the disk. This interpretation is generally used to analyse SEDs. However, we need to keep in mind that the grains which can emit the most are those which have absorbed most of the incident energy, i.e., with about $\lambda \sim 2\pi a$. So emission at different wavelengths trace at the same time different disk's temperatures and various grain sizes. This is represented in a schematic view in Fig. 1.10.

Finally, the notion of optical depth is important to interpret the emission that one receives from a disk. Indeed, part of the stellar emission or dust thermal emission can be obscured by dust grains along the line of sight (dl), either due to absorption or to scattering. This leads to the attenuation of the incident energy by a factor $1 - e^{-\tau_\nu}$, where τ_ν is the optical depth: $\tau_\nu = \int \rho_d(\kappa_\nu^{abs} + \kappa_\nu^{scat})dl$. If $\tau_\nu \gg 1$, most of the emission is obscured by the dust, this corresponds to an optically thick region. This assumption is valid in dense regions (such as the inner regions of the disk) or for wavelengths with high opacities such as in the optical or infrared. In that case, we can only detect emission up to the so-called $\tau_\nu = 1$ surface, the rest is invisible to the observer. The other extreme is the optically thin regime, where $\tau_\nu \ll 1$. In that case, all dust emitting at these wavelengths can be seen, so the dust mass can be directly related to the observed flux (see equation 2.1, in Chapter 2).

1.4.2 *Radio interferometry with ALMA*

To be able to spatially resolve protoplanetary disks and study their structure, high angular resolution observations are needed. As an example, the Kuiper belt extends between 30 and 50 au from the Sun, which suggests that the protoplanetary disk at the origin of the solar system was larger than this size. Thus, to resolve this disk at a typical distance of 140 pc (mean distance of Taurus, Zucker et al., 2019), the observations need to have an angular resolution smaller than 0.3". The typical angular scale ($\Delta\theta$) that a single dish telescope can achieve corresponds to the diffraction limit: $\Delta\theta \propto \lambda/D$, with λ the wavelength of the observations and D the diameter of the telescope. Observations at 1 mm reaching 0.3" angular resolution would thus need a telescope of 1 km of diameter! As building such large telescope is not possible, the technical solution to reach high angular resolution at millimeter wavelengths is to use interferometry. In that case, the largest separation (or baseline) of individual antennas determines the resolution of the telescope.

1.4.2.a. The Atacama Large Millimeter Array

The Atacama Large Millimeter Array (ALMA, Fig. 1.11), located in the Chajnantor plateau in the Atacama desert, is the current best (sub-)millimeter interferometer both in terms of sensitivity and angular resolution. During my PhD, I used mainly ALMA observations, so this section focuses on the description of this millimeter interferometer and on the calibration steps needed for reducing ALMA data.

ALMA consists in 66 high precision 12 m and 7 m antennas, that can be arranged in different configurations over the year. The maximum distance between 12 m antennas can vary from 150 meters to 16 kilometers, which allows to observe with different spatial resolutions. For example, the angular resolutions achieved at 1.3 mm range from 1.5" to 0.04". At the largest array configuration, ALMA can reach similar angular resolution as large optical/IR telescopes, such as the VLT or HST for example, which typically achieve $\sim$ 0.04" of angular resolution (respectively at 1.4 μm and 0.4 μm).

ALMA is based on heterodyning, meaning that the incoming signal mixed with a local oscillator in the receiver frontend, which lowers the frequency to make it easier to detect, and then combined in a correlator. The instrument can be set up to observe at different wavelengths, with various bandwidth and spectral resolution depending on the purpose of the observations. The bandwidths and spectral resolution modes can be separated into two groups. On the one hand, ALMA offers large bandwidth with small spectral resolution, best for continuum (dust) observations. On the other hand, one can access to high spectral resolution, with the price of small bandwidth, more interesting for line emission. Also, as mentioned previously, ALMA can provide data at different wavelengths. These are separated into 8 frequency bands, starting at 100 GHz (3 mm, band 3) and ending at 870 GHz (0.3 mm, band 10).

Figure 1.11 – ALMA.

1.4.2.b. *Basics of interferometry*

Because ALMA is an interferometer, it samples the Fourier transform of the sky brightness distribution. The link between the observed visibility function $\mathcal{V}(u,v)$ and the sky brightness $I(x,y)$ is given by the van Cittert-Zernike theorem (van Cittert, 1934; Zernike, 1938) :

$$\mathcal{V}(u,v) = \int\int PB(x,y)I(x,y)e^{2\pi i(ux+vy)}dxdy = Ae^{i\phi} \tag{1.18}$$

where $PB(x,y)$ corresponds to the primary beam, the relative sensitivity of each antenna. Each pair of antenna is associated to a position in the uv-plane, which describes the separation of pairs of antennas as seen from the source at a particular instant in time. The resulting visibility point is characterized by an amplitude (A) and a phase (ϕ), as presented in equation 1.18.

During my PhD, I used CASA (Common Astronomy Software Application, McMullin et al., 2007) to handle visibilities. In particular, this software was useful for calibration and to reconstruct images from the visibilities. I will now detail the ideal ALMA data reduction steps.

1.4.2.c. *Calibration of ALMA observations*

During the observations, several factors can corrupt the data. As an example, the presence of a cloud during the observations can produce a phase or an amplitude error. The phase error originates from the fact that the light path of different incident beams may vary with time and spatial position inside the cloud, leading to a delay between the different beams. On the other hand, the amplitude error comes from absorption by the cloud. This implies that various calibration steps have to be applied to the observed visibilities to recover the true visibility function. In general, the effects corrupting the visibility function impact independently its amplitude or its phase. To illustrate the steps required to calibrate ALMA observations, I represent a sequence of real observations in Fig. 1.12. These observations are analysed in Chapter 4.

One of the first calibration step is the correction for water vapor variation along the light of sight of each antenna, which can cause large delay/phase variations. The atmospheric water vapor content is measured very regularly during the observations by external radiometers (WVR) located on each 12 m antenna. Then, during the calibration, a CASA task converts the measured water vapor emission into a predicted antenna delay, which is applied on the data.

Along with the delays, the amplitude sensitivity and noise contribution of each antenna (and receiver frontend) have to be measured and calibrated out. Several times during the observations (see 'Calibrate Atmosphere' scans in Fig. 1.12), the antennas response is measured off source (in a blank region of the sky). This calibration step is called Tsys (system temperature measurement). As well as measuring the noise contribution from the atmosphere, frontend and antenna, this measurement allows to directly detect if an antenna is defective during the observations.

Finally, the last calibration step which does not require any specific external calibration source is the antenna position updates. Indeed, the position of each antenna has to be known very accurately in order to correctly calculate the delays between the different antennas. The antenna position table is determined regularly by the observatory and applied to the data during this calibration.

Then, the following calibration steps require the observations of several astronomical calibrators, which are needed for bandpass, flux, amplitude and phase calibration. Note that calibrators are generally chosen among bright quasars and that a unique calibrator can be used for several calibration purposes. At the start of observing each calibrator, a pointing calibration is made to correctly align the pointing of the individual antennas. Before observing the science target, a large fraction of the observing time has to be spent on the bandpass calibrator. This calibration estimates the relative amplitude and phase between the different frequency channels of each spectral window. It is observed only once. Afterwards, the amplitude of each antenna is scaled so that the flux matches that of the flux calibrator. The typical flux calibration error of ALMA varies between 5% and 20% depending on the observing frequency (see the ALMA Technical Handbook[2]). Finally, the visibilities have to be correctly aligned with one another on a point source, and corrected for amplitude and phase temporal variations. One of the most important calibrations is indeed the phase calibration, also known as the 'gain' calibration, as it tracks the complex gains (amplitude and phase). It is usually estimated after all other calibrations have been made. To do

---

[2] https://almascience.eso.org/documents-and-tools/latest/documents-and-tools/cycle8/alma-technical-handbook

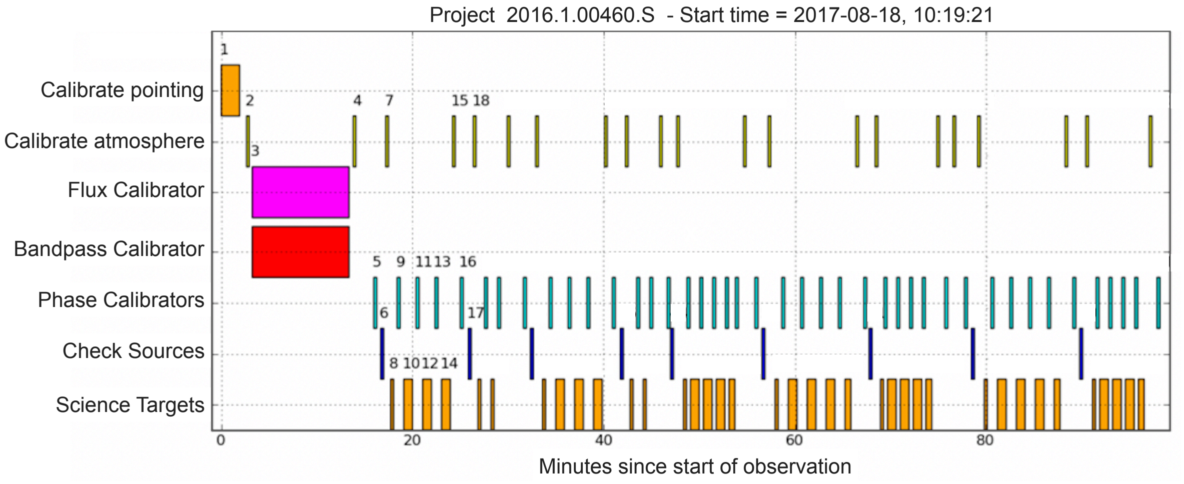

Figure 1.12 – Example of a real sequence of ALMA observations, later studied in Chapter 4. The first 18 scans only are numbered, they observe different calibrators (6 first lines) and a science target. Note that water vapor is also measured in all scans on calibrators.

this calibration, a phase calibrator, selected to be unresolved at the resolution of the observations, is observed extremely regularly between each observation of the science target (see Fig. 1.12). This allows to monitor changes in phase and amplitude between antennas during the observations and to apply the relevant corrections to the science target. Finally, note that to be able to estimate the accuracy of the phase calibration, a check source is generally observed once before the science target. The check source is selected to be about at the same distance to the phase calibrator than the science target, to have a comparable intensity with the science target, and to be unresolved by the observations. Then applying all the calibration steps to the check source should allow to verify that they were correctly performed.

During my PhD, I reduced several ALMA datasets. Except for one particularly complex dataset (see Chapter 4), the standard calibration provided by the observatory was generally adequate to calibrate the data.

1.4.2.d. Image reconstruction

Once all calibration steps are performed, it is possible to reconstruct an image from the visibility points, by taking the inverse Fourier transform of the visibilities (see equation 1.18). However, as the sampling of the uv-plane is not complete, complex algorithms have been developed to reconstruct the images. During my PhD, I used the `clean` and `tclean` tasks of CASA to reconstruct the images. These iterative functions proceed by several steps. The first step is to compute a dirty beam and dirty image of the observations. The designation *dirty* represents objects that are directly obtained from the visibilities. The reconstructed image is associated to a beam pattern, which corresponds to the point spread function of the instrument. Then, a point source (or a larger region when using the `multiscale` option) centered on the maximum intensity of the dirty map is subtracted from the dirty map. This second step is repeated several times, replacing the dirty map by the remaining map from previous iterations (residual map). It stops when a sensitivity or iteration threshold is reached. Lastly, the final image is generated by adding the model map (composed of all point sources subtracted from the dirty image), convolved to the resolution of the observation, and the residual map (i.e., noise map).

Note that there are many options for the cleaning of the images. In particular, it is possible either to image each channel maps separately or together, which respectively allows line or continuum imaging. Another important option is the weighting parameter applied to each baseline used to reconstruct the image. There are three different options: 1/ *Natural* weighting, which allows to minimise the noise in the image but at the expense of lower resolution in the reconstructed image, by applying a larger weight to the baselines with the lowest noise level (or highest density in the uv-plane), 2/ *Uniform* weighting, which applies a larger weight to long baselines, favoring the angular resolution, and 3/ *Briggs* weighting, which allows a compromise between the two strategies. Indeed the robust parameter of the Briggs method can vary between -2, for a natural weighting, and 2 for uniform weighting. Using a Briggs robust parameter of 0.5 is generally a good compromise between sensitivity and angular resolution.

Finally, it is sometimes possible to perform a last calibration step to improve the image quality. Self-calibration consists in using the source itself to estimate the variation of phase (or amplitude) with time. If the source is bright enough, this last reduction step can significantly improve the quality of the final image (lower rms and higher dynamical range) as it allows a continuous monitor of the sky variations directly on the source.

1.4.3 *Scattered light observations and basics of polarization*

During my PhD, I also used scattered light images from VLT/SPHERE (Spectro-Polarimetic High contrast imager for Exoplanets REsearch, Beuzit et al., 2019) and from HST (Hubble Space Telescope), which trace small grains well mixed with the gas. One of the difficulties of observing protoplanetary disks at optical/NIR wavelengths is that the star is bright (see typical Class II SED in Fig. 1.1). Thus, several techniques have to be considered to increase the contrast of the disks compared to their host stars. One of them is to use a coronagraph. This device allows to hide emission up to a given angular radius (see a coronagraph profile in Fig. 3.7). It has the advantage of removing efficiently stellar emission, but also prevents the observations from recovering disk emission from the central regions.

Another technique which allows to increase the contrast of the disk compared to the star is to study polarized light. Indeed, stellar emission is globally unpolarized, while the reprocessed light coming from the disk is linearly polarized at optical/NIR wavelengths (due to scattering by small grains). Polarimetric differential imaging (PDI) is a commonly used technique to remove unpolarized emission from scattered light observations. It consists in observing a system simultaneously with two perpendicular polarization filters and then to subtract the two resulting images from each other. Unpolarized stellar light will cancel out while polarized emission from the disk remains. This technique allows to increase the contrast between the disk and the star, making the study of the disk easier. Note that both HST and SPHERE can use a coronagraph, and the instrument IRDIS (Infra-Red Dual-band Imager and Spectrograph, Dohlen et al., 2008) of SPHERE is designed to detect polarized intensity. In the next paragraphs, I present how polarized light can be described and some characteristics of polarized light from protoplanetary disks.

The usual way for characterising polarization in scattered light observations is to use the Stokes formalism (Stokes, 1851), where light can be described by four vectors: I, Q, U, and V. I represents the total intensity, Q and U the two components of linear polarization and V the component of circular polarisation. These vectors can be combined to obtain quantities easier to interpret such as polarized intensity (PI) and polar Stokes components (Q_ϕ and U_ϕ, Schmid et al., 2006):

$$\mathrm{PI} = \sqrt{Q^2 + U^2} \tag{1.19}$$

$$Q_\phi = +Q\cos(2\phi) + U\sin(2\phi) \tag{1.20}$$

$$U_\phi = -Q\sin(2\phi) + U\cos(2\phi) \tag{1.21}$$

where $\phi = \arctan(y/x)$ corresponds to the angle measured north to east with respect to the position of the star. This angle ϕ is purely geometric on the image and centered on the star. A positive signal in Q_ϕ indicates a polarization in the azimuthal direction (negative signal is in the radial direction), while U_ϕ represents the polarization inclined by $\pm 45°$ from this direction.

For protoplanetary disks Q_ϕ and U_ϕ values are generally easier to interpret than Q and U. Indeed, for single scattering events, photons are expected to be polarized orthogonally to the scattering plane, which is defined by the line of sight and the direction of the incident stellar emission (radially in the plane of the disk). This implies that the disk emission would be polarized in the azimuthal direction and included only in the (positive) Q_ϕ component, U_ϕ becoming a proxy for the noise. However, multiple scattering events might occur, for example in very inclined disks. This would imply that the incident emission might not come only from the radial direction as in the single scattering case, which can lead to some degree of polarization not necessarily in the azimuthal direction. In that case, part of the physical signal will also be included in the U_ϕ component (Canovas et al., 2015). As I did not reduce scattered light data, I refer the reader to de Boer et al. (2020) and van Holstein et al. (2020) for a detailed description of the calibration steps of IRDIS observations.

In the complex environment of a protoplanetary disk, there are no global analytic solutions to the equations of radiative transfer. Numerical methods are necessary to solve these equations and to interpret the structure of protoplanetary disks. During my thesis, I used extensively the radiative transfer code MCFOST (Menard, 1991; Pinte et al., 2006; Pinte et al., 2009), which I will briefly describe in this section.

MCFOST is a versatile 3D radiative transfer code, able to model SED as well as continuum dust and line emission (for example CO). To compute the model images, the code uses a fixed parametric disk structure and dust properties. However, note that various developments allowed to couple MCFOST with different codes, for example with PHANTOM (Price et al., 2018b), which enables to obtain radiative transfer images from a code solving hydrodynamic equations. MCFOST uses two different methods to produce images. First, it solves the temperature structure of the disk using a Monte Carlo method. Then, ray tracing is used to produce the SED and mono-chromatic images. I will describe these two steps in the following subsections.

1.5.1 *Solving the temperature structure*

MCFOST solves the temperature structure of the disk using a Monte Carlo method, commonly used in this type of codes. It consists in the generation of photon packets, either from the stellar photosphere or through thermal emission of the disk itself. Then, each photon packet is stochastically propagated through the disk. The propagation includes the effects of scattering, where an incident photon is re-emitted with same wavelength but in another direction, and also the effect of absorption and re-emission by the dust grains. In the case of absorption, MCFOST uses the method described by Bjorkman and Wood (2001), where the idea is to consider absorption and re-emission as a scattering event which would be isotropic and change the wavelength of re-emission accordingly to the temperature of the cell. A photon packet will thus propagate through the disk from a scattering event (real or faking absorption) to the next, which might change its initial direction and frequency. It keeps propagating until it exits the disk.

Absorption is the most relevant parameter for estimating the disk's temperature. Indeed, as a photon packet is absorbed and re-emitted by a cell, it deposits some energy into the cell. As described in details in Pinte et al. (2006), MCFOST determines the temperature of a cell i following Lucy (1999, describing the concept of mean intensity in a cell), by solving:

$$\int_0^\infty \kappa_i^{abs}(\lambda) B_\lambda(T_i) d\lambda = \frac{L_\star}{4\pi V_i N_\gamma} N_{\gamma\, abs,i} \tag{1.22}$$

where κ_i^{abs} is the absorption opacity of the cell, $B_\lambda(T_i)$ the Planck function at the temperature T_i of the cell, and $L_\star$ the stellar luminosity, V_i the volume of the cell, N_γ the total number of emitted photons, and $N_{\gamma\, abs,i}$ the number of absorbed photons in cell i. The temperature structure is computed at the end, when all photons have been propagated through the disk. Note that if an infinite number of photon were propagated through the disk, the temperature structure would be perfectly converged. However, for computational reason, only a finite number of packets can be considered. Then, not all paths can be covered and there can be some errors in the temperature of each cell. The errors are small if a sufficiently large number of photons are considered.

1.5.2 *Computing the SED and intensity maps*

The method presented in the previous subsection allows a fast convergence of the temperature profile, but is fairly slow to compute SED. Thus, after this first step, MCFOST calculates the SED and/or intensity maps using another method, based on direct ray-tracing. This method integrates the energy that would reach the observer following rays of photons. Packets of photons are emitted both from the star and the disk (thermal emission), with probabilities described in Pinte et al. (2009). The ray-tracing method implements scattering and takes into account that, after each scattering event, a fraction of the energy is removed from the incident photon due to absorption. This procedure allows the code to be relatively fast in generating SED and images.

1.5.3 *Parametric disk structure*

Before providing any physical parameters, the grid geometry and the numbers of photons required for each step of calculation need to be set. Then, MCFOST requires a relatively simple parametrisation to describe the disk structure. During my PhD, I always assumed an axisymmetric disk and a gas to dust ratio of 100. The following list enumerates the free parameters to describe a region of the disk, and note that several regions with different parameters can be set (allowing to model rings, gaps...).

- *Stellar parameters:* T_{eff}, $R_\star$, and $M_\star$. The two first parameters are required to compute the stellar luminosity following equation 1.1, while the stellar mass is important whenever kinematics is involved, e.g., line profiles or channel maps.
- *Disk orientation:* Inclination (i) and distance (d)
- *Disk mass:* M_{dust} and gas-to-dust ratio
- *Radial structure:* As described in Section 1.2.2, the radial structure of a protoplanetary disk can be described by a truncated power law (equation 1.10) or by a tapered edge structure (equation 1.11). Both are described by an inner and outer radius (R_{in} and R_{out}), a surface density exponent (p) and a critical radius for the tapered edge-structure (R_c).
- *Vertical structure:* The disk's scale height is parametrized by equation 1.7, which is described by the following free parameters: $H_{100\,\mathrm{au}}$ and β. Alternatively, note that MCFOST also includes a few parametrizations for vertical settling, for example following Fromang and Nelson (2009, see equation 1.17). In that case the settling efficiency in the disk depends on the viscosity parameter α.

- *Grain properties:* The dust composition and grain sizes (a_{min} and a_{max}) are free parameters. Additionally the number density of dust particles is described with a power law of the grain size $dn(a) \propto a^{-a_{exp}}\, da$.

1.6 OUTLINE OF THIS THESIS

During my PhD, I aimed to provide new observational constraints on various evolutionary processes in protoplanetary disks. I used multi-wavelength observations, mainly comparing ALMA millimeter observations with optical/infrared scattered light images to probe various disk's regions and grain sizes. The main questions that I focused on during my PhD are related to the formation of planets in a protoplanetary disk. In particular, I worked on the dust mass dissipation timescale of disks, the formation of cavities in transition disks and explored other dust evolution mechanisms such as radial drift and vertical settling.

In Chapter 2, I present the study of ALMA observations of 31 protoplanetary disks in the intermediately aged Chamaeleon II star-forming region (4 ± 2 Myr). By comparing the distributions of dust-to-stellar mass ratios with several other star-forming regions in the age range of $1 - 10$ Myr, I found that disks become less massive with time: the older the region, the smaller the ratio. This is consistent with predictions. Additionally, based on gas detection rates of different star-forming regions, I investigated the dissipation of cold gas (^{12}CO) in protoplanetary disks. The detections rates decrease with the age of the region, which shows that the gas also dissipates with time. Finally, for the resolved disks, I also compared the gas and dust major axis sizes, aiming to add constraints on radial drift efficiency. The typical size ratio between dust and gas is about 3, which is likely due to radial drift of dust grains.

In Chapter 3, I present the modeling and observations focusing on two transition disks (J1608 and J1852), observed with SPHERE (near-infrared, μm sized grains) and ALMA (millimeter wavelengths and grain sizes). By performing radiative transfer modeling and comparing with the observations, I constrained the radial and vertical extent of different grains sizes. I find that large grains are less extended radially and vertically than small grains, at least in J1608, the most inclined and best resolved system of the study. Additionally, to assess planet formation as a potential origin for the cavities of transition disks, I gathered a sample of 22 transition disks with scattered light and millimeter observations. By comparing the cavity sizes with predictions from hydrodynamical simulations, I found that 15 disks have cavities that can be explained by a planet of less than 13 Jupiter masses, while the others require either the presence of a more massive companion or of several low-mass planets. In most cases, giant planets might be at the origin of most cavities observed in transition disks.

In Chapter 4, I present the analysis of the continuum emission of a survey of 12 edge-on disks observed with ALMA. The edge-on configuration is particularly favorable for the study of vertical settling as it allows to directly constrain the millimeter vertical extent of disks. For most sources, we find that the millimeter continuum emission is more compact than the scattered light, both in the vertical and radial directions, which is consistent with vertical settling and radial drift of the larger grains. In this chapter, I aimed to add constraints on both mechanisms.

Finally, I show the latest version of my first author papers in Appendix A and the first page of my published co-authored publications in Appendix B.

2

PROBING PROTOPLANETARY DISK EVOLUTION IN THE CHAMAELEON II STAR-FORMING REGION

Contents

2.1 INTRODUCTION

While a large variety of planets are observed in different exoplanet surveys (Clanton and Gaudi, 2016; Baron et al., 2019; Fernandes et al., 2019), it is still not clear how these planets form. In particular, gas giant planets must form before the protoplanetary disk has dissipated most of its gas content. As mentioned in Section 1.3.1, several studies showed that the fraction of disks detected at infrared wavelengths decreases with time, with a typical timescale of about 2.5 Myr (Mamajek, 2009; Ribas et al., 2015). However, near infrared observations probe hot dust in the inner regions of disks while the timescale for giant planet formation is rather set by the global gas and dust mass dissipation timescale. To test disk evolutionary models and find the dominant mass dissipation mechanism(s), further observational constraints on the dissipation of the mass are needed.

Millimeter and submillimeter surveys are particularly useful to probe the disk's dust and gas content. Several surveys of various star-forming regions have been conducted at millimeter wavelengths, mostly focusing on star-forming regions of $1-3$ Myr (Andrews et al., 2013; Pascucci et al., 2016; Ansdell et al., 2016; Cazzoletti et al., 2019; van Terwisga et al., 2019). They showed that the disk dust masses estimated in these young regions is commonly smaller than those measured in the more evolved Upper Sco star-forming region ($5-10$ Myr, Barenfeld et al., 2016), which suggests the dissipation of the disk dust mass with time.

In this chapter, I present an ALMA survey of protoplanetary disks located in the intermediately aged Chamaeleon II star-forming region (4 ± 2 Myr, hereafter Cha II). The study of this region complements previous ALMA surveys as it allows to probe an age/evolutionary stage little studied until now, where disk dissipation is expected to be advanced. In this chapter, I focus in particular on the evolution of the disks masses and sizes with time. I describe the observations and data reduction in Section 2.2. The continuum and CO line measurements are presented in Section 2.3. Then, in Section 2.4, I compare the dust and gas sizes, and estimate the dust and gas masses of the detected sources. Finally, in Section 2.5, I compare evolution of the dust to stellar mass ratio and gas detection rates for Cha II to other star-forming regions of different ages. In this chapter, most of the text originates from an article in preparation, but I complement the analysis with additional details.

2.2 OBSERVATIONS AND DATA REDUCTION

2.2.1 *Target selection*

In this study, we selected a sample of 31 disks out of the 63 young stellar objects of the Cha II star-forming region (Spezzi et al., 2013). We selected these targets because they all show an infrared excess at 70 μm, as observed by *Herschel* (Spezzi et al., 2013), while the unobserved Class II sources were not detected at 70 μm by Herschel. Thus, our survey is likely complete for the brightest Class II disks of Cha II. The sample includes one Class I source, one "flat spectrum" source and 27 Class II sources; two secondary sources (around Hn 24 and Sz 59) were also detected with our cycle 2 ALMA observations. I report the physical parameters of the sources in Table 2.1.

2.2.2 *ALMA observations*

We used band 6 observations (Project ID: 2013.1.00708.S, PI: Ménard) obtained on 2015 August 27. The spectral setup was such that 2 spectral windows were used for continuum, giving a mean continuum frequency of 225.7 GHz (1.33 mm) and the other three spectral windows were set-up to include 3 CO isotopologue lines. They covered the ^{12}CO, ^{13}CO, and C^{18}O $J = 2 - 1$ transitions at 230.538 GHz, 220.399 GHz and 219.56 GHz. Each line spectral window has a native 0.33 km s^{-1} velocity resolution. I used the CASA pipeline (version 4.3.1) to calibrate the raw data.

The continuum images were extracted from the calibrated visibilities over the continuum channels using the CASA `clean` function with a Briggs robust weighting parameter of +0.5. To maximize the dynamic range of the brightest sources (CM Cha, Hn 22, Hn 23, IRAS12496-7650, IRAS12500-7658, Sz 58 and Sz 61), I performed self-calibration. The continuum images are presented in Fig. 2.1. They achieve an average beam size of $0.48'' \times 0.25''$ for the continuum.

I also extracted ^{12}CO, ^{13}CO and C^{18}O channel maps from the calibrated visibilities after subtracting the continuum from the spectral windows containing line emission using the `uvcontsub` routine in CASA. Note that for the brightest sources, I also applied the continuum self-calibration solutions to the gas line data. The sources were cleaned with 0.35 km s^{-1} velocity resolution, with a Briggs robust weighting parameter of 0. The achieved angular resolution is in average $0.51'' \times 0.28''$ for the CO lines.

For the detected sources in the channel maps of each isotopologue, I generated moment 0 (Fig. 2.2) and moment 1 maps (Fig. 2.3) showing respectively the integrated line emission and the velocity gradient. These maps were obtained by using the channels where the source was detected (see Fig. 2.2 for details). Additionally, the moment 1 maps were generated for pixels detected by more than 3σ in each velocity channel.

For each source, I also generated line profiles from the CO channel maps, over a range from -10 to $+15$ km s^{-1}. The spatial range used to generate each line profile varies according to the detectability of the source. When the sources were detected in the molecule, line profiles were produced on their 3σ contours. When the sources were not detected in CO, I also generated a line profile in order to get a consistent method to evaluate the RMS. I used a square of size $1'' \times 1''$ (close to the mean size of the detected sources), centered near the phase center to extract the spectrum and calculate the RMS. The ^{12}CO and ^{13}CO line profiles are shown on Fig. 2.2 for the sources that were detected in the corresponding lines.

Source	RA (h m s)	Dec (deg ′ ″)	Class[a]	SpT[a]	$M_\star/M_\odot$ [b]
J13022287-7734494	13 02 22.9	-77 34 49.4	II	M5	0.16 ± 0.1
J13071806-7740529	13 07 18.1	-77 40 52.9	II	M4.5	0.20 ± 0.1
J13082714-7743232	13 08 27.1	-77 43 23.3	II	M4.5	0.20 ± 0.1
CM Cha	13 02 13.6	-76 37 57.8	II	K7	0.63 ± 0.1
Hn 22	13 04 22.9	-76 50 05.5	II	M2	0.40 ± 0.1
Hn 23	13 04 24.1	-76 50 01.2	II	K5	0.97 ± 0.2
Hn 24 A	13 04 55.7	-77 39 49.6	II	M0	0.52 ± 0.1
Hn 24 B*	13 04 55.6	-77 39 51.0	-	-	-
Hn 25	13 05 08.6	-77 33 42.6	II	M2.5	0.34 ± 0.1
Hn 26	13 07 48.5	-77 41 21.4	II	M2	0.41 ± 0.1
IRAS12496-7650	12 53 17.2	-77 07 10.6	II	F0	> 1.4
IRAS12500-7658	12 53 42.9	-77 15 11.5	I	K5	0.06 ± 0.1
IRAS12535-7623	12 57 11.7	-76 40 11.1	II	M0	0.49 ± 0.1
ISO-CHAII 13	12 58 06.8	-77 09 09.5	II	M7	0.07 ± 0.1
J130059.3-771403	13 00 59.3	-77 14 02.7	II	K3	-
J130521.7-773810	13 05 21.7	-77 38 10.3	F	-	-
J130529.0-774140	13 05 29.0	-77 41 40.1	II	-	-
Sz 46	12 56 33.7	-76 45 45.4	II	M1	0.49 ± 0.1
Sz 49	13 00 53.2	-76 54 15.2	II	M0.5	0.56 ± 0.1
Sz 50	13 00 55.3	-77 10 22.2	II	M3	0.32 ± 0.1
Sz 51	13 01 58.9	-77 51 21.9	II	K8.5	0.63 ± 0.1
Sz 52	13 04 24.9	-77 52 30.3	II	M2.5	0.35 ± 0.1
Sz 53	13 05 12.7	-77 30 52.6	II	M1	0.49 ± 0.1
Sz 54	13 05 20.7	-77 39 01.6	II	K5	0.86 ± 0.2
Sz 56	13 06 38.8	-77 30 35.3	II	M4	0.23 ± 0.1
Sz 58	13 06 57.5	-77 23 41.6	II	K5	1.03 ± 0.2
Sz 59 A	13 07 09.2	-77 30 30.5	II	K7	0.69 ± 0.1
Sz 59 B*	13 07 09.7	-77 30 30.2	-	-	-
Sz 61	13 08 06.3	-77 55 05.2	II	K5	0.89 ± 0.2
Sz 62	13 09 50.4	-77 57 24.0	II	M2.5	0.27 ± 0.1
Sz 63	13 10 04.2	-77 10 44.8	II	M3	0.28 ± 0.1

Table 2.1 – Stellar parameters. Coordinates are from the SIMBAD database except for the secondary of the Hn 24 and Sz 59 binaries. These two were estimated from our images (marked by *).
References: (a) Spezzi et al. (2013), (b) This work. The stellar masses were calculated from the PMS tracks by Baraffe et al. (2015), using luminosities and temperatures from Spezzi et al. (2008) rescaled using individual distances from GAIA DR2 (Gaia Collaboration et al., 2018). The errors are estimated based on the uncertainty assumed for the stellar effective temperature (see Section 2.5.1).

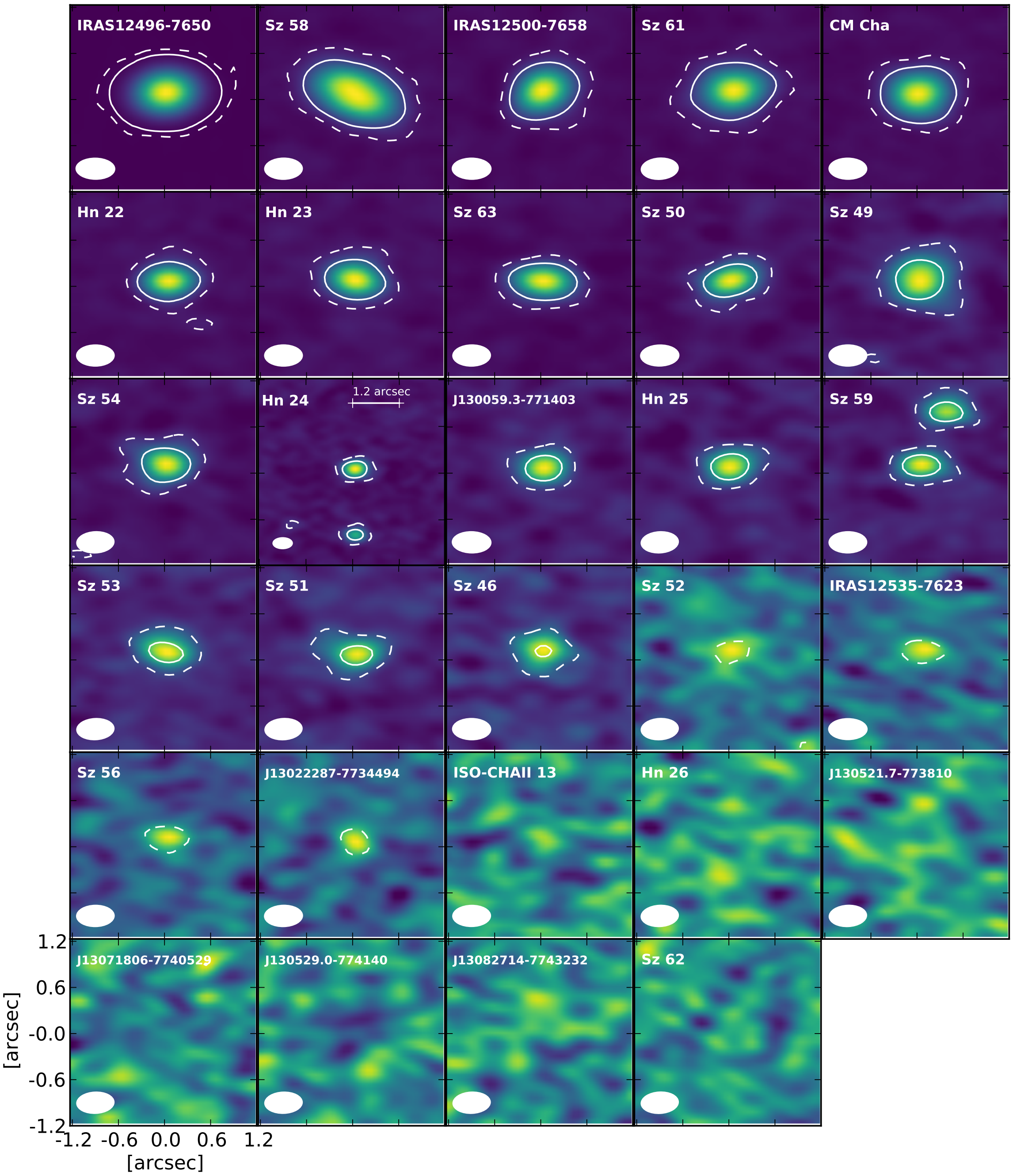

Figure 2.1 – Continuum images ordered by decreasing fluxes. Images are 2.4″ × 2.4″ except for Hn 24 where we use 4.8″ × 4.8″ to show the secondary source. The beam is shown in the lower left corner of each panel. 3σ and 15σ contours are shown in dashed and solid lines, respectively. The colormap is chosen to go from from -3σ to the maximum intensity of each image.

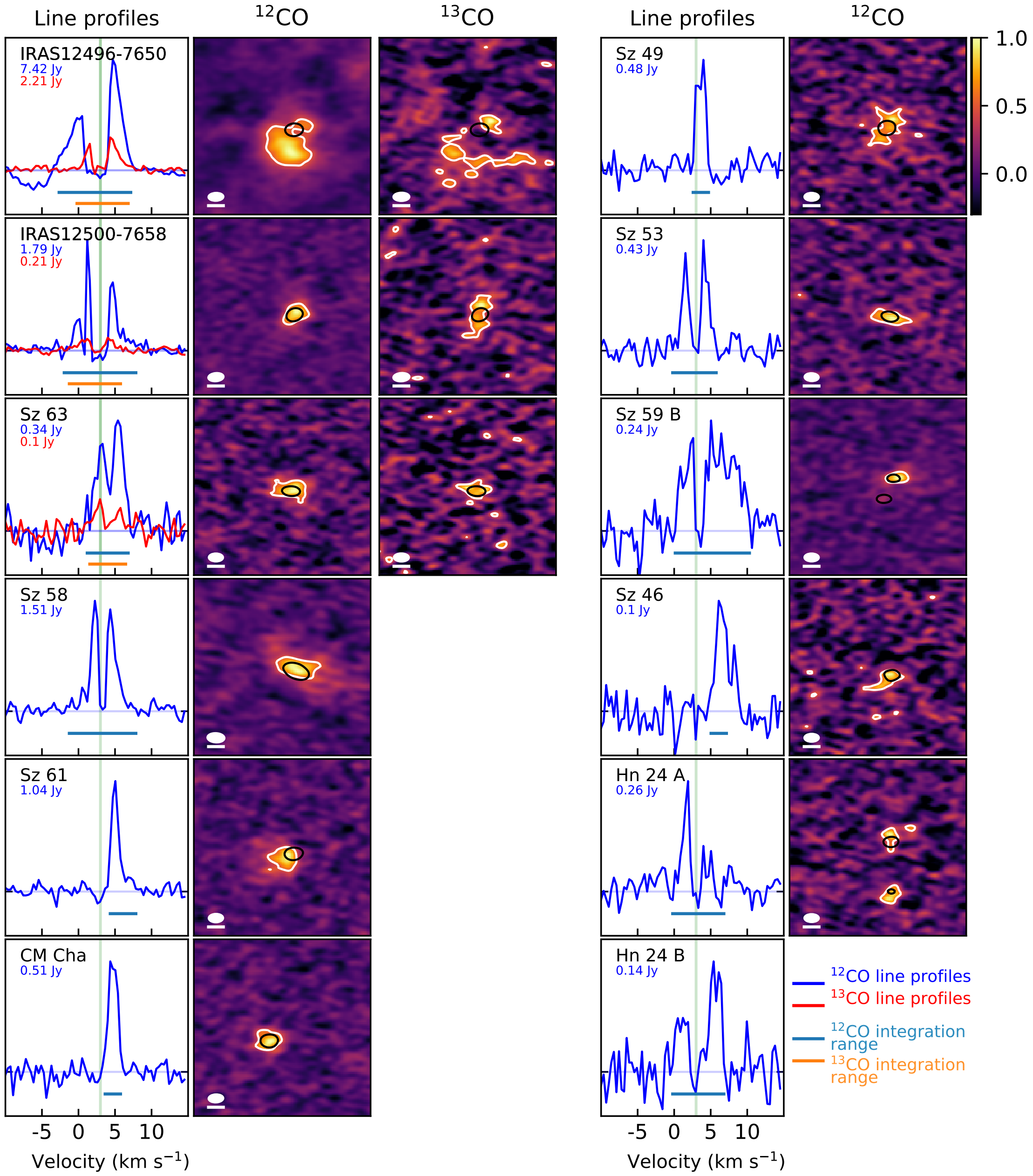

Figure 2.2 – Line profiles (left panels), ^{12}CO normalized moment 0 maps (middle panels) and ^{13}CO normalized moment 0 maps (right panels) for the sources detected in the respective lines (2 sources per row). For each source, we display the continuum contours at 50% of the continuum peak (black line) and the CO contours at 50% of the CO peak (white line) on the CO moment 0 maps. The CO beam size is shown in the bottom left corner of each panel, along with a white line representing a 0.5″ scale. On the line profiles plots, we also show a green vertical line at 3 km s^{-1}, where the cloud absorption is estimated, and the size of the integration range to used estimate the ^{12}CO and ^{13}CO fluxes. The maximum fluxes of each line profile are displayed in the top left side of the panels, colored in blue for ^{12}CO and in red for ^{13}CO.

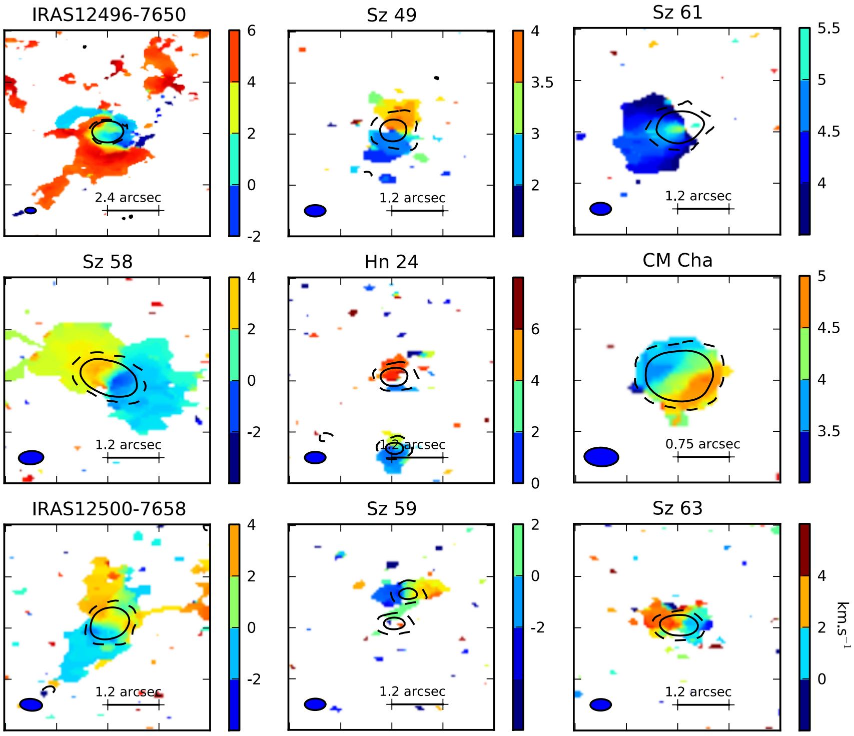

Figure 2.3 – Moment 1 maps for ^{12}CO detected sources, the color coding corresponds to the radio velocity expressed in km s^{-1}. Beam sizes are shown in the bottom left corner, and scales are presented in the bottom right corner. The contours represent the 3σ and 15σ levels of the corresponding continuum emission.

2.3 RESULTS

2.3.1 *Continuum emission*

We measure the continuum emission by fitting an elliptical Gaussian model to the visibility data, using the CASA `uvmodelfit` task. This model has six free parameters: integrated flux density ($F_{1.3\text{mm}}$), full width half maximum (hereafter FWHM) along the major axis ($R_{50\%,\,1.3\text{mm}}$), aspect ratio of the axes (r, such that *minor axis fwhm* = $R_{50\%,\,1.3\text{mm}} \times r$), position angle (PA), right ascension ($\Delta\alpha$) and declination ($\Delta\delta$) of the phase center. For the sources where the Gaussian model did not converge, we fitted the visibilities with a point source model with only three free parameters ($F_{1.3\text{mm}}$, $\Delta\alpha$, $\Delta\delta$). Table 2.2 gives the measured 1.3 mm continuum flux, major and minor axis sizes, and position angle of each source. Right ascensions and declinations obtained from the fits are consistent with the SIMBAD coordinates within a few tenths of arcseconds.

Out of the 31 sources of the sample, 24 are detected above a 3σ significance threshold, and 14 of them are resolved. The continuum images are presented in Fig 2.1. In this figure, binaries in the fields of Sz 59 and Hn 24 are visible. We measure a separation of 0.70″ and PA of -25° for Sz 59 from the continuum fits, which is consistent with the measurement by Geoffray and Monin (2001). In the field of Sz 59, the companions have similar continuum fluxes and sizes. In addition, we discover a new visual binary, as Hn 24 B is not referenced in the literature. From the continuum uv-plane fit, we derive the components' locations (Table 2.1). We measure a separation of 1.67″, a PA of 0° and a flux ratio in the continuum of 2. At 1.3 mm, the secondary is unresolved and smaller than the (resolved) primary.

2.3.2 *CO line emission*

We measure the line fluxes by integrating the line profiles over their spectral widths, which we determined by visual inspection of the channel maps. For the detected sources, I represent the line width by horizontal lines at the bottom of each panels of Fig. 2.2. The mean line width of the detected sources is ~ 6.3 km s^{-1}. For these sources, we evaluated the flux error as the RMS times the width of the line. On the other hand, we report upper limits for the non-detections. They correspond to 3 times the RMS of the line profile, integrated over a line width of 6.3 km s^{-1}. We present the integrated fluxes and uncertainties for the three isotopologues in Table 2.3. Additionally, we estimate the ^{12}CO emission size of the resolved sources by fitting an elliptical Gaussian to the moment 0 maps. We report the major axis FWHM of ^{12}CO emission ($R_{50\%,^{12}\mathrm{CO}}$) in the second to last column of Table 2.3.

Out of 31 targets observed, 12 are detected in ^{12}CO, 3 in ^{13}CO and none in C^{18}O. All the sources detected in ^{13}CO are also detected in ^{12}CO, and all the sources detected in ^{12}CO are detected in the continuum. Each source detected in a CO isotopologue is also resolved. Hn 24 is the only identified continuum binary that is detected in the ^{12}CO line. In contrast with the continuum fluxes, where Hn 24 A and Hn 24 B have a factor of two difference in flux, the ^{12}CO fluxes are similar for both sources. This is expected if the two disks have different dust masses (as indicated by their difference in continuum emission, assuming it is optically thin), but similar sizes and temperatures, that would lead to similar line fluxes in the optically thick ^{12}CO.

However, we caution for the presence of significant foreground absorption for all sources. From the moment 0 maps displayed in Fig. 2.2, we see that for some sources the line emission is not centered on the continuum (e.g., Sz 61), which suggests that we are missing part of the emission for each of them. Furthermore, some line profiles are also asymmetric (e.g., CM Cha) and/or have minima (absorption) that go down to the continuum level (e.g., IRAS12500-7658). This is not compatible with a Keplerian profile unless there is foreground absorption. The large cloud absorption is located around 3 km s^{-1} (green line on Fig. 2.2). It is compatible with Mizuno et al. (2001) study, which gave estimations of $+2.9 \pm 2.8$ km s^{-1}. Thus, even for the detected sources, the CO fluxes and sizes are likely lower limits only.

Source	$F_{1.3mm}$ (mJy)	$R_{50\%, 1.3mm}$ (mas)	*Minor axis fwhm* (mas)	PA (deg)	M_{dust} ($M_\oplus$)
J13022287-7734494	0.87 ± 0.15				1.84 ± 0.32
J13071806-7740529	< 0.51				< 0.93
J13082714-7743232	< 0.51				< 1.19
CM Cha	38.76 ± 0.23	315 ± 5	315 ± 9	35 ± 57	34.08 ± 0.20
Hn 22	21.81 ± 0.17	175 ± 6	110 ± 12	-51 ± 4	28.47 ± 0.22
Hn 23	20.75 ± 0.19	190 ± 4	190 ± 13	158 ± 57	17.95 ± 0.16
Hn 24 A	10.52 ± 0.19	193 ± 15	193 ± 33	67 ± 57	8.44 ± 0.15
Hn 24 B	5.05 ± 0.16				5.85 ± 0.18
Hn 25	5.38 ± 0.18	195 ± 25			6.21 ± 0.19
Hn 26	< 0.51				< 0.64
IRAS12496-7650	708.60 ± 0.27	354 ± 1	321 ± 1	125 ± 1	247.80 ± 0.09
IRAS12500-7658	49.60 ± 0.26	258 ± 5	258 ± 11	-84 ± 57	266.50 ± 1.40
IRAS12535-7623	1.09 ± 0.18				0.60 ± 0.10
ISO-CHAII 13	< 0.51				< 2.28
J130059.3-771403	5.68 ± 0.19	188 ± 15		4 ± 9	6.57 ± 0.22
J130521.7-773810	< 0.51				< 0.61
J130529.0-774140	< 0.51				< 0.59
Sz 46	3.73 ± 0.20	221 ± 49			4.26 ± 0.23
Sz 49	10.92 ± 0.26	401 ± 14	311 ± 31	-1 ± 7	14.61 ± 0.35
Sz 50	10.96 ± 0.20	169 ± 15	169 ± 33	64 ± 57	5.71 ± 0.19
Sz 51	4.30 ± 0.18	249 ± 33	133 ± 49	-70 ± 10	4.58 ± 0.19
Sz 52	1.16 ± 0.24	461 ± 131			1.72 ± 0.35
Sz 53	4.81 ± 0.20	307 ± 32	168 ± 44	65 ± 8	5.59 ± 0.35
Sz 54	10.54 ± 0.18	586 ± 9	131 ± 28	12 ± 6	7.01 ± 0.12
Sz 56	1.00 ± 0.15				1.09 ± 0.16
Sz 58	60.72 ± 0.30	699 ± 5	347 ± 39	61 ± 1	51.12 ± 0.25
Sz 59 A	4.99 ± 0.16	114 ± 37			4.23 ± 0.13
Sz 59 B	4.29 ± 0.16	97 ± 22			4.98 ± 0.19
Sz 61	41.32 ± 0.23	310 ± 3	310 ± 9	-11 ± 57	33.05 ± 0.17
Sz 62	< 0.51				< 0.65
Sz 63	19.79 ± 0.21	369 ± 9	183 ± 11	83 ± 1	26.56 ± 0.28

Table 2.2 – 1.3 mm continuum properties. Gaussian (point source) models were fitted in the uv plane for detected (undetected) sources. We report the continuum fluxes ($F_{1.3mm}$), the resolved major and minor axis FWHM (respectively $R_{50\%, 1.3mm}$ and *Minor axis fwhm*), the position angles (PA) and the estimated dust masses (see Section 2.4.2). Some sources are only resolved in the major axis direction, for these sources we do not report any size in the minor axis.

Source	$F_{^{12}CO}$ (Jy km s^{-1})	$F_{^{13}CO}$ (Jy km s^{-1})	$F_{C^{18}O}$ (Jy km s^{-1})	$R_{50\%,^{12}CO}$ (mas)	$R_{50\%,^{12}CO}$/ $R_{50\%,\,1.3mm}$
J13022287-7734494	< 0.14	< 0.14	< 0.12		
J13071806-7740529	< 0.15	< 0.14	< 0.10		
J13082714-7743232	< 0.11	< 0.16	< 0.10		
CM Cha	0.67 ± 0.04	< 0.19	< 0.09	680 ± 100	2.2 ± 0.3
Hn 22	< 0.13	< 0.15	< 0.10		
Hn 23	< 0.13	< 0.14	< 0.10		
Hn 24 A	0.35 ± 0.04	< 0.15	< 0.11	540 ± 160	2.8 ± 0.9
Hn 24 B	0.33 ± 0.04	< 0.15	< 0.11	950 ± 400	
Hn 25	< 0.15	< 0.14	< 0.11		
Hn 26	< 0.13	< 0.13	< 0.12		
IRAS12496-7650	20.58 ± 1.66	5.26 ± 0.33	< 0.16	1520 ± 110	4.3 ± 0.3
IRAS12500-7658	2.93 ± 0.22	0.60 ± 0.06	< 0.14	840 ± 100	3.3 ± 0.4
IRAS12535-7623	< 0.15	< 0.15	< 0.10		
ISO-CHAII 13	< 0.14	< 0.15	< 0.09		
J130059.3-771403	< 0.15	< 0.16	< 0.11		
J130521.7-773810	< 0.16	< 0.14	< 0.10		
J130529.0-774140	< 0.13	< 0.14	< 0.11		
Sz 46	0.12 ± 0.01	< 0.13	< 0.11	1020 ± 270	4.6 ± 1.6
Sz 49	0.61 ± 0.04	< 0.17	< 0.10	1360 ± 280	3.4 ± 0.7
Sz 50	< 0.17	< 0.17	< 0.13		
Sz 51	< 0.14	< 0.15	< 0.09		
Sz 52	< 0.13	< 0.16	< 0.12		
Sz 53	0.84 ± 0.06	< 0.15	< 0.10	1370 ± 220	4.5 ± 0.9
Sz 54	< 0.14	< 0.12	< 0.11		
Sz 56	< 0.11	< 0.13	< 0.09		
Sz 58	4.01 ± 0.24	< 0.15	< 0.11	1990 ± 220	2.8 ± 0.3
Sz 59 A	< 0.16	< 0.14	< 0.11		
Sz 59 B	1.14 ± 0.09	< 0.14	< 0.11	780 ± 130	8.0 ± 2.3
Sz 61	1.31 ± 0.08	< 0.16	< 0.11	1020 ± 150	3.3 ± 0.5
Sz 62	< 0.14	< 0.14	< 0.11		
Sz 63	1.04 ± 0.07	0.21 ± 0.03	< 0.12	1190 ± 150	3.2 ± 0.4

Table 2.3 – Integrated fluxes for the CO isotopologues derived from the line profiles and ^{12}CO sizes. As the continuum of Hn 24 B was not resolved, we do not report CO/continuum size ratio for this source.

2.4 DISK MASSES AND SIZES

2.4.1 *Continuum vs CO sizes*

Measuring and comparing disk sizes as seen in dust and gas tracers is particularly important to constrain evolutionary mechanisms. In Section 2.3.1 and Section 2.3.2, I presented the estimates of the major axis sizes (FWHM) of the continuum and ^{12}CO emission line. Those are reported in Table 2.2 and Table 2.3, respectively. Additionally, the gas to continuum size ratio is presented in the last column of Table 2.3. We find that the ^{12}CO emission is systematically larger than its continuum counterpart, with a median size ratio of 3.3.

Before discussing the implications of these results, note that the sizes were measured by fitting an elliptical Gaussian to each source, respectively in the uv-plane for the continuum and in the image plane for the gas, which might lead to systematic differences in the size estimation. To quantify the impact of using different measurement methods, I compared the sizes obtained using Gaussian fits either in the image- or in the uv-plane for 11 objects, well resolved in continuum. In Fig. 2.4, I present the size ratio obtained for these sources using the two methods. The ratios uv / image measurements are between 0.7 and 1.05 between the two techniques. So the image plane estimation, deconvolved from the beam, gives larger values than those found in the uv-plane, in average 1.1 times larger. However, the CO to continuum size ratios estimated for our data are significantly larger than this size difference (median size ratio of 3.3, Table 2.3). This implies that the differences measured are not an artefact of the measurement method.

Previous studies have reported similarly large size differences between gas and continuum measurements, both for individual Herbig AeBe and for T Tauri stars (e.g., van der Plas et al., 2017a; Facchini et al., 2019). It can have several explanations. Indeed, the ^{12}CO emission is optically thick while the dust continuum is optically thinner, making the CO disk easier to detect at large distances even if the solids are distributed as far outside as the gas (e.g., Woitke et al., 2016). Additionally, protoplanetary disks are also accreting onto the central star and angular momentum conservation implies that beyond a certain radius, the gas disk has to expand outward (see equation 1.8). Conversely, millimeter-sized grains are expected to drift inward rapidly, making the continuum disk look smaller, with a sharp outer edge at millimeter wavelengths (see Section 1.3.2).

Using thermochemical models, Trapman et al. (2019) find that a ratio $R_{90\%,^{12}\mathrm{CO}}/R_{90\%,\,1.3\mathrm{mm}} \geq 4$ requires dust evolution and radial drift. Note that in this study, we compare the FWHM of the gas with that of the continuum rather than the radius which encompass 90% of the flux of both tracers as is done by Trapman et al. (2019). When applying their results to our Cha II sample, we find that grain growth and radial drift are needed to reproduce the high values of gas to dust size ratio observed in several disks. Additionally, we observe that the average size difference is lower in the 2 ± 1 Myr old Lupus star-forming region (Ansdell et al., 2018) than in the 4 ± 2 Myr old Cha II. Indeed, Ansdell et al. (2018) estimate an average gas to dust

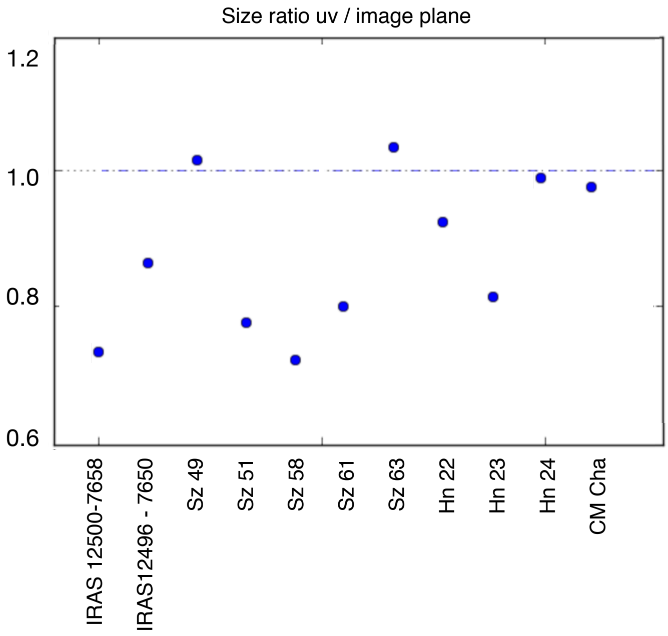

Figure 2.4 – Size ratio of 11 sources, estimated using different measurement methods. I divide the size obtained by fitting a Gaussian in the uv plane by that fitting a Gaussian in the image plane. In average, the sizes estimated from fitting in the uv plane are 0.9 times smaller than those estimated in the image plane.

size ratio of about 2 for 22 disks in Lupus. This difference is also consistent with disk evolution. Indeed, as mentioned previously, the millimeter dust grains are expected to drift inward with time while the gas spread to larger radius, which leads to an increase of $R_{^{12}CO}/R_{1.3mm}$ with time.

2.4.2 *Continuum masses*

Assuming that the continuum emission is optically thin at 1.3 mm, it is possible to infer the disk dust mass (M_{dust}) from the continuum millimetric flux (F_ν) at a given wavelength (e.g., Hildebrand, 1983):

$$M_{\text{dust}} = \frac{F_\nu d^2}{\kappa_\nu B_\nu(T_{\text{dust}})} \tag{2.1}$$

We take a grain opacity κ_ν of 2.3 $cm^2.g^{-1}$ at 230 GHz (Beckwith et al., 1990), with $\kappa_\nu \propto \nu^{0.4}$ (as in Andrews et al., 2013). We use individual distances from Gaia DR2 (Gaia Collaboration et al., 2018) for sources that have an error on the distance smaller than 15 pc. When the error is larger than 15 pc, we adopt the weighted mean distance of the well characterized objects: 198 pc (Dzib et al., 2018). We adopt the relationship of T_{dust} with $L_\star$ from Andrews et al. (2013), inferred with a grid of radiative transfer models: $T_{dust} = 25K\,(L_\star/L_\odot)^{1/4}$. We used the luminosities determined by Spezzi et al. (2008), rescaled to the Gaia DR2 distances. For the sources that were not characterized spectrally (see Table 2.1), we applied a characteristic dust

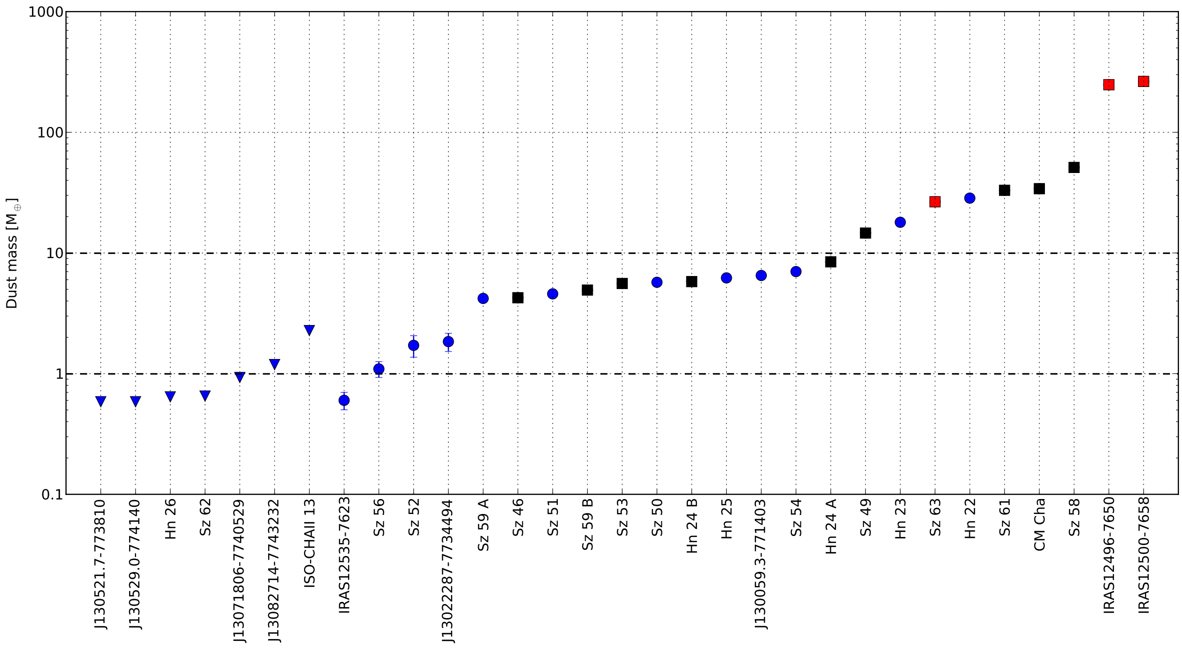

Figure 2.5 – Dust masses for the 31 sources in our Cha II sample expressed in Earth masses and ordered by increasing dust mass (Table 2.2). Black and red squares correspond to ^{12}CO and ^{13}CO detected sources, respectively. Round symbols show continuum only detected sources and the downward-facing triangles correspond to 3σ upper limits for non detections.

temperature of $T_{\rm dust} = 20\,$K, the median temperature for Taurus disks (Andrews and Williams, 2005). Fig. 2.5 shows the detections and upper limits of our dust mass estimates. The values are reported in Table 2.2, they range from $\sim 0.6\,M_\oplus$ (IRAS12535-7623) to $\sim 266.5\,M_\oplus$ (IRAS12500-7658).

We note however, that the scaling relation between $T_{\rm dust}$ and $L_\star$ was calibrated for luminosities larger than $0.1\,L_\odot$. In our sample, 5 objects have luminosities smaller than this value, including IRAS12500-7658 and ISO-CHAII 13 that have luminosities close to $0.01\,L_\odot$ (Spezzi et al., 2008). For these two sources, the estimation of the mass is probably overestimated by a factor ~ 2 (van der Plas et al., 2016).

2.4.3 *CO masses*

Determining gas masses from observations is a difficult task. Indeed, most of the gas is in the form of H_2, which is very difficult to detect since it does not have a permanent dipole moment and does not emit significantly. Lines of less abundant molecules (e.g., CO, HD) are possible to use, but they probe specific temperatures and are affected by chemistry, corresponding to different regions of the disk. Moreover, gas emission lines are often optically thick, meaning that, as opposed to dust emission, line fluxes do not trace directly the gas mass.

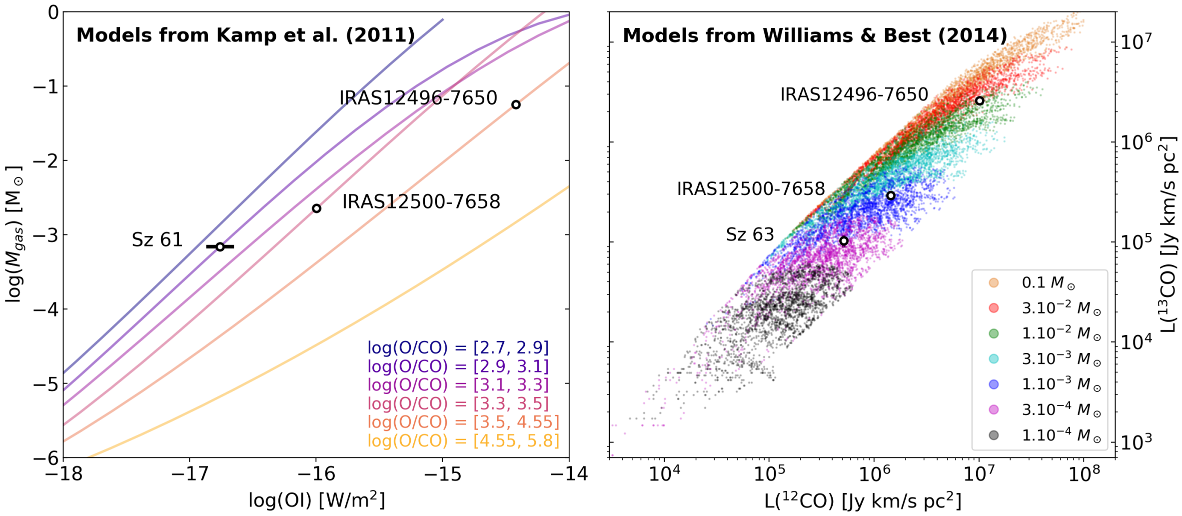

Figure 2.6 – Gas mass estimates. Left: Models from Kamp et al. (2011) with the 3 sources observed and detected in both ^{12}CO and [OI] 63 μm. Dashed curves correspond to models for six different [OI]/CO ratios. Right: Models from Williams and Best (2014) showing the 3 sources detected in ^{12}CO and ^{13}CO.

Nevertheless, several models that attempt to infer gas masses from observations are available in the literature. From chemistry and physical modeling, Kamp et al. (2011) estimate gas masses with a precision of about an order of magnitude using [OI] 63 μm combined with ^{12}CO $J = 2 - 1$ emission lines. For several bins of [OI]/CO flux ratio, they fitted their disk models by third order polynomial curves to obtain gas masses from the [OI] fluxes. In our Cha II sample, only three sources that are detected in ^{12}CO have also been detected in [OI] (Riviere-Marichalar et al., 2015). They have flux ratios, log([OI]/CO), of 4.1 ± 0.2, 3.4 ± 0.2 and 2.9 ± 0.4 (respectively for IRAS12496-7650, IRAS12500-7658 and Sz 61). These ratios are consistent within the errors with the polynomial curves constructed for log([OI]/CO) between 3.5 and 4.55, 3.3 and 3.5, and the curve between 2.9 and 3.1 respectively, so they can be displayed on these curves in the left panel of Fig. 2.6. This panel shows the gas mass estimations for those three sources. The represented curves are derived for smaller intervals of [OI]/CO than in Kamp et al. (2011), for six ranges in [OI]/CO ratio (Kamp et al., private communication). The estimated masses are reported in the first column of Table 2.4. They were obtained after rescaling the Cha II [OI] fluxes from 198 pc to 140 pc (used for the model grid), and give an order of magnitude estimate for disk masses.

Williams and Best (2014) also developed a parametrized grid of models to study CO emission depending on various disk parameters. Based on a relatively simple CO chemistry that takes into account freeze-out onto dust grains at low temperatures near the disk midplane, photodissociation in the upper disk atmosphere and assuming some initial molecular abundances, they estimate the gas masses using ^{13}CO and C^{18}O fluxes or ^{12}CO and ^{13}CO fluxes. As none of our Cha II sources were detected in C^{18}O, we estimate gas masses from their ^{12}CO and ^{13}CO grid. In those models, the

	Kamp et al. (2011)	Williams and Best (2014)	G/D ratio = 100
IRAS12496-7650	5.6×10^{-2}	2.0×10^{-2}	7.4×10^{-2}
IRAS12500-7658	2.2×10^{-3}	1.0×10^{-3}	8.0×10^{-2}
Sz 61	7.0×10^{-4}		1.0×10^{-2}
Sz 63		3.0×10^{-4}	8.0×10^{-3}

Table 2.4 – Gas masses from different methods given in $M_{\odot}$. The last column reproduces the dust masses of Table 2.2 considering a gas to dust mass ratio of 100. When considering only the errors on the dust mass (Table. 2.2), the typical error on this value is about 10^{-4}. For the other methods, the uncertainty of the measurements is about of 1 order of magnitude for Kamp et al. (2011), at least a factor of ∼ 3 for Williams and Best (2014)

gas structure is an exponentially tapered disk profile in hydrostatic equilibrium. Gas masses estimated using this method are shown on the right panel of Fig. 2.6. The second column of Table 2.4 presents the masses obtained for the 3 sources detected in both isotopologues.

Finally, I estimated the gas masses with a third method that used the dust masses estimated from the 1.3 mm continuum (Table 2.2). I assumed a standard gas to dust ratio of 100. These values are given in the last column of Table 2.4.

For the two sources for which we could infer gas masses from the two models, IRAS12496-7650 and IRAS12500-7658, the results are consistent between the Kamp et al. (2011) method and the Williams and Best (2014) models within a factor of 3. This consistency between two different models suggests that the results are robust, but further studies are required. In particular, note that the CO abundances are not known very precisely which implies that the gas mass estimates provided by these two methods are precise to about an order of magnitude. Additionally, the CO fluxes might be highly impacted by foreground absorption (see Section 2.3.2), which would lead to higher disk masses for both models (higher ^{12}CO fluxes and reduced [OI]/CO).

The third method tested here, using the dust masses and assuming a gas to dust ratio of 100, gives masses that are up to one order of magnitude larger than the estimates using the methods of either Williams and Best (2014) or Kamp et al. (2011). This is consistent with results from previous studies on a large sample of Lupus protoplanetary disks (Ansdell et al., 2016; Miotello et al., 2017), and suggests either that the gas to dust ratio in those disks is lower than the canonical ISM value, or that the CO is under-abundant compared to H_2 in these disks (e.g., review by Bergin and Williams, 2018). However, further investigations with lower gas-to-dust ratio and estimating uncertainties of each method are needed to confirm this statement. This analysis was out of the scope of the paper and could only be applied to few sources so we did not keep it in the latest version of the article.

2.5 COMPARISONS WITH OTHER STAR-FORMING REGIONS

2.5.1 *Luminosity functions*

Over the last years, observations of nearby star-forming regions have shown that the disk dust mass tends to decrease with age, which can be a sign for disk dissipation (e.g., Ansdell et al., 2016). This evidence was mostly driven by the comparison of young star-forming regions ($1-3\,$Myr, e.g., Lupus) with the older Upper Sco ($5-10\,$Myr) but a small number of studies focused on intermediately aged regions (e.g., σ-Orionis, Ansdell et al., 2017). In this section, we expand the study of cumulative dust mass distribution to the intermediately aged $4\pm2\,$Myr Cha II star-forming region, aiming to add constraints on the evolution of dust mass with time.

Additionally, these surveys of complete star-forming regions revealed a correlation between $M_{\rm dust}$ and $M_\star$ (e.g., Andrews et al., 2013; Pascucci et al., 2016). Although this relation might evolve with time, when assuming a dust temperature scaling with luminosity in equation 2.1, they showed that the dust mass is about proportional to the stellar mass[1]: $M_{\rm dust} \propto M_\star$. Because of this relation, lower stellar masses are expected to correspond to lower disk dust masses. Then, comparing the dust mass distributions of star-forming regions with different stellar mass distributions might lead to inadequate conclusions. In this context, our analysis consists in comparing millimeter luminosity functions, i.e., cumulative disk dust mass distributions, as well as dust-to-stellar mass ratio distributions for different star-forming regions. Using this ratio allows us to reduce the impact of potentially different distributions of stellar mass, and to the first order, to study the evolution of $M_{\rm dust}$ as a function of time.

2.5.1.a. Sample

In this analysis, we consider 6 star-forming regions observed at millimeter wavelengths and for which stellar masses can be well estimated. Those are Upper Sco (Barenfeld et al., 2016), Cha II (this study), IC 348 (Ruíz-Rodríguez et al., 2018), Cha I (Pascucci et al., 2016), Lupus (both band 7 and band 6 surveys, Ansdell et al., 2016; Ansdell et al., 2018) and Taurus (Andrews et al., 2013). The main characteristics of all regions (age, average distance, observed frequency and smallest detected dust mass) are reported in Table 2.5. Note that because objects of different SED classes are most likely in a different evolutionary stage, we selected only the Class II objects from all studies. For Upper Sco, they are the objects classified as 'Full', 'Transitional' and 'Evolved' in Table 1 of Barenfeld et al. (2016).

Also, note that we did not include several millimeter surveys in this analysis, either because they lack of stellar masses estimates (e.g., σ-Orionis, Ophiuchus or OMC-2, respectively in Ansdell et al., 2017; Cieza et al., 2018; van Terwisga et al., 2019), or because not all Class II of the region were observed (e.g., Serpens, CrA, Law et al.,

---

[1] When taking a constant $T_{\rm dust} = 20\,$K, those studies usually find $M_{\rm dust} \propto M_\star^2$ (e.g., Ansdell et al., 2017).

Region	Published age (Myr)	Distance (pc)	Obs freq (GHz)	$\mathrm{M}_{\mathrm{dust,min}}$ ($\mathrm{M}_\oplus$)	Detections/Total sources
Upper Sco	$5-11^{a,b}$	145 ± 10	341.1	0.17	53/75
Cha II	$2-6^{c}$	198 ± 6^{A}	225.7	0.60	19/23
IC 348	$2-3^{d}$	310 ± 20^{d}	225.7	0.52	33/67
Cha I	$2-4^{e,f}$	192 ± 6^{A}	338.0	0.54	60/76
Lupus b7	$1-3^{g}$	160 ± 4^{A}	335.8	0.16	51/57
Lupus b6			225.5	0.60	62/66
Taurus	$1-2^{h}$	141 ± 7^{B}	225.0	1.08	92/164

Table 2.5 – Parameters of star-forming regions. The sensitivity limits ($\mathrm{M}_{\mathrm{dust,min}}$) correspond to the lowest detected dust mass of each star-forming region.
References: (a) Pecaut et al. (2012), (b) Herczeg and Hillenbrand (2015), (c) Spezzi et al. (2008), (d) Ruíz-Rodríguez et al. (2018), (e) Pascucci et al. (2016), (f) Luhman (2007), (g) Ansdell et al. (2016), (h) Andrews et al. (2013), (A) Dzib et al. (2018), (B) Zucker et al. (2019)

2017; Cazzoletti et al., 2019). For example, note that analysing Gaia DR2 data, Galli et al. (2020) identified 28 new Class II since the ALMA survey of CrA (probing 43 Class II sources, Cazzoletti et al., 2019).

2.5.1.b. Methods

INDIVIDUAL DISTANCES. First, for each object included in the published millimeter surveys, I looked for the individual distance through the Gaia archive [2] (Gaia Collaboration et al., 2018). I used the individual stellar distances whenever the errors are smaller than 15 pc. For the sources with larger errors or that are not in the catalog, the weighted averaged distance of the corresponding association is adopted. The published ages and mean distances are reported in Table 2.5.

STELLAR MASSES. Because the obtained distances can be different from previous estimates (see e.g., de Zeeuw et al., 1999; Voirin et al., 2018; Long et al., 2017; Andrews et al., 2013, for older values), the stellar luminosity might change as well, which impacts the stellar mass estimated. For this reason, I recalculated homogeneously the stellar masses of all objects in this study. I used the Bayesian method described in Andrews et al. (2013) and Pascucci et al. (2016) to find the stellar age and mass of the evolutionary model that best matches the observed effective temperature T and luminosity L of each object. For each source, I computed the following likelihood function:

$$F(T,L|\hat{T},\hat{L}) = \frac{1}{2\pi\sigma_T\sigma_L} \times \exp\left(-0.5 \times \left[\frac{(T-\hat{T})^2}{\sigma_T^2} + \frac{(L-\hat{L})^2}{\sigma_L^2}\right]\right) \tag{2.2}$$

---

[2] http://gaia.ari-heidelberg.de/singlesource.html

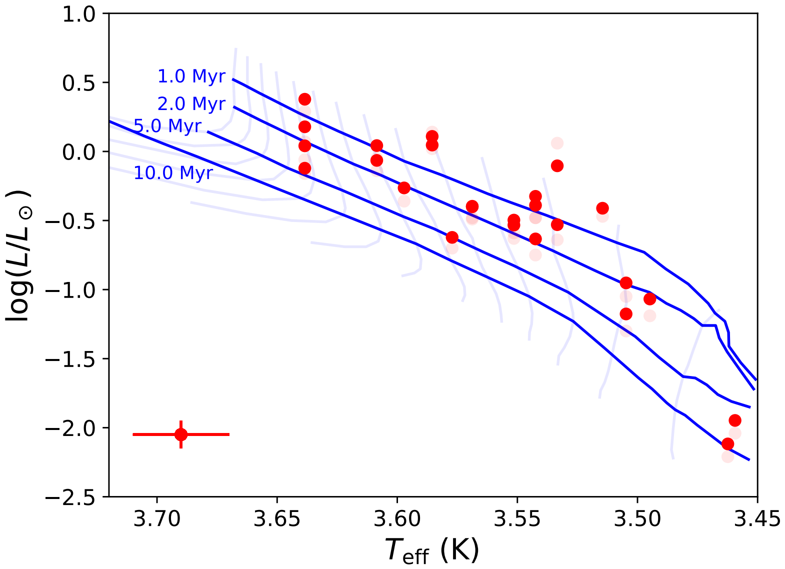

Figure 2.7 – HR diagram showing the Cha II sources included in our ALMA sample. The faint lines correspond to evolutionary tracks for different stellar masses, between 0.1 and 1.4 $M_{\odot}$ by steps of 0.1 $M_{\odot}$, and the solid lines to different isochrones (from Baraffe et al., 2015). The faint points are calculated with a distance of 178 pc, while the colored points are calculated with the latest Gaia distances. I represent the typical errors used for this analysis in the bottom left corner of the plot.

where $\hat{T}$ and $\hat{L}$ are the model grid temperatures and σ_T , σ_L the uncertainties associated with T and L. For this analysis, I used isochrones from Baraffe et al. (2015), in the range 0.5 to 50 Myr. The tracks were interpolated to probe the mass range from 0.05 to 1.4 $M_{\odot}$, by steps of 0.01 $M_{\odot}$. The assumed uncertainties in $\log(L_\star)$ and $\log(T_\star)$ are 0.1 and 0.02 respectively, which correspond to the upper values of the uncertainties in Spezzi et al. (2008). The stellar mass and age associated to each object correspond to the model for which the likelihood function is maximum.

I used stellar luminosities and temperatures from Andrews et al. (2013), Alcalá et al. (2017), Manara et al. (2017) and Luhman (2007), Ruíz-Rodríguez et al. (2018), Spezzi et al. (2008), and Barenfeld et al. (2016) for Taurus, Lupus, Cha I, IC 348, Cha II, and Upper Sco respectively, rescaling the luminosity to each individual stellar distance as detailed previously.

I show an example of HR diagram in Fig. 2.7, including the Cha II sources of our ALMA sample. For the complete population, the median age of the sources obtained with this technique is about 2 Myr. This is on the lower side of the typical age range associated to Cha II: 4 ± 2 Myr (Spezzi et al., 2008). The difference might be related to changes in the evolutionary models considered or because we now use the most recent Gaia distances. Previous to Gaia, the average distance assumed for the Cha II star-forming region was 178 pc (Whittet et al., 1997), while the most recent estimations give it at 198 pc in average (Dzib et al., 2018). This has a direct impact on the luminosity of the objects as can be seen in Fig. 2.7 (see faint and colored points). Because the objects are seen further away, their luminosity is higher. For low mass pre-main sequence stars, younger than $\sim 5 - 10\,\mathrm{Myr}$, this corresponds to younger objects in the evolutionary tracks (see Fig. 2.7). Further discussion on the age uncertainties have been presented in Section 1.1.2. Note that for the other star-forming regions included in this study, we also find slight modifications in the average age, the general ranking remaining consistent with previous studies. However, as the estimation of the ages of stellar associations is out of the scope of this study, we choose to keep using the published age of each star-forming region rather than the median age estimated by our method. On the other hand, the errors on stellar mass estimates are typically $\sim 0.2\,\mathrm{M}_\odot$ for solar type stars and we use our stellar mass estimates in the rest of the analysis.

DUST MASSES. Similarly, we recalculated the dust masses in a homogeneous way from millimeter or sub-millimetrer fluxes using equation 2.1 in Section 2.4.2. We adopt the same temperature-luminosity relation and grain opacities as described previously, as well as the most recent distances.

SAMPLE SELECTION. Because most of the samples used are only complete down to the brown dwarf limit, we considered only stars with derived masses above $0.1\,\mathrm{M}_\odot$. Moreover, as Baraffe et al. (2015) tracks stop at $\mathrm{M}_\star = 1.4\,\mathrm{M}_\odot$, we decided not to include stars where the fit of isochrone produces this value. I/ present the number of sources considered in this study in Table 2.5, along with the number of detected sources. All regions show comparable stellar mass distributions, except IC 348 which contains no stars between 0.9 and $1.4\,\mathrm{M}_\odot$.

2.5.1.c. Cumulative distributions

In order to compare all star-forming regions together, I used the Kaplan-Meier estimator (Kaplan and Meier, 1958) to generate the cumulative distributions of the dust masses and dust to stellar mass ratio of all star-forming regions. This estimator has been used in previous protoplanetary disks studies (e.g., Ansdell et al., 2016; Law et al., 2017) and has various other application fields as well (medicine for example). The Kaplan-Meier estimator is a non parametric method used to estimate the survival function from lifeline data. Compared to a simple histogram, this method is interesting because it takes into account the non detections (i.e., upper limits). The probability of sources to have a dust mass greater than M_dust with the Kaplan-Meier estimator is defined as follows:

$$\hat{S}(\mathrm{M}_\mathrm{dust}) = \prod_{\mathrm{M}_i < \mathrm{M}_\mathrm{dust}} \left(1 - \frac{d_i}{n_i}\right) \tag{2.3}$$

where d_i is the number of *detected* sources with exactly the mass M_i and n_i the total number of objects in the sample with $M_\mathrm{dust} \geq M_i$. I show an example of a fictional dataset in Fig. 2.8. I considered 13 disks with masses between 1 and 5, 4 of which being actually non detections, so upper limits. In the top right corner of the figure, I

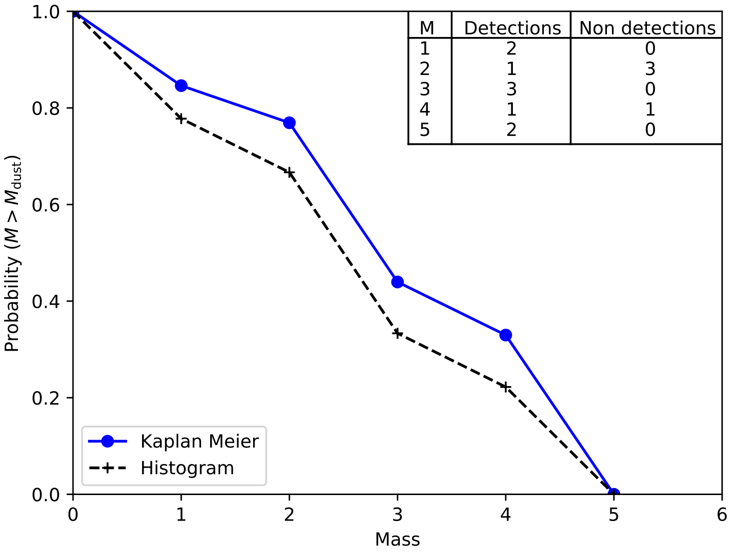

M	Detections	Non detections
1	2	0
2	1	3
3	3	0
4	1	1
5	2	0

Figure 2.8 – Example of cumulative distribution curves, obtained only with the detections (black curve) or with the Kaplan-Meier estimator including non detections (blue). The top right table indicates the sample considered to produce this plot, with M being the fictional mass of the objects.

indicate the number of sources detected for each bin of mass along with the number of sources with upper limits. The blue curve corresponds to the distribution obtained with the Kaplan-Meier estimator and the black one is a normalized histogram, considering only the detections. We can see that the Kaplan-Meier curve obtains larger probabilities than the histogram curve. For instance, in the example the probability of having a disk with a mass of 3 is higher when using the Kaplan-Meier estimator. This is because there is one disk, potentially more massive than 3, which was not detected (it has a mass upper limit of 4). This disk is not taken into account in the histogram method but the Kaplan-Meier estimator does consider it, which increases the probability of finding a disk more massive than 3. In practice, I used the `lifelines` package in Python to generate the cumulative distributions[3]. To conclude on this estimator, note that for most observed distributions, the upper limits are mostly located at the lower mass end of the distributions, which implies that the distributions obtained with the Kaplan-Meier estimator are not as dramatically different as in the example of Fig. 2.8. Only Taurus has a lot of non detections around low mass stars, which leads to non detections distributed over a large range of dust to stellar mass ratio and not only to the lower end.

In this work, we generate two families of cumulative distributions. First, as in previous studies, we estimate the cumulative distributions of $M_{\rm dust}$. They are shown in the left panel of Fig. 2.9, and scaled so that the maximum of each distribution

---

[3] See documentation at http://lifelines.readthedocs.io/

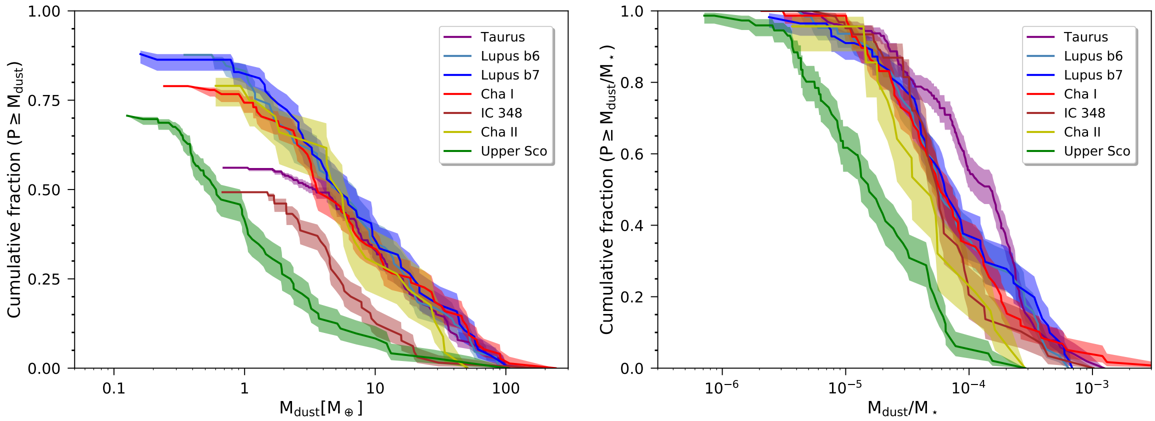

Figure 2.9 – **Left:** Cumulative distribution of the dust mass, generated by the Kaplan-Meier estimator and normalized by the fraction of detected sources in each star-forming regions.
Right: Cumulative distribution of the dust to stellar mass ratio generated by the Kaplan-Meier estimator. We indicate 1σ confidence intervals.

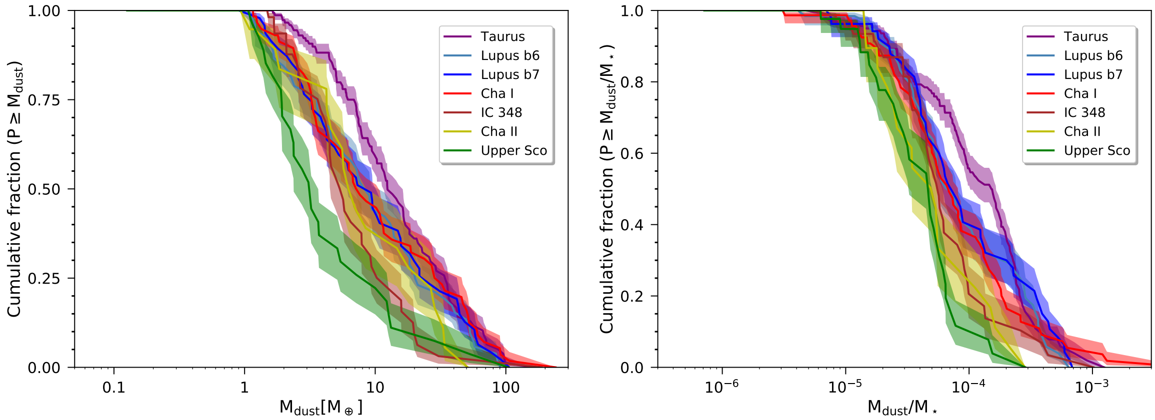

Figure 2.10 – Same as Fig. 2.9, but considering all systems with disk masses smaller than $1.08\,M_{\oplus}$ (the lowest mass detected in Taurus) as non detections.

Region	Published age (Myr)	Median $M_{\rm dust}$ ($M_\oplus$)	Median $M_{\rm dust}/M_\star$ (10^{-5})
Upper Sco	$5-11$	0.6 ± 0.2	1.6 ± 0.3
Cha II	$2-6$	5.6 ± 1.0	4.9 ± 1.4
IC 348	$2-3$	~ 1.5	5.4 ± 0.7
Cha I	$2-4$	3.5 ± 1.0	5.9 ± 1.2
Lupus b7	$1-3$	5.3 ± 1.6	6.4 ± 1.4
Lupus b6		5.4 ± 1.7	5.8 ± 1.1
Taurus	$1-2$	3.3 ± 0.8	15.2 ± 3.1

Table 2.6 – Median dust mass and dust to stellar mass ratio for each star-forming region, as estimated from the cumulative distributions presented in Fig. 2.9.

corresponds to the fraction of detected sources in each sample. We find that most distributions, including that of Cha II, have similar medians and shapes. However, Upper Sco and IC 348 show a noticeable difference compared with the other distributions, with median dust masses up to one order of magnitude smaller than in other regions. The median dust masses are reported in Table 2.6. This might be related to different effects such as differences in stellar populations with other regions (e.g., no stars between 0.9 and 1.4 $M_\odot$ in IC 348) or to the scaling factor used for the $M_{\rm dust}$ distribution, which might have to be modified if the samples are found not to be complete. For comparison, the median mass of the Class II objects studied in this work is found to be at least a factor of 5 smaller than masses of Class 0 and Class I objects in Orion star-forming region, as can be seen in Fig. 15 of Tobin et al. (2020). This suggests that Class II objects have evolved and lost dust mass since the first stages of their evolution.

Additionally, in order to limit the effect of different stellar population, we estimate the cumulative distributions of the dust-to-stellar mass ratio, which are shown in the right panel of Fig. 2.9. Again, we find that most regions have similar shapes. Only Taurus shows a different shape than in the plot of $M_{\rm dust}$, breaking away from the other curves, mostly because a large fraction of the non-detections are around low mass stars, which correspond to large $M_{\rm dust}/M_\star$ ratio. Moreover, the distributions appear shifted to progressively lower mass ratios as the age of the region increases (see median $M_{\rm dust}/M_\star$ ratio in Table 2.6). In the following subsection, we aim to estimate statistically whether all distributions of $M_{\rm dust}/M_\star$ are similar or not, looking for a potential evolutionary trend.

2.5.1.d. Statistical test

The observed ranking of the disk-to-stellar mass ratios is suggestive of an evolution of the disk properties with time. To test the significance of the observed shift in the mass ratio distributions, we performed a statistical test on all star-forming regions.

We use the logrank test, a non parametric method that compares the cumulative distributions of two samples, taking into account non-detections. This test is implemented in the `lifeline` Python package. The null hypothesis is that distributions of all regions are equal at all mass ratio. We performed one-by-one comparisons and present them in Table 2.7. The probabilities that the null hypothesis is correct (also called p-values) are shown in the bottom-left part of the table, and their interpretations are reported in the top-right side of the table. Regions that are statistically distinct (i.e., with p-values ≤ 0.001) are characterized by the symbol '***'. The symbols '**' and '*' are used for p-values between $0.001 - 0.05$ and $0.05 - 0.1$ corresponding to regions that are gradually less statistically different. Regions that are statistically indistinguishable (p-values > 0.1) are shown by the symbol '-'. Note that before adopting the logrank test, which was used by several other protoplanetary disks studies (e.g., Cazzoletti et al., 2019), I also tried the Kruskal-Wallis test (Kruskal and Wallis, 1952). The latter gives similar results but it is more reductive than the logrank test. Indeed, the Kruskal-Wallis test does not take into account the non detections, and also the null hypothesis is that all populations have the same median (rather than a global comparison of the distributions).

Using the $M_{\rm dust}/M_\star$ ratio, we find that Upper Sco is statistically different from all other star-forming regions (Table 2.7). Taurus is also statistically different from Cha II and marginally from IC 348 and Cha I. Although we see a progressive decline of the median of ratio with increasing age, these shifts are not significant at the 3σ level when the age difference is too small (≤ 2 Myr). Larger samples would be needed to confirm the observed trend. However, when larger time baselines are considered (≥ 3 Myr), the evolution of the luminosity function becomes significant. This result strongly suggests that disks evolve gradually with time, with a decrease of the relative mass of their millimetric dust grains compared with the star. This could be explained by accretion of those grains on the central star, formation of planets, or because, as grains grow bigger with time the millimeter wavelength opacity decreases. The lack of 3σ significance for small age differences may be corrected when more sensitive surveys are performed, larger samples are observed, or more accurate ages are available.

In parallel to the decrease of the median dust-to-stellar mass ratio with time (Table 2.5), a change in the detected disk fraction is observed in IR studies (Ribas et al., 2014). This indicates that not only the number of disks detected is declining with time, but also that the remaining disks have a lower mass. The global dust content of the disk seems to decrease with time.

2.5.1.e. Possible limitations of the luminosity functions analysis

Comparison between complete but inhomogeneous samples requires care. Here, all samples were observed with close but yet different sensitivities. The cumulative distributions were generated using the Kaplan-Meier estimator that considers the upper limits of non-detections. Nevertheless, to confirm the robustness of the analysis, I also performed the same analysis considering a common dust mass limit. In Fig. 2.10,

	Upper Sco	Cha II	IC348	Cha I	Lupus B7	Lupus B6	Taurus
Upper Sco		**	***	***	***	***	***
Cha II	0.01		-	-	**	*	***
IC348	9×10^{-7}	0.3		-	-	-	**
Cha I	$< 1 \times 10^{-7}$	0.2	0.6		-	-	**
Lupus b7	$< 1 \times 10^{-7}$	0.04	0.5	0.8		-	-
Lupus b6	$< 1 \times 10^{-7}$	0.06	0.8	0.9	0.4		*
Taurus	$< 1 \times 10^{-7}$	0.0003	0.02	0.04	0.2	0.07	

Table 2.7 – Results of pair comparisons with the logrank test applied on the ratio $M_{dust}/M_{\star}$. The lower left half of the table represents p-values for pairs comparisons, and the upper right half corresponds to the interpretation of the test. A p-value lower than 0.001 (***) corresponds to regions statistically distinct, p-values higher than 0.1 (-) to regions statistically similar, and P-values between 0.001 and 0.05 (**), and between 0.05 and 0.1 (*) to regions that are marginally different.

$M_{lim} = 1.08 M_{\oplus}$	Upper Sco	Cha II	IC348	Cha I	Lupus B7	Lupus B6	Taurus
Upper Sco		-	*	**	***	***	***
Cha II	0.4		-	-	**	**	***
IC348	0.07	0.4		-	-	-	**
Cha I	0.004	0.1	0.4		-	-	-
Lupus b7	0.0007	0.02	0.2	0.7		-	-
Lupus b6	0.001	0.03	0.4	0.97	0.4		-
Taurus	1×10^{-7}	0.0006	0.02	0.1	0.4	0.2	

Table 2.8 – Same as Table. 2.7, but considering all systems with disk masses smaller than $1.08\,M_{\oplus}$ (the lowest mass detected in Taurus) as non detections.

I show the distributions of $M_{\rm dust}$ and $M_{\rm dust}/M_\star$ when considering all systems with disk masses smaller than $1.08\,M_\oplus$ (the lowest mass detected in Taurus, see Table 2.5) as non detections. In that case the cumulative distribution of $M_{\rm dust}$ goes to 1 because we probe all disks which are more massive than the adopted limit. The results of the logrank test for these distributions are presented in Table 2.8. Although less significant, the results are similar to those presented above in this section: regions with an important difference in age are statistically different. Thus, by re-observing the same samples with higher sensitivities, and possibly with a homogeneous angular resolution, we do not expect significant changes in the results.

Binary systems were not filtered out from the samples, all the more so for unresolved binaries. However, binary systems have been shown to disperse their disk faster than single star systems (Cieza et al., 2009). Studying binaries in Taurus, Kraus and Ireland (2012) showed that this is particularly true for close binaries, with separations smaller than 40 au. At larger separation, disks around binaries are detected with similar occurrence than around single stars. In Ophiuchus, Cox et al. (2017) showed that the median flux around binaries is systematically 60% of the flux around single stars. In this study, we found that 5%, 12.5%, 40%, 10% and 32% of the sources used in the respective distributions of Upper Sco, Cha II, Cha I, Lupus and Taurus are known as binaries stars. Only one disk (non-detected) of IC 348 is a binary, of separation larger that 80 au (Ruíz-Rodríguez et al., 2018). However, a very limited fraction are known close binaries ($r < 40$ au): less than 1% of the considered stars in Upper Sco, Cha II and Lupus, and $\sim$ 8% in Cha I and Taurus. Therefore, binaries are not expected to modify the distributions significantly.

To convert the observed fluxes into dust masses, we also assumed that disks were always optically thin. However, this assumption might be partially incorrect. Indeed, recent observations of disks using high angular resolution have revealed that substructures are ubiquitous (Andrews et al., 2018b; Long et al., 2018), and in most cases associated to optically thick regions (e.g., Huang et al., 2018a; Dent et al., 2019). Additionally, a scaling relation between the millimeter flux and the disk size has been measured in a large number of disks, which also suggests that protoplanetary disks are partly optically thick (Tripathi et al., 2017; Andrews et al., 2018a). Nevertheless, the disks are not found to be totally optically thick so assuming the opposite (i.e., that dust is optically thin) gives a first order estimate of the minimal dust mass present in a disk, which we see decreases with the age of the star-forming region.

We also used a scaling relation between $T_{\rm dust}$ and $L_\star$ in the conversion process. This relationship was proposed and tested by Andrews et al. (2013) using radiative transfer models with a fixed outer radius ($r_{\rm out}$ = 200 au) and for a range of luminosity between 0.1 and $100\,L_\odot$. Using this equation for smaller disks or less luminous stars is expected to lead to over-estimations of the dust mass (van der Plas et al., 2016). However, we find that the average disk outer radius and the fraction of sources with lower luminosity are about similar in each study (see also Hendler et al., 2020). This should affect all distributions in a similar way. To ease the comparison with other studies, we have used the prescription from Andrews et al. (2013) throughout.

Finally, the interpretation of the distribution functions presented here relies on the age of each individual region based on previous studies, in most cases anterior to GAIA. The GAIA DR2 data release now provides individual distances for most stars. Although we have used the new distances to re-evaluate the stellar luminosities and therefore masses of each star, we have chosen not to re-assess the age of each association. This should be done in future studies.

2.5.2 *Gas detection rates*

The above subsection only applies to the evolution of dust mass, which we probe with continuum emission. However the disk mass is dominated by gas. Measuring the gas mass in protoplanetary disks is notably difficult (see Section 2.4.3). Instead, here we focus on the gas detection rates with the aim of comparing the respective detection rates of CO gas and dust continuum from disks of different ages. To do so, we gathered ALMA and SMA millimetric measurements to characterize the cold disk regions (continuum and CO isotopologues rotational lines), in the same star-forming regions as in the previous section. Samples are complete in the sense of ALMA capability in snapshot surveys, except for Taurus where only a limited number of sources was observed (only in ^{13}CO) using IRAM interferometer, leading to an incomplete survey.

In order to compare the different star-forming regions with each other, we selected subsamples of disks with similar spectral type distributions (K & M stars). This made necessary to remove the F0 disk (IRAS12496-7650) from our Cha II study. Then, only stars with disks detected in millimeter dust are considered, so that we compare gas detections in systems that posses a dusty disk with comparable mass limit.

Table 2.9 shows the detection rates in CO isotopologues for dusty disks in star-forming regions of different ages. For the two transitions traced, in the three probed isotopologues, a larger fraction of disks is detected in young regions than in older ones. This indicates that for young star-forming regions most of the disks that are detected in dust are also detected in ^{12}CO $-$ ^{13}CO, while for older regions the fraction of targets with detected dust and gas is lower. This decrease in detection rates from younger to older regions shows that CO emission is reduced with time. Moreover, as all of our targets are selected to be detected in dust with a similar mass limit (see Table 2.5), the apparent decrease of gas detection fraction suggests that CO dissipates faster than dust. This would imply either a decreasing gas to dust ratio or a decreasing abundance of these species, for example by a change of state from gas to ice or by photo-dissociation as the ^{12}CO becomes progressively optically thinner and less self-shielded. The small size of our samples and the fact that surveys were likely not performed with the exact same setup prevent from drawing definitive conclusions but the tentative evidence for a different evolutionary timescale for gas versus dust has potential interesting consequences.

	Transition	^{12}CO (%)	^{13}CO (%)	C^{18}O (%)
Upper Sco [a]	$3-2$	47		
Cha I [b,c]	$3-2$	> 26	26	2
Lupus [d]	$3-2$	> 58	58	18
Cha II	$2-1$	52	9	0
Lupus [e]	$2-1$	68	28	11
Taurus [f,g]	$2-1$	> 89	89	

Table 2.9 – Detection rates of CO isotopologues for sources detected in dust, ordered by decreasing age of the system, and separated accordingly to the transition observed. According to the isotopologue ratio, we expect to detect more sources in ^{12}CO than in ^{13}CO. This is indicated through lower limits in Cha I, Lupus and Taurus, where no ^{12}CO study are available. The Taurus survey in ^{13}CO is also not complete. *References:* (a) Barenfeld et al. (2016), (b) Pascucci et al. (2016), (c) Long et al. (2017), (d) Ansdell et al. (2016), (e) Ansdell et al. (2018), (f) Andrews et al. (2013), (g) Guilloteau et al. (2013)

Compiling results from *Herschel* using the [OI] 63 μm line, on disks detected in dust in Upper Sco, Cha II and Taurus (Mathews et al., 2013; Riviere-Marichalar et al., 2015; Howard et al., 2013), we find a similar trend. Gas in disks located in young regions is more often detected (91% in Taurus) than for disks in older regions (43% in Cha II and 17% in Upper Sco). In the context of photoevaporation models (e.g., Owen et al., 2011; Alexander et al., 2014), individual disks are thought to dissipate slowly in the first million years, while a photoevaporative flow removes gas from the disk. In this scenario, dust is not affected by the photoevaporative flow. This could explain our observations, where, as the age of the region increases, fewer of the disks detectable in dust are detectable in gas.

2.6 CONCLUSIONS

We have used ALMA to conduct a millimeter survey of 31 protoplanetary disks in the Chamaeleon II star-forming region. This region is particularly interesting to study disk evolution as its intermediate age of 4 ± 2 Myr is comparable to the median disk lifetime. Our ALMA observations cover the 1.3 mm continuum as well as the ^{12}CO, ^{13}CO and C^{18}O $J = 2-1$ lines. Out of 31 sources, 24 were detected in the continuum, 12 were detected in ^{12}CO, 3 in ^{13}CO and none in C^{18}O. The measured dust masses range from 270 $M_\oplus$ down to 0.6 $M_\oplus$. The CO disk sizes are found to be on average more than 3 times larger than the 1.3 mm continuum disk sizes. This can not be explained by optical depth effect only: grain growth and radial drift are needed to reproduce such difference in size.

A comparison of cumulative distributions between Cha II and 5 other star-forming regions shows that the dust mass to stellar mass ratio declines with time. This trend is statistically significant when the age difference is large. However, the ranking of the dust-to-stellar mass ratio distribution also holds for associations with small age differences. The correct ranking of the 6 distributions (or of their medians) is suggestive of a global evolutionary trend, although the significance between 2 adjacent curves remains at a statistical level $< 3\sigma$ for now. Further surveys including older star-forming regions or better age estimates will clarify that claim.

We also compared gas detection rates for various disks detected in millimeter continuum emission located in five star-forming regions. We find that gas is less likely to be detected in older regions than in younger ones. This suggests that either gas dissipates faster than dust, or that disks have a reduced gas to dust ratio (or CO abundance) when their age increases. However, the limited sample size and observational setups prevent us from drawing definitive conclusions.

To conclude, this work allowed to add statistical constraints on disk dissipation with time, and to evidence the effect of radial drift between star-forming regions of different ages (Cha II and Lupus). Having more constraints on these two mechanisms is important to understand the timescale available for planet formation. In the other projects of my PhD, I looked for further evidence of some of these evolutionary processes (in particular radial drift and vertical settling) in various individual objects.

3

SPATIAL SEGREGATION OF DUST GRAINS IN TRANSITION DISKS: NEW OBSERVATIONS OF J1608 & J1852

Contents

3.1 INTRODUCTION

Currently a large variety of substructures have been identified in protoplanetary disks, both using infrared and millimeter observations. A number of studies revealed rings (e.g., Huang et al., 2018b; Long et al., 2018; Muro-Arena et al., 2018), lopsided emission (e.g., Casassus et al., 2013; Cazzoletti et al., 2018b), spirals (e.g., Huang et al., 2018c; Benisty et al., 2017), and shadows (e.g., Benisty et al., 2018; Muro-Arena et al., 2020). Transition disks in particular, historically identified from their lack of infrared flux in their spectral energy distribution, possess an inner region depleted of dust and a large variety of substructures. Among other mechanisms (e.g., photoevaporation or dead zones, Owen et al., 2011; Pinilla et al., 2016), planets interacting with the disk can open the inner cavity and lead to the apparition of such structures. Planets are expected to shape the disk differently according to their mass. In particular, the relative cavity radius of different dust grain sizes depends on the planetary mass. Multi-wavelength observations at high angular resolution allow to test the potential presence of a planet carving the cavity. Additionally, observations at several wavelengths allow to characterize the efficiency of several evolutionary mechanisms affecting the dust, such as radial drift and vertical settling which I was particularly focusing on during my PhD.

In this chapter, I present the study of scattered light and millimeter observations of two transition disks, 2MASS J16083070-3828268 and RXJ1852.3-3700 (hereafter J1608 and J1852, respectively), observed with VLT/SPHERE and ALMA. Both disks are located in close-by star-forming regions, respectively Lupus and Corona Australis. I report all the relevant stellar parameters in Table 3.1. In this study, I modeled both disks using a radiative transfer code, aiming to bring constraints on radial and vertical segregation of dust particles with different sizes. This allows to discuss the efficiency of vertical settling and radial drift in these disks and additionally to estimate if planets can be at the origin of their cavities.

In this chapter, most of the text originates directly from Villenave et al. (2019), but I complement the analysis with additional details. In Section 3.2, I present the observations and data reduction, with SPHERE observations in Section 3.2.1, ALMA in Section 3.2.2 and the spectral energy distributions in Section 3.2.3. Then, the modeling procedure and results are detailed in Section 3.3. Finally, I present the comparison of our results with a larger sample of transition disks in Section 3.4.

3.2 OBSERVATIONS AND DATA REDUCTION

3.2.1 *SPHERE observations*

3.2.1.a. Observations and data reduction

Both disks around J1608 and J1852 were observed with IRDIS (Dohlen et al., 2008) sub-instrument of SPHERE (Beuzit et al., 2008) mounted on the Very Large Telescope. The observations were carried out in dual-polarization imaging mode (DPI, Langlois

Parameters		J1608	J1852
RA	(h m s)	16 08 30.7	18 52 17.3
Dec	(deg ′ ″)	-38 28 26.8	-37 00 11.9
Distance[a]	(pc)	156 ± 6	146 ± 1
Av	(mag)	0.1	1.0
SpT		K2	K2
Teff	(K)	4800	4850
$R_\star$	($R_\odot$)	2.00	1.17
$\dot{M}$	($M_\odot.yr^{-1}$)	10^{-9}	10^{-9}
$M_\star$[b]	($M_\odot$)	1.4 ± 0.1	1.0 ± 0.1
Age[b]	(Myr)	$8.3^{+4.4}_{-2.1}$	> 14

Table 3.1 – Stellar parameters.

(a) Gaia Collaboration et al. (2018), (b) Stellar masses and ages are calculated by Garufi et al. (2018) using Gaia DR2 distances and stellar tracks by Siess et al. (2000).

References: Alcalá et al. (2017) and Manara et al. (2014)

et al., 2014), in both J ($\lambda_J = 1.245\,\mu$m) and H-band ($\lambda_H = 1.625\,\mu$m) for J1608, and in H-band only for J1852.

J1852 was observed as part of the SPHERE Guaranteed Time Observations (GTO) program on May 15, 2017 (ID: 099.C-0147, PI: Beuzit), in H-band and using a coronograph, while J1608 was observed during the nights of June 18, and July 23, 2017 (ID: 099.C-0891, PI: Benisty). During the first epoch (June 18, 2017), we observed J1608 in H-band, with a coronagraphic mask (N_ALC_YJH_S, 0.185″ in diameter; Martinez et al., 2009; Carbillet et al., 2011). During the second epoch and to confirm the presence of a cavity, the disk was observed in J-band, without coronagraph.

The weather conditions were very different between each observation. In particular, the observations of J1852 were performed with relatively poor conditions, with a seeing of $\sim$ 1.2″. On the other hand, for J1608, the seeing was rather good during the first night (between 0.65″and 0.9″), and relatively poor during the second night (between 1.2″and 1.9″). Thus, for this target, I chose to focus on the modeling of the observations taken with the best observing conditions (during the first night, H-band, using a coronagraph). To illustrate the effect of seeing on the data, I represent the profile of the point spread function (PSF) reference images for the H-band observations of both J1608 and J1852 in Fig. 3.1. We consider that the PSF represents the angular resolution of the observations. On this figure, one can clearly see that the PSF of J1852 is broader than that of J1608. Due to the poorer weather conditions, the angular resolution of J1852 is slightly lower than that of J1608. Also, the PSF of J1852 presents side lobes which possibly indicate the poor correction by the adaptive optics system.

The images of J1608 and J1852 were reduced by collaborators (C. Ginski and J. de Boer) who generated total intensity and Stokes Q and U polarized maps, following the

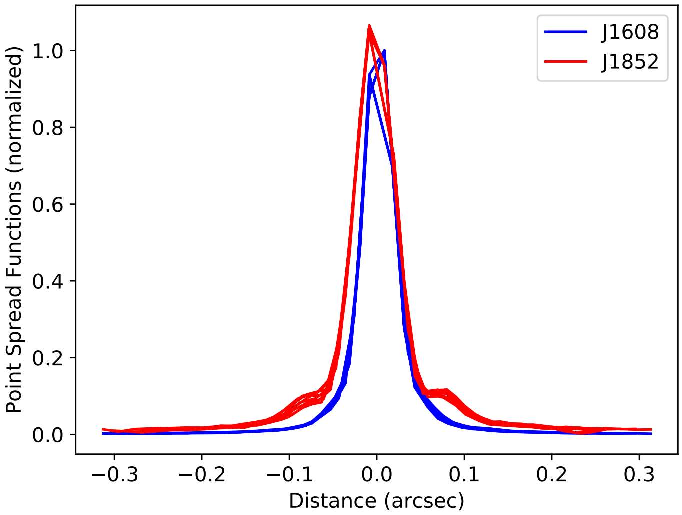

Figure 3.1 – Radial cuts on the PSF for the H-band observations of J1608 and J1852. J1852 presents side lobes and has a broader profile than J1608, indicating poorer weather conditions.

approach detailed in Ginski et al. (2016). Then, I computed the polarized intensity (PI) and the polar Stokes components Q_ϕ and U_ϕ of each disks using equations 1.19, 1.20, and 1.21.

3.2.1.b. Results

The reduced images of both disks are shown in Fig. 3.2. As a reminder, note that assuming single scattering events, the disk emission is expected to be included only in the Q_ϕ component, U_ϕ becoming a proxy for the noise (see additional discussion in Section 1.4.3). J1608 appears to be relatively inclined, in both images with and without the coronagraph. We detect two lobes southeast and northwest of the star, as well as a faint line of scattered light to the southwest that we interpret as the rear-facing side of the disk closest to us. In the Q_ϕ maps, the disk shows emission above the noise level up to 0.54″ along the major axis. The central cavity is clearly visible in both the coronagraphic and non-coronagraphic images. Additionally, there is no clear emission from the northeast of the star, corresponding to emission from the far side of the disk being scattered backwards toward us.

In the coronagraphic images of J1852 (bottom panels, Fig. 3.2), we observe two rings in the Q_ϕ map, with peak values located at 0.125″ and 0.295″ from the star along the major axis. The inner ring is cut off by the coronagraph and the peak radius may lie within this. The outer ring seems to be slightly off-centered compared to the inner ring ($\sim 0.01''$, 1 pixel), which is likely an effect of the inclination and flaring of the disk surface (e.g., de Boer et al., 2016; Ginski et al., 2016; Avenhaus et al., 2018). Finally, we note that the disk displays emission above the noise level as far as 0.4″along its major axis.

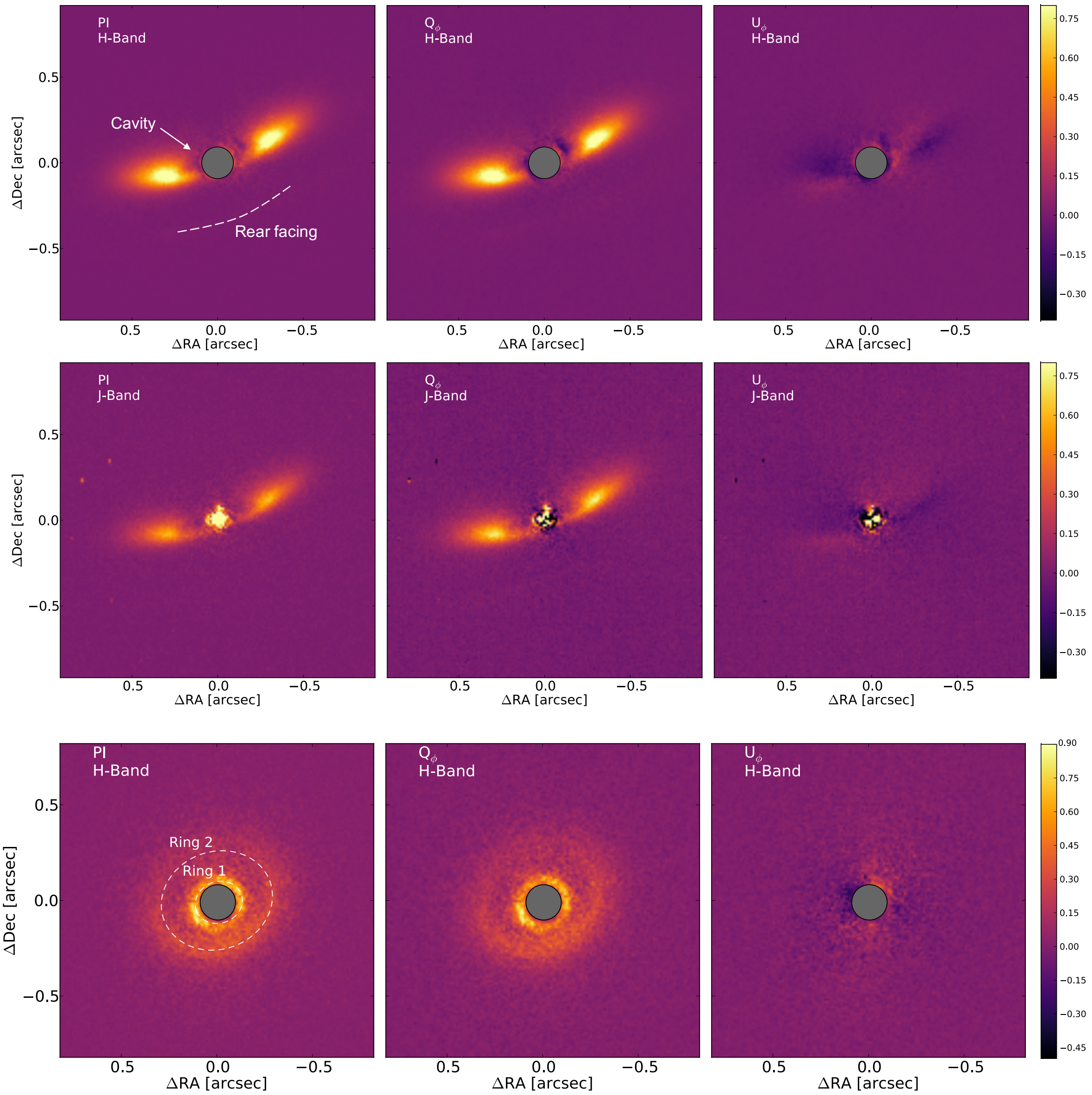

Figure 3.2 – Normalized polarized intensity (left panel), Q_ϕ (middle), and U_ϕ (right) maps of J1608 and J1852.
Top: H-band observations of J1608, obtained with a coronagraph, which is represented by the gray circle of diameter 0.185″. The dashed line in the left panel traces the faint scattered light from the rear-facing side of the disk (see also Fig. 3.11).
Middle: J-band observations of J1608, obtained without coronagraph.
Bottom: H-band observations of J1852, with a coronagraph. The dashed ellipses in the left panel represent the two scattered light rings (see text for details).
Each Q_ϕ and U_ϕ maps are normalized to the maximum of Q_ϕ.

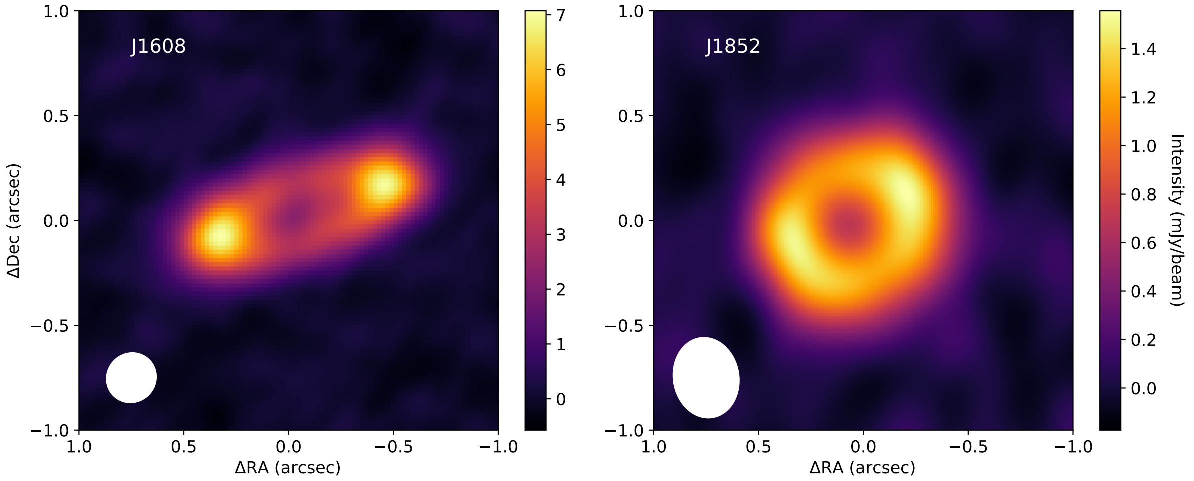

Figure 3.3 – ALMA continuum images of J1608 and J1852. The beam size is represented by an ellipse in the bottom left corner of each pannel.

3.2.2 *ALMA observations*

3.2.2.a. Observations and data reduction

J1608 was observed as part of a large survey of disks in the Lupus clouds. In this work, we used the band 6 observations (1.3 mm, Project ID: 2015.1.00222.S, PI: Williams) obtained on July 23, 2016, at a resolution of 0.24″ × 0.23″, and cleaned with a Briggs robust weighting parameter of +0.5. The data reduction of the continuum and line emission is presented in detail in Ansdell et al. (2018).

For J1852, we use ALMA data observed on September 22, 2016, in band 3 (3 mm, Project ID: 2015.1.01083.S, PI: Morino). The four continuum spectral windows were centered respectively on 91.5 GHz, 93.4 GHz, 101.5 GHz and 103.5 GHz. I used the CASA pipeline to calibrate the data and extracted the continuum images using the CASA `clean` task, with a Briggs robust parameter of +0.5. I performed self-calibration to improve the image quality and obtained a beam of 0.38″ × 0.31″.

3.2.2.b. Results

The continuum images of both disks are shown in Fig. 3.3 The large axis ratio observed in J1608 confirms that the disk is highly inclined. Moreover, the presence of two blobs with higher intensity along the major axis, located at 0.4″ from the star, denote emission coming from an optically thin ring. On the other hand, the image of J1852 shows one unique ring, peaking at 0.3″ along the major axis. The shape of the ALMA observations contrast with the SPHERE images which is likely related to the fact that we probe different grain sizes and regions of the disk.

Additionally, ^{12}CO $2-1$ transition was available in the observations of J1608. In order to characterize the radial location of the gas in this disk, I calculated the position-velocity (PV) diagram of this line (see Fig. 3.4), with a velocity resolution of 0.11 km s^{-1}. This diagram represents the intensity of the line, for each velocity

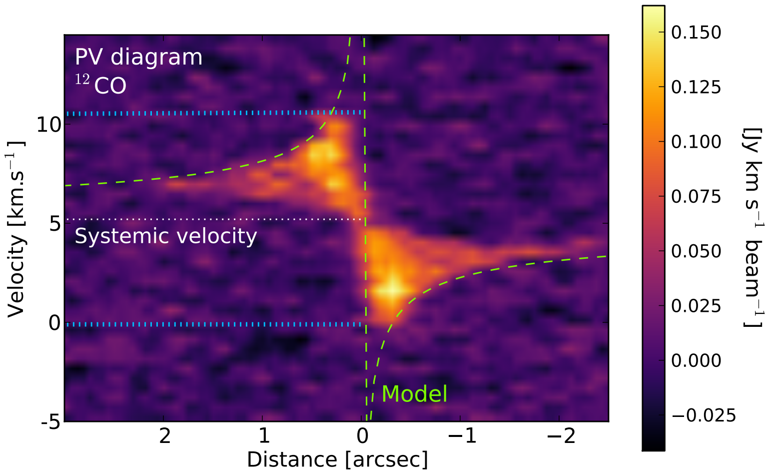

Figure 3.4 – Position-velocity diagram of the ^{12}CO $J = 2-1$ emission in J1608. The green dashed line corresponds to the Keplerian velocity of a disk at 74° of inclination around a 1.4 $M_\odot$ star. The highest velocity with emission is about 5.3 km s^{-1} from the systemic velocity. It corresponds to a gas cavity radius of $\sim$ 48 au, and is indicated by the blue lines.

channel (y-axis) as a fonction of the distance to the central star (x-axis). For a Keplerian rotation, the material reaches high velocities close to the star, while further away the disk is expected to rotate slower. The PV diagram of J1608 shown in Fig. 3.4 presents the characteristic shape of Keplerian rotation. From the center of this diagram, we can retrieve the systemic velocity of the source to be $+5.2 \pm 0.4$ km s^{-1} (LSR). We also note that, contrary to what is expected from Keplerian rotation of a continuous disk, no velocities higher than 5.3 km s^{-1} with respect to the star are detected (blue dotted lines in Fig. 3.4). This indicates the presence of an inner cavity devoid of gas. I modeled the disk velocities with Keplerian motion (assuming $M_\star = 1.4\,M_\odot$, i= 74°) and infered that the inner radius of the gas cavity is $\sim$ 48 au. This is in agreement with the outcome of previous thermo-chemical modeling of the CO observations (47 au, van der Marel et al., 2018).

3.2.3 *Spectral energy distributions*

To obtain a more complete view of the structure of both disks, we compiled their SED using Vizier or the VO SED Analyser [1] (VOSA, Bayo et al., 2008). For J1608, we complement this SED with the low-resolution Spitzer/IRS spectrum from the CASSIS database (Lebouteiller et al., 2011). The SEDs are shown on Fig. 3.5.

For both disks the SEDs show a steep increase longwards of 20 μm, typical of transition disks. Although J1852 does not show any clear near-IR excess, a silicate feature at 10 μm is present, characteristics of the presence of small hot grains close to the star (Silverstone et al., 2006; Hughes et al., 2010).

---

[1] http://svo2.cab.inta-csic.es/theory/vosa50

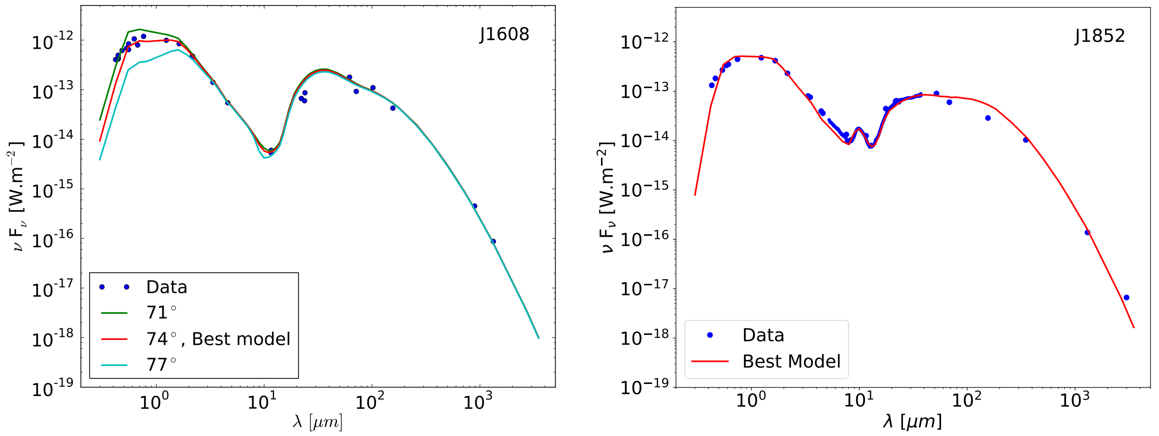

Figure 3.5 – Spectral energy distribution of J1852 and J1608 (blue circles) and our best model (red line). For J1608, I also indicate the effect of inclination at optical wavelengths. The models are corrected by interstellar extinction (Av).

3.3 RADIATIVE TRANSFER MODELING

3.3.1 *Methodology and model setup*

In order to understand the physical structure of the two observed TDs, I modeled both their SPHERE and ALMA images using the radiative transfer code MCFOST presented in Section 1.5. An iterative process is followed to find a model that reproduces well the SED and the images. Considering the complexity of our observations, the aim was not to find the best-fit model, but rather a representative one. For each set of parameters, I computed the SED, the millimeter continuum image as well as the near-IR polarized intensity, Stokes Q and U maps. All images are initially generated with infinite angular resolution, and then convolved with a PSF reference image of the SPHERE observations (see profiles on Fig. 3.1) or with the ALMA 2D Gaussian beam.

To match better the observations, we also add noise to our scattered light predictions. It is estimated at each point of the map from the U_ϕ image of our observations (as in Muro-Arena et al., 2018). For each point in the U_ϕ map, we consider an aperture in which we determine the rms of the intensity. The aperture is taken as 4 pixels of diameter, which is close to the FWHM of the PSF of each target (3.5 pixels for J1608 and 4.3 pixels for J1852). As our sources are inclined, the U_ϕ image might contain some physical signal (Canovas et al., 2015). Thus, in each aperture we subtract its mean value (physical signal) before extracting the rms. For each corresponding pixel in the model image, we simulate the noise by adding a Gaussian random number of the same rms centered on 0. The resulting noise maps are shown in Fig. 3.6, where the noise is normalized to the maximum intensity of the PI maps. We find that the noisiest region of both maps is located at the edges of the coronagraph. Note that we

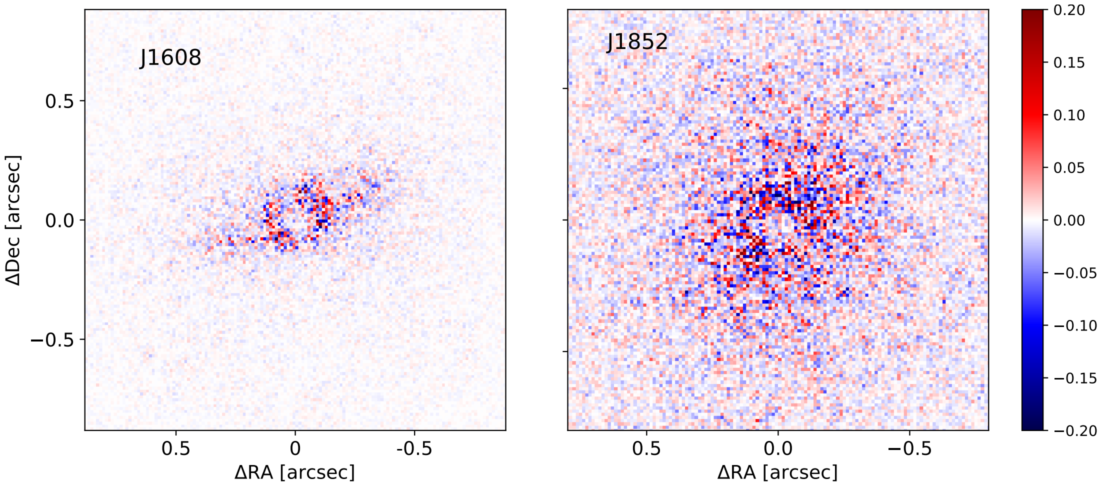

Figure 3.6 – Noise maps of J1608 and J1852, scaled to the maximum of the PI maps. The peak noise is found at the edges of the coronagraph.

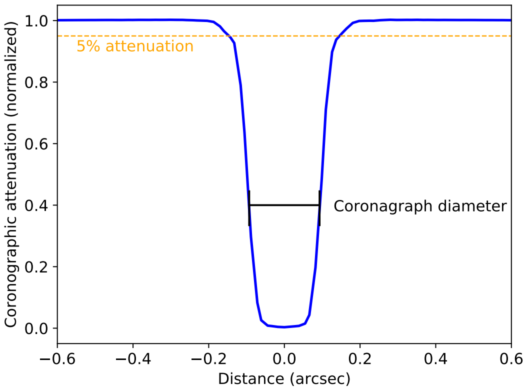

Figure 3.7 – Profile of the coronagraphic attenuation applied in our model of J1852. *Adapted from Wilby et al. (in prep.)*

did not add noise to the millimeter maps predictions, because the signal to noise of the observations is larger.

Since some emission very close to the coronagraph is modeled in the J1852 image, I applied a 2D attenuation map due to the coronagraph (Wilby et al., in prep.). A radial cut on this attenuation map is shown on Fig. 3.7. The mask removes all signal inside the coronagraph mask radius (0.093″), with gradually decreasing attenuation down to 5% at a radius of 0.15″. Finally, after convolving the models to the correct angular resolution and as for the observations, we compute the PI, Q_ϕ and U_ϕ maps using equations 1.19, 1.20, and 1.21. To find a good model, we only compare the observed and synthetic PI images. After this is done, we compared also the observed and predicted Q and U.

For the modelisation, we define various axisymmetric disk zones to reproduce the observed features of the two disks and assume a gas-to-dust ratio of 100. For each region, we define the disk height and the surface density profiles as in equations 1.7 and 1.10 (truncated power low). In all our models, we fix the surface density exponent to $p = 1$. We use astronomical silicates (assumed to be compact spheres) with a number density described with a power law of the grain size $\mathrm{dn(a)} \propto a^{-3.5}\,\mathrm{da}$ (Mathis et al., 1977). For each region, our free parameters are the inner and outer radius ($R_{\mathrm{in}} - R_{\mathrm{out}}$), the dust mass and the scale height ($\mathrm{H}_{100\,\mathrm{au}}$).

For both disks, we mimic dust settling by modeling separately the spatial distribution of small ($0.01 - 0.5\,\mu$m) and large grains ($10 - 1000\,\mu$m). We fixed the flaring exponent β to 1.1 for all type of grains. The results are summarized in Table 3.2 and described in detail in the following two subsections. Additionally, Fig. 3.14 shows a schematic representation of the structure obtained for large and small grains in both disks.

3.3.2 *Modeling J1608*

3.3.2.a. Large grains

We first aim to reproduce the thermal emission detected in the ALMA band 6 data by considering a ring of large grains. We adjust the dust mass to fit the total millimeter flux and modify the radial and vertical extent of the ring to match the images. Our convolved model at 1.3 mm is presented in the top-center panel of Fig. 3.8. The right panel of this figure shows radial cuts along the major and minor axis, both for the model and the observations. In our model, the radial position of the maxima as well as the radial extent in each cut are well reproduced. However, the model overestimates the flux in the inner region of the disk (i.e., inside the gap) by about 30%.

The radial width of the ring made of large grains has to be sufficiently small so that the position and shape of the maxima of the cut along the major axis matches the data. We find that, for the large grains ring, a radial width of about 10 au is consistent with the data, with $\mathrm{R}_{\mathrm{in}} \sim 77$ au. However, a narrower ring would still reproduce the observations.

To reproduce the observed aspect ratio of the disk and the SED, a high inclination is needed ($\sim 74°$). In Figure 3.5, I show the effect of the inclination on the SED. We see that models at lower (71°) or larger (77°) inclinations do not match the photometry at $\sim \mu$m wavelengths. If the inclination is too large the photosphere is highly occulted at short wavelengths. Also, note that the inclination has very little effect at larger wavelengths.

Finally, the fluxes of the peaks and depth of the gap along the minor axis depend both on the radial width and the vertical thickness of the disk. If the scale height of the large grains is too large, after convolution by the beam, the two sides of the ring would appear as connected, leading to a flat intensity profile along the minor axis. On the other hand, if the zone of large grains is too vertically thin for a given disk mass, the fluxes at the peaks of the minor axis cut would become too large. The

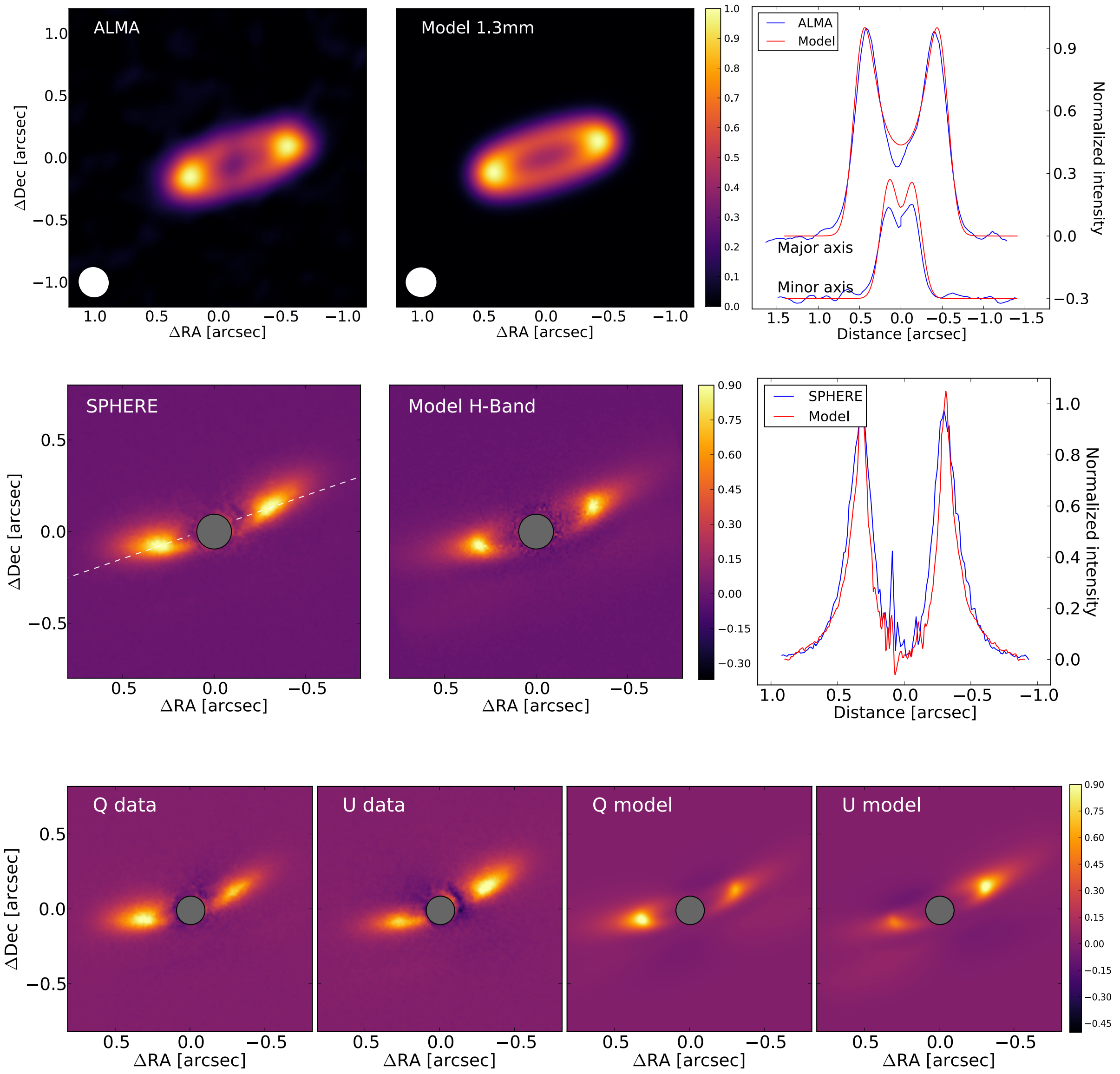

Figure 3.8 – Data and model images of J1608.

Top: ***Left:*** Normalized ALMA band 6 image (peak flux of 7.1 mJy). The beam is shown in the bottom left of the image. ***Middle:*** Normalized model obtained after convolution by a beam of $0.24'' \times 0.23''$. ***Right:*** Radial cuts along the major and minor axis, with each map normalized to its maximum. For clarity, the cut along the minor axis is shifted by -0.3 in normalized intensity. The peaks are located at $0.4''$ (62 au) along the major axis and $0.14''$ (22 au) along the minor axis.

Middle: ***Left:*** Observed PI image. ***Middle:*** PI model map. Both maps are normalized to their maximum. ***Right:*** Radial cuts along the major axis for the PI images of the data and model, smoothed with a Gaussian kernel with a standard deviation of 9 mas. The position of the cut is indicated by the dotted line in the left panel.

Bottom: Q and U normalized maps of the data and model without noise.

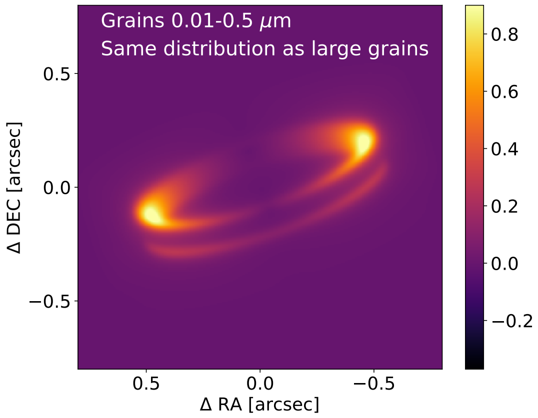

Figure 3.9 – Synthetic scattered light image of J1608 computed assuming the same spatial distribution for small grains and large grains, without adding noise. It does not provide a good match of the data, which indicates that there is a difference in spatial segregation between small and large grains.

appropriate scale height in our modeling, $H_{100\,\mathrm{au}}$, is between 1 and 5 au, which is similar to the value obtained for HL Tau (1 au at 100 au, Pinte et al., 2016). All the model's parameters are presented in Table 3.2.

3.3.2.b. Small grains

The synthetic scattered light image computed assuming the same spatial distribution for small and large grains does not provide a good match to the images (see Fig. 3.9). To reproduce the observations, the radial extent of small grains and their scale height need to be larger than those of the large grains, from 50 to 150 au radially, and about 12 au vertically at 100 au. Note that this layer is already included in the millimeter predictions displayed in Fig. 3.8, but does not contribute significantly at millimeter wavelengths. The scattered light image of our model is presented in the middle panel of Fig. 3.8, with a cut along the major axis direction. The cuts were smoothed with a Gaussian kernel with a FWHM of 50% the measured image resolution ($\sim$ 10 mas). The inner radius of the small grains distribution is very close to that of the gas, as estimated from the PV diagram (48 au, see Fig. 3.4), consistent with the expectation that these grains are well coupled to the gas (see Section 1.3.2).

We also note that, in the observations, no scattered light is detected from the northeast part of the disk (see Fig. 3.2). Geometrically, the existence of the bottom line located in the southwest suggests that it traces the part of the disk nearest to us, while the northeast region would correspond to the more distant side of the disk. This implies that the phase function of the polarized intensity is such that there is no or very little backward scattering (on the assumption that the disk is axisymmetric). The polarized intensity is the product of the polarization degree and the total intensity. While the polarization degree from backward scattering is similarly low for all grain

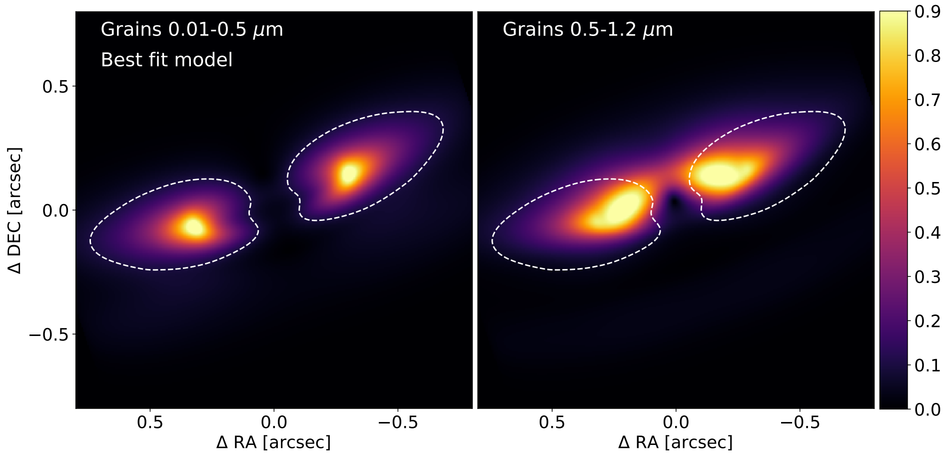

Figure 3.10 – Model of the scattered light emission for J1608, using the grain size from the best fit model and slightly larger grains, without adding noise. The largest grains emit efficiently in backward scattering which is not see in our observations. I use a different colorscale than in Fig. 3.8 to increase the contrast of the feature.

size (see Fig. 7 of Keppler et al., 2018), the phase function of the intensity varies significantly with the grain size. We reproduce this feature by selecting grains smaller than 0.5 μm. For grains with an intermediate size (between 0.5 and 1.2 μm), backward scattering is very efficient, which leads to a significant signal northeast of the disk coming from its far side. I show the effect of the grain sizes on backward scattering with our model of J1608 in Fig. 3.10. In both panels, the dashed line indicates the position of the two lobes for the models with grain sizes between 0.01 and 0.5 μm. The smallest grain population reproduces better the observations which suggests that grains between 0.5 and 1.2 μm are not a dominant population in this disk.

To summarize, we are able to recreate the general structure seen in J1608, with two lobes along the major axis, no emission from the northeast region of the disk (backward scattering) and a faint line south of the disk, but these characteristics are not perfectly reproduced. For example the southern line is brighter in our model than in the observations (see Fig. 3.11). To reproduce better this part of the image, the layer of small grains scattering light must be thinner vertically, but this in turn has an impact on the extent of the lobes. Moreover, the southern line is closer to the star than in the data. A way to push this line further would be for example to increase the mass of the scattering grains, the scale height or the inclination. However, each case would lead to an extinction of the photosphere that is not observed in the SED. Thus the model that we present here is a compromise to reproduce both the ALMA and SPHERE images, together with the SED. This should be considered as a working model to derive the main structural characteristics of the J1608 system. These are: 1/ a high inclination, 2/ large grains more compact vertically and radially than the small grains, and 3/ a distribution of size in small grains that produces low polarized intensity in backward scattering.

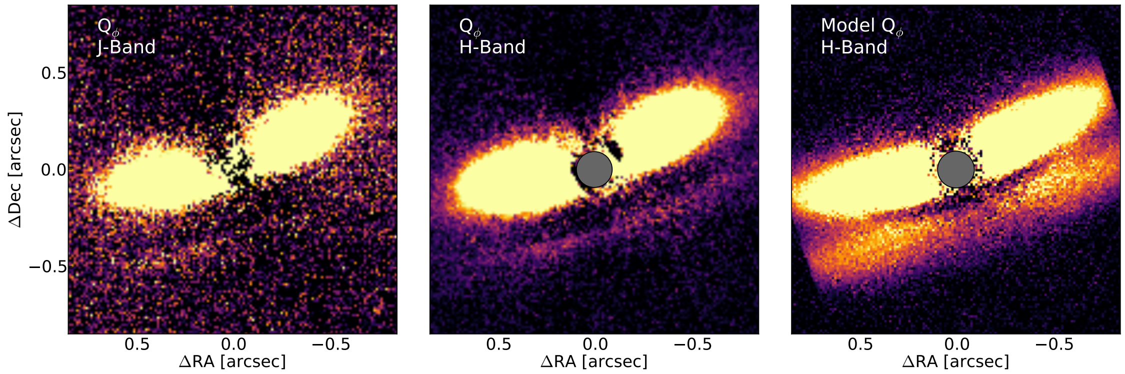

Figure 3.11 – Q$_\phi$ images of J1608 in J-band (non coronagraphic, left panel), H-band (coronagraphic, middle panel), and H-band model image (right panel) with a dynamical range from 0 to 5% of the maximum of each image. The bottom line of the disk is seen more clearly in the data than in Fig. 3.2 thanks to an increased contrast. It appears to be too bright in the model compared to the data.

3.3.3 *Modeling J1852*

The SED of J1852 (right panel of Fig. 3.5) shows a steep increase around 20 μm, typical of transition disks, due to the outer edge of the cavity. A clear silicate feature at 10 μm is present, characteristic of small hot grains close to the star. While the scattered light image (see Fig. 3.2) shows signal just outside of the coronagraph, there is no corresponding clear millimeter emission at the same location. The scattered light image shows a second bright ring at 0.295″, which does correspond to the ring detected in the millimeter image.

To reproduce the scattered light and SED features, we consider three zones in our model: 1/ a tenuous inner disk region, solely required to reproduce the silicate feature, 2/ an inner ring, responsible for the sharp jump in the mid-IR SED and for the emission seen in the SPHERE image just outside of the coronagraph radius, and finally, 3/ an outer ring, to account for the second brightness increase in the near-IR polarized image and the millimeter ring. The three zones are described in the following sections, after which we will detail the strategy modeling the millimeter data. The model of J1852 is presented in Fig. 3.12. The structure is illustrated in the bottom panel of Fig. 3.14.

3.3.3.a. *Small grains*

Inner disk. The inner region, responsible for the silicate emission around 10 μm in the SED, is modeled by small grains ($0.01 - 5\,\mu$m) between 0.1 and 5 au. To reproduce the shape of the emission of the inner disk, we consider a mixture of silicate, composed at 65% of olivine (Dorschner et al., 1995) and 35% of astronomical silicates (Draine and Lee, 1984). However, note that these parameters are not well-constrained.

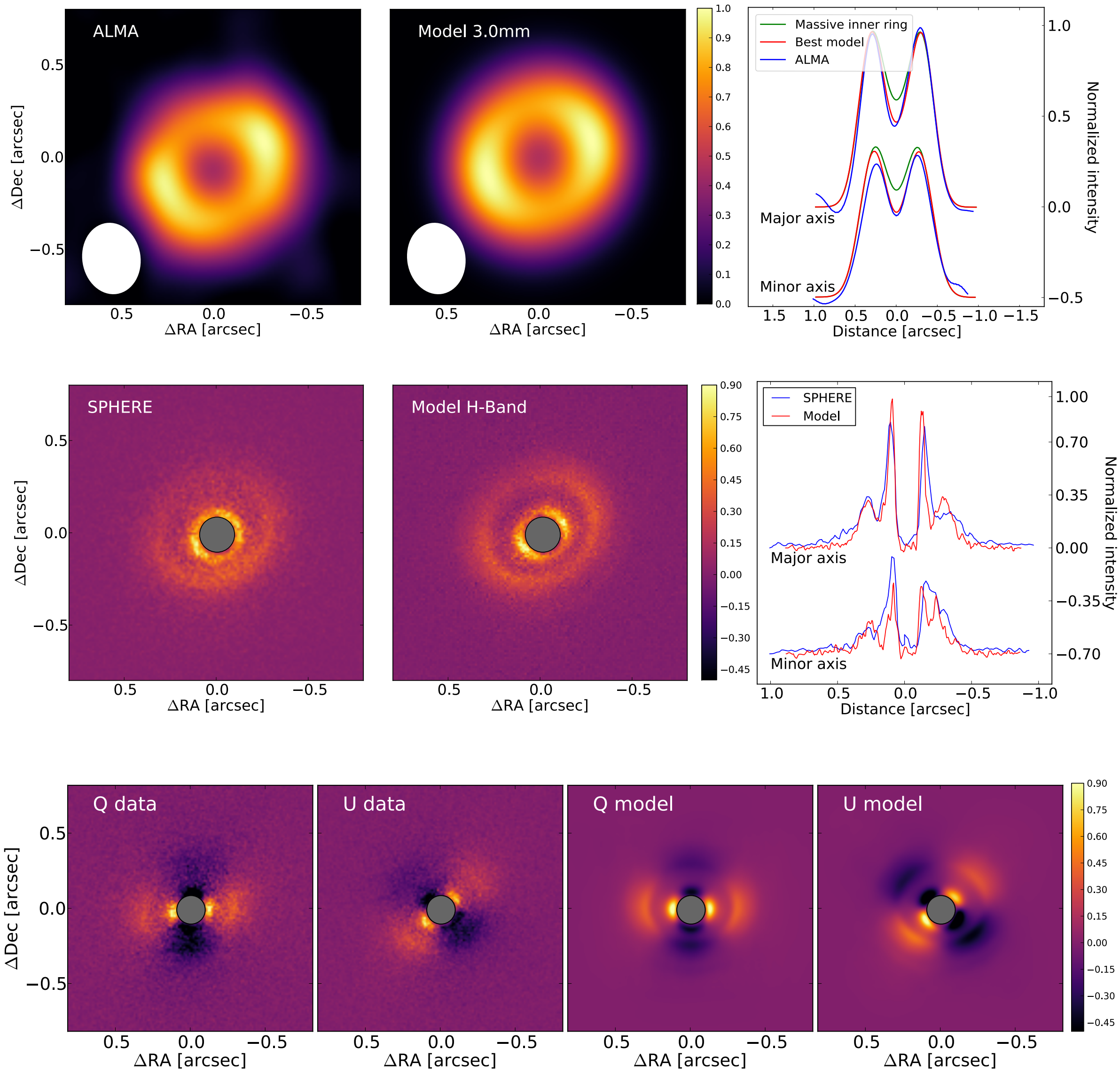

Figure 3.12 – Data and model images of J1852.

Top: ***Left:*** Normalized ALMA band 3 image (peak flux is 1.5 mJy). The beam is represented in the bottom left corner of the image. ***Middle:*** Normalized model obtained after convolution by a beam of $0.38'' \times 0.31''$. ***Right:*** Cuts along the major and minor axis, with each map normalized to its maximum. For clarity, the cut along the minor axis is shifted by -0.5 in normalized intensity. The peaks are located at $0.3''$ (44 au) along the major axis. The green curve corresponds to a model in which the dust mass of the inner ring is $2 \cdot 10^{-6}\,M_\odot$ instead of $3 \cdot 10^{-7}\,M_\odot$ for the best model. A massive inner ring in the millimeter is not consistent with the data.

Middle: ***Left:*** Observed PI image. ***Middle:*** PI model map. Both maps are normalized to their maximum. ***Right:*** Radial cuts along the major and minor axis for the PI images of the data and the model. Each curve is smoothed by Gaussian kernel with a standard deviation of 11 mas.

Bottom: Q and U normalized maps of the data and model without noise.

Inner ring. The position of the wall in the SED traces the dust temperature, which is dependent on both the inner radius and the dust size. For simplicity, we chose to use the same grain size distribution as for J1608. As the inner radius of J1852 is likely located behind the coronagraph, we constrained it using the SED. We reproduce well the inner ring by defining its radial extent between 15 and 22 au, with a scale height $H_{100\,\mathrm{au}}$ of 15 au.

Outer ring. To reproduce the peak of intensity around 0.295″ (~ 43 au), an increase of the surface density in the small grains is needed, between 42 and 65 au. The mass of this region is adjusted to reproduce the relative brightness of the rings and the SED. The scale height is fixed to be the same as that of the inner ring.

Our model reproduces relatively well the position and the brightness of the peaks along the major and minor axis directions. The second ring shows an offset to the center as seen in the data. However, we were not able to reproduce the surface brightness inside the gap between the inner and outer ring in the southern part of the disk. This region is twice brighter in the data than in the model. In our model the gap is empty and the ring edges are sharp, while in practice, a low surface density of small grains could be filling it.

3.3.3.b. Large grains

Unlike J1608, we do not have sufficiently high angular resolution data of J1852 to show that the large grains are radially distributed differently to the small grains, so for now we assume that they are radially co-located. We adjusted the total mass of the large grains to reproduce the observed SMA flux at 1 mm and the ALMA 3 mm flux in the SED. Also, to match the relative flux in the center of the millimeter ring, we needed to allocate a small fraction of mass to the inner ring. In the top-right panel of Fig. 3.12, I show the millimeter cuts for the best model (in red) and for a second model (in green) for which the mass of the inner disk is about one order of magnitude larger than in the best model. This second model does not fit the center of the cuts, which indicates that the inner ring is not massive in millimeter grains.

With our assumptions on the radial structure and grain composition of the large grain population, we inferred its scale height from the effect on the 100 μm emission. Indeed when the scale height is larger, as more grains receive light from the star, they warm up and emit more at 100 μm (Dullemond and Dominik, 2004; Woitke et al., 2016). To fit the SED, it was necessary to reduce the scale height of the large grains to about 1 au at 100 au. However, it should be noted that modeling the SED is degenerate. In particular, changing the minimum size of the large grain population (a_{min} in Table 3.2) from 10 to 300 μm, we find that the small and large grain populations could be distributed similarly and share the same scale height, while leading to similar excess and images as in the previous model.

		J1608	J1852	
Inclination	$(^\circ)$	74	30	
PA	$(^\circ)$	19	34	
			Inner disk	
$a_{\mathrm{min}} - a_{\mathrm{max}}$	$(\mu\mathrm{m})$	-	$0.01 - 5$	
$R_{\mathrm{in}} - R_{\mathrm{out}}$	(au)	-	$0.1 - 5$	
Dust mass	$(\mathrm{M}_\odot)$	-	$9 \cdot 10^{-11}$	
$\mathrm{H}_{100\mathrm{au}}$	(au)	-	0.9	
			Outer disk	
			Small grains	
$a_{\mathrm{min}} - a_{\mathrm{max}}$	$(\mu\mathrm{m})$	$0.01 - 0.5$	$0.01 - 0.5$	
$R_{\mathrm{in}} - R_{\mathrm{out}}$	(au)	$50 - 150$	$15 - 22$	$42 - 65$
Dust mass	$(\mathrm{M}_\odot)$	$2 \cdot 10^{-6}$	$2 \cdot 10^{-8}$	$7 \cdot 10^{-7}$
$\mathrm{H}_{100\mathrm{au}}$	(au)	12	15	
			Large grains	
$a_{\mathrm{min}} - a_{\mathrm{max}}$	$(\mu\mathrm{m})$	$10 - 1000$	$10 - 1000$	
$R_{\mathrm{in}} - R_{\mathrm{out}}$	(au)	$77 - 87$	$15 - 22$	$42 - 65$
Dust mass	$(\mathrm{M}_\odot)$	$5 \cdot 10^{-5}$	$3 \cdot 10^{-7}$	$7 \cdot 10^{-5}$
$\mathrm{H}_{100\mathrm{au}}$	(au)	$1 - 5$	$1 - 15$	

Table 3.2 – Parameters for our radiative transfer models. Each parameter was adjusted during the modeling, except for the grain size ($a_{\mathrm{min}} - a_{\mathrm{max}}$).

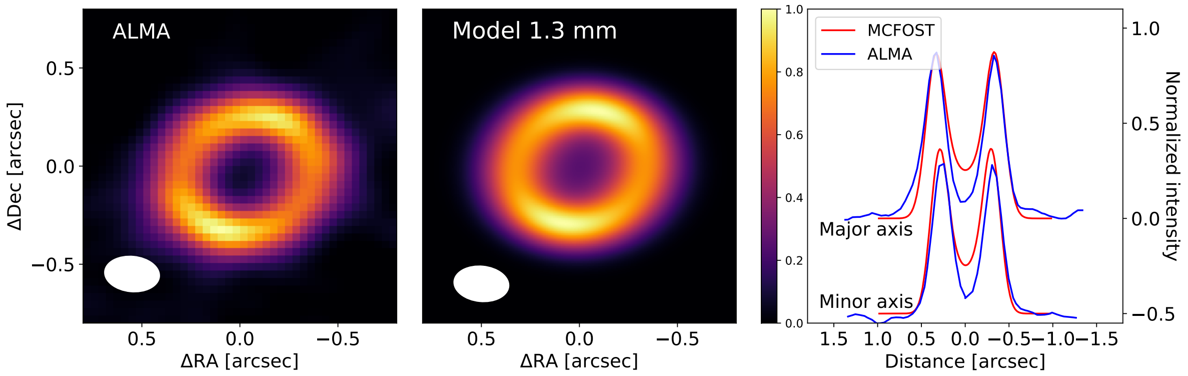

Figure 3.13 – **Left:** Normalized ALMA band 6 image of J1852 (peak flux is 7.3 mJy). The beam is represented in the bottom left corner of the image.
Middle: Normalized model obtained after convolution by a beam of $0.28'' \times 0.18''$.
Right: Cuts along the major and minor axis, with each map normalized to its maximum. For clarity, the cut along the minor axis is shifted by -0.5 in normalized intensity.

Since the study was published, band 6 observations of J1852 with a better angular resolution than our band 3 data became public (Project ID: 2015.1.01083.S, PI: Morino). I show the data products (delivered by ALMA) in the left panel of Fig. 3.13, and the image of our model computed at the same wavelength in the middle panel of this figure. The model matches very well the observations. The only big difference is found in the center of the ring, where the flux is higher than in the observations. This suggests that the inner ring is likely less massive than what is assumed in our model (see also the non detection of the inner ring at millimeter wavelengths in Francis and van der Marel, 2020).

3.4 DISCUSSION

3.4.1 *Dust vertical distribution*

The radiative transfer modeling of J1608 indicates that small and large grains have a different spatial distribution (see Table 3.2). Small grains ($< 1\,\mu$m) are found to be more extended vertically than large grains ($> 10\,\mu$m). We find small grains up to a height of 15 au at 100 au, in agreement with other results around T Tauri stars (e.g., Burrows et al., 1996; Wolff et al., 2017; Pohl et al., 2017a). In contrast, to reproduce the ALMA image and SEDs, the height of the large grain layer at 100 au has to be of a few astronomical units.

In this work, we compare our results with ideal MHD simulations by Fromang and Papaloizou (2006). In this numerical study, the authors considered a strongly magnetized and turbulent disk, with a viscous coefficient of $\alpha \approx 1.5 \times 10^{-2}$ and no grain growth. They obtain that the scale height of 10 cm bodies ($St = 0.1$) is about $H_{100\,\mathrm{mm}} \approx 0.23\,H_{\mathrm{gas}}$ (equation 43 of Fromang and Papaloizou, 2006), which

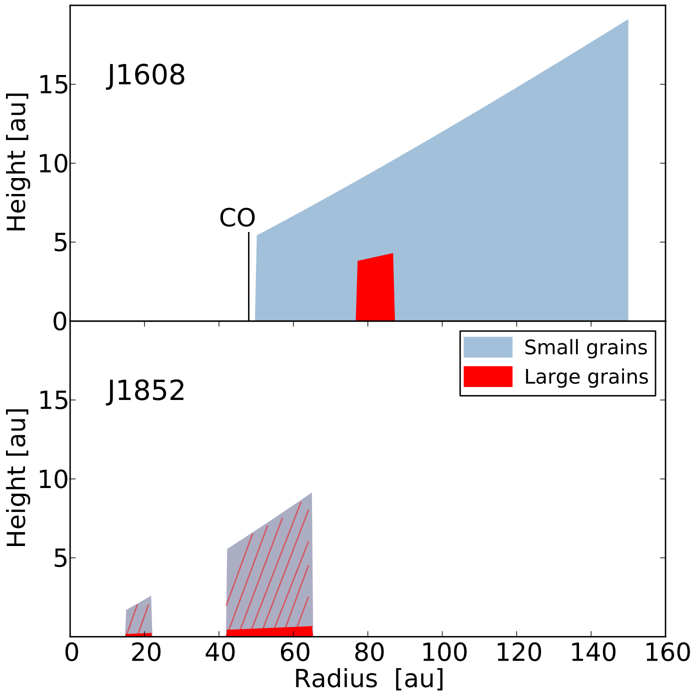

Figure 3.14 – Modeled radial and vertical structure for small and large grains in J1608 and J1852, in linear scale. The vertical black line indicates the inner radius of the disk in CO, as measured on the PV-diagram (Fig. 3.4). The red hatches in J1852 represent the uncertainty on the scale height of the large grain population that is not well constrained by our model. The innermost disk of J1852, located between 0.2 and 2 au, is too small to be visible in this representation.

seems too large to account for current estimates from observations. If we assume that scattered light traces the gas and that all light at 1.3 mm is emitted by grains of similar size (Draine, 2006), the modeling of J1608 gives millimeter dust scale height of the order of 1 to 5 au at 100 au, which corresponds to $H_{1.3\,\mathrm{mm}} = 0.08 - 0.41\,H_{\mathrm{gas}}$. This is similar or smaller than the predictions of Fromang and Papaloizou (2006) for particles 100 times larger, which are expected to be considerably more settled. This suggests that ideal MHD induced turbulence is too strong to reproduce the observations.

On the other hand, settling is more efficient for disks with low turbulence (Dullemond and Dominik, 2004), if the grain size distribution contains fewer small grains or if the gas-to-dust ratio is low (Mulders and Dominik, 2012). Moreover, in the outer parts of the disk the ionization fraction might be such that a perfect coupling to magnetic field is unlikely, and non-ideal effects might be expected. In this context, Riols and Lesur (2018) showed that ambipolar diffusion allows much more efficient settling of large grains than in perfect MHD models, allowing to reproduce the constraints on HL Tau (see further discussion in Chapter 4).

3.4.2 *Dust radial distribution*

OUTER RADIUS. Our model of J1608 shows that small grains extend to larger radii than large grains (see Table 3.2). This is expected as small grains are predicted to be well coupled to the gas, well detected beyond the ring seen in the ALMA image. On the other hand, large grains are (partially) decoupled from the gas, and experience radial drift and dust trapping. Earlier studies have shown that the gas outer radii extend further than the ones measured in the millimeter continuum. An average ratio between the gas and millimeter dust outer disk radii of 1.96 ± 0.04 was found in 22 disks of the Lupus star forming region (Ansdell et al., 2018). This trend is also observed in 12 disks in Chamaeleon II (see Chapter 2) and in individual disks such as PDS 70 where the gas is detected up to 160 au and millimeter dust up to 110 au (Long et al., 2018). Note however that the sensitivity limits between the ALMA observations in CO and those in polarized scattered light are different. The outermost radius at which scattered light is detected depends on the stellar illumination (which drops as r^{-2}). Besides the sensitivity limits, the difference between gas/small grains and large grains can be due to optical depth effects combined with radial drift of the large grains (Facchini et al., 2017). Depending on the inclination of the system, the vertical height of small grains can also have a large effect on their detectable radius. If the vertical height of small grains decreases after some radius, the surface layers could be located in the shadow of the inner region and would not be detected in scattered light (Muro-Arena et al., 2018).

INNER RADIUS. From the PV diagram shown in Fig. 3.4 and our modeling, we found that both the small grains and gas in J1608 extend inwards of the large grains, indicating that the cavity is not completely empty. Likewise, an inner ring in scattered light is detected inside the millimeter cavity of J1852. A similar conclusion was reached on several other transition disks, which show a CO cavity smaller than the millimeter dust cavity, such as Sz 91 (Canovas et al., 2015; Canovas et al., 2016) or RXJ1604.3-2130A (Zhang et al., 2014) for example. In each of these systems, the authors found the CO to extend at least 20 au inward of the outer edge of the millimeter dust cavity. These differences in inner radius could be related to the mechanisms responsible for the cavities in transition disks, which we explore in the next subsection.

3.4.3 *Comparison with other transition disks and cavity origins*

Several mechanisms have been proposed to explain the origin of cavities in transition disks: photoevaporation (Owen et al., 2011), dead zones (Flock et al., 2015; Pinilla et al., 2016), opacity effect via grain growth (Dullemond and Dominik, 2005; Birnstiel et al., 2012), or planetary/stellar companion interacting with the disk (Crida and Morbidelli, 2007; Facchini et al., 2013).

In this work, I explored in more details the potential planetary origin of cavities of transition disks. Several numerical and analytical works showed that planets of mass larger than 1 $\mathrm{M_J}$ can carve gaps in the gas and induce large perturbations in the gas surface density (Dong and Fung, 2017). In turn, they generate pressure maxima that trap dust particles. In this case, the inner region of the disk is depleted of millimeter grains, while smaller grains can flow inside the planet's orbit, and potentially be detected in scattered light (de Juan Ovelar et al., 2013; Dong et al., 2015a).

For this analysis, I used specifically the results from de Juan Ovelar et al. (2013), who performed synthetic observations of hydrodynamical and dust evolution simulations, considering a massive planet on a circular orbit. The initial parameters for the 2D hydrodynamical simulations are a viscous parameter of $\alpha = 10^{-3}$, a surface density profile of $\Sigma \propto r^{-1}$ and a temperature profile following $T \propto r^{-1/2}$, and they are run for 1000 planetary orbits. The obtained maps are then azimuthally averaged to be used as initial conditions for dust evolution simulations (3 Myr of evolution). The 1D dust evolution simulations include grain coagulation and fragmentation associated with radial drift, turbulent mixing and gas drag. Finally, the synthetic images are produced from the distributions of dust and gas using the MCMax radiative transfer code.

Using these synthetic images, de Juan Ovelar et al. (2013) found that as the mass of the planet increases, the position of the millimeter ring moves further away from the planet's orbit while the outer radius of the scattered light cavity does not change. They derived an analytic formula relating the planet mass (M_p) with the ratio (f) between the position of the so-called 'scattered light wall' to that of the ALMA peak:

$$f(M_p) = c\left(\frac{M_p}{M_J}\right)^{\gamma} \tag{3.1}$$

where c is a constant and γ an exponent which increases with the orbital radius of the planet. In the simulations, the scattered light wall is defined as the radial location where the scattered light signal is half of the difference between the flux measured at the peak of the wall and the minimum flux in the gap.

To study the possibility of planets being at the origin of the cavities observed in transition disks, I compiled a sample of 22 disks that have both scattered light and millimeter observations, as presented in Table 3.3, and compared them to the results from the simulations by de Juan Ovelar et al. (2013). The sample includes two known binary systems, V4046 Sgr and HD 142527 (Quast et al., 2000; Biller et al., 2014). The eccentric binary companion in HD 142527 is likely responsible for the cavity (Price et al., 2018a), but this is probably not the case for the very close binary system V4046 Sgr (2.4 days period, Quast et al., 2000; D'Orazi et al., 2018). All sources show a resolved dust cavity in the millimeter and, except Oph IRS 48 and Sz 91 for which we consider respectively VISIR and Subaru observations, all have scattered light observations with VLT/SPHERE. The outer radius of the scattered light cavity and millimeter peak are reported in Table 3.3. I re-scaled the published values using the latest distances from GAIA DR2 (Gaia Collaboration et al., 2018). In this analysis, we only considered the position of the main cavity, regardless of the presence of an inner disk within the first few au. For 5 of the 22 disks considered in this analysis, the scattered light cavity may be located inside the coronagraphic mask radius, giving the upper limits in Table 3.3. For the small fraction of transition disks that possesses multiple rings in scattered light, we report the position of the scattered light ring that is the closest to the millimeter peak emission (for the following objects: HD 169142, V4046 Sgr, J1852, HD 97048, Lk Ca 15, Sz 91 and HD 34282). For J1608, which has a large inclination, we chose to estimate the ALMA and SPHERE peaks on our model, after computing it face-on. Finally, note that several disks included in this study present important azimuthal asymmetries. Those are mainly spirals in scattered light observations (as in HD 143006, CQ Tau, HD 135344B, MWC 758, HD 142527) and crescent like features at millimeter wavelengths (in HD 143006, HD 135344B, Oph IRS 48, MWC 758, HD 34282, HD 142527). While these features are not predicted in the synthetic dust images from de Juan Ovelar et al. (2013) (because the authors used a 1D code for dust evolution), they might be generated by planets in the disks (see the gas distribution in Fig. 1 of de Juan Ovelar et al. 2013, and e.g., Bae et al. 2016; Baruteau et al. 2019).

As the position of the wall defined by de Juan Ovelar et al. (2013) is usually not explicitly published in the literature, we consider both the inner radius of the disk beyond the cavity, as seen in scattered light, and the position of the peak in polarized intensity (respectively referred to as $R_{\mathrm{in,PI}}$ and $R_{\mathrm{peak,PI}}$ in Table 3.3). Considering the position of the cavity instead of that of the wall tends to over-estimate the planet mass, and inversely under-estimates it when the position of the peak is used. We also note that the models were specifically calculated for R band scattered light observations and band 7 (850 μm), and only for a planet in a circular orbit. However, little difference is expected for such small variations in wavelength, as can be seen by comparing the theoretical profiles of R-band and H-band in Fig. 3 of de Juan Ovelar et al. (2013).

In Fig. 3.15, I show the radius of the scattered light cavity ($R_{\mathrm{cav,PI}}$), defined as the mean between $R_{\mathrm{in,PI}}$ and $R_{\mathrm{peak,PI}}$, as a function of the radius of the millimeter ring ($R_{\mathrm{peak,mm}}$). We observe that for each system the scattered light cavity radius is smaller than the millimeter radius (see the green line), with about one third of the disks having a ratio smaller than 0.5 (see Table 3.3). The models of de Juan Ovelar et al. (2013) would imply companion masses above 13 M_J for ratios lower than 0.48 when the planet is located at 20 au, 0.53 when it is at 40 au, and 0.56 at 60 au (red shaded area). As can be seen in Fig. 3.15, fifteen disks in our sample are above the red shaded area. This indicates ratios larger than the ones given above, placing the possible companions in the planetary mass regime. PDS 70 is the only system where a few Jupiter mass planet has been imaged in the main cavity (Keppler et al., 2018; Müller et al., 2018), while HD 142527 has a stellar companion. For the other disks considered (namely UX Tau A, HD 143006, DoAr44, CQ Tau, HD 135344B, RY Lup and MWC758), the ratio (or its upper limit) would lead to objects in the stellar or brown dwarf regime. These disks appear in the red shaded area in Fig. 3.15.

To confirm the possible presence of planets in the gaps of all these transition disks, I performed a literature search on direct imaging surveys searching for planets. Except for PDS 70 and claims of candidate companions in the disks of HD 100546 (Quanz et al., 2015; Currie et al., 2014), HD 169142 (Biller et al., 2014; Reggiani et al., 2014),

Source	d (pc)	Band	$R_{\rm peak,mm}$ (au)	$R_{\rm in,PI}$ (au)	$R_{\rm peak,PI}$ (au)	Ratio
HD 100546	110 ± 1	B7 - R′	15.0	12.0	14.0	0.81, 0.96
HD 169142	114 ± 1	B6 - J	21.7	16.0	20.5	0.74, 0.94
V4046 Sgr	72 ± 1	B6 - H	27.0	15.3	26.9	0.57, 0.99
UX Tau A	140 ± 2	B6 - H	33.2	$<$ 14		< 0.42
HD 100453	104 ± 1	B6 - R′	33.3	14.6	18.5	0.44, 0.55
T Cha	110 ± 1	B3 - H	36.8	28.8	31.4	0.78, 0.85
HD 143006	166 ± 4	B6 - J	40.0	18.2	30.0	0.45, 0.75
DoAr44	146 ± 1	B7 - H	42.7	$<$ 14		< 0.33
CQ Tau	163 ± 2	B6 - J	47.3	$<$ 4		< 0.08
J1852	146 ± 1	B3 - H	43.8	34.7	43.1	0.79, 0.98
HD 135344B	136 ± 2	B7 - R	54.6	18.3	23.5	0.34, 0.43
HD 97048	185 ± 1	B7 - J	55.4	45.9	54.4	0.83, 0.98
LkCa 15	159 ± 1	B7 - J	64.0	53.7	64	0.84, 1.0
Oph IRS 48	134 ± 2	B9 - Q	70.6	33.3	59.1	0.47, 0.84
RY Lup	159 ± 2	B7 - H	71.9	$<$ 15		< 0.20
MWC758	160 ± 2	B7 - Y	80.0	$<$ 15		< 0.19
PDS 70	113 ± 1	B7 - J	81.0	45.0	54.0	0.56, 0.67
J1608	156 ± 6	B6 - H	81.0	45.0	49.9	0.56, 0.82
RXJ1604.3-2130A	150 ± 1	B6 - R′	83.0	54.9	63.7	0.66, 0.77
Sz 91	159 ± 2	B7 - Ks	87.5	46.0	50.9	0.52, 0.58
HD 34282	312 ± 5	B7 - J	133.9	124.2	132.7	0.93, 0.99
HD 142527	157 ± 1	B7 - Ks	165, 205	78.5	157.0	0.38, 0.95

Table 3.3 – Position of millimeter and scattered light cavities for 22 transition disks, ordered by increasing millimeter cavity size. Known binary systems are indicated with the name in italic. We report the peak of the millimeter intensity beyond the cavity, along with the position of the inner radius and peak in scattered light. When the cavity is not detected down to the coronagraph radius in scattered light, we use the symbol <. The position of the scattered light cavity ($R_{cav,PI}$), defined as the mean between $R_{in,PI}$ and $R_{peak,PI}$, is used in Fig. 3.15.

References: HD 100546: Pinilla et al. (2018a) and Garufi et al. (2016), HD 169142: Fedele et al. (2017), Pohl et al. (2017b), and Bertrang et al. (2018), V4046 Sgr: Rosenfeld et al. (2013) and Avenhaus et al. (2018), HD 100453: van der Plas et al. (2019) and Benisty et al. (2017), T Cha: Hendler et al. (2018) and Pohl et al. (2017a), UX Tau: Pinilla et al. (2018a), Menard et al. (2020); HD 143006: Benisty et al. (2018) and Pérez et al. (2018a), DoAr44: Casassus et al. (2018) and Avenhaus et al. (2018), CQ Tau: Pinilla et al. (2018a); Benisty et al. (in prep.), J1852: This work, HD 97048: van der Plas et al. (2017b) and Ginski et al. (2016), LkCa 15: Andrews et al. (2011), Thalmann et al. (2015), and Thalmann et al. (2016), HD 135344B: Pinilla et al. (2018a) and Stolker et al. (2016), Oph IRS 48: van der Marel et al. (2013), Bruderer et al. (2014), and Geers et al. (2007), RY Lup: Pinilla et al. (2018a) and Langlois et al. (2018), MWC758: Marino et al. (2015) and Benisty et al. (2015), RXJ1604.3-2130A: Pinilla et al. (2018b) and Pinilla et al. (2015), PDS 70: Long et al. (2018) and Keppler et al. (2018), J1608: Ansdell et al. (2016), This work, Sz 91: Canovas et al. (2016) and Tsukagoshi et al. (2014), HD 34282: van der Plas et al. (2017a), de Boer et al. (in prep.), HD 142527: Boehler et al. (2017) and Avenhaus et al. (2014).

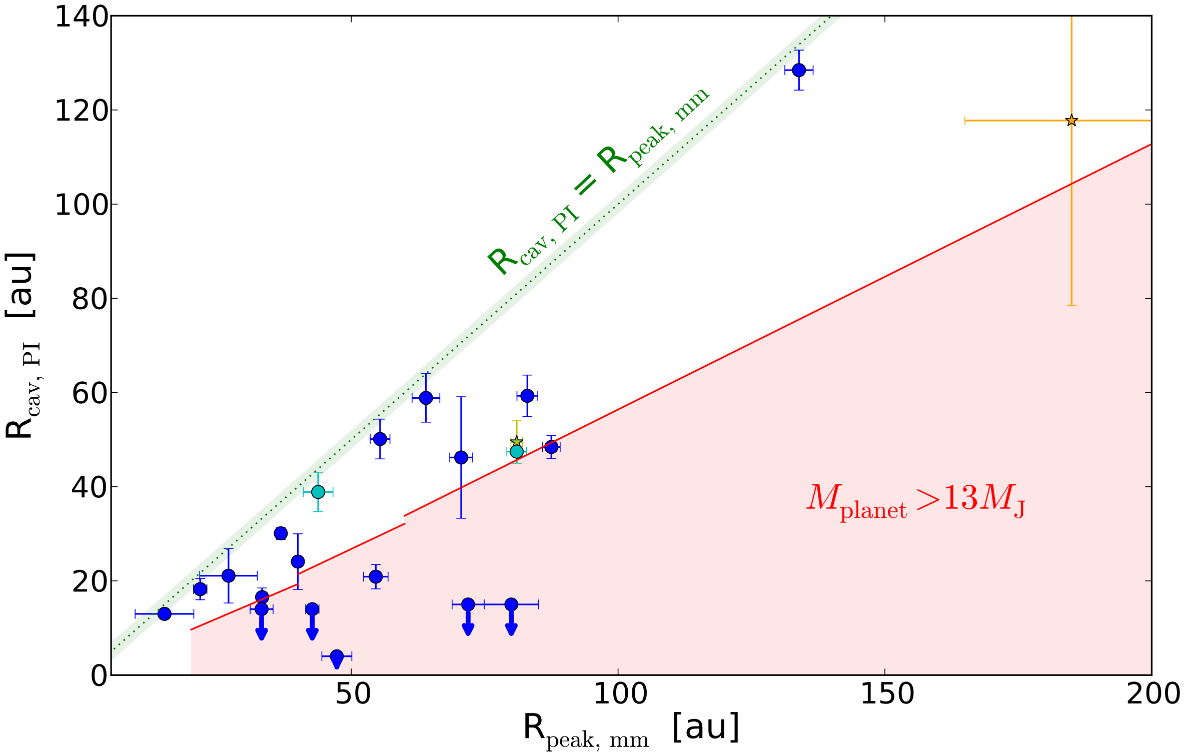

Figure 3.15 – Comparison of the cavity sizes as measured in the millimeter and in scattered light for a sample of 22 transition disks. The cyan points correspond to the two systems modeled in this paper, while the yellow star symbols refer to HD 142527 that has a stellar companion in the cavity, and PDS 70 where a planet has been detected. The upper limits, indicated with arrows, refer to systems for which scattered light cavities could not be measured down to the coronagraphic radius. Horizontal bars correspond to one tenth of the millimeter beam, while vertical bars represent the interval between the cavity radius and the peak in scattered light (Table 3.3). The red region shows the ratio for which the planet mass inferred with the prescription of de Juan Ovelar et al. (2013) is larger than 13 Jupiter masses. The three breaks correspond to their models with planets at radii of 20, 40 and 60 au, respectively.

Lk Ca 15 (Kraus and Ireland, 2012; Sallum et al., 2015) and MWC758 (Reggiani et al., 2018), no planets were found in most disks included in our study, up to a sensitivity of $\sim 10\,\mathrm{M_J}$ at 0.25″. This is most problematic for the systems in which the model predicted the presence of a planet larger than $13\,\mathrm{M_J}$. An alternative scenario to explain the small ratio between the radius of the scattered light cavity and the millimeter peak could be that the cavities are caused by several lower mass planets, which would allow small grains to fill the cavity, while large grains are retained in the outer disk (Rosotti et al., 2016; Dipierro and Laibe, 2017). In this case, no gap would be detected in scattered light, while a clear ring would appear in the millimeter images.

3.5 CONCLUSIONS

This work focused on new polarized scattered light and millimeter observations of two transition disks, namely 2MASS J16083070-3828268 (J1608) and RXJ1852.3-3700 (J1852). The image of J1608 reveals a relatively inclined disk ($\sim 74°$) with a large cavity of about 50 au in scattered light. We also detect a faint line, in the southwest, that we interpret as tracing the rear-facing side of the disk. The second disk of our study, J1852, shows scattered light just beyond the coronagraph radius, a gap between 22 and 42 au and an outer ring up to 65 au. A cavity inward of the first ring, as inferred from the SED, is located behind the coronagraph.

I modeled both scattered light and millimeter images (tracing small and large dust grains, respectively), together with the SED, using a radiative transfer code. The modeling of the relatively inclined disk J1608 indicates that small and large grains have a different spatial distributions. Radially, small grains are more extended inward and outward than the large grains, by respectively 30 au and 60 au. Vertically, the large grains have to be located within a height of $H_{100\mathrm{au}} = 1 - 5\,\mathrm{au}$, while the small grains extend vertically up to $H_{100\mathrm{au}} = 12\,\mathrm{au}$. We follow a similar procedure for J1852 and propose a model with a spatial segregation between grain sizes. However, the angular resolution of the millimeter observations is too low to constrain the radial extent of large grains, and the disk is not inclined enough to allow us to strongly constrain the relative vertical extents of various grain sizes. So, our modeling of the images and SED for this object remains degenerate.

The radial and vertical segregation in particle sizes observed in J1608 is likely a consequence of both vertical settling and dust radial drift that occur during the evolution of the disks. Vertical settling in low turbulence disks and/or following non-ideal MHD effects such as ambipolar diffusion can explain the relatively small scale height inferred for the large grain population. The difference in the outer extents (as measured in scattered light and millimeter emission) could result from radial drift, optical depth and illumination effects, while the difference in the inner radius of the outer disk, might be related to the presence of planet(s).

I compiled a sample of 22 transition disks imaged with both ALMA and SPHERE, and find that scattered light is detected inside the millimeter cavity in all of the disks. The observed spatial difference in millimeter and far-IR observations is used to identify a segregation in particle sizes, and infer the proposed companion mass responsible for the cavity using the prescription of de Juan Ovelar et al. (2013). We show that in 15 objects, including the two disks modeled in this study, the cavities could be explained by the presence of a giant planet. The seven other disks of the sample show large ratios between the position of the scattered light and the millimeter cavity, suggestive of a companion above the planetary mass regime, or alternatively, of a multiple planetary system.

As of today, apart from PDS 70 (Keppler et al., 2018), direct imaging surveys with results available in the literature did not provide the detection of other such objects within a transition disk. New deeper observations with direct imaging instruments, or search for non-Keplerian motions in the gas kinematics with ALMA (Pérez et al., 2015; Pérez et al., 2018b; Teague et al., 2018; Pinte et al., 2018) might lead to further detections.

4

EDGE-ON CONTINUUM SURVEY WITH ALMA

Contents

4.1 INTRODUCTION

The process of planet formation requires small submicron-sized particles to grow up to large pebbles and boulders that will eventually aggregate to form planetesimals and planets. Given the short lifetimes of disks, such efficient growth has to occur in the highest density regions of protoplanetary disks, i.e., the inner regions, dust traps, and/or the disk midplane. Yet, vertical settling, which allows to increase the dust density in the disk midplane, remains poorly constrained (see Chapter 1). The comparison of observations at widely different wavelengths, for example optical/NIR and (sub)millimeter, can help to constrain the settling strength.

Up to now, most studies of protoplanetary disks focused on substructures, such as rings, gaps, and spirals, which naturally led to observations of low inclination systems ($\leq 70^\circ$, where 0° is face-on), where they are more readily visible. Some of these studies showed that the gas is often more radially extended than the millimeter-sized dust (Ansdell et al., 2018; Facchini et al., 2019, this thesis - Chapter 2), which is likely a combined effect of optical depth and dust radial drift (Facchini et al., 2017). However, although important to constrain radial drift, dedicated comparisons of the radial distribution of different dust grains sizes remain sparse (see e.g., Pinilla et al., 2015; Villenave et al., 2019).

For relatively face-on disks, it is difficult to estimate the difference in vertical extent between gas and dust grains, detailed modeling of narrow rings and gaps features is required (e.g., Pinte et al., 2016). On the other hand, edge-on disks offer a unique perspective, as they allow us to directly observe their vertical structure. Previous studies of highly inclined disks using different wavelengths indicate that the grains are stratified, with larger dust closer to the disk midplane (Glauser et al., 2008; Duchêne et al., 2003; Duchêne et al., 2010; Villenave et al., 2019), as predicted by models. However, even for these systems, the vertical extent of the midplane remains poorly constrained in early studies, limited by the resolution of the observations.

In this chapter, I present a survey of 12 edge-on disks observed with ALMA at high angular resolution ($\sim 0.1''$). The sample was selected based on SEDs and HST images, and most of the targets were observed at multiple millimeter bands. After describing the sample and the data reduction in Section 4.2, I present the fluxes, brightness temperatures, as well as the radial and vertical extents of all disks in Section 4.3. Section 4.4 compares our results with a fiducial radiative transfer model. We focused on the vertical extent of the disks, their radial extent, and investigate optical depth in the disks by studying the brightness temperature and spectral indices of the sources. Most of the text of this chapter originates directly from Villenave et al. (2020), but I complement the analysis with additional details. Note also that between the submission of the manuscript and the PhD defense, the paper was slightly modified through the refereeing process. The latest analysis is included in the final version of the paper, in Appendix A. This chapter focuses on the dust emission, but a preliminary analysis of the ^{12}CO emission is presented in Chapter 5.

4.2 OBSERVATIONS AND DATA REDUCTION

4.2.1 *Target selection*

In this study, we selected a sample of twelve highly inclined disks. All sources were identified as candidates from their Spectral Energy Distribution (SED, see Stapelfeldt et al., 2014, and Stapelfeldt et al., in prep) and confirmed as edge-on disks (hereafter EOD) according to their optical or near-infrared scattered-light images. The ALMA observations targeted 8 sources located in the Taurus star-forming region, 3 in Chamaeleon I, and 1 in Ophiuchus (see Table 4.1). Most of the observations presented in this work were part of our cycle 4 and 5 survey of edge-on disks (Project 2016.1.00460.S, PI: Ménard), but we also included complementary observations of Tau 042021, HH 30, and Oph 163131 from previous programs (Projects 2013.1.01175.S, 2016.1.01505.S, and 2016.1.00771.S, PIs: Dougados, Louvet, and Duchêne).

I report the spectral types and stellar masses of the sources in Table 4.2. As the spectral features associated with the central source are still visible for edge-on disks through the scattered light (Appenzeller et al., 2005), the spectral types could be determined from spectroscopy (Luhman, 2007; Luhman et al., 2010, Flores et al., in prep). However, the edge-on configuration does not allow a direct estimate of the stellar luminosity, because due to their large inclinations most of the stellar light is obscured by the disk. Thus, we report dynamical stellar masses estimated from CO emission (Simon et al., 2019, Flores et al. in prep).

At optical and NIR wavelengths, edge-on disk systems highlight extended nebulosities on both sides of a dark lane, tracing the disk midplane. Because of severe extinction in the dark lane, the central star is usually undetected at optical/NIR wavelengths, also resulting in fainter systems for a given spectral type and distance. In a few cases, the brightness distribution of the nebulosities has also been observed to vary significantly (Stapelfeldt et al., 1999). These facts combine to render parallax measurements difficult and the distances determined by Gaia can be plagued by large errors. For our targets, we decided to adopt the average distance of the parent star forming-regions instead; 140 pc for the sources in Taurus and Ophiuchus (Kenyon et al., 2008; Ortiz-León et al., 2018; Cánovas et al., 2019) and 192 pc for those in Chamaeleon I (Dzib et al., 2018).

Four of the observed disks are part of multiple systems: HK Tau B, HV Tau C, Haro 6-5B, and HH 48 NE (Stapelfeldt et al., 1998; Stapelfeldt et al., 2003; Krist et al., 1998; Haisch et al., 2004) with apparent companion separations larger than 2.4". While HH 30 has been suggested to be a binary on the basis of jet wiggles and a disk central hole in lower resolution and signal to noise ratio millimeter continuum maps (Guilloteau et al., 2008), higher resolution ALMA observations do not confirm the central hole (Louvet et al., 2018), but neither do they exclude the possibility of spectroscopic binary. The other targets in the sample are not known to be in multiple systems.

Full name	Adopted name	RA (h m s)	Dec (° ′ ″)	SFR
2MASS J04202144+2813491	Tau 042021	04 20 21.4	+28 13 49.2	Taurus
HH 30	HH 30	04 31 37.5	+18 12 24.5	Taurus
IRAS 04302+2247	IRAS 04302	04 33 16.5	+22 53 20.4	Taurus
HK Tau B	HK Tau B	04 31 50.6	+24 24 16.4	Taurus
HV Tau C	HV Tau C	04 38 35.5	+26 10 41.3	Taurus
IRAS 04200+2759	IRAS 04200	04 23 07.8	+28 05 57.5	Taurus
FS Tau B	Haro 6-5B	04 22 00.7	+26 57 32.5	Taurus
IRAS 04158+2805	IRAS 04158	04 18 58.1	+28 12 23.4	Taurus
2MASS J16313124-2426281	Oph 163131	16 31 31.3	-24 26 28.5	Ophiuchus
ESO-Hα 569	ESO-Hα 569	11 11 10.8	-76 41 57.4	Cha I
ESO-Hα 574	ESO-Hα 574	11 16 02.8	-76 24 53.2	Cha I
HH 48 NE	HH 48 NE	11 04 22.8	-77 18 08.0	Cha I

Table 4.1 – Adopted name, stellar coordinates (in J2000), and corresponding star forming region (SFR) of the disks included in this study.

Source	SpT^{a,b}	M$_\star^c$ (M$_\odot$)	PA (°)	$i_{\rm AxisRatio}$ (°)
Tau 042021	M1		-16	> 85
HH 30	M0		121	$> 85^A$
IRAS 04302	K6−M3.5	$1.3 - 1.7$	175	> 84
HK Tau B	M0.5	0.89 ± 0.04	41	> 83
HV Tau C	K6	1.33 ± 0.04	108	> 80
IRAS 04200	M3.5−M6	0.52 ± 0.04	129	67 ± 4
Haro 6-5B	K5		145	74 ± 2
IRAS 04158	M5.25		92	62 ± 3
Oph 163131	K4−K5^d	1.2 ± 0.2^d	49	> 80
ESO-Hα 569	M2.5		144	> 64
ESO-Hα 574	K8		141	> 69
HH 48 NE	K7		75	> 68

Table 4.2 – Stellar and disks parameters.
SpT: Spectral type, M$_\star$: Stellar masses, from dynamical estimates based on gas emission, PA: Position angle of the disks from their millimeter images, $i_{\rm AxisRatio}$: Estimation of the inclination inferred from the millimetric mean axis ratio in continuum. These values are lower limits when the disks are not resolved along their minor axis by more than 2 beams, or when the measured inclination is too high not to be influenced by the physical vertical extent of the disk.
References: (a) Luhman (2007), (b) Luhman et al. (2010), (c) Simon et al. (2019), (d) Flores et al. (in prep), (A) Louvet et al. (2018).

4.2.2 *ALMA observations*

The twelve targets considered in this analysis come from four different projects, which had different sensitivity, angular resolution and observing frequency. In this section, I describe the most important parameters of each observations and my contribution to obtain the final images. Except for HH 30, which was reduced by collaborators, I calibrated and reduced all datasets to produce the final images. In this chapter, we focus on the continuum data. The reduction and a preliminary analysis of the ^{12}CO data is presented in Chapter 5.

To summarize the observations, four sources were observed in only one band with moderate angular resolution (ALMA band 7 or band 6), 6 sources in two bands (band 7 and 4), and 2 were observed in three bands (band 7, 6, and 4). As a reminder, band 7, 6, and 4 respectively correspond to the following wavelengths: 0.9 mm, 1.3 mm and 2.06 mm.

4.2.2.a. Observations of HH 30

We include multi-wavelength, band 4, 6, and 7, observations of HH 30. The data reduction of each observation have been performed by collaborators. In particular, the band 6 observations were published in Louvet et al. (2018, Project 2013.1.01175.S, PI: Dougados), and the band 4 and 7 (Project 2016.1.01505.S, PI: Louvet) were reduced by Y. Boehler at IPAG. Table 4.3 summarizes the most important parameters of the observations.

4.2.2.b. Observations of Tau 042021 and Oph 163131

We also include band 6 observations of Tau 042021 and Oph 163131 (Project 2016.1.00771.S, PI: Duchêne). Both observations were performed with two array configurations as can be seen in Table 4.3. I used the CASA pipeline (version 4.7) to calibrate the data of both configurations for each source.

Note that for Oph 163131, I also reduced the gas data, targeting the three CO isotopologues. I am thus involved in two complementary studies on this source. Flores et al. (in prep) studies the temperature structure of the disk by modeling the emission lines, while Wolff et al. (in prep) analyses dust emission performing a model of the HST and ALMA images.

4.2.2.c. Chameleon I survey

Most of our sources were observed as part of project 2016.1.00460.S, which was divided into two groups, targeting respectively 7 sources located in Taurus and 3 in Chameleon I. The three Chamaeleon sources (ESO-Hα 569, ESO-Hα 574, and HH 48 NE) were observed in band 7 with a compact configuration only (see Table 4.3). I calibrated the compact configuration observations with the CASA pipeline version 4.7.

Source	Band	Obs. date	Baselines (m − km)	N_{ant}	T_{int} (min)	v_{CASA}	PWV (mm)
(1)	(2)	(3)	(4)	(5)	(6)	(7)	(8)
HH 30	7	14, 15 & 21/10/2016	19 − 2.5	42 − 46	174	4.7	0.58
	6	19 & 21/07/2015	13 − 1.6	42	78	4.3	0.56
	4	23/10/2016	19 − 1.8	48	12	4.7	1.77
		12/09/2017	41 − 9.5	44	31	4.7	1.70
Tau 042021	6	05/12/2016	15 − 0.7	41	7.5	4.7	1.60
		21/10/2016	18 − 1.8	44	25	4.7	0.35
Oph 163131	6	25/04/2017	15 − 0.5	41	8.5	4.7	1.30
		07/07/2017	17 − 2.6	44	27	4.7	0.65
Survey Cha I[a]	7	15/11/2016	15 − 0.9	42	1.1	4.7	0.50
Survey Taurus[b]	7	24/11/2016	15 − 0.7	43	1.1	4.7	0.55
		18/08/2017	21 − 3.6	43	3.7	5.1	0.38
	4	27/09/2017	41 − 14.9	43	6.7	5.1	1.39

Table 4.3 – Summary of the main observational parameters of the datasets included in the study.
Column 1: Target name, Column 2: Observing band, Column 3: Observing date, Column 4: Minimum and maximum baseline range, Column 5: Number of antennas, Column 6: On source integrating time, Column 7: Calibrating CASA version, Column 8: Precipitable water vapor during the observations.
(a) The Chamaeleon I sources included in the survey are ESO-Hα 569, ESO-Hα 574, and HH 48 NE.
(b) The Taurus sources included in the survey are Tau 042021, IRAS 04302, HK Tau B, HV Tau C, IRAS 04200, Haro 6-5B, and IRAS 04158.

4.2.2.d. Taurus survey

The Taurus sources included in program 2016.1.00460.S are: Tau 042021, IRAS 04302, HK Tau B, HV Tau C, IRAS 04200, Haro 6-5B, and IRAS 04158. They were observed in band 4 and band 7 (see Table 4.3). I calibrated the raw band 4 data using the CASA pipeline version 5.1.

The band 7 observations of the Taurus sources were performed with both a compact and an extended array configuration. I calibrated the compact configuration observations with the CASA pipeline version 4.7.

Contrary to previously mentioned datasets, for the extended configuration of the band 7 survey (observing 7 Taurus sources), I could not simply execute the ALMA-provided script to calibrate the data. When using it, only HK Tau B was properly calibrated while noise was obtained in all other fields. It took several months of tests to understand the reason of this failure.

The first step of our investigation was to dig into the provided calibration script. For this dataset, the calibration was not performed with the CASA pipeline but with a manual calibrating script. I checked all steps of this manual calibration (see Section 1.4.2). For the first ones, namely correcting for water vapor in the high site (WVR), for the antenna temperatures ($T_{\rm sys}$), and for the antenna positions, the calibrating plots were regular. Afterwards, the script added a model from the flux calibrator, in our case the bandpass calibrator (J0510+1800, see Table 4.4), that I checked was correct according to the calibrator catalogue. Then, the script calculated the bandpass correction, which estimates the response of the interferometer at different frequencies, and the amplitude and phases corrections for each sources. All calibration plots appeared regular too. However, the application of these tables to each target was not calibrating properly, so I looked carefully at this last step. We found that for most sources, there was a mismatch of a few of MHz between the spectral windows of a target and its corresponding phase calibrator. In Fig. 4.1, I show the example of HV Tau C, reporting several sections of the `listobs` task in CASA. The top table of this figure shows two consecutive scans, the first (scan 31) observes the science target, and the second the official phase calibrator (J0438+3004, scan 32). Both sources were observed at different spectral windows (see column "Spw ID"). The bottom table of Fig. 4.1 displays the properties of the spectral windows. The third column of this table reports the central frequency of each spectral windows. There is a mismatch in the frequency used between the source and phase calibrator of a few MHz. This was also the case for the following sources: HK Tau B, IRAS 04200, and IRAS 04302. After performing some tests, we found that this little difference in observing frequency is sufficient to lead to a totally incorrect phase calibration. The phase calibrator and the source need to be observed with the exact same spectral setup for the phase calibration to work correctly. For the flux and bandpass calibration, such small differences in spectral windows between the calibrator and the science targets are not an issue.

When looking carefully at the spectral setup of the dataset, we found that three sources (Tau 042021, Haro 6-5B, IRAS 04158) could be calibrated with the supplied

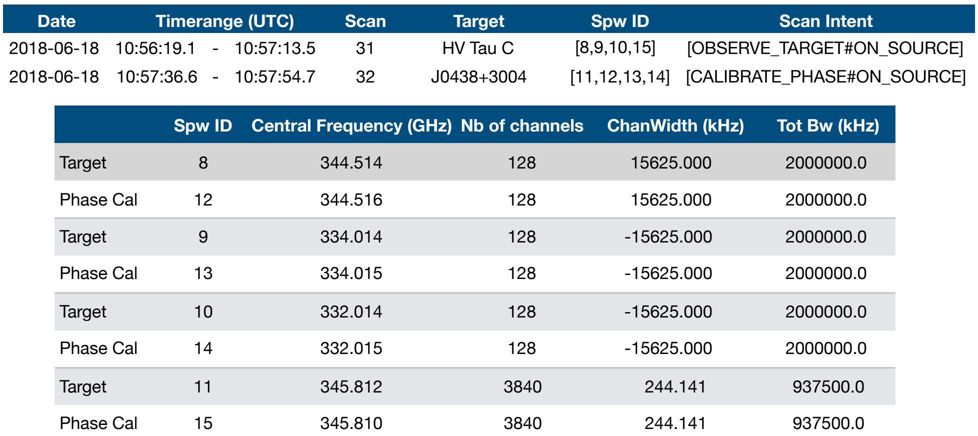

Date	Timerange (UTC)	Scan	Target	Spw ID	Scan Intent
2018-06-18	10:56:19.1 - 10:57:13.5	31	HV Tau C	[8,9,10,15]	[OBSERVE_TARGET#ON_SOURCE]
2018-06-18	10:57:36.6 - 10:57:54.7	32	J0438+3004	[11,12,13,14]	[CALIBRATE_PHASE#ON_SOURCE]

	Spw ID	Central Frequency (GHz)	Nb of channels	ChanWidth (kHz)	Tot Bw (kHz)
Target	8	344.514	128	15625.000	2000000.0
Phase Cal	12	344.516	128	15625.000	2000000.0
Target	9	334.014	128	-15625.000	2000000.0
Phase Cal	13	334.015	128	-15625.000	2000000.0
Target	10	332.014	128	-15625.000	2000000.0
Phase Cal	14	332.015	128	-15625.000	2000000.0
Target	11	345.812	3840	244.141	937500.0
Phase Cal	15	345.810	3840	244.141	937500.0

Figure 4.1 – Example of scans and spectral windows in the extended configuration of the band 7 observations of project 2016.1.00460.S.

ALMA phase calibrator. In the provided calibration script, they were mistakenly calibrated with the solutions from the bandpass calibrator. For the 4 remaining targets (namely HK Tau B, HV Tau C, IRAS 04200, and IRAS 04302), the spectral window setup used for the supplied phase calibrator was different to that of the science target, and so, these data could not be reduced as simply.

For HK Tau B, the more distant bandpass calibrator could be used as a phase calibrator, as it was initially done in the ALMA provided calibrating script. For the three other sources (HV Tau C, IRAS 04200 and IRAS 04302), we first tried to use selfcalibration as to perform the calibration in phase. In order to see if such calibration would induce some artefact, I first tested this method on Tau 042021, a bright, extended source of the sample which could also be calibrated using the provided phase calibrator. The results, shown in Fig. 4.2, are convincing: the reconstructed image using selfcalibration (left panel) is similar to the image obtained after phase calibrating with the provided phase calibrator (right panel). Thus, we first calibrated the three sources in phase using the selfcalibration method. For IRAS 04302, we obtained a reasonable solution by averaging all spectral windows, to the cost of a significantly poorer angular resolution. However, for the fainter and smaller HV Tau C and IRAS 04200, the images obtained after selfcalibration were doubtful. As can be seen in Fig. 4.3, the selfcalibration generated a point source at the phase center of both fields. This structure being absent from the likely optically thinner band 4 observations, we estimated that it was a calibration artefact due to selfcalibration. Looking for another solution for phase calibration, we realized that it was possible to use the check sources as phase calibrators. Indeed, the check source is observed at the exact same frequency than the science target. In that case, the calibrator was only observed once before each of the science targets (rather than bracketing it in time, see Fig. 1.12); which increased the phase calibration uncertainties of these objects. However, this allowed to obtain more reliable band 7 images for HV Tau C and IRAS 04200. Note that for an unclear reason, using the check source was not a better solution for IRAS 04302 and we kept the selfcalibrated image.

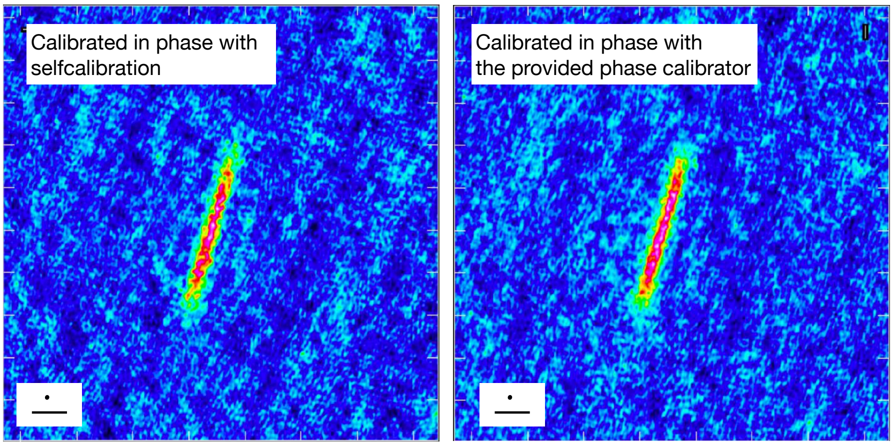

Figure 4.2 – Different phase calibrations of Tau 042021. The beam size and a 0.5″ scale are represented in the bottom left corner of each panels respectively by an ellipse and an horizontal line.

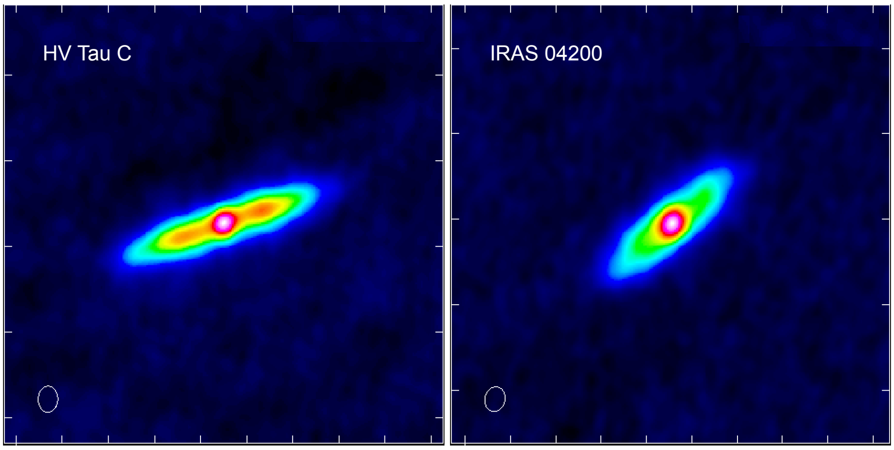

Figure 4.3 – Representation of the preliminary images obtained for HV Tau C and IRAS 04200, using selfcalibration to calibrate the source in phase. An artificial point source can be seen in the center of each target.

Sources	Bandpass & Flux	Phase	Phase calibration
Tau 042021	J0510+1800	J0438+3004	Standard
IRAS 04302	J0510+1800	IRAS 04302	Selfcalibration
HK Tau B	J0510+1800	J0510+1800	Bandpass used
HV Tau C	J0510+1800	J0440+2728	Check source used
IRAS 04200	J0510+1800	J0433+2905	Check source used
Haro 6-5B	J0510+1800	J0426+2327	Standard
IRAS 04158	J0510+1800	J0422+3058	Standard

Table 4.4 – Calibration sources of the band 7 survey.

To summarize, after various investigations, we managed to calibrate all science targets of the dataset. We calibrated Tau 042021, Haro 6-5B and IRAS 04158 with their ALMA supplied phase calibrator, HK Tau B with the bandpass calibrator, HV Tau C and IRAS 04200 with their check sources, and used selfcalibration to calibrate IRAS 04302. This is summarized in Table 4.4.

4.2.3 *Imaging the continuum*

For all sources, I extracted the images from the visibilities with the `clean` task, using a Briggs robust weighting parameter of 0.5. Note that when the data were taken with several array configurations, I generated the images by combining all configurations. To reduce the noise level and improve the dynamical range of the images, I applied phase self-calibration on the sources with the highest signal to noise, namely for the band 7 of HK Tau B, Tau 042021, Haro 6-5B, and the band 6 of Oph 163131. I report the final beam sizes in Table 4.5 and present the final images in Fig. 4.4. Note that to be able to compare the physical sizes of the sources and to compute spectral index maps I also generated recentered maps with similar angular resolution. This is described in the next section.

4.2.4 *Astrometric accuracy and map registration*

ALMA maps are subject to astrometric uncertainties due to limited signal to noise on the phase calibrator and errors in the phase referenced observations related to poor weather or antenna position errors. To be able to compute accurate spectral index maps (see Section 4.3.5), the images at the different wavelengths have to be accurately aligned, and need to have similar angular resolution. In the following paragraph, I discuss the registration of our images.

For each source and band, we perform simple Gaussian fits in the image plane to estimate the centroid position. The offsets between band 4 and band 7 ranged from 2 mas for Tau 042021, and IRAS 04200, up to $60-90$ mas for HH 30, HV Tau C, and

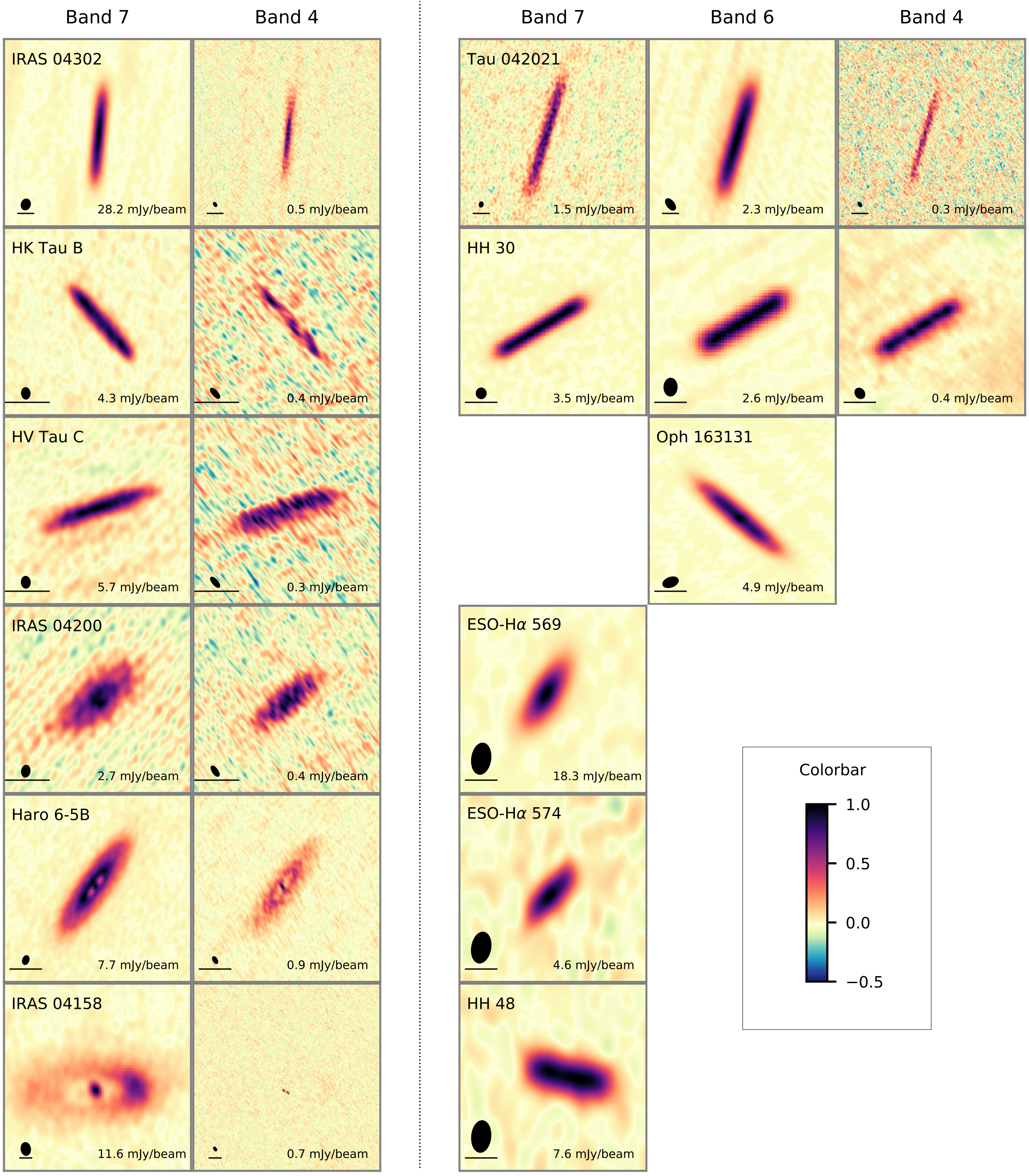

Figure 4.4 – Images of all sources included in this study, normalized to their peak intensity. Each column is a different band and each line two different sources (each side of the dashed vertical line). The peak emission is reported in the bottom right corner of the image, and we show the beam size (ellipse) and a 0.5″scale (dark line) in the bottom left.

Sources	B7 (″)	B6 (″)	B4 (″)	Restored B4 & B7 (″)
Tau 042021	0.12 × 0.08	0.37 × 0.18	0.11 × 0.04	0.12 × 0.08
HH 30	0.14 × 0.13	0.26 × 0.18	0.15 × 0.12	0.15 × 0.12
IRAS 04302	0.30 × 0.24		0.09 × 0.04	0.30 × 0.24
HK Tau B	0.11 × 0.07		0.12 × 0.04	0.12 × 0.08
HV Tau C	0.11 × 0.08		0.12 × 0.04	0.12 × 0.08
IRAS 04200	0.11 × 0.074		0.11 × 0.04	0.11 × 0.11
Haro 6-5B	0.12 × 0.07		0.10 × 0.04	0.12 × 0.08
IRAS 04158	0.48 × 0.30		0.11 × 0.04	
Oph 163131		0.23 × 0.13		
ESO-Hα 569	0.48 × 0.28			
ESO-Hα 574	0.47 × 0.28			
HH 48 NE	0.48 × 0.28			

Table 4.5 – Beam sizes of our observations, and restored beam used to compute brightness temperatures and spectral index maps.

IRAS 04302. Most are larger than expected from source proper motion between the different executions. For standard observations using bright phase calibrators taken in good weather conditions, the expected astrometric accuracy for each band is 10% of the beam (see ALMA Technical Handbook [1]). This would correspond to about 20 mas relative registration between the bands. The band offsets were significantly larger between the observations of HH 30, IRAS 04302, and HV Tau C. However, we note that for these three disks, different phase calibrators were used between the observations. Moreover, for IRAS 04302 and HV Tau C, the standard phase calibration could not be performed (see above); in particular, we used the check source of HV Tau C for its calibration, and could only perform self-calibration of IRAS 04302 in band 7, thus losing the absolute astrometry. In addition, the weather conditions during the band 7 extended configuration observations were relatively poor, with phase rms of $\sim 64^\circ$ on the longest baselines. This is likely to deteriorate the positional accuracy. Overall, the astrometric accuracy of our observations is not sufficient to confirm any significant motion or shift of the sources between the two bands. Because models of edge-on disks also show that offsets between bands should remain minimal compared to the beam size (e.g., Galván-Madrid et al., 2018), we registered our images to a common center in both bands. We aligned the band 4 and band 7 observations using the `fixplanets` task in CASA [2].

---

[1] https://almascience.eso.org/documents-and-tools/latest/documents-and-tools/cycle8/alma-technical-handbook

[2] We note that we set the option `fixuvw` to True when applying the `fixplanets` task, which is similar to using the `fixvis` task.

Finally, to be able to compute spectral index maps, we also recompute the maps to get a unique angular resolution for each source observed both in band 4 and band 7. To do so, we first re-imaged each source using the same `uvrange` and applying a `uvtaper` to limit the effect of flux filtering and of different uvcoverage. Then, to obtain exactly the same angular resolution between both bands, we used the `imsmooth` CASA task. The restored beam sizes are reported in the last column of Table 4.5.

4.3 RESULTS

4.3.1 *Continuum emission*

All millimeter-wavelength continuum images are presented in Fig. 4.4. The majority of the disks show an elongated emission shape, with large axis ratios and in several cases a roughly constant surface brightness along the major axis, confirming that they are highly inclined.

Two disks in the sample, however, present a different shape. Haro 6-5B and IRAS 04158 show a ring and some centrally peaked emission. As in previous CARMA observations (Sheehan and Eisner, 2017), the band 7 image of IRAS 04158 reveals a highly asymmetric ring (brighter on the western side) with a compact source towards the center. We evaluate the position of the rings in Section 4.3.3. This ring is not detected in our band 4 observations, mostly due to the lack of short spacing baselines (filtering of large scale features) and flux dilution into small beams. However, the band 4 observations clearly resolve the emission at the center of the ring into two point sources. IRAS 04158 is a binary system. I am involved in a detailed analysis focusing on this source. We find that hydrodynamical simulations using some orbital parameters for the binary are able to reproduce the shape of the circumbinary disk (Ragusa et al., in prep).

The total continuum flux density of each source is measured by integrating the signal, down to the 3σ noise level, within elliptical apertures tailored to each source. The flux densities are reported in Table 4.6. The absolute calibration errors for ALMA are about 5% at the lower frequencies up to $\sim$ 10% at band 7 (see ALMA Technical Handbook[3]). We use 10% error values throughout Table 4.6. We note that although the phase calibration method used for the extended configuration observations in band 7 was non-standard (see Section 4.2.2), the flux calibration followed the usual procedure and, accordingly, the flux calibration uncertainty should be nominal. Additionally, we checked that the flux of the compact and extended configurations of the band 7 survey are consistent.

---

[3] https://almascience.nrao.edu/documents-and-tools/latest/documents-and-tools/cycle7/alma-technical-handbook

Source	F_{B7} (mJy)	F_{B6} (mJy)	F_{B4} (mJy)	α_{mm}
Tau 042021	124.2 ± 12.4	47.2 ± 4.7	15.4 ± 1.5	2.5 ± 0.1
HH 30	54.5 ± 5.5	22.3 ± 0.1^a	6.9 ± 0.7	2.5 ± 0.1
IRAS 04302	267.5 ± 26.8		37.2 ± 3.7	2.3 ± 0.1
HK Tau B	55.6 ± 5.6		4.4 ± 0.4	3.0 ± 0.2
HV Tau C	90.6 ± 9.1		11.6 ± 1.2	2.2 ± 0.2
IRAS 04200	65.6 ± 6.6		11.6 ± 1.2	2.1 ± 0.4
Haro 6-5B	340.9 ± 34.1		35.3 ± 3.5	2.6 ± 0.1
IRAS 04158	$259.2 \pm 25.9^*$		$2.0 \pm 0.2^*$	2.9 ± 0.6
Oph 163131	125.8 ± 2.4^b	44.8 ± 4.5		2.6 ± 0.1
ESO-Hα 569	40.2 ± 4.0			2.3 ± 0.2
ESO-Hα 574	9.3 ± 0.9			
HH 48 NE	31.0 ± 3.1			

Table 4.6 – New millimeter fluxes, derived spectral indices and mass limits. The fluxes are measured using elliptical apertures centred on the targets. The millimeter spectral indices were calculated using the fluxes in this table together with literature measurements (references for these are reported below).

(*) Band 7: Total flux for the disk and central binary. Band 4: Only flux from the central binary.

References: (a) Louvet et al. (2018), (b) Cox et al. (2017).

References used to compute the global spectral indices: Tau 042021: Andrews et al. (2013), HH 30: Louvet et al. (2018), IRAS 04302: Moriarty-Schieven et al. (1994), Gräfe et al. (2013), and Wolf et al. (2003), HK Tau B: Duchêne et al. (2003), HV Tau C: Andrews et al. (2013) and Duchêne et al. (2010), IRAS 04200: Andrews et al. (2013), Haro 6-5B: Dutrey et al. (1996), IRAS 04158: Andrews et al. (2008) and Motte and André (2001), Oph 163131: Cox et al. (2017), ESO-Hα 569: Wolff et al. (2017)

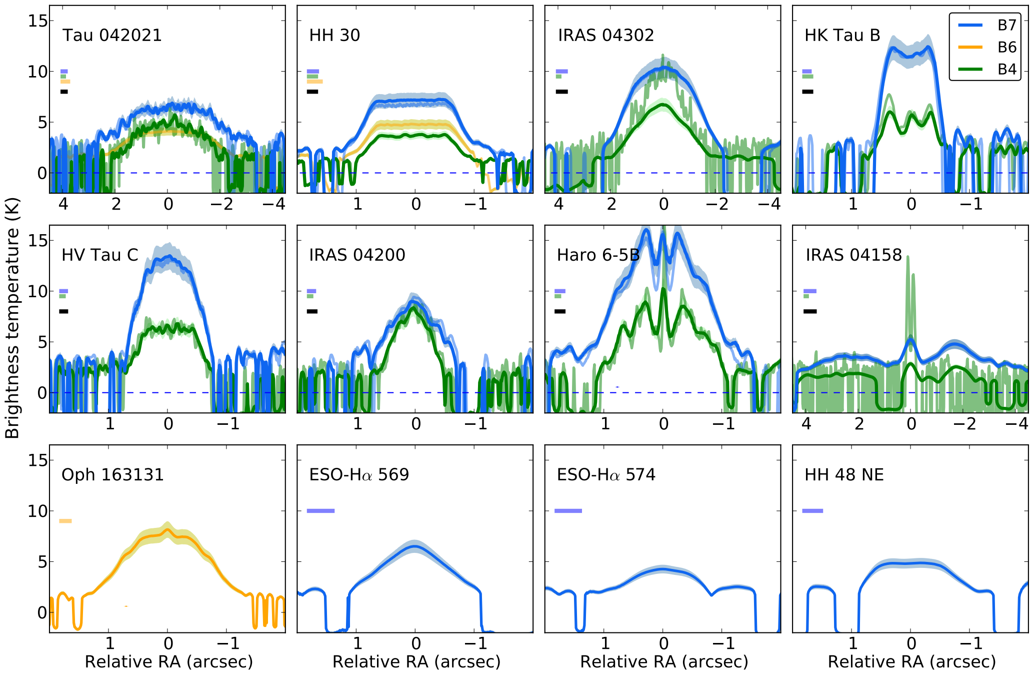

Figure 4.5 – Observed brightness temperatures as a function of radial distance. Solid lines were computed with the same angular resolution, while the light lines have the original angular resolution. We report the beam sizes in the direction of the cut as horizontal lines in the left part of each plot. The restored beam corresponds to the black line. Error bars correspond to 10% of the brightness temperature.

4.3.2 *Brightness temperatures*

The brightness temperature of a source corresponds to the temperature of an optically thick blackbody at the corresponding wavelength. I inferred the brightness temperatures of the disks by inverting the Planck equation on our continuum images, without using the Rayleigh-Jeans approximation ($h\nu \ll k_B T$) which might not be appropriate for our observations. To ease the comparison for each source, I computed the brightness temperatures from the band 7 and band 4 maps computed at the same angular resolution (see Section 4.2.4). I report the *peak* brightness temperatures in Table 4.7 and show the brightness temperature profiles measured along the major axis direction in Fig. 4.5. In this figure, the solid lines correspond to cuts on the images with the restored beam, while light colored lines are for the best angular resolution. Note that the beam sizes of the band 6 observations of Tau 042021 and HH 30 are significantly larger than the restored beam. Thus, it is not possible to compare directly the band 6 brightness temperatures to the band 4 and band 7 temperatures shown in Fig. 4.5, the beam dilution will be different. Finally, a direct comparison of brightness temperature between sources is difficult as they would have different levels of beam dilution.

We note that, even for the most resolved sources (i.e., least impacted by beam dilution), the inferred brightness temperatures are lower or comparable to those

Sources	B7 (K)	B4 (K)
Tau 042021	$6.9^{\dagger}$	$5.3^{\dagger}$
HH 30	7.2	3.7
IRAS 04302	10.3	$6.7^{\dagger}$
HK Tau B	11.4	$5.4^{\dagger}$
HV Tau C	13.5	6.8
IRAS 04200	$9.1^{\dagger}$	$8.7^{\dagger}$
Haro 6-5B	$15.8^{\dagger}$	$9.9^{\dagger}$
IRAS 04158	5.2	
ESO-Hα 569	6.5	
ESO-Hα 574	4.3	
HH 48 NE	4.9	

Table 4.7 – Peak brightness temperatures. The uncertainties are limited by errors in flux calibration and can thus be estimated by 10% of the reported brightness temperature peak. The reported peak brightness temperatures were computed using the same beam in both bands (see Table 4.5 for details). We only report the peak band 7 brightness temperature of IRAS 04158 as the disk is not detected in band 4.
$^{(\dagger)}$ Well resolved sources in all directions.

required to be in the Rayleigh-Jeans regime, respectively $T > 16.2\,\mathrm{K}$ for band 7 and 6.8 K for band 4. This strengthens our choice not to use this approximation. Additionally, we find that the band 4 brightness temperatures are systematically lower than the band 7 ones.

4.3.3 *Radial extent*

To characterize the radial extent of the disks, we present cuts along the major axis of each disk in Fig. 4.6. The cuts are normalized to their maximum intensity. For Tau 042021, IRAS 04302 and HV Tau C, for which the band 4 emission is very noisy, we estimate the normalizing factor as the amplitude of the Gaussian best fitting the curves. All sources are well resolved along their major axis.

4.3.3.a. Morphology

For several sources, the brightness profile is flat along the major axis direction and drops steeply at the edges. This is particularly true for HH 30, HK Tau B, HV Tau C, and HH 48 NE. The lack of a central brightness peak further supports the idea that these disks are optically thick and highly inclined, so that we are viewing only the outer optically-thick edge. This idea will be tested further in Section 4.4.2 (Fig. 4.12). Conversely, the disks of Tau 042021, IRAS 04302, IRAS 04200, ESO-Hα 569, and ESO-

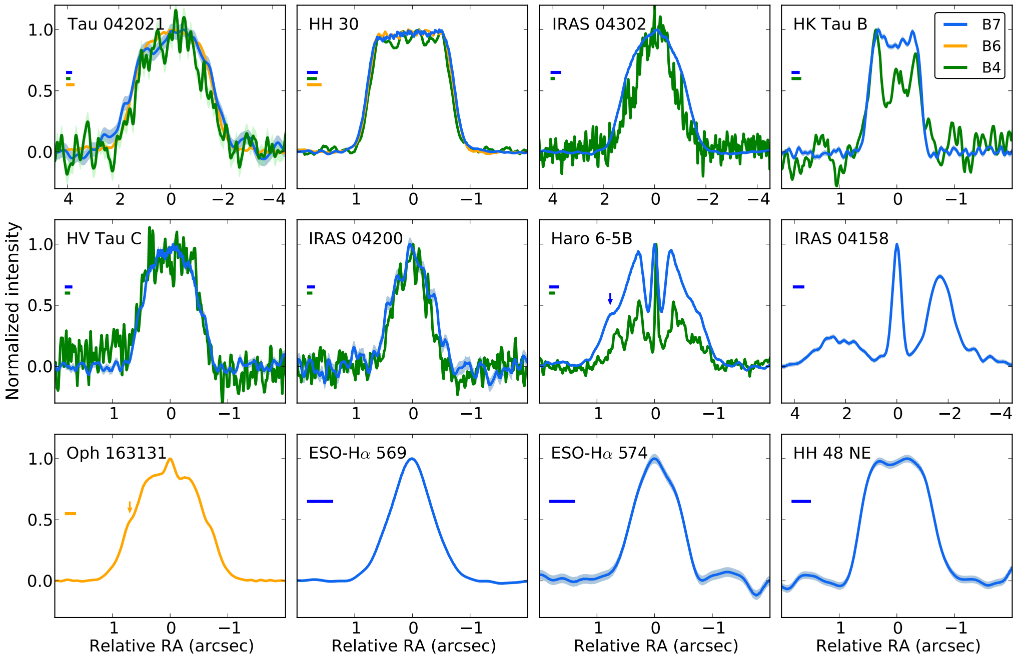

Figure 4.6 – Normalized major axis intensity profiles. The light shading corresponds to the normalized rms in each band. The beam sizes in the direction of the cut are shown in the left part of each plot as horizontal lines. We indicate the shoulders of Haro 6-5B and Oph 163131 by an arrow. Note that we smoothed the cuts through Tau 042021 by convolving them by a 1-D Gaussian of the beam width, to reduce the noise and make the plot clearer.

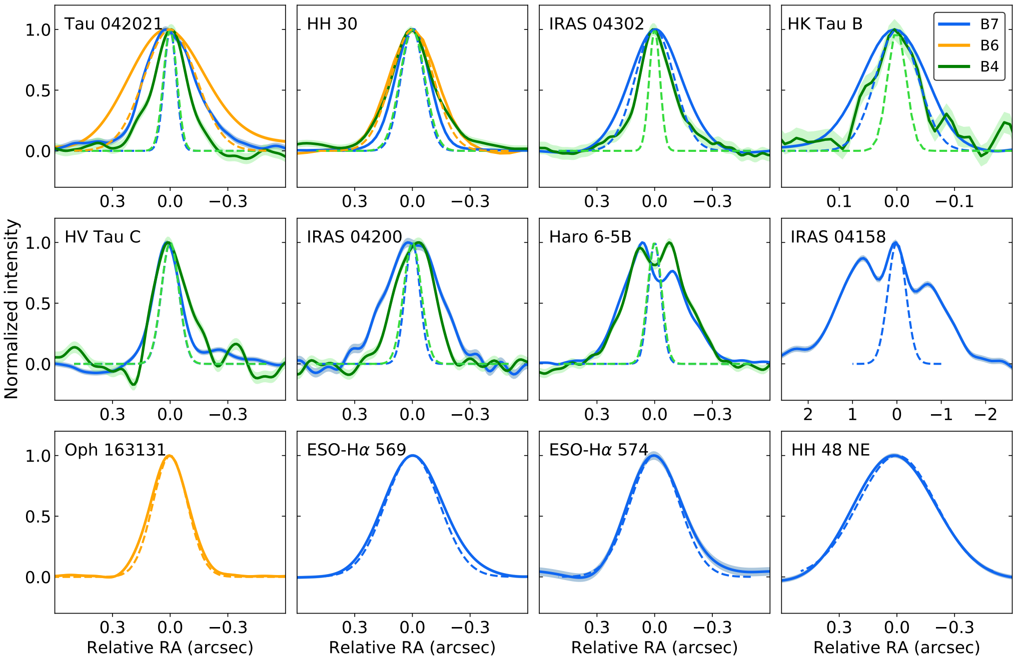

Figure 4.7 – Normalized averaged minor axis intensity profiles. For the most inclined sources (resp. least inclined: IRAS 04200, Haro 6-5B, and IRAS 04158), these were obtained by averaging minor axis intensity cuts over the whole major axis of the disk (resp. over the central 0.3”). The light shading correspond to the normalized rms in each band. The beam sizes in the direction of the minor axis are shown as dotted Gaussian of the corresponding color.

Hα 574 show more centrally peaked emission without a clear plateau, suggesting that they are optically thinner and/or viewed with a lower inclination, less edge-on. Additionally, we note that the radial brightness profile of HK Tau B shows hints of rising at the edges. While this is a marginal (3σ) feature, this may indicate the presence of a ring (or transition disk).

Finally, three disks (Haro 6-5B, IRAS 04158, and Oph 163131) show symmetric shoulders or clear evidence of ring like features:

- The main ring of Haro 6-5B peaks at $\sim 0.29''$ (41 au) in both bands. Furthermore, a shoulder seen in band 7 is associated with a peak in the higher-resolution band 4 cut; this would correspond to a fainter ring located at $\sim 0.77''$ (108 au).
- The brightness asymmetry of the outer ring in IRAS 04158 is very clear in the major-axis cut: its western side is about 3 times brighter than the eastern side. We also note that the ring is slightly off-centered compared to the central binary. The western side of the disk peaks at $\sim 1.71''$ (239 au), while the eastern side peaks at $\sim 2.28''$ (319 au) from the center. We fit Gaussians on each side of the disk in the radial profile and find that the eastern ring is about 1.7 times wider than the western ring (with full width half maximum, FWHM, of 1.98″ and 1.18″ respectively).
- We also find that Oph 163131 displays a relatively flat profile in the inner 0.5″, but has a sharp central peak. It has symmetric shoulders at $\sim 0.70''$, which suggests that this disk contains two rings, and is viewed slightly away from edge-on. Further modeling of this source, focusing on dust emission, will be presented in a separate analysis in which I am involved (Wolff et al., in prep). Additionally, higher angular resolution (0.02″) obtained during ALMA cycle 6 (Project 2018.1.00958.S, PI: Villenave) reveal the presence of the rings. A preliminary analysis of the images is presented in Chapter 5.

4.3.3.b. Size estimations

For this study, we aimed at determining the disks radial extent to look for size variation with wavelength. To determine the sizes, we first normalized the major axis cuts presented in Fig. 4.6, as mentioned in the beginning of this section. Then, for each source, we estimate the relevant 3σ noise level in the image with the worst signal-to-noise ratio, either band 4 or band 7. This 3σ level is converted into a fraction of the peak, in percent. The sizes in both bands are then measured at the same level, i.e., at the same fraction of the peak. The disk sizes along their major axis are reported in Table 4.8. The errors correspond to a tenth of the beam size along the major axis direction.

Along with the major axis size, we also estimate the apparent sharpness of the disk's edges, as measured in the image plane. To do so, we measure the fractional range of radius over which the millimeter emission decreases from 80% to 20% of the peak emission, called $\Delta r/r$. We define Δr by $\Delta r = |r_{80\%} - r_{20\%}|$ and the normalisation radius by $r = |r_{80\%} + r_{20\%}|/2$. We chose this flux range because the radial profiles can usually be well approximated by straight lines in this interval. We report the values

Source	B7 (″)	B6 (″)	B4 (″)	Optical/NIR (″)	$\Delta r/r$
Tau 042021	4.10 ± 0.01	3.76 ± 0.02	3.67 ± 0.01	5.0	0.6 ± 0.1
HH 30	1.85 ± 0.01	1.82 ± 0.02	1.73 ± 0.01	3.1	0.2 ± 0.1
IRAS 04302	3.15 ± 0.03		2.84 ± 0.01		0.7 ± 0.1
HK Tau B	0.99 ± 0.01		0.99 ± 0.01	1.3	0.2 ± 0.1
HV Tau C	1.20 ± 0.01		1.18 ± 0.01	0.8	0.5 ± 0.1
IRAS 04200	1.00 ± 0.01		0.85 ± 0.01		1.0 ± 0.1
Haro 6-5B	2.06 ± 0.01		1.74 ± 0.01	2.3	$0.8 \pm 0.1^{\dagger}$
IRAS 04158	7.47 ± 0.03			13.6	
Oph 163131	1.30 ± 0.03^{a}	2.50 ± 0.01		2.6	0.7 ± 0.1
ESO-Hα 569	1.88 ± 0.04			2.0	0.9 ± 0.2
ESO-Hα 574	1.35 ± 0.04			1.2	0.7 ± 0.2
HH 48 NE	1.72 ± 0.03			1.3	0.4 ± 0.1

Table 4.8 – Major axis sizes for millimeter and optical/NIR images, and estimates of the mean deconvolved major axis sharpness of the millimeter data. The errors in the millimeter sizes correspond to one tenth of the beam width in the major axis direction. When possible, the $\Delta r/r$ ratios correspond to their averaged values between the band 7 and band 4. All are deconvolved by the beam.
$^{(\dagger)}\Delta r/r$ of the band 7 only.
References: $^{(a)}$ FWHM from Cox et al. (2017) fitting a Gaussian

of $\Delta r/r$ in the last column of Table 4.8. The values are the mean of the estimations in band 4 and band 7 and they are deconvolved by the beam size. Sharp outer edges have small Δr and hence small $\Delta r/r$. Additionally, the disk size slightly affects the value of the ratio. For example, a typical beam with a FWHM of 0.1″ would have $\Delta r/r \simeq 0.1$ when calculated in a small disk similar to HK Tau B ($r = 0.5''$), or $\Delta r/r \simeq 0.04$ in a disk as large as IRAS 04302 ($r = 1.2''$). All the disks in our sample have $\Delta r/r$ values larger than 0.2, which corresponds to shallower outer edges than the typical beam.

We find two different families of objects when comparing the radial extent of the disks in band 4 and band 7. Four sources (Tau 042021, IRAS 04302, IRAS 04200, and Haro 6-5B) show a band 7 size more extended than the band 4 by more than 2 beams. When compared at the same angular resolution, these sources have band 7 major axis sizes on average 15% larger than that of the band 4. The outer edges of these four sources are well resolved and they have an average apparent sharpness of $\Delta r/r \sim 0.8$, much shallower than the beam.

For the three remaining sources (HH 30, HK Tau B, HV Tau C), no difference in radial extent is found between band 7 and band 4. This might suggest the presence of dust traps at the outer edges of these disks, which can slow radial drift and lead particles to stop at particular radial locations (Powell et al., 2019). Including HH 48 NE, these four sources have the sharpest edges, with $\Delta r/r$ between 0.2 and 0.5, i.e., only just resolved. The edges of these disks are only marginally shallower than the typical beam.

4.3.4 *Disk extent perpendicular to the midplane*

For the most inclined systems, the intensity maps shown in Fig. 4.4 have very elongated, linear shapes rather than elliptical ones, so we generate the minor axis profiles by taking the mean of the cuts at all distances along the major axis. In that case, the size of the minor axis is dominated by the vertical extent of the disk perpendicular to the midplane. For the least inclined sources where a clear ellipticity is visible in the image (namely IRAS 04200, Haro 6-5B, and IRAS 04158), we generate the minor axis profiles by averaging over a restricted range, only ±0.15″ around the center of the disk. In that case, the minor axis is dominated by the projection of the disk radius. We show the averaged brightness profile along the minor axis for all sources in Fig. 4.7. Dashed lines trace the Gaussian beam profiles along the cut direction. We find that six out of the twelve disks of our sample are well-resolved along the minor axis, having a width more than twice the beam width. They are Tau 042021, IRAS 04200, Haro 6-5B (in both band 7 and band 4), IRAS 04158 (in band 7), and IRAS 04302, HK Tau B (in band 4). Additionally, the minor axis profiles of Haro 6-5B and IRAS 04158 reveal the presence of rings, and we see a clear asymmetry in the band 7 cut of Haro 6-5B.

We measure the minor axis sizes by fitting Gaussians to the generated profiles, Gaussians being good first approximations. For Haro 6-5B and IRAS 04158 for which the cuts show ring features, we estimate the FWHM directly through the cuts, by reading the size of the disk at 50% of the peak flux. We report the resulting FWHM in Table 4.9, where the errors correspond to a tenth of the beam size projected in the direction of the cut.

In order to extract the intrinsic vertical extent of the disks, we also deconvolve the minor axis sizes by the beam size in the direction of the cut, assuming both profiles are Gaussian. These values are presented in Table 4.10. We estimate the uncertainties on the deconvolved minor axis sizes by propagating the errors. From Gaussian fits of the calibration sources, we estimate that the error on the beam size is about 10% of the beam major axis size (from band 7 observations taken in the most extended array configuration). For the least resolved disks, i.e., for Oph 163131, ESO-Hα 569, ESO-Hα 574, and HH 48 NE, we only report upper limits. We estimate the uncertainties on the deconvolved minor axis sizes by propagating the errors, assuming that the error on the beam size is 10% of the beam major axis size.

Finally, note that even for the most inclined disks, the minor axis size is related but is not a measurement of the FWHM of the dust's vertical density profile at a given radius. Indeed, observations are measuring the integrated intensity along the line of sight over the whole disk (i.e., from several radii) and are affected by optical depth effects. This second point implies that if the disk is optically thick, observations probe

Source	Minor B7 (″)	Minor B6 (″)	Minor B4 (″)
Tau 042021	$0.32 \pm 0.01^{\dagger}$	0.49 ± 0.03	$0.21 \pm 0.01^{\dagger}$
HH 30	0.21 ± 0.01	0.29 ± 0.03	0.27 ± 0.02
IRAS 04302	0.32 ± 0.02		$0.21 \pm 0.01^{\dagger}$
HK Tau B	0.13 ± 0.01		$0.10 \pm 0.01^{\dagger}$
HV Tau C	0.17 ± 0.01		0.19 ± 0.01
IRAS 04200*	$0.33 \pm 0.01^{\dagger}$		$0.23 \pm 0.01^{\dagger}$
Haro 6-5B*	$0.35 \pm 0.01^{\dagger}$		$0.35 \pm 0.01^{\dagger}$
IRAS 04158*	$2.36 \pm 0.05^{\dagger}$		
Oph 163131	0.16 ± 0.07^{a}	0.23 ± 0.02	
ESO-Hα 569	0.37 ± 0.03		
ESO-Hα 574	0.33 ± 0.03		
HH 48 NE	0.49 ± 0.05		

Table 4.9 – Full width half maximum of the (averaged) minor axis profiles. The uncertainties correspond to one tenth of the beam size along the cut direction.
(∗) Disks with inclination lower than 75°. Their minor axis size is likely dominated by the radial extent of the disk over its vertical extent, as opposed to more inclined disks. (†) Resolved by more than 2 beams in the minor axis direction. These are the ones for which the deconvolved minor axis size should be the most reliable (see Table 4.10).
References: (a) Cox et al. (2017)

Source	Deconvolved B7 (″)	Deconvolved B6 (″)	Deconvolved B4 (″)
Tau 042021	$0.31 \pm 0.01^{\dagger}$	0.37 ± 0.06	$0.20 \pm 0.01^{\dagger}$
HH 30	0.16 ± 0.02	0.14 ± 0.07	0.22 ± 0.02
IRAS 04302	0.21 ± 0.05		$0.20 \pm 0.01^{\dagger}$
HK Tau B	0.10 ± 0.01		$0.09 \pm 0.01^{\dagger}$
HV Tau C	0.13 ± 0.02		0.16 ± 0.02
IRAS 04200*	$0.31 \pm 0.01^{\dagger}$		$0.21 \pm 0.01^{\dagger}$
Haro 6-5B*	$0.34 \pm 0.01^{\dagger}$		$0.34 \pm 0.01^{\dagger}$
IRAS 04158*	$2.31 \pm 0.05^{\dagger}$		
Oph 163131		< 0.14	
ESO-Hα 569	< 0.13		
ESO-Hα 574	< 0.21		
HH 48 NE	< 0.24		

Table 4.10 – Deconvolved full width half maximum of the (averaged) minor axis profiles.
(∗) and (†) as in Table 4.9.

the dust $\tau = 1$ surface, which might be located at a few gas scale height above the midplane. Along this chapter, we use the term *dust scale height* to describe the vertical density profile of dust grains at a given radius. We use the same definition as for the gas pressure scale height (e.g., Fromang and Nelson, 2009).

We also estimate the disk inclinations from the measured axis ratio in all bands, and report them in Table 4.2. For consistency, we use the FWHM of the major axis sizes (cut at 50% of the peak flux) to estimate the inclination, as opposed to the size at 3σ reported in Table 4.8. For the sources that are not resolved in the vertical direction (Oph 163131, ESO-Hα 569, ESO-Hα 574, HH 48 NE) and those with the smallest axis ratio (Tau 042021, IRAS 04302, HK Tau B, HV Tau C), we present these values as lower limits. Indeed, for the most inclined systems, i.e. those with the smallest axis ratio, the minor axis size might not be dominated by the inclination but by the actual vertical thickness of the disks, which leads to lower apparent inclinations based on the axis ratio only. Except IRAS 04200, Haro 6-5B, and IRAS 04158, all resolved disks have an inclination larger than 75°. We note that Tau 042021 is the only disk more inclined than 85° which is resolved along its minor axis in both band 7 and band 4. For this disk, the band 7 appears about 1.5 times more extended vertically than the band 4. This is discussed in more detail in Section 4.4.1.

4.3.5 *Estimation of spectral indices*

Using the continuum fluxes from our survey and (sub)millimeter fluxes from the literature, we estimate the global millimeter spectral index α_{mm} for each source. We use a least-squares fit of all photometric points between 800 μm and 3.3 mm. We find $\alpha_{mm} \leq 3$ for all disks, as can be seen in Table 4.6.

Global spectral indices do not take into account the spatial distribution of the emission. Thus, for sources with multiple millimeter images, we computed spectral index maps using the band 4 and band 7 observations imaged at the same angular resolution (see Section 4.2.4). The size of the recovered beam is reported in Table 4.5. We generated the spectral index maps pixel-by-pixel by applying the CASA task `immath`. Finally, to lower the noise level in the spectral index map, we applied a filter to keep only the pixels with emission well above the noise level (5σ) in both the band 4 and the band 7 images. The final maps and cuts along the major and minor axis are displayed in Fig. 4.8.

We find that the spectral index increases with radius for most sources, albeit with larger uncertainties at larger radii due to the lower signal-to-noise ratio. Similarly, the spectral index also rises along the minor axis direction for two disks, Tau 042021 and IRAS 04200. Previous studies identified similar increases in the radial direction in several disks seen at lower inclinations (e.g., Pinte et al., 2016; Dent et al., 2019). The increases were attributed to changes in the dust size distribution and/or to lower optical depths at large radii. Very inclined systems on the other hand are optically

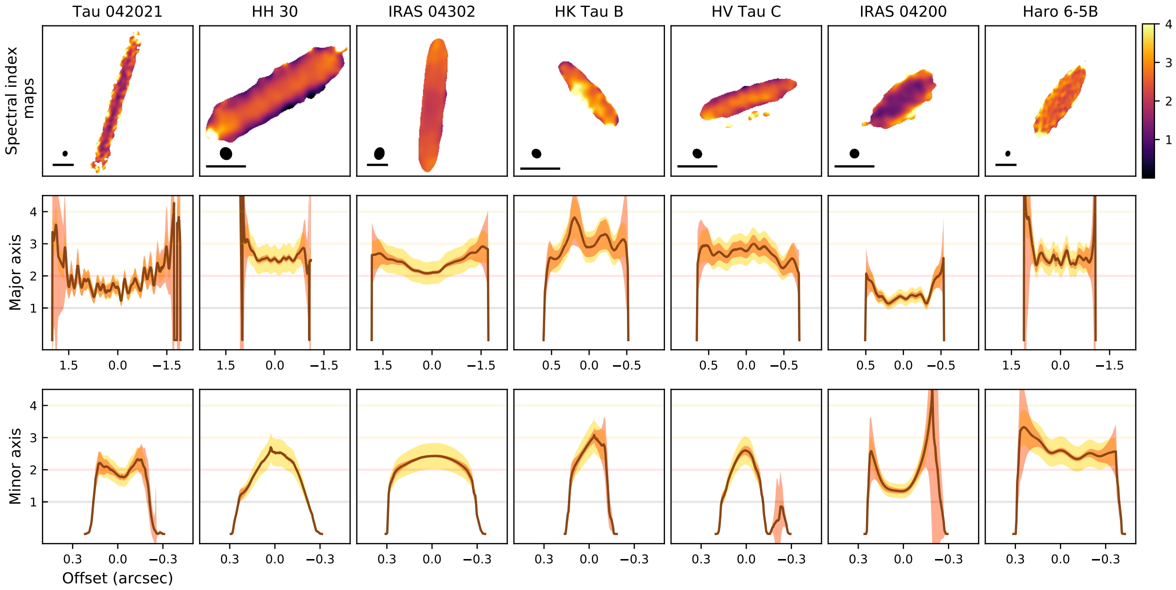

Figure 4.8 – **Top row:** Spectral index maps, applying a filter to keep only the pixels with more emission than 5σ in both bands. The beam size is shown in the bottom left corner, along with a dark line representing a 0.5″ scale.
Middle row: Spectral index cuts along the major axis.
Bottom row: Spectral index profiles along the minor axis, averaged as done for Fig. 4.7 (see text Section 4.3.4).
For all cuts, yellow errors correspond to a flux calibration error of 10% in both bands, while orange errors are estimated from the signal-to-noise in each band. The x-axis corresponds to the offset to the center of the disk in arcseconds.

thicker than low inclination disks for the same mass, as can be seen in Fig. 4.17. This is due to projection effects, because the line-of-sight crosses the disk over a longer distance. This suggests that spectral index variations are dominated by changes of optical depth inside the disk rather than by grain growth in our sample (see also our radiative transfer model, Fig. 4.18). However, at the outer edges, where the disks become optically thinner, spectral index variations are enhanced by changes in the dust size distribution (see e.g., Tau 042021, IRAS 04302, IRAS 04200, and Haro 6-5B, where we found large differences in major axis sizes between band 7 and band 4). We also note that HH 30 and HV Tau C show the opposite behavior of Tau 042021 and IRAS 04200 along the minor axis, their spectral indices decrease. However, neither of them is well resolved along the minor axis, so variations can be more affected by beam dilution and are less reliable.

Finally, we obtain spectral index values lower than 2 in the innermost regions of two disks: namely Tau 042021 and IRAS 04200 (see also our radiative transfer model, Fig. 4.18). Such low values have also been measured in the inner regions of other disks (e.g., Huang et al., 2018a; Dent et al., 2019), and have often been interpreted as flux calibration errors because in the Rayleigh-Jeans regime α should not be smaller than 2. However, considering a 10% flux calibration error (yellow shaded regions in Fig. 4.8), the lowest α values measured in Tau 042021 and IRAS 04200 can not be reconciled with $\alpha = 2$. Recent studies showed that low dust temperatures (outside the Rayleigh Jeans regime) or dust scattering in optically thick regions can reduce significantly the emission of a disk. In both cases, the spectral index can be even lower than 2 (e.g., Liu, 2019; Zhu et al., 2019). In the context of highly inclined disks such as Tau 042021 and IRAS 04200, which are optically thick (see Fig. 4.17), both explanations are equally valid to explain low spectral indices observed. Modeling is needed to determine which one is dominant.

To summarize, because of the high inclination of our sources, we interpret the observed variation of spectral indices along the major and minor axis as being dominated by optical depth changes in the disks. Additionally, we find that the low spectral index values measured in Tau 042021 and IRAS 04200 can either be related to low dust temperatures or to dust scattering in optically thick regions.

4.3.6 *Comparison with optical and NIR images*

We present overlays of optical and NIR images with our band 7 observations in Fig. 4.9. For most disks, we use HST optical images but prefer (space-based or ground-based) near-infrared (NIR) images in a handful of cases to reduce confusion with extended nebulosity (3 sources, see references in Fig. 4.9). All scattered light images show the same characteristic features, with two bright reflection nebulae separated by a dark lane tracing the obscuration of direct starlight by the edge-on disk. As opposed to the scattered light images, the millimeter data appear as very flat disks. All sources are found much less extended vertically in the millimeter than in scattered light, the result of a combination of opacity effects and vertical settling. Most of them also appear less extended radially, which can be linked to dust radial drift or opacity effects.

Thanks to several collaborators (G. Duchene, Z. Telkamp, and H. Williams), we estimated the scattered light major axis sizes by following the spine of each nebulae. The method is described in more details in Appendix D of the paper (see the draft in Appendix A). The scattered light radial sizes are reported in Table 4.8. We could not estimate the scattered light sizes for two disks of the sample: for IRAS 04302 because we likely do not see the disk but the envelope; and for IRAS 04200 because the bright point source in the northern nebulae prevented the method to converge. Also, we indicate that our scattered light radial sizes might be under-estimated because lower illumination or lower sensitivity in the outer regions might reduce the apparent optical/NIR size (see for example Muro-Arena et al., 2018). A complete analysis will require the use of tracers of the gas distribution, which we postpone to a future paper (see Chapter 5).

Despite this, we find that most sources are larger radially in scattered light than in the millimeter, albeit with a few exceptions, the most obvious case being HV Tau C. ESO-Hα 574 and HH 48 NE, although formally more compact in scattered as estimated with our algorithm, have very similar sizes and will require deeper millimeter data for confirmation. The ratios of scattered light over thermal continuum band 7 sizes

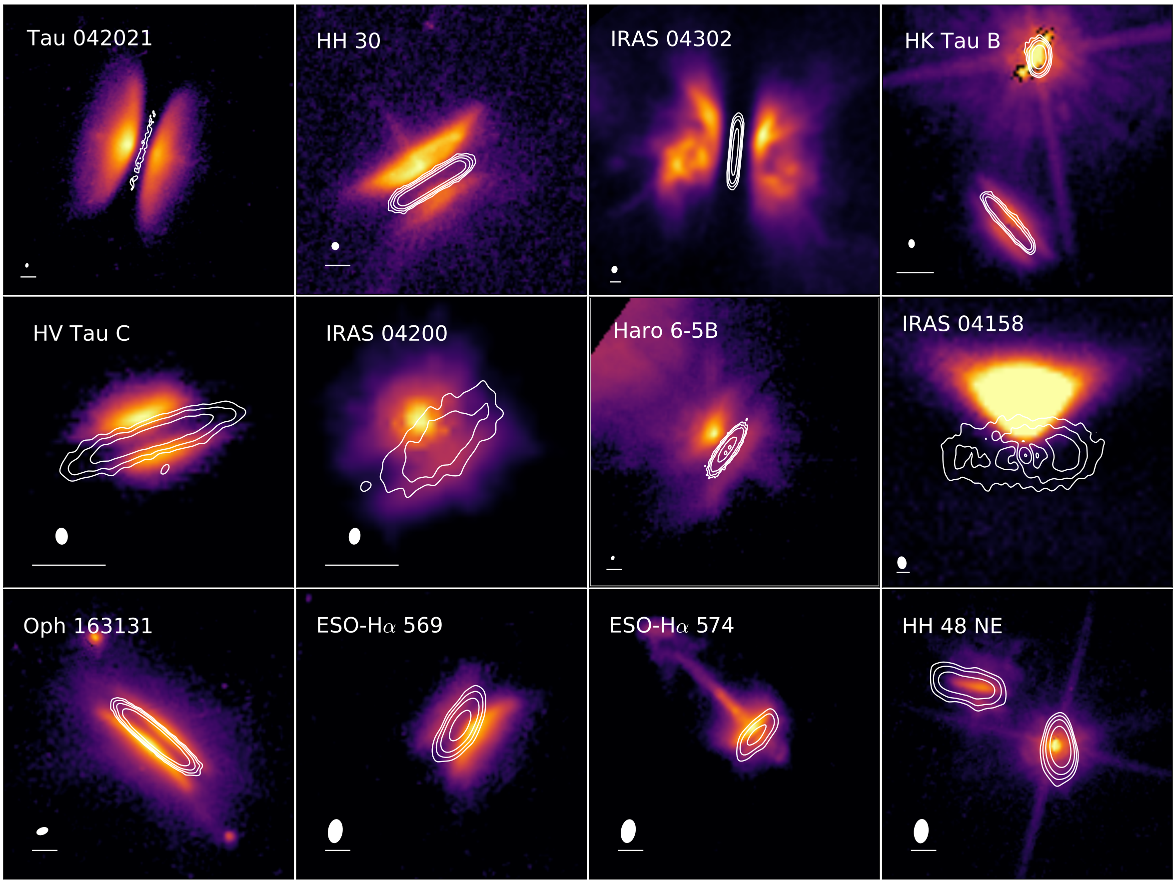

Figure 4.9 – Overlay of scattered light (colors, in logarithmic scales) and ALMA band 7 continuum images (5, 10, 20 and 50σ contours) for all sources in this study, except for Oph 163131 for which we show the band 6 image. The scattered light images are plotted between 3σ (except for IRAS 04302 and IRAS 04158, where we use respectively 60 and 1σ to increase the contrast) and their maximum brightness (except for IRAS 04158, for which we take a lower value to increase the contrast). The ellipse and horizontal line in the bottom left corner indicate the beam size of the ALMA image and a 0.5″ scale.
References: Scattered light images, **2.2 μm:** HV Tau C: Duchêne et al. (2010); **1.9 μm:** IRAS 04302: Padgett et al. (1999); **1.6 μm:** Haro 6-5B: Padgett et al. (1999); **0.8 μm:** Tau 042021: Duchêne et al. (2014), HH 30: Watson and Stapelfeldt (2004), IRAS 04158: Glauser et al. (2008), ESO-Hα 569: Wolff et al. (2017), HH 48 NE: Stapelfeldt et al. (2014); **0.6 μm:** IRAS 04200: Stapelfeldt et al. (in prep), Oph 163131: Stapelfeldt et al. (2014), ESO-Hα 574: Stapelfeldt et al. (2014); **0.4 μm:** HK Tau B: Duchêne et al. (in prep).

are between 0.7 and 2.0. This is in general consistent with predictions from radial drift theory: the objects with clear evidence for radial drift being those in which scattered light disk (small grains) is significantly larger than the millimeter continuum disk (large grains). Additionally, while we do not quantify explicitly the vertical extent of the scattered light images, Fig. 4.9 clearly shows that all disks are significantly more extended vertically in scattered light than at millimeter wavelengths. This indicates that vertical settling is occurring in these disks, which will be further studied in Section 4.4.1.

4.4 DISCUSSION

In this section, we aim at interpreting the vertical and radial structure of our highly inclined disks, using radiative transfer modeling. We use the radiative transfer code MCFOST (Pinte et al., 2006; Pinte et al., 2009, see Section 1.5). Note that a large fraction of this section has been updated in the revised version of the paper, I refer the reader to the final version of the paper in Appendix A, and present the submitted version of the paper in the manuscript.

As modeling each individual disk is beyond the scope of this study, we use the comprehensive model of HL Tau presented in Pinte et al. (2016) as our fiducial disk model. This model is relevant as it is one of the few characterizing the millimeter scale height of a protoplanetary disk. The authors assumed that dust grains are affected by settling and follow the vertical density profile described in Fromang and Nelson (2009, equation 1.17 reported in Section 1.3.2 of this thesis). From the contrast ratio of HL Tau's gaps and rings along the minor axis direction, Pinte et al. (2016) constrained the millimeter dust vertical distribution, expressed in terms of a "scale height", to $h_{1\mathrm{mm}} = 0.7\,\mathrm{au}$ at 100 au. Indeed, as can be seen in Fig. 4.10, the rings are less visible

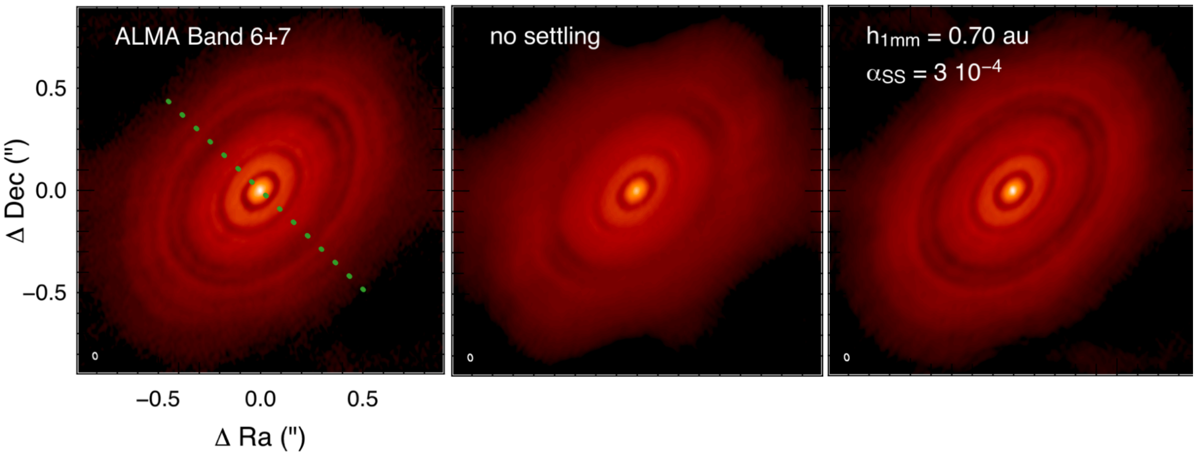

Figure 4.10 – Effect of dust settling on the appearance of the HL Tau model. Along the minor axis, the rings are seen more clearly in the model with settling (right panel) than in the model without settling (middle panel), which suggests that this disk has a very thin millimeter vertical extent. *Adapted from Fig. 4 of Pinte et al. (2016)*

in the minor axis direction when no settling is considered. As of now, we will refer to this model with settling as our *fiducial model*. We note that the HL Tau model contains several rings and gaps and has an outer radius of about 140 au (Pinte et al., 2016).

In order to understand the observable effects of vertical settling, we also consider the HL Tau model without settling. In this case, all grain sizes are fully mixed with the gas and so the millimeter dust scale height, h_{1mm}, is equal to h_{gas}, which is 10 au at a radius of 100 au. Similarly to the fiducial model, radial drift is not included in the calculation of the model without settling.

The models were calculated at a distance of 140 pc, which is similar to the average distance to Taurus molecular cloud where most sources of our sample are located (see Table 4.1). We recomputed the models at 0.89 mm (resp. 2.06 mm) for inclinations between 82.5° and 90°. In Fig. 4.11, I show the resulting MCFOST images. Without convolving the images by a beam, we note that we can distinguish the rings for the fiducial model (at the lowest inclinations) but not for the models without settling. This is directly related to the small vertical extent of the millimeter grains in the fiducial model and was an argument to estimate the millimeter scale height of HL Tau by Pinte et al. (2016).

To be able to perform a direct comparison of the models with our observations, I produced synthetic images using the `simobserve` and `simanalyze` tasks of the CASA simulator. I used the same antenna configuration, date and integration time as in the observations, which allows to achieve a similar uv coverage than in our data (either band 4 or the extended configuration of band 7). Finally, I generated band 7 and band 4 images with a similar resolution to the restored beam presented previously (see Table 4.5), by using a `uvtaper`. This results in beam sizes of $\sim 0.11 \times 0.07''$ for the band 7 synthetic images and $\sim 0.13 \times 0.08''$ for the band 4. The synthetic band 7 images (0.89 mm) are presented in Fig. 4.12.

4.4.1 *Vertical extent*

4.4.1.a. Effect of inclination on the vertical extent of the fiducial model

In the top panels of Fig. 4.12, I show the synthetic images of our fiducial model at several inclinations, while the bottom panels present images of the radiative transfer model without settling. The disk appears much more extended vertically for the case without settling than for the fiducial model. As the inclination approaches 90°, without settling, the high optical depth in the midplane results in a clear low intensity lane in the midplane separating the two sides of the disk, while for lower inclination the bottom (far) side of the disk is about 4 times fainter than the top (near) side. As the angular resolution is similar and the signal to noise is greater than 14 for all targets such an asymmetry would be detectable easily in our observations. However, neither the vertical asymmetry nor the dark lane in the midplane are present in our data. Interestingly, they can hardly be seen in the model that includes settling (top row of the Fig. 4.12). This clearly suggests that these disks have a small millimeter

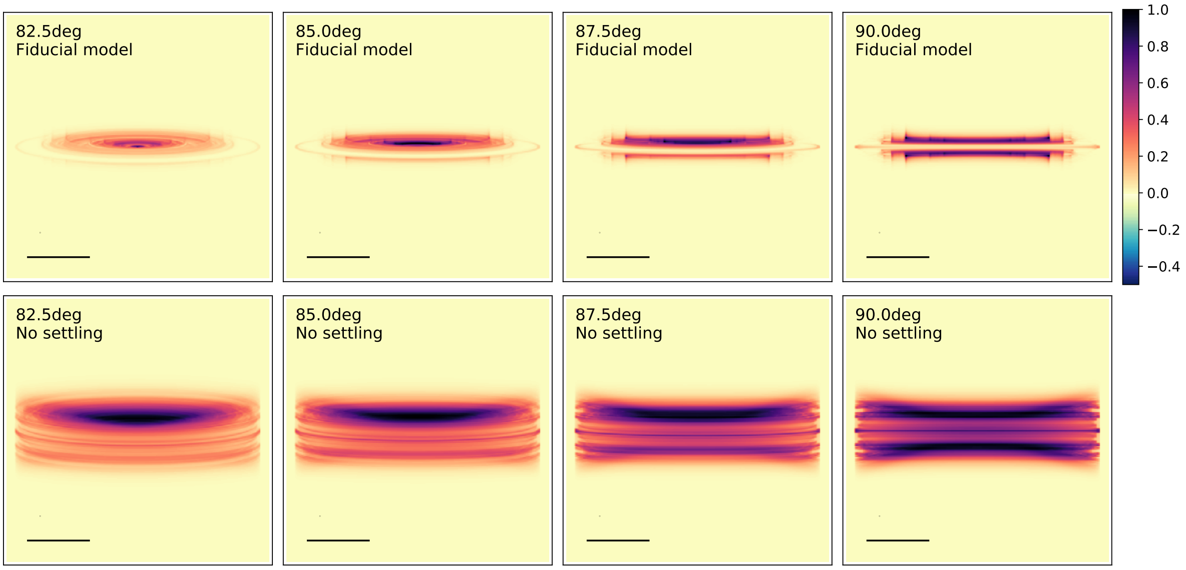

Figure 4.11 – **Top:** Model from Pinte et al. (2016) at 0.89 mm (band 7), computed at high inclination and including settling ($h_{1mm} = 0.70$ au, fiducial model).
Bottom: Same models at 0.89 mm but without including settling ($h_{1mm} = h_{gas} = 10$ au). The horizontal lines of the model without settling are likely numerical artefacts. All images are normalized to their peak surface brightness.
The horizontal line in the bottom left of each pannels represents a 0.5″ scale.

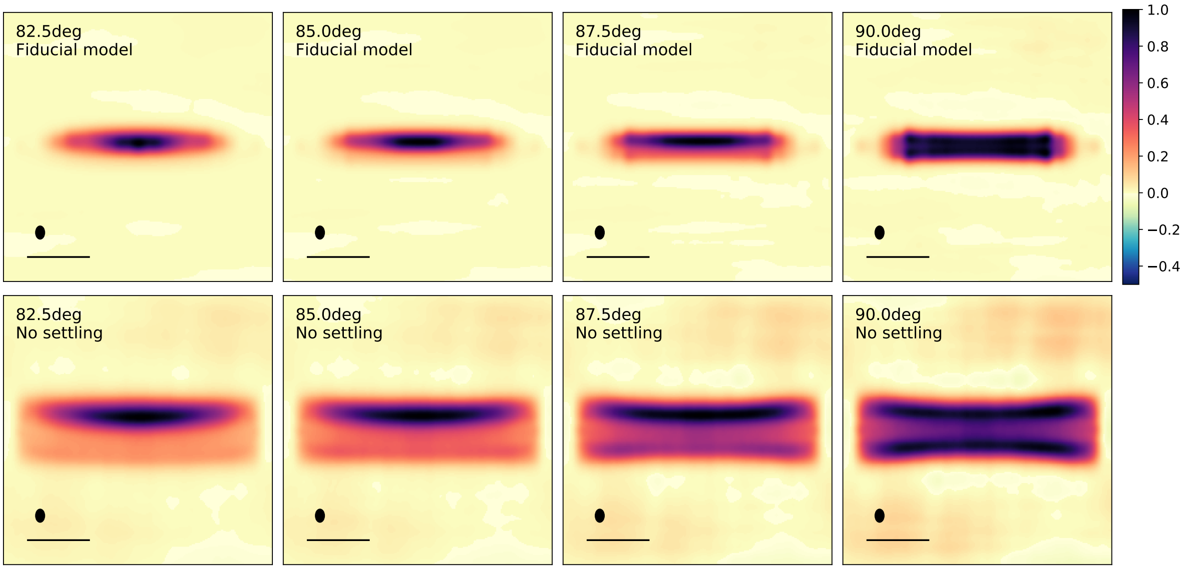

Figure 4.12 – Same as Fig. 4.11 but convolved to the resolution of the observations through the CASA simulator. The horizontal line represents a 0.5″ scale, and the ellipse shows the beam size.

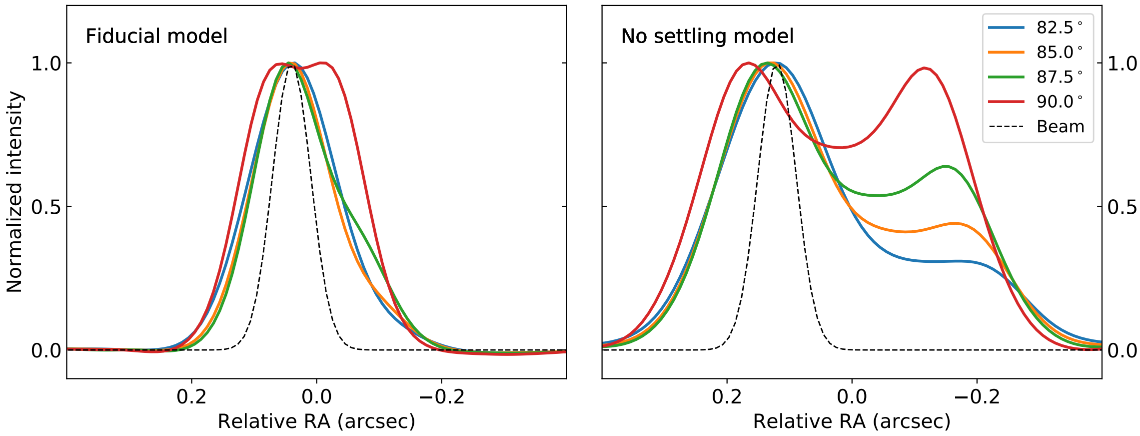

Figure 4.13 – Minor axis profiles for the fiducial model (left) and the model without settling (right), computed as in Fig. 4.7. The models were computed in band 7, so at 0.89 mm. All cuts are normalized to their peak surface brightness and I indicate the beam size as a dotted Gaussian in both panels.

dust scale height, closer to 1 au than to 10 au at a radius of 100 au. Because the gas scale height, indirectly probed by scattered light observations of micron-sized grains, is typically $\sim$ 10 au at 100 au (e.g., Burrows et al., 1996; Stapelfeldt et al., 1998), our results suggest that significant vertical settling of the millimeter dust has occurred in the present sample of protoplanetary disks.

To quantify further the compatibility of our fiducial, settled, model with the observations, I generated minor axis profiles following the method presented in Section 4.3.4. The profiles were generated by taking the mean minor axis cuts over the full radial extent of the disk. The minor axis profiles of the fiducial model and of the model without settling are shown in Fig. 4.13. Additionally, I report the deconvolved minor axis sizes for both models in Table 4.11. At 90°, the deconvolved FWHM of the minor axis profiles are about 0.18″ in band 7 and about 0.13″ in band 4. For comparison, the width of the model without settling measured on the cuts is about 0.45″ in band 7 and 0.42″ in band 4, at 90°. Considering only the three most inclined systems that are resolved by more than 2 beams in the vertical direction in our data (Tau 042021, IRAS 04302, and HK Tau B), we find that the average band 4 deconvolved width is about 0.16″. This minor axis size of millimeter grains is definitively closer to that of our fiducial model than to that of our model without settling. As noted previously, this indicates that for these systems the millimeter scale height would be closer to 1 au than to 10 au at 100 au. This suggests that the process of vertical dust settling is likely advanced in these disks, therefore increasing significantly the concentration of dust mass in the disk midplane.

Vertical settling models show that the turbulence generated self-consistently by ideal MHD or vertical shear instabilities are likely too strong to lead to millimeter scale height as small as 1 au at r = 100 au for gas scale heights of 10 au at 100 au (Flock et al., 2017). On the other hand, non ideal effects such as ohmic resistivity or ambipolar diffusion lead to lower turbulence and thus to very thin millimeter grains layers (Riols

	Fiducial model		No settling model		
Incl	Minor B7	Minor B4	Minor B7	Minor B4	$\Delta r / r_{\text{fiducial}}$
(°)	(″)	(″)	(″)	(″)	
82.5	0.15	0.13	0.23^a	0.32^a	1.2 ± 0.6
85	0.14	0.10	0.23^a	0.40	1.0 ± 0.5
87.5	0.15	0.11	0.43	0.42	0.7 ± 0.3
90	0.18	0.13	0.44	0.42	0.3 ± 0.1

Table 4.11 – Effect of inclination on model disk thickness and edge sharpness for our both radiative transfer models. I show the deconvolved minor axis sizes (FWHM) using the beam size in the direction of the cut, and the averaged deconvolved $\Delta r / r$ of the fiducial model. The average major axis size of the model is about 1.5″.
$^{(a)}$: Due to our definition of minor axis sizes (full width half maximum) and the shape of the minor axis profiles of the model at the lowest inclinations, the sizes are underestimated.

and Lesur, 2018). Those mechanisms might be dominant in the sample of disks analysed in this study. Detailed modeling of each individual object is needed to obtain a quantitative estimate of the millimeter and gas scale height of the disks.

4.4.1.b. Comparison with a published model of HK Tau B

HK Tau B is the only Class II disk of the sample which is well resolved by ALMA in the minor axis direction (in band 4), for which the scattered light image has been modeled. Stapelfeldt et al. (1998) estimated the scale height of micron-sized grains to be of the order of 3.9 au at 50 au (8.3 au at 100 au, assuming a flaring exponent of 1.1 as in Stapelfeldt et al., 1998). The parameters of this model are reported in their Table 1 and the 0.8 μm image of the model can be found in their Fig. 3. Aiming for a quantitative comparison of scale height between millimeter and micron-sized grains, we computed their best model C at millimeter wavelengths using the radiative transfer code MCFOST. We assumed that grains are fully mixed (i.e., no settling) and produce synthetic images using the CASA simulator with the same uv coverage as in our observations. To obtain a similar opacity of $\kappa \sim 120\,\text{cm}^2/\text{g}$ at 0.8 μm, we use dust grains (silicates) with sizes from 0.01 μm to 15 cm, and assume a number density described with a power law of the grain size $dn(a) \propto a^{-3.5} da$. This leads to opacities of about 4.8 cm^2/g and 2.6 cm^2/g respectively at 0.89 mm and 2.06 mm, which is comparable to standard assumptions (e.g., Ansdell et al., 2016). We show the results in Fig. 4.14.

We find that the model by Stapelfeldt et al. (1998) does not reproduce well the millimeter images of HK Tau B. Along the major axis, the model is too peaked at the center (less flat-topped) and more extended in the radial direction than the actual millimeter data. The more peaked profile suggests that the observed millimeter

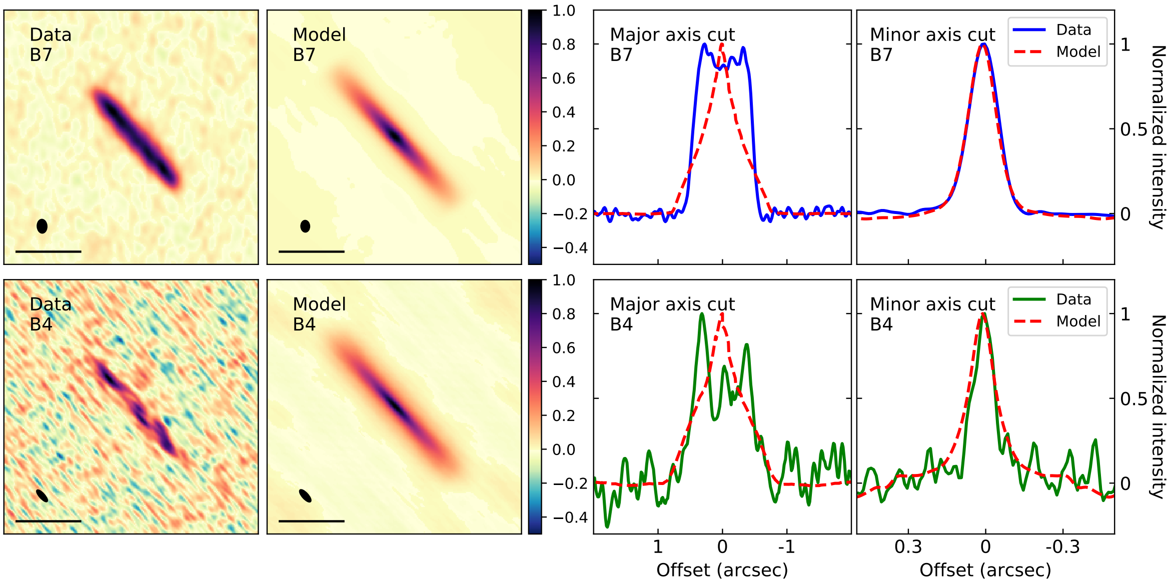

Figure 4.14 – **Left panels:** ALMA data of HK Tau B.
Middle-left panels: Millimeter images of the best model C of Stapelfeldt et al. (1998), assuming well mixed grains. They were computed for the same uv-coverage as in the data. The contours represent 30% of the maximum intensity of the data of the same band.
Middle-right panels: Major axis cuts of the data and the models in band 7 and band 4.
Right panels: Minor axis cuts, performed as in Section 4.3.4.

disk is more optically thick than what is predicted by the model. While the best model of Stapelfeldt et al. (1998) contains a full disk at an inclination of 85°, we suggest that a higher inclination (closer to 90°, see Fig. 4.12) or the presence of a large inner cavity would reproduce better the major axis brightness profile. Along the minor axis, the band 4 cut indicates that the model by Stapelfeldt et al. (1998) is also more extended vertically than the data (see right panels of Fig. 4.14). As previously proposed by Duchêne et al. (2003), this hints for vertical segregation of dust grains in this disk, millimeter grains being located in a vertically thinner layer than micron-sized grains. However the low signal to noise of the band 4 data and the low angular resolution in band 7 prevent us from a strong conclusion on the presence of vertical settling.

4.4.1.c. Vertical settling in Tau 042021

Tau 042021 is the only edge-on disk clearly resolved vertically in both band 7 and band 4. For this disk, the band 7 appears about 1.5 times more extended vertically than the band 4 (see Table 4.9). We note that Tau 042021 is only marginally resolved in band 6, so the size at this wavelength is uncertain. For our radiative transfer model without settling (including only optical depth effects), we find a band 7 to band 4 minor axis ratio of about 1.1 at $i = 90°$ (see table 4.11), significantly smaller than the observed value. Although this model is not unique, it indicates that opacity effects are not sufficient to produce the large difference in minor axis size observed, which suggests that grain-size-dependent vertical settling is occurring in this disk as well. In this section, we compare the measured minor axis ratio with predictions from several vertical settling models. We assume that the disk is perfectly edge-on so that variations along the minor axis are dominated by differences in vertical extent between bands rather than projections of the disk radius.

From the minor axis ratio measured in Tau 042021, one can estimate the scaling of the minor axis size (S_d) with grain size (a) assuming $S_d \propto a^{-m}$. Assuming that most of the emission comes from grains of the optimal size ($a \approx \lambda/2\pi$), we obtain: $m = -\log(S_{d,b7}/S_{d,b4})/\log(a_{b7}/a_{b4}) \sim 0.5$. Additionally, if we assume S_d is directly proportional to the dust "scale height" ($\mathrm{h_d}$), an exponent of $m = 0.5$ has been predicted for large grains in the context of a 1-D diffusion theory (Dubrulle et al., 1995). Performing numerical simulations including non-ideal MHD effects such as ambipolar diffusion, Riols and Lesur (2018) also estimated a relationship of dust scale height with grain size with an exponent of 0.5, valid for large grains ($St \gtrsim 10^{-2}$). For comparison, using the standard disk model presented in Riols and Lesur (2018, equation 13), at 100 au, grains of the optimal size emitting in band 7 would have Stokes numbers larger than $2.5 \cdot 10^{-2}$, which implies that such scale height relationship is expected.

In the settling model considered for our fiducial model, the dust scale height varies as: $\mathrm{h}_d \propto a^{-0.2}$ (Fromang and Nelson, 2009). This leads to a smaller minor axis ratio in our fiducial radiative transfer model than in the observations (~ 1.25 for an inclination of 90°, see Table 4.11). However, note that this expression was estimated for small grains ($St \leq 10^{-2}$) and might not apply for the grain sizes that we are probing at millimeter wavelengths.

To summarize, we find that the large minor axis difference observed in Tau 042021 at different millimeter wavelengths has to be associated with strong settling. While ideal MHD simulations predict a settling less efficient than observed, a simple 1-D diffusion theory (in the case of strong settling, Dubrulle et al., 1995) or numerical simulations including non-ideal MHD effects (Riols and Lesur, 2018) provide for now the best consistency with the observations.

4.4.1.d. Radial variation of vertical extent in IRAS 04302

The high resolution band 4 disk image of IRAS 04302 shows evidence of flaring, i.e., the extent perpendicular to the disk midplane at large radii is broader than at the center (see Fig. 4.4). This is in contrast with the other disks in our survey, which are flatter or unresolved. Fig. 4.15 compares the minor axis cuts at different radii in IRAS 04302 with the other well-resolved edge-on disk with large signal to noise: Tau 042021. In the latter case, the vertical extent appears quasi constant as a function of radius, whereas it is $\sim 50\%$ larger in IRAS 04302 at a projected radius of 100 au (0.7") than at the center. This might be related to differences in optical depth or settling between the disks. However, IRAS 04302 is the only Class I object in our sample (Gräfe et al., 2013) and the scattered light image does not show the flared

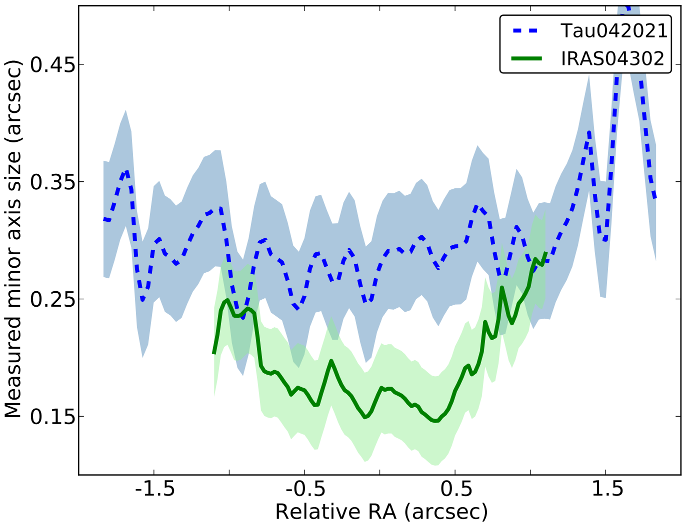

Figure 4.15 – Minor axis full width half maximum as a function of radius for IRAS 04302 (band 4) and Tau 042021 (band 7). The errors correspond to the standard deviation of the curves.

upper surface of a disk, like in the other objects (Class II, see Fig. 4.9), but instead traces an envelope. Objects like this one, and HH 212 a Class 0 (Lee et al., 2017), open the possibility to do comparative studies of disk evolution in the early phases.

4.4.2 *Radial extent*

4.4.2.a. Effect of inclination on the radial brightness profile of the models

In this section, we investigate the effect of inclination on the observed radial brightness profiles. To do so, I produced major axis cuts of the fiducial and no settling radiative transfer models, as in Section 4.3.3. They are presented in Fig. 4.16. First, we note that for the fiducial model, most cuts show an increase of intensity around 0.5″ and 0.9″, which are related to the rings and gaps present in the HL Tau model.

Along the major axis, the effect of inclination on the shape of the brightness profile is very clear both in the images and in the cuts. At an inclination of 82.5°, the image and cut show a steep increase of intensity at the center, very similar to our observations of Oph 163131. On the contrary, for the fully edge-on configuration ($i = 90°$), the major axis brightness profile is flat at all radii and drops steeply, like our observations of HH 30, HK Tau B, HV Tau C and HH 48 NE. Between these extreme cases, the cuts show a less extended plateau and shallower outer edges than for the 90° case, likely related to lower optical depth than in the edge-on case. The cuts on the model without settling on the other hand do not show the rings, but they present similar trends on the sharpness of the edges as defined between 20% and 80% of the peak intensity.

We estimate the apparent sharpness ($\Delta r/r$) for the fiducial models as in Section 4.3.3 and report them in Table 4.11. Although the measurement of this parameter is affected

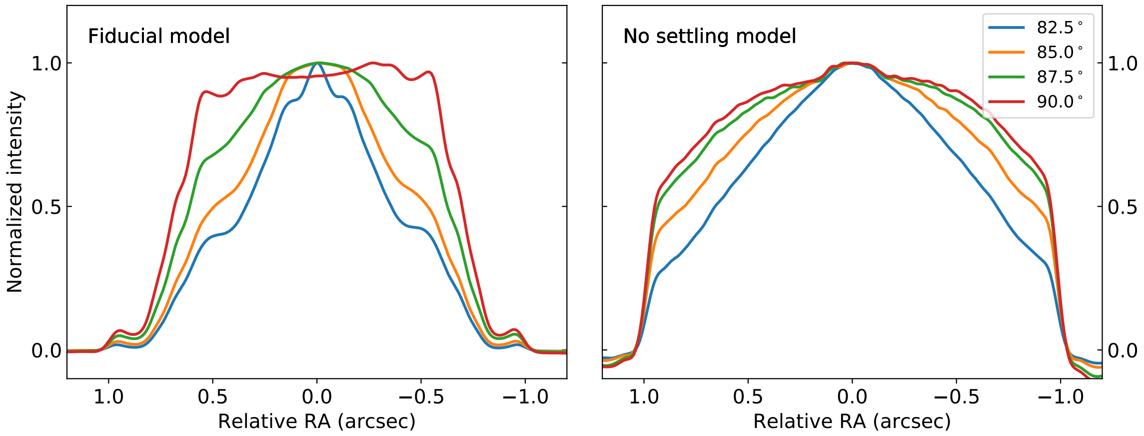

Figure 4.16 – Major axis profiles for the fiducial model (left) and the model without settling (right), computed as in Fig. 4.6. The models were computed in band 7 (0.89 mm). All cuts are normalized to their peak surface brightness.

by the presence of rings in the model (leading to the large uncertainties on $\Delta r/r$ at small inclinations), the variations of the sharpness are indicative of the effect of inclination. We find that the apparent sharpness of the disk significantly increases with increasing inclination. When the model is computed at 82.5°, we obtain $\Delta r/r \sim 1.1$, while we find $\Delta r/r \sim 0.3$ for 90°.

Three disks in our sample show edges as sharp as 0.3. These are HH 30, HK Tau B, HH 48 NE, which suggests that these disks are the most inclined of the sample. Larger values of $\Delta r/r$ might indicate that the disks are either less inclined than 90°, less massive and optically thinner than the radiative transfer model considered here, or simply less resolved along the major axis. Nonetheless, the sharpness of the radial brightness distribution seems to be a good tracer of disk inclination.

4.4.2.b. Comparison with a radial drift model

Similarly to previous multi-wavelengths studies (e.g., Pérez et al., 2012; Tripathi et al., 2018; Powell et al., 2019), our observations show that 4 disks have major axis sizes that decrease with wavelength (namely Tau 042021, IRAS 04302, IRAS 04200, Haro 6-5B, see Table 4.8 and the radial variation of the spectral index in Fig. 4.8). For these disks, the average size difference between band 7 and band 4 observations is about 15%. Estimating the major axis sizes from our fiducial radiative transfer model described in Section 4.4 (which does not include radial drift), we find that opacity effects alone predict a difference of only a few percents between bands, which is not sufficient to reproduce the observations. In this section, we compare the measured radial differences with an analytical radial drift model, presented by Birnstiel and Andrews (2014). Similarly to other theoretical models, they showed that inward dust migration of single size particles spontaneously produces a sharp edge in the dust density distribution (Birnstiel and Andrews, 2014; Facchini et al., 2017; Powell et al., 2019). Birnstiel and Andrews (2014) computed an analytical formula to infer the position of the disk outer edge in a disk with radial drift only (see their equation

B9). The vertical extent of the grains is not considered in their model. They assume a smooth tapered-edge gas surface density profile and parametrize the turbulence following Shakura and Sunyaev (1973).

Assuming that the band 7 and band 4 emission only originate from grains of the optimal size ($a \approx \lambda/2\pi$), the model by Birnstiel and Andrews (2014) predicts a size difference in surface density between band 7 and band 4 of about 25% (after 0.1 Myr). While the predicted effect is marginally too strong, the absolute disk sizes are more problematic. When grains of 0.1 μm detectable in scattered light are expected to be found up to 135 au after 0.1 Myr, the model predicts that grains emitting most at 0.89 mm should have drifted to 42 au. This corresponds to a micron/millimeter disk radius ratio greater than 3, which is more than 1.5 times larger than the largest ratio measured in our data.

Part of these differences might be explained because the observations are not probing the surface density of the disk, because several grain sizes (that might have drifted to different radii) have to be considered rather than a unique one, or because our disks are older than 0.1 Myr so they might be affected by viscous spreading as well. Besides, as discussed previously (Section 4.3.6), we note the scattered light images might not always trace the whole disks, since they require illumination (and sufficient optical depth) to trace the disk all the way to the edge. This can lead to apparent sizes in scattered light that are smaller than the real radial extent of small grains. However, the small expected sizes at millimeter wavelengths suggest that this radial drift model is too efficient to reproduce the observations (see also Brauer et al., 2007). The existence of pressure fluctations in the disks (e.g., rings and gaps tracing pressure bumps and dust traps) rather than smooth power low surface density profiles are expected to slow down the drift efficiently (see, e.g., Gonzalez et al., 2017; Pinilla et al., 2012a) and help reconcile models with observations. We speculate that the disks included in our study may have complex radial structures to slow down the radial migration of dust.

4.4.3 *Effect of inclination on global disk properties*

Most Class II disk surveys in close-by star-forming regions estimate dust masses directly from the measured integrated fluxes assuming optically thin disks, irrespective of the disk inclinations (e.g., Andrews et al., 2013; Ansdell et al., 2016; van der Plas et al., 2016, this thesis - Chapter 2). However, because of the projection effect, the optical depth along the line-of-sight increases with inclination and will affect the observed flux. In this section, we investigate the impact of inclination on integrated fluxes, derived dust masses, and integrated spectral indices. Finally, we also discuss the measured brightness temperatures obtained for our disks in the context of optical depth.

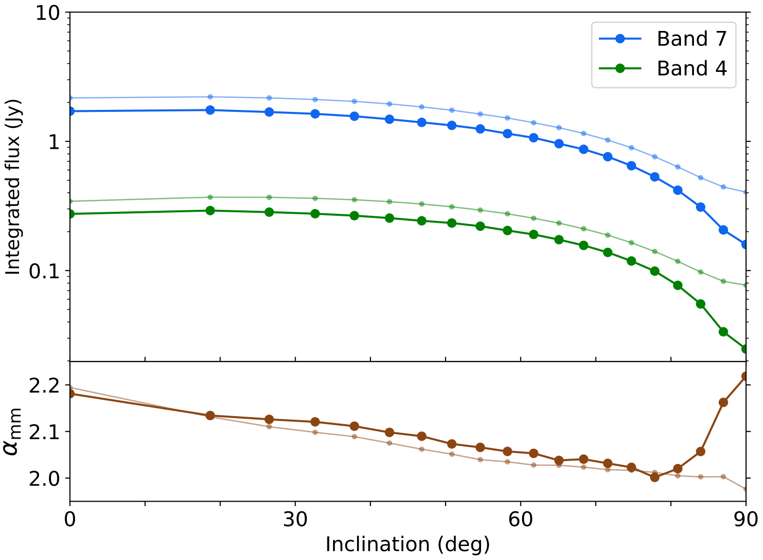

Figure 4.17 – **Top:** Variation of the band 7 and band 4 integrated fluxes of the fiducial (with settling, solid lines) and the radiative transfer model without settling (light lines) as a function of the inclination.
Bottom: Variation of the integrated spectral index for the fiducial model.

4.4.3.a. Flux densities and derived masses

We present the variation of the integrated band 7 and band 4 fluxes in our radiative transfer models (with and without settling) as a function of inclination in Fig. 4.17. Overall, the emitted flux density of the disk becomes attenuated by up to an order of magnitude with increasing inclination. This is due to a combination of the increasing optical depth, a lower average dust temperature seen by the observer for high inclinations, and to geometrical effects (reduced emitting surface with increasing inclination). In this model, from $\sim 60°$ to $90°$, the flux density and thus the derived disk mass would appear significantly smaller than for the same disk viewed at intermediate inclinations (by up to ~ 10 times for the fiducial model). The amplitude of the attenuation depends on the model's parameters. The effects of dust scattering are fully included in the radiative transfer calculations. Note that in Fig 4.17, the model without settling is brighter than the fiducial model for all inclinations. This effect is likely dominated by a difference in dust temperatures in the disk midplane between the different models. With settling (fiducial model) the temperature of the dust is slightly lower than for the un-settled model because the disk intersects less starlight overall than in the settled case, resulting in a lower integrated flux.

This raises the question of the reliability of disk masses derived purely from millimeter fluxes. We focus here on the edge-on disks of our sample. For a direct comparison with previous studies, we assume optically thin and isothermal dust emission at sub-millimeter wavelengths. In that case the flux (F_ν) is directly related to the dust mass following: $M_{\text{dust}} = F_\nu d^2/\kappa_\nu B_\nu(T_{\text{dust}})$, where d is the disk distance to the Sun, $B_\nu(T_{\text{dust}})$ the Planck function evaluated at a mean representative dust

Sources	$M_{\mathrm{dust\,B7}}$ ($M_\oplus$)
Tau 042021	> 25.5
HH 30	> 11.2
IRAS 04302	> 54.8
HK Tau B	> 11.4
HV Tau C	> 18.6
IRAS 04200	> 13.4
Haro 6-5B	> 69.8
IRAS 04158	> 53.1
Oph 163131	> 25.8
ESO-Hα 569	> 13.6
ESO-Hα 574	> 3.1
HH 48 NE	> 7.1

Table 4.12 – Mass limits. Dust masses are estimated from the band 7 fluxes (Table 4.6), assuming optically thin emission, and therefore are lower limits (see text for details).

temperature T_{dust}, and κ_ν the *dust* grain opacity. We use typical values of $T_{\mathrm{dust}} = 20\,\mathrm{K}$ and $\kappa_\nu = 3.4\,\mathrm{cm}^2\,\mathrm{g}^{-1}$, as in Ansdell et al. (2016, and references therein) to estimate the dust mass of the disks in the sample and for the fiducial model, using the band 7 fluxes. For the data, the results are reported in Table 4.12. As noted above, the masses are almost certainly underestimated and so we quote them as lower limits.

By applying the formula directly we find a mean dust mass of about $25\,M_\oplus$ for the 6 edge-on disks more inclined than $75°$. For comparison, at an inclination of $90°$, the estimated dust mass of the fiducial model is 3 times lower than the real dust mass (for an inclination of $0°$, the estimated mass is 3 times larger than the real mass). Without full modelling, it is difficult to find a reliable correction factor for individual sources to compensate the attenuation due to inclination. The disk masses of our highly inclined sample are probably a few times larger, i.e., up to $\sim 75\,M_\oplus$ when applying the same factor of 3. This would be on the high end of the dust mass distributions of Taurus or Lupus star-forming regions (mean of $15\,M_\oplus$, Ansdell et al., 2016, see Chapter 2, Fig. 2.9).

This result suggests that our sample of edge-on disks is biased towards massive disks. This is a direct consequence of the important attenuation caused by the high inclination, making the starlight and the disk emission fainter. This may also explain, at least partly, why the number of known edge-on disks with resolved images remains sparse, even today. A comprehensive study of the biases affecting the edge-on disk population and their detection will be presented in Angelo et al. (in prep).

4.4.3.b. *Integrated spectral indices*

The median spectral index of the edge-on disks in this study, $\bar{\alpha}_{mm} = 2.5 \pm 0.3$, is similar to previous measurements of intermediate-inclination disks, i.e., 2.3 ± 0.1 in the Lupus and Taurus star-forming regions (Ribas et al., 2017; Ansdell et al., 2018). At first glance, this is surprising as edge-on disks are expected to appear more optically thick, but Sierra and Lizano (2020) showed that the spectral index is only mildly dependent on inclination based on an extensive study.

To further understand the integrated α_{mm} for edge-on disks, we computed them for our radiative transfer models with and without settling. The expected values at different inclinations are shown in the bottom panel of Fig. 4.17. We find that for both models the variation of spectral index with inclination is relatively small ($2 \lesssim \alpha_{mm} \lesssim 2.2$), in agreement with Sierra and Lizano (2020). This is because the model used for our analysis is known to be optically thick at these frequencies even at low inclinations and because large grains are included in the model (Pinte et al., 2016; Carrasco-González et al., 2019). The small difference in integrated spectral index observed between our sample of edge-on disks and disks at lower inclinations can be explained if most disks are partially optically thick at millimeter wavelengths and/or if grains have grown to millimeter/centimeter sizes. Grain growth is known to have occurred in Class II disks, leading to low spectral indices (Ricci et al., 2010; Testi et al., 2014). Similarly, recent imaging campaigns have revealed that ring structures are very common in protoplanetary disks (Huang et al., 2018b; Long et al., 2018) and generally associated with optically thick regions with large grains (e.g., Dent et al., 2019). So far, the edge-on disks in our sample appear similar to the disks observed on other surveys, except from their viewing angle.

Interestingly, for inclinations greater than 80°, we find a clear difference in the integrated spectral index between the models with and without settling. While at these inclinations the spectral index decreases in the model without settling (see also Galván-Madrid et al., 2018), we find that the integrated spectral index increases for the fiducial settled model, reaching about 2.2 at 90°. This can be explained if the contribution of the optically thick midplane decreases with increasing inclination while the contribution of the upper layers (rich in small grains with higher β values) increases with increasing inclination, leading to higher values of the integrated spectral indices for the settled model. Said differently, for very large inclinations several line-of-sights do not cross the disk midplane containing large grains but cross mostly the high altitude layers above and below it. Since these layers are optically thinner and contain only small grains, the spectral index increases.

This effect can for example be seen on our radiative transfer models presented in Fig. 4.18 (see also Tau 042021 in Fig. 4.8). In Fig. 4.18, I show the spectral index maps and major axis cuts of the fiducial and no settling models at 85° and 90° of inclination. In both cases, we see that the spectral index is higher in the upper layers than in the disk midplane, accordingly to what was just described. However, in the fiducial model, the values reached in the upper layers are higher than those reached

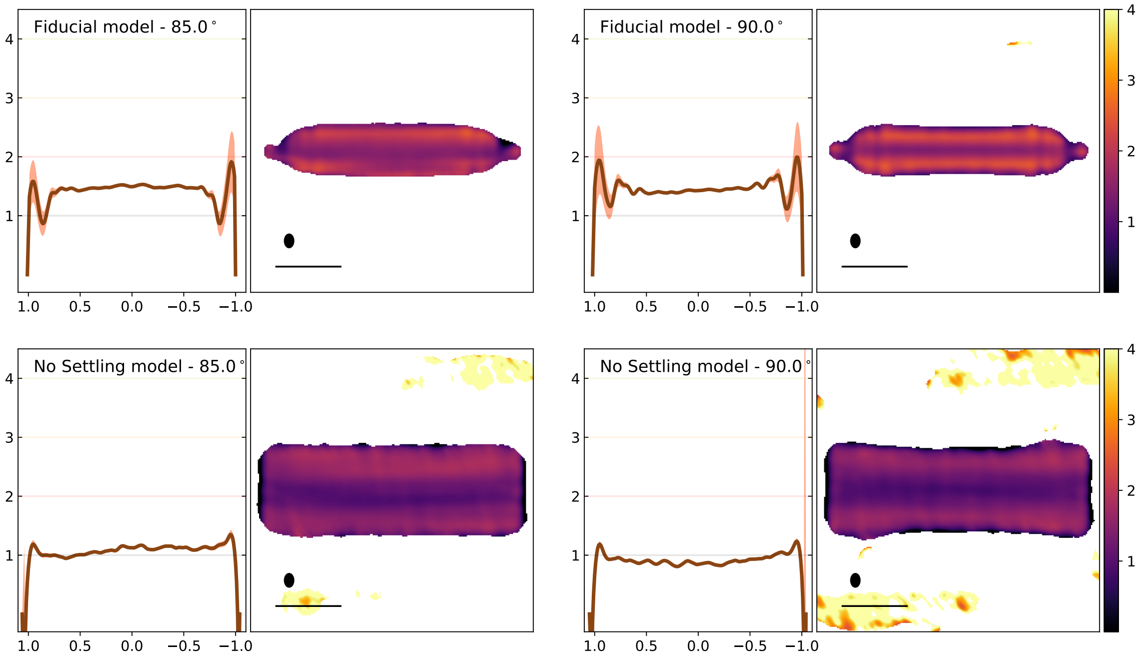

Figure 4.18 – Spectral index cuts along the major axis, for the fiducial model (top row) and the model without settling (bottom row) computed at different inclinations (85° and 90°). The orange errors in the cuts are estimated from the signal to noise in each band. The x-axis corresponds to the relative offset in arcseconds (different scales between panels). The right panels show the spectral index maps of the same models, applying a filter to keep only the pixels with more emission than 5σ in both bands. We also show the beam size and a 0.5″ scale in the bottom left corned of the image.

in the model without settling. This illustrates why the integrated spectral index appears higher in the fiducial model than the in no settling model at high inclinations. However, further studies are required to investigate this effect (e.g., Sierra and Lizano, 2020) and its applicability to specific objects.

Finally, from the spectral index major axis cuts shown in Fig. 4.18, we also see a slight increase of spectral index at larger radius for all models. As size selective dust radial drift is not included in the models, this variation corresponds to changes in optical depth only. Several disks in our study, namely Tau 042021, IRAS 04302, IRAS 04200, Haro 6-5B, show stronger variations along the major axis direction than the models. This suggests that these disks are also affected by size selective radial drift. To confirm this interpretation, note that the band 4 and band 7 sizes are found to be largely different in these four sources.

4.4.3.c. *Brightness temperatures*

Assuming that scattering is negligible and that the dust temperature is high enough (e.g., in the Rayleigh-Jeans limit) and constant over the emitting region, the brightness temperature of dust emission at frequency ν can be expressed as $T_B =$

$\eta_c\ T_p\ (1 - e^{-\tau_\nu})$, where τ_ν is the optical depth of the medium, T_p the mean dust physical temperature, and η_c the fraction of beam covered by the source (see e.g., Wilson et al., 2009). In the isothermal optically thick limit ($\tau_\nu \gg 1$), for a source filling the beam (but smaller than the largest angular scale of the interferometric observations) the brightness temperature corresponds to $T_p - 2.7\,\mathrm{K}$, because the cosmic microwave background (CMB) is resolved out by the interferometer. For compact sources, beam dilution would reduce the observed brightness temperatures below T_p. Scattering is also known to decrease dust emission from very optically thick regions, which would also effectively lead to lower observed brightness temperatures (Zhu et al., 2019). The brightness temperatures of the disks of this survey were estimated in Section 4.3.1. The major axis cuts of the brightness temperature are presented in Fig. 4.5 and we report the peak brightness temperatures in Table 4.7.

We estimate a mean peak brightness temperature of 10.6 K for the three resolved sources in band 7. These values are particularly low compared to previous estimates on other disks around stars of similar spectral types. As an example, Andrews et al. (2018b) derived a mean brightness temperature peak of 66.5 K for the 17 disks of the DSHARP sample around K & M stars observed in band 6. These disks have a mean inclination of 42°, while all disks of our study are more inclined than 65°. The brightness temperatures we derive for our disks are also much lower than the traditional $T_{dust} = 20\,\mathrm{K}$ assumed in flux-to-mass conversions (see e.g., Section 4.4.3).

Although the measured brightness temperatures are integrated over some vertical extent because of the beam size, and therefore include a vertical temperature gradient, for the well-resolved disks T_B does provide a reasonable estimate of the temperature of the outer midplane where the line-of-sight optical depth reaches unity. This is the case for Tau 042021 for example. The low brightness temperatures measured in these optically-thick edge-on systems is likely to reflect the midplane temperature in the cold outer radii of the disks.

In Fig. 4.19, I present the brightness temperature cuts at several inclinations computed for the fiducial radiative transfer model and that without including vertical settling. In both models, we find that as the inclination increases, the peak temperature decreases. This indicates that the disk becomes optically thicker with inclination. As mentioned previously, this suggests that the highest inclinations the millimeter emission likely originates in the outer regions of the disk (radially).

Additionally, we find that the band 4 brightness temperatures are always lower than the band 7 brightness temperatures. The brightness temperature differences are smaller for the model without settling than for the fiducial model, which suggests that vertical segregation of dust grains increases brightness temperature differences between millimeter bands. We note that we also detect large variations in brightness temperatures between bands in the observations (Fig. 4.5), which can be related with differences in opacity or spatial segregation between band 7 and band 4 emitting grains.

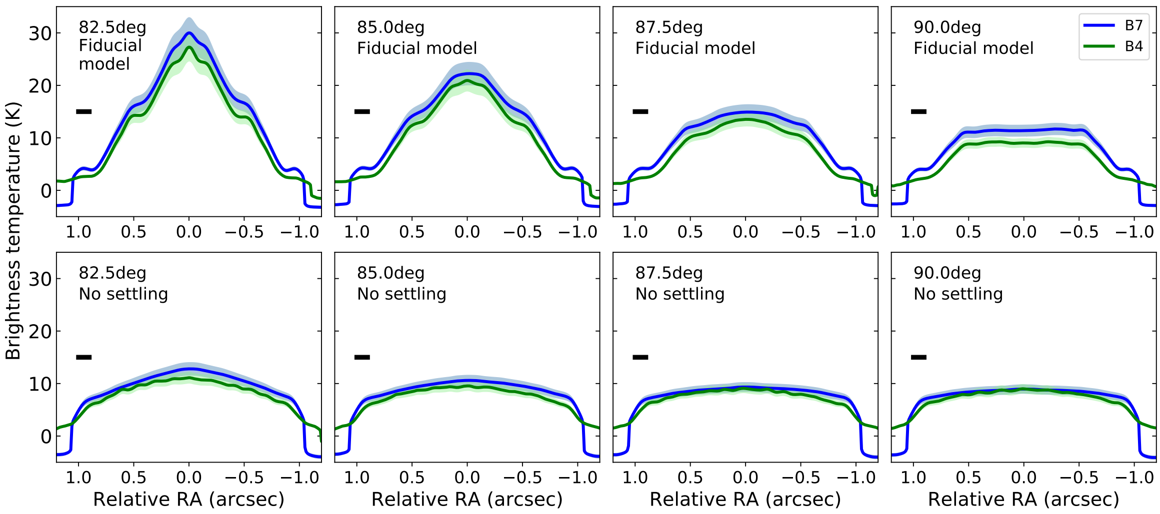

Figure 4.19 – Brightness temperatures as a function of the radial distance for the radiative transfer models shown in Fig. 4.12, computed at different inclinations. We report the beam size in the direction of the cut in the top left corner of each panels.
Top: Fiducial model.
Bottom: Model without settling.

4.5 CONCLUSIONS

We presented high angular resolution ALMA band 7 and band 4 observations of 12 highly-inclined disks previously selected from the shape of their scattered light images. All disks are well resolved along the major axis and 6 are also resolved in the direction perpendicular to the disk midplane in at least one millimeter band. Several disks show flat surface brightness profiles along their major axis with a steep drop off at their outer edge, indicating their large inclination and significant optical depth.

Haro 6-5B and IRAS 04158 are the least inclined disks of the sample ($< 75°$) and both show a distinct ring and an isolated emission peak at the center. At the highest angular resolution, the point source at the center of IRAS 04158 is a binary source.

The analysis of global quantities such as integrated fluxes, spectral indices, and brightness temperatures shows that the highly inclined disks of our sample have (at least partly) optically thick emission. Because of the low brightness temperatures and small beam sizes, we conclude that the emission originates from the outer radii of the disks, with a peak brightness temperature below 10 K for half the sources in band 7.

We also find that the median spectral index in our disk sample is similar to that of disks seen at lower inclinations. This can be explained if disks at intermediate inclination are already partly optically thick (which implies significant scattering even at millimeter wavelengths) and/or if grains have grown to millimeter/centimeter sizes in all cases.

All disks were observed at several wavelengths with similar angular resolution, from the optical to the millimeter range. This enables a comparison of the radial extent of different grain populations in the disks (i.e., grain sizes). We assumed that the small dust responsible for the scattered light in the optical is tracing closely the gas distribution. Most disks have larger radial sizes in the optical/NIR than at millimeter wavelengths indicative of dust radial drift, the larger particles having drifted inward. Three of the disks have the same radial extent in both millimetric bands; these ones also have the sharpest apparent outer edges: $\Delta r/r \sim 0.3$. Four sources have band 7 emission which is radially more extended than band 4, by about 15% on average. However, current radial drift models predict larger differences - both between optical and millimeter, and between band 7 and band 4 - than we actually observe. This suggests that other mechanisms such as pressure traps are likely present in these disks to slow down or halt the radial drift.

The peculiar viewing angle of the disks presented in this survey allows us to obtain more direct information on their vertical structures. First of all, the direct comparison of the ALMA observations with scattered light data shows that these disks have larger vertical sizes in the optical/NIR than at millimeter wavelengths, indicative of the different optical depths and of vertical dust settling. To further estimate the vertical distribution of millimeter grains (parametrized as a "scale height"), we compared the shape of ALMA observations with the radiative transfer model of HL Tau published in Pinte et al. (2016). We recomputed the model at 90° of inclination, with the same angular resolution as our data, and considered two different values for the scale height of millimeter grains. We find that the disks of our survey are compatible with millimeter dust "scale heights" of a few au at $r = 100$ au: these disks are much thinner at millimeter wavelengths than the gas traced by the small dust, which has a typical scale height of 10 au (Burrows et al., 1996; Stapelfeldt et al., 1998).

On a case by case basis, for HK Tau B, a more detailed comparison of the ALMA images with a published scattered light model (re-computed at millimeter wavelengths) also indicates significant differences in vertical extent between millimeter and micron-sized grains, as previously suggested by Duchêne et al. (2003). Also, for Tau 042021, the only edge-on disk well resolved in the two millimeter bands, we find that the band 7 emission is about 1.5 times more extended vertically than the band 4. This ratio is expected for relatively large dust grains in the simple 1-D diffusion theory or numerical simulations including non-ideal MHD effects (Dubrulle et al., 1995; Riols and Lesur, 2018), further supporting the idea that strong vertical dust settling as taken place, leading to an increase in dust concentration in the disk midplane.

Finally, we find evidence of a more flared structure in IRAS 04302, suggesting that the millimeter grains in this Class I source are less settled. The millimeter dust in this disk may be in transition between the vertically unsettled structures seen in some Class 0 objects and the flatter dust found in our Class II disks.

5

ON GOING PROJECTS

Contents

In Chapter 4 I presented a survey of 12 edge-on disks where we analysed their continuum millimeter emission to obtain direct constraints on the vertical extent of millimeter-sized dust grains in protoplanetary disks. We find that the disks are extremely thin at millimeter wavelength (in the continuum). However, in order to be able to add even stronger contraints on vertical settling and thus on disk turbulence and on the processes of planet formation, follow-up studies are needed. In this section, I present several projects on which I have been recently working on.

In Section 5.1, I present a preliminary analysis of the ^{12}CO emission of most disks included in the continuum edge-on survey. Then in Section 5.2, I discuss some results from a cycle 6 proposal of which I am PI, that observed Oph 163131 in band 6 at very high angular resolution ($\sim 0.02''$). I reduced the data and I started to work on a radiative transfer model to understand the physical structure of the disk. All the work presented in this chapter has not yet been published.

5.1 EDGE-ON ^{12}CO SURVEY

In order to constrain which mechanisms drive the turbulence in disk, it is important to estimate observationally the dust to gas vertical (size) ratio, i.e., the settling efficiency. In Chapter 4 we used the small grains as a proxy for the gas distribution, as observed in scattered light by HST. In this section, I present some new images and first ideas of analysis of the ^{12}CO $J = 3 - 2$ emission (central frequency 345.796 GHz) of the edge-on disks analysed in Chapter 4. I have currently only reduced data from the sources included in project 2016.1.00460.S (PI: Ménard), so compared to the analysis presented in Chapter 4, HH 30 and Oph 163131 are missing.

5.1.1 *Imaging the gas*

The observational setup of the data was presented in Section 4.2.2 of Chapter 4. To produce the CO images, I first substracted the continuum images using the `uvcontsub` CASA task and applied the continuum selfcalibration solutions when available. I imaged the CO emission line with the `tclean` task, using a Briggs robust weighting parameter of 0.5 and the `multiscale` option. Additionally, for the sources with the lowest signal to noise (namely Tau 042021, HK Tau B, HV Tau C, Haro 6-5B, IRAS 04200, and IRAS 04158), I used the `uvtaper` option to increase the beam size and improve the signal to noise. The final angular resolutions range between $0.13'' \times 0.12''$ and $0.52'' \times 0.31''$ (see Table 5.1).

From the channel maps, I created moment 0 and moment 1 maps using the `immoment` task of CASA. The moment maps were generated over pixels brighter than 3 times the rms and included within the mask used to clean the different channel maps. The moment 0 image showing the integrated ^{12}CO intensity are presented in Fig. 5.1 and the moment 1 maps showing the velocity maps are displayed in Fig. 5.2, both with the continuum contour at 20% overlayed. Finally, I present an overlay of the HST scattered light images, CO moment 0 and millimeter continuum images in Fig. 5.3

Source	CO beam (″)
Tau 042021	0.26 × 0.24
IRAS 04302	0.47 × 0.36
HK Tau B	0.13 × 0.13
HV Tau C	0.14 × 0.13
IRAS 04200	0.24 × 0.23
Haro 6-5B	0.16 × 0.14
IRAS 04158	0.23 × 0.20
ESO-Hα 569	0.49 × 0.30
ESO-Hα 574	0.49 × 0.30
HH 48 NE	0.52 × 0.31

Table 5.1 – CO beams.

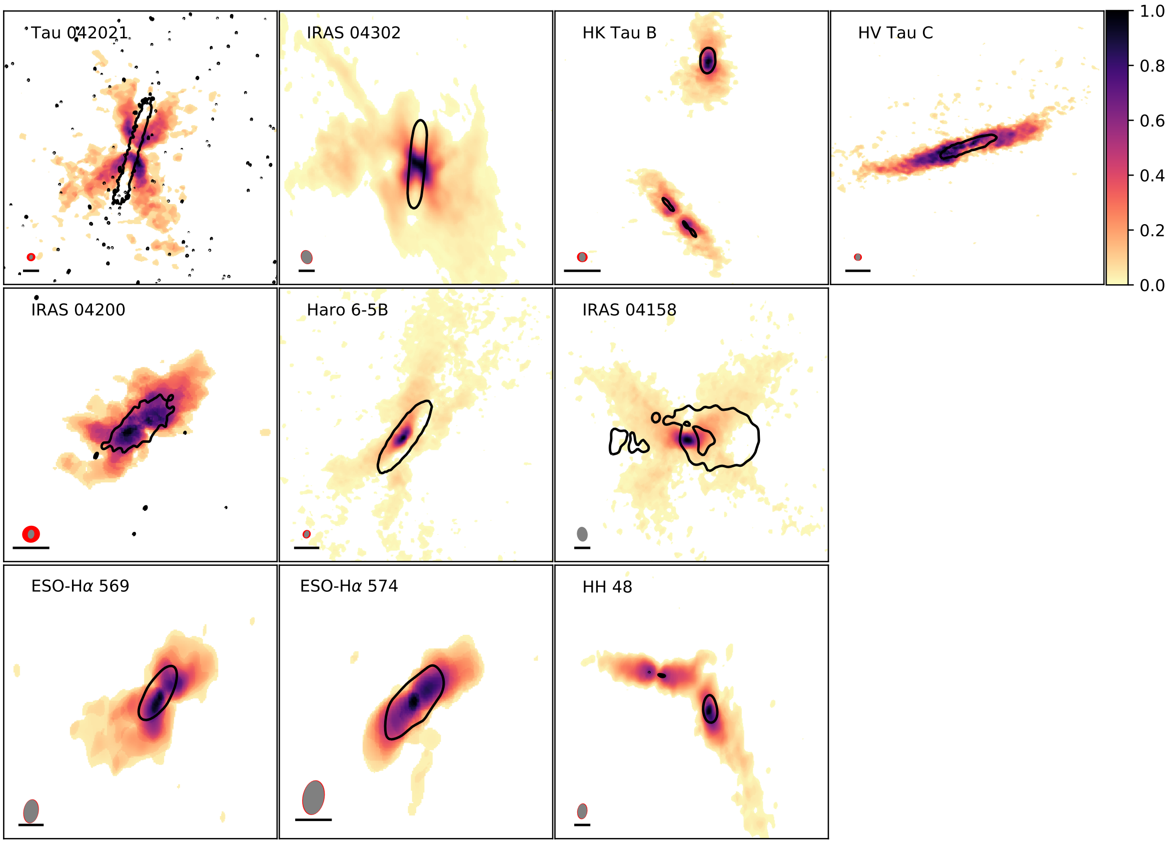

Figure 5.1 – Overlay of moment 0 maps and continuum in contour (20% levels). The CO and continuum beam sizes are shown in the bottom left corner (respectively in red and grey), along with a dark line representing a 0.5″ scale.

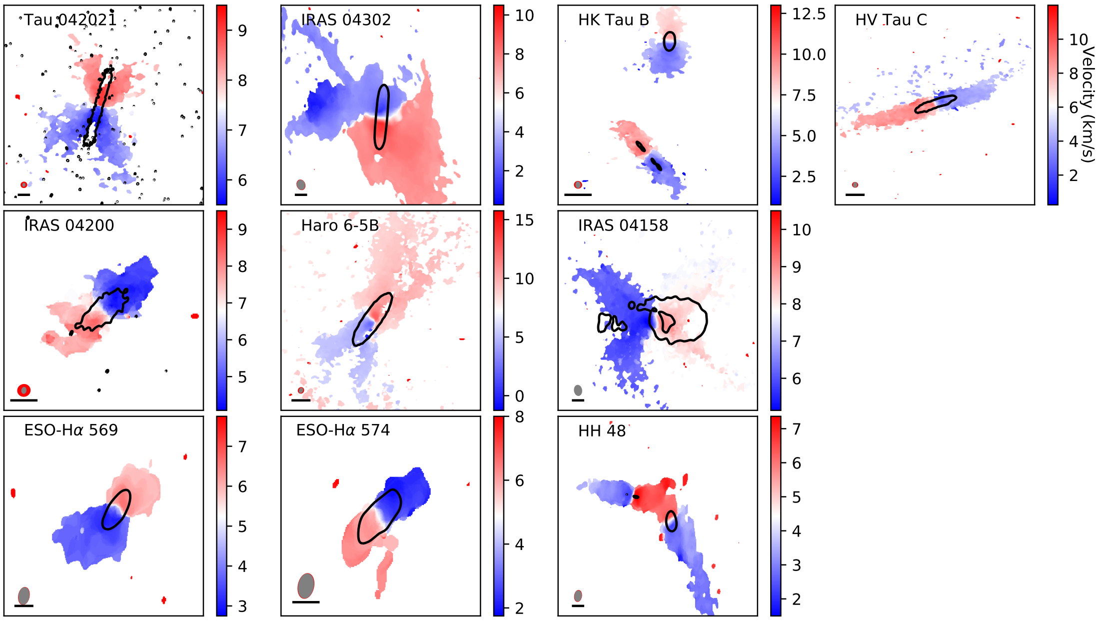

Figure 5.2 – Overlay of normalized moment 1 maps and continuum in contour (20% levels). The CO and continuum beam sizes are shown in the bottom left corner (respectively in red and grey), along with a dark line representing a 0.5″ scale.

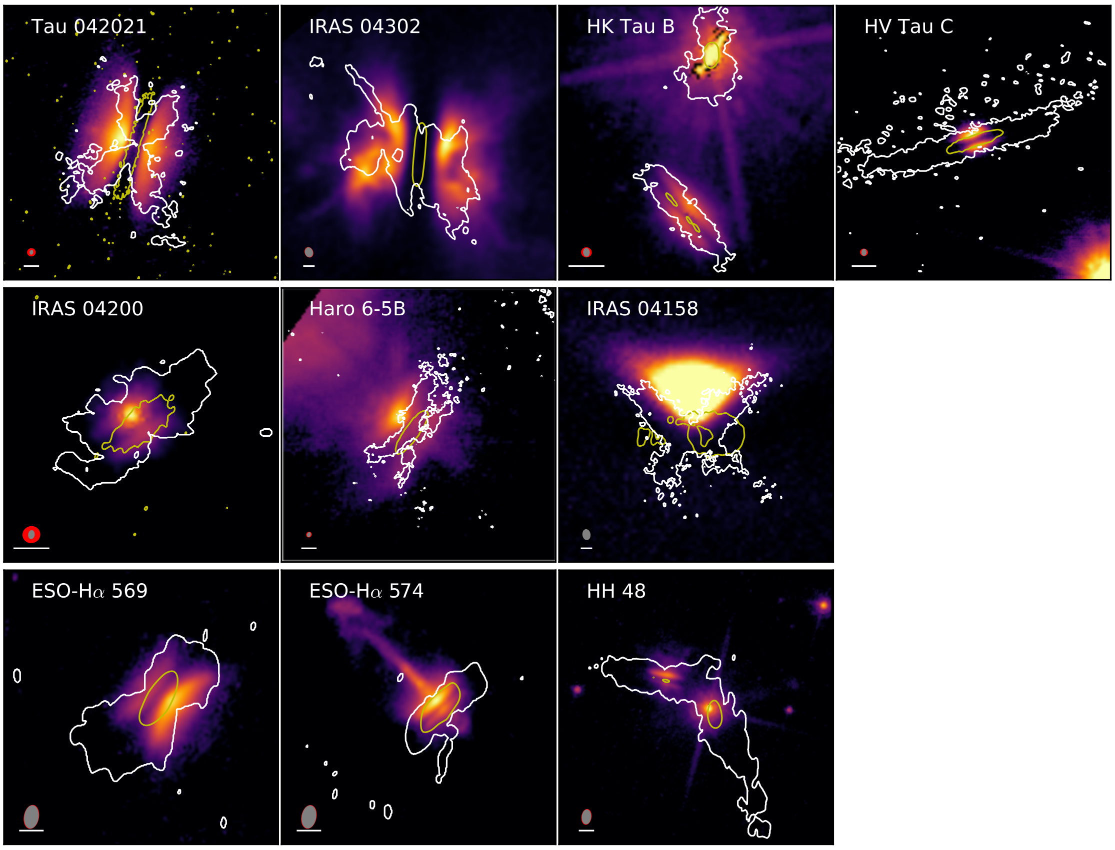

Figure 5.3 – Overlay of HST, moment 0 (2% contours, white) and continuum 20% contours (yellow). The CO and continuum beam sizes are shown in the bottom left corner (respectively in red and grey), along with a white line representing a 0.5″ scale.

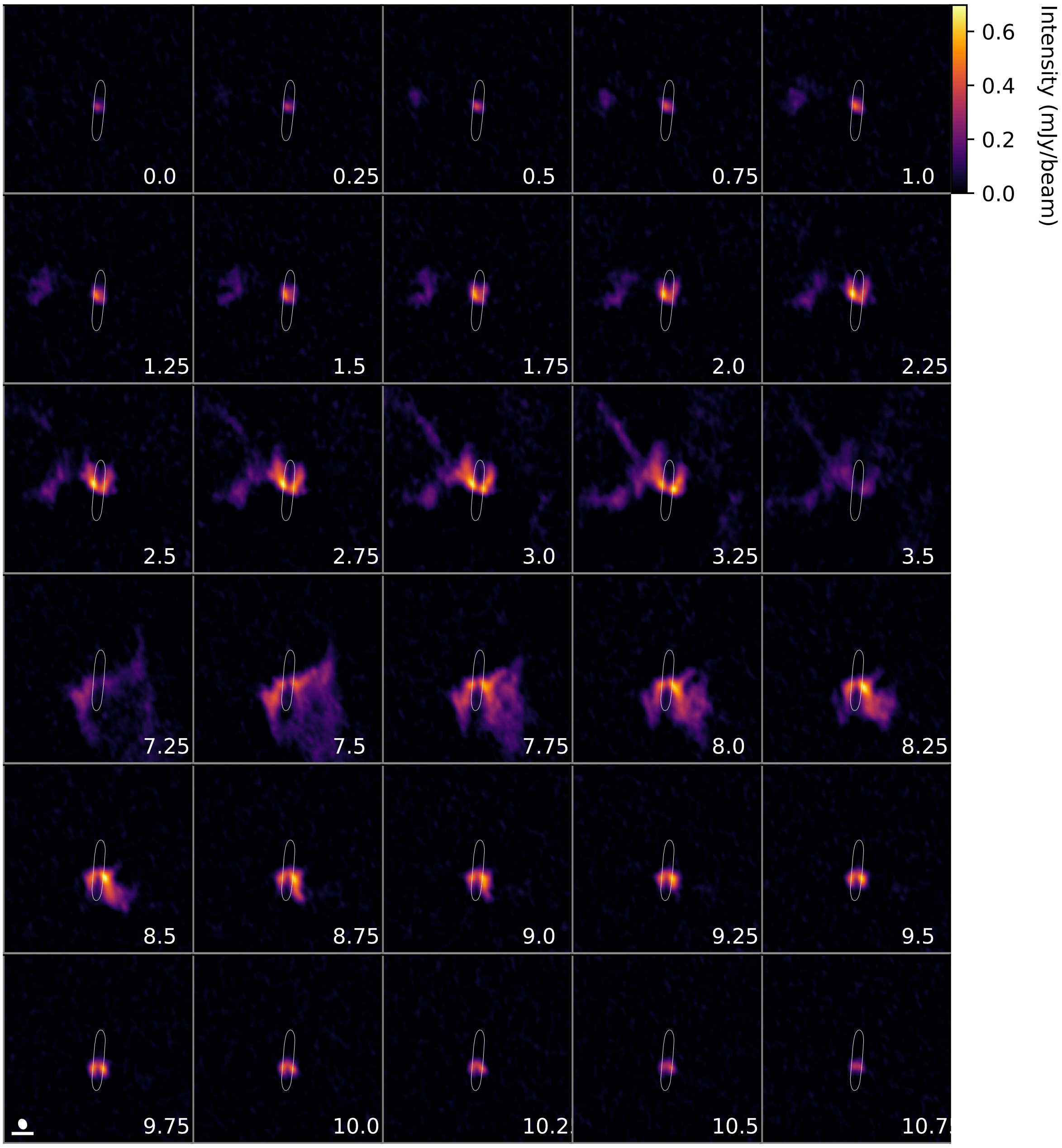

Figure 5.4 – Channel maps of IRAS 04302 along with the continuum emission (20% contours). The velocities between 3.5 and 7.25 km/s are not represented as CO is not detected (potentially because of cloud or envelope absorption). The synthesized beam and a 0.5″ scale are represented in the bottom left panel, and the velocities are reported in the bottom right corner of each panels (in km/s).

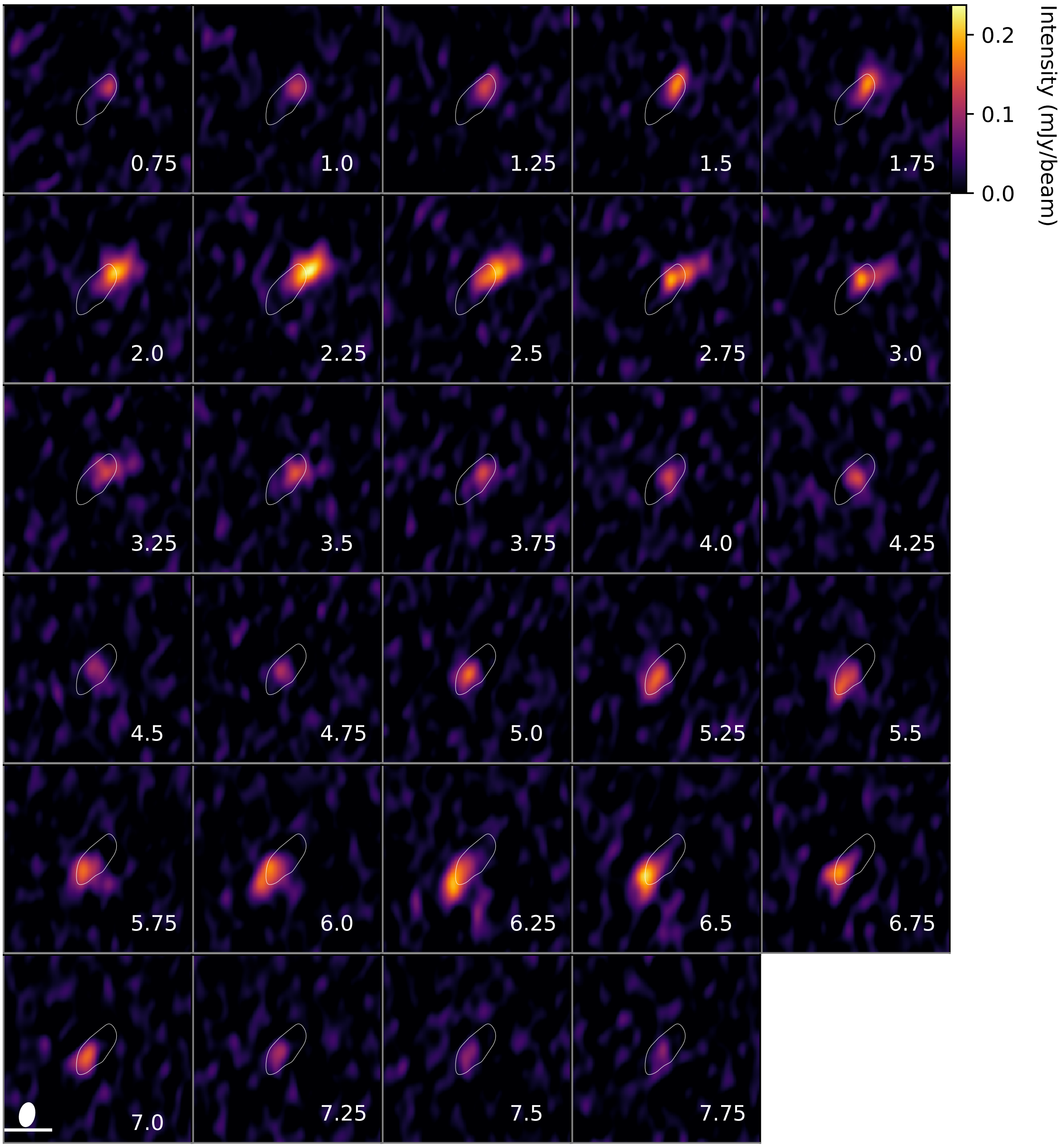

Figure 5.5 – Channel maps of ESO-Hα 574 along with the continuum emission (20% contours). The synthesized beam and a 0.5″ scale are represented in the bottom left panel, and the velocities are reported in the bottom right corner of each panels (in km/s).

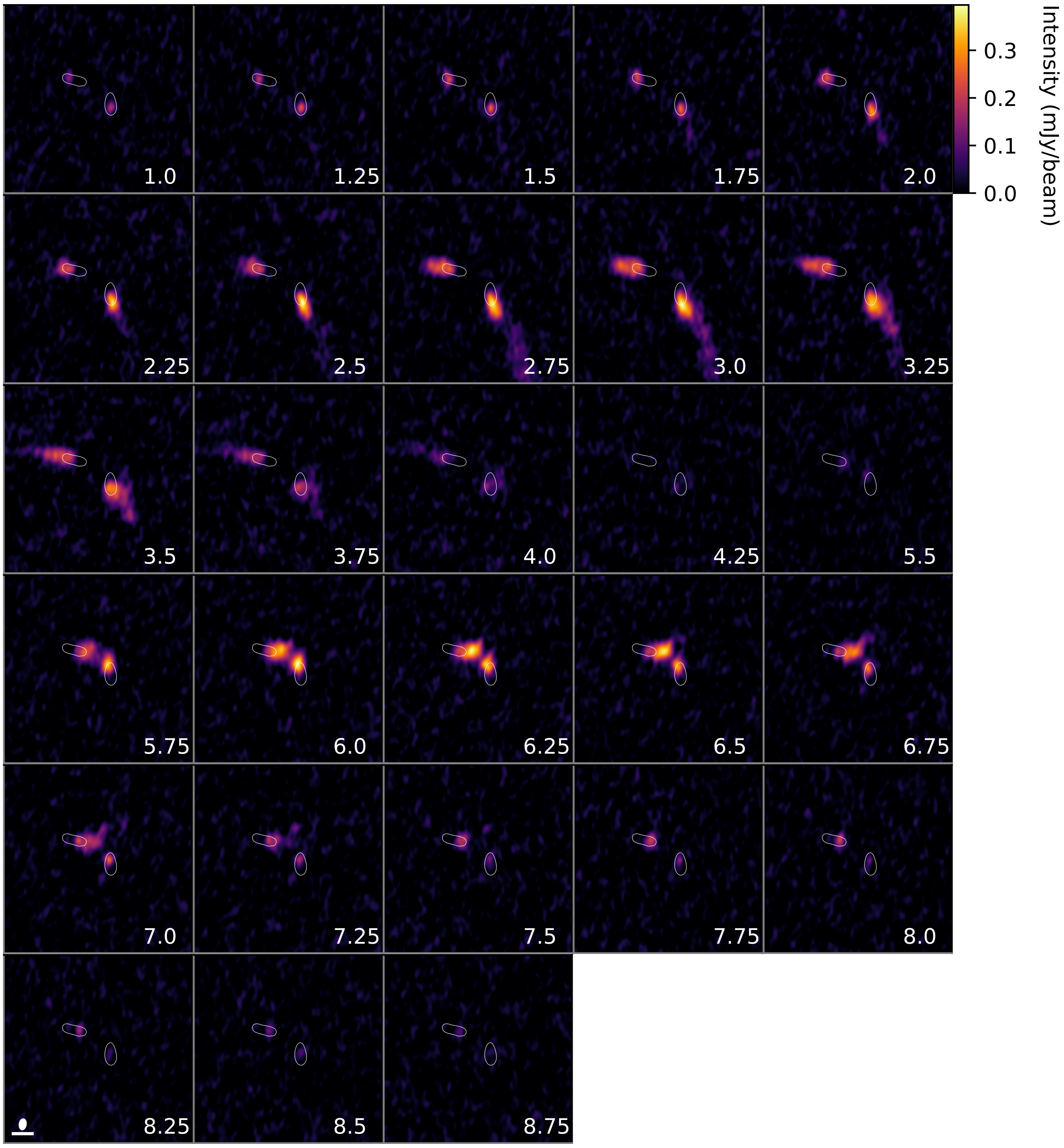

Figure 5.6 – Channel maps of HH 48 NE along with the continuum emission (20% contours). The velocities between 4.25 and 5.5 km/s are not represented because CO is not detected. The synthesized beam and a 0.5″ scale are represented in the bottom left panel, and the velocities are reported in the bottom right corner of each panels (in km/s).

5.1.2 *Results and future analysis*

From the moment maps shown in Fig. 5.1 and Fig. 5.2, we find that the gas emission extends further out than the continuum both radially and vertically. This is similar to the results obtained in Section 4.3.6 (Fig. 4.9) comparing the millimeter continuum emission with HST scattered light images and this supports the fact that these disks are subject to radial drift and vertical settling. A detailed analysis is still to be performed but we can notice several interesting features.

- First, we find that in most cases, the scattered light and ^{12}CO gas emission seem to correspond tightly (see e.g., Tau 042021 and HK Tau B in Fig. 5.3). This is consistent with small grains being well mixed with the gas.
  However, some disks present important differences between scattered light and gas emission. For example, the ^{12}CO emission of HV Tau C is significantly more extended radially than the scattered light emission. This is likely related to lower illumination in the outer regions of the disks, which lead to lower intensity in scattered light. Another example of differences between scattered light and gas emission is IRAS 04158, where both tracers do not seem to be co-located. This potentially indicates that the scattered light emission is significantly optically thicker than ^{12}CO emission. Detailed studies will help to understand better the coupling of small grains with gas.
- From the moment maps we can see that some disks present some interesting features, sometimes non Keplerian. To illustrate this statement, I represent the channel maps of three sources in Figs. 5.4, 5.5, and 5.6 (IRAS 04302, ESO-Hα 574, and HH 48 NE). In Fig. 5.2, we see an elongated structure on the northeast side of the continuum emission of IRAS 04302. In the channel maps, it is best seen between 0.5 and 3.5 km/s (Fig. 5.4). This structure might correspond to an outflow. Additionally, some extended emission is detected in the southwest of the source (between 7.25 and 8.5 km/s), which could be related to emission from an envelope.
  The second source for which I represented the channel maps, ESO-Hα 574, shows some extended emission in the south-west (see Fig. 5.2). While this structure is relatively clear in the moment maps (Fig. 5.1 and 5.2), we can see that it is only marginally above the noise level in the channel maps (between 5.75 and 6.5 km/s, Fig. 5.5).
  As a third example, I represent the channel maps of the two sources of HH48 in Fig. 5.6. They seem connected on the red-shifted side of the emission (see moments maps in Fig. 5.2 and channel maps between 5.75 and 7.0 km/s, Fig. 5.6). If the disks are in the same plane, such interaction might lead to disk truncation. Individual studies of these features should allow to reveal their physical origin.
- Having in mind that the top row of Figs. 5.1 and 5.2 corresponds to the most inclined sources of the sample (and that IRAS 04302 is a class I with an extended envelope), we can see two different types of disks. While Tau 042021 and IRAS 04302 are very extended in the vertical direction compared to the contin-

uum, HK Tau B and HV Tau C appear extremely flat. This suggests a difference in the physical processes present in the disks, potentially with the flat disks being colder than the flared ones. A detailed comparison of the two different types of objects is needed to understand the origin of these differences.

— Finally, studying the gas emission of edge-on disks will allows us to obtain dynamical estimates of stellar masses. Currently, no estimation of stellar masses are available for the majority of these disks (see Table 4.2), because due to their large inclinations most of the stellar light is obscured. Since vertical settling and radial drift are related to viscosity and stellar gravity, estimating the mass of the star is important to test these models. An interesting study can be to look for any connections between stellar masses and the observed disks vertical extent.

5.2 HIGH ANGULAR RESOLUTION OBSERVATIONS OF OPH 163131

I am also currently working on high angular resolution observations of Oph 163131 which I obtained during ALMA cycle 6 (project: 2018.1.00958.S, PI: Villenave). We observed the source at the highest angular resolution possible in band 6, in order to resolve the vertical extent of this disk which appears very thin in scattered light observations. I have already reduced the data, which I present in subsection 5.2.1 and I am working on a radiative transfer model of the new ALMA data to understand the physical structure of the disk.

5.2.1 *Observations and data reduction*

The spectral setup of the cycle 6 observations was divided in three continuum spectral windows, of rest frequencies 229.0 GHz, 243.5 GHz, and 246.0 GHz, and an fourth spectral window including the ^{12}CO transition at 230.538 GHz. The line spectral window has a native velocity resolution of 0.64 km s^{-1}. The data were obtained on June 8, 2019, with baselines ranging from 80 m to 16 km. The total observing time on source was about 2 hours and 30 minutes. The raw data were calibrated using the CASA pipeline version 5.4.

To produce the final images, I combined the cycle 6 observations with previous lower angular resolution observations from cycle 4 (Project 2016.1.00771.S, PI: Duchêne) presented in Section 4.2.2. To maximize the dynamical range of the image, I performed self-calibration on the cycle 4 continuum observations, but the limited signal to noise prevented from using selfcalibration on the cycle 6 observations. I extracted the continuum images using the CASA `tclean` task on the combined dataset, with a Briggs parameter of +0.5 and using the multiscale deconvolver. The resulting beam size is $0.024'' \times 0.020''$ ($\sim 3 \times 3.5$ au at 146 pc, Wolff et al., in prep). Note that a shift of about $0.05''$ ($\sim$ 20% of the cycle 4 beam) was present between the cycle 4 and cycle 6 observations, which is roughly consistent with the astrometric accuracy of ALMA (see

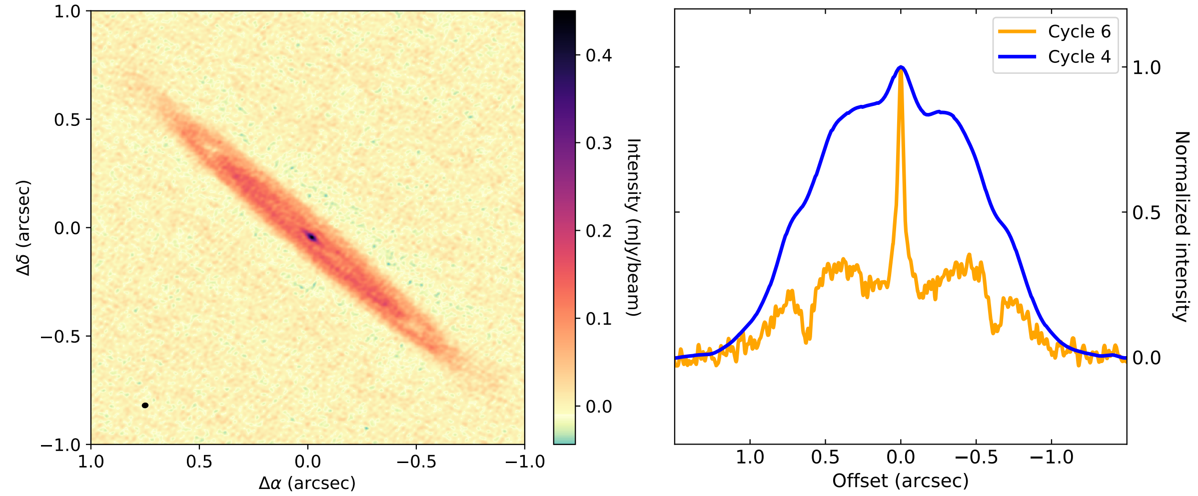

Figure 5.7 – **Left:** Continuum image of Oph 163131. The beam size is indicated by an ellipse in the bottom left corner of the plot.
Right: Normalized cuts along the major axis of the new image and previous cycle 4 observations of Oph 163131. The structure is much clearer at the highest angular resolution available. Note that the cuts are normalized so that their maximum is unity but the total intensities of both cycle 4 and cycle 6 images are similar.

ALMA Technical Handbook [1]). Thus, before producing the combined image, I aligned both observations using the `fixplanet`.

After applying the continuum self-calibration solutions to all spectral windows, I extracted the emission lines from the calibrated visibilities by subtracting continuum emission using the `uvcontsub` task in CASA. I used 0.7 km s^{-1} velocity resolution and a Briggs parameter of 0.5 to create the line images. Additionally, to increase the signal to noise of the ^{12}CO observations, I applied a uv-taper while generating the images. The average resulting beam for the line is $0.081'' \times 0.07''$. Finally, I generated moment 0 and 1 maps including only pixels above 3 times the rms.

5.2.2 *Results*

The continuum observations of Oph 163131 are shown in Fig. 5.7, along with a major axis cut. The high angular resolution of the image reveals a lot of substructures even if the disk is highly inclined. In particular, we see a centrally peaked unresolved region, a non-empty gap (hereafter called plateau) from about 0.1″ (15 au) with increasing intensity up to 0.5″ (74 au) where we see a first ring, and a second ring peaking at 0.72″ (106 au). The second ring is separated from the first one by a clear a gap between 0.6″ and 0.65″. Note that there were hints for these substructures with previous observations (see cycle 4 cut in the right panel of Fig. 5.7) but they were unresolved as with the current observations.

---

[1] https://almascience.eso.org/documents-and-tools/latest/documents-and-tools/cycle8/alma-technical-handbook

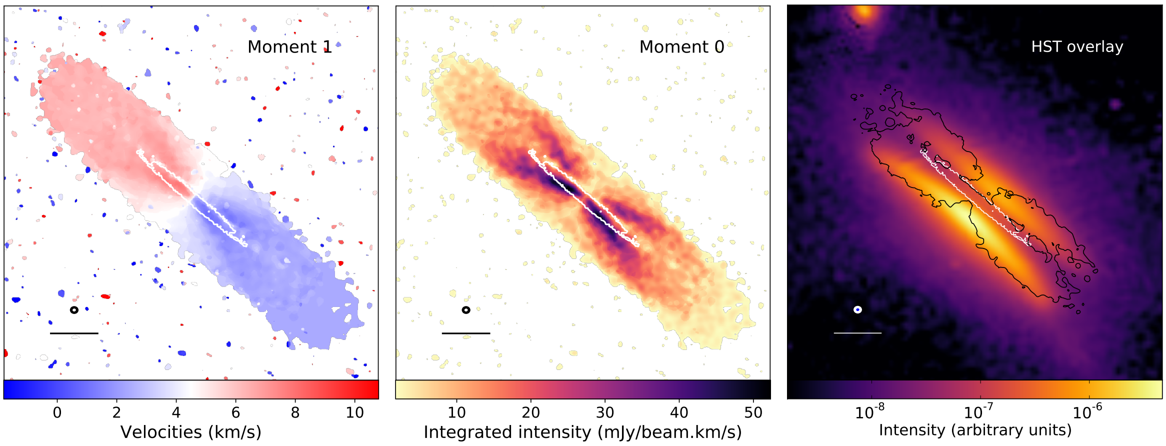

Figure 5.8 – **Left:** Moment 1 map,**Middle:** Moment 0 map, **Right:** Overlay of the HST image (colors), continuum contours (in white) and ^{12}CO moment 0 contours (in black). In each panel, an horizontal line in the bottom left corner indicates the 0.5″size. The continuum and CO beams are represented by blue and white ellipses in the bottom left corner of each panels (inversed colors).

The moment 0 and moment 1 maps of Oph 163131 are shown in Fig. 5.8. The disk appears significantly more extended in the radial and vertical direction than the continuum, indicating that large grains are less extended radially and vertically than the gas. Additionally, the overlay of the gas emission with the HST scattered light image presented in the same figure shows that both tracers have a similar radial and vertical extent. This indicates that micron sized grains are well mixed with the gas, validating the assumption we made in Chapter 4.

5.2.3 *Preliminary analysis*

In order to obtain new constraints on vertical settling and radial drift, I started to model the disk with MCFOST. This is still work in progress, but the first results indicate that:

- To reproduce the cut along the major axis direction, the vertical extent of millimeter grains has to be extremely thin (< 3 au at 100 au).
- The disk plateau between 0.1 and 0.5″ can only be reproduced by a disk region with increasing surface density with radius ($p = -1$), while the rings are well matched by the typical surface density with $p = 1$ (see equation 1.10).
- The current best model (which contains only grains larger than 10 μm) is optically thick at millimeter wavelengths, but reaches an integrated flux at millimeter wavelengths about an order of magnitude smaller than the observed one. Some preliminary tests show that adding a layer of small grains more extended vertically than the millimeter grains allows to increase the total flux emitted at millimeter wavelengths. This is likely because the presence of small grains modifies the temperature structure of the disk, by scattering energy back to the

disk surface. This makes the midplane warmer than without the small grains and thus allows it to emit more at millimeter wavelengths. Additionally, having a layer of small grains more extended vertically (e.g., 10 au at 100 au) is justified by HST observations of the disk (Wolff et al., in prep). It is also consistent with vertical settling in the disk.

Once a good model for the continuum is obtained, I plan to perform a direct comparison of the model and data in the visibility plane. Then, I aim to produce ^{12}CO model maps to estimate the difference in vertical extent between the two observables. This will allow to quantify precisely the settling efficiency within the disk and to estimate the potential gas to dust mass ratio in the disk midplane. With these values, we should be able to predict whether streaming instabilities can be triggered within the disk or not.

6

CONCLUSIONS AND PERSPECTIVES

6.1 SUMMARY

My PhD work consisted in using multi-wavelength observations to constrain several evolutionary mechanisms in protoplanetary disks. My main interests are to study observationally dust radial drift and vertical settling, but I also worked on global disk dispersion and the formation of cavities in transition disks. I used mostly ALMA millimeter observations, which I learned to calibrate and analyse during this thesis. Continuum millimeter observations probe large millimeter grains, which are expected to be decoupled from the gas. This implies that these grains are predicted to be less extended both radially and vertically than the gas (see Section 1.3.2). To add constraints on radial drift and vertical settling, I compared continuum millimeter observations to gas emission lines (mainly using ^{12}CO) or scattered light observations. The latter are a proxy for gas observations because scattered light trace small micron sized grains which are well mixed with the gas.

The first project of my thesis allowed to study the *global evolution of disks*. In particular, I analysed the dissipation of disks with time by studying the relatively old Cha II star-forming region (4 ± 2 Myr, Chapter 2). I showed that the disk dust mass, as estimated from continuum millimeter emission, is statistically smaller in Cha II than in younger associations such as Lupus and Taurus. Conversely, the Cha II disks are statistically more massive than those of the older Upper Sco region. This is consistent with a smooth dissipation of the disk with time, as predicted from the evolution of viscous disks (see Section 1.2.2).

In parallel, I showed that the gas detection rates in disks detected in dust also decrease with time. This suggests that gas dissipates faster than dust (see also Fedele et al., 2010), implying that the timescale available for giant planet formation might be even shorter than the typical dust dissipation timescale (a few Myr, Ribas et al., 2014).

In the second project, I studied a large sample of transition disks observed at several wavelengths in order to *test whether their cavities could be opened by planets* (see Chapter 3). I showed that in 15 out of the 22 disks studied, the cavities could be explained by a giant planet. For the remaining disks of the sample, the cavity might be opened by a companion above the planetary mass regime, or by multiple low mass planets. This result is in agreement with the growing idea that protoplanetary disks are actually planet-hosting disks.

For all projects of my thesis, I also studied the *radial extent of protoplanetary disks*. In agreement with theoretical predictions, I find that both the gas and small micron-sized grains are more extended radially than larger millimeter-sized grains. This is the case for the 12 Cha II disks detected in ^{12}CO emission (Chapter 2), for J1608, the most resolved disk of Chapter 3 modeled with radiative transfer, as well as for the edge-on disks presented in Chapter 4. In particular, the 12 Cha II disks show an average gas to dust ratio in radial extent greater than 3. This large ratio can likely not be reproduced only by differences in optical depth between the two tracers, so it is highly suggestive that radial drift and grain growth are happening in the disks.

Additionally, the gas to dust size ratio measured in the Cha II disks is larger than what is observed in 22 disks of the younger Lupus star-forming region (ratio ~ 2 in Lupus, Ansdell et al., 2018). This is likely a direct observation of the combined effects of inward drift of the millimeter grains and the outward expansion of the gas between $1-3\,$Myr (Lupus) and $2-6\,$Myr (Cha II), which are predicted from the evolution a standard viscous disk (see Section 1.2.2) and from the interaction of dust with the slower gas (see Section 1.3.2).

However, while the drift timescale of millimeter sized grains is predicted to be very fast ($\ll$ few Myr), all the disks studied in this thesis where gas is more extended than dust are relatively large (> several tens of au). This suggests that some mechanisms are able to slow down radial drift in most disks that I analysed during my PhD. Following the results from recent high angular resolution surveys (e.g., Andrews et al., 2018b; Long et al., 2018), there is a growing conviction that substructures, and rings in particular, are universal in disks. Those are generally associated to pressure traps, where dust particles accumulate, possibly allowing to solve the radial drift issue (Pinilla et al., 2012b). However, the origin of these substructures remains unclear. While planets within the disks are often proposed to explain the substructures, the question of how such planets could form so early in the disk remains. Alternatively, other scenario able to create substructures involve for example ice lines (Okuzumi et al., 2016), MHD-driven winds (e.g., Suzuki et al., 2016; Riols et al., 2020b) or self-induced dust traps (Gonzalez et al., 2017). Those could be responsible for a first generation of substructures, allowing to form the first planets, later creating more substructures.

Finally, my work allowed to add important observational constraints on the *vertical structure of protoplanetary disks*. In Chapter 3 and Chapter 4, I compared scattered light and millimeter images of several disks. Using radiative transfer modeling, I showed that small micron sized grains are more extended in the vertical direction than millimeter sized grains, for at least one object studied in Chapter 3 (J1608, at least a factor 2 in vertical extent). For the edge-on survey, the comparison of the gas and scattered light vertical extent with that of the millimeter grains leads to similar conclusions (see Fig. 4.9 and Fig. 5.1), in agreement with efficient vertical settling in a large number of disks.

In order to quantify the settling efficiency, I worked on some of the first direct observational constraints on the vertical extent of millimeter dust in protoplanetary disks. The large inclination of the edge-on disks studied in Chapter 4 indeed offers a unique perspective to estimate directly their vertical structure. I showed that the most resolved disks of the survey are compatible with millimeter vertical "scale heights" of a few au at 100 au. This is about a factor 10 smaller than the typical gas scale height (e.g., Stapelfeldt et al., 1998) and is consistent with previous observational studies (e.g., Pinte et al., 2016). This value indicates that settling is efficient in protoplanetary disks, leading to a very flat disk of millimeter sized grains where the gas to dust ratio is smaller than in the ISM. Pinte et al. (2016) showed for example that, at 100 au, a gas to dust ratio of 1 is reached for 10 cm grains in the similarly flat HL Tau disk (1 au at 100 au for millimeter grains). This gas to dust ratio, likely present in most of the edge-on disks (since they all appear vertically thin at millimeter wavelengths), is expected to be low enough to trigger streaming instabilities (Youdin and Goodman, 2005), which allow grains to form planetesimals in a very short timescale. Additionally, an increased solid density favors mechanisms such as pebble accretion (Ormel and Klahr, 2010; Lambrechts and Johansen, 2012), which accelerate even further the formation of planetesimals in disks. If vertical settling is fast enough, it can be a mechanism helping the formation of planets in the earliest stages of disk evolution.

6.2 PERSPECTIVES

While disk dissipation, radial drift or the opening mechanisms of transition disks have been studied in details prior to my PhD work, the analysis of the vertical structure of protoplanetary disks is relatively new, particularly using the edge-on viewing angle. Previous observational studies of disk vertical structure have been performed through the analysis of gas emission lines of relatively low inclination disks (e.g., Dartois et al., 2003; Pinte et al., 2018; Teague et al., 2019) or of inclined systems but with low angular resolution preventing from resolving their vertical extent (Dutrey et al., 2017; Teague et al., 2020). The analysis of a large number of edge-on disks presented in Chapter 4 consisted in one of the first study of vertically resolved observations of protoplanetary disks at millimeter wavelengths. We showed that the disks are extremely thin at millimeter wavelengths which indicates that settling is important and turbulence is low. However, these conclusions have been derived from a detailed analysis of the millimeter dust emission only, provided that the scattered light images appear more extended vertically.

A direct extension of this study would be to perform a *detailed analysis of the vertical extent of the gas in edge-on disks*. Directly comparing the vertical extent of the gas and millimeter dust is essential because predictions from settling models constrain the scale height ratio between dust and gas. Thus, obtaining an observational scale height ratio is expected to allow to discriminate between the settling models, and so, might allow to identify the dominant turbulent mechanism in the outer disk of protoplanetary disks. Currently, theoretical studies have predicted the vertical extent of disks for various turbulence-driving mechanisms (e.g., ideal-MHD, Fromang and Nelson 2009, vertical shear instability, Flock et al. 2017, ambipolar diffusion, Riols and Lesur 2018, gravito-turbulent disks, Riols et al. 2020a). Low turbulence able to reproduce the observations seems to occur in disks where non ideal MHD effects dominate. However, further observational and theoretical studies are needed to explore other possibilities and improve the comparison with data.

The analysis of the gas seen in edge-on disks will also allow to estimate precisely their *temperature structure* (Dutrey et al., 2017; Pinte et al., 2018; Teague et al., 2020, Flores et al., in prep). This value is extremely important as dust thermal emission and molecular chemistry depend on the disk temperature. Additionally, the gas pressure scale height is directly related to the temperature profile of the disk. Being able to quantify the disk's temperature should allow to estimate if temperature difference is at the origin of the variety in vertical extent observed from scattered light and ^{12}CO observations of edge-on disks (see Chapter 5, and Stapelfeldt et al., 2014).

Along those lines, *increasing the number of edge-on disks resolved in the vertical direction at millimeter wavelengths* will enable us to look for correspondence between the scattered light and millimeter vertical extent, answering the following question: are vertically thin disks in scattered light also thinner at millimeter wavelength? This will allow to gain significant insights on the physics governing the vertical extent of protoplanetary disks.

In order to perform such analysis, note that several disks were resolved in the vertical direction in the survey presented in Chapter 4 and I also obtained high angular resolution ($\sim 0.02''$) observations of Oph 163131 with ALMA (see Chapter 5, Section 5.2.1). Some preliminary results suggest that indeed thin disks in scattered light observations are also thin at millimeter wavelengths (and conversely). However, detailed modeling of these disks and other promising targets should allow to get precise observational constraints on the vertical structure of several protoplanetary disks. In particular, the comparison of the vertical extent of Class II targets with that of younger Class 0 or Class I objects would be highly interesting to look for evolution of settling with time.

Finally, obtaining vertically resolved *observations at several wavelengths for a large number of edge-on disks* is important to constrain the effect of vertical settling on the different grain sizes. Currently, scattered light (between 0.4 μm and 2.2 μm) and millimeter (2.06 mm and 0.89 mm) observations are available on the edge-on disks of our sample. This allows to probe large grains in the disk midplane as well as small grains more mixed with the gas. In the near future, the James Webb Space Telescope (JWST) will provide images at intermediate wavelengths, from 0.6 to 26 μm, although with a limited angular resolution ($\sim 0.3''$ at 10 μm). Only the largest disks (e.g., Tau 042021) are expected to be vertically resolved by JWST observations. For these disks, JWST will allow to probe intermediate grain sizes, between the micron sized particles studied with optical/NIR observations and the millimeter grains probed by millimeter observations. These intermediate grains are likely affected in an intermediate way by vertical settling, although the impact of settling on these intermediate grains has not been studied in great details by numerical studies. Comparing these three grain populations will be important to add constraints on vertical and radial segregation.

Interestingly, JWST will be very sensitive which also enables it to probe many gas lines from the surface layers of protoplanetary disks, enabling to study in greater details the chemistry of protoplanetary disks. Additionally, extending the study of edge-on disks to larger wavelengths (e.g., centimeter with the VLA, future ALMA upgrades, and SKA), which are likely optically thinner would allow to get strong constraints on the vertical extent of protoplanetary disks.

At the same time, ESO is currently building the ELT (Extremely Large Telescope) on Cerro Armazones in Chile[1]. Thanks to its large primary mirror of 39 m of diameter and the adaptive optics systems associated to each instrument, the ELT should reach an angular resolution about 5 times smaller than the VLT, and increase the collecting area by more than one order of magnitude compared to previous instrumentation. This will allow to detect fainter objects and to study the finest structures of protoplanetary disks. In particular, the high sensitivity provided by this telescope should allow to increase the population of known planets around young stars or even inside protoplanetary disks, which could help to understand better the origin of the substructures commonly observed in disks. These upcoming facilities will thus permit to build answers on several remaining questions of this field, such as the origin of substructures of disks, how turbulence is generated and at what strength, and finally, how exoplanets planet form.

---

[1] The GMT and TMT are other 30-m class telescopes under-construction.

A

FIRST AUTHOR PUBLICATIONS

In this appendix, I present all my first authored publications. They are either in preparation or already published. I described each in Chapter 2, 3, and 4 of this thesis.

- ***M. Villenave****, F. Ménard , W. Dent, G. van der Plas et al.*, in preparation
  Probing protoplanetary disk evolution in the Chamaeleon II star-forming region.
- ***M. Villenave****, F. Ménard , W. Dent, G. Duchêne et al.*, 2020, A&A, in press
  Observations of edge-on protoplanetary disks with ALMA. I. Results from continuum data.
- ***M. Villenave****, M. Benisty, W. Dent, F. Ménard et al.*, 2019, A&A, 624, A7
  Spatial segregation of dust grains in transition disks. SPHERE observations of 2MASS J16083070-3828268 and RXJ1852.3-3700.

Astronomy & Astrophysics manuscript no. output
June 26, 2020

Probing protoplanetary disk evolution in the Chamaeleon II region

M. Villenave[1,2], F. Ménard[2], W. R. F. Dent[3], G. van der Plas[2], M. Benisty[4,2], J. P. Williams[5], C. Caceres[6,8], H. Canovas[9], L. Cieza[10], A. Hales[3,11], I. Kamp[12], C. Pinte[13,2], D. A. Principe[14], M. R. Schreiber[6,7], and A. Riols[1]

[1] European Southern Observatory, Alonso de Córdova 3107, Vitacura, Casilla 19001, Santiago 19, Chile e-mail: `marion.villenave@univ-grenoble-alpes.fr`
[2] Univ. Grenoble Alpes, CNRS, IPAG, F-38000 Grenoble, France.
[3] Joint ALMA Observatory, Alonso de Córdova 3107, Vitacura 763-0355, Santiago, Chile
[4] Unidad Mixta Internacional Franco-Chilena de Astronomía, CNRS/INSU UMI 3386 and Departamento de Astronomía, Universidad de Chile, Casilla 36-D, Santiago, Chile
[5] Institute for Astronomy, University of Hawaii, Honolulu, Hawaii, USA
[6] Milenium Nucleus for Planet Formation, Universidad de Valparaiso, Av. Gran Bretaña 1111, Valparaiso, Chile
[7] Universidad de Valparaiso, Instituto de Fisica y Astronomia, Avenida Gran Bretaña 1111, Valparaiso, Chile
[8] Departamento de Ciencias Fisicas, Facultad de Ciencias Exactas, Universidad Andres Bello. Av. Fernandez Concha 700, Las Condes, Santiago, Chile
[9] European Space Astronomy Centre (ESA), Camino Bajo del Castillo s/n, 28692, Villanueva de la Cañada, Madrid, Spain.
[10] Núcleo de Astronomía, Facultad de Ingeniería y Ciencias, Universidad Diego Portales, Av. Ejercito 441, Santiago, Chile
[11] National Radio Astronomy Observatory, 520 Edgemont Road, Charlottesville, Virginia, 22903-2475, United States
[12] Kapteyn Astronomical Institute, University of Groningen, Landleven 12, NL-9747 AD Groningen, The Netherlands
[13] Monash Centre for Astrophysics (MoCA) and School of Physics and Astronomy, Monash University, Clayton Vic 3800, Australia
[14] Massachusetts Institute of Technology, Kavli Institute for Astrophysics, Cambridge, MA 02109, USA

Received xx / Accepted xx

ABSTRACT

Context. Characterizing the evolution of protoplanetary disks is necessary to improve our understanding of planet formation. Constraints on both dust and gas are needed to determine the dominant disk dissipation mechanisms.

Aims. We aim to measure disk dust masses and gas detection rates in the Chamaeleon II (Cha II) star-forming region. At that age (~ 4 ± 2 Myr), disks evolve and dissipate rapidly. We aim to compare Cha II with younger and older regions, in the 1 to 10 Myr age range.

Methods. We used ALMA to survey 31 sources in Cha II. Continuum data at 1.33 mm is exploited to estimate the dust masses, and CO isotopologues observations are used to infer the gas detection rate.

Results. We detected 24 sources in the continuum, 12 in ^{12}CO, 3 in ^{13}CO and none in C^{18}O. Most disk dust masses are smaller than 10 $M_\oplus$ under standard assumptions for dust temperatures and opacities. Disk radii measured in dust are ~3 times smaller than those of ^{12}CO, which can be explained by a combination of opacity, grain growth and radial drift effects. By comparing consistent estimations of the distributions of disk-to-stellar-mass ratios with five other star-forming regions in the age range of 1-10 Myr, we find that disks become less massive with time: the older the region, the smaller the ratio. When compared by pairs, star-forming regions with large age differences (≥ 3 Myr) have disk-to-stellar mass ratios that are statistically different (i.e., they have evolved). More closely aged regions have ratios that are not statistically different, although the same trend may be present. Considering gas evolution by comparing CO detection rates for disks with detected dust, we find that the fraction of disks detectable in gas also decreases with age, in accordance with disk evolution models. This suggests that either gas dissipates faster than dust, or that older disks have a reduced CO abundance.

Key words. Protoplanetary disks - Techniques: interferometric - Stars: formation - Stars: circumstellar matter - Stars: variables: T Tauri

1. Introduction

Planetary systems form from the gas- and dust-rich disks that orbit young stars. Currently more than 4100 planets around main sequence stars are confirmed (exoplanet.eu), revealing a wide diversity in the architecture of exoplanetary systems (Borucki et al. 2010; Howard et al. 2010; Mayor et al. 2011). To identify the origins of such diverse planetary systems, it is essential to understand how planets form. Current models indicate that the architectures of planetary systems are dictated by the initial dust and gas content of protoplanetary disks and their evolution (Raymond et al. 2007; Dawson et al. 2014). A better characterization of the physical properties and evolutionary mechanisms of protoplanetary disks is therefore essential towards the understanding of planet formation.

In a review comparing more than twenty star-forming regions observed at near-infrared (NIR) wavelengths, Mamajek (2009) showed that the evolution with time of the disk fraction can be described by an exponential with a typical timescale of 2.5 Myr (see also Ribas et al. 2014). This timescale varies slightly between low and high mass stars, suggesting that disks around higher mass stars dissipate faster than around low mass stars (Ribas et al. 2015; Mamajek 2009). However, NIR emission probes hot dust in the inner regions of disks. The timescale for giant planet formation is rather set by the global gas and dust mass dissipation rather than the hot dust dissipation timescale alone.

To test disk evolutionary models and find the dominant mass dissipation mechanism(s), observational constraints on mass are needed. Millimeter and submillimeter surveys are particularly useful to probe the disk's dust and gas content. Several surveys of star-forming regions have been conducted at millimeter wavelengths, generally focused on 1-3 Myr regions (Andrews et al. 2013; Pascucci et al. 2016; Ansdell et al. 2016; Cazzoletti et al. 2019; van Terwisga et al. 2019). They showed that the disk dust masses estimated in these young regions is in general smaller than those measured in the more evolved Upper Sco star-forming region (5-10 Myr Barenfeld et al. 2016). This suggested the dissipation of the disk dust mass with time. Those surveys also found a correlation between dust and stellar mass.

In this paper, we extend these studies and present an ALMA survey of protoplanetary disks located in the intermediate age Chamaeleon II (Cha II) star-forming region. Cha II is located ~ 198 ± 6 pc away (Dzib et al. 2018). With an age of 4 ± 2 Myr (Spezzi et al. 2008), this makes it a good choice to study the decline of gas and dust content. Compared to the σ-Orionis star-forming region of about the same age, Cha II offers a different environment, not influenced by OB stars.

We describe our ALMA observations and data reduction in Section 2. The continuum and CO line measurements are presented in Section 3, and properties derived from the data are given in Section 4. Then, in Section 5, we compare the dust to stellar mass ratio and gas detection rates for Cha II to other star-forming regions of different ages. Our results are summarized in Section 6.

2. Observations and data reduction

2.1. Sample

Cha II contains 63 known young stellar objects (YSOs) including 38 Class II sources (Spezzi et al. 2013). We observed 31 members of Cha II with the Atacama Large Millimeter Array (ALMA) during Cycle 2. The sample contains mainly classical T Tauri stars, whose physical parameters are given in Table 1. Two objects in the sample have been classified as binary systems previously, namely Sz 59 (also called BK Cha) and Sz 62 (Correia et al. 2006; Geoffray & Monin 2001). The sample includes one Class I source, one "flat spectrum" source and 27 Class II sources; two secondary sources (around Hn 24 and Sz 59) were also detected.

The targets were selected because they show an infrared (IR) excess at 70 μm, as observed by *Herschel* (Spezzi et al. 2013). The remaining eleven unobserved Class II systems of Cha II have stellar masses in the range from 0.1 to 0.6 $M_\odot$ (Fig. 1). Except for one source, they are not detected at 70 μm by Herschel. Comparing their IR properties with those of the undetected sources in our ALMA sample, it is most likely that they would not have been detected with ALMA either, given our observation set-up. Thus although we observed only 70% of the known Class II objects, our survey is probably complete for the brightest Class II disks of Cha II.

2.2. ALMA observations

Our ALMA Cycle 2 observations (Project 2013.1.00708.S, PI: Ménard) were obtained on 2015 August 27, with an array configuration made of 40 antennas with baselines ranging from 26 to 1170 m.

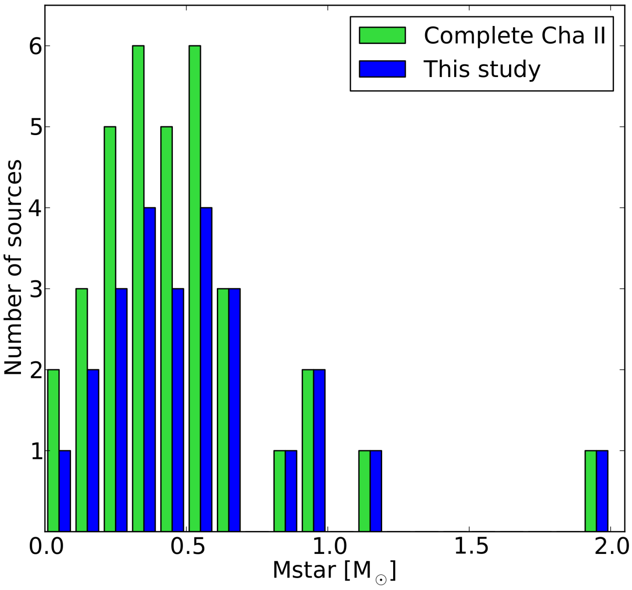

Fig. 1. Distribution of stellar masses for the Cha II members of Class II. The full sample from Spezzi et al. (2013, in blue) and our ALMA sample (in green) are compared.

The continuum spectral windows were centered on 234.2 and 217.2 GHz, giving a mean continuum frequency of 225.7 GHz (1.33 mm). The other two spectral windows were set-up to include 3 CO isotopologue lines. They covered the ^{12}CO, ^{13}CO, and C^{18}O $J = 2 - 1$ transitions at 230.538 GHz, 220.399 GHz and 219.56 GHz. Each spectral window had 152-160 km s^{-1} velocity bandwidth and 0.33 km s^{-1} velocity resolution. Integration time was 2.5 min "on-source" per target giving an average continuum RMS of 0.17 mJy beam^{-1}. The raw data were calibrated using the CASA package (version 4.3.1).

We extracted the continuum images from the calibrated visibilities over the continuum channels by using the CASA `clean` function with a Briggs robust weighting parameter of +0.5. To maximize the dynamic range of the brightest sources, we performed a phase-only self-calibration on CM Cha, Hn 22, Hn 23, IRAS12500-7658, Sz 58 and Sz 61. In the case of the brightest target, IRAS12496-7650 (also called DK Cha), phase and amplitude self-calibration were performed. This improved the signal-to-noise ratio by more than 30%. We present the continuum images in Fig 2. They achieve an averaged angular resolution of 0.48″×0.25″.

We extracted ^{12}CO, ^{13}CO and C^{18}O channel maps from the calibrated visibilities by subtracting the continuum from the spectral windows containing line emission using the `uvcontsub` routine in CASA. For the brightest sources, we also applied the continuum selfcalibration solution to the gas line data. We cleaned the sources with velocity channels of 0.35 km s^{-1}, and with a Briggs robust weighting parameter of 0, providing a good compromise between spatial resolution and sensitivity. We obtain an average angular resolution of 0.51″×0.28″ for the CO lines.

For the detected sources, from the CO channel maps of each isotopologue, we created moment 0 showing the integrated line emission (see Fig. 3 for the sources detected in ^{12}CO). The maps were obtained by using the channels where the source was detected. For each source, we also generated line profiles from the CO channel maps, over a range from -10 to +15 km s^{-1}. The spatial range used to generate each line profile varied according

Table 1. Observed Cha II ALMA sample.

Source	RA (h.m.s)	Dec (deg.m.s)	SpT[a]	Class[a]	$M_\star/M_\odot$ [b]
J13022287-7734494	13 02 22.9	-77 34 49.4	M5	II	0.16
J13071806-7740529	13 07 18.1	-77 40 52.9	M4.5	II	0.20
J13082714-7743232	13 08 27.1	-77 43 23.3	M4.5	II	0.20
CM Cha	13 02 13.6	-76 37 57.8	K7	II	0.63
Hn 22	13 04 22.9	-76 50 05.5	M2	II	0.40
Hn 23	13 04 24.1	-76 50 01.2	K5	II	0.97
Hn 24 A	13 04 55.7	-77 39 49.6	M0	II	0.52
Hn 24 B*	13 04 55.6	-77 39 51.0	-	-	-
Hn 25	13 05 08.6	-77 33 42.6	M2.5	II	0.34
Hn 26	13 07 48.5	-77 41 21.4	M2	II	0.41
IRAS12496-7650	12 53 17.2	-77 07 10.6	F0	II	>1.4
IRAS12500-7658	12 53 42.9	-77 15 11.5	K5	I	0.06
IRAS12535-7623	12 57 11.7	-76 40 11.1	M0	II	0.49
ISO-CHAII 13	12 58 06.8	-77 09 09.5	M7	II	0.07
J130059.3-771403	13 00 59.3	-77 14 02.7	K3	II	-
J130521.7-773810	13 05 21.7	-77 38 10.3	-	F	-
J130529.0-774140	13 05 29.0	-77 41 40.1	-	II	-
Sz 46	12 56 33.7	-76 45 45.4	M1	II	0.49
Sz 49	13 00 53.2	-76 54 15.2	M0.5	II	0.56
Sz 50	13 00 55.3	-77 10 22.2	M3	II	0.32
Sz 51	13 01 58.9	-77 51 21.9	K8.5	II	0.63
Sz 52	13 04 24.9	-77 52 30.3	M2.5	II	0.35
Sz 53	13 05 12.7	-77 30 52.6	M1	II	0.49
Sz 54	13 05 20.7	-77 39 01.6	K5	II	0.86
Sz 56	13 06 38.8	-77 30 35.3	M4	II	0.23
Sz 58	13 06 57.5	-77 23 41.6	K5	II	1.03
Sz 59 A	13 07 09.2	-77 30 30.5	K7	II	0.69
Sz 59 B*	13 07 09.7	-77 30 30.2	-	-	-
Sz 61	13 08 06.3	-77 55 05.2	K5	II	0.89
Sz 62	13 09 50.4	-77 57 24.0	M2.5	II	0.27
Sz 63	13 10 04.2	-77 10 44.8	M3	II	0.28

Notes. Coordinates are from the SIMBAD database except for the secondary of the Hn 24 and Sz 59 binaries. These two were estimated from our images (marked by *).

References. (a) Spezzi et al. (2013), (b) This work. Stellar masses are calculated from the PMS tracks by Baraffe et al. (2015), using luminosities and temperatures from Spezzi et al. (2008) rescaled using individual distances from Gaia DR2 (Gaia Collaboration et al. 2018), see Section 5.1.

to the detectability of the source. When the sources were detected in the molecule, line profiles were produced on the pixels detected by more than 3σ. When sources were not detected in CO, we also generated line profiles in order to get a consistent method to evaluate the RMS. We used a square of size $1''\times1''$ (close to the mean size of the detected sources), centered near the phase center to extract the spectrum and calculate the RMS. ^{12}CO and ^{13}CO line profiles are shown on the left panels of Fig. 3 for the sources that were detected in ^{12}CO.

3. ALMA results

3.1. Continuum emission

We measure the continuum emission by fitting an elliptical Gaussian model to the visibility data, using the CASA `uvmodelfit` task. This model has six free parameters: integrated flux density ($F_{1.3\mathrm{mm}}$), full width half maximum (hereafter FWHM) along the major axis ($R_{50\%,\,1.3\mathrm{mm}}$), aspect ratio of the axes (r such that Minor axis fwhm = $R_{50\%,\,1.3\mathrm{mm}}\times r$), position angle (PA), right ascension and declination of the phase center. For the sources where the Gaussian model did not converge, we fitted the visibilities with a point source model with only three free parameters (F_{cont}, $\Delta\alpha$, $\Delta\delta$). Table 2 gives the measured 1.3 mm continuum fluxes, major and minor axis, and position angles along with their associated uncertainties. Right ascensions and declinations obtained from the fits are consistent with the SIMBAD coordinates within a few tenths of arcsec.

Out of the 31 sample sources, 24 are detected above a 3σ significance threshold and 14 of them are resolved. Continuum images are presented in Fig 2. In this figure, binaries in the fields of Sz 59 and Hn 24 are visible. We measure a separation of $0.70''$ and PA of -25° for Sz 59 from the continuum fits, which is consistent with the measurement by Geoffray & Monin (2001). In the field of Sz 59, the companions have similar continuum fluxes and sizes. In addition, we discover a new visual binary, as Hn 24 B is not referenced in the literature. From the continuum uv-plane fit, we derive the components' locations (Table 1). We measure a separation of $1.67''$, a PA of 0° and a flux ratio in the continuum of 2. At 1.3 mm, the secondary is unresolved, and smaller than the (resolved) primary.

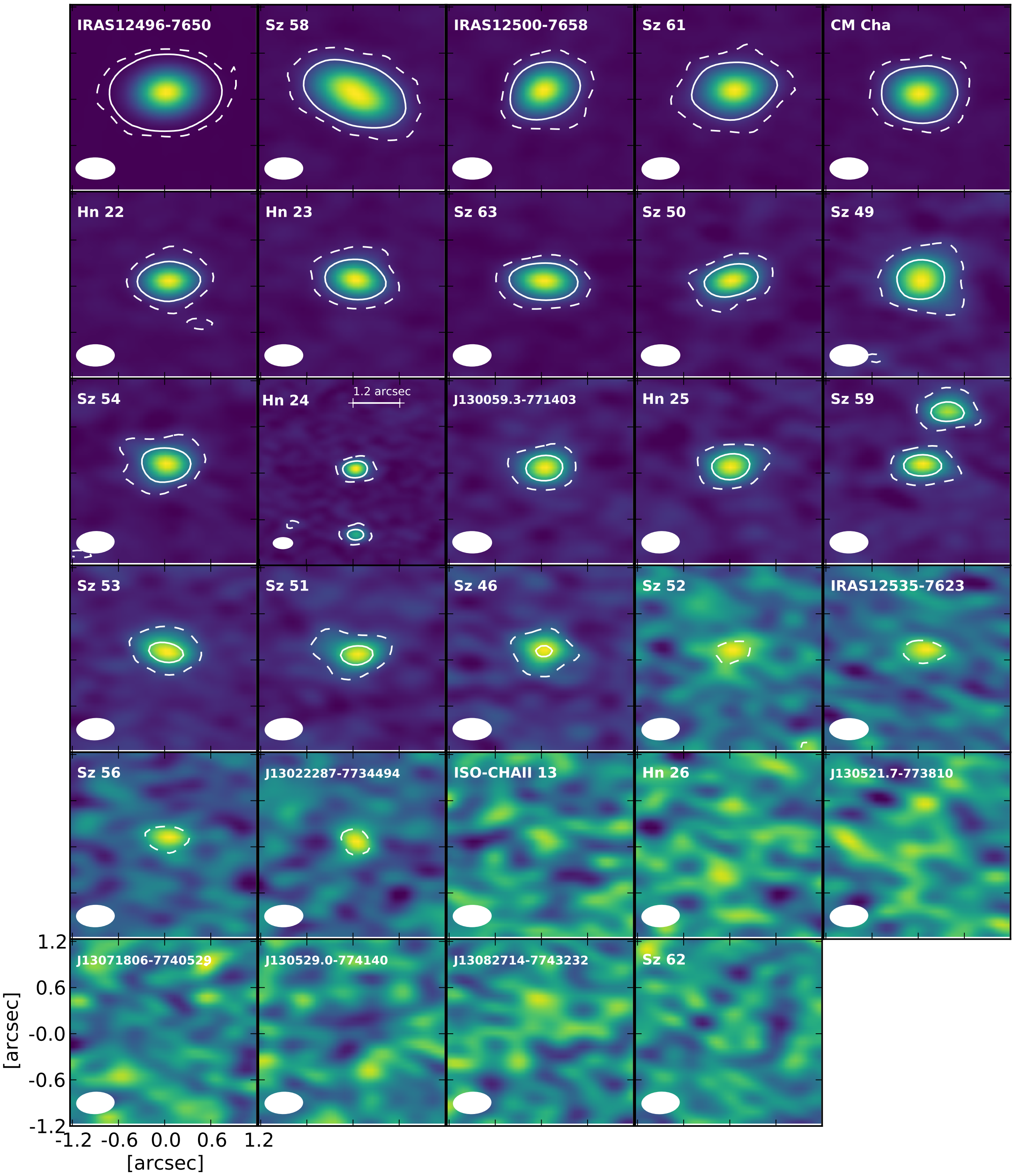

Fig. 2. Continuum images ordered by decreasing fluxes. Images are 2.4″×2.4″ except for Hn 24 where we use 4.8″×4.8″ to show the secondary source. The beam is shown in the lower left corner of each panel. 3 σ and 15 σ contours are shown in dashed and solid lines, respectively. The colormap is chosen to go from from -3 σ to the maximum intensity of each image.

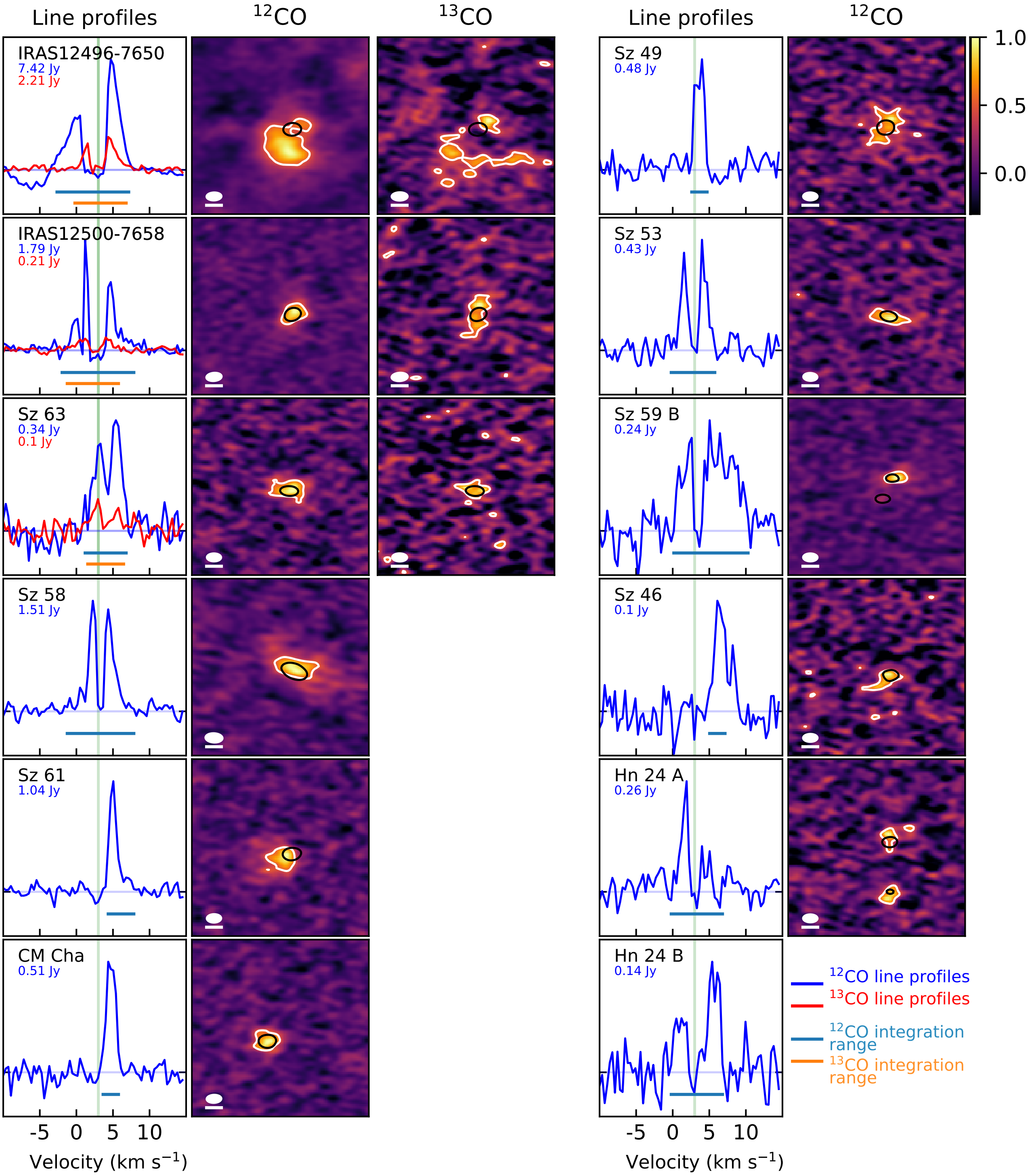

Fig. 3. Line profiles (left panels), ^{12}CO normalized moment 0 maps (middle panels) and ^{13}CO normalized moment 0 maps (right panels) for the sources detected in ^{12}CO. For each source, we display the continuum contours at 50% of the continuum peak (white line) and the CO contours at 50% of the CO peak (black line) on the CO moment 0 maps. The beam size is shown in the bottom left corner of each panel, along with a white line representing a 0.5″scale. On the line profiles plots (left panels), we also show a green vertical line at 3 km s^{-1}, where the cloud absorption is estimated, and the size of the integration range to estimate the ^{12}CO and ^{13}CO fluxes reported in Table 3. The maximum fluxes of each line profile is displayed in the top left side of the panels, colored in blue for ^{12}CO and in red for ^{13}CO.

Table 2. 1.3 mm continuum properties.

Source	$F_{1.3mm}$ (mJy)	$R_{50\%,\,1.3mm}$ (mas)	Minor axis fwhm (mas)	PA (deg)	M_{dust} ($M_{\oplus}$)
J13022287-7734494	0.87 ± 0.15	$<$	$<$		1.84 ± 0.32
J13071806-7740529	< 0.51				< 0.93
J13082714-7743232	< 0.51				< 1.19
CM Cha	38.76 ± 0.23	315 ± 5	315 ± 9	35 ± 57	34.08 ± 0.20
Hn 22	21.81 ± 0.17	175 ± 6	110 ± 12	-51 ± 4	28.47 ± 0.22
Hn 23	20.75 ± 0.19	190 ± 4	190 ± 13	158 ± 57	17.95 ± 0.16
Hn 24 A	10.52 ± 0.19	193 ± 15	193 ± 33	67 ± 57	8.44 ± 0.15
Hn 24 B	5.05 ± 0.16	$<$	$<$		5.85 ± 0.18
Hn 25	5.38 ± 0.18	195 ± 25	$<$		6.21 ± 0.19
Hn 26	< 0.51				< 0.64
IRAS12496-7650	708.60 ± 0.27	354 ± 1	321 ± 1	125 ± 1	247.80 ± 0.09
IRAS12500-7658	49.60 ± 0.26	258 ± 5	258 ± 11	-84 ± 57	266.50 ± 1.40
IRAS12535-7623	1.09 ± 0.18				0.60 ± 0.10
ISO-CHAII 13	< 0.51				< 2.28
J130059.3-771403	5.68 ± 0.19	188 ± 15		4 ± 9	6.57 ± 0.22
J130521.7-773810	< 0.51				< 0.61
J130529.0-774140	< 0.51				< 0.59
Sz 46	3.73 ± 0.20	221 ± 49			4.26 ± 0.23
Sz 49	10.92 ± 0.26	401 ± 14	311 ± 31	-1 ± 7	14.61 ± 0.35
Sz 50	10.96 ± 0.20	169 ± 15	169 ± 33	64 ± 57	5.71 ± 0.19
Sz 51	4.30 ± 0.18	249 ± 33	133 ± 49	-70 ± 10	4.58 ± 0.19
Sz 52	1.16 ± 0.24	461 ± 131			1.72 ± 0.35
Sz 53	4.81 ± 0.20	307 ± 32	168 ± 44	65 ± 8	5.59 ± 0.35
Sz 54	10.54 ± 0.18	586 ± 9	131 ± 28	12 ± 6	7.01 ± 0.12
Sz 56	1.00 ± 0.15				1.09 ± 0.16
Sz 58	60.72 ± 0.30	699 ± 5	347 ± 39	61 ± 1	51.12 ± 0.25
Sz 59 A	4.99 ± 0.16	114 ± 37			4.23 ± 0.13
Sz 59 B	4.29 ± 0.16	97 ± 22			4.98 ± 0.19
Sz 61	41.32 ± 0.23	310 ± 3	310 ± 9	-11 ± 57	33.05 ± 0.17
Sz 62	< 0.51				< 0.65
Sz 63	19.79 ± 0.21	369 ± 9	183 ± 11	83 ± 1	26.56 ± 0.28

Notes. Gaussian (point source) models were fitted in the uv plane for detected (undetected) sources. We report the continuum fluxes ($F_{1.3mm}$), the resolved major and minor axis FWHM (respectively $R_{50\%,\,1.3mm}$ and minor axis fwhm), the position angles (PA) and the estimated dust masses. Some sources are only resolved in the major axis direction, for these sources we do not report any size in the minor axis.

3.2. CO Line Emission

We measure the line fluxes by integrating the line profile over a spectral range which we determined by visual inspection of the channel maps. For the detected sources, the mean line width is ~6.3 km s^{-1}. We represent the line width by horizontal lines at the bottom of each (left) panels of Fig. 3. For the detected sources, the flux error corresponds to the RMS of the line profile integrated over the width of the emission. On the other hand, we report upper limits for the non-detections. They correspond to 3 times the RMS of the line profile, integrated over a line width of 6.3 km s^{-1}. We present the integrated fluxes and uncertainties for the three isotopologues in Table 3. Additionally, we estimate the ^{12}CO emission size of the resolved sources by fitting an elliptical Gaussian to the moment 0 maps. We report the major axis FWHM of ^{12}CO emission ($R_{50\%,^{12}CO}$) in the second to last column of Table 3.

Out of 31 targets observed, 12 are detected in ^{12}CO, 3 in ^{13}CO and none in C^{18}O. All the sources detected in ^{13}CO are also detected in ^{12}CO, and all the sources detected in ^{12}CO are detected in the continuum. Each source detected in a CO isotopologue is also resolved. Hn 24 is the only continuum binary with both components detected in the ^{12}CO line. In contrast with the continuum fluxes, where Hn 24 A and Hn 24 B have a factor of two difference in flux, the ^{12}CO fluxes are similar for both sources. This is expected if the two disks have different dust masses (as indicated by their difference in continuum emission, assuming it is optically thin), but similar sizes and temperatures, that would lead to similar line fluxes in the optically thick ^{12}CO. From the line profiles (Fig. 3), we observe an apparent velocity difference of about 4 km s^{-1}, not inconsistent with them being a bound binary.

However, we caution for the presence of significant foreground absorption for all sources. From the moment 0 maps displayed in Fig. 3, we see that for some sources the line emission is not centered on the continuum (e.g., Sz 61), which suggests that we are missing part of the emission for each of them. Furthermore, some line profiles are also asymmetric (e.g., CM Cha) and/or have minima (absorption) that go down to the continuum level (e.g., IRAS12500-7658). This is not compatible with a Keplerian profile without absorption. The large cloud absorption is located around 3 km s^{-1} (green line on Fig. 3). It is compatible with Mizuno et al. (2001) study, which gave estimations of $+2.9 \pm 2.8$ km s^{-1}. Thus, even for the detected sources, the CO fluxes and sizes are likely lower limits only.

Table 3. Integrated fluxes for the CO isotopologues derived from the line profiles and ^{12}CO size of the detected sources.

Source	$F_{^{12}CO}$ (Jy km s^{-1})	$F_{^{13}CO}$ (Jy km s^{-1})	$F_{C^{18}O}$ (Jy km s^{-1})	$R_{50\%,^{12}CO}$ (mas)	$R_{50\%,^{12}CO}$ / $R_{50\%,\,1.3mm}$
J13022287-7734494	< 0.14	< 0.14	< 0.12		
J13071806-7740529	< 0.15	< 0.14	< 0.10		
J13082714-7743232	< 0.11	< 0.16	< 0.10		
CM Cha	0.67 ± 0.04	< 0.19	< 0.09	680 ± 100	2.2 ± 0.3
Hn 22	< 0.13	< 0.15	< 0.10		
Hn 23	< 0.13	< 0.14	< 0.10		
Hn 24 A	0.35 ± 0.04	< 0.15	< 0.11	540 ± 160	2.8 ± 0.9
Hn 24 B	0.33 ± 0.04	< 0.15	< 0.11	950 ± 400	
Hn 25	< 0.15	< 0.14	< 0.11		
Hn 26	< 0.13	< 0.13	< 0.12		
IRAS12496-7650	20.58 ± 1.66	5.26 ± 0.33	< 0.16	1520 ± 110	4.3 ± 0.3
IRAS12500-7658	2.93 ± 0.22	0.60 ± 0.06	< 0.14	840 ± 100	3.3 ± 0.4
IRAS12535-7623	< 0.15	< 0.15	< 0.10		
ISO-CHAII 13	< 0.14	< 0.15	< 0.09		
J130059.3-771403	< 0.15	< 0.16	< 0.11		
J130521.7-773810	< 0.16	< 0.14	< 0.10		
J130529.0-774140	< 0.13	< 0.14	< 0.11		
Sz 46	0.12 ± 0.01	< 0.13	< 0.11	1020 ± 270	4.6 ± 1.6
Sz 49	0.61 ± 0.04	< 0.17	< 0.10	1360 ± 280	3.4 ± 0.7
Sz 50	< 0.17	< 0.17	< 0.13		
Sz 51	< 0.14	< 0.15	< 0.09		
Sz 52	< 0.13	< 0.16	< 0.12		
Sz 53	0.84 ± 0.06	< 0.15	< 0.10	1370 ± 220	4.5 ± 0.9
Sz 54	< 0.14	< 0.12	< 0.11		
Sz 56	< 0.11	< 0.13	< 0.09		
Sz 58	4.01 ± 0.24	< 0.15	< 0.11	1990 ± 220	2.8 ± 0.3
Sz 59 A	< 0.16	< 0.14	< 0.11		
Sz 59 B	1.14 ± 0.09	< 0.14	< 0.11	780 ± 130	8.0 ± 2.3
Sz 61	1.31 ± 0.08	< 0.16	< 0.11	1020 ± 150	3.3 ± 0.5
Sz 62	< 0.14	< 0.14	< 0.11		
Sz 63	1.04 ± 0.07	0.21 ± 0.03	< 0.12	1190 ± 150	3.2 ± 0.4

1

4. Disk sizes and masses

4.1. Continuum vs CO sizes

Measuring and comparing disk sizes as seen in dust and gas tracers is particularly important to constrain evolutionary mechanisms. In Section 3.1 and Section 3.2, we estimated the major axis sizes (FWHM) of the continuum and ^{12}CO emission line. Those are reported in Table 2 and Table 3. Additionally, we present the gas to continuum size ratio in the last column of Table 3. We find that the ^{12}CO emission is systematically larger than its continuum counterpart, with a median size ratio of 3.3.

Before discussing the implications of these results, we note that the sizes were measured by fitting an elliptical Gaussian to each source, respectively in the uv-plane for the continuum and in the image plane for the gas, which might lead to systematic differences in the size estimation. To quantify the impact of using different measurement methods, we compared the size estimates obtained using Gaussian fits either in the image- or in the uv-plane for 10 objects. We calculated a mean discrepancy ratio for the major axis sizes of ~1.1 between the two techniques, the image plane estimation, deconvolved from the beam, giving larger values than those found in the uv-plane. However, the CO to continuum size ratios estimated in this work (see Table 3) are significantly larger than this size difference. This implies that the differences measured are not an artifact of the measurement method.

Previous studies have reported similarly large size differences between gas and continuum measurements, both for individual Herbig AeBe and for T Tauri stars (e.g., Facchini et al. 2019; van der Plas et al. 2017). It can have several explanations. Indeed, the ^{12}CO emission is optically thick while the dust continuum is optically thinner, making the CO disk easier to detect at large distances even is the solids are distributed as far outside as the gas (e.g., Woitke et al. 2016). Additionally, protoplanetary disks are also accreting onto the central star and angular momentum conservation implies that beyond a certain radius, the gas disk has to expand outward. Conversely, millimeter-sized grains can drift inward rapidly, making the continuum disk look smaller, with a sharp outer edge at millimeter wavelengths.

Using thermochemical models, Trapman et al. (2019) find that a ratio $R_{90\%,^{12}CO}/R_{90\%,\,1.3mm} \geq 4$ requires dust evolution and radial drift. In this study, we compare the FWHM of the gas with that of the continuum rather than the radius which encompass 90% of the flux of both tracers as in done by Trapman et al. (2019). When applying their results to our Cha II sample, we find that grain growth and radial drift are needed to reproduce the high values of gas to dust size ratio observed in several disks. Additionally, we observe that the average size difference is lower in the 2 ± 1 Myr old Lupus star-forming region (Ansdell et al. 2018) than in the 4 ± 2 Myr old Cha II. Indeed, Ansdell et al. (2018) estimate an average gas to dust size ratio of about 2 for 22 disks in the younger Lupus star-forming region (2 ± 1 Myr). This is consistent with disk evolution. The millimeter dust grains

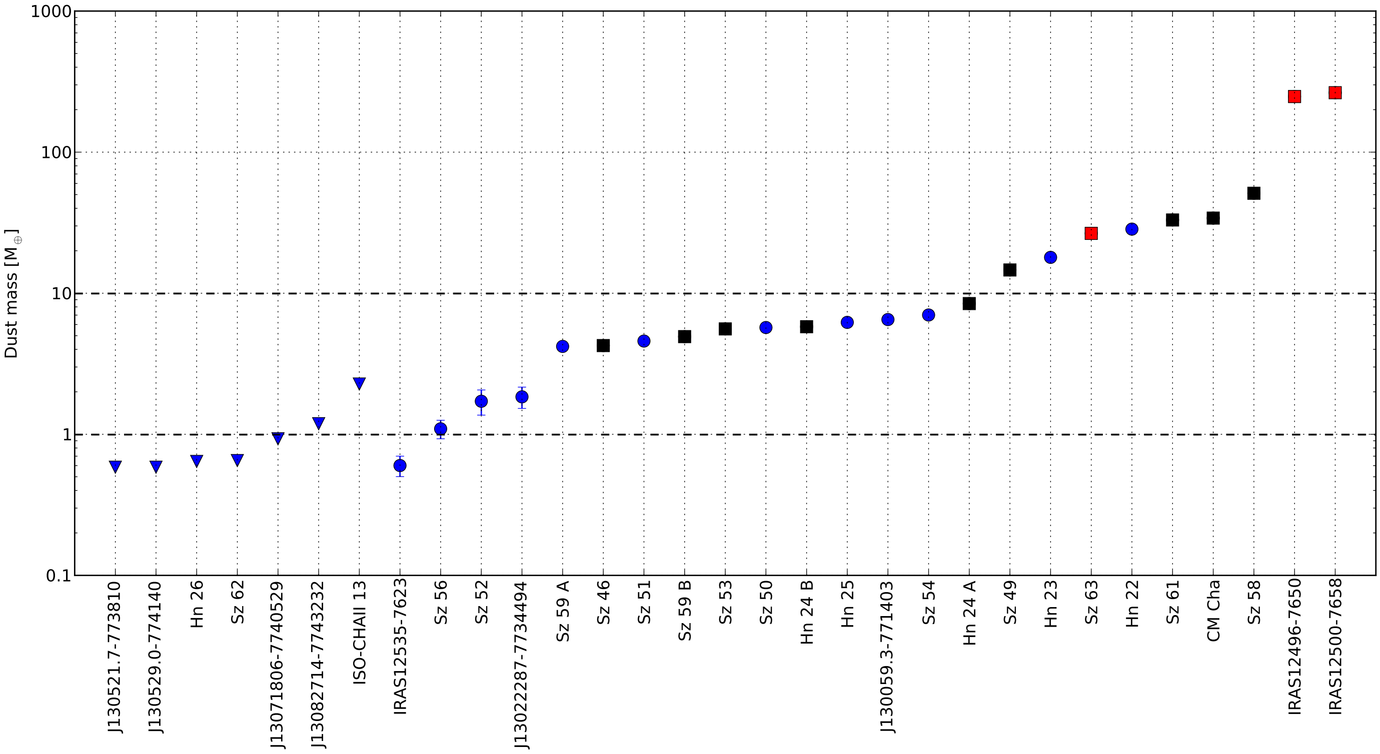

Fig. 4. Dust masses for the 31 sources in our Cha II sample expressed in Earth masses, ordered by increasing dust mass (Table 2). Black and red squares correspond to ^{12}CO and ^{13}CO detected sources, respectively. Round symbols show continuum only detected sources and the downward-facing triangles correspond to 3 σ upper limits for non detections.

are expected to drift inward with time while the gas spread to larger radius, which leads to an increase of $R_{^{12}CO}/R_{1.3mm}$ with time.

4.2. Dust Masses

Assuming that the continuum emission is optically thin at 1.3 mm, it is possible to infer the disk dust mass (M_{dust}) from the continuum millimetric flux (F_ν) at a given wavelength (e.g., Hildebrand 1983):

$$M_{\rm dust} = \frac{F_\nu d^2}{\kappa_\nu B_\nu(T_{\rm dust})} \quad (1)$$

We take a grain opacity κ_ν of 2.3 cm^2.g^{-1} at 230 GHz (Beckwith et al. 1990), with $\kappa_\nu \propto \nu^{0.4}$ (as other studies and consistently with recent integrated spectral index measurements Andrews et al. 2013; Ribas et al. 2017). We use individual distances from *Gaia DR2* (Gaia Collaboration et al. 2018) for sources that have an error on the distance smaller than 15 pc. When the error is larger than 15 pc, we adopt the weighted mean distance of the well characterized objects: 198 pc (Dzib et al. 2018). We adopt the relationship of T_{dust} with $L_\star$ from Andrews et al. (2013), inferred with a grid of radiative transfer models: $T_{dust} = 25K\,(L_\star/L_\odot)^{1/4}$. We used the luminosities determined by Spezzi et al. (2008), rescaled to the Gaia DR2 distances. For the sources that were not characterized spectrally, we applied a characteristic dust temperature of $T_{dust} = 20$ K, the median temperature for Taurus disks (Andrews & Williams 2005). Fig. 4 shows the detections and upper limits of our dust mass estimates. The values are given in Table 2. They range from ~0.6 (IRAS12535-7623) to ~266.5 $M_\oplus$ (IRAS12500-7658). We note however, that the scaling relation between T_{dust} and $L_\star$ was calibrated for luminosities larger than 0.1 $L_\odot$. In our sample, 5 objects have luminosities smaller than this value, including IRAS12500-7658 and ISO-CHAII 13 that have luminosities close to 0.01 $L_\odot$. For these two sources, the estimation of the mass is probably overestimated by a factor ~2 (van der Plas et al. 2017).

5. Discussion - Comparison with other regions

5.1. Luminosity functions

Over the last years, observations of nearby star-forming regions have shown a tendency for disk dust mass to decrease with age, which can be a sign for disk dissipation (e.g., Ansdell et al. 2016). This evidence was mostly driven by the comparison of young star-forming regions (1 – 3 Myr, e.g., Lupus) with the older Upper Sco (5-10 Myr) but a small number studied intermediately aged regions (e.g., Ansdell et al. 2017). In this section, we expand the study of cumulative dust mass distribution to the intermediately aged 4±2 Myr Cha II star-forming region, aiming to add constraints on the evolution of dust mass with time.

Additionally, these studies revealed a correlation between M_{dust} and $M_\star$ (e.g., Andrews et al. 2013; Pascucci et al. 2016). Although this relation might evolve with time, when assuming a dust temperature scaling with luminosity in Eq. (1), they showed that the dust mass is about proportional to the stellar mass[2]: $M_{dust} \propto M_\star$. Because of this relation, lower stellar masses are expected to lead to lower dust masses. Then, comparing the dust mass distributions of star-forming regions with different stellar

---

[2] When taking a constant $T_{dust} = 20$ K, those studies usually find $M_{dust} \propto M_\star^2$ (e.g., Ansdell et al. 2017).

mass distributions might lead to inadequate conclusions. In this context, our analysis consists in comparing millimeter luminosity functions, i.e., cumulative disk dust mass distributions, as well as dust-to-stellar mass ratio distributions for different star-forming regions. Using this ratio allows us to reduce the impact of potentially different $M_\star$ distributions and, to the first order, to study the evolution of $M_{\rm dust}$ with $M_\star$ as a function of time.

Methods. In this analysis, we consider 7 star-forming regions observed at millimeter wavelengths, and for which stellar masses can be well estimated. Those are Upper Sco (Barenfeld et al. 2016), Cha II (this study), IC 348 (Ruíz-Rodríguez et al. 2018), Cha I (Pascucci et al. 2016), Lupus (both band 7 and band 6 surveys, Ansdell et al. 2016, 2018) and Taurus (Andrews et al. 2013). We show the main characteristics of all regions (age, average distance, observed frequency and smallest detected dust mass) in Table 4. We note that because objects of different SED classes are most likely in a different evolutionary stage, we selected only the Class II objects from all studies. For Upper Sco, they are the objects classified as 'Full', 'Transitional' and 'Evolved' in Table 1 of Barenfeld et al. (2016). We note that we did not include several millimeter surveys in this analysis, either because lack of stellar masses (e.g., σ-Orionis, Ophiuchus or OMC-2, respectively in Ansdell et al. 2017; Cieza et al. 2018; van Terwisga et al. 2019), or because not all Class II of the region were observed (e.g., Serpens, CrA, Law et al. 2017; Cazzoletti et al. 2019). For example, we note that analysing Gaia DR2 data, Galli et al. (2020) identified 28 new Class II were identified since the ALMA survey of CrA (probing 43 Class II sources, Cazzoletti et al. 2019).

In order to provide a meaningful comparison of all regions, we recalculated both the dust and stellar masses in a coherent and homogeneous manner. Additionally, we use individual stellar distances for the first time. Whenever errors are smaller than 15 pc, we assign the latest distance of the source from the *Gaia DR2* catalog (Gaia Collaboration et al. 2018), while for sources with larger errors or that are not in the catalog, we used the weighted averaged distance of the association (see Table 4).

We determine stellar masses using isochrones from Baraffe et al. (2015), in the range 0.5 to 50 Myr. The tracks were interpolated to probe the mass range from 0.05 to 1.4 $M_\odot$, by steps of 0.01 $M_\odot$. We adopt the Bayesian method described in Andrews et al. (2013) and Pascucci et al. (2016) to assign a stellar mass and an age by minimizing a likelihood function. The assumed uncertainties in $\log(L_\star/L_\odot)$ and $\log(T_\star)$ are 0.1 and 0.02 respectively, which correspond to the upper values for uncertainties in Spezzi et al. (2008). We use stellar luminosities and temperatures from Andrews et al. (2013), Alcala et al. (2017), Manara et al. (2017) and Luhman (2007), Ruíz-Rodríguez et al. (2018) and Barenfeld et al. (2016) for Taurus, Lupus, Cha I,, IC 348 and Upper Sco respectively. We note that, before estimating the stellar masses, we rescaled the luminosities to each individual stellar distance.

We also recalculated dust masses in an homogeneous way from millimeter or sub-millimetre fluxes using Eq. (1) from Sect. 4.2. We use the same temperature-luminosity relation and grain opacity as previously, and adopt the most recent distances. We note that that using the simplifying assumption of $T_{\rm dust}$ = 20 K does not change the statistical results presented in this section. Also, it should be noticed that our analysis includes surveys of star-forming regions observed at different frequencies (see Table 4).

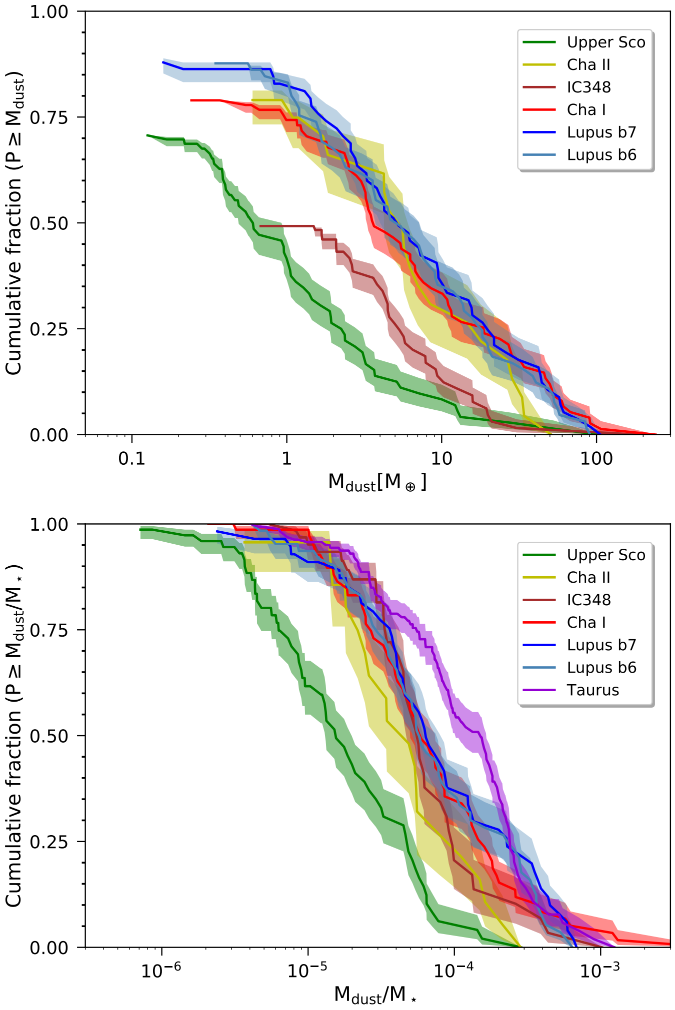

Fig. 5. Top: Cumulative distribution of the dust mass, generated by the Kaplan-Meier estimator and normalized by the fraction of detected sources in each star-forming regions. Bottom: Cumulative distribution of the dust to stellar mass ratio generated by the Kaplan-Meier estimator. We indicate 1σ confidence intervals.

Because most of the samples used are only complete down to the brown dwarf limit, we considered only stars with derived masses above 0.1 $M_\odot$. Moreover, as Baraffe et al. (2015) tracks stop at $M_\star$=1.4 $M_\odot$, we decided not to include stars where the fit of isochrone produces this value. We present the number of sources considered in this study in Table 4, along with the number of detected sources. All regions show comparable stellar mass distributions, except IC 348 which contain no stars between 0.9 and 1.4 $M_\odot$.

Cumulative distributions. In order to compare all star-forming regions together, we generate two families of cumulative distributions. We used the Kaplan-Meier estimator in the `lifelines` package in Python[3], which takes into account upper limits and was used in previous studies (e.g., Ansdell et al. 2016; Law et al. 2017).

First, as in previous studies, we estimate the cumulative distributions of $M_{\rm dust}$. They are shown in the top panel of Fig. 5, and scaled so that the maximum of each distribution corresponds to the fraction of detected sources in each sample. We find that most

---

[3] See documentation at http://lifelines.readthedocs.io/

Table 4. Parameters of star-forming regions.

Region	Published age (Myr)	Distance (pc)	Obs freq (GHz)	$M_{\rm dust,min}$ ($M_\odot$)	Detections/ Total sources	Median $M_{\rm dust}$ ($M_\oplus$)	Median $M_{\rm dust}/M_\star$ (10^{-5})
Upper Sco	5 – $11^{1,2}$	145 ± 10	341.1	0.17	53/75	0.6 ± 0.2	1.6 ± 0.3
Cha II	2 – 6^{3}	198 ± 6^{9}	225.7	0.60	19/23	5.6 ± 1.0	4.9 ± 1.4
IC 348	2 – 3^{4}	310 ± 20^{10}	225.7	0.52	33/67	∼ 1.5	5.4 ± 0.7
Cha I	2 – $4^{5,6}$	192 ± 6^{9}	338.0	0.54	60/76	3.5 ± 1.0	5.9 ± 1.2
Lupus	1 – 3^{7}	160 ± $4^{9,*}$	335.8	0.16	51/57	5.3 ± 1.6	6.4 ± 1.4
Lupus			225.5	0.60	62/66	5.4 ± 1.7	5.8 ± 1.1
Taurus	1 – 2^{8}	141 ± 7^{11}	225.0	1.08	92/164	3.3 ± 0.8	15.2 ± 3.1

Notes. Sensitivity limits correspond to the reported rms for each study scaled to the distance of Cha II. In Cha I and Lupus, samples were separated in two subsamples leading to two values for the rms. For Taurus, we report the range of rms values presented in the original study. In the third column, we show the mean distance of each region.

References. 1/ Pecaut et al. (2012), 2/ Herczeg & Hillenbrand (2015), 3/ Spezzi et al. (2008), 4/ Ruíz-Rodríguez et al. (2018), 5/ Pascucci et al. (2016), 6/ Luhman (2007), 7/ Ansdell et al. (2016), 8/ Andrews et al. (2013), 9/ Dzib et al. (2018) 10/ Ortiz Leon 2018, (*): we used the average distance of the lupus cloud for the least characterized sources 11/ Zucker, Speagle, Schafly 2019

distributions, including that of Cha II, have similar medians and shapes, but Upper Sco and IC 348 show a noticeable difference compared with the others, with median dust masses about an order of magnitude smaller than in other regions (see before last column of Table 4). This might be related to different effects such as differences in stellar populations with other regions (e.g., no stars between 0.9 and 1.4 $M_\odot$ in IC 348) or to the scaling factor used for the $M_{\rm dust}$ distribution, which might have to be modified if the samples are found not to be complete.For comparison, we note that the median mass of the Class II objects studied in this work is found to be at least a factor of 5 smaller than masses of Class 0 and Class I objects in Orion star-forming region, as can be seen in Figure 15 of Tobin et al. (2020). This suggests that Class II objects have evolved and lost dust mass since the first stages of their evolution.

Additionally, in order to limit the effect of different stellar population, we estimate cumulative distributions of dust-to-stellar mass ratio, which are shown in the bottom panel of Fig. 5. As highlighted by the position of the 25%, 50% and 75% levels, we find that most regions appear to have similar shapes. Only Taurus shows a different shape than in the plot of $M_{\rm dust}$, breaking away from the other curves, mostly because a large fraction of the non-detections are around low mass stars, which correspond to a large $M_{\rm dust}/M_\star$ ratio. Additionally, except for CrA which is likely a young region, we find that the distributions appear shifted to progressively lower mass ratios as the age of the region increases (see median ratio in Table 4). In the following subsection, we aim to estimate statistically whether all distributions of $M_{\rm dust}/M_\star$ are similar or not, looking for a potential evolutionary trend.

Statistical test. The observed ranking of the disk-to-star mass ratios is suggestive of an evolution of the disk properties with time. To test the significance of the observed shift in the mass ratio functions, we performed a statistical test on all star-forming regions. We use the logrank test, a non parametric method that compares the survival distributions of two samples, taking into account non-detections. The null hypothesis is that distributions of all regions are equal at all mass ratio. We performed one-by-one comparisons, and present them in Table 5. P-values are shown in the bottom-left part of the table, while their interpretations are shown in the top-right side of the table. Regions that are statistically distinct (i.e., with P-values ≤ 0.001) are characterized by the symbol '***'. The symbols '**' and '*' are used for P-values between 0.001-0.05 and 0.05-0.1 corresponding to regions that are gradually less statistically different. Regions that are statistically indistinguishable (P-values > 0.1) are shown by the symbol '-'.

Using the $M_{\rm dust}/M_\star$ ratio, we find that Upper Sco is statistically different from all other star-forming regions. Taurus is also statistically different from Cha II and marginally from IC 348 and Cha I. Although we see a progressive decline of the median of ratio with increasing age, these shifts are not significant at the 3σ level when the age difference is too small (≤ factor of 2). Larger samples would be needed to confirm the observed trend. However, when larger time baselines are considered (≥ factor of 3), the evolution of the luminosity function becomes significant. This result strongly suggests the fact that disks evolve gradually with time, with a decrease of the relative mass of their millimetric dust grains compared with the star. This could be explained by accretion of those grains on the central star, formation into planets, or because, as grains grow bigger with time, a decrease in the millimeter wavelength opacity. The lack of 3-sigma significance for small age differences may be corrected when more sensitive surveys are performed, larger samples are observed, or more accurate ages are available.

In parallel to the decrease of the median dust-to-stellar mass ratio with time (Table 4), a change in the detected disk fraction is observed in IR studies (Ribas et al. 2014). This indicates that not only the number of disks detected is declining with time, but also that the remaining disks have a lower mass. The global dust content of the disk seems to decrease with time.

Possible limitations

Binary systems were no filtered out from the samples, all more so for unresolved binaries. However, binary systems have been shown to disperse their disk faster than single star systems (Cieza et al. 2009). Studying binaries in Taurus, Kraus et al. (2012) showed that this is particularly true for close binaries, with separations smaller than 40 au. At larger separation, disks around binaries are detected with similar occurrence than around single stars. In Ophiuchus, Cox et al. (2017) showed that the median flux around binaries is systematically 60% the flux around single stars. In this study, we found that 5%, 12.5%, 40%, 10% and 32% of the sources used in the respective distributions of Upper Sco, Cha II, Cha I, Lupus and Taurus are known as binaries

Table 5. Results of pair comparisons with the logrank test applied on the ratio $M_{dust}/M_\star$.

	Upper Sco	Cha II	IC348	Cha I	Lupus B7	Lupus B6	Taurus
Upper Sco		**	***	***	***	***	***
Cha II	0.01		-	-	**	*	***
IC348	9e-7	0.3		-	-	-	**
Cha I	< 1e-7	0.2	0.6		-	-	**
Lupus B7	< 1e-7	0.04	0.5	0.8		-	-
Lupus B6	< 1e-7	0.06	0.8	0.9	0.4		*
Taurus	< 1e-7	3e-4	0.02	0.04	0.2	0.07	

Notes. The lower left half of the table represents P-values for pairs comparisons, and the upper right half corresponds to the interpretation of the test. A P-value lower than 0.001 (***) corresponds to regions statistically distinct, P-values higher than 0.1 (-) to regions statistically similar, and P-values between 0.001 and 0.05 (**), and between 0.05 and 0.1 (*) to regions that are marginally different.

stars. Only one disk (non-detected) of IC 348 is a binary, of separation larger that 80 au (Ruíz-Rodríguez et al. 2018). However, a very limited fraction are known close binaries (r < 40 au): less than 1% of the considered stars in Upper Sco, Cha II and Lupus, and ~ 8% in Cha I and Taurus. Therefore, binaries are not expected to modify the distributions significantly.

Comparison between inhomogenous samples requires care. Here, all samples were observed with close but yet different sensitivities. The cumulative distributions were generated using the Kaplan-Meier estimator that considers the upper limits of non-detections. In Appendix A, we performed the analysis considering this time that each distribution had a similar disk mass detection limit. The results are similar to those presented above in this section. Thus, by re-observing the same samples with higher sensitivities, and possibly with an homogeneous angular resolution, we do not expect significant changes in the results, in particular in that of M_{dust}.

To convert the observed fluxes into dust masses, we also assumed that disks were always optically thin. This assumption should be generally verified given the observed fluxes. We also used a scaling relation between T_{dust} and $L_\star$ in the conversion process. This relationship was proposed and tested by Andrews et al. (2013) using radiative transfer models with a fixed outer radius (r_{out} = 200 au) and for a range of luminosity between 0.1 and 100 $L_\odot$. Using this equation for smaller disks or less luminous stars is expected to lead to overestimations of the dust mass (see van der Plas et al. 2016). However, we find that average disk outer radii and the fraction of sources with lower luminosity are about similar in each study, which should affect all distributions in a similar way. To ease the comparison with other studies, we have used the prescription from Andrews et al. (2013) throughout.

Finally, the interpretation of the distribution functions presented here relies on the age of each individual region based on previous studies, in most cases anterior to Gaia. The Gaia DR2 data release now provides individual distances for most stars. Although we have used the new distances to re-evaluate the stellar luminosities (and therefore masses) for each star, we have not re-assessed the age of each association. Additionally, the cumulative mass ratio distribution function is probably also affected by the stellar environment. Thus, we have not included regions like Sigma Orionis.

5.2. Gas detection rates

The above subsection only applies to the evolution of dust mass, which we probe with continuum emission. However the disk mass is dominated by gas. Measuring the gas mass in protoplanetary disks is notably difficult (see for example Williams & Best 2014; Kamp et al. 2011). Instead, here we will focus on the gas detection rates with the aim of comparing the respective detection rates of CO gas and dust continuum from disks of different ages. To do so, we gathered ALMA and SMA millimetric measurements to characterize the cold disk regions (continuum and CO isotopologues rotational lines), in the same regions as in the previous section. Samples are complete in the sense of ALMA capability in snapshot surveys, except for Taurus star-forming region where only a limited number of sources was observed (only in ^{13}CO) using IRAM interferometer, leading to an incomplete survey.

Table 6. Detection rates of CO isotopologues for sources detected in dust, ordered by decreasing age of the system separated accordingly to the transition observed.

	Transition	^{12}CO (%)	^{13}CO (%)	C^{18}O (%)
Upper Sco[1]	3-2	47		
Cha I[2,3]	3-2	> 26	26	2
Lupus[4]	3-2	> 58	58	18
Cha II	2-1	52	9	0
Lupus[5]	2-1	68	28	11
Taurus[6,7]	2-1	> 89	89	

Notes. According to the isotopologue ratio, we expect to detect more sources in ^{12}CO than in ^{13}CO. This is indicated through lower limits in Cha I, Lupus and Taurus, where no ^{12}CO study are available. The Taurus survey in ^{13}CO is also not complete.

References. 1/ Barenfeld et al. (2016), 2/ Pascucci et al. (2016), 3/ Long et al. (2017), 4/ Ansdell et al. (2016), 5/ Ansdell et al. (2018), 6/Andrews et al. (2013), 7/ Guilloteau et al. (2013)

In order to compare the different star-forming regions with each other, we selected subsamples of disks with similar spectral type distributions (K & M stars). This made necessary to remove the F0 disk (IRAS12496-7650) from our Cha II study. Then, only stars with disks detected in cold dust are considered, so that we compare gas detections in systems that posses a dusty disk with comparable mass limit.

Table 6 shows the detection rates CO isotopologues for dusty disks in star-forming regions of different ages. For the two transitions traced, in the three probed isotopologues, a larger fraction of disks is detected in young regions than in older ones. This indicates that for young star-forming regions most of the disks that are detected in dust are also detected in ^{12}CO-^{13}CO, while for older regions the fraction of targets with detected dust and gas is lower. This decrease in detection rates from younger to older regions shows that CO emission is reduced with time. Moreover, as all of our targets are selected to be detected in dust with a similar mass limit, the apparent decrease of gas detection fraction suggests that CO dissipates faster than dust. This would imply either a decreasing gas to dust ratio or a decreasing abundance of these species, for example by change of state from gas to ice or by photo-dissociation as the ^{12}CO becomes progressively optically thinner and less self-shielded. The small size of our samples and the fact that surveys were likely not performed with the exact same setup prevent from drawing definitive conclusions but the tentative evidence for a different evolutionary timescale for gas versus dust has potential interesting consequences.

Compiling results from *Herschel* Space Observatory using the [OI] 63 μm line, on disks detected in dust in Upper Sco, Cha II and Taurus (Mathews et al. 2013; Riviere-Marichalar et al. 2015; Howard et al. 2013), we find a similar trend. Gas in disks located in young regions is more often detected (91% in Taurus) that for disks in older regions (43% in Cha II and 17% in Upper Sco). In the context of photoevaporation models (e.g., Owen et al. 2011; Alexander et al. 2014), individual disks are thought to dissipate slowly in the first million years, while a photoevaporative flow removes gas from the disk. In this scenario, dust is not affected by the photoevaporative flow. This could explain our observations, where, as the age of the region increases, fewer of the disks detectable in dust are detectable in gas.

6. Conclusions

We have used ALMA to conduct a high-sensitivity millimetric survey of 31 protoplanetary disks in the Cha II star-forming region. This region is particularly interesting to study disk evolution as its intermediate age of 4 ± 2 Myr is comparable to the median disk lifetime.

1. Our ALMA observations cover the 1.3 mm continuum as well as the ^{12}CO, ^{13}CO and C^{18}O $J = 2-1$ lines. Out of 31 sources, 24 were detected in the continuum, 12 were detected in ^{12}CO, 3 in ^{13}CO and none in C^{18}O. Measured dust masses ranged from 270 down to 0.6 $M_\oplus$.
2. CO disk sizes are found to be on average more than 3 times larger than 1.3 mm continuum disk sizes. This can not be explained by optical depth effect only: grain growth and radial drift are needed to reproduce such difference in size.
3. A comparison of cumulative distributions between Cha II and 5 other star-forming regions shows that the dust mass to stellar mass ratio declines with time.
4. We suggest a steady evolution with age. This trend is statistically significant when the age difference is large. However, the ranking of the disk to stellar mass ratio distribution also holds for associations with small age differences. The correct ranking of the 6 distributions (or of their medians) is suggestive of a global evolutionary trend, although the significance between 2 adjacent curves remains at a statistical level $< 3\sigma$ for now. Further surveys will clarify that claim.
5. For disks detected in dust in five star-forming regions, we compared gas detection rates. We find that gas is less likely to be detected in older regions than in younger ones. This suggests that either gas dissipates faster than dust, or that disks have a reduced gas to dust ratio (or CO abundance) when their age increases. However, the limited sample size and observational setups prevent us to draw definitive conclusions.

Acknowledgements. This paper makes use of the following ALMA data: ADS/JAO.ALMA#2013.1.00708.S. ALMA is a partnership of ESO (representing its member states), NSF (USA), and NINS (Japan), together with NRC (Canada), NSC and ASIAA (Taiwan), and KASI (Republic of Korea), in cooperation with the Republic of Chile. The Joint ALMA Observatory is operated by ESO, AUI/NRAO, and NAOJ. The National Radio Astronomy Observatory is a facility of the National Science Foundation operated under cooperative agreement by Associated Universities, Inc. CC acknowledges support from project CONICYT PAI/Concurso Nacional Insercion en la Academia, convocatoria 2015, folio 79150049, and support from ICM Núcleo Milenio de Formación Planetaria, NPF. The National Radio Astronomy Observatory is a facility of the National Science Foundation operated under cooperative agreement by Associated Universities, Inc. L.C. acknowledges support from CONICYT FONDECYT grant 1171246. MV, FM, MB and GvdP acknowledge funding from ANR of France under contract number ANR-16-CE31-0013 (Planet Forming Disks). CP acknowledges funding from the Australian Research Council via FT170100040 and DP180104235.

References

Alcala, J. M., Manara, C. F., Natta, A., et al. 2017, A&A, 600, A20
Alexander, R., Pascucci, I., Andrews, S., Armitage, P., & Cieza, L. 2014, Protostars and Protoplanets VI, 475
Andrews, S. & Williams, J. P. 2005, ApJ
Andrews, S. M., Rosenfeld, K. A., Kraus, A. L., & Wilner, D. J. 2013, AJ, 771
Ansdell, M., Williams, J. P., Manara, C. F., et al. 2017, AJ, 153
Ansdell, M., Williams, J. P., Trapman, L., et al. 2018, ApJ
Ansdell, M., Williams, J. P., van der Marel, N., et al. 2016, AJ, 828
Baraffe, I., Homeier, D., Allard, F., & Chabrier, G. 2015, A&A, 577, A42
Barenfeld, S. A., Carpenter, J. M., Ricci, L., & Isella, A. 2016, AJ, 827
Beckwith, S., Sargent, A. I., Chini, R., & Gusten, R. 1990, ApJ, 99
Borucki, W. J., Koch, D., Basri, G., & Team, K. S. 2010, Nat
Cazzoletti, P., Manara, C. F., Baobab Liu, H., et al. 2019, A&A, 626, A11
Cieza, L. A., Padgett, D. L., Allen, L. E., et al. 2009, ApJ, 696, L84
Cieza, L. A., Ruíz-Rodríguez, D., Hales, A., et al. 2018, MNRAS, 2538
Correia, S., Zinnecker, H., Ratzka, T., & Sterzik, M. 2006, A&A, 459, 909
Cox, E. G., Harris, R. J., Looney, L. W., et al. 2017, ApJ
Dawson, R. I., Murray-Clay, R. A., & Johnson, J. A. 2014, ApJ, 798, 66
Dzib, S. A., Loinard, L., Ortiz-León, G. N., Rodríguez, L. F., & Galli, P. A. B. 2018, ApJ, 867, 151
Facchini, S., van Dishoeck, E. F., Manara, C. F., et al. 2019, A&A, 626, L2
Gaia Collaboration, Brown, A. G. A., Vallenari, A., et al. 2018, A&A
Galli, P. A. B., Bouy, H., Olivares, J., et al. 2020, A&A, 634, A98
Geoffray, H. & Monin, J.-L. 2001, A&A, 369
Guilloteau, S., Folco, E. D., Dutrey, A., et al. 2013, A&A, 549
Herczeg, G. J. & Hillenbrand, L. A. 2015, 808, 23
Hildebrand, R. H. 1983, QJRAS
Howard, A. W., Marcy, G. W., Johnson, J. A., et al. 2010, Sci
Howard, C. D., Sandell, G., D.Vacca, W., et al. 2013, AJ, 776
Kamp, I., Woitke, P., Pinte, C., et al. 2011, A&A, 532
Kraus, A. L., Ireland, M. J., Hillenbrand, L. A., & Martinache, F. 2012, ApJ, 745, 19
Law, C. J., Ricci, L., Andrews, S. M., Wilner, D. J., & Qi, C. 2017, AJ
Long, F., Herczeg, G. J., Pascucci, I., et al. 2017, ApJ, 844, 99
Luhman, K. L. 2007, ApJ SS, 173, 104
Mamajek, E. E. 2009, in American Institute of Physics Conference Series, ed. T. Usuda, M. Tamura, & M. Ishii, Vol. 1158, 3–10
Manara, C. F., Testi, L., Herczeg, G. J., et al. 2017, A&A, 604, A127
Mathews, G. S., Pinte, C., Duchene, G., Williams, J. P., & Menard, F. 2013, A&A, 558
Mayor, M., Marmier, M., Lovis, C., et al. 2011, ArXiv e-prints, arXiv:1109.2497
Mizuno, A., Yamaguchi, R., Tachihara, K., et al. 2001, PASJ, 53
Owen, J. E., Clarke, C. J., & Ercolano, B. 2011, MNRAS
Pascucci, I., Testi, L., Herczeg, G. J., et al. 2016, ApJ, 831, 125
Pecaut, M. J., Mamajek, E. E., & Bubar, E. J. 2012, ApJ, 746
Raymond, S. N., Scalo, J., & Meadows, V. 2007, ApJ, 669, 606
Ribas, A., Bouy, H., & Merín, B. 2015, A&A, 576, A52
Ribas, Á., Espaillat, C. C., Macías, E., et al. 2017, ApJ, 849, 63
Ribas, A., Merín, B., Bouy, H., & Maud, L. T. 2014, 561, A54
Riviere-Marichalar, P., Bayo, A., Kamp, I., et al. 2015, A&A, 575
Ruíz-Rodríguez, D., Cieza, L. A., Williams, J. P., et al. 2018, MNRAS, 478, 3674
Spezzi, L., Alcalá, J. M., Covino, E., et al. 2008, AJ
Spezzi, L., Cox, N., Prusti, T., et al. 2013, A&A
Tobin, J. J., Sheehan, P., Megeath, S. T., et al. 2020, arXiv e-prints, arXiv:2001.04468
Trapman, L., Facchini, S., Hogerheijde, M. R., van Dishoeck, E. F., & Bruderer, S. 2019, A&A, 629, A79
van der Plas, G., Menard, F., Canovas, H., et al. 2017, A&A
van der Plas, G., Menard, F., Ward-Duong, K., et al. 2016, ApJ, 819
van Terwisga, S. E., Hacar, A., & van Dishoeck, E. F. 2019, A&A, 628, A85
Williams, J. P. & Best, W. M. J. 2014, ApJ
Woitke, P., Min, M., Pinte, C., et al. 2016, A&A, 586, A103

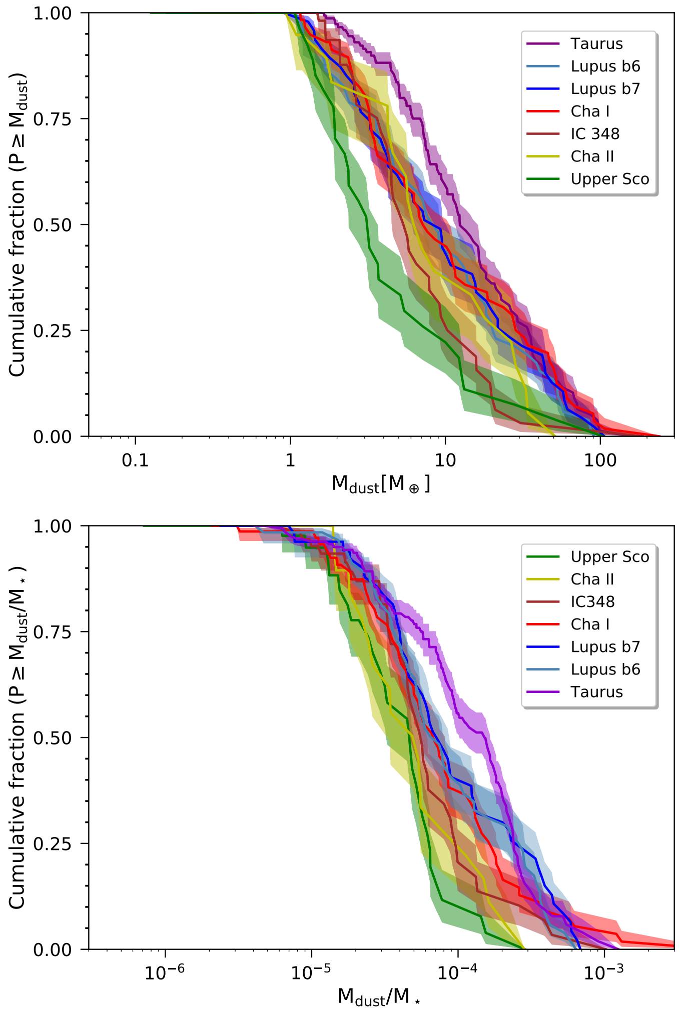

Fig. A.1. Cumulative distributions as in Fig. 5 considering disks with smaller masses than $1.08 M_{\oplus}$ as non-detections.

Appendix A: Cumulative distributions curves

Even though the Kaplan-Meier estimator and the logrank test take into account the non-detections, we performed the analysis considering a common dust mass limit. On Fig A.1, we show the distributions functions of M_{dust} and $M_{dust}/M_{\star}$ when considering all systems with disk masses smaller than $1.08 \cdot M_{\oplus}$ (the lowest mass detected in Taurus) as non detections. The results of the logrank test are also presented in Table A.1. As in Sect. 5.1, regions with an important difference in age are statistically different. However, it is harder to say that older regions such as Upper Sco and Cha II have lower dust to stellar mass ratio than older regions, the main difference between the curves being their shapes.

Table A.1. Results of pair comparisons with the logrank test applied on the ratio $M_{dust}/M_{\star}$.

Mlim = 1.08Mearth	Upper Sco	Cha II	IC348	Cha I	Lupus B7	Lupus B6	Taurus
Upper Sco		-	*	**	***	***	***
Cha II	0.4		-	-	**	**	***
IC348	0.07	0.4		-	-	-	**
Cha I	0.004	0.1	0.4		-	-	-
Lupus B7	0.0007	0.02	0.2	0.7		-	-
Lupus B6	0.001	0.03	0.4	0.97	0.4		-
Taurus	1e-7	0.0006	0.02	0.1	0.4	0.2	

Notes. The lower left half of the table represents P-values for pairs comparisons, and the upper right half corresponds to the interpretation of the test. A P-value lower than 0.001 (***) corresponds to regions statistically distinct, P-values higher than 0.1 (-) to regions statistically similar, and P-values between 0.001 and 0.05 (**), and between 0.05 and 0.1 (*) to regions that are marginally different.

Astronomy & Astrophysics manuscript no. edge-on-survey_arxiv
September 18, 2020

Observations of edge-on protoplanetary disks with ALMA

I. Results from continuum data

M. Villenave[1,2], F. Ménard[1], W. R. F. Dent[3], G. Duchêne[4,1], K. R. Stapelfeldt[5], M. Benisty[6,1], Y. Boehler[1], G. van der Plas[1], C. Pinte[7,1], Z. Telkamp[4], S. Wolff[8], C. Flores[9], G. Lesur[1], F. Louvet[10], A. Riols[1], C. Dougados[1], H. Williams[11,4], and D. Padgett[5]

[1] Univ. Grenoble Alpes, CNRS, IPAG, 38000 Grenoble, France.
e-mail: `marion.villenave@univ-grenoble-alpes.fr`
[2] European Southern Observatory, Alonso de Córdova 3107, Vitacura, Casilla 19001, Santiago 19, Chile
[3] Joint ALMA Observatory, Alonso de Córdova 3107, Vitacura 763-0355, Santiago, Chile
[4] Astronomy Department, University of California, Berkeley, CA 94720, USA
[5] Jet Propulsion Laboratory, California Institute of Technology, 4800 Oak Grove Drive, Pasadena, CA 91109, USA
[6] Unidad Mixta Internacional Franco-Chilena de Astronomía (CNRS, UMI 3386), Departamento de Astronomía, Universidad de Chile, Camino El Observatorio 1515, Las Condes, Santiago, Chile
[7] Monash Centre for Astrophysics (MoCA) and School of Physics and Astronomy, Monash University, Clayton Vic 3800, Australia
[8] Leiden Observatory, Leiden University, 2300 RA Leiden, The Netherlands
[9] Institute for Astronomy, University of Hawaii, 640 N. Aohoku Place, Hilo, HI 96720, USA
[10] AIM Paris-Saclay Département d'Astrophysique, CEA, CNRS, Univ. Paris Diderot, CEA-Saclay, F-91191 Gif-sur-Yvette Cedex, France
[11] School of Physics & Astronomy, University of Minnesota, 116 Church Street SE, Minneapolis, MN 55455 USA

September 18, 2020

arXiv:2008.06518v2 [astro-ph.SR] 17 Sep 2020

ABSTRACT

Aims. We aim to study vertical settling and radial drift of dust in protoplanetary disks from a different perspective: an edge-on view. An estimation of the amplitude of settling and drift is highly relevant to understanding planet formation.
Methods. We analyze a sample of 12 HST-selected edge-on protoplanetary disks (i.e., seen with high inclinations) for which the vertical extent of the emission layers can be constrained directly. We present ALMA high angular resolution continuum images ($\sim 0.1''$) of these disks at two wavelengths, 0.89 mm and 2.06 mm (respectively ALMA bands 7 and 4), supplemented with archival band 6 data (1.33 mm) where available.
Results. Several sources show constant brightness profiles along their major axis with a steep drop at the outer edges. Two disks have central holes with additional compact continuum emission at the location of the central star. For most sources, the millimeter continuum emission is more compact than the scattered light, both in the vertical and radial directions. Six sources are resolved along their minor axis in at least one millimeter band, providing direct information on the vertical distribution of the millimeter grains. For the second largest disk of the sample, Tau 042021, the significant difference in vertical extent between band 7 and band 4 suggests efficient size-selective vertical settling of large grains. Furthermore, the only Class I object in our sample shows evidence of flaring in the millimeter. Along the major axis, all disks are well resolved. Four of them are larger in band 7 than in band 4 in the radial direction, and three have a similar radial extent in all bands. These three disks are also the ones with the sharpest apparent edges (between 80% and 20% of the peak flux, $\Delta r/r \sim 0.3$), and two of them are binaries. For all disks, we also derive the millimeter brightness temperature and spectral index maps. We find that all edge-on disks in our sample are likely optically thick and that the dust emission reveals low brightness temperatures in most cases (brightness temperatures ≤ 10 K). The integrated spectral indices are similar to those of disks at lower inclination.
Conclusions. The comparison of a generic radiative transfer disk model with our data shows that at least three disks are consistent with a small millimeter dust scale height, of a few au (measured at r=100 au). This is in contrast with the more classical value of $h_g \sim 10$ au derived from scattered light images and from gas line measurements. These results confirm, by direct observations, that large (millimeter) grains are subject to significant vertical settling in protoplanetary disks.

Key words. Protoplanetary disks – Stars: formation – Stars: circumstellar matter – Stars: variables: T Tauri

1. Introduction

The process of planet formation requires small submicron-sized particles to grow up to large pebbles and boulders that will eventually aggregate to form planetesimals and planets. Given the short lifetimes of disks, such efficient growth has to occur in the highest density regions of protoplanetary disks, that is to say, the inner regions and/or the disk midplane. Gas drag, the interaction of dust (in Keplerian rotation) with the gas orbiting around the central star at slower (sub-Keplerian) velocities, is at the origin of the vertical settling to the midplane and of the inward radial drift of large (e.g., millimeter-sized) dust grains (Weidenschilling 1977; Barrière-Fouchet et al. 2005). Unlike the larger grains, micron-sized particles are well coupled to the gas and are located in similar regions, well-mixed with the gas. The characteristic timescale of radial drift is predicted to be about a hundred times longer than that of vertical settling (Laibe et al. 2014). However, the strength of these effects is not yet well constrained and depends in particular on the disk viscosity and/or turbulence, on the gas-to-dust ratio, and on the initial grain size distribution (Fromang & Papaloizou 2006; Dullemond & Dominik 2004; Mulders & Dominik 2012). The comparison of observations at widely different wavelengths, for example optical-NIR (near-infrared) and (sub)millimeter, can help to constrain the settling intensity and radial drift of dust grains. Moreover, by performing multi-wavelength observations in the millimeter, one can achieve spectral index measurements and, assuming optically thin emission, interpret the findings in terms of grain growth (e.g., Guilloteau et al. 2011; Pérez et al. 2012).

Up to now, most studies of protoplanetary disks have focused on radial features, such as rings, gaps, and spirals, which naturally led to observations of low inclination systems ($\leq 70^\circ$), where they are more readily visible. Some of these studies showed that the gas is often more radially extended than the millimeter-sized dust (Ansdell et al. 2018; Facchini et al. 2019), which is likely a combined effect of optical depth and dust radial drift (Facchini et al. 2017). However, though it is important to constrain radial drift, dedicated comparisons of the radial distribution of different dust grains sizes remain sparse (see e.g., Pinilla et al. 2015; Long et al. 2018).

For relatively face-on disks, it is difficult to estimate the difference in vertical extent between gas and dust grains. Detailed modeling of ring and gap features is required (e.g., Pinte et al. 2016). On the other hand, edge-on disks offer a unique perspective, as they allow us to directly observe their vertical structure. Previous studies of edge-on disks at different wavelengths indicate that the grains are stratified, with larger dust closer to the disk midplane (Glauser et al. 2008; Duchêne et al. 2003, 2010; Villenave et al. 2019), as predicted by models. However, even for these very inclined systems, the vertical extent of the midplane remains poorly constrained in early studies, limited by the resolution of the observations.

In this work, we present a survey of edge-on disks observed with the Atacama Large Millimeter Array (ALMA) at high angular resolution ($\sim$0.1″). The sample was selected based on Hubble Space Telescope (HST) images and most of the targets were observed at multiple millimeter bands. After describing the sample and the data reduction in Section 2, we present the fluxes, brightness temperatures, spectral indices, and the radial and vertical extents of all disks in Section 3. Section 4 compares our results with a toy model. We focus on the vertical and radial extent of the disks, and investigate optical depth in the disks by studying the brightness temperature and spectral indices of the sources. Finally, we summarize our conclusions in Section 5.

2. Observations and data reduction

2.1. Target selection

In this study, we selected a sample of twelve highly inclined disks. All sources were identified as candidates from their Spectral Energy Distribution (SED, see Stapelfeldt et al. 2014, and Stapelfeldt et al., in prep) and confirmed as edge-on disks (hereafter EOD) according to their optical or near-infrared HST scattered-light images. At these wavelengths, edge-on disks are inclined enough so that the star is not in direct view of the observer. The ALMA observations targeted 8 sources located in the Taurus star-forming region, 3 in Chamaeleon I, and 1 in Ophiuchus. Most of the observations presented in this work were part of our cycle 4 and 5 survey of edge-on disks (Project 2016.1.00460.S, PI: Ménard), but we also included complementary observations of Tau 042021, HH 30, and Oph 163131 from previous programs (Projects 2013.1.01175.S, 2016.1.01505.S, and 2016.1.00771.S, PIs: Dougados, Louvet, and Duchêne).

We report the coordinates, spectral types, and stellar masses of the sources in Table 1. As the spectral features associated with the central source are still visible for edge-on disks through the scattered light (Appenzeller et al. 2005), the spectral types could be determined from spectroscopy (Luhman 2007; Luhman et al. 2010, Flores et al., in prep). However, the edge-on configuration does not allow a direct estimate of the stellar luminosity. Thus, we report dynamical stellar masses estimated from CO emission.

At optical and NIR wavelengths, edge-on disk systems highlight extended nebulosities on both sides of a dark lane, tracing the disk midplane. Because of severe extinction in the dark lane, the central star is usually undetected at optical-NIR wavelengths, also resulting in fainter systems for a given spectral type and distance. In a few cases, the brightness distribution of the nebulosities has also been observed to vary significantly (Stapelfeldt et al. 1999). These facts combine to render parallax measurements difficult and the distances determined by GAIA can be plagued by large errors. For our targets, we decided to adopt the average distance of the parent star-forming regions instead; 140 pc for the sources in Taurus and Ophiuchus (Kenyon et al. 2008; Ortiz-León et al. 2018; Cánovas et al. 2019) and 192 pc for those in Chamaeleon I (Dzib et al. 2018).

Four of the observed disks are part of multiple systems: HK Tau B, HV Tau C, Haro 6-5B, and HH 48 NE (Stapelfeldt et al. 1998, 2003; Krist et al. 1998; Haisch et al. 2004) with apparent companion separations larger than 2.4″. While HH 30 has been suggested to be a binary on the basis of jet wiggles and a disk central hole in lower resolution and signal-to-noise ratio millimeter continuum maps (Guilloteau et al. 2008), higher resolution ALMA observations do not confirm the central hole (Louvet et al. 2018). Neither do they exclude the possibility of spectroscopic binary. The other targets in the sample are not known to be in multiple systems.

2.2. ALMA edge-on survey

Our ALMA cycle 4 and 5 observations (Project 2016.1.00460.S, PI: Ménard) were divided into two groups, targeting respectively seven sources located in Taurus and three in Chameleon I. The observations were performed in

Table 1. Stellar parameters.

Full name	Adopted name	RA (h m s)	Dec (° ′ ″)	SFR	SpT^{a,b}	M$_\star$^{c} (M$_\odot$)
2MASS J04202144+2813491	Tau 042021	04 20 21.4	+28 13 49.2	Taurus	M1	
HH 30	HH 30	04 31 37.5	+18 12 24.5	Taurus	M0	
IRAS 04302+2247	IRAS 04302	04 33 16.5	+22 53 20.4	Taurus	K6-M3.5	$1.3-1.7$
HK Tau B	HK Tau B	04 31 50.6	+24 24 16.4	Taurus	M0.5	0.89 ± 0.04
HV Tau C	HV Tau C	04 38 35.5	+26 10 41.3	Taurus	K6	1.33 ± 0.04
IRAS 04200+2759	IRAS 04200	04 23 07.8	+28 05 57.5	Taurus	M3.5-M6	0.52 ± 0.04
FS Tau B	Haro 6-5B	04 22 00.7	+26 57 32.5	Taurus	K5	
IRAS 04158+2805	IRAS 04158	04 18 58.1	+28 12 23.4	Taurus	M5.25	
2MASS J16313124-2426281	Oph 163131	16 31 31.3	-24 26 28.5	Ophiuchus	K4-K5^{d}	1.2 ± 0.2^{d}
ESO-Hα 569	ESO-Hα 569	11 11 10.8	-76 41 57.4	Cha I	M2.5	
ESO-Hα 574	ESO-Hα 574	11 16 02.8	-76 24 53.2	Cha I	K8	
HH 48 NE	HH 48 NE	11 04 22.8	-77 18 08.0	Cha I	K7	

Notes. Coordinates are J2000. SFR: Star-forming region, SpT: Spectral type, M$_\star$: Stellar masses, from dynamical estimates based on gas emission.

References. $^{(a)}$ Luhman (2007), $^{(b)}$ Luhman et al. (2010), $^{(c)}$ Simon et al. (2019), $^{(d)}$ Flores et al. (in prep)

band 7 (0.89 mm) and in band 4 (2.06 mm). We present the different setups in the following section.

2.2.1. Band 7 survey

The band 7 observations of the Taurus sources (Tau 042021, IRAS 04302, HK Tau B, HV Tau C, IRAS 04200, Haro 6-5B, and IRAS 04158) were performed with both a compact and an extended array configuration. For the Chamaeleon sources (ESO-Hα 569, ESO-Hα 574, and HH 48 NE), only the compact configuration was observed. The observational setup is summarized in Table 2. The spectral setup was divided into three continuum spectral windows, with dual polarization, 2 GHz bandwidth spectral windows centered at 344.5, 334.0, and 332.0 GHz, and one spectral window set to observe the ^{12}CO J$=3-2$ transition at 345.796 GHz. In this paper, we focus on the continuum data which has a geometric mean frequency of 336.8 GHz (0.89 mm). The reduction and analysis of the CO data will be presented in a separate study. Because the observations were performed over two cycles, different versions of CASA have been used for the calibration.

We calibrated the raw data of the compact array executions using the pipeline from CASA package version 4.7. The raw data of the extended configuration observations of the Taurus sources was manually calibrated, using CASA version 5.1. Whenever possible we used the supplied ALMA phase calibrator in the dataset (for Tau 042021, Haro 6-5B, IRAS 04158). However, for four targets (namely HK Tau B, HV Tau C, IRAS 04200, and IRAS 04302), the spectral window setup used for the supplied phase calibrator was different from that of the science target. These data could not be reduced using the standard pipeline. For HV Tau C and IRAS 04200, it was possible to use the check source as a phase calibrator, and for HK Tau B, the more distant bandpass calibrator could be used. In these cases, the calibrator was only observed once before each of the science targets (rather than bracketing it in time); this increased the phase calibration uncertainties for these objects. IRAS 04302 did not have a usable phase calibrator. However, this source is bright and extended, and self-calibration using the average of all spectral windows could be performed without an initial phase reference. Consequently for this target, there was no absolute astrometric solution in the extended configuration data; also the achievable angular resolution was somewhat worse than the other sources of the sample.

2.2.2. Band 4 survey

The band 4 observations of the edge-on survey were only performed for the sources located in Taurus (Tau 042021, IRAS 04302, HK Tau B, HV Tau C, IRAS 04200, Haro 6-5B, and IRAS 04158). The continuum spectral windows were centered on 138, 140, 150, and 152 GHz, with a geometric mean frequency of 145.0 GHz (2.06 mm). The relevant parameters of the observations are reported in Table 2. The raw data were pipeline calibrated using the CASA package, version 5.1.

2.3. Archival and literature data

2.3.1. ALMA observations of HH 30

We include multi-wavelength, band 4, 6, and 7, observations of HH 30 in the present study. The observational setup and data reduction of the band 6 observations are presented in Louvet et al. (2018, Project 2013.1.01175.S, PI: Dougados). We also use new band 4 and band 7 cycle 4 observations (Project 2016.1.01505.S, PI: Louvet), and present the data reduction in the following paragraphs.

The band 7 observations of HH 30 were performed with only one array configuration, in four executions between October 14 and October 21, 2016 (see Table 2). The dual polarization spectral setup included two 2 GHz bandwidth spectral windows for the continuum emission, centered at 331.6 and 344.8 GHz, and two other spectral windows set to observe the ^{13}CO and C^{18}O J=3-2 emission. Here we present only the continuum observations. The observations were calibrated by the ALMA pipeline using CASA 4.7.

The band 4 observations were performed with two configurations: a compact configuration and an extended con-

Table 2. ALMA observations.

Source (1)	Band (2)	Obs. date (3)	Config. (4)	Baselines (5)	N$_{ant}$ (6)	t$_{int}$ (min) (7)	v$_{\rm CASA}$ (8)	Project ID (9)
Survey Tau[a]	7	24/11/2016	C40-4	15 m−0.7 km	43	1.1	4.7	2016.1.00460.S
		18/08/2017	C40-7	21 m−3.6 km	43	3.7	5.1	2016.1.00460.S
	4	27/09/2017	C40-8/9	41 m−14.9 km	43	6.7	5.1	2016.1.00460.S
Survey Cha[b]	7	15/11/2016	C40-4/6	15 m−0.9 km	42	1.1	4.7	2016.1.00460.S
HH 30	7	14, 15, 21/10/2016	C40-6	19 m−2.5 km	42-46	174	4.7	2016.1.01505.S
	6	19, 21/07/2015	C34-6/7	13 m−1.6 km	42	78	4.3	2013.1.01175.S
	4	23/10/2016	C40-6	19 m−1.8 km	48	12	4.7	2016.1.01505.S
		12/09/2017	C40-8/9	41 m− 9.5 km	44	31	4.7	2016.1.01505.S
Tau 042021	6	05/12/2016	C40-3	15 m− 0.7 km	41	7.5	4.7	2016.1.00771.S
		21/10/2016	C40-6	18 m− 1.8 km	44	25	4.7	2016.1.00771.S
Oph 163131	6	25/04/2017	C40-3	15 m−0.5 km	41	8.5	4.7	2016.1.00771.S
		07/07/2017	C40-5	17 m− 2.6 km	44	27	4.7	2016.1.00771.S

Notes. Column 1: Target name, Column 2: Observing band, Column 3: Observing date, Column 4: ALMA array configuration, Column 5: Minimum and maximum baseline range, Column 6: Number of antennas, Column 7: On source integrating time, Column 8: Calibrating CASA version. (a) The Taurus sources included in the survey are Tau 042021, IRAS 04302, HK Tau B, HV Tau C, IRAS 04200, Haro 6-5B, and IRAS 04158. (b) The Chamaeleon I sources included in the survey are ESO-Hα 569, ESO-Hα 574, and HH 48 NE.

figuration (see Table 2). The ALMA correlator was configured to record dual polarization with four separate continuum spectral windows of 2 GHz each centered at 138, 140, 150, and 152 GHz. The observations were calibrated by the pipeline using CASA 4.7.

2.3.2. ALMA observations of Tau 042021 and Oph 163131

We also include band 6 cycle 4 observations of Tau 042021 and Oph 163131 (Project 2016.1.00771.S, PI: Duchêne). Although the spectral setup targeted emission lines of three CO isotopologues, we focus here on the continuum data. An analysis of the line emission of Oph 163131 will be presented in a separate study (Flores et al., in prep).

For both sources, the two continuum spectral windows were centered on 216.5 and 232.3 GHz leading to a geometric mean frequency of 224.4 GHz (1.34 mm). The detailed observational setup is presented in Table 2. Data from both configurations were reduced using the pipeline from CASA package version 4.7.

2.4. ALMA imaging

We constructed the images from the calibrated visibilities with a Briggs robust weighting parameter of 0.5, except for the band 6 of HH 30 for which we used the reduction presented in Louvet et al. (2018, robust of 0.56). When the data were taken with several array configurations (see Table 2), the images were generated by combining the visibilities from the compact and extended configurations. The only exception is IRAS 04158 for which we show the band 7 compact configuration observations only. We applied self-calibration on the sources with the highest signal-to-noise ratio (on at least one array configuration). In band 7 this corresponds to Tau 042021, IRAS 04302, HK Tau B, and Haro 6-5B, in band 6 to Tau 042021 and Oph 163131, and to only HH 30 in band 4. For the Taurus survey, this leads to typical beam sizes of about $0.11'' \times 0.07''$ in band 7 and about $0.11'' \times 0.04''$ in band 4. For the other sources, the beam sizes range from $0.23 \times 0.13''$ to $0.48 \times 0.30''$. The beam sizes of each observations are reported in Table A.1, and we present the images in Fig. 1.

Additionally, we also recompute the maps to get a unique angular resolution for each source observed both in band 4 and band 7 (except for IRAS 04158, for which the disk is not detected in band 4). To do so, we first re-imaged each source using the same `uvrange` and applying a `uvtaper` to limit the effect of flux filtering and of different uvcoverage. Then, to obtain exactly the same angular resolution between both bands, we used the `imsmooth` CASA task. The restored beam sizes are reported in the last column of Table A.1.

2.5. Astrometric accuracy and map registration

ALMA maps are subject to astrometric uncertainties due to limited signal-to-noise on the phase calibrator and errors in the phase referenced observations related to weather or antenna position errors. To compute accurate spectral index maps (see Section 3.3), the images at the different wavelengths have to be accurately aligned. In this section, we discuss the registration of our images.

For each source and band, we performed simple Gaussian fits in the image plane to estimate the centroid position. The offsets between band 4 and band 7 ranged from 2 mas (milliarcseconds) for Tau 042021 and IRAS 04200, up to 60 - 90 mas for HH 30, HV Tau C, and IRAS 04302. Most are larger than expected from source proper motion between the different executions and from the astrometric accuracy of ALMA (10% of the synthesized beam, see ALMA Technical Notebook). However, for the three disks with the largest offsets (HH 30, HV Tau C, and IRAS 04302), different phase calibrators were used between the observations. In addition, the standard phase calibration could not be performed for the band 7 data of IRAS 04302 and HV Tau C (see above), and the weather conditions during the band 7 extended configuration observations were relatively poor, with phase rms of $\sim 64°$ on the longest baselines. This will also deteriorate the positional accuracy. Overall, the astrometric accuracy of our observations is not sufficient to confirm any significant motion or shift of the sources between the two bands.

Table 3. Millimeter fluxes.

Sources	F_{B7} (mJy)	F_{B6} (mJy)	F_{B4} (mJy)
Tau 042021	124.2 ± 12.4	47.2 ± 4.7	15.4 ± 1.5
HH 30	54.5 ± 5.5	22.3 ± 0.1^a	6.9 ± 0.7
IRAS 04302	267.5 ± 26.8		37.2 ± 3.7
HK Tau B	55.6 ± 5.6		4.4 ± 0.4
HV Tau C	90.6 ± 9.1		11.6 ± 1.2
IRAS 04200	65.6 ± 6.6		11.6 ± 1.2
Haro 6-5B	340.9 ± 34.1		35.3 ± 3.5
IRAS 04158	$259.2 \pm 25.9^*$		$2.0 \pm 0.2^*$
Oph 163131	125.8 ± 2.4^b	44.8 ± 4.5	
ESO-Hα 569	40.2 ± 4.0		
ESO-Hα 574	9.3 ± 0.9		
HH 48 NE	31.0 ± 3.1		

Notes. Total fluxes are measured using elliptical apertures centred on the targets. (*) Band 7: Total flux for the disk and central binary. Band 4: Only flux from the central binary.

References. (a) Louvet et al. (2018), (b) Cox et al. (2017).

Table 4. Peak brightness temperatures.

Sources	B7 (K)	B4 (K)
Tau 042021	$6.9^\dagger$	$5.3^\dagger$
HH 30	7.2	3.7
IRAS 04302	10.3	$6.7^\dagger$
HK Tau B	11.4	$5.4^\dagger$
HV Tau C	13.5	6.8
IRAS 04200	$9.1^\dagger$	$8.7^\dagger$
Haro 6-5B	$15.8^\dagger$	$9.9^\dagger$
IRAS 04158	5.2	
ESO-Hα 569	6.5	
ESO-Hα 574	4.3	
HH 48 NE	4.9	

Notes. The uncertainties are limited by errors in flux calibration and can thus be estimated by 10% of the reported brightness temperature peak. The reported peak brightness temperatures were computed using the same beam in both bands (see Table A.1). We only report the peak band 7 brightness temperature of IRAS 04158 because the disk is not detected in band 4. (†) Well resolved sources in all directions.

Because models of edge-on disks also show that offsets between bands should remain minimal compared to the beam size, we registered our images to a common center in both bands. We aligned the band 4 and band 7 observations using the `fixplanets` task in CASA[1].

3. Results

3.1. Continuum emission and brightness temperatures

All millimeter-wavelength continuum images are presented in Fig. 1. The majority of the disks in our sample show an elongated emission shape, with large axis ratios and in several cases roughly constant surface brightness along the major axis, confirming that they are highly inclined.

Two disks in the sample, however, present a different shape. Haro 6-5B and IRAS 04158 show the presence of a ring and central emission peak. We evaluate the position of the rings in Section 3.2.1. As in previous CARMA observations (Sheehan & Eisner 2017), the band 7 image of IRAS 04158 reveals a highly asymmetric ring (brighter on the western side) with a compact source toward the center. This ring is not detected in our band 4 observations, mostly due to flux dilution into small beams. However, the band 4 observations clearly resolve the emission at the center of the ring into two point sources. IRAS 04158 is a binary system. A detailed analysis of this source will be presented in a dedicated study (Ragusa et al., in prep).

The total continuum flux density of each source is measured by integrating the signal, down to the 3σ noise level, within elliptical apertures tailored to each source. The flux densities are reported in Table 3. We use 10% error values throughout Table 3, which correspond to the typical flux calibration errors of ALMA (see ALMA Technical Handbook[2]). We note that although the phase calibration method used for the extended configuration observations in band 7 was non-standard (see Section 2.2.1), the flux calibration followed the usual procedure and, accordingly, the flux calibration uncertainty should be nominal. We checked that the integrated fluxes recovered using the compact configuration band 7 observations or both compact and extended configurations jointly are consistent within 10%.

To further investigate the disk properties, we calculate the brightness temperature, T_B, maps of each source. To ease the comparison between bands, we estimate the brightness temperatures from the band 7 and band 4 maps computed at the same angular resolution (see Section 2.4). We do not use the Rayleigh-Jeans approximation. We show the brightness temperature profiles measured along the major axis in Fig. B.1 and report the *peak* brightness temperatures in Table 4.

We note that, even for the most resolved sources (i.e., least impacted by beam dilution), the inferred brightness temperatures are lower or comparable to those required to be in the Rayleigh-Jeans regime, respectively $T > 16.2$ K for band 7 and 6.8 K for band 4. This strengthens our choice not to use this approximation. Additionally, we find that the band 4 brightness temperatures are systematically lower than the band 7 ones.

3.2. Surface brightness profiles

3.2.1. Radial extent

To characterize the radial extent of the disks, we present cuts along the major axis of each disk in Fig. 2. The cuts are normalized to their maximum intensity. For Tau 042021, IRAS 04302 and HV Tau C, for which the band 4 emission is very noisy, we estimate the normalizing factor as the amplitude of the Gaussian best fitting the curves. All sources are well resolved along their major axis.

---

[1] We note that we set the option `fixuvw` to True when applying the `fixplanets` task, which is similar to using the `fixvis` task.

[2] https://almascience.eso.org/documents-and-tools/latest/documents-and-tools/cycle8/alma-technical-handbook

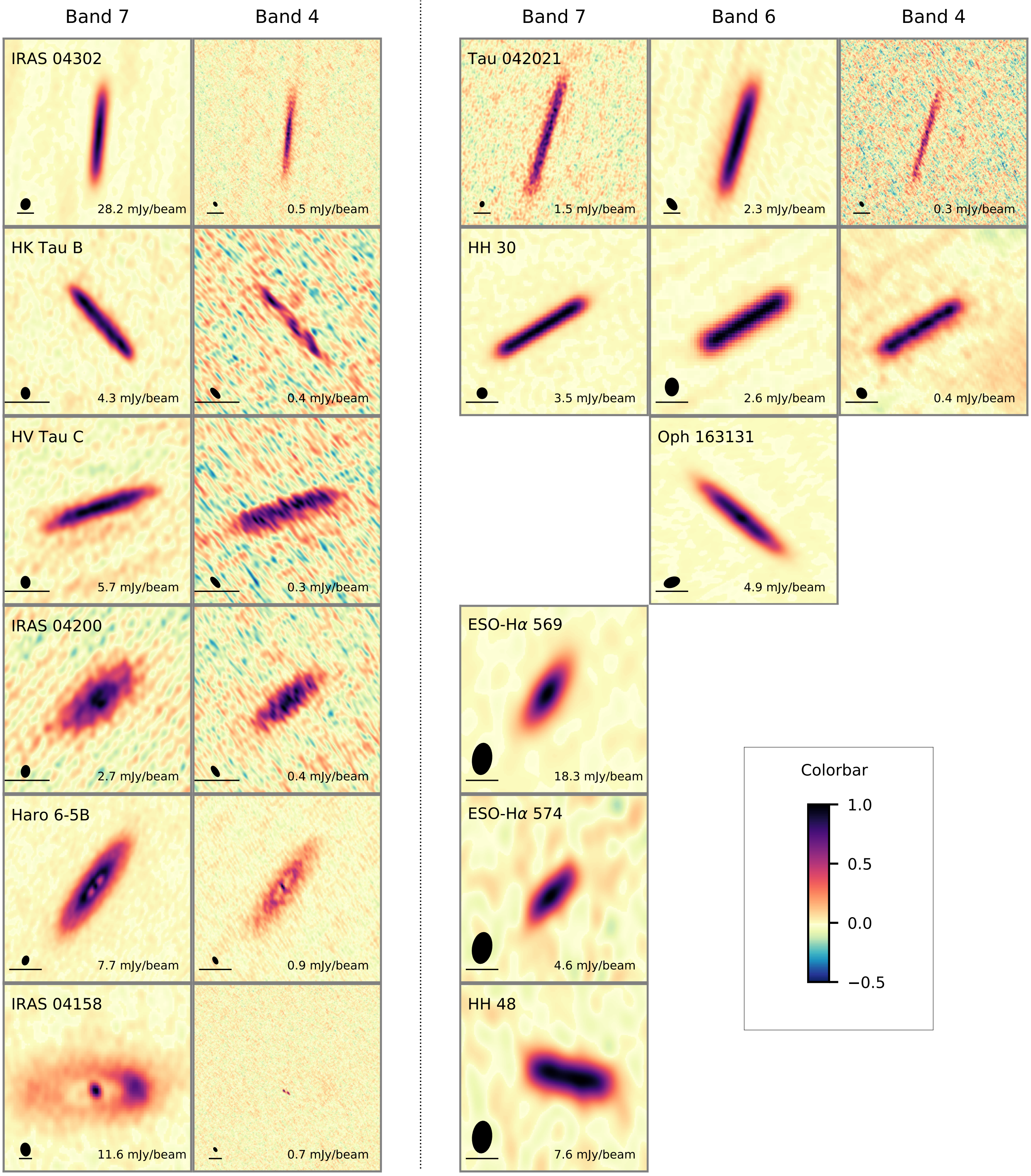

Fig. 1. Images of all sources included in this study normalized to their peak intensity (reported in the bottom right corner of each image). Each column corresponds to a different band and each line displays two sources, separated by the vertical dashed line. We show the beam size (ellipse) and a 0.5″ scale (dark line) in the bottom left corner of each panel.

Morphology. For several sources, the brightness profile is flat along the major axis direction and drops steeply at the edges. This is particularly true for HH 30, HK Tau B, HV Tau C, and HH 48 NE. The lack of a central brightness peak further supports the idea that these disks are optically thick and highly inclined, so that we are viewing only the outer optically-thick edge. Conversely, the disks of Tau 042021, IRAS 04302, IRAS 04200, ESO-Hα 569, and ESO-Hα 574 show more centrally peaked emission without a clear plateau, suggesting that they are optically thinner and/or viewed with a lower inclination, less edge-on. We note that the radial brightness profile of HK Tau B shows hints of rising at the edges. While this is a marginal (3σ)

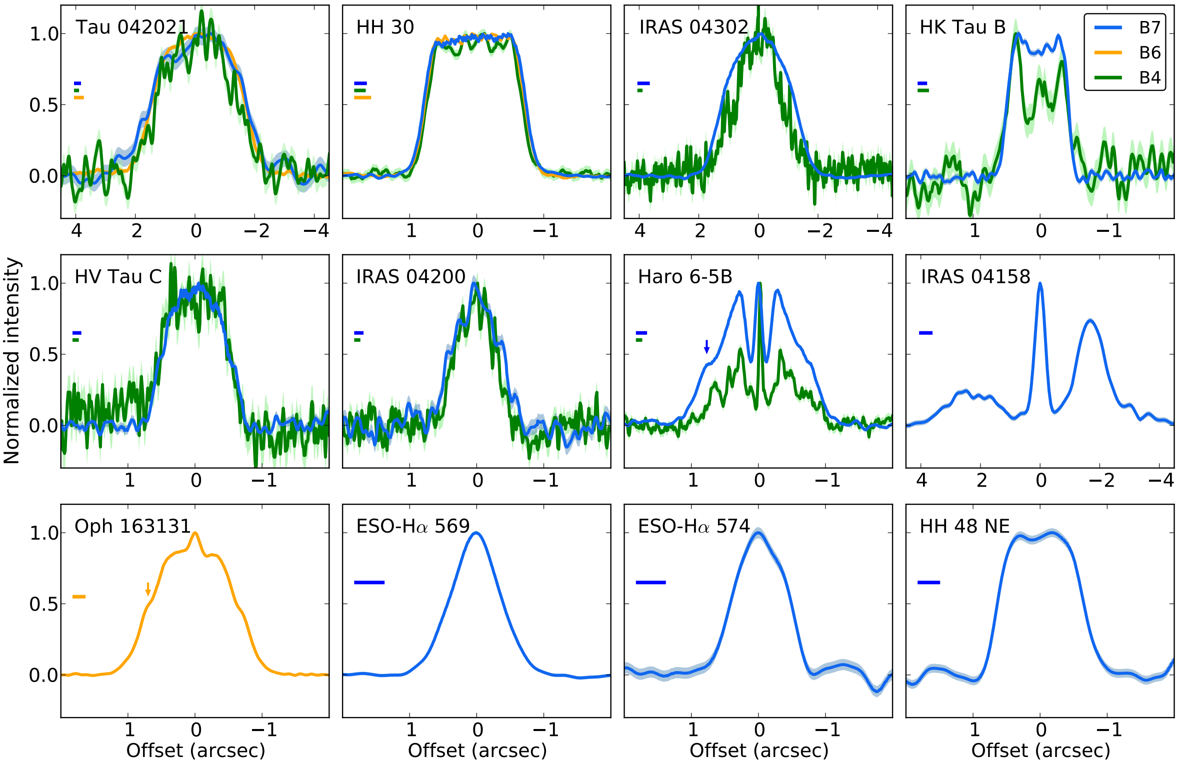

Fig. 2. Normalized major axis intensity profiles. Data in the three bands are represented by the green (band 4), orange (band 6) and blue (band 7) lines. The light shading corresponds to the normalized rms in each band. The beam sizes in the direction of the cut are shown in the left part of each plot as horizontal lines. We indicate the shoulders of Haro 6-5B and Oph 163131 by an arrow. We smoothed the cuts through Tau 042021 by convolving them by a 1-D Gaussian of the beam width, to reduce the noise and make the plot clearer.

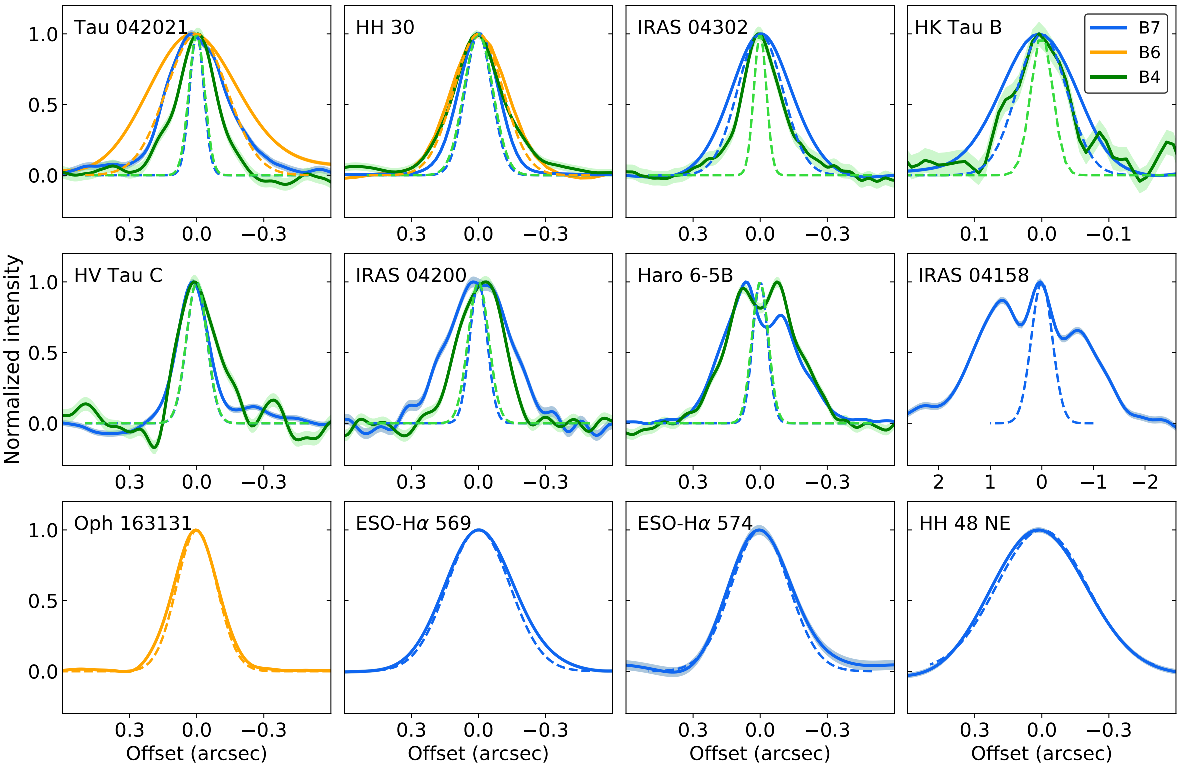

Fig. 3. Normalized averaged minor axis intensity profiles. For the most inclined sources (resp. least inclined: IRAS 04200, Haro 6-5B, and IRAS 04158), these were obtained by averaging minor axis intensity cuts over the whole major axis extent of the disk (resp. over the central 0.3″). The light shading correspond to the normalized rms in each band. The beam sizes in the direction of the minor axis are shown as dotted Gaussian of the corresponding color.

Table 5. Position angle, inclination, major axis sizes, and estimates of the mean deconvolved major axis sharpness of the millimeter data.

Sources	PA (°)	$i_{\mathrm{AxisRatio}}$ (°)	B7 (″)	B6 (″)	B4 (″)	Optical-NIR (″)	$\Delta r/r$
Tau 042021	-16	> 85	4.10 ± 0.01	3.76 ± 0.02	3.67 ± 0.01	5.0	0.6 ± 0.2
HH 30	121	$> 85^{a}$	1.85 ± 0.01	1.82 ± 0.02	1.73 ± 0.01	3.1	0.2 ± 0.1
IRAS 04302	175	> 84	3.15 ± 0.03		2.84 ± 0.01		0.7 ± 0.1
HK Tau B	41	> 83	0.99 ± 0.01		0.99 ± 0.01	1.3	0.2 ± 0.1
HV Tau C	108	> 80	1.20 ± 0.01		1.18 ± 0.01	0.8	0.5 ± 0.2
IRAS 04200	129	69 ± 2	1.00 ± 0.01		0.85 ± 0.01		1.0 ± 0.4
Haro 6-5B	145	74 ± 2	2.06 ± 0.01		1.74 ± 0.01	2.3	$0.8 \pm 0.3^{\dagger}$
IRAS 04158	92	62 ± 3	7.47 ± 0.03			13.6	
Oph 163131	49	> 80		2.50 ± 0.01		2.6	0.7 ± 0.2
ESO-Hα 569	144	> 64	1.88 ± 0.04			2.0	0.9 ± 0.2
ESO-Hα 574	141	> 69	1.35 ± 0.04			1.2	0.7 ± 0.2
HH 48 NE	75	> 68	1.72 ± 0.03			1.3	0.4 ± 0.1

Notes. For each source, the errors in the millimeter sizes correspond to one tenth of the beam width in the major axis direction. When possible, the $\Delta r/r$ ratios correspond to their averaged values between the band 7 and band 4. All are deconvolved by the beam. We also indicate an estimate of the inclination inferred from the millimetric mean axis ratio. These are lower limits when the disks are not resolved along their minor axis in all bands by more than 2 beams, or when the measured inclination is too high not to be influenced by the physical vertical extent of the disk. $^{(\dagger)}\Delta r/r$ of the band 7 only.

References. $^{(a)}$ Louvet et al. (2018)

feature, this may indicate the presence of a ring (or transition disk).

Finally, three disks (Haro 6-5B, IRAS 04158, and Oph 163131) show symmetric shoulders or clear evidence of ring like features. The main ring of Haro 6-5B peaks at ∼0.29″ (41 au) in both bands. Furthermore, a shoulder seen in band 7 is associated with a peak in the higher-resolution band 4 cut; this would correspond to a fainter ring located at ∼0.77″ (108 au). The brightness asymmetry of the outer ring in IRAS 04158 is very clear in the major-axis cut: its western side is about 3 times brighter than the eastern side. We also note that the ring is slightly off-centered compared to the central binary. The western side of the disk peaks at ∼1.71″ (239 au), while the eastern side peaks at ∼2.28″ (319 au) from the center. We fit Gaussians on each side of the disk in the radial profile and find that the eastern ring is about 1.7 times wider than the western ring (with full width half maximum, FWHM, of 1.98″ and 1.18″ respectively). We also find that Oph 163131 displays a relatively flat profile in the inner 0.5″, but has a sharp central peak. It has symmetric shoulders at ∼0.70″ radius, which suggests that this disk contains two rings and is viewed slightly away from edge-on. Further modeling of this source, focusing on dust emission, will be presented in a separate analysis (Wolff et al., in prep).

Size estimations. To determine the sizes, we first normalized the major axis cuts presented in Fig. 2, as mentioned in the beginning of this section. Then, for each source, we estimate the relevant 3σ noise level in the image with the worst signal-to-noise ratio, either band 4 or band 7. This 3σ level is converted into a fraction of the peak, in percent. The sizes in both bands are then measured at the same level, which means at the same fraction of the peak. The size of the disks along their major axis are reported in Table 5. The errors correspond to a tenth of the beam size along the major axis direction. We verified that using the FWHM of the cut profiles instead of the 3σ levels yields similar conclusions. This is also the case for the cuts obtained from the maps computed with a similar uv-coverage.

Along with the major axis size, we also estimate the apparent sharpness of the disk edges, as measured in the image plane. To do so, we measure the fractional range of radius over which the millimeter emission decreases from 80% to 20% of the peak emission, called $\Delta r/r$. We define Δr by $\Delta r = |r_{80\%} - r_{20\%}|$ and the normalization radius by $r = |r_{80\%} + r_{20\%}|/2$. We chose this flux range because the radial profiles can usually be well approximated by straight lines in this interval. We report the values of $\Delta r/r$ in the last column of Table 5. The values are the mean of the estimations in band 4 and band 7, and they are deconvolved by the beam size. Sharp outer edges have small Δr and hence small $\Delta r/r$. For example, a typical beam with a FWHM of 0.1″ would have $\Delta r/r \simeq 0.1$ when calculated in a small disk similar to HK Tau B ($r = 0.5''$), or $\Delta r/r \simeq 0.04$ in a disk as large as IRAS 04302 ($r = 1.2''$). All the disks in our sample have $\Delta r/r$ values larger than 0.2, which corresponds to shallower outer edges than the typical beam.

We find two different families of objects when comparing the radial extent of the disks in band 4 and band 7. Four sources (Tau 042021, IRAS 04302, IRAS 04200, and Haro 6-5B) show a band 7 size more extended than the band 4 by more than 2 beams. When compared with the same angular resolution and uv-coverage, these sources have band 7 major axis size on average 12% larger than that of the band 4. As the band 7 shorter wavelength traces smaller particles than those probed by band 4, the smaller sizes in band 4 suggest that the larger particles have drifted inward relative to the smaller ones. The outer edges of these four sources are well resolved and they have an average apparent sharpness of $\Delta r/r \sim 0.8$, much shallower than the beam.

For the three remaining sources (HH 30, HK Tau B, HV Tau C), no difference in radial extent is found between band 7 and band 4. This might suggest the presence of dust traps at the outer edges of these disks, which can slow radial drift and lead particles to stop at particular radial locations (Powell et al. 2019; Long et al. 2020). Including HH 48 NE, these four sources have the sharpest edges, with $\Delta r/r$ between 0.2 and 0.5. The edges of these disks are only marginally shallower than the typical beam. We note that 3 out of these 4 systems are known binaries and dynamical interactions may also lead to sharp outer edges.

3.2.2. Disk extent perpendicular to the midplane

For the most inclined systems, the brightness maps shown in Fig. 1 have very elongated, linear shapes rather than elliptical ones, so we generate the minor axis profiles by taking the mean of the cuts at all distances along the major axis. In that case, the size of the minor axis is dominated by the vertical extent of the disk perpendicular to the midplane. For the less inclined sources where a clear ellipticity is visible in the image (namely IRAS 04200, Haro 6-5B, and IRAS 04158), we generate the minor axis profiles by averaging over a restricted range, only $\pm 0.15''$ around the center of the disk. In that case, the minor axis is dominated by the projection of the disk radius. We show the averaged brightness profile along the minor axis for all sources in Fig. 3. Dashed lines trace the Gaussian beam profiles along the cut direction.

We find that six out of the twelve disks of our sample are well-resolved along the minor axis, having a width more than twice the beam width. They are Tau 042021, IRAS 04200, Haro 6-5B (in both band 7 and band 4), IRAS 04158 (in band 7), and IRAS 04302, HK Tau B (in band 4). Additionally, the minor axis profiles of Haro 6-5B and IRAS 04158 reveal the presence of rings, and we see a clear asymmetry in the band 7 cut of Haro 6-5B.

We measure the minor axis sizes by fitting Gaussians to the generated profiles, Gaussians being good first approximations. For Haro 6-5B and IRAS 04158 for which the cuts show ring features, we estimate the FWHM directly through the cuts, without fitting a Gaussian. We report the resulting FWHM in Table 6, where the errors correspond to a tenth of the beam size projected in the direction of the cut[3].

In order to extract the intrinsic vertical extent of the disks, we also deconvolve the minor axis sizes by the beam, assuming that both profiles are Gaussian. These values are presented in the last columns of Table 6. For the least resolved disks (i.e., for Oph 163131, ESO-Hα 569, ESO-Hα 574, and HH 48 NE), we only report upper limits. We estimate the uncertainties on the deconvolved minor axis sizes by propagating the errors, assuming that the error on the beam size is 10% of the beam major axis size.

We also estimate the disk inclinations from the measured axis ratio in all bands, and report them in Table 5. For consistency, we use the FWHM of the major axis sizes (cut at 50% of the peak flux) to estimate the inclination, as opposed to the size at 3σ reported in Table 5. For the sources that are not resolved in the vertical direction (Oph 163131, ESO-Hα 569, ESO-Hα 574, HH 48 NE) and those with the smallest axis ratio (Tau 042021, IRAS 04302, HK Tau B, HV Tau C), we present these values as lower limits. Indeed, for the most inclined systems (i.e. those with the smallest axis ratio), the minor axis size might not be dominated by the inclination but by the actual vertical thickness of the disks, which leads to lower apparent inclinations based on the axis ratio only. Except IRAS 04200, Haro 6-5B, and IRAS 04158, all resolved disks have an inclination larger than 75°. We note that Tau 042021 is the only highly inclined disk resolved along its minor axis in both band 7 and band 4. For this disk, the band 7 appears about 1.5 times more extended vertically than the band 4.

3.3. Estimation of spectral indices

The millimeter spectral index, defined as $F_\nu \propto \nu^{\alpha_{mm}}$, can be used to study optical depth and grain growth in a disk (see e.g., review by Williams & Cieza 2011). Indeed, assuming scattering is negligible, the millimeter intensity can be expressed as $I_\nu = B_\nu(T)(1 - e^{-\tau_\nu})$, in which $B_\nu(T)$ is the Planck function and τ_ν the dust optical depth (which is proportional to the dust absorption coefficient, $\kappa_\nu \propto \nu^\beta$). In the Rayleigh-Jeans regime and for optically thin emission, we expect $\alpha \approx 2 + \beta \geq 2$. Small ISM-like grains have a β parameter of 1.5-2 (e.g., Li & Draine 2001), while grains of millimeter or centimeter sizes are expected to have a β parameter closer to 0 (e.g., Pavlyuchenkov et al. 2019). Low values of spectral indices ($\alpha \leq 3$) are usually interpreted either in terms of the emission being optically thick or that the dust grain size distribution has grown significantly to reach millimeter/centimeter for the maximum sizes (e.g., Testi et al. 2014).

Using the continuum fluxes from our survey and (sub)millimeter fluxes from the literature, we estimate the global millimeter spectral index α_{mm} for each source. We use a least-squares fit of all photometric points between 800 μm and 3.3 mm. We find $\alpha_{mm} \leq 3$ for all disks, as can be seen in Table 7.

Global spectral indices do not take into account the spatial distribution of the emission. Thus, for sources with multiple millimeter images, we computed spectral index maps using the band 4 and band 7 observations. We generated the spectral index maps pixel-by-pixel by applying the CASA task `immath` on the band 7 and band 4 maps computed to a unique resolution (see Section 2.4). Finally, to lower the noise level in the spectral index map, we applied a filter to keep only the pixels with emission well above the noise level (5σ) in both the band 4 and the band 7 images. The final maps and cuts along the major and minor axis are displayed in Fig. 4.

We find that the spectral index increases with radius for most sources, albeit with larger uncertainty at larger radii due to the lower signal-to-noise ratio. Similarly, the spectral index also rises along the minor axis direction for two disks, Tau 042021 and IRAS 04200. Previous studies identified similar increases in the radial direction in several disks seen at lower inclinations (e.g., Pinte et al. 2016; Dent et al. 2019). The increases were attributed to changes in the dust

---

[3] We note that even for the most inclined disks, the minor axis size is related but is not a measurement of an equivalent "dust scale height" at a given radius. Indeed, observations are measuring the integrated intensity along the line-of-sight over the whole disk (i.e., from several radii) and are affected by optical depth effects.

Table 6. Full width half maximum of the (averaged) minor axis profiles, measured and deconvolved by the beam size.

Sources	Minor B7 ($''$)	Minor B6 ($''$)	Minor B4 ($''$)	Deconvolved B7 ($''$)	Deconvolved B6 ($''$)	Deconvolved B4 ($''$)
Tau 042021	$0.32 \pm 0.01^{\dagger}$	0.49 ± 0.03	$0.21 \pm 0.01^{\dagger}$	$0.31 \pm 0.01^{\dagger}$	0.37 ± 0.06	$0.20 \pm 0.01^{\dagger}$
HH 30	0.21 ± 0.01	0.29 ± 0.03	0.27 ± 0.02	0.16 ± 0.02	0.14 ± 0.07	0.22 ± 0.02
IRAS 04302	0.32 ± 0.02		$0.21 \pm 0.01^{\dagger}$	0.21 ± 0.05		$0.20 \pm 0.01^{\dagger}$
HK Tau B	0.13 ± 0.01		$0.10 \pm 0.01^{\dagger}$	0.10 ± 0.01		$0.09 \pm 0.01^{\dagger}$
HV Tau C	0.17 ± 0.01		0.19 ± 0.01	0.13 ± 0.02		0.16 ± 0.02
IRAS 04200*	$0.33 \pm 0.01^{\dagger}$		$0.23 \pm 0.01^{\dagger}$	$0.31 \pm 0.01^{\dagger}$		$0.21 \pm 0.01^{\dagger}$
Haro 6-5B*	$0.35 \pm 0.01^{\dagger}$		$0.35 \pm 0.01^{\dagger}$	$0.34 \pm 0.01^{\dagger}$		$0.34 \pm 0.01^{\dagger}$
IRAS 04158*	$2.36 \pm 0.05^{\dagger}$			$2.31 \pm 0.05^{\dagger}$		
Oph 163131	0.16 ± 0.07^{a}	0.23 ± 0.02			< 0.14	
ESO-Hα 569	0.37 ± 0.03			< 0.13		
ESO-Hα 574	0.33 ± 0.03			< 0.21		
HH 48 NE	0.49 ± 0.05			< 0.24		

Notes. The uncertainties on the measured minor axis sizes correspond to one tenth of the beam size along the cut direction. (*) Disks with inclination lower than 75°. Their minor axis size is likely dominated by the radial extent of the disk over its vertical extent, as opposed to more inclined disks. (†) Resolved by more than 2 beams in the minor axis direction. These are the ones for which the deconvolved minor axis size should be the most reliable.

References. (a) Cox et al. (2017)

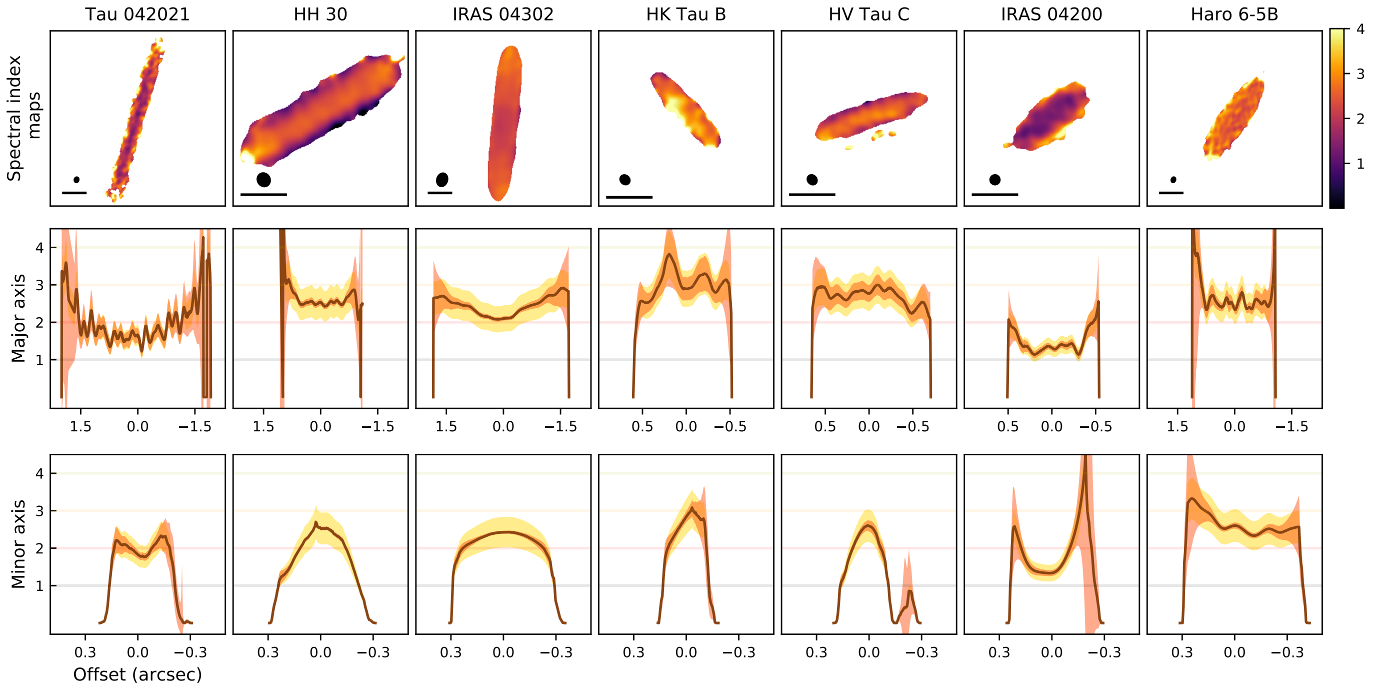

Fig. 4. *Top row:* Spectral index maps, applying a filter to keep only the pixels with more emission than 5σ in both bands. The beam size is shown in the bottom left corner, along with a dark line representing a $0.5''$ scale. *Middle row:* Spectral index cuts along the major axis. *Bottom row:* Spectral index profiles along the minor axis, averaged as done for Fig. 3 (see text Section 3.2.2). For all cuts, yellow errors correspond to a flux calibration error of 10% in both bands, while orange errors are estimated from the signal-to-noise in each band. The x-axis corresponds to the offset to the center of the disk in arcseconds.

size distribution and/or to lower optical depths at large radii. Very inclined systems on the other hand appear optically thicker than low inclination ones for the same mass. This is due to projection effects, because the line-of-sight crosses the disk over a longer distance. This suggests that, for the most inclined disks of our sample, spectral index variations are dominated by changes of optical depth inside the disk (i.e., opacity effects) rather than by grain growth (see also our radiative transfer model, Appendix C). However, at the outer edges (both radially and vertically), where the disks become optically thinner, spectral index variations are enhanced by changes in the dust size distribution (see e.g., Tau 042021, IRAS 04302, IRAS 04200, and Haro 6-5B, where we found large differences in major axis sizes between band 7 and band 4). We also note that HH 30, IRAS 04302, HK Tau B, and HV Tau C show the opposite behavior of Tau 042021 and IRAS 04200 along the minor axis, their spectral indices decrease. However, none

Table 7. Integrated spectral indices.

Sources	α_{mm}
Tau 042021	2.5 ± 0.1
HH 30	2.5 ± 0.1
IRAS 04302	2.3 ± 0.1
HK Tau B	3.0 ± 0.2
HV Tau C	2.2 ± 0.2
IRAS 04200	2.1 ± 0.4
Haro 6-5B	2.6 ± 0.1
IRAS 04158	2.9 ± 0.6
Oph 163131	2.6 ± 0.1
ESO-Hα 569	2.3 ± 0.2

Notes. The millimeter spectral indices were calculated using the fluxes from Table 3 together with literature measurements (references for these are reported below). No spectral indices are reported for ESO-Hα 574 and HH 48 NE because they were observed in only one millimeter band.

References. Tau 042021: Andrews et al. (2013), HH 30: Louvet et al. (2018), IRAS 04302: Moriarty-Schieven et al. (1994); Gräfe et al. (2013); Wolf et al. (2003), HK Tau B: Duchêne et al. (2003), HV Tau C: Andrews et al. (2013); Duchêne et al. (2010), IRAS 04200: Andrews et al. (2013), Haro 6-5B: Dutrey et al. (1996), IRAS 04158: Andrews et al. (2008); Motte & André (2001), Oph 163131: Cox et al. (2017), ESO-Hα 569: Wolff et al. (2017)

of them is well resolved along the minor axis at the resolution of the restoring beam, so variations can be more affected by beam dilution and are less reliable.

Finally, we point out that we obtain spectral index values lower than 2 in the innermost regions of two disks: namely Tau 042021 and IRAS 04200 (see also our radiative transfer model, Appendix C). Such low values have also been reported in the inner regions of other disks (e.g., Huang et al. 2018a; Dent et al. 2019), and have often been interpreted as flux calibration errors because in the Rayleigh-Jeans regime α should not be smaller than 2. However, considering a 10% flux calibration error (yellow shaded regions in Fig. 4), the lowest α values measured in Tau 042021 and IRAS 04200 can not be reconciled with $\alpha = 2$. Recent studies showed that low dust temperature (outside the Rayleigh Jeans regime) or dust scattering in optically thick regions can reduce significantly the emission of a disk. In both cases, the spectral index can be even lower than 2 (e.g., Liu 2019; Zhu et al. 2019). In the context of highly inclined disks such as Tau 042021 and IRAS 04200, which are optically thick, both explanations are equally valid to explain low spectral indices observed. Modeling is needed to determine which one is dominant.

To summarize, because of the high inclination of our sources, we interpret the observed variation of spectral indices along the major axis as being dominated by optical depth changes in the disks. Additionally, we find that the low spectral index values measured in Tau 042021 and IRAS 04200 can either be related to low dust temperatures or to dust scattering in optically thick regions.

3.4. Comparison with optical and NIR images

We present overlays of optical and NIR images with our band 7 observations in Fig. 5. For most disks, we use HST optical images but prefer (space-based or ground-based) near-infrared (NIR) images in a handful of cases to reduce confusion with extended nebulosity (see references in Fig. 5). All scattered light images show the same characteristic features, with two bright reflection nebulae separated by a dark lane tracing the obscuration of direct starlight by the edge-on disk. As opposed to the scattered light images, the millimeter data appear as very flat disks. All sources are found much less extended vertically in the millimeter than in scattered light, the result of a combination of opacity effects and vertical settling. Most of them also appear less extended radially, which can be linked to dust radial drift or opacity effects.

We estimate the scattered light major axis sizes by following the spine of each nebula (see method in Appendix D) and report the inferred radial sizes in Table 5. We could not estimate the scattered light sizes for two disks of the sample: for IRAS 04302 because we do not see the disk but the envelope; and for IRAS 04200 because the bright point source in the northern nebulae prevented the method to converge. Also, we indicate that our scattered light radial sizes might be under-estimated because lower illumination or lower sensitivity in the outer regions might reduce the apparent optical-NIR size (see for example Muro-Arena et al. 2018). A complete analysis will require the use of tracers of the gas distribution, which we postpone to a future paper.

Despite this, we find that most sources are larger radially in scattered light than in the millimeter, albeit with a few exceptions, the most obvious case being HV Tau C. ESO-Hα 574, and HH 48 NE, although formally more compact in scattered as estimated with our algorithm, have very similar sizes and will require deeper millimeter data for confirmation.

The ratios of scattered light over thermal continuum band 7 sizes are between 0.7 and 2.0. This is in general consistent with predictions from radial drift theory: the objects with clear evidence for radial drift being those in which scattered light disk (small grains) is significantly larger than the millimeter continuum disk (large grains). While we do not quantify explicitly the vertical extent of the scattered light images, Fig. 5 clearly shows that all disks are significantly more extended vertically in scattered light than at millimeter wavelengths, which indicates vertical settling has occurred in each disk.

4. Discussion

In this section, we use the brightness profiles of the highly inclined disks of our sample to discuss critically the amplitude of vertical dust settling, radial drift, and the effects of the enhanced optical depth due to projection effects. To this effect we constructed several toy disk models and performed radiative transfer with the MCFOST code (Pinte et al. 2006, 2009) to produce synthetic images for comparison with the data. The toy models include a disk without rings or gaps and have an outer radius of 140 au (1″). We assume that the surface density follows a truncated power law. The synthetic images are computed with and without vertical dust settling.

For the model without settling (NS), the dust is well mixed with the gas and assumed to have a scale height of 10 au at a radius of 100 au. For the model with dust settling (S), we assume that, as a function of size, dust follows

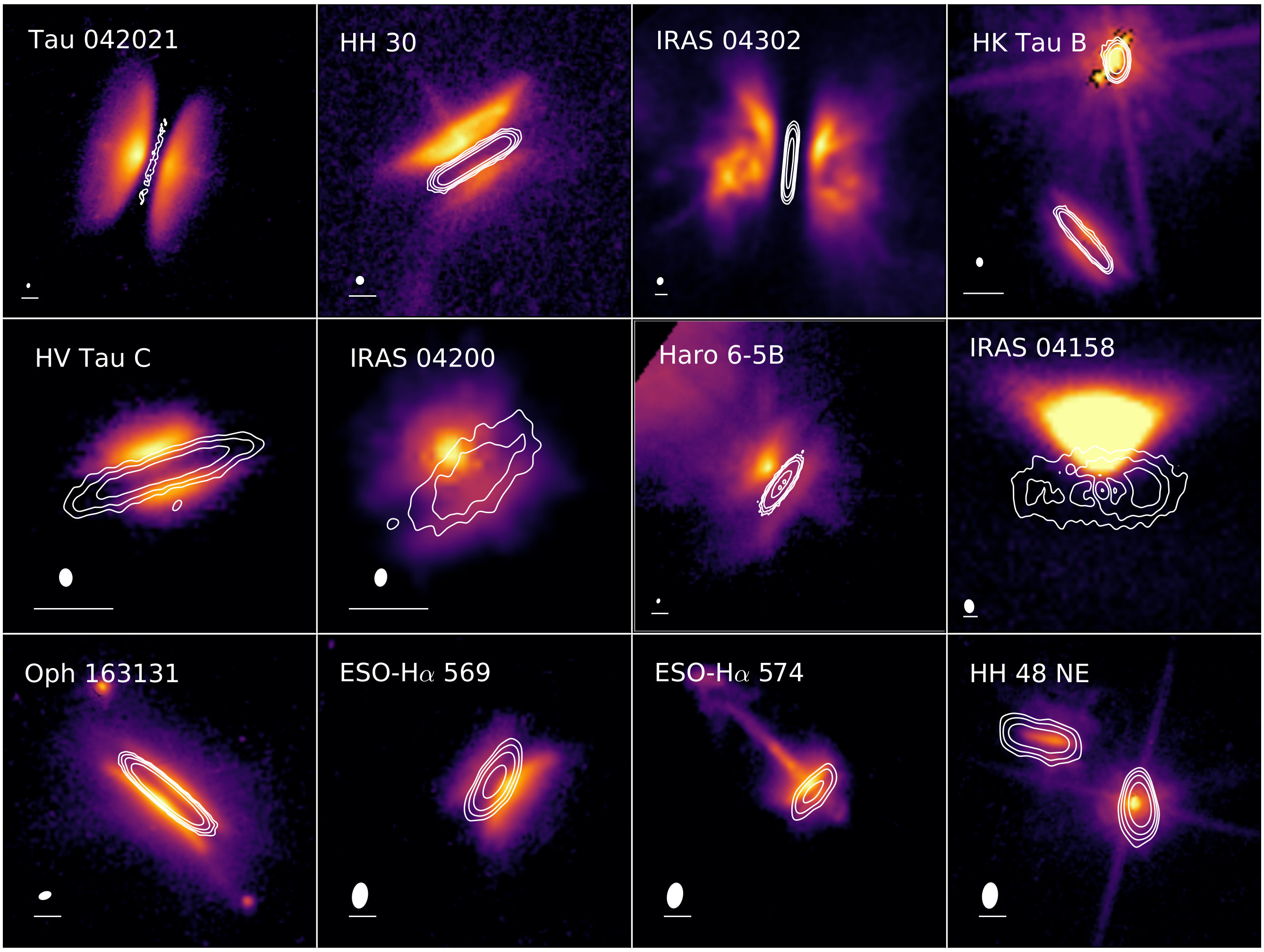

Fig. 5. Overlay of scattered light (colors, in logarithmic scales) and ALMA band 7 continuum images (5, 10, 20, and 50σ contours) for all sources in this study, except for Oph 163131 for which we show the band 6 image. The scattered light images are plotted between 3σ (except for IRAS 04302 and IRAS 04158, where we use respectively 60 and 1σ to increase the contrast) and their maximum brightness (except for IRAS 04158, for which we take a lower value to increase the contrast). The ellipse and horizontal line in the bottom left corner indicate the beam size of the ALMA image and a 0.5″scale.

References. Scattered light images, **2.2 μm:** HV Tau C: Duchêne et al. (2010); **1.9 μm:** IRAS 04302: Padgett et al. (1999); **1.6 μm:** Haro 6-5B: Padgett et al. (1999); **0.8 μm:** Tau 042021: Duchêne et al. (2014), HH 30: Watson & Stapelfeldt (2004), IRAS 04158: Glauser et al. (2008), ESO-Hα 569: Wolff et al. (2017), HH 48 NE: Stapelfeldt et al. (2014); **0.6 μm:** IRAS 04200: Stapelfeldt et al. (in prep), Oph 163131: Stapelfeldt et al. (2014), ESO-Hα 574: Stapelfeldt et al. (2014); **0.4 μm:** HK Tau B: Duchêne et al. (in prep).

the vertical density profile prescribed by Fromang & Nelson (2009). Following the results from Pinte et al. (2016) for HL Tau, a very flat disk when observed with ALMA, we set the vertical distribution of the millimeter dust (expressed in terms of a "scale height") to be $h_{1\mathrm{mm}} = 0.7$ au at 100 au. This corresponds to a disk viscosity coefficient of $\alpha = 3 \cdot 10^{-4}$.

The toy model is also calculated for two different dust masses in order to probe the effect of optical depth. We consider intermediate to high mass disk models based on the upper limits on the dust mass derived for our sample of highly inclined disks (Section 4.3.1). We use $M_{\mathrm{dust}} = 1 \cdot 10^{-3} M_\odot$ for high mass disk models (HM), and $M_{\mathrm{dust}} = 5 \cdot 10^{-5} M_\odot$ for low mass models (LM). In total four different sets of images are calculated. We use a distance of 140 pc.

We computed the models at 0.89 mm (resp. 2.06 mm) for inclinations between 75° and 90°, and produced synthetic images using the CASA simulator with the same uv-coverage as our band 7 (resp. band 4) data. The synthetic band 7 images (0.89 mm) of each model are presented in Fig. 6. The band 4 images are qualitatively similar as those presented in Fig. 6 but slightly less extended in the vertical direction.

We also generated band 7 and band 4 model images with a unique angular resolution using a `uv-taper`. Using these maps, we computed the brightness temperatures and spectral index maps of the models, which are presented in Appendix B and C.

4.1. Constraints from the surface brightness profiles

4.1.1. Vertical extent

For the high and low mass models presented in Fig. 6, we see that the disks appear less extended in the minor axis di-

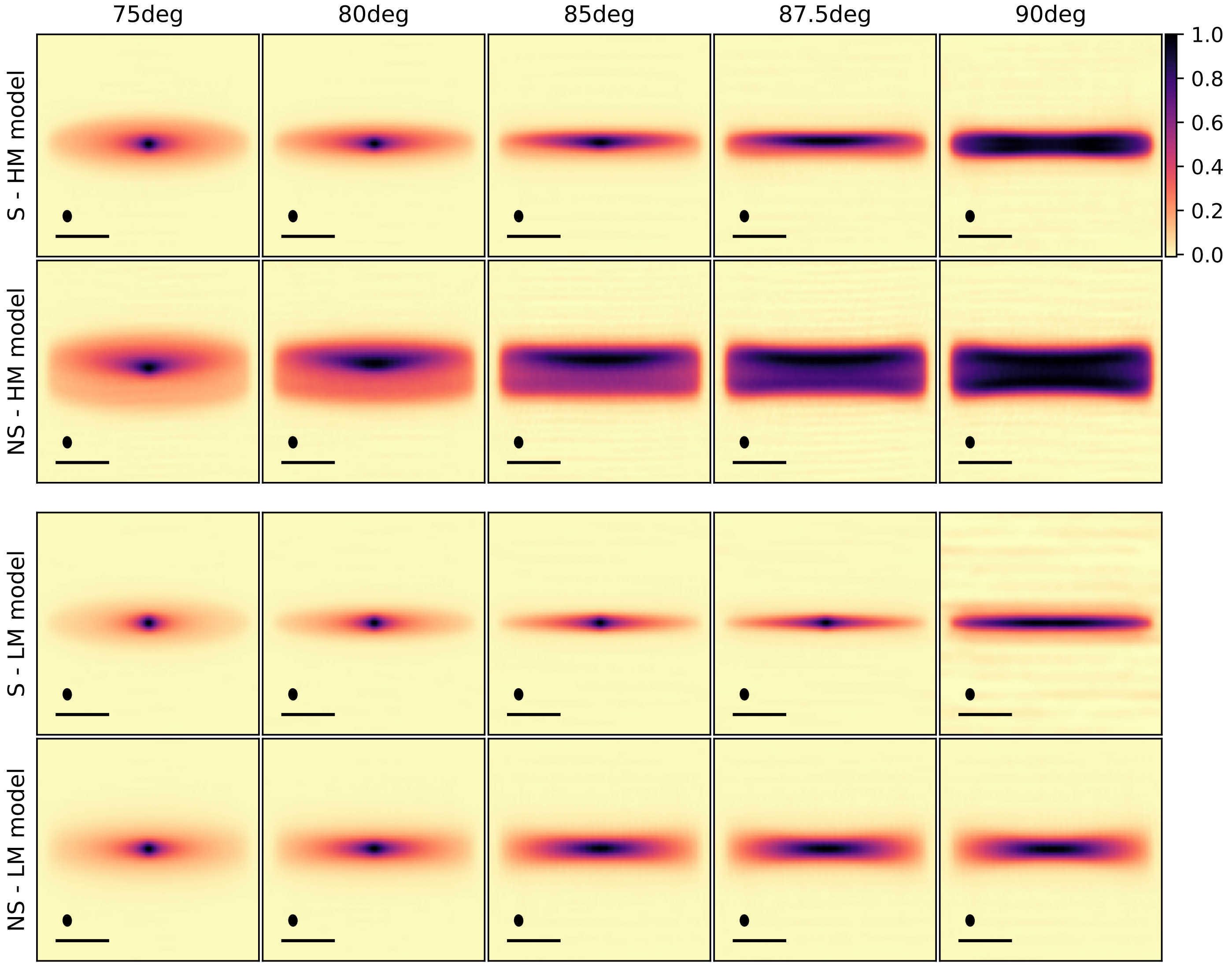

Fig. 6. Radiative transfer models computed at 0.89 mm (band 7), for different inclinations. *Top and third row:* High and low mass settling models ($h_{1mm} = 0.70$ au at r=100 au), *Second and bottom row:* High and low mass No Settling models ($h_{1mm} = h_{gas} = 10$ au at r=100 au). The beam size and a 0.5″ scale bar are shown in the bottom left corner of each panel.

rection when settling is included. For the high mass model without settling (model NS-HM), we find that as the inclination approaches 90°, the high optical depth in the midplane results in a clear low intensity lane, separating the two sides of the disk. On the other hand, at lower inclinations the bottom (far) side of the disk is about 5-6 times fainter than the top (near) side. This is visible directly in Fig. 6 and highlighted in a different way by showing cuts along the minor axis in Fig. 7 for inclinations of 80° (fainter back side) and 90° (dark lane). As the angular resolution is similar and the signal-to-noise is greater than 14 for all targets included in this study, such an asymmetry would be detectable easily in our observations. However, neither the vertical asymmetry nor the dark lane in the midplane are present in our data. This configuration (NS-HM) can be ruled out. Interestingly, the features can hardly be seen in the high mass model which includes settling, nor in any of the low mass models. If the disks included in our sample are as massive as the high mass model, this would indicate that they have a small millimeter dust scale height, closer to 1 au than to 10 au at a radius of 100 au. This is similar to the results of Pinte et al. (2016) for the disk of HL Tau.

To go further, the deconvolved minor axis sizes of the models can be compared with the average size obtained for the most inclined disks of our sample (i.e., with $i > 80°$). For the data, the mean deconvolved minor axis size is about 0.18″ in band 7 (0.17″ in band 4, see Table 6). Except for the high mass model without settling (model NS-HM), which is more than twice as thick as the observations (deconvolved minor axis size ∼ 0.4″ at 80° and 90°), all models studied in this section are compatible with the vertical extent measured in the data (in band 7, typical deconvolved sizes of ∼ 0.2″ for S-HM, NS-LM at 80° and 90°, and for S-LM at 80°, and ∼ 0.1″ for S-LM at 90°). Thus, the vertical extent alone is not sufficient to distinguish whether vertical settling is required to explain the observations or not.

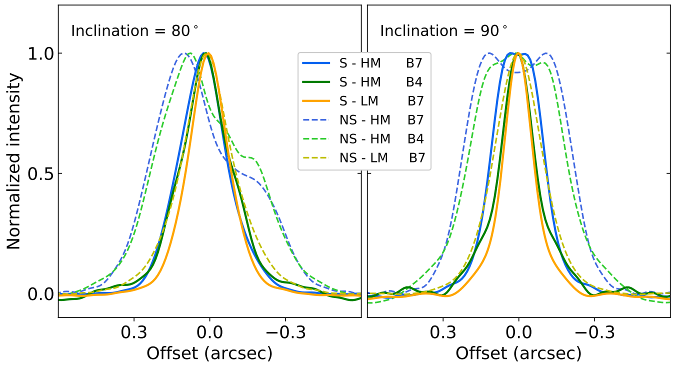

Fig. 7. Normalized averaged minor axis profiles for the high and low mass settling models (solid lines) and No Settling models (dashed lines) computed at 0.89 mm (band 7), at 80° (left panel) and 90° (right panel).

4.1.2. Radial brightness profile

We now investigate the effect of inclination on the observed radial brightness profiles. To do so, we produce major axis cuts of our radiative transfer models, as in Section 3.2.1, and present them in Fig. 8. We also estimate the apparent sharpness between 20% and 80% of the peak flux ($\Delta r/r$) for our models as in Section 3.2.1, and report them in Table 8.

Along the major axis, the effect of inclination on the shape of the brightness profile is very clear both in the images (Fig. 6) and in the cuts (Fig. 8). For all models, at the lowest inclinations, the images and cuts show a steep increase in intensity at the center, and low apparent edge sharpness ($\Delta r/r > 1$ for $i < 80°$). On the contrary, for the fully edge-on configuration ($i = 90°$), the major axis brightness profile of the high mass models is flat at all radii and drops steeply ($\Delta r/r \sim 0.2$ at 90° for both high mass models S-HM and NS-HM). Between these extreme cases, the cuts show a less extended plateau and shallower outer edges than for the 90° case, related to lower optical depth than in the edge-on case. We note that in the low mass models, which are optically thinner, the flat plateau along the major axis direction is never reached and the apparent disk sharpness is always larger than $\Delta r/r > 0.6$. Nevertheless, we find that, independently of the dust mass assumed for the models, the apparent sharpness of the disk outer edge increases with increasing inclination.

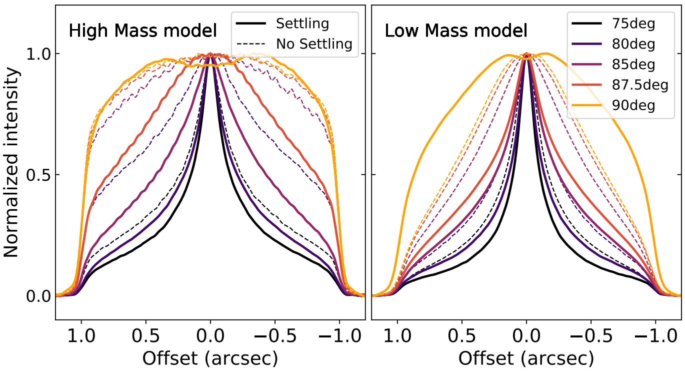

Fig. 8. Normalized major axis intensity profiles for the high mass (left) and low mass (right) models at 0.89 mm, for different inclinations between 75° and 90°.

Table 8. Effect of inclination on the apparent edge sharpness $\Delta r/r$ for our radiative transfer models.

Incl (deg)	S - HM	NS - HM	S - LM	NS - LM
75	1.7 ± 0.3	1.7 ± 0.2	1.5 ± 0.4	1.5 ± 0.3
80	1.7 ± 0.2	1.2 ± 0.1	1.6 ± 0.3	1.6 ± 0.3
85	1.5 ± 0.1	0.4 ± 0.1	1.6 ± 0.2	1.2 ± 0.1
87.5	0.9 ± 0.1	0.2 ± 0.1	1.6 ± 0.2	1.0 ± 0.1
90	0.2 ± 0.1	0.2 ± 0.1	0.6 ± 0.1	1.0 ± 0.1

Three disks in our sample show edges as sharp as 0.3. They are HH 30, HK Tau B, and HH 48 NE. The comparison with models suggests that these disks are the most inclined of the sample. Additionally, these disks present flat radial brightness profiles that the low mass models are unable to reproduce. This indicates that they are optically thicker than the low mass model, likely because they are more massive. In Section 4.1.1, we have shown that a more massive disk, while leading to a flat profile along the major axis direction also presents a larger vertical extent. Our high mass model without settling is inconsistent with the observations (see Fig. 6, NS-HM model). This implies that vertical settling is needed to explain both the flat radial profile and small apparent vertical extent of these three disks. For these systems the millimeter scale height would be closer to 1 au than to 10 au at 100 au, therefore increasing significantly the concentration of dust mass in the disk midplane. Although we can not confirm vertical settling for the other sources, we believe that their vertical structure is likely similar and governed by settling, in particular because of the large vertical size difference between the scattered light and thermal emission images.

Vertical settling models show that the turbulence generated self-consistently by ideal MHD or vertical shear instabilities are likely too strong to lead to millimeter scale height as small as 1 au at r = 100 au for gas scale heights of 10 au at 100 au (Flock et al. 2017, 2020). On the other hand, non-ideal effects such as ohmic resistivity or ambipolar diffusion lead to lower turbulence and thus to very thin millimeter grain layers (Riols & Lesur 2018). Those mechanisms may well be dominant in the sample of disks analyzed here. Detailed modeling of each individual object is needed to obtain a quantitative estimate of the millimeter dust and gas scale height of the disks.

4.2. Comparison with a radial drift model

Similarly to previous multi-wavelength studies (e.g., Pérez et al. 2012; Tripathi et al. 2018; Powell et al. 2019), our observations show that 4 disks have major axis sizes that decrease with wavelength (namely Tau 042021, IRAS 04302, IRAS 04200, Haro 6-5B, see Table 5 and the radial variation of their spectral index in Fig. 4). For these disks, the average size difference between band 7 and band 4 observations is about 12%. Estimating the major axis sizes from our radiative transfer models described in Section 4 (which do not include radial drift), we find that opacity effects alone predict a difference of only a few percents between bands, which is not sufficient to reproduce the observations. In this section, we compare the measured radial differences with an analytical radial drift model, presented by Birnstiel & Andrews (2014). Similarly to other theoretical models, they showed that inward dust migration of single size particles spontaneously produces a sharp edge in the dust density distribution (Birnstiel & Andrews 2014; Facchini et al. 2017; Powell et al. 2019). Birnstiel & Andrews (2014) computed an analytical formula to infer the position of the disk outer edge in a disk with radial drift only (see their equation B9). The vertical extent of the grains is not considered in their model. They assume a smooth tapered-edge gas surface density profile and parametrize the turbulence following Shakura & Sunyaev (1973).

Assuming that the band 7 and band 4 emission only originate from grains of the optimal size ($a \approx \lambda/2\pi$), the model by Birnstiel & Andrews (2014) predicts a size difference in surface density between band 7 and band 4 of about 25% (after 0.1 Myr). While the predicted effect is marginally too strong, the absolute disk sizes are more problematic. When grains of 0.1 μm detectable in scattered light are expected to be found up to 135 au after 0.1 Myr, the model predicts that grains emitting most at 0.89 mm should have drifted to 42 au. This corresponds to a micron/millimeter disk radius ratio greater than 3, which is more than 1.5 times larger than the largest ratio measured in our data. Part of these differences might be explained because the observations are not probing the surface density of the disk, because several grain sizes (that might have drifted to different radii) have to be considered rather than a unique one, or because our disks are older than 0.1 Myr so they might be affected by viscous spreading as well. Besides, as discussed previously (Section 3.4), we note the scattered light images might not always trace the whole disks, since they require illumination (and sufficient optical depth) to trace the disk all the way to the edge. This can lead to apparent sizes in scattered light that are smaller than the real radial extent of small grains. However, the small expected sizes at millimeter wavelengths suggest that this radial drift model is too efficient to reproduce the observations (see also Brauer et al. 2007). The existence of pressure fluctuations in the disks (e.g., rings and gaps tracing pressure bumps and dust traps) rather than smooth power law surface density profiles are expected to slow down the drift efficiently (see, e.g., Gonzalez et al. 2017; Pinilla et al. 2012) and help reconcile models with observations. We speculate that the disks included in our study may have complex radial structures to slow down the radial migration of dust.

4.3. Effect of inclination on global values

Most Class II disk surveys in close-by star-forming regions estimate dust masses directly from the measured integrated fluxes assuming optically thin disks, irrespective of the disk inclinations (e.g., Andrews et al. 2013; Ansdell et al. 2016; van der Plas et al. 2016). However, because of the projection effect, the optical depth along the line-of-sight increases with inclination and will affect the observed flux. In this section, we investigate the impact of inclination on integrated fluxes, dust mass estimations, and integrated spectral indices. Finally, we also discuss the measured brightness temperatures obtained for our disks in the context of optical depth.

4.3.1. Flux density and derived masses

We present the variation of the integrated band 7 and band 4 fluxes in our high mass radiative transfer models (with and without settling) as a function of inclination in Fig. 9. The effects of dust scattering are fully included in the radiative transfer calculations. Overall, the emitted flux density of the disk becomes attenuated by up to an order of magnitude with increasing inclination. This is due to a combination of the increasing optical depth, a lower average dust temperature seen by the observer for high inclinations, and to geometrical effects (reduced emitting surface with increasing inclination). In this model, from ~60° to 90°, the flux density and thus the derived disk mass would appear significantly smaller than for the same disk viewed at intermediate inclinations (by up to ~10 times for the high mass settled model). The amplitude of the attenuation depends on the parameters of the model. We note that in Fig. 9, the model without settling is brighter than the corresponding settled model for all inclinations. This is due to temperature differences between the settled and no settling models, to differences in optical depths and to geometrical effects. Similar behaviors are seen in the low mass models which are not represented.

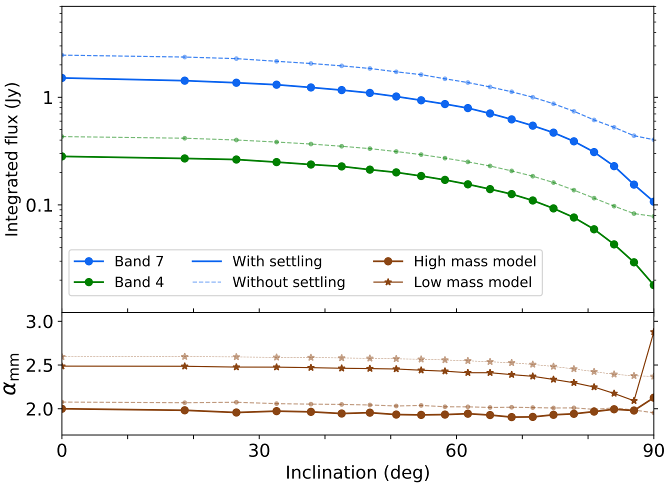

Fig. 9. *Top:* Variation of the band 7 and band 4 integrated fluxes of the high mass radiative transfer models with settling (thick lines) and without settling (thin lines) as a function of the inclination. *Bottom:* Variation of the integrated spectral index with inclination for both high and low mass radiative transfer models, with or without including settling.

This raises the question of the reliability of disk masses derived purely from millimeter fluxes, in particular for surveys where the disks are not well resolved and inclinations cannot be estimated. We focus here on the highly inclined disks of our sample. For a direct comparison with previous studies, we assume optically thin and isothermal dust emission at sub-millimeter wavelengths. In that case the flux (F_ν) is directly related to the dust mass following: $M_{\rm dust} = F_\nu d^2/\kappa_\nu B_\nu(T_{\rm dust})$, where d is the disk distance to the Sun, $B_\nu(T_{\rm dust})$ the Planck function evaluated at a mean representative dust temperature $T_{\rm dust}$, and κ_ν the *dust* grain opacity. We use typical values of $T_{\rm dust} = 20\,{\rm K}$ and $\kappa_\nu = 3.4\,{\rm cm^2\,g^{-1}}$, as in Ansdell et al. (2016, and references therein) to estimate the dust mass of the disks in the sample, using the band 7 fluxes. For the data, the results are reported in Table 9. As noted above, these masses are almost certainly underestimated and so we quote them as lower limits.

Table 9. Mass limits.

Sources	$M_{\rm dust\,B7}$ ($M_\oplus$)
Tau 042021	> 25.5
HH 30	> 11.2
IRAS 04302	> 54.8
HK Tau B	> 11.4
HV Tau C	> 18.6
IRAS 04200	> 13.4
Haro 6-5B	> 69.8
IRAS 04158	> 53.1
Oph 163131	> 25.8
ESO-Hα 569	> 13.6
ESO-Hα 574	> 3.1
HH 48 NE	> 7.1

Notes. Dust masses are estimated from the band 7 fluxes (Table 3), assuming optically thin emission, and therefore are lower limits (see text for details).

By applying the formula directly we find a mean dust mass of about 25 M$_\oplus$ for the 6 edge-on disks more inclined than 75°. For comparison, at an inclination of 90°, the estimated dust mass of both the high mass and low mass settled models are more than 3 times lower than the real dust mass. Without full modeling, it is difficult to find a reliable correction factor for individual sources to compensate the attenuation due to inclination. The disk masses of our highly inclined sample are probably a few times larger, that is up to ∼75 M$_\oplus$ when applying the same factor of 3. This is on the high end of the dust mass distributions of Taurus or Lupus star-forming regions (mean of 15 M$_\oplus$, Ansdell et al. 2016).

This result suggests that our sample of edge-on disks is biased toward more massive disks. This is a direct consequence of the important attenuation caused by the high inclination, making the starlight and the disk emission fainter. This may also explain, at least partly, why the number of known edge-on disks with resolved images remains sparse, even today. A comprehensive study of the biases affecting the edge-on disk population and their detection will be presented in Angelo et al. (in prep).

4.3.2. Integrated spectral indices

The median spectral index of the edge-on disks in our study, $\bar{\alpha}_{mm} = 2.5 \pm 0.3$, is similar to previous measurements of intermediate-inclination disks, for example 2.3 ± 0.1 in the Lupus and Taurus star-forming regions (Ribas et al. 2017; Ansdell et al. 2018). At first glance, this is surprising as edge-on disks are expected to appear more optically thick, but Sierra & Lizano (2020) showed that the spectral index is only mildly dependent on inclination based on an extensive study.

To further understand the integrated α_{mm} for edge-on disks, we computed them for our radiative transfer models. The expected values at different inclinations are shown in the bottom panel of Fig. 9. We find that the variation of spectral index with inclination is relatively small ($1.9 \lesssim \alpha_{mm} \lesssim 2.2$ for the high mass settled model, and $2.1 \lesssim \alpha_{mm} \lesssim 2.5$ for the low mass settling model for inclinations lower than 87°), in agreement with Sierra & Lizano (2020). This is because the models are (at least partially) optically thick even at low inclination and because large grains are included (maximum grain size is 3 mm). The small difference in integrated spectral index observed between our sample of edge-on disks and disks at lower inclinations can be explained if most disks are partially optically thick at millimeter wavelengths and/or if grains have grown to millimeter/centimeter sizes. Grain growth is known to have occurred in class II disks, leading to low spectral indices (Ricci et al. 2010; Testi et al. 2014). Similarly, recent imaging campaigns have revealed that ring structures are very common in protoplanetary disks (Huang et al. 2018b) and generally associated with optically thick regions with large grains (e.g., Dent et al. 2019). So far, the edge-on disks in our sample appear similar to the disks observed on other surveys, except from their viewing angle.

Interestingly, for inclinations greater than 70° for the high mass or 87° for the low mass model, we find a clear difference in the integrated spectral index between the models with and without settling. While at these inclinations the spectral index decreases in the models without settling (see also Galván-Madrid et al. 2018), we find that the integrated spectral index increases for the settled models, reaching about 2.2 at 90° for the high mass model (2.8 for the low mass model). This can be explained by the contribution of the optically thick midplane that decreases for increasing inclination (as it appears colder) while the contribution of the upper layers (rich in small grains with higher β values) increases, leading to higher values of the integrated spectral indices for the settled model (see, e.g., Fig. C.1). Said differently, for very large inclinations several line-of-sights do not cross the disk midplane containing large grains but only the high altitude layers above and below it. Since these layers are optically thinner and contain only small grains, the spectral index increases. However, further studies are required to investigate this effect (e.g., Sierra & Lizano 2020) and its applicability to specific objects.

4.3.3. Brightness temperatures

Assuming that scattering is negligible and that the dust temperature is high enough (e.g., in the Rayleigh-Jeans limit) and constant over the emitting region, the brightness temperature of dust emission at frequency ν can be expressed as $T_B = \eta_c\ T_p\ (1 - e^{-\tau_\nu})$, where τ_ν is the optical depth of the medium, T_p the mean dust physical temperature (see e.g., Wilson et al. 2009), and η_c the fraction of beam covered by the source. In the isothermal optically thick limit ($\tau_\nu \gg 1$), for a source filling the beam (but smaller than the largest angular scale of the interferometric observations) the brightness temperature corresponds to $T_p - 2.7$ K, because the cosmic microwave background (CMB) is resolved out by the interferometer. For compact sources, beam dilution would reduce the observed brightness temperatures below T_p. Scattering is also known to decrease dust emission from very optically thick regions, which would also effectively lead to lower observed brightness temperatures (Zhu et al. 2019). The brightness temperatures were estimated in Section 3.1. Major axis cuts are presented in Fig. B.1 and we report the peak brightness temperatures in Table 4.

We estimate a mean peak brightness temperature of 10.6 K for the three best resolved sources in band 7 (Tau 042021, IRAS 04200, and Haro 6-5B). These values are particularly low compared to previous estimates on other disks around stars of similar spectral types. As an example, Andrews et al. (2018) derived a mean brightness temperature peak of 66.5 K for the 17 disks of the DSHARP sample around K & M stars observed in band 6. These disks have a mean inclination of 42°, while all disks of our study are more inclined than 65°. The brightness temperatures we derive for our disks are also much lower than the traditional $T_{dust} = 20\,\mathrm{K}$ assumed in flux-to-mass conversions (see e.g., Section 4.3.1).

Although the measured brightness temperatures are integrated over some vertical extent because of the beam size, and therefore include a vertical temperature gradient, for the well-resolved disks T_B does provide a reasonable estimate of the temperature of the outer midplane where the line-of-sight optical depth reaches unity. This is the case for Tau 042021 for example. The low brightness temperatures measured in these optically-thick edge-on systems is likely to reflect the midplane temperature in the cold outer radii of the disks. This in agreement with the idea that the disks appear optically thick because of projection effect.

4.4. Individual targets

4.4.1. HK Tau B: Comparison with a published model

HK Tau B is the only Class II disk of the sample which is resolved by ALMA in the minor axis direction (in band 4) and for which the scattered light image has been modeled previously. Stapelfeldt et al. (1998) estimated the scale height of micron-sized grains to be on the order of 3.9 au at 50 au (8.3 au at 100 au, assuming a flaring exponent of 1.1 as in Stapelfeldt et al. 1998). Aiming for a quantitative comparison of scale height between millimeter and micron-sized grains, we computed their best model C at millimeter wavelengths (at 0.89 mm and 2.06 mm) using the radiative transfer code MCFOST. The parameters of the model are reported in Table 1 of Stapelfeldt et al. (1998) and the 0.8 μm image of the model can be found in their Fig. 3. Following the results of Duchêne et al. (2003), we adopt revised opacities in our model, leading to a revised disk dust mass of $5.9\times10^{-5}\,\mathrm{M}_\odot$ to match the observed millimeter fluxes. We use silicate dust grains with sizes from 0.01 μm to 15 cm and assume a number density described with a power law of the grain size $dn(a) \propto a^{-3.5}da$. This yields opacities of $4.8\,\mathrm{cm}^2/\mathrm{g}$ and $2.6\,\mathrm{cm}^2/\mathrm{g}$ (per dust mass) respectively at 0.97 mm and 2.06 mm. Assuming a gas-to-dust mass ratio of 100, this is comparable to standard assumptions (e.g., Beckwith et al. 1990, $0.048\,\mathrm{cm}^2/\mathrm{g}$ and $0.026\,\mathrm{cm}^2/\mathrm{g}$ of gas and dust, respectively). For a direct comparison, we assume that grains of all sizes are fully mixed and produce synthetic images using the CASA simulator with the same uv coverage as in our observations. We show the results in Fig. 10.

We find that the model does not reproduce well the millimeter images of HK Tau B. Along the major axis, the model is too peaked at the center (less flat-topped) and more extended in the radial direction than the actual millimeter data. As discussed in Section 4.1.2, the more peaked profile suggests that the observed millimeter disk is more optically thick than what is predicted by the model. While the best model of Stapelfeldt et al. (1998) contains a full disk at an inclination of 85°, we suggest that a higher inclination, closer to 90° (see Section 4.1.2), or the presence of a large but unresolved inner cavity would reproduce better the major axis brightness profile.

Along the minor axis, the band 4 cut indicates that the model is also more extended vertically than the data (see Fig. 10). As previously proposed by Duchêne et al. (2003) this hints for vertical segregation of dust grains in this disk, millimeter grains being located in a vertically thinner layer than micron-sized grains. However the low signal-to-noise of the band 4 data and the low angular resolution in band 7 prevent us from a strong conclusion.

4.4.2. Vertical settling in Tau 042021

Tau 042021 is the only edge-on disk clearly resolved vertically in both band 7 and band 4. For this disk, the band 7 appears about 1.5 times more extended vertically than the band 4 (see Table 6). We note that Tau 042021 is only marginally resolved in band 6, so the size at this wavelength is uncertain. For our high mass radiative transfer model without settling (i.e., including only optical depth effects), we find a band 7 to band 4 minor axis ratio of about 1.1 at $i = 90°$ (respectively 1.2 for the low mass settled model), significantly smaller than the observed value. Although this model is not unique, it indicates that opacity effects are not sufficient to produce the large difference in minor axis size observed, which suggests that grain-size-dependent vertical settling is occurring in this disk as well. In this section, we compare the measured minor axis ratio with predictions from several vertical settling models. We assume that the disk is perfectly edge-on so that variations along the minor axis are dominated by differences in vertical extent between bands rather than projections of the disk radius.

From the minor axis ratio measured in Tau 042021, one can estimate the scaling of the minor axis size (S_d) with grain size (a) assuming $S_d \propto a^{-m}$. Assuming that most of the emission comes from grains of the optimal size ($a \approx \lambda/2\pi$), we obtain: $m = -\log(S_{d,b7}/S_{d,b4})/\log(a_{b7}/a_{b4}) \sim 0.5$.

If we additionally assume that S_d is directly proportional to the dust "scale height" ($\mathrm{h_d}$), an exponent of $m = 0.5$ has been predicted for large grains in the context of a 1-D diffusion theory (Dubrulle et al. 1995). Performing numerical simulations including non-ideal MHD effects such as ambipolar diffusion, Riols & Lesur (2018) also estimated a relationship of dust scale height with grain size with an exponent of 0.5, valid for large grains ($St \gtrsim 10^{-2}$). For comparison, using the standard disk model presented in Riols & Lesur (2018, equation 13), at 100 au, grains of the optimal size emitting in band 7 would have Stokes numbers larger than $2.5 \cdot 10^{-2}$.

On the other hand, Fromang & Nelson (2009) estimated that in the case of ideal MHD, the dust scale height varies as: $\mathrm{h_d} \propto a^{-0.2}$. Settling obtained with ideal MHD is expected to be less efficient than other models previously discussed. However, we note that this expression was estimated for small grains ($St \leq 10^{-2}$) and might not apply for the grain sizes that we are probing at millimeter wavelengths.

To summarize, we find that the large minor axis difference observed in Tau 042021 at different millimeter wavelengths has to be associated with strong settling. To compare our observations with settling models, we make the assumption that the measured minor axis extent is proportional to the real dust scale height. While ideal MHD simulations predict a settling less efficient than observed, a simple 1-D diffusion theory (in the case of strong settling,

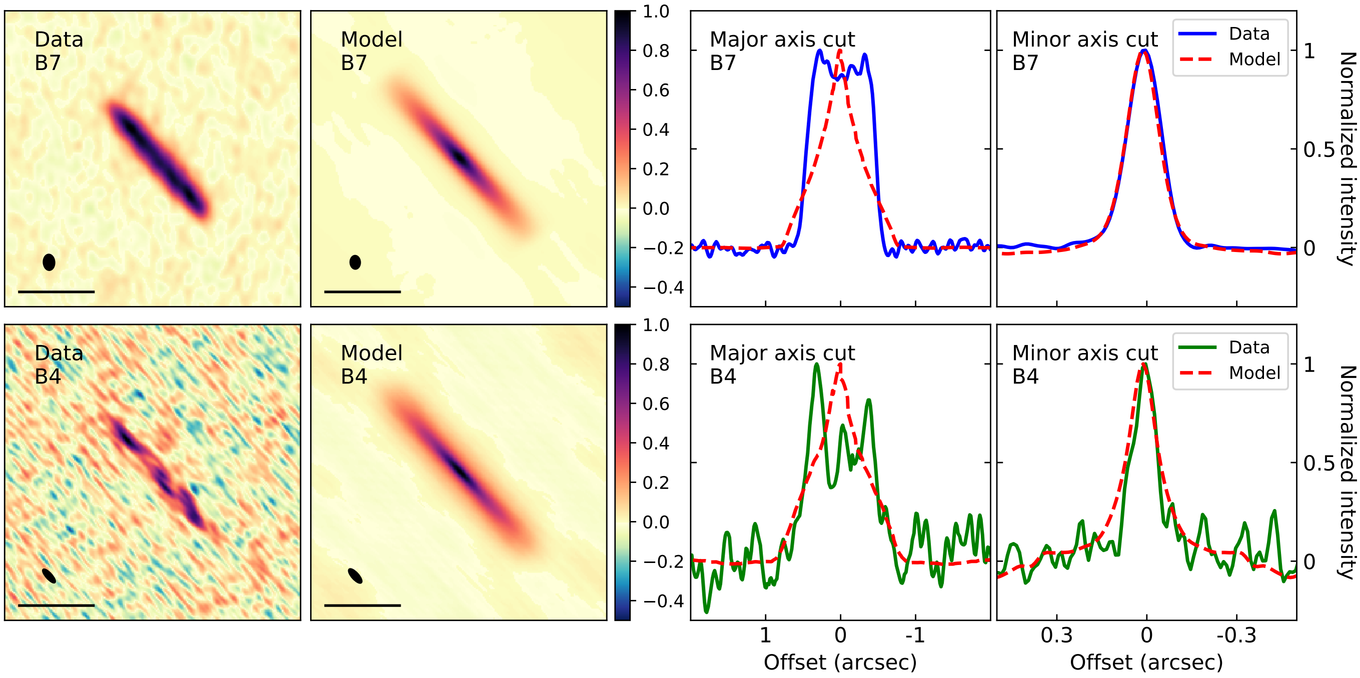

Fig. 10. *Left panels:* ALMA data of HK Tau B. In all the figure, top row is band 7 and bottom row is band 4. *Middle-left panels:* Millimeter images of the best model C of Stapelfeldt et al. (1998), assuming well mixed grains. They were computed for the same uv-coverage as in the data. *Middle-right panels*: Major axis cuts of the model and the data. *Right panels*: Averaged minor axis cuts of the data and the models, performed as in Section 3.2.2.

Dubrulle et al. 1995) or numerical simulations including non-ideal MHD effects (Riols & Lesur 2018) provide for now the best consistency with the observations.

4.4.3. Radial variation of vertical extent in IRAS 04302

The high resolution band 4 disk image of IRAS 04302 shows evidence of flaring: the extent perpendicular to the disk midplane at large radii is broader than at the center (see Fig. 1). This is in contrast with the other disks in our survey, which are flatter or unresolved. Fig. 11 compares the minor axis sizes at different radii in IRAS 04302 with the other well-resolved edge-on disk with large signal-to-noise: Tau 042021. In the latter case, the vertical extent appears quasi constant as a function of radius with only a slight increase in the outer regions, whereas it is ∼50% larger in IRAS 04302 at a projected radius of 100 au (0.7″) than at the center. This might be related to differences in optical depth or settling between the disks. Additionally, IRAS 04302 is the only Class I object in our sample (Gräfe et al. 2013) and the scattered light image does not show the flared upper surface of a disk, like in the other objects (Class II, see Fig. 5), but instead traces an envelope. Objects like this one, and HH 212 a Class 0 (Lee et al. 2017), open the possibility to do comparative studies of disk evolution in the early phases.

5. Summary and conclusions

We presented high angular resolution ALMA band 7 and band 4 observations of 12 highly-inclined disks previously selected from the shape of their scattered light images. All disks are well resolved along the major axis and 6 are also resolved in the direction perpendicular to the disk midplane

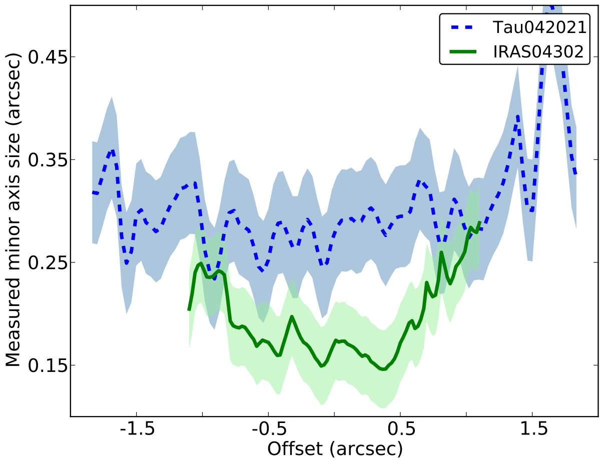

Fig. 11. Minor axis size as a function of radius for IRAS 04302 (band 4) and Tau 042021 (band 7). The errors correspond to the standard deviation of the curves.

in at least one millimeter band. Several disks show flat surface brightness profiles along their major axis with a steep drop off at their outer edge, indicating their large inclination and significant optical depth.

Haro 6-5B and IRAS 04158 are the least inclined disks of the sample (less than 75°) and both show a distinct ring and an isolated emission peak at the center. At the highest angular resolution, the point source at the center of IRAS 04158 is a binary source.

The analysis of global quantities such as integrated fluxes, spectral indices, and brightness temperatures shows that the highly inclined disks of our sample have (at least partly) optically thick emission. Because of the low brightness temperatures and small beam sizes, we conclude that the emission originates from the outer radii of the disks, with a peak brightness temperature below 10 K for half the sources in band 7.

We also found that the median spectral index in our disk sample is similar to that of disks seen at lower inclinations. This can be explained if disks at intermediate inclination are already partly optically thick (which implies significant scattering even at millimeter wavelengths) and/or if grains have grown to millimeter/centimeter sizes in all cases.

All disks were observed at several wavelengths with similar angular resolution, from the optical to the millimeter range. This enables a comparison of the radial extent of different grain populations in the disks (i.e., grain sizes). We assumed that the small dust responsible for the scattered light in the optical is tracing closely the gas distribution. Most disks have larger radial sizes in the optical-NIR than at millimeter wavelengths indicative of dust radial drift, the larger particles having drifted inward. Three of the disks have the same radial extent in both millimetric bands; these ones also have the sharpest apparent outer edges (estimated between 20% and 80% of the peak flux): $\Delta r/r \sim 0.3$. Four sources have band 7 emission which is radially more extended than band 4, by about 12% on average. However, current radial drift models predict larger differences - both between optical and millimeter, and between band 7 and band 4 - than we actually observe. This suggests that other mechanisms such as pressure traps are likely present in these disks to slow down or halt the radial drift.

The peculiar viewing angle of the disks presented in this survey allows us to obtain more direct information on their vertical structures. First of all, the direct comparison of the ALMA observations with scattered light data shows that these disks have larger vertical sizes in the optical-NIR than at millimeter wavelengths, indicative of the different optical depths and of vertical dust settling. To further estimate the vertical distribution of millimeter grains (parametrized as a "scale height"), we compared the shape of ALMA observations with four radiative transfer toy models of different mass, which include or not vertical settling. We computed the models at high inclinations, with the same angular resolution as our data, and considered two different values for the scale height of millimeter grains. We find that at least three disks of our survey require that the millimeter dust "scale heights" is low, of order of a few au at r=100 au: these disks are vertically thin at millimeter wavelengths. This is much thinner than the gas traced by the small dust, which has a typical scale height of 10 au (Burrows et al. 1996; Stapelfeldt et al. 1998).

On a case by case basis, for HK Tau B, a more detailed comparison of the ALMA images with a published scattered light model (re-computed at millimeter wavelengths) also suggests differences in vertical extent between millimeter and micron-sized grains, as previously suggested by Duchêne et al. (2003). Also, for Tau 042021, the only edge-on disk well resolved in the two millimeter bands, we find that the band 7 emission is about 1.5 times more extended vertically than the band 4. Assuming that the measured vertical extent is directly proportionnal to the dust scale height, this ratio is expected for relatively large dust grains in the simple 1-D diffusion theory or numerical simulations including non-ideal MHD effects (Dubrulle et al. 1995; Riols & Lesur 2018), further supporting the idea that strong vertical dust settling has taken place, leading to an increase in dust concentration in the disk midplane.

Finally, we find evidence of a more flared structure in IRAS 04302, suggesting that the millimeter grains in this Class I source are less settled. The millimeter dust in this disk may be in transition between the vertically unsettled structures seen in some Class 0 objects, and the flatter dust found in our Class II disks.

In forthcoming studies, we will present the CO gas distribution measured in these disks. We will also produce more detailed case by case models of selected targets to quantify the dust and gas density distribution profiles.

Acknowledgements. The authors thank the referee for the constructive comments which improved significantly the paper. The authors also thank Laura Perez and Eric Villard for useful discussions. MV, FM, MB, GvdP, CP acknowledge funding from ANR of France under contract number ANR-16-CE31-0013. This project was financially supported in 2019 and 2020 by the CNRS as part of its programme 80|PRIME. GD and ZT acknowledge support from NASA under grant 80NSSC18K0442 and NSF grant AST-1518332. KRS acknowledges funding from the Space Telescope Science Institute under GO grant 12514. CP acknowledges funding from the Australian Research Council via FT170100040 and DP180104235. FL acknowledges the support of the Fondecyt program No3170360. This paper makes use of the following ALMA data: ADS/JAO.ALMA#2016.1.00460.S, ADS/JAO.ALMA#2016.1.01505.S, ADS/JAO.ALMA#2016.1.00771.S and ADS/JAO.ALMA#2013.1.01175.S. ALMA is a partnership of ESO (representing its member states), NSF (USA) and NINS (Japan), together with NRC (Canada), MOST and ASIAA (Taiwan), and KASI (Republic of Korea), in cooperation with the Republic of Chile. The Joint ALMA Observatory is operated by ESO, AUI/NRAO and NAOJ.

References

Andrews, S. M., Huang, J., Pérez, L. M., et al. 2018, The Astrophysical Journal, 869, L41
Andrews, S. M., Liu, M. C., Williams, J. P., & Allers, K. N. 2008, ApJ, 685, 1039
Andrews, S. M., Rosenfeld, K. A., Kraus, A. L., & Wilner, D. J. 2013, ApJ, 771, 129
Ansdell, M., Williams, J. P., Trapman, L., et al. 2018, ApJ, 859, 21
Ansdell, M., Williams, J. P., van der Marel, N., et al. 2016, ApJ, 828, 46
Appenzeller, I., Bertout, C., & Stahl, O. 2005, A&A, 434, 1005
Barrière-Fouchet, L., Gonzalez, J. F., Murray, J. R., Humble, R. J., & Maddison, S. T. 2005, A&A, 443, 185
Beckwith, S. V. W., Sargent, A. I., Chini, R. S., & Guesten, R. 1990, AJ, 99, 924
Birnstiel, T. & Andrews, S. M. 2014, ApJ, 780, 153
Brauer, F., Dullemond, C. P., Johansen, A., et al. 2007, A&A, 469, 1169
Burrows, C. J., Stapelfeldt, K. R., Watson, A. M., et al. 1996, ApJ, 473, 437
Cánovas, H., Cantero, C., Cieza, L., et al. 2019, A&A, 626, A80
Cox, E. G., Harris, R. J., Looney, L. W., et al. 2017, ApJ, 851, 83
Dent, W. R. F., Pinte, C., Cortes, P. C., et al. 2019, MNRAS, 482, L29
Dubrulle, B., Morfill, G., & Sterzik, M. 1995, Icarus, 114, 237
Duchêne, G., McCabe, C., Pinte, C., et al. 2010, ApJ, 712, 112
Duchêne, G., Ménard, F., Stapelfeldt, K., & Duvert, G. 2003, A&A, 400, 559
Duchêne, G., Stapelfeldt, K., Isella, A., et al. 2014, in IAU Symposium, Vol. 299, Exploring the Formation and Evolution of Planetary Systems, ed. M. Booth, B. C. Matthews, & J. R. Graham, 111–112
Dullemond, C. P. & Dominik, C. 2004, A&A, 421, 1075
Dutrey, A., Guilloteau, S., Duvert, G., et al. 1996, A&A, 309, 493
Dzib, S. A., Loinard, L., Ortiz-León, G. N., Rodríguez, L. F., & Galli, P. A. B. 2018, ApJ, 867, 151
Facchini, S., Birnstiel, T., Bruderer, S., & van Dishoeck, E. F. 2017, A&A, 605, A16

Facchini, S., van Dishoeck, E. F., Manara, C. F., et al. 2019, A&A, 626, L2

Flock, M., Nelson, R. P., Turner, N. J., et al. 2017, ApJ, 850, 131

Flock, M., Turner, N. J., Nelson, R. P., et al. 2020, arXiv e-prints, arXiv:2005.11974

Fromang, S. & Nelson, R. P. 2009, A&A, 496, 597

Fromang, S. & Papaloizou, J. 2006, A&A, 452, 751

Galván-Madrid, R., Liu, H. B., Izquierdo, A. F., et al. 2018, ApJ, 868, 39

Glauser, A. M., Ménard, F., Pinte, C., et al. 2008, A&A, 485, 531

Gonzalez, J. F., Laibe, G., & Maddison, S. T. 2017, MNRAS, 467, 1984

Gräfe, C., Wolf, S., Guilloteau, S., et al. 2013, A&A, 553, A69

Guilloteau, S., Dutrey, A., Pety, J., & Gueth, F. 2008, A&A, 478, L31

Guilloteau, S., Dutrey, A., Piétu, V., & Boehler, Y. 2011, A&A, 529, A105

Haisch, Karl E., J., Greene, T. P., Barsony, M., & Stahler, S. W. 2004, AJ, 127, 1747

Huang, J., Andrews, S. M., Cleeves, L. I., et al. 2018a, ApJ, 852, 122

Huang, J., Andrews, S. M., Dullemond, C. P., et al. 2018b, ApJ, 869, L42

Kenyon, S. J., Gómez, M., & Whitney, B. A. 2008, Low Mass Star Formation in the Taurus-Auriga Clouds, ed. B. Reipurth, Vol. 4, 405

Krist, J. E., Stapelfeldt, K. R., Burrows, C. J., et al. 1998, ApJ, 501, 841

Laibe, G., Gonzalez, J.-F., Maddison, S. T., & Crespe, E. 2014, MNRAS, 437, 3055

Lee, C.-F., Li, Z.-Y., Ho, P. T. P., et al. 2017, ApJ, 843, 27

Li, A. & Draine, B. T. 2001, ApJ, 554, 778

Liu, H. B. 2019, ApJ, 877, L22

Long, F., Pinilla, P., Herczeg, G. J., et al. 2020, arXiv e-prints, arXiv:2006.03120

Long, F., Pinilla, P., Herczeg, G. J., et al. 2018, ApJ, 869, 17

Louvet, F., Dougados, C., Cabrit, S., et al. 2018, A&A, 618, A120

Luhman, K. L. 2007, The Astrophysical Journal Supplement Series, 173, 104

Luhman, K. L., Allen, P. R., Espaillat, C., Hartmann, L., & Calvet, N. 2010, The Astrophysical Journal Supplement Series, 186, 111

Moriarty-Schieven, G. H., Wannier, P. G., Keene, J., & Tamura, M. 1994, ApJ, 436, 800

Motte, F. & André, P. 2001, A&A, 365, 440

Mulders, G. D. & Dominik, C. 2012, A&A, 539, A9

Muro-Arena, G. A., Dominik, C., Waters, L. B. F. M., et al. 2018, A&A, 614, A24

Ortiz-León, G. N., Loinard, L., Dzib, S. A., et al. 2018, ApJ, 869, L33

Padgett, D. L., Brandner, W., Stapelfeldt, K. R., et al. 1999, AJ, 117, 1490

Pavlyuchenkov, Y., Akimkin, V., Wiebe, D., & Vorobyov, E. 2019, MNRAS, 486, 3907

Pérez, L. M., Carpenter, J. M., Chandler, C. J., et al. 2012, ApJ, 760, L17

Pinilla, P., Birnstiel, T., Ricci, L., et al. 2012, A&A, 538, A114

Pinilla, P., van der Marel, N., Pérez, L. M., et al. 2015, A&A, 584, A16

Pinte, C., Dent, W. R. F., Ménard, F., et al. 2016, ApJ, 816, 25

Pinte, C., Harries, T. J., Min, M., et al. 2009, A&A, 498, 967

Pinte, C., Ménard, F., Duchêne, G., & Bastien, P. 2006, A&A, 459, 797

Powell, D., Murray-Clay, R., Pérez, L. M., Schlichting, H. E., & Rosenthal, M. 2019, ApJ, 878, 116

Ribas, Á., Espaillat, C. C., Macías, E., et al. 2017, ApJ, 849, 63

Ricci, L., Testi, L., Natta, A., & Brooks, K. J. 2010, A&A, 521, A66

Riols, A. & Lesur, G. 2018, A&A, 617, A117

Shakura, N. I. & Sunyaev, R. A. 1973, A&A, 500, 33

Sheehan, P. D. & Eisner, J. A. 2017, ApJ, 851, 45

Sierra, A. & Lizano, S. 2020, arXiv e-prints, arXiv:2003.02982

Simon, M., Guilloteau, S., Beck, T. L., et al. 2019, arXiv e-prints, arXiv:1908.10952

Stapelfeldt, K. R., Duchêne, G., Perrin, M., et al. 2014, in IAU Symposium, Vol. 299, Exploring the Formation and Evolution of Planetary Systems, ed. M. Booth, B. C. Matthews, & J. R. Graham, 99–103

Stapelfeldt, K. R., Krist, J. E., Ménard, F., et al. 1998, ApJ, 502, L65

Stapelfeldt, K. R., Ménard, F., Watson, A. M., et al. 2003, ApJ, 589, 410

Stapelfeldt, K. R., Watson, A. M., Krist, J. E., et al. 1999, ApJ, 516, L95

Testi, L., Birnstiel, T., Ricci, L., et al. 2014, in Protostars and Planets VI, ed. H. Beuther, R. S. Klessen, C. P. Dullemond, & T. Henning, 339

Tripathi, A., Andrews, S. M., Birnstiel, T., et al. 2018, ApJ, 861, 64

van der Plas, G., Ménard, F., Ward-Duong, K., et al. 2016, ApJ, 819, 102

Villenave, M., Benisty, M., Dent, W. R. F., et al. 2019, A&A, 624, A7

Watson, A. M. & Stapelfeldt, K. R. 2004, ApJ, 602, 860

Weidenschilling, S. J. 1977, MNRAS, 180, 57

Williams, J. P. & Cieza, L. A. 2011, ARA&A, 49, 67

Wilson, T. L., Rohlfs, K., & Hüttemeister, S. 2009, Tools of Radio Astronomy

Wolf, S., Padgett, D. L., & Stapelfeldt, K. R. 2003, ApJ, 588, 373

Wolff, S. G., Perrin, M. D., Stapelfeldt, K., et al. 2017, ApJ, 851, 56

Zhu, Z., Zhang, S., Jiang, Y.-F., et al. 2019, ApJ, 877, L18

Appendix A: Beam sizes

We present the beam sizes obtained for the different observations in Table A.1. The last column describes the beam size of the maps used to compute the brightness temperatures and the spectral index maps.

Appendix B: Brightness temperature cuts

We present brightness temperature cuts along the major axis for all disks in Fig. B.1. Solid lines represent the band 7 and band 4 cuts computed with the same beam, for which we reported the peak temperature in Table 4. We also show the brightness temperatures calculated with the resolution of the images presented in Fig. 1 in light colors. We note that, as the beam sizes of the band 6 observations of Tau 042021 and HH 30 are significantly larger than the restored beam (see Table A.1), it is not possible to compare directly the band 6 brightness temperatures to band 4 and band 7, the beam dilution will be different. Moreover, a direct comparison of brightness temperature between sources is difficult as they would have different levels of beam dilution.

In Fig. B.1, we find that most sources do not show strong differences in brightness temperatures between the different angular resolution studied. Only the band 4 observations of Haro 6-5B and IRAS 04302 show important variations of the brightness temperature with the beam size. The temperatures obtained with the restored beam are smaller than those with the original angular resolution. For both objects, this likely indicates that the disk (or central point source for Haro 6-5B) is significantly less resolved with the restored beam than at the original angular resolution. This leads to a lower brightness temperature due to beam dilution.

In Fig. B.2, we present brightness temperature cuts at several inclinations computed for our radiative transfer models with and without including vertical settling. We also report the peak brightness temperatures obtained for our models in Table B.1. In each model, we find that as the inclination increases, the peak temperature decreases. This indicates that the disk becomes optically thicker with inclination. At the highest inclinations millimeter emission likely originates in the outer radii of the disk. We note that this is presumably also the case for several disks of our survey in which low brightness temperatures are measured even if they are well resolved (for example for Tau 042021).

Additionally, we find that, in the low mass models, the band 4 brightness temperatures are lower than the band 7 brightness temperatures. This is not the case for the high mass model where the band 4 brightness temperature can sometimes be higher than the band 7 temperature. In the observations, we detect large variations in brightness temperatures between bands (Fig. B.1, Table 4). While this suggest that the disks are optically thinner than the high mass models, further studies are needed to explain the differences in brightness temperature measured in the observations.

Appendix C: Spectral index maps of the high mass settled model

In order to interpret the spectral index maps shown in Fig. 4, we computed the spectral index map of our high mass settled radiative transfer model presented in Section 4 (the most representative of our observations, see Section 4.1), for inclinations between 75° and 90°. We show the maps on the top row of Fig. C.1, and display the major axis cuts in the disk midplane in the middle row and the averaged minor axis profiles in the bottom row. As in Section 3.2.2, we obtained the minor axis profiles over the full major axis for the disks that do not show ellipticity (i.e., more inclined than 80°), and over $\pm 0.15''$ for the least inclined models.

The spectral index maps of the models show several features also seen in the observations. First, for most inclinations, it reaches values lower than two in the midplane (as for Tau 042021 and IRAS 04200), which can indicate low temperatures or important scattering in the disk midplane. Second, at the highest inclinations, there is a slight increase in α_{mm} along the major axis, which is related to optical depth effects only. This variation is smaller than for several sources of our sample (e.g., Tau 042021, IRAS 04302, IRAS 04200 and Haro 6-5B) which suggests that these disks are affected by radial drift. Finally, for inclinations larger than 85°, the spectral index increases along the minor axis, similarly to what is measured in Tau 042021, which is likely related to optical depth effect and vertical settling.

Appendix D: Estimation of scattered light sizes

Here we describe a method to estimate the radial extent of edge-on disks as observed in scattered light. To measure the extents of the scattered light images of the disks, we first find a set of points to define the spine of each nebula. To this end, we extract cuts along the minor axis of the disk. When this cut contains two clear local maxima, we compute the centroid in a small region surrounding the peaks. If the two nebula are partially blended, or hard to disentangle, we perform a two-Gaussian fit, forcing the same FWHM of the two nebulae. The center of each Gaussian then defines the location of the spines. The process is initiated at the disk's axis of symmetry and we proceed outward on each side until the surface brightness drops below $1-7\%$ of the peak surface brightness, depending on the signal-to-noise of the image and adjusted to match the visually detectable edge of the disk. The result is two sets of points that define the spines of the bright and counter nebulae (blue and red points in Fig. C.1). Outliers, due to bad pixels or substructure in the disk, are excluded based on deviations from a running median. We then fit second-order polynomial functions to each nebula, which provides adequate morphological information while minimizing sensitivity to noise and low-level departures from symmetry. The radial extent (diameter) of the disk is then defined as the maximum distance between identified spine points along the major axis. We present an example of fit in Fig. D.1.

Table A.1. Beam sizes of our observations and restored beam used to compute brightness temperatures and spectral index maps.

Sources	B7		B6		B4		Restored B4 & B7	
	FWHM (″)	PA (°)	FWHM (″)	PA (°)	FWHM (″)	PA (°)	FWHM (″)	PA (°)
Tau 042021	0.12×0.08	-13	0.37×0.18	38	0.11×0.04	33	0.12×0.08	-13
HH 30	0.14×0.13	2	0.26×0.18	-2	0.15×0.12	39	0.15×0.12	38
IRAS 04302	0.30×0.24	-17			0.09×0.04	34	0.30×0.24	-17
HK Tau B	0.11×0.07	3			0.12×0.04	42	0.12×0.08	42
HV Tau C	0.11×0.08	4			0.12×0.04	41	0.12×0.08	-4
IRAS 04200	0.11×0.07	-8			0.11×0.04	35	0.11×0.11	35
Haro 6-5B	0.12×0.07	-19			0.10×0.04	30	0.12×0.08	-19
IRAS 04158	0.48×0.33	8			0.11×0.04	36		
Oph 163131			0.23×0.13	-70				
ESO-Hα 569	0.48×0.28	-8						
ESO-Hα 574	0.47×0.28	-10						
HH 48 NE	0.48×0.28	-5						

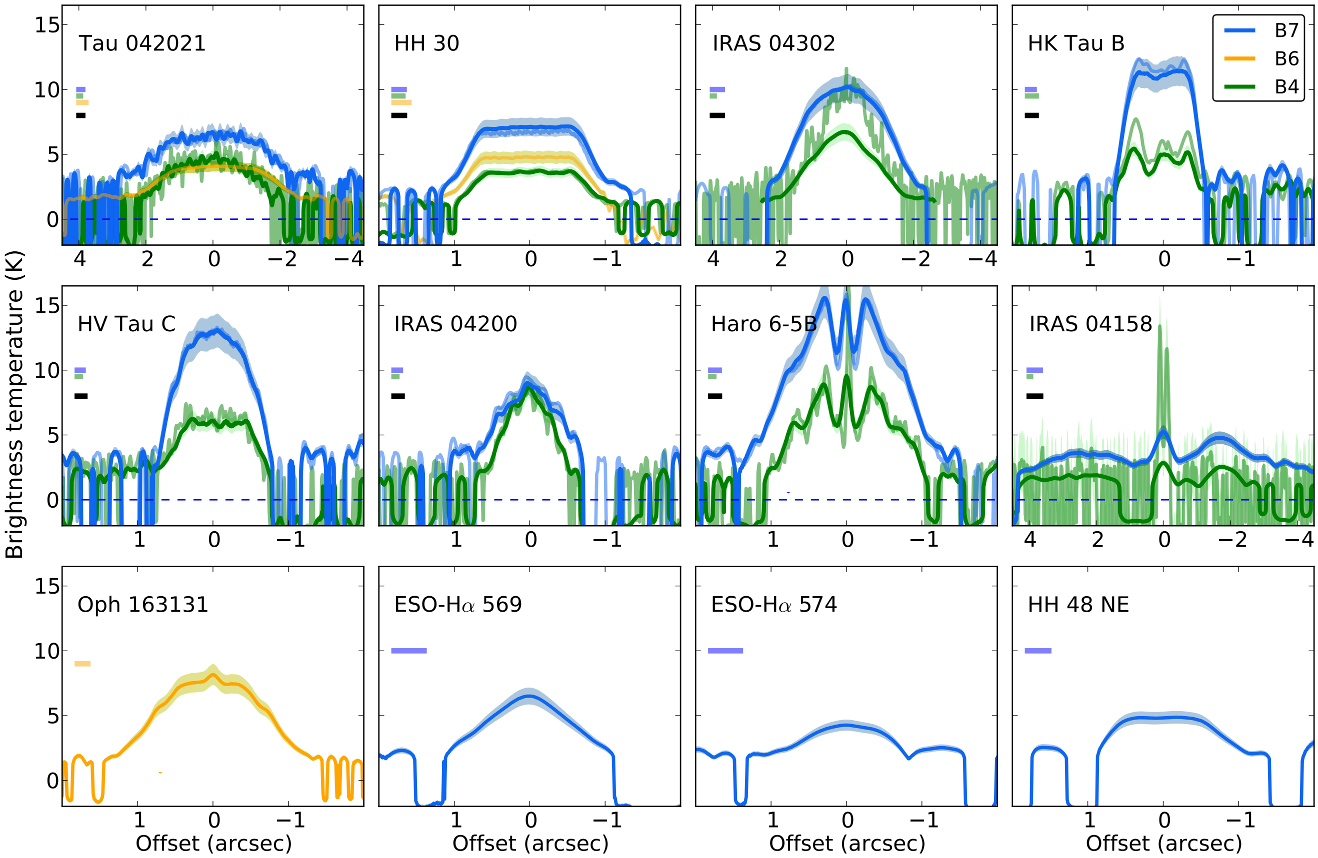

Fig. B.1. Observed brightness temperatures as a function of the radial distance to the central star. Solid lines profiles (band 7 and band 4 only) were computed with the same angular resolution (restored beam in Table A.1), while the light lines have the original angular resolution. We report the beam sizes in the direction of the cut as horizontal lines in the left part of each plot. The restored beam corresponds to the black line. Error bars correspond to 10% of the brightness temperature.

Table B.1. Peak brightness temperatures for our radiative transfer models

	S-HM		NS - HM		S-LM		NS - LM	
Incl (°)	B7 (K)	B4 (K)	B7 (K)	B4 (K)	B7 (K)	B4 (K)	B7 (K)	B4 (K)
75	28.9	31.6	26.4	30.0	17.7	13.5	22.4	17.6
80	24.0	25.5	15.2	16.7	16.1	12.6	18.3	15.0
85.0	15.5	17.3	11.0	11.1	13.0	10.6	13.9	11.8
87.5	10.3	10.9	10.5	10.7	10.1	7.8	12.7	10.8
90.0	8.0	6.8	10.3	10.5	5.4	3.1	12.4	10.5

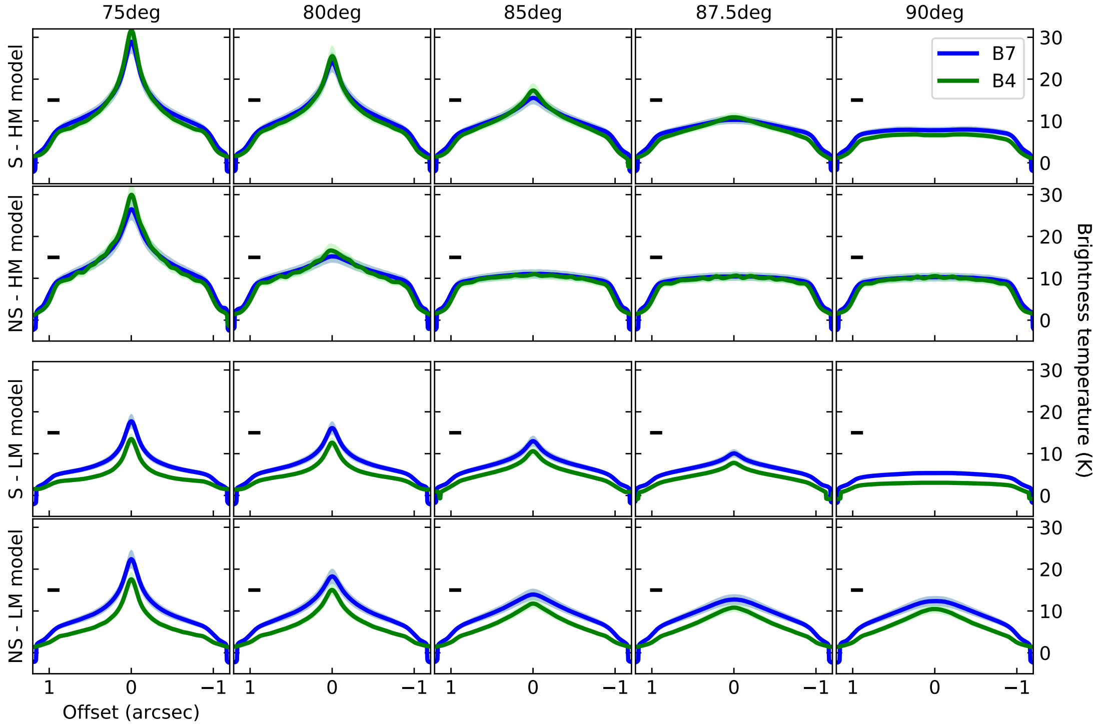

Fig. B.2. Brightness temperatures as a function of the radial distance for the radiative transfer models presented in Section 4, computed at different inclinations. *Top and third row:* High and low mass settling models, *Second and bottom row:* High and low mass No Settling models. We report the beam size in the direction of the cut in the left part of each panel.

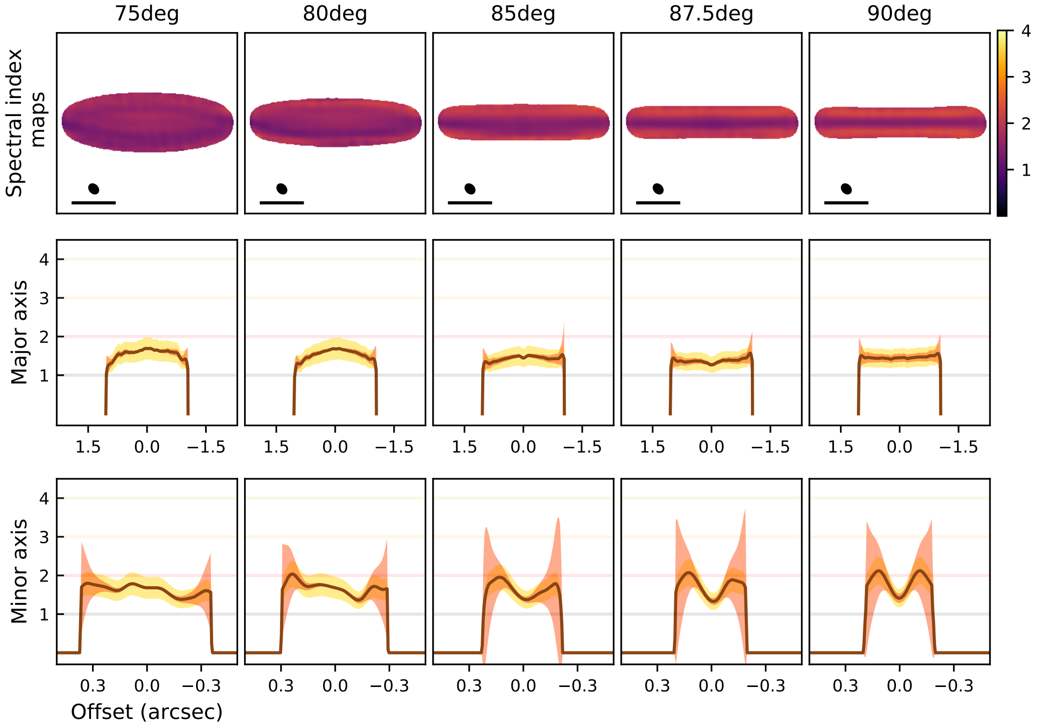

Fig. C.1. *Top row:* Spectral index maps of the high mass settled model, applying a filter to keep only the pixels with more emission than 5σ in both bands. The beam size is shown in the bottom left corner, along with a dark line representing a $0.5''$ scale. *Middle row:* Spectral index cuts along the major axis. *Bottom row:* Spectral index profiles along the minor axis, averaged along the major axis. For all cuts, yellow errors correspond to a flux calibration error of 10% in both bands, while orange errors are estimated from the signal-to-noise in each band. The x-axis corresponds to the offset to the center of the disk in arcseconds.

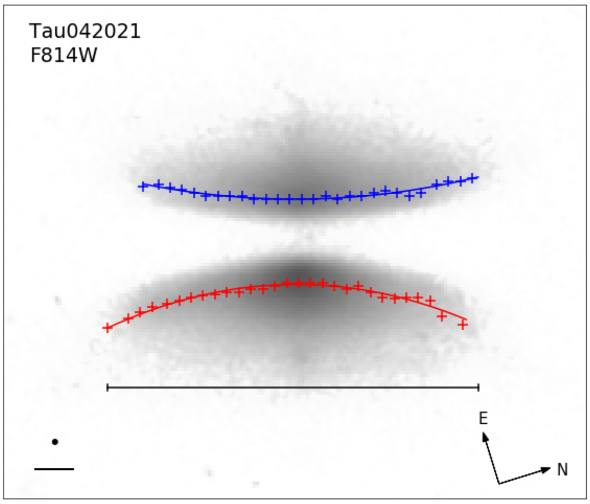

Fig. D.1. Example of scattered light size estimate in Tau 042021. We represent the two spines of the nebula by the blue and red curves. The adopted radial size corresponds to the horizontal line, the maximum distance between spine points along the major axis.

A&A 624, A7 (2019)
https://doi.org/10.1051/0004-6361/201834800

Astronomy & Astrophysics

Spatial segregation of dust grains in transition disks[★]

SPHERE observations of 2MASS J16083070-3828268 and RXJ1852.3-3700

M. Villenave[1,2], M. Benisty[1,3,4], W. R. F. Dent[5], F. Ménard[1], A. Garufi[6], C. Ginski[7], P. Pinilla[8], C. Pinte[9,1], J. P. Williams[10], J. de Boer[11], J.-I. Morino[12], M. Fukagawa[12], C. Dominik[7], M. Flock[13], T. Henning[13], A. Juhász[14], M. Keppler[13], G. Muro-Arena[7], J. Olofsson[15,16], L. M. Pérez[4], G. van der Plas[1], A. Zurlo[17,18,19], M. Carle[19], P. Feautrier[1], A. Pavlov[13], J. Pragt[20], J. Ramos[13], J.-F. Sauvage[19,21], E. Stadler[1], and L. Weber[22]

(Affiliations can be found after the references)

Received 7 December 2018 / Accepted 6 February 2019

ABSTRACT

Context. The mechanisms governing the opening of cavities in transition disks are not fully understood. Several processes have been proposed, but their occurrence rate is still unknown.

Aims. We present spatially resolved observations of two transition disks, and aim at constraining their vertical and radial structure using multiwavelength observations that probe different regions of the disks and can help understanding the origin of the cavities.

Methods. We have obtained near-infrared scattered light observations with VLT/SPHERE of the transition disks 2MASS J16083070-3828268 (J1608) and RXJ1852.3-3700 (J1852), located in the Lupus and Corona Australis star-forming regions respectively. We complement our datasets with archival ALMA observations, and with unresolved photometric observations covering a wide range of wavelengths. We performed radiative transfer modeling to analyze the morphology of the disks, and then compare the results with a sample of 20 other transition disks observed with both SPHERE and ALMA.

Results. We detect scattered light in J1608 and J1852 up to a radius of 0.54″ and 0.4″ respectively. The image of J1608 reveals a very inclined disk ($i \sim 74°$), with two bright lobes and a large cavity. We also marginally detect the scattering surface from the rear-facing side of the disk. J1852 shows an inner ring extending beyond the coronagraphic radius up to 15 au, a gap and a second ring at 42 au. Our radiative transfer model of J1608 indicates that the millimeter-sized grains are less extended vertically and radially than the micron-sized grains, indicating advanced settling and radial drift. We find good agreement with the observations of J1852 with a similar model, but due to the low inclination of the system, the model remains partly degenerate. The analysis of 22 transition disks shows that, in general, the cavities observed in scattered light are smaller than the ones detected at millimeter wavelengths.

Conclusions. The analysis of a sample of transition disks indicates that the small grains, well coupled to the gas, can flow inward of the region where millimeter grains are trapped. While 15 out of the 22 cavities in our sample could be explained by a planet of less than 13 Jupiter masses, the others either require the presence of a more massive companion or of several low-mass planets.

Key words. protoplanetary disks – techniques: polarimetric – radiative transfer – scattering

1. Introduction

The variety of physical and structural conditions in protoplanetary disks – the birthplace of planets – might be responsible for the diversity observed in the exoplanet population. Studying disk evolution through the analysis of protoplanetary disks with depleted regions and/or clear signs of evolution could provide indirect constraints on the way in which planets form. Thanks to new capabilities of high resolution instruments such as ALMA, VLT/SPHERE and Gemini/GPI, many features have been identified in protoplanetary disks and in particular in transition disks (TDs). A number of studies reveal rings (e.g., Isella et al. 2016; Pohl et al. 2017b; Muro-Arena et al. 2018), lopsided emission (e.g., Casassus et al. 2013; Cazzoletti et al. 2018), spirals (e.g., Pérez et al. 2016; Dong et al. 2018; Muto et al. 2012; Stolker et al. 2017; Benisty et al. 2017; Uyama et al. 2018), and shadows (e.g., Marino et al. 2015; Stolker et al. 2017; Casassus et al. 2018; Benisty et al. 2018). Among other mechanisms, planets interacting with the disk can form such structures. Although challenging, the observation and/or hints of forming planets within disks have been reported in recent studies (Keppler et al. 2018; Pinte et al. 2018; Teague et al. 2018).

Interaction with a planetary or stellar companion is also thought to result in the large cavities observed in circumbinary or transition disks (e.g., Muñoz & Lai 2016; Rosotti et al. 2016; Dipierro & Laibe 2017; Price et al. 2018). Such disks were identified from a lack of emission in the near-infrared (IR) in their spectral energy distribution (SED), which indicates a dust depleted inner region (Strom et al. 1989). Other mechanisms such as photo-evaporation (Owen et al. 2011) or the presence of a dead zone (Flock et al. 2015; Pinilla et al. 2016) are potential processes that could open such cavities. Each mechanism is expected to shape the inner disk differently, and can result in a cavity radius that depends on the dust grain size. However, their respective importance is currently not well constrained.

While μm-sized dust are coupled to the gas that orbits at sub-Keplerian speed, larger grains are increasingly decoupled. Their interactions with the gas lead simultaneously to inward radial

---

[★] Based on observations performed with SPHERE/VLT under program ID 099.C-0891(A) and 099.C-0147(A).

drift and vertical settling (Weidenschilling 1977; Dullemond & Dominik 2004). Thus, the large grains are expected to be located in a more compact region radially and to be less extended vertically than smaller grains. However, the strength of these effects is not yet well constrained. Grains of different sizes would also be trapped more or less efficiently by a pressure maximum, which can be generated at the outer edge of dead zones or by a planet in the disk.

The combination of high-resolution observations at different wavelengths is key for quantifying both the radial and vertical distribution of dust grains, and in particular, the degree of dust settling. It can therefore help to differentiate the various mechanisms that can generate cavities in transition disks. While direct imaging with SPHERE traces polarized scattered light by small grains (<few μm) well coupled to the gas and located in the surface layers, ALMA observations probe thermal emission of larger grains (>50 μm), partially decoupled from the gas and located in the midplane. The combination of both tracers therefore allows one to trace and compare different dust grain populations.

In this paper, we present scattered light images of two transition disks, 2MASS J16083070-3828268 and RXJ1852.3-3700 (hereafter J1608 and J1852, respectively) observed with VLT/SPHERE. We complement our observations with ALMA archival data. We aim to model both disks using a radiative transfer code and to bring constraints on the radial segregation of dust particles, on vertical settling and on the origin of their cavities. In Sect. 2, we present the two transition disks, and in Sect. 3, the observations and data reduction. The modeling procedure and results are detailed in Sect. 4. We compare our results with a larger sample of transition disks in Sect. 5. Finally, the conclusions are presented in Sect. 6.

2. Stellar and disk properties

J1608 and J1852 are two transition disks around K2 stars, located in close-by star-forming regions. Using VLT/X-shooter spectroscopy, mass accretion rates of $\sim 10^{-9}\ M_\odot\ \mathrm{yr}^{-1}$ were found for both objects, typical of transition disks and indicating that the inner disk regions still hold significant gas content (Alcala et al. 2017; Manara et al. 2014). In this paper, we will use the stellar ages and masses re-estimated by Garufi et al. (2018) using the latest Gaia DR2 distances (Gaia Collaboration et al. 2018) and stellar tracks by Siess et al. (2000). J1608 is found to be younger than J1852 although age estimates appear uncertain. We report the stellar parameters in Table 1. All the radial extents provided in physical units in the following have been scaled to the Gaia DR2 distances.

J1608 is located at 156 pc (Gaia Collaboration et al. 2018) in the Lupus III cloud. It has been observed with ALMA in Band 7 and Band 6 (~0.89 mm and ~1.33 mm, respectively; Ansdell et al. 2016, 2018). J1608 is one of the most massive disks of the Lupus millimeter survey with ~80 $M_\oplus$ of dust. It possesses a large cavity in the continuum and is highly inclined (>70°; Ansdell et al. 2016). From the Band 6 observations, Ansdell et al. (2018) find a gas radial extent about twice as large as that of the dust. Pinilla et al. (2018b) modeled the Band 7 continuum emission with a radially asymmetric Gaussian ring model and found that the peak intensity of the ring is located at ~61 au. This is consistent with the dust and line modeling of the ALMA data by van der Marel et al. (2018) that constrains the outer radius of the dust and gas cavity respectively to 59 au and 47 au.

Table 1. Stellar parameters.

Parameters		J1608	J1852
RA	(h m s)	16 08 30.7	18 52 17.3
Dec	(deg ′ ″)	−38 28 26.8	−37 00 11.9
Distance[a]	(pc)	156 ± 6	146 ± 1
Av	(mag)	0.1	1.0
SpT		K2	K2
T_{eff}	(K)	4800	4850
$R_\star$	($R_\odot$)	2.00	1.17
$\dot{M}$	($M_\odot \cdot \mathrm{yr}^{-1}$)	10^{-9}	10^{-9}
$M_\star$[b]	($M_\odot$)	1.4 ± 0.1	1.0 ± 0.1
Age[b]	(Myr)	$8.3^{+4.4}_{-2.1}$	>14

Notes. [(a)]Gaia Collaboration et al. (2018), [(b)]stellar masses and ages are calculated by Garufi et al. (2018) using Gaia DR2 distances and stellar tracks by Siess et al. (2000).

References. Alcala et al. (2017); Manara et al. (2014).

J1852 is one of the oldest systems in the Corona Australis association (CrA; Neuhaeuser et al. 2000), located at a distance of 146 pc (Gaia Collaboration et al. 2018). Gas emission lines of [Ne II], [H I] and [O I] were detected (Rigliaco et al. 2015; Pascucci et al. 2007; Geers et al. 2012; Riviere-Marichalar et al. 2016), using Spitzer and Herschel data. While no spectroscopic binary was found in the system (Kohn et al. 2016), a candidate companion located at 3″ (~ 440 au) separation, was identified with SUBARU (Uyama et al. 2017a). Follow-up observations are needed to confirm if it is a bound companion or a background object.

SMA observations, with rather low resolution (1.0″ × 1.7″), show that the disk has a relatively low inclination (~30°; Hughes et al. 2010). From SED modeling, Hughes et al. (2010) inferred the presence of a cavity up to 16 au,with an optically thick inner disk closer to the star, more recently confirmed by van der Marel et al. (2016). Geers et al. (2012) presented a thermo-chemical model explaining the upper limits for the [OI] and CO emission lines, and found that the gas is either optically thin and co-located with the dust (16–500 au), or possibly radially concentrated in an optically thick region (16–70 au).

We selected these two transition disks around K2 stars with similar stellar properties, but seen at different inclinations to investigate the differences in their structure and the mechanisms that can be responsible for their inner cavities.

3. Observations and data reduction

3.1. Observations

Both disks were observed with the InfraRed Dual band Imager and Spectrograph (IRDIS; Dohlen et al. 2008) sub-instrument of SPHERE (Beuzit et al. 2008) mounted on the Very Large Telescope. Observations were carried out in dual-polarization imaging mode (DPI; Langlois et al. 2014), in both J ($\lambda_J = 1.245\ \mu$m) and H-Band ($\lambda_H = 1.625\ \mu$m) for J1608, and in H-Band only for J1852.

We observed J1608, during the nights of June 18, and July 23, 2017 (ID 099.C-0891, PI: Benisty). During the first epoch (June 18, 2017), we observed J1608 in H-Band, with an apodized Lyot coronagraphic mask (N_ALC_YJH_S, 0.185″ in diameter; Martinez et al. 2009; Carbillet et al. 2011). The observations consisted of 56 exposures of 32 seconds each,

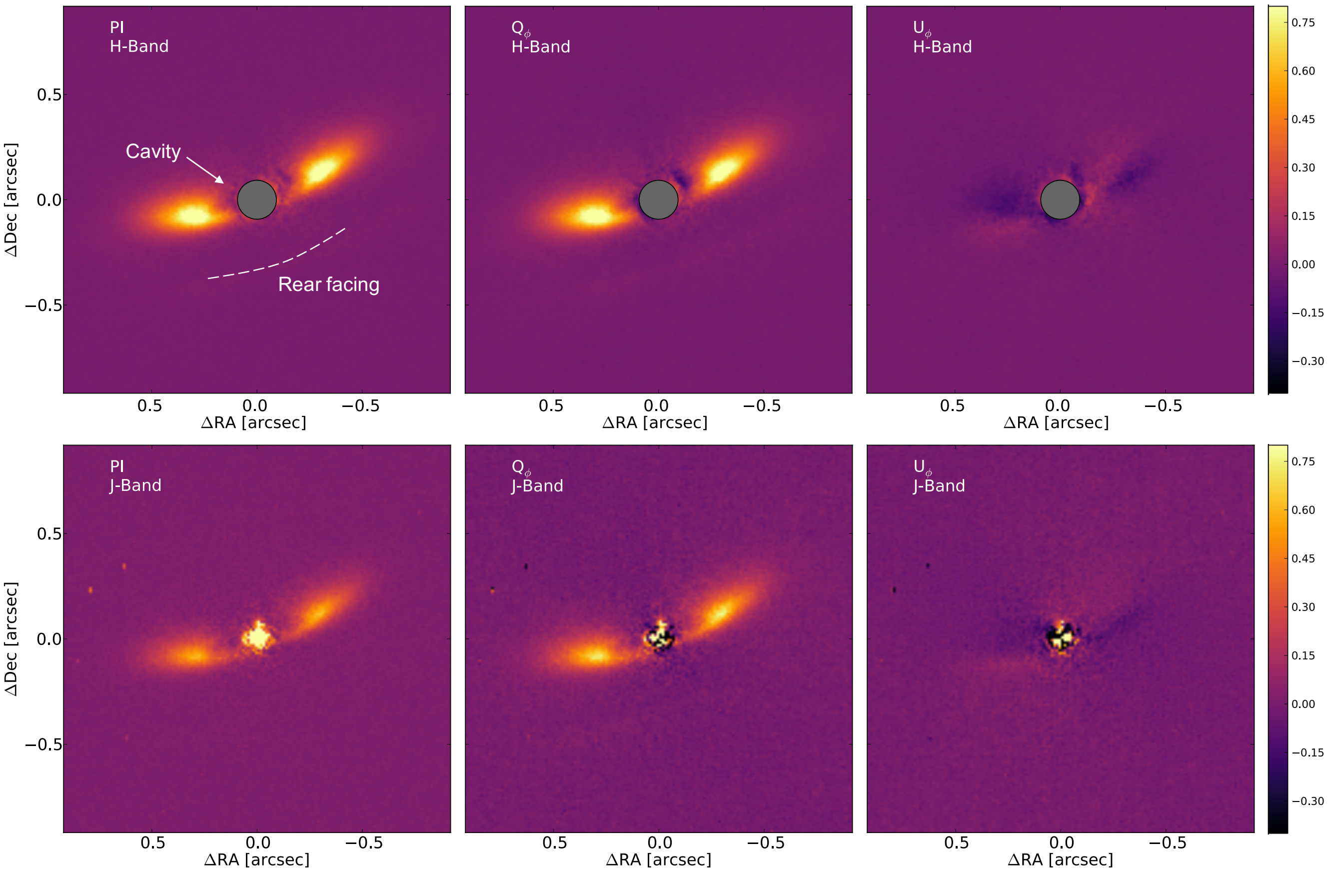

Fig. 1. Normalized polarized intensity map (*left panel*), Q_ϕ (*middle panel*), and U_ϕ (*right panel*) maps of J1608. *Top panel*: H-Band observations, obtained with a coronagraph as illustrated by the grey circle of diameter 0.185″. The dashed line in the left panel traces the faint scattered light from the rear-facing near side of the disk (see Fig. A.1). *Bottom panel*: J-band observations, obtained without coronagraph. Each Q_ϕ and U_ϕ maps are normalized to the maximum of Q_ϕ.

corresponding to about 30 minutes on source. Conditions were good, with a seeing between 0.65″ and 0.9″ during the night. To confirm the presence of a cavity, we also performed non-coronagraphic observations on July 23, 2017, in J-band, with about 80 seconds on source, by exposures of 2 seconds. Weather conditions were relatively poor with a seeing between 1.2″ and 1.9″ during these observations.

J1852 was observed as part of the SPHERE guaranteed time observations (GTO) program on May 15, 2017 (ID 099.C-0147, PI: Beuzit). Observations were performed in H-Band, using the same coronagraph as for J1608, and consisted in 12 exposures of 64 seconds each. The seeing was around 1.2″ during the observations.

We reduced the data to generate the total intensity map and Stokes Q and U polarized maps, following the approach detailed in Ginski et al. (2016). The polarized intensity (PI) image is computed from the Stokes Q and U components:

$$\mathrm{PI} = \sqrt{Q^2 + U^2}. \tag{1}$$

We also define the polar Stokes components Q_ϕ and U_ϕ as in Schmid et al. (2006):

$$Q_\phi = +Q\cos(2\phi) + U\sin(2\phi), \tag{2}$$

$$U_\phi = -Q\sin(2\phi) + U\cos(2\phi), \tag{3}$$

where $\phi = \arctan(\frac{y}{x})$ corresponds to the azimuthal angle as measured north to east with respect to the position of the star (centered in the image). The positive signal in Q_ϕ is the polarization in the azimuthal direction (negative signal is in the radial direction), while U_ϕ represents the polarization inclined by 45° from this direction. In the case of single scattering events, a photon is expected to be polarized orthogonally to the scattering plane, defined by the light source, the scattering particle and the observer. Thus, in this scenario, all the polarized signal should be included in the Q_ϕ component. Canovas et al. (2015) showed however, that if the disk is too inclined and/or multiple scattering events occurs, the polarization is not necessarily perpendicular to the scattering plane. Then, part of the astrophysical signal will be included in the U_ϕ component. This effect was indeed observed in the very inclined (∼69°) disk around T Cha, leading to a large U_ϕ/Q_ϕ peak-to-peak value (Pohl et al. 2017b).

3.2. Results

Our reduced images are shown in Figs. 1 and 2 for J1608 and J1852. J1608 appears to be very inclined, in images both with and without the coronagraph. We detect two lobes southeast and northwest of the star, as well as a faint line of scattered light[1] to the southwest that we interpret as the rear-facing side of the disk closest to us. The presence of this line will be discussed further in the modeling in Sect. 4.3. In the Q_ϕ maps, the disk shows emission above the noise level up to 0.54″ along the major axis. The central cavity is clearly visible in both the coronagraphic and

---

[1] We show the faint southwest emission with a more favorable dynamic range in Fig. A.1.

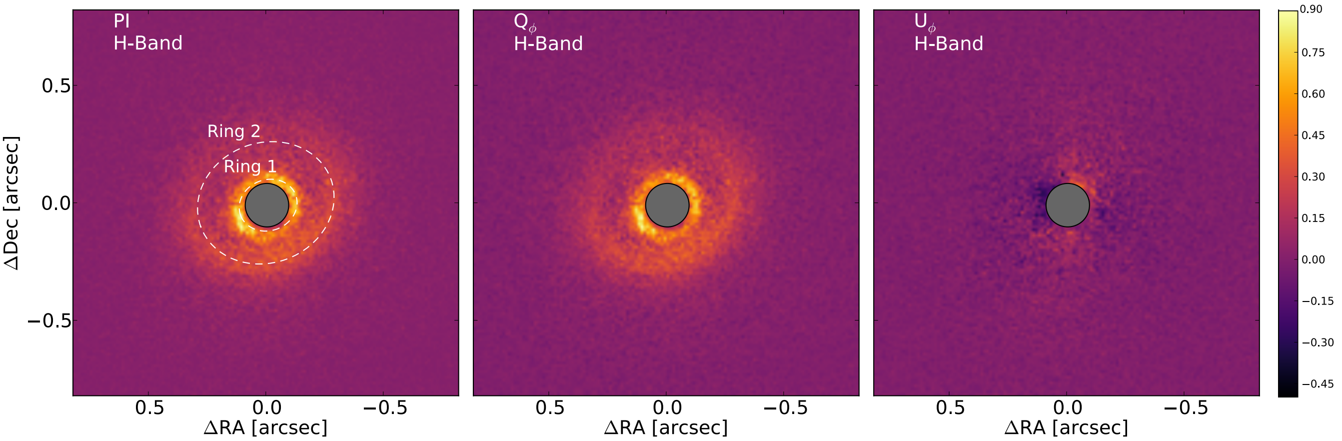

Fig. 2. Normalized polarized intensity map (*left panel*), Q_ϕ (*middle panel*), and U_ϕ (*right panel*) maps of J1852, observed in *H*-Band with a coronagraph. The Q_ϕ and U_ϕ maps are normalized to the maximum of Q_ϕ. The dashed ellipses in the left panel represent the two scattered light rings (see text for details).

non-coronagraphic images. We note that there is no clear emission from the northeast of the star, corresponding to emission from the far side of the disk being scattered backwards toward us. In Sect. 4.3, we will focus on the modeling of the coronagraphic *H*-Band image as the data were taken in better observing conditions, have a higher signal to noise ratio, and look very similar to the non-coronagraphic *J*-band data.

In the coronagraphic images of J1852 (Fig. 2), we observe two rings in the Q_ϕ map, with peak values located at 0.125″ and 0.295″ from the position of the star along the major axis. The inner ring is cut off by the coronagraph and the peak radius may lie within this. The outer ring seems to be slightly off-centered compared to the inner ring (~0.01″, 1 pixel), likely an effect of the inclination and flaring of the disk surface (e.g., de Boer et al. 2016; Ginski et al. 2016; Avenhaus et al. 2018). This is modeled in Sect. 4.4. The disk displays emission above the noise level as far as 0.4″along its major axis.

3.3. Complementary data

ALMA archival data. J1608 was observed as part of a large survey of disks in the Lupus clouds. In this work, we use the Band 6 observations (Project ID: 2015.1.00222.S, PI: Williams) obtained on July 23, 2016, at a resolution of 0.24″ × 0.23″, cleaned with a Briggs robust weighting parameter of +0.5. The data reduction of the continuum and line emission is presented in details in Ansdell et al. (2018).

We show the position-velocity (PV) diagram of the ^{12}CO 2-1 transition in Fig. 3, obtained with a velocity resolution of 0.11 km s^{-1}. From the PV diagram, we retrieve the systemic velocity of the source to be +5.2 ± 0.4 km s^{-1} (LSR). We also note that no velocity higher than 5.3 km s^{-1} with respect to the star is detected, indicating the presence of an inner cavity in the gas. Modeling the disk velocities with Keplerian motion (assuming $M_\star = 1.4\,M_\odot$, $i = 74°$), we infer that the inner radius of the gas cavity is ~48 au, in agreement with the outcome of thermo-chemical modeling of the CO observations (47 au; van der Marel et al. 2018).

The ALMA continuum image is shown in the left panel of Fig. 4. The large axis ratio indicates that the disk is highly inclined. Moreover, the presence of two blobs with higher intensity along the major axis, located at 0.4″ from the star, denote emission coming from an optically thin ring.

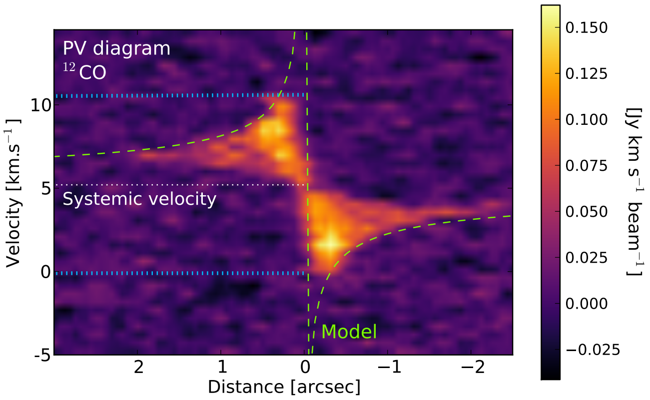

Fig. 3. Position-velocity diagram of the ^{12}CO 2-1 emission in J1608. The green dashed line corresponds to the Keplerian velocity of a disk at 74° of inclination around a 1.4 $M_\odot$ star. The highest velocity with emission is about 5.3 km s^{-1} from the systemic velocity. It corresponds to a gas cavity radius of ~48 au, and is indicated by the blue lines.

For J1852, we use ALMA data observed on September 22, 2016, in Band 3 (~3 mm, Project ID: 2015.1.01083.S, PI: Morino). The four continuum spectral windows were centered respectively on 91.5 GHz, 93.4 GHz, 101.5 GHz and 103.5 GHz. We used the CASA pipeline to calibrate the data and extracted the continuum images using the CASA `clean` task, with a Briggs robust parameter of +0.5. The final image, after performing phase only self-calibration, is presented in the left panel of Fig. 8, with the achieved beam of 0.38″ × 0.31″. The image shows one unique ring, peaking at 0.3″ along the major axis.

Spectral energy distributions. We compiled the SED of J1608 using Vizier, to which we add the millimeter fluxes at 0.88 mm and 1.3 mm obtained from Ansdell et al. (2016) and Ansdell et al. (2018), respectively. The SED of J1852 was computed using the VO SED Analyser[2] (VOSA; Bayo et al. 2008). We complement this SED with the low-resolution Spitzer/IRS spectrum from the CASSIS database (Lebouteiller et al. 2011). The SEDs are shown on Figs. 6 and 7.

The SEDs of the two disks show a steep increase longwards of 20 μm, typical of transition disks. Although J1852 does not

---

[2] http://svo2.cab.inta-csic.es/theory/vosa50

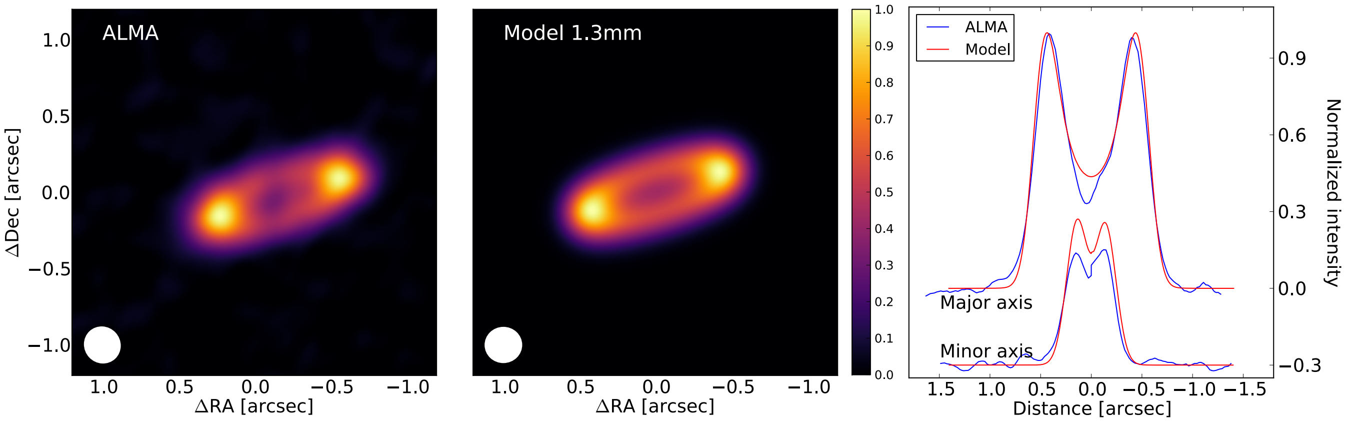

Fig. 4. *Left panel*: normalized ALMA Band 6 image of J1608, with a peak flux of 7.1 mJy. The beam is shown in the bottom left of the image. *Middle panel*: normalized model obtained after convolution by a beam of $0.24'' \times 0.23''$. *Right panel*: radial cuts along the major and minor axis, with each map normalized to its maximum. For clarity, the cut along the minor axis is shifted by −0.3 in normalized intensity. The peaks are located at 0.4″(62 au) along the major axis and 0.14″(22 au) along the minor axis.

show any clear near-IR excess, a silicate feature at 10 μm is present, characteristics of the presence of small hot grains close to the star (Silverstone et al. 2006; Hughes et al. 2010).

4. Radiative transfer modeling

4.1. Methodology

In order to understand the physical structure of the two observed TDs, we construct models using the radiative transfer code `mcfost` (Pinte et al. 2006, 2009). This code computes the thermal structure of the disk using a Monte Carlo method and produces images by ray-tracing. An iterative process is done to find a model that reproduces well the SED and the images. Considering the complexity of our observations, we do not aim to find the best-fit model, but rather a representative one. For each set of parameters, we compute the SED, the millimeter continuum image as well as the near-IR polarized intensity, Stokes Q and U maps. All images are initially generated with infinite angular resolution, and then convolved with a point spread function reference image (PSF; in practice, a non-coronagraphic or FLUX image of the star) or the ALMA 2D Gaussian beam.

We also add noise to our scattered light predictions. We estimate it at each point of the map from the U_ϕ image of our observations (as in Muro-Arena et al. 2018). For each point in the U_ϕ map, we consider an aperture in which we determine the root mean square (rms) of the intensity. The aperture is taken as 4 pixels of diameter, which is close to the FWHM of the point spread functions of each target (3.5 pixels for J1608 and 4.3 pixels for J1852). As our sources are inclined, the U_ϕ image might contain some physical signal (Canovas et al. 2015). Thus, in each aperture we subtract its mean value (physical signal) before extracting the rms. For each corresponding pixel in the model image, we simulate the noise by adding a Gaussian random number of the same rms centered on 0.

Since we will model emission very close to the coronagraph in the J1852 image, we apply a 2D attenuation map due to the coronagraph (Wilby et al. in prep.). This numerical mask removes all signal inside the coronagraph mask radius (0.093″), with gradually decreasing attenuation down to 5% at a radius of 0.15″. Finally, we compute the PI, Q_ϕ and U_ϕ maps using Eqs. (1)–(3). In this work, we compare the observed and synthetic PI images. A comparison between the observed and predicted Q and U as well as the Q_ϕ and U_ϕ maps are presented in Appendix A.

4.2. Model setup

We define various axisymmetric disk zones to reproduce the observed features of the two disks and assume a gas-to-dust ratio of 100. For each region, we define the disk height as a power-law:

$$H(R) = H_{100\,\mathrm{au}}(R/100\,\mathrm{au})^{\beta}, \tag{4}$$

where β is the flaring exponent, R the radius and $H_{100\,\mathrm{au}}$ is the scale height at a radius of 100 au. A simple description of the surface density profile is adopted for each region of our disks, with a single power law: $\Sigma(R) \propto R^p$. In all our modeling we choose $p = -1$. We use astronomical silicates (similar to those shown in Fig. 3 of Draine & Lee 1984) with a number density described with a power law of the grain size $dn(a) \propto a^{-3.5}$ da (Mathis et al. 1977). For each region, our free parameters are the inner and outer radius (R_{in}–R_{out}), the dust mass and the scale height ($H_{100\,\mathrm{au}}$).

For both disks, we mimic dust settling by modeling separately the extents of small (0.01−0.5 μm) and large grains (10−1000 μm). We fixed the flaring exponent β to 1.1 for all type of grains. The results are summarized in Table 2 and described in detail in the following two subsections.

4.3. Modeling J1608

Large grains. We first aim to reproduce the thermal emission detected in the ALMA Band 6 data with a ring of large grains, adjusting the dust mass to fit the total millimeter flux. Our convolved model prediction at 1.3 mm is presented in the center panel of Fig. 4. The right panel of this figure shows radial cuts along the major and minor axis. In our model, the radial position of the maxima as well as the radial extent in each cut are well reproduced. However, the model overestimates the flux in the inner region of the disk (i.e., inside the gap) by about 30%.

To reproduce the observed aspect ratio of the disk, a high inclination (~74°) is needed. However, we find that the inclination should not be larger than 80°, otherwise the photosphere would be occulted at short wavelengths, in contradiction with the shape of the SED (see for example the SED of the edge-on disk ESO-Hα 569; Wolff et al. 2017). The radial width of the ring made of large grains has to be sufficiently small so that the position and shape of the maxima of the cut along the major axis match the data. We find that a radial width for the large grains ring of about 10 au is consistent with the data, with $R_{\mathrm{in}} \sim 77$ au. However, a narrower ring would still reproduce the observations.

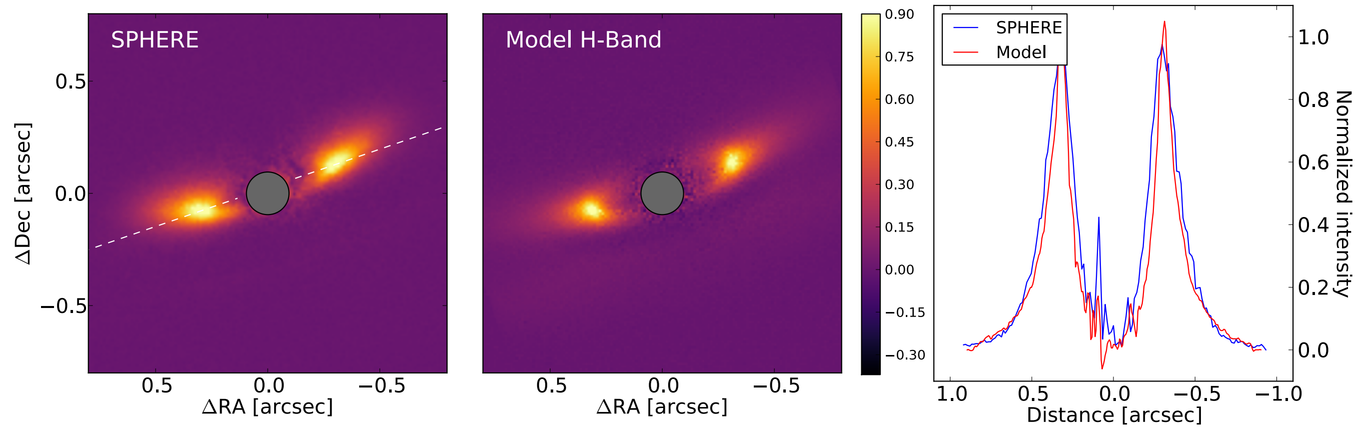

Fig. 5. *Left panel*: observed polarized intensity of J1608. *Middle panel*: PI model map. Both maps are normalized to their maximum. *Right panel*: radial cuts along the major axis for the PI images of the data and model, smoothed with a Gaussian kernel with a standard deviation of 9 mas. The position of the cut is indicated by the dotted line in the left panel.

Table 2. Parameters for our radiative transfer models.

		J1608	J1852	
Inclination	(°)	74	30	
PA	(°)	19	34	
			Inner disk	
$a_{\rm min}$–$a_{\rm max}$	(μm)	–	0.01–5	
$R_{\rm in}$–$R_{\rm out}$	(au)	–	0.1–5	
Mass	($M_\odot$)	–	$9 \cdot 10^{-11}$	
$H_{\rm 100au}$	(au)	–	0.9	
		Small grains	Small grains	
$a_{\rm min}$–$a_{\rm max}$	(μm)	0.01–0.5	0.01–0.5	
$R_{\rm in}$–$R_{\rm out}$	(au)	50–150	15–22	42 – 65
Mass	($M_\odot$)	2×10^{-6}	2×10^{-8}	7×10^{-7}
$H_{\rm 100au}$	(au)	12	15	
		Large grains	Large grains	
$a_{\rm min}$–$a_{\rm max}$	(μm)	10–1000	10–1000	
$R_{\rm in}$–$R_{\rm out}$	(au)	77–87	15–22	42–65
Mass	($M_\odot$)	5×10^{-5}	3×10^{-7}	7×10^{-5}
$H_{\rm 100au}$	(au)	5	1	

Notes. Each parameter was adjusted during the modeling, except for the grain size ($a_{\rm min}$–$a_{\rm max}$).

Finally, the fluxes of the peaks and depth of the gap along the minor axis depend both on the radial width and the vertical thickness of the disk. If the scale height of the large grains is too large, after convolution by the beam, the two sides of the ring would appear as connected, leading to a flat intensity profile along the minor axis. On the other hand, if the zone of large grains is too thin vertically for a given disk mass, the fluxes at the peaks of the minor axis cut would become too large. The appropriate scale height in our modeling is between 3 and 5 au at 100 au, which is similar to the value obtained for HL Tau (1 au at 100 au; Pinte et al. 2016). We note that a smaller scale height, such as in HL Tau, can not be excluded by our model. We show the non-convolved model in Appendix A. All the model's parameters are presented in Table 2.

Small grains. The synthetic scattered light image computed assuming the same spatial distribution for small grains and large grains does not provide a good match to the images. To reproduce the observations, the radial extent of small grains and their scale height need to be larger than those of the large grains, from 50 to 150 au radially, and about 12 au vertically at 100 au. We note that this layer is already included in the millimeter predictions displayed in Fig. 4, but does not contribute significantly at millimeter wavelengths. The scattered light image of our model is presented in Fig. 5, with a cut along the major axis direction. The cuts were smoothed with a Gaussian kernel with a FWHM of 50% the measured image resolution (~10 mas). The inner radius of the small grains distribution is very close to that of the gas, as estimated from the PV diagram (48 au, see Fig. 3), consistent with the expectation that these grains are well coupled to the gas.

We note that, in the observation, no scattered light is detected from the northeast part of the disk (Fig. 5). Geometrically, the existence of the bottom line located in the southwest suggests that it traces the part of the disk nearest to us, while the northeast region would correspond to the more distant side of the disk. This implies that the phase function of the polarized intensity is such that there is no or very little backward scattering (on the assumption that the disk is axisymmetric). The polarized intensity is the product of the polarization degree and the total intensity. While the polarization degree from backward scattering is similarly low for all grain sizes (see Fig. 7 of Keppler et al. 2018), the phase function of the intensity varies significantly with the grain size. We reproduce this feature by selecting grains smaller than 0.5 μm. Grains larger than 1.2 μm also have a very small efficiency for backward scattering. However, with such grains our models showed that the position of the maximum intensity along the major axis is independent of the inner radius position and located further out than seen in the data. These grains are therefore not compatible with the observations. For grains with an intermediate size (between 0.5 and 1.2 μm), backward scattering is very efficient, which would lead to a significant signal northeast of the disk coming from its far side.

We show the SED compared to that of the model in Fig. 6. All the model parameters are presented in Table 2, and a schematic representation of our model is shown in the top panel of Fig. B.1.

We note that we are able to recreate the same general structure as seen in J1608, with two lobes along the major axis, no emission from the northeast region of the disk (backward

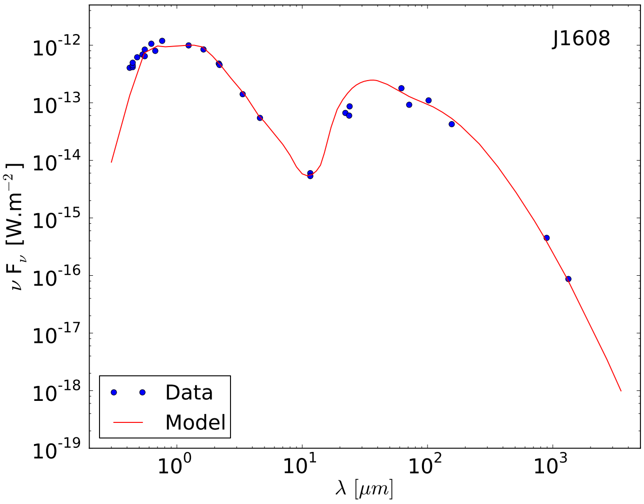

Fig. 6. Spectral energy distribution of J1608 (blue circles) and our model prediction (red line). The model is corrected by the Av.

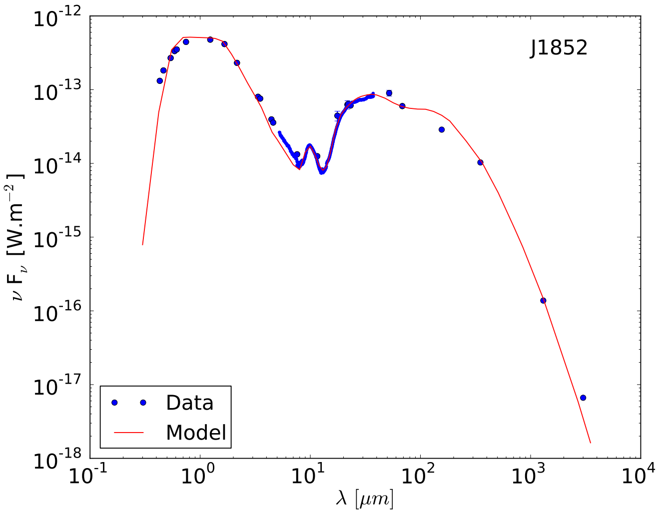

Fig. 7. Spectral energy distribution of J1852 (blue circles) and our model (red line). The model is corrected by the Av.

scattering) and a faint line south of the disk, but these characteristics are not perfectly reproduced. For example the southern line is brighter in our model than in the observations (see Fig A.1). To reproduce better this part of the image, the layer of small grains scattering light must be thinner vertically, but this in turn has an impact on the extent of the lobes. Moreover, the southern line is closer to the star than in the data. A way to push this line further would be for example to increase the mass of the scattering grains, the scale height or the inclination. However, each case would lead to an extinction of the photosphere that is not observed in the SED. Thus the model that we present here is a compromise to reproduce both the ALMA and SPHERE images, together with the SED. This should be considered as a working model to derive the main structural characteristics of the J1608 system. These are: (1) a high inclination, (2) large grains more concentrated vertically and radially than the small grains, and (3) a distribution of size in small grains that produces low polarized intensity in backward scattering.

4.4. Modeling J1852

The SED of J1852 shows a steep increase around 20 μm, typical of transition disks, due to the outer edge of the cavity. A clear silicate feature at 10 μm is present, characteristic of small hot grains close to the star. While scattered light image shows signal just outside of the coronagraph, there is no corresponding clear millimeter emission at the same location. The scattered light image shows a second bright ring at 0.295″, which does correspond to the ring detected in the millimeter image.

To reproduce the scattered light and SED features, we consider three zones in our model: (1) a tenuous inner disk region, solely required to reproduce the silicate feature, (2) an inner ring, responsible for the sharp jump in the mid-IR SED and for the emission seen in the SPHERE image just outside of the coronagraph radius, and finally, (3) an outer ring, to account for the second brightness increase in the near-IR polarized image and the millimeter ring. The structure is illustrated in the bottom panel of Fig. B.1. The three zones are described in the following sections.

Inner disk. The inner region, responsible for the silicate emission around 10 μm in the SED, is modeled by small grains (0.01–5 μm) between 0.1 and 5 au, although this is not well-constrained. To reproduce the shape of the emission, we consider a mixture of silicate, composed at 65% of olivine (Dorschner et al. 1995) and 35% of astronomical silicates (Draine & Lee 1984).

Inner ring. The position of the wall in the SED traces the dust temperature, which is dependent on both the inner radius and the size of the dust. For simplicity, we chose to use the same grain size distribution as for J1608. As the inner radius of J1852 is likely located behind the coronagraph, we constrained it using the SED. We reproduce well the inner ring by defining its radial extent between 15 and 22 au, with a scale height of 15 au at 100 au.

Outer ring. To reproduce the peak of intensity around 0.295″ (~43 au), an increase of the surface density in the small grains is needed, between 42 and 65 au. The mass of this region is adjusted to reproduce the relative brightness of the rings and the SED. The scale height is fixed to be the same as that of the inner ring.

Our model (Fig. 9) reproduces relatively well the position and the brightness of the peaks in the major and minor axis directions. The second ring shows an offset to the center as seen in the data. However, we were not able to reproduce the surface brightness inside the gap between the inner and outer ring in the southern part of the disk. This region is twice brighter in the data than in the model. In our model the gap is empty and the ring edges are sharp, while in practice, a low surface density of small grains could be filling it.

Large grains. Unlike J1608, we do not have sufficient high resolution data to show that the large grains are radially distributed differently to the small grains (see Fig. 8), so for now we assume that they are radially co-located. We adjusted the total mass of the large grains to reproduce the observed SMA flux at 1 mm and the ALMA 3 mm flux in the SED, allocating a small fraction of mass to the inner ring to account for the scattered light data. The large beam considered in this work also dilutes the emission of the inner ring (as modeled here), making it very difficult to detect (see Appendix A). With our assumptions on the radial structure and grain composition of the large grain population, we inferred its scale height from the effect on

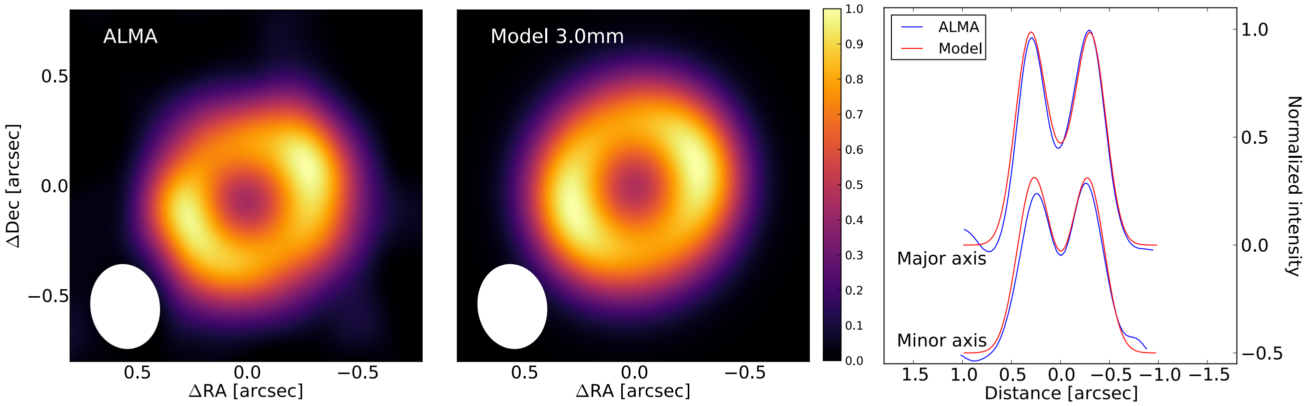

Fig. 8. *Left panel*: normalized ALMA Band 3 image of J1852 (peak flux is 1.5 mJy). The beam is represented in the bottom left of the image. *Middle panel*: normalized model obtained after convolution by a beam of 0.38″ × 0.31″. *Right panel*: cuts along the major and minor axis, with each map normalized to its maximum. For clarity, the cut along the minor axis is shifted by −0.5 in normalized intensity. The peaks are located at 0.3″(44 au) along the major axis.

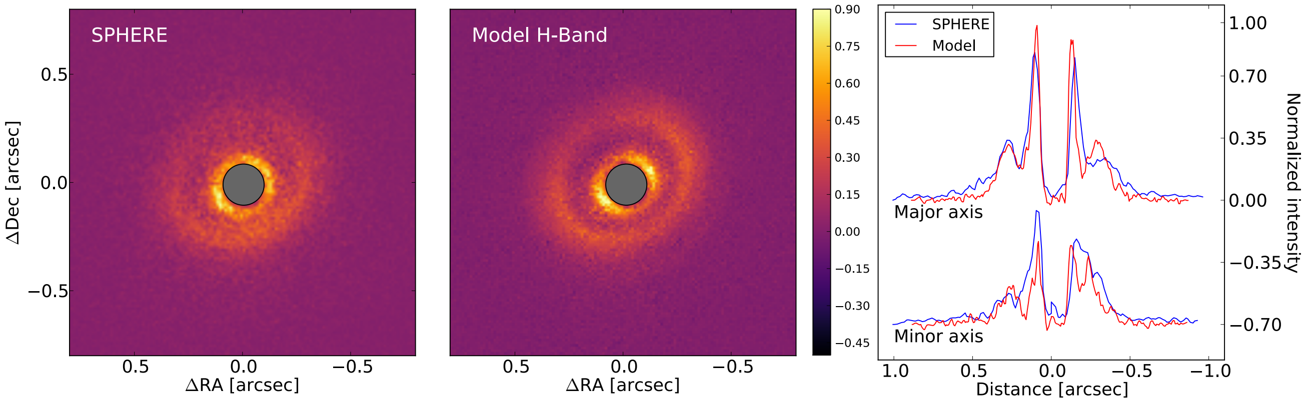

Fig. 9. *Left panel*: observed PI image of J1852. *Middle panel*: PI model map. Both maps are normalized to their maximum. *Right panel*: radial cuts along the major and minor axis for the PI images of the data and the model. Each curve is convolved with a Gaussian kernel with a standard deviation of 11 mas.

the 100 μm emission. Indeed when the scale height is larger, as more grains receive light from the star, they warm up and emit more at 100 μm (Dullemond & Dominik 2004; Woitke et al. 2016). To fit the SED, it was necessary to reduce the scale height of the large grains to about 1 au at 100 au. However, it should be noted that modeling the SED is degenerate. In particular, changing the minimum size of the large grain population ($a_{\min}$ in Table 2) from 10 to 300 μm, we find that the small and large grain populations could be distributed similarly and share the same scale height, while leading to similar excess and images as in the previous model.

5. Discussion

5.1. Dust vertical settling

Our radiative transfer modeling of J1608 indicates that small and large grains have a different spatial distribution (see Table 2). Small grains (<1 μm) are found to be more extended vertically than large grains (>10 μm). Small grains are found up to a height of 15 au at 100 au, in agreement with other results around T Tauri stars (e.g., Burrows et al. 1996; Wolff et al. 2017; Pohl et al. 2017b). In contrast, to reproduce the ALMA image and SEDs, the height of the large grain layer at 100 au has to be of a few astronomical units.

The need for stratification of dust grains was already suggested in earlier studies. Duchêne et al. (2003) showed that a perfect mixing of dust grains is not able to reproduce simultaneously HST scattered light images and IRAM millimeter images of HK Tau B, implying that vertical settling is occurring. Such a radial stratification of the dust distribution was also highlighted by Pinte et al. (2007) while modeling IR and optical scattered light images of GG Tau. In all cases, small grains are inferred to be located at the disk surface while large grains are found closer to the mid-plane, a natural outcome of vertical settling.

Vertical settling of particles occurs simultaneously with radial drift due to the effect of stellar gravity and gas drag on the dust (Weidenschilling 1977). Because the pressure force acts only on the gas, the gas rotates at sub-Keplerian speed, while decoupled dust grains rotate faster, at Keplerian speed. The gas drag on the dust particles leads to inward drift. Moreover, through the stellar gravity and the interaction with the surrounding gas, dust grains settle onto the midplane, with a different efficiency depending on the coupling of the grains. Small grains are well coupled to the gas and hence are located at similar scale heights; large grains are relatively decoupled from the gas, and settle to the midplane (Barrière-Fouchet et al. 2005). Laibe et al. (2014) found that vertical settling is much faster than the radial drift of the particles, even when taking into account grain growth.

Fromang & Papaloizou (2006) carried out ideal magnetohydrodynamic (MHD) simulations to quantify the effect of magnetic field on dust settling. They consider a strongly magnetized and turbulent disk, with a viscous coefficient of $\alpha \approx 1.5 \times 10^{-2}$ in the simulation, and no grain growth. They find that the scale height of 10 cm bodies is about $H_{100\,\mathrm{mm}} \approx 0.23\,H_{\mathrm{gas}}$ (Eq. (43) of Fromang & Papaloizou 2006), which seems too large to account for current estimates from observations. If we assume that scattered light traces the gas and that all light at 1.3 mm is emitted by grains of similar size (Draine 2006), the modeling of J1608 gives mm dust scale heights on the order of $H_{1.3\,\mathrm{mm}} = 0.41\,H_{\mathrm{gas}}$. This is similar or smaller than the predictions of Fromang & Papaloizou (2006) for particles 100 times larger, which are expected to be considerably more settled.

On the other hand, Dullemond & Dominik (2004) showed analytically that settling is more efficient for disks with low turbulence. It is also is more efficient if the grain size distribution contains fewer small grains or if the gas-to-dust ratio is low (Mulders & Dominik 2012). Moreover, in the outer parts of the disk the ionization fraction might be such that a perfect coupling to magnetic field is unlikely, and non-ideal effects might be expected. In this context, Riols & Lesur (2018) showed that ambipolar diffusion allows much more efficient settling of large grains than in perfect MHD models, allowing to reproduce the constraints on HL Tau.

5.2. Dust radial distribution

Outer radius. Our model of J1608 shows that small grains extend to larger radii than large grains (Table 2). This is expected as small grains are predicted to be well coupled to the gas, well detected beyond the ring seen in the ALMA image. On the other hand, large grains are (partially) decoupled from the gas, and experience radial drift and dust trapping. Earlier studies have shown that the gas outer radii extend further than the ones measured in the millimeter continuum. An average ratio between the gas and dust outer disk radii of 1.96 ± 0.04 was found in 22 disks of the Lupus star forming region (Ansdell et al. 2018). This trend is also observed in 12 disks in Chamaeleon II (Villenave et al. in prep) and in individual disks such as PDS 70 where the gas is detected up to 160 au and millimeter dust up to 110 au (Long et al. 2018). We note, however, that the sensitivity limits between the ALMA observations in CO and those in polarized scattered light are different. The outermost radius at which scattered light is detected depends on the stellar illumination (which drops as r^{-2}). Besides the sensitivity limits, the difference between gas/small grains and large grains can be due to optical depth effects combined with the radial drift of the large grains (Facchini et al. 2017). Depending on the inclination of the system, the vertical height of small grains can also have a large effect on their detectable radius. If the vertical height of small grains decreases after some radius, the surface layers could be located in the shadow of the inner region and would not be detected in scattered light (Muro-Arena et al. 2018).

Inner radius. From the PV diagram shown in Fig. 3 and our modeling, we found that both the small grains and gas in J1608 extend inwards of the large grains, indicating that the cavity is not completely empty. Likewise, an inner ring in scattered light is detected inside the millimeter cavity of J1852. A similar conclusion was reached on several other transition disks, which show a CO cavity smaller than the millimeter dust cavity, such as Sz 91 (Canovas et al. 2015, 2016) or RXJ1604.3-2130A (Zhang et al. 2014) for example. In each of these systems, the authors found the CO to extend at least 20 au inward of the outer edge of the millimeter dust cavity. These differences in inner radius could be related to the mechanisms responsible for the cavities in transition disks, which we explore in the next subsection.

5.3. Comparison with other transition disks

Several mechanisms have been proposed to explain the origin of cavities in transition disks: photoevaporation (Owen et al. 2011), dead zones (Flock et al. 2015; Pinilla et al. 2016), opacity effect via grain growth (Dullemond & Dominik 2005; Birnstiel et al. 2012), or planetary or stellar companion interacting with the disk (Crida & Morbidelli 2007; Facchini et al. 2013). Recent studies showed that most of the transition disks studied at high angular resolution (a sample biased toward the brightest objects) still have moderate accretion rates (Manara et al. 2014) and rather small CO cavities. Thus, photoevaporation might not be the main mechanism in this sample (Pinilla et al. 2018b; van der Marel et al. 2018).

Dead-zones are low ionization regions in which magneto-rotational instability is suppressed (Blaes & Balbus 1994; Flock et al. 2012). In such regions the rate of gas flow decreases, leading to accumulation of gas at the outer edge of the region. The pressure bump is able to trap particles and stop the radial drift of large grains, which leads to a ring-like morphology for the millimeter dust as observed in transition disks (Pinilla et al. 2016). Synthetic scattered light and millimeter continuum images of disk with a dead zone in the inner 30 au show that the inner edge of the ring is located at about the same radius in both tracers. If a dead zone and a MHD wind act together however, a larger difference in inner radii could be observed.

Dust depleted cavities can also be generated by planets. Planets of mass larger than 1 M_J can carve gaps in the gas and induce large perturbations in the gas surface density (Dong & Fung 2017), in turn generating pressure maxima that trap dust particles. In this case, the inner region of the disk is depleted in millimeter grains, while smaller grains can flow inside the planet's orbit, and potentially be detected in scattered light (de Juan Ovelar et al. 2013; Dong et al. 2015).

To assess the origin of the cavity in transition disks, we compiled a sample of 22 disks that have both scattered light and millimeter observations, as presented in Table 3. This sample includes two known binary systems, HD 142527 and V4046 Sgr (Biller et al. 2014; Quast et al. 2000). The excentric binary companion in HD 142527 is likely responsible for the cavity (Price et al. 2018), but this is probably not the case for the very close binary system V4046 Sgr (2.4 days period; Quast et al. 2000; D'Orazi et al. 2018). All sources show a resolved dust cavity in the millimeter and, except Oph IRS 48 and Sz 91 for which we consider respectively VISIR and Subaru observations, all have scattered light observations with VLT/SPHERE. We report the outer radius of the scattered light cavity and millimeter peak in Table 3. We re-scale the published values using the latest distances from Gaia DR2 (Gaia Collaboration et al. 2018). In this analysis, we only consider the position of the main cavity, regardless of the presence of an inner disk within the first few au. For 5 of the 22 disks considered in this analysis, the scattered light cavity may be located inside the coronagraphic mask radius, giving the upper limits in Table 3. For the small fraction of transition disks that possesses multiple rings in scattered light, we report the position of the scattered light ring that is the closest to the millimeter peak emission (for the following objects: HD 169142, V4046 Sgr, J1852, HD 97048, Lk Ca 15, Sz 91 and HD 34282). For J1608, which has a large inclination, we chose to estimate the ALMA and SPHERE peaks on our model, after computing it face-on.

From synthetic observations, calculated after hydrodynamical and dust evolution simulations and considering massive planets on a circular orbit, de Juan Ovelar et al. (2013) found

Table 3. Position of millimeter and scattered light cavities for 22 transition disks, ordered by increasing millimeter cavity size.

Source	d (pc)	Band	$R_{\rm peak,mm}$ (au)	$R_{\rm in,PI}$ (au)	$R_{\rm peak,PI}$ (au)	Ratio
HD 100546	110 ± 1	B7 – R'	15.0	12.0	14.0	0.81, 0.96
HD 169142	114 ± 1	B6 – J	21.7	16.0	20.5	0.74, 0.94
V4046 Sgr	72 ± 1	B6 – H	27.0	15.3	26.9	0.57, 0.99
UX Tau A	140 ± 2	B6 – H	33.2	< 14		< 0.42
HD 100453	104 ± 1	B6 – R'	33.3	14.6	18.5	0.44, 0.55
T Cha	110 ± 1	B3 – H	36.8	28.8	31.4	0.78, 0.85
HD 143006	166 ± 4	B6 – J	40.0	18.2	30.0	0.45, 0.75
DoAr44	146 ± 1	B7 – H	42.7	< 14		< 0.33
CQ Tau	163 ± 2	B6 – J	47.3	< 4		< 0.08
J1852	146 ± 1	B3 – H	43.8	34.7	43.1	0.79, 0.98
HD 135344B	136 ± 2	B7 – R	54.6	18.3	23.5	0.34, 0.43
HD 97048	185 ± 1	B7 – J	55.4	45.9	54.4	0.83, 0.98
LkCa 15	159 ± 1	B7 – J	64.0	53.7	64	0.84, 1.0
Oph IRS 48	134 ± 2	B9 – Q	70.6	33.3	59.1	0.47, 0.84
RY Lup	159 ± 2	B7 – H	71.9	< 15		< 0.20
MWC758	160 ± 2	B7 – Y	80.0	< 15		< 0.19
PDS 70	113 ± 1	B7 – J	81.0	45.0	54.0	0.56, 0.67
J1608	156 ± 6	B6 – H	81.0	45.0	49.9	0.56, 0.82
RXJ1604.3-2130A	150 ± 1	B6 – R'	83.0	54.9	63.7	0.66, 0.77
Sz 91	159 ± 2	B7 – Ks	87.5	46.0	50.9	0.52, 0.58
HD 34282	312 ± 5	B7 – J	133.9	124.2	132.7	0.93, 0.99
HD 142527	157 ± 1	B7 – Ks	165, 205	78.5	157.0	0.38, 0.95

Notes. Known binary systems are indicated with the name in italic. We report the peak of the millimeter intensity beyond the cavity, along with the position of the inner radius and peak in scattered light. When the cavity is not detected down to the coronagraph radius in scattered light, we use the symbol <. The position of the scattered light cavity ($R_{\rm cav,PI}$), defined as the mean between $R_{\rm in,PI}$ and $R_{\rm peak,PI}$, is used in Fig. 10.
References. HD 100546: Pinilla et al. (2018b); Garufi et al. (2016), HD 169142: Fedele et al. (2017); Pohl et al. (2017a); Bertrang et al. (2018), V4046 Sgr: Rosenfeld et al. (2013); Avenhaus et al. (2018), HD 100453: van der Plas et al. (2019); Benisty et al. (2017), T Cha: Hendler et al. (2018); Pohl et al. (2017b), UX Tau: Pinilla et al. (2018b), Menard (in prep.); HD 143006: Benisty et al. (2018); Pérez et al. (2018a), DoAr44: Casassus et al. (2018); Avenhaus et al. (2018), CQ Tau: Pinilla et al. (2018b); Benisty (in prep), J1852: This work, HD 97048: van der Plas et al. (2017b); Ginski et al. (2016), LkCa 15: Andrews et al. (2011); Thalmann et al. (2015, 2016), HD 135344B: Pinilla et al. (2018b); Stolker et al. (2016), Oph IRS 48: van der Marel et al. (2013); Bruderer et al. (2014); Geers et al. (2007), RY Lup: Pinilla et al. (2018b); Langlois et al. (2018), MWC758: Marino et al. (2015); Benisty et al. (2015), RXJ1604.3-2130A: Pinilla et al. (2018a, 2015), PDS 70: Long et al. (2018); Keppler et al. (2018), J1608:Ansdell et al. (2016), This work, Sz 91: Canovas et al. (2016); Tsukagoshi et al. (2014), HD 34282: van der Plas et al. (2017a), de Boer (in prep.), HD 142527: Boehler et al. (2017); Avenhaus et al. (2014).

that as the mass of a planet in a disk increases, the position of the millimeter ring moves further away from the planet's orbit while the outer radius of the scattered light cavity does not. They derived an analytic formula relating the planet mass with the ratio between the position of the so-called "scattered light wall" to that of the ALMA peak. The scattered light wall is defined as the radial location where the scattered light signal is half of the difference between the flux measured at the peak of the wall and the minimum flux in the gap. As the position of the wall is usually not explicitly published in the literature, we use both the inner radius of the disk beyond the cavity, as seen in scattered light, and the position of the peak in polarized intensity (respectively referred to as $R_{\rm in,PI}$, and $R_{\rm peak,PI}$, in Table 3). Considering the position of the cavity instead of that of the wall tends to overestimate the planet mass, and inversely under-estimate it when the position of the peak is used. We also note that the models were specifically calculated for R band scattered light observations and Band 7 (850 μm), and only for a planet in a circular orbit. However, little difference is expected for such small variations in wavelength, as can be seen by comparing the theoretical profiles of Band R and Band H in Fig. 3 of de Juan Ovelar et al. (2013).

We show in Fig. 10 the radius of the scattered light cavity ($R_{\rm cav,PI}$), defined as the mean between $R_{\rm in,PI}$ and $R_{\rm peak,PI}$, as a function of the radius of the millimeter ring ($R_{\rm peak,mm}$). We observe that for each system the scattered light cavity radius is smaller than the millimeter radius (green line), with about one third of the disks having a ratio smaller than 0.5 (see Table 3). The models of de Juan Ovelar et al. (2013) would imply companion masses above 13 M_J for ratios lower than 0.48 when the planet is located at 20 au, 0.53 when it is at 40 au, and 0.56 at 60 au. As can be seen in Fig. 10, fifteen disks in our sample (namely HD 100546, HD 169142, V4046 Sgr, HD 100453, T Cha, J1852, HD 97048, Lk Ca 15, Oph IRS 48, PDS 70, J1608, RXJ1604.3-2130A, Sz 91, HD 34282 and HD 142527) are above the red shaded area. This indicates ratios larger than the ones given above, placing the possible companions in the planetary mass regime. PDS 70 is the only system where a few Jupiter mass planet was imaged in the main cavity (Keppler et al. 2018; Müller et al. 2018), while HD 142527 has a stellar companion. For the other disks considered (namely UX Tau A, HD 143006, DoAr44, CQ Tau, HD 135344B, RY Lup and MWC758), the ratio (or its upper limit) would lead to objects in the stellar or brown dwarf regime. These disks appear in the red shaded area in Fig. 10.

Several direct imaging surveys have been carried out searching for companions. Kraus et al. (2008, 2011) performed a high-resolution imaging studies of Taurus-Auriga and Upper Sco star-forming regions to identify companions down to 8 to 12 M$_J$.

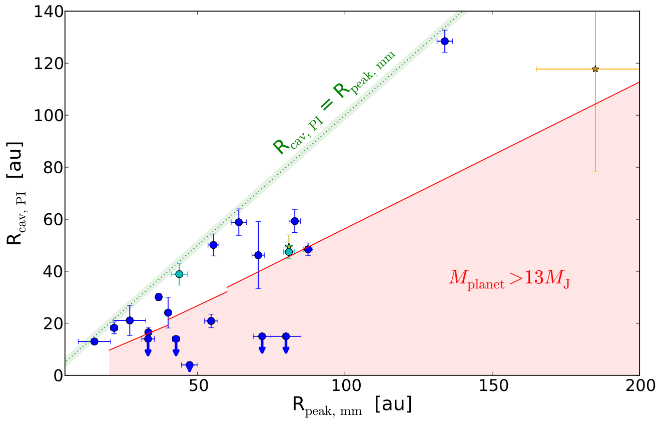

Fig. 10. Comparison of the cavity sizes as measured in the millimeter and in scattered light for a sample of 22 transition disks. The cyan points correspond to the two systems modeled in this paper, while the yellow star symbols refer to HD 142527 that has a stellar companion in the cavity, and PDS 70 where a planet has been detected. The upper limits, indicated with arrows, refer to systems for which scattered light cavities could not be measured down to the coronagraphic radius. Horizontal bars correspond to one tenth of the millimeter beam, while vertical bars represent the interval between the cavity radius and the peak in scattered light (Table 3). The red region shows the ratio for which the planet mass inferred with the prescription of de Juan Ovelar et al. (2013) is larger than 13 Jupiter masses. The three breaks correspond to their models with planets at radii of 20, 40 and 60 au, respectively.

More recently, Subaru high-contrast observations of 68 young stellar objects were performed (SEEDS survey; Uyama et al. 2017b), reaching typical limits of 10 M_J at 0.5″ (~70 au at 140 pc) and 6 M_J at 1″. The SEEDS survey covered 12 disks of our sample[3], without a planet detection. For HD 169142, T Cha, HD 135344B, HD 97048 and RY Lup, detection limits were also presented in individual studies, that reached sensitivity of ~ 10 M_J at 0.25″(Ligi et al. 2018; Pohl et al. 2017b; Maire et al. 2017; Ginski et al. 2016; Langlois et al. 2018). We also note that claims of candidate companions were made in the disks of HD 100546 (Quanz et al. 2015; Currie et al. 2014), HD 169142 (Biller et al. 2014; Reggiani et al. 2014), Lk Ca 15 (Kraus & Ireland 2012; Sallum et al. 2015) and MWC758 (Reggiani et al. 2018), without having been firmly confirmed until now.

An alternative scenario to explain the small ratio between the radius of the scattered light cavity and the millimeter peak could be that the cavities are caused by several lower mass planets, which would allow small grains to fill the cavity, while large grains are retained in the outer disk (Rosotti et al. 2016; Dipierro & Laibe 2017). In this case, no gap would be detected in scattered light, while a clear ring would appear in the millimeter images.

6. Conclusion

In this paper, we present new polarized scattered light observations of two transition disks, namely 2MASS J16083070-3828268 (J1608) and RXJ1852.3-3700 (J1852). The image of J1608 reveals a highly inclined disk (~74°) with a large cavity of about 50 au in scattered light. We also detect a faint line, in the southwest, that we interpret as tracing the rear-facing side of the disk. The second disk of our study, J1852, shows scattered light (referred to as an inner ring) just beyond the coronagraph radius, a gap between 22 and 42 au and an outer ring up to 65 au. A cavity inward of the first ring, as inferred from the SED, is located behind the coronagraph.

We modeled both scattered light and millimeter images (that trace small and large dust grains, respectively), together with the SED, using radiative transfer. Our modeling of the highly inclined disk J1608 indicates that small and large grains have a different spatial distribution. Radially, small grains are more extended inward and outward than the large grains, by respectively 30 au and 60 au. Vertically, at a radius of 100 au, we constrain the large grains to be located within a height of 5 au, while the small grains extend vertically up to 12 au. We follow a similar procedure for J1852 and propose a model with a spatial segregation between grain sizes. However, the disk is not inclined enough to allow us to strongly constrain the relative vertical extents of various grain sizes, and so our modeling of the images and SED for this object remains degenerate.

The radial and vertical segregation in particle sizes observed in J1608 is likely a consequence of both vertical settling and dust radial drift that occur during the evolution of the disks. Vertical settling in low turbulence disks and/or following non-ideal MHD effects such as ambipolar diffusion can explain the relatively small scale height inferred for the large grain population. The difference in the outer extents (as measured in scattered light and millimeter emission) could result from radial drift, optical depth and illumination effects, while the difference in the inner radius of the outer disk, might be related to the presence of planet(s).

We compile a sample of 22 transition disks imaged with both ALMA and SPHERE, and find that scattered light is detected inside the millimeter cavity in all of the disks. We use the observed spatial difference in mm and far-IR distributions to identify a segregation in particle sizes, and infer the proposed companion mass responsible for the cavity using the prescription of de Juan Ovelar et al. (2013). We show that in 15 objects, including the two disks modeled in this study, the cavities could be explained by the presence of a giant planet. The seven other disks of the sample show large ratios between the position of the scattered light and the millimeter cavity, suggestive of a companion above the planetary mass regime, or alternatively, of a multiple planetary system.

As of today, apart from PDS 70 (Keppler et al. 2018), direct imaging surveys with results available in the literature, did not provide the detection of other such objects within a transition disk. New deeper observations with direct imaging instruments, or search for non-Keplerian motions in the gas kinematics with ALMA (Pérez et al. 2015, 2018b; Teague et al. 2018; Pinte et al. 2018) might lead to further detections.

Acknowledgements. MV, MB, FM, GvdP, CP acknowledge funding from ANR of France under contract number ANR-16-CE31-0013 (Planet Forming Disks). M.F. received funding from the European Research Council (ERC) under the European Union's Horizon 2020 research and innovation programme (grant agreement n° 757957). J. O. acknowledges financial support from the ICM (Iniciativa Científica Milenio) via the Núcleo Milenio de Formación Planetaria grant, from the Universidad de Valparaíso, and from Fondecyt (grant 1180395). L.P. acknowledges support from CONICYT project Basal AFB-170002 and from FONDECYT Iniciación project #11181068. A.Z. acknowledges support from the CONICYT + PAI/ Convocatoria nacional subvención a la instalación en la academia, convocatoria 2017 + Folio PAI77170087. This paper makes use of the following ALMA data: ADS/JAO.ALMA#2015.1.00222.S and ADS/JAO.ALMA#2015.1.01083.S. ALMA is a partnership of ESO (representing its member states), NSF (USA) and NINS (Japan), together with NRC (Canada), MOST and ASIAA (Taiwan), and KASI (Republic of Korea), in cooperation with the Republic of Chile. The Joint ALMA Observatory is operated by ESO, AUI/NRAO and NAOJ. This publication makes use of VOSA, developed under the Spanish Virtual Observatory project supported

---

[3] Namely UX Tau A, HD 143006, DoAr44, CQ Tau, J1852, HD 135344B, Lk Ca 15, Oph IRS 48, MWC 758, RXJ1604.3-2130A, Sz 91, HD 34282.

from the Spanish MINECO through grant AyA2017-84089. SPHERE is an instrument designed and built by a consortium consisting of IPAG (Grenoble, France), MPIA (Heidelberg, Germany), LAM (Marseille, France), LESIA (Paris, France), Laboratoire Lagrange (Nice, France), INAF–Osservatorio di Padova (Italy), Observatoire de Genéve (Switzerland), ETH Zurich (Switzerland), NOVA (Netherlands), ONERA (France) and ASTRON (Netherlands) in collaboration with ESO. SPHERE was funded by ESO, with additional contributions from CNRS (France), MPIA (Germany), INAF (Italy), FINES (Switzerland) and NOVA (Netherlands). SPHERE also received funding from the European Commission Sixth and Seventh Framework Programmes as part of the Optical Infrared Coordination Network for Astronomy (OPTICON) under grant number RII3-Ct-2004-001566 for FP6 (2004–2008), grant number 226604 for FP7 (2009–2012) and grant number 312430 for FP7 (2013–2016). We also acknowledge financial support from the Programme National de Planétologie (PNP) and the Programme National de Physique Stellaire (PNPS) of CNRS-INSU in France. This work has also been supported by a grant from the French Labex OSUG2020 (Investissements d'avenir – ANR10 LABX56). The project is supported by CNRS, by the Agence Nationale de la Recherche (ANR-14-CE33-0018). It has also been carried out within the frame of the National Centre for Competence in Research PlanetS supported by the Swiss National Science Foundation (SNSF). MRM, HMS, and SD are pleased to acknowledge this financial support of the SNSF. Finally, this work has made use of the the SPHERE Data Centre, jointly operated by OSUG/IPAG (Grenoble), PYTHEAS/LAM/CESAM (Marseille), OCA/Lagrange (Nice) and Observtoire de Paris/LESIA (Paris).

References

Alcala, J. M., Manara, C. F., Natta, A., et al. 2017, A&A, 600, A20
Andrews, S. M., Rosenfeld, K. A., Wilner, D. J., & Bremer, M. 2011, ApJ, 742, L5
Ansdell, M., Williams, J. P., van der Marel, N., et al. 2016, ApJ, 828, 46
Ansdell, M., Williams, J. P., Trapman, L., et al. 2018, ApJ, 859, 21
Avenhaus, H., Quanz, S. P., Schmid, H. M., et al. 2014, ApJ, 781, 87
Avenhaus, H., Quanz, S. P., Garufi, A., et al. 2018, ApJ, 863, 44
Barrière-Fouchet, L., Gonzalez, J. F., Murray, J. R., Humble, R. J., & Maddison, S. T. 2005, A&A, 443, 185
Bayo, A., Rodrigo, C., Barrado Y Navascués, D., et al. 2008, A&A, 492, 277
Benisty, M., Juhasz, A., Boccaletti, A., et al. 2015, A&A, 578, L6
Benisty, M., Stolker, T., Pohl, A., et al. 2017, A&A, 597, A42
Benisty, M., Juhász, A., Facchini, S., et al. 2018, A&A, 619, A171
Bertrang, G. H. M., Avenhaus, H., Casassus, S., et al. 2018, MNRAS, 474, 5105
Beuzit, J.-L., Feldt, M., Dohlen, K., et al. 2008, in Ground-based and Airborne Instrumentation for Astronomy II, Vol. 7014, 701418
Biller, B. A., Males, J., Rodigas, T., et al. 2014, ApJ, 792, L22
Birnstiel, T., Andrews, S. M., & Ercolano, B. 2012, A&A, 544, A79
Blaes, O. M., & Balbus, S. A. 1994, ApJ, 421, 163
Boehler, Y., Weaver, E., Isella, A., et al. 2017, ApJ, 840, 60
Bruderer, S., van der Marel, N., van Dishoeck, E. F., & van Kempen T. A. 2014, A&A, 562, A26
Burrows, C. J., Stapelfeldt, K. R., Watson, A., et al. 1996, ApJ, 473, 437
Canovas, H., Ménard, F., de Boer, J., et al. 2015, A&A, 582, L7
Canovas, H., Caceres, C., Schreiber, M. R., et al. 2016, MNRAS, 458, L29
Carbillet, M., Bendjoya, P., Abe, L., et al. 2011, Exper. Astron., 30, 39
Casassus, S., van der Plas, G., Perez, S. M., et al. 2013, Nature, 493, 191
Casassus, S., Avenhaus, H., Pérez, S., et al. 2018, MNRAS, 477, 5104
Cazzoletti, P., van Dishoeck, E. F., Pinilla, P., et al. 2018, A&A, 619, A161
Crida, A., & Morbidelli, A. 2007, MNRAS, 377, 1324
Currie, T., Muto, T., Kudo, T., et al. 2014, ApJ, 796, L30
de Boer, J., Salter, G., Benisty, M., et al. 2016, A&A, 595, A114
de Juan Ovelar, M., Min, M., Dominik, C., et al. 2013, A&A, 560, A111
Dipierro, G., & Laibe, G. 2017, MNRAS, 469, 1932
Dohlen, K., Langlois, M., Saisse, M., et al. 2008, in Ground-based and Airborne Instrumentation for Astronomy II, Vol. 7014, 70143L
Dong, R., & Fung, J. 2017, ApJ, 835, 146
Dong, R., Zhu, Z., & Whitney, B. 2015, ApJ, 809, 93
Dong, R., Liu, S.-Y., Eisner, J., et al. 2018, ApJ, 860, 124
D'Orazi, V., Gratton, R., Desidera, S., et al. 2018, Nat. Astron., 172
Dorschner, J., Begemann, B., Henning, T., Jaeger, C., & Mutschke, H. 1995, A&A, 300, 503
Draine, B. T. 2006, ApJ, 636, 1114
Draine, B. T., & Lee, H. M. 1984, ApJ, 285, 89
Duchêne, G., Ménard, F., Stapelfeldt, K., & Duvert, G. 2003, A&A, 400, 559
Dullemond, C. P., & Dominik, C. 2004, A&A, 421, 1075
Dullemond, C. P., & Dominik, C. 2005, A&A, 434, 971
Facchini, S., Lodato, G., & Price, D. J. 2013, MNRAS, 433, 2142
Facchini, S., Birnstiel, T., Bruderer, S., & van Dishoeck, E. F. 2017, A&A, 605, A16
Fedele, D., Carney, M., Hogerheijde, M. R., et al. 2017, A&A, 600, A72
Flock, M., Henning, T., & Klahr, H. 2012, ApJ, 761, 95
Flock, M., Ruge, J. P., Dzyurkevich, N., et al. 2015, A&A, 574, A68
Fromang, S., & Papaloizou, J. 2006, A&A, 452, 751
Gaia Collaboration (Brown, A. G. A., et al.) 2018, A&A, 616, A1
Garufi, A., Quanz, S. P., Schmid, H. M., et al. 2016, A&A, 588, A8
Garufi, A., Benisty, M., Pinilla, P., et al. 2018, A&A, 620, A94
Geers, V. C., Pontoppidan, K. M., van Dishoeck, E. F., et al. 2007, A&A, 469, L35
Geers, V. C., Gorti, U., Meyer, M. R., et al. 2012, ApJ, 755
Ginski, C., Stolker, T., Pinilla, P., et al. 2016, A&A, 595, A112
Hendler, N. P., Pinilla, P., Pascucci, I., et al. 2018, MNRAS, 475, L62
Hughes, A. M., Andrews, S. M., Wilner, D. J., et al. 2010, ApJ, 140, 887
Isella, A., Guidi, G., Testi, L., et al. 2016, Phys. Rev. Lett., 117, 251101
Keppler, M., Benisty, M., Müller, A., et al. 2018, A&A, 617, A44
Kohn, S. A., Shkolnik, E. L., Weinberger, A. J., Carlberg, J. K., & Llama, J. 2016, ApJ, 820, 2
Kraus, A. L., & Ireland, M. J. 2012, ApJ, 745, 5
Kraus, A. L., Ireland, M. J., Martinache, F., & Lloyd, J. P. 2008, ApJ, 679, 762
Kraus, A. L., Ireland, M. J., Martinache, F., & Hillenbrand, L. A. 2011, ApJ, 731, 8
Laibe, G., Gonzalez, J.-F., Maddison, S. T., & Crespe, E. 2014, MNRAS, 437, 3055
Langlois, M., Dohlen, K., Vigan, A., et al. 2014, in Ground-based and Airborne Instrumentation for Astronomy V, Vol. 9147, 91471R
Langlois, M., Pohl, A., Lagrange, A. M., et al. 2018, A&A, 614, A88
Lebouteiller, V., Barry, D. J., Spoon, H. W. W., et al. 2011, ApJS, 196, 8
Ligi, R., Vigan, A., Gratton, R., et al. 2018, MNRAS, 473, 1774
Long, Z. C., Akiyama, E., Sitko, M., et al. 2018, ApJ, 858, 112
Maire, A. L., Stolker, T., Messina, S., et al. 2017, A&A, 601, A134
Manara, C. F., Testi, L., Natta, A., et al. 2014, A&A, 568, A18
Marino, S., Casassus, S., Perez, S., et al. 2015, ApJ, 813, 76
Martinez, P., Dorrer, C., Kasper, M., Boccaletti, A., & Dohlen, K. 2009, A&A, 500, 1281
Mathis, J. S., Rumpl, W., & Nordsieck, K. H. 1977, ApJ, 217, 425
Muñoz, D. J., & Lai, D. 2016, ApJ, 827, 43
Mulders, G. D., & Dominik, C. 2012, A&A, 539, A9
Müller, A., Keppler, M., Henning, T., et al. 2018, A&A, 617, L2
Muro-Arena, G. A., Dominik, C., Waters, L. B. F. M., et al. 2018, A&A, 614, A24
Muto, T., Grady, C. A., Hashimoto, J., et al. 2012, ApJ, 748, L22
Neuhaeuser, R., Walter, F. M., Covino, E., et al. 2000, A&A, SS, 146, 323
Owen, J. E., Ercolano, B., & Clarke, C. J. 2011, MNRAS, 412, 13
Pascucci, I., Hollenbach, D., Najita, J., et al. 2007, ApJ, 663
Pérez, L. M., Carpenter, J. M., Andrews, S. M., et al. 2016, Science, 353, 1519
Pérez, S., Dunhill, A., Casassus, S., et al. 2015, ApJ, 811, L5
Pérez, L. M., Benisty, M., Andrews, S. M., et al. 2018a, ApJ, 869, L50
Pérez, S., Casassus, S., & Benítez-Llambay, P. 2018b, MNRAS, 480, L12
Pinilla, P., de Boer, J., Benisty, M., et al. 2015, A&A, 584, L4
Pinilla, P., Flock, M., Ovelar, M. d. J., & Birnstiel, T. 2016, A&A, 596, A81
Pinilla, P., Benisty, M., de Boer, J., et al. 2018a, ApJ, 868, 85
Pinilla, P., Tazzari, M., Pascucci, I., et al. 2018b, ApJ, 859, 32
Pinte, C., Fouchet, L., Ménard, F., Gonzalez, J. F., & Duchêne, G. 2007, A&A, 469, 963
Pinte, C., Menard, F., Duchene, G., & Bastien, P. 2006, A&A, 459, 797
Pinte, C., Harries, T. J., Min, M., et al. 2009, A&A, 498, 967
Pinte, C., Dent, W. R. F., Ménard, F., et al. 2016, ApJ, 816, 25
Pinte, C., Price, D. J., Ménard, F., et al. 2018, ApJ, 860, L13
Pohl, A., Benisty, M., Pinilla, P., et al. 2017a, ApJ, 850, 52
Pohl, A., Sissa, E., Langlois, M., et al. 2017b, A&A, 605, A34
Price, D. J., Cuello, N., Pinte, C., et al. 2018, MNRAS, 477, 1270
Quanz, S. P., Amara, A., Meyer, M. R., et al. 2015, ApJ, 807, 64
Quast, G. R., Torres, C. A. O., de La Reza, R., da Silva, L., & Mayor, M. 2000, in IAU Symposium, Vol. 200, 28
Reggiani, M., Quanz, S. P., Meyer, M. R., et al. 2014, ApJ, 792, L23
Reggiani, M., Christiaens, V., Absil, O., et al. 2018, A&A, 611, A74
Rigliaco, E., Pascucci, I., Duchene, G., et al. 2015, ApJ, 801, 31
Riols, A., & Lesur, G. 2018, A&A, 617, A117
Riviere-Marichalar, P., Merín, B., Kamp, I., Eiroa, C., & Montesinos, B. 2016, A&A, 594, A59
Rosenfeld, K. A., Andrews, S. M., Wilner, D. J., Kastner, J. H., & McClure, M. K. 2013, ApJ, 775, 136
Rosotti, G. P., Juhasz, A., Booth, R. A., & Clarke, C. J. 2016, MNRAS, 459, 2790
Sallum, S., Follette, K. B., Eisner, J. A., et al. 2015, Nature, 527, 342
Schmid, H. M., Joos, F., & Tschan, D. 2006, A&A, 452, 657
Siess, L., Dufour, E., & Forestini, M. 2000, A&A, 358, 593
Silverstone, M. D., Meyer, M. R., Mamajek, E. E., et al. 2006, ApJ, 639, 1138
Stolker, T., Dominik, C., Avenhaus, H., et al. 2016, A&A, 595, A113

Stolker, T., Sitko, M., Lazareff, B., et al. 2017, ApJ, 849, 143
Strom, K. M., Strom, S. E., Edwards, S., Cabrit, S., & Skrutskie, M. F. 1989, AJ, 97, 1451
Teague, R., Bae, J., Bergin, E. A., Birnstiel, T., & Foreman-Mackey, D. 2018, ApJ, 860, L12
Thalmann, C., Mulders, G. D., Janson, M., et al. 2015, ApJ, 808, L41
Thalmann, C., Janson, M., Garufi, A., et al. 2016, ApJ, 828, L17
Tsukagoshi, T., Momose, M., Hashimoto, J., et al. 2014, ApJ, 783, 90
Uyama, T., Hashimoto, J., Kuzuhara, M., et al. 2017a, AJ, 153, 106
Uyama, T., Hashimoto, J., Kuzuhara, M., et al. 2017b, AJ, 153, 106
Uyama, T., Hashimoto, J., Muto, T., et al. 2018, AJ, 156, 63
van der Marel, N., van Dishoeck, E. F., Bruderer, S., et al. 2013, Science, 340, 1199
van der Marel, N., Verhaar, B. W., van Terwisga, S., et al. 2016, A&A, 592, A126
van der Marel, N., Williams, J. P., Ansdell, M., et al. 2018, ApJ, 859, 21
van der Plas, G., Ménard, F., Canovas, H., et al. 2017a, A&A, 607, A55
van der Plas, G., Wright, C. M., Ménard, F., et al. 2017b, A&A, 597, A32
van der Plas, G., Ménard, F., Gonzalez, J. F., et al. 2019, A&A, in press, DOI: 10.1051/0004-6361/201834134
Weidenschilling, S. J. 1977, MNRAS, 180, 57
Woitke, P., Min, M., Pinte, C., et al. 2016, A&A, 586, A103
Wolff, S. G., Perrin, M. D., Stapelfeldt, K., et al. 2017, ApJ, 851, 56
Zhang, K., Isella, A., Carpenter, J. M., & Blake, G. A. 2014, ApJ, 791, 42

---

[1] Univ. Grenoble Alpes, CNRS, IPAG, 38000 Grenoble, France
e-mail: `villenam@univ-grenoble-alpes.fr`
[2] European Southern Observatory, Alonso de Córdova 3107, Vitacura, Casilla 19001, Santiago 19, Chile
[3] Unidad Mixta Internacional Franco-Chilena de Astronomía (CNRS, UMI 3386), Departamento de Astronomía, Universidad de Chile, Camino El Observatorio 1515, Las Condes, Santiago, Chile
[4] Departamento de Astronomía, Universidad de Chile, Camino El Observatorio 1515, Las Condes, Santiago, Chile
[5] Joint ALMA Observatory, Alonso de Córdova 3107, Vitacura 763-0355, Santiago, Chile
[6] INAF, Osservatorio Astrofisico di Arcetri, Largo Enrico Fermi 5, 50125 Firenze, Italy
[7] Anton Pannekoek Institute for Astronomy, University of Amsterdam, Science Park 904, 1098XH Amsterdam, The Netherlands
[8] Department of Astronomy/Steward Observatory, The University of Arizona, 933 North Cherry Avenue, Tucson, AZ 85721, USA
[9] Monash Centre for Astrophysics (MoCA) and School of Physics and Astronomy, Monash University, Clayton, Victoria 3800, Australia
[10] Institute for Astronomy, University of Hawaii, Honolulu, HI, USA
[11] Leiden Observatory, Leiden University, PO Box 9513, 2300 RA Leiden, The Netherlands
[12] National Astronomical Observatory of Japan, Osawa 2-21-1, Mitaka, Tokyo 181-8588, Japan
[13] Max Planck Institute for Astronomy, Königstuhl 17, 69117 Heidelberg, Germany
[14] Institute of Astronomy, Madingley Road, Cambridge CB3 OHA, UK
[15] Facultad de Ciencias, Instituto de Física y Astronomía, Universidad de Valparaíso, Av. Gran Bretaña 1111, 5030 Casilla, Valparaíso, Chile
[16] Núcleo Milenio Formación Planetaria – NPF, Universidad de Valparaíso, Av. Gran Bretaña 1111, Valparaíso, Chile
[17] Núcleo de Astronomía, Facultad de Ingeniería y Ciencias, Universidad Diego Portales, Av. Ejercito 441, Santiago, Chile
[18] Escuela de Ingeniería Industrial, Facultad de Ingeniería y Ciencias, Universidad Diego Portales, Av. Ejercito 441, Santiago, Chile
[19] Aix Marseille Université, CNRS, LAM, 13388 Marseille, France
[20] NOVA Optical Infrared Instrumentation Group, Oude Hoogeveensedijk 4, 7991 PD Dwingeloo, The Netherlands
[21] DOTA, ONERA, Université Paris Saclay, 91123 Palaiseau France
[22] Geneva Observatory, University of Geneva, Chemin des Mailettes 51, 1290 Versoix, Switzerland

Appendix A: Additional maps

Saturated J1608 Q_ϕ image. To visualize better the faint line south of J1608, we show the Q_ϕ image of the H and J-band observations in Fig. A.1, while saturating the image for brightness larger than 5% of the maximum intensity of the map. The right panel also shows our Q_ϕ model image with the same dynamical range.

Model Q_ϕ and U_ϕ images. As we show and model the polarized intensity image in the main text, we present in Figs. A.2 and A.3, the individual Q_ϕ and U_ϕ model predictions for J1608 and J1852, respectively. The Q_ϕ images are very similar to our model polarized intensity images that reproduce well the data. In addition, when compared to Figs. 1 and 2, we see that the regions with positive and negative intensity in the U_ϕ images are also a good match to the data.

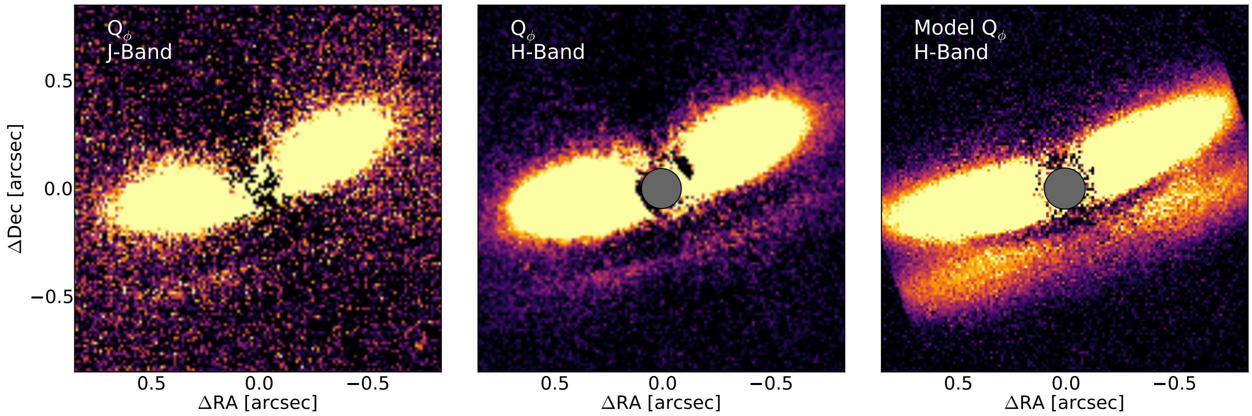

Fig. A.1. The Q_ϕ images of J1608 in J (non coronagraphic) and H-Band (coronagraphic) with a dynamical range from 0 to 5% of the maximum of each image are showed in the *left and middle panels*, respectively. The bottom line of the disk is seen more clearly in the data than in Fig. 1, and appears to be too bright in the model (*right panel*).

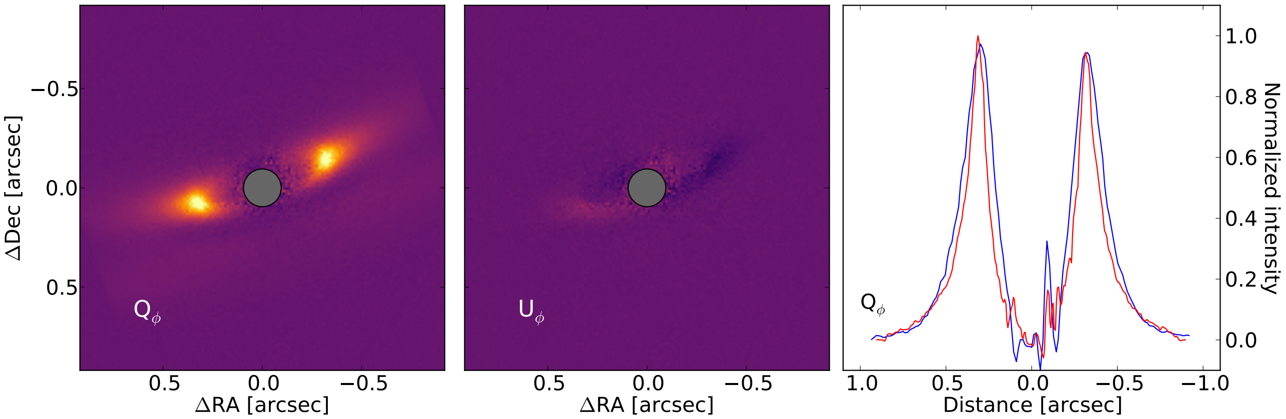

Fig. A.2. *Left and middle panels*: Q_ϕ and U_ϕ images of our model of J1608, respectively. The colorscale used in the same as in Fig. 5. *Right panel*: radial cuts along the major axis, compared to the data.

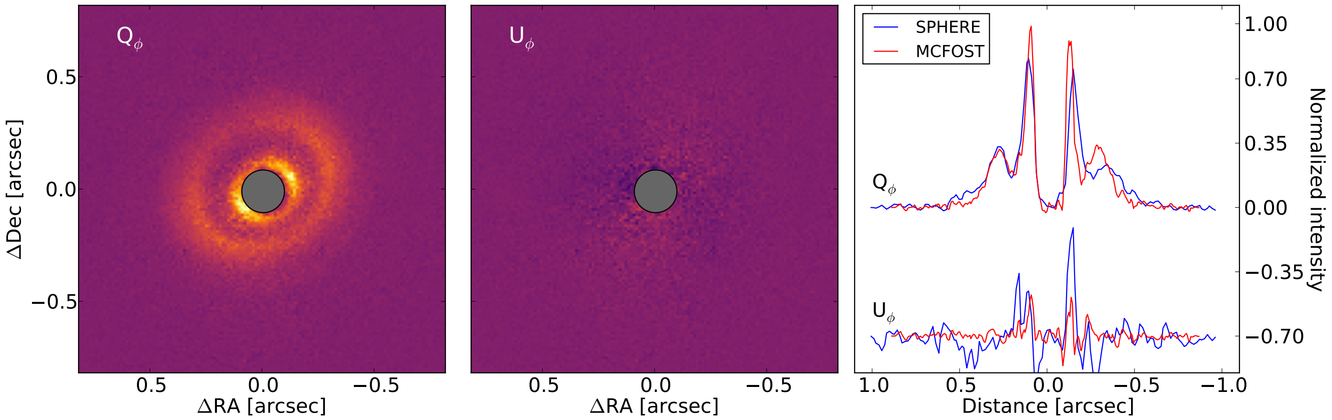

Fig. A.3. *Left and middle panels*: Q_ϕ and U_ϕ images of our model of J1852, respectively. The colorscale used in the same as in Fig. 9. *Right panel*: radial cuts along the major axis, compared to the data.

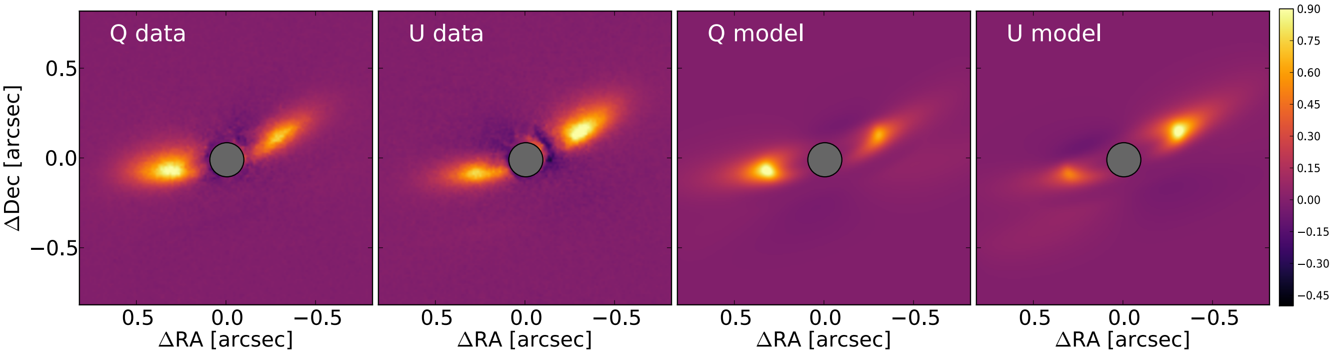

Fig. A.4. J1608 Q and U normalized maps of the data and model without noise.

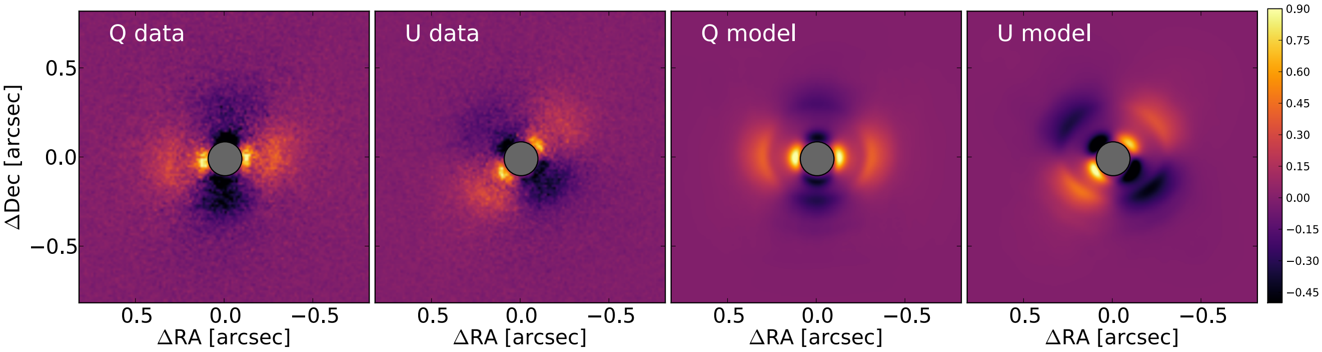

Fig. A.5. J1852 Q and U normalized maps of the data and model without noise.

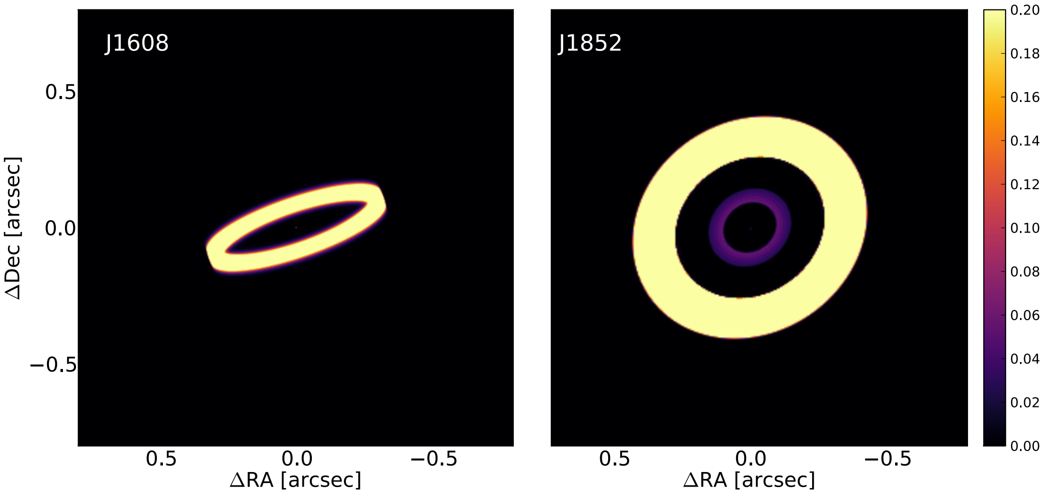

Fig. A.6. Synthetic millimeter predictions of our models for J1608 in Band 6 (*left panel*) and J1852 in Band 3 (*right panel*), before convolution by the ALMA beam.

Model Q and U images. We show the Q and U maps of both data and models (without any noise) in Figs. A.4 and A.5. In J1608, the east/west asymmetry in the lobe is reproduced, and in J1852 we clearly see the two rings in the model images.

Model millimeter images before convolution by the beam. In Fig. A.6, we show our synthetic millimeter predictions for J1608 and J1852 before convolution by the corresponding ALMA beam.

Appendix B: Model schematic representation

We show a schematic representation of our models in Fig. B.1, that shows the clear spatial segregation in particle sizes for J1608. As explained in the main text, our model of J1852 remains degenerate. With a grain size distribution as given in Table 2, that uses a minimum grain size of 10μm for the large grain population, we obtain a good model represented in the bottom panel of Fig. B.1. However, with a minimum grain size to 300 μm, both small and large grain population could be mixed up to the same height. We therefore represent the height of the small grain population with red hatches to show this uncertainty.

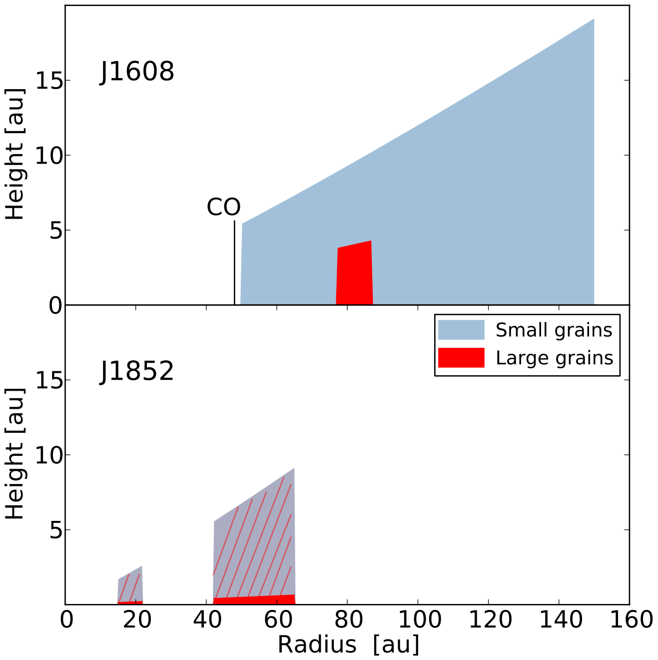

Fig. B.1. Modeled radial and vertical structure for small and large grains in J1608 and J1852, in linear scale. The vertical black line indicates the inner radius of the disk in CO, as measured on the PV-diagram (Fig. 3). The red hatches in J1852 represent the uncertaincy on the scale height of the large grain population that is not well constrained by our model. The innermost disk of J1852, located between 0.2 and 2 au, is too small to be visible in this representation.

B

CO-AUTHORED PUBLICATIONS

In this appendix, I present the first page of all my published co-authored publications. I participated in the interpretation and discussion of the results.

- *F. Ménard, N. Cuello, C. Ginski, ..., **M. Villenave**, et al.*, 2020, A&A, 639, L1
  Ongoing flyby in the young multiple system UX Tauri

- *M. Keppler, A. Penzlin, M. Benisty, ..., **M. Villenave**, et al.*, 2020, A&A, 639, A62
  A gap, shadows, spirals, streamers: SPHERE observations of binary-disk in GG Tau A

- *G. Muro-Arena, C. Ginski, C. Dominik, ..., **M. Villenave**, et al.*, 2020, A&A, 636, L4
  Spirals inside the millimeter cavity of transition disk SR 21

- *G. Muro-Arena, M. Benisty, C. Ginski, ..., **M. Villenave**, et al.*, 2020, A&A, 635, A121
  Shadowing and multiple rings in the protoplanetary disk of HD 139614

- *A. Garufi, M. Benisty, P. Pinilla, ..., **M. Villenave**, et al.*, 2018, A&A, 620, A94
  Evolution of protoplanetary disks from their taxonomy in scattered light: spirals, rings, cavities, and shadows.

- *M. Benisty, A. Juhász, S. Facchini, ..., **M. Villenave**, et al.*, 2018, A&A, 619, A171
  Shadows and asymmetries in the T Tauri disk HD 143006: evidence for a misaligned inner disk.

- *G. Muro-Arena, C. Dominik, L. Waters, ..., **M. Villenave**, et al.*, 2018, A&A, 614, A24
  Dust modeling of the combined ALMA and SPHERE datasets of HD 163296. Is HD163296 really a Meeus group II disk ?

- *A. Pohl, M. Benisty, P. Pinilla, ..., **M. Villenave**, et al.*, 2017, ApJ, 850, 1
  The circumstellar disk HD 169142: gas, dust and planets acting in concert ?

A&A 639, L1 (2020)
https://doi.org/10.1051/0004-6361/202038356

Astronomy & Astrophysics

LETTER TO THE EDITOR

Ongoing flyby in the young multiple system UX Tauri[⋆]

F. Ménard[1], N. Cuello[1,2,3], C. Ginski[4,5], G. van der Plas[1], M. Villenave[1,6], J.-F. Gonzalez[3], C. Pinte[7,1], M. Benisty[1], A. Boccaletti[8], D. J. Price[7], Y. Boehler[1], S. Chripko[9], J. de Boer[5], C. Dominik[4], A. Garufi[10], R. Gratton[11], J. Hagelberg[12], Th. Henning[13], M. Langlois[3], A. L. Maire[14,13], P. Pinilla[13], G. J. Ruane[15], H. M. Schmid[16], R. G. van Holstein[5,6], A. Vigan[17], A. Zurlo[17,18,19], N. Hubin[20], A. Pavlov[13], S. Rochat[1], J.-F. Sauvage[21,17], and E. Stadler[1]

[1] Univ. Grenoble Alpes, CNRS, IPAG, 38000 Grenoble, France
e-mail: `francois.menard@univ-grenoble-alpes.fr`
[2] Instituto de Astrofísica, Pontificia Universidad Católica de Chile, Santiago, Chile
[3] Univ Lyon, Univ Claude Bernard Lyon1, Ens de Lyon, CNRS, Centre de Recherche Astrophysique de Lyon UMR5574, 69230 Saint-Genis-Laval, France
[4] Sterrenkundig Instituut Anton Pannekoek, Science Park 904, 1098 XH Amsterdam, The Netherlands
[5] Leiden Observatory, Leiden University, PO Box 9513, 2300 RA Leiden, The Netherlands
[6] European Southern Observatory, Alonso de Córdova 3107, Casilla 19001 Vitacura, Santiago, Chile
[7] School of Physics and Astronomy, Monash University, Clayton, Vic 3800, Australia
[8] LESIA, Observatoire de Paris, Université PSL, CNRS, Sorbonne Université, Univ. Paris Diderot, Sorbonne Paris Cité, 5 place Jules Janssen, 92195 Meudon, France
[9] CECI, Université de Toulouse, CNRS, CERFACS, Toulouse, France
[10] INAF, Osservatorio Astrofisico di Arcetri, Largo Enrico Fermi 5, 50125 Firenze, Italy
[11] INAF, Osservatorio Astronomico di Padova, Vicolo dell'Osservatorio 5, 35122 Padova, Italy
[12] Geneva Observatory, University of Geneva, Chemin des Mailettes 51, 1290 Versoix, Switzerland
[13] Max Planck Institute for Astronomy, Königstuhl 17, 69117 Heidelberg, Germany
[14] STAR Institute, Université de Liège, Allée du Six Août 19c, 4000 Liège, Belgium
[15] Jet Propulsion Laboratory, California Institute of Technology, 4800 Oak Grove Dr., Pasadena, CA 91109, USA
[16] Institute for Particle Physics and Astrophysics, ETH Zurich, Wolfgang-Pauli-Strasse 27, 8093 Zurich, Switzerland
[17] Aix Marseille Université, CNRS, CNES, LAM, Marseille, France
[18] Núcleo de Astronomía, Facultad de Ingeniería y Ciencias, Universidad Diego Portales, Av. Ejercito 441, Santiago, Chile
[19] Escuela de Ingeniería Industrial, Facultad de Ingeniería y Ciencias, Universidad Diego Portales, Av. Ejercito 441, Santiago, Chile
[20] European Southern Observatory (ESO), Karl-Schwarzschild-Str. 2, 85748 Garching, Germany
[21] DOTA, ONERA, Université Paris Saclay, 91123 Palaiseau, France

Received 5 May 2020 / Accepted 1 June 2020

ABSTRACT

We present observations of the young multiple system UX Tauri to look for circumstellar disks and for signs of dynamical interactions. We obtained SPHERE/IRDIS deep differential polarization images in the *J* and *H* bands. We also used ALMA archival CO data. Large extended spirals are well detected in scattered light coming out of the disk of UX Tau A. The southern spiral forms a bridge between UX Tau A and C. These spirals, including the bridge connecting the two stars, all have a CO (3–2) counterpart seen by ALMA. The disk of UX Tau C is detected in scattered light. It is much smaller than the disk of UX Tau A and has a major axis along a different position angle, suggesting a misalignment. We performed PHANTOM SPH hydrodynamical models to interpret the data. The scattered light spirals, CO emission spirals and velocity patterns of the rotating disks, and the compactness of the disk of UX Tau C all point to a scenario in which UX Tau A has been perturbed very recently (∼1000 years) by the close passage of UX Tau C.

Key words. protoplanetary disks – circumstellar matter – stars: pre-main sequence – binaries: general

1. Introduction

Star formation occurs in molecular clouds where the stellar density is higher than in the field and the probability for encounters and dynamical interactions is enhanced. The presence of other stars in the vicinity of a forming young stellar and planetary system can dramatically affect the disk morphology and evolution (Pfalzner 2003; Vincke et al. 2015; Bate 2018).

The probability of a system to undergo a flyby decreases rapidly with time in a stellar association in unison with the stellar density, which decreases with cluster expansion. During the first million years of a stellar cluster, Pfalzner (2013) and Winter et al. (2018a) estimated that the probability of a stellar encounter can be on the order of 30% for solar-type stars, a flyby being defined in this case as a single passage within 100–1000 au. These calculations assumed a background stellar density that is larger than in Taurus. In Taurus the stellar density is low (1–10 stars pc^{-3}) and at first sight the flyby rate would be equivalently low. However, the stellar distribution in Taurus is patchy; several denser groups have been identified in Taurus (e.g., Joncour et al. 2018) and there is a higher probability that encounters might happen in these groups.

Clarke & Pringle (1993) considered coplanar parabolic encounters between equal-mass stars with periastron separations

---

[⋆] Movies associated to Fig. 3 are available at https://www.aanda.org

A&A 639, A62 (2020)
https://doi.org/10.1051/0004-6361/202038032

Astronomy & Astrophysics

Gap, shadows, spirals, and streamers: SPHERE observations of binary-disk interactions in GG Tauri A*

M. Keppler[1], A. Penzlin[2], M. Benisty[3,4], R. van Boekel[1], T. Henning[1], R. G. van Holstein[5,6], W. Kley[2], A. Garufi[7], C. Ginski[8,5], W. Brandner[1], G. H.-M. Bertrang[1], A. Boccaletti[9], J. de Boer[5], M. Bonavita[10,11], S. Brown Sevilla[1], G. Chauvin[3,4], C. Dominik[8], M. Janson[12], M. Langlois[13,14], G. Lodato[15], A.-L. Maire[16,1], F. Ménard[3], E. Pantin[17], C. Pinte[18,3], T. Stolker[19], J. Szulágyi[20], P. Thebault[21], M. Villenave[3], A. Zurlo[22,23,14], P. Rabou[3], P. Feautrier[3], M. Feldt[1], F. Madec[14], and F. Wildi[24]

(Affiliations can be found after the references)

Received 26 March 2020 / Accepted 15 May 2020

ABSTRACT

Context. A large portion of stars is found to be part of binary or higher-order multiple systems. The ubiquity of planets found around single stars raises the question of whether and how planets in binary systems form. Protoplanetary disks are the birthplaces of planets, and characterizing them is crucial in order to understand the planet formation process.

Aims. Our goal is to characterize the morphology of the GG Tau A disk, one of the largest and most massive circumbinary disks. We also aim to trace evidence for binary-disk interactions.

Methods. We obtained observations in polarized scattered light of GG Tau A using the SPHERE/IRDIS instrument in the H-band filter. We analyzed the observed disk morphology and substructures. We ran 2D hydrodynamical models to simulate the evolution of the circumbinary ring over the lifetime of the disk.

Results. The disk and also the cavity and the inner region are highly structured, with several shadowed regions, spiral structures, and streamer-like filaments. Some of these are detected here for the first time. The streamer-like filaments appear to connect the outer ring with the northern arc. Their azimuthal spacing suggests that they may be generated through periodic perturbations by the binary, which tear off material from the inner edge of the outer disk once during each orbit. By comparing observations to hydrodynamical simulations, we find that the main features, in particular, the gap size, but also the spiral and streamer filaments, can be qualitatively explained by the gravitational interactions of a binary with a semimajor axis of ~35 au on an orbit coplanar with the circumbinary ring.

Key words. stars: individual: GG Tau A – protoplanetary disks – methods: observational – methods: numerical – techniques: high angular resolution – techniques: polarimetric

1. Introduction

Almost half of all main-sequence solar-type stars are found in binary or higher-order multiple systems (e.g., Raghavan et al. 2010; Duchêne & Kraus 2013), and it is thought that the fraction of multiple systems is even higher among pre-main sequence stars (e.g., Duchêne 1999; Kraus et al. 2011). More than 4000 detections of extrasolar planets around single stars to date show that the assembly of planetary bodies is a common byproduct of star formation. The high abundance of multiple stars on the one hand and planetary companions on the other hand thus raises the question about the possible formation pathways and prevalence of planets in multiple systems.

While our understanding of the building-up of planets within protoplanetary disks around single stars has significantly advanced in the past years, less is known about the conditions of planet formation in multiple systems (e.g., Thebault & Haghighipour 2015). In contrast to the single-star case, the evolution of material in the circumbinary and individual circumstellar disks in multiple systems will (depending on the binary parameters such as mass ratio, orbital separation, and eccentricity) be dominated by the gravitational perturbation of the central binary. As a consequence, the binary-disk interaction has severe implications for the planet formation process. Tidal interactions exerted by the binary are expected to truncate the individual circumstellar disks, reducing their masses, outer radii, and viscous timescales (e.g., Papaloizou & Pringle 1977; Artymowicz & Lubow 1994; Rosotti & Clarke 2018). In addition, the tidal torques will truncate the circumbinary disk from the inner edge by opening a large inner cavity. Despite the resulting separation of circumbinary and circumstellar material, gas streams through the gap may form, supplying the circumstellar disks with material from the outer circumbinary disk (e.g., Artymowicz & Lubow 1996; Muñoz et al. 2020). While observational trends infer binary interaction to be indeed destructive for disks in many cases (e.g., Bouwman et al. 2006; Duchêne 2010; Harris et al. 2012; Cox et al. 2017; Akeson et al. 2019; Manara et al. 2019), potentially impeding the formation of planets, several massive disks around binary systems are known and have been observed at high angular resolution (e.g., UY Aur, HD142527, HD 34700 A; Hioki et al. 2007; Tang et al. 2014; Avenhaus et al. 2017; Monnier et al. 2019).

Despite the potential complications for planet formation induced by the gravitational perturbations from the binary, more

---

* Based on observations performed with VLT/SPHERE under program ID 198.C-0209(N).

Open Access funding provided by Max Planck Society.

A&A 636, L4 (2020)
https://doi.org/10.1051/0004-6361/202037656

Astronomy & Astrophysics

LETTER TO THE EDITOR

Spirals inside the millimeter cavity of transition disk SR 21[⋆]

G. A. Muro-Arena[1], C. Ginski[1,2], C. Dominik[1], M. Benisty[3,4], P. Pinilla[5], A. J. Bohn[2], T. Moldenhauer[6], W. Kley[6], D. Harsono[2], T. Henning[5], R. G. van Holstein[2,7], M. Janson[8], M. Keppler[5], F. Ménard[3], L. M. Pérez[9], T. Stolker[10], M. Tazzari[11], M. Villenave[3], A. Zurlo[12], C. Petit[13], F. Rigal[1], O. Möller-Nilsson[5], M. Llored[14], T. Moulin[3], and P. Rabou[3]

[1] Anton Pannekoek Institute for Astronomy, University of Amsterdam, Science Park 904, 1098XH Amsterdam, The Netherlands
e-mail: `g.a.muroarena@uva.nl`
[2] Leiden Observatory, Leiden University, PO Box 9513, 2300 RA Leiden, The Netherlands
[3] Univ. Grenoble Alpes, CNRS, IPAG, 38000 Grenoble, France
[4] Unidad Mixta Internacional Franco-Chilena de Astronomía (CNRS, UMI 3386), Departamento de Astronomía, Universidad de Chile, Camino El Observatorio 1515, Las Condes Santiago, Chile
[5] Max Planck Institute for Astronomy, Königstuhl 17, 69117 Heidelberg, Germany
[6] Institut für Astronomie und Astrophysik, Universität Tübingen, Auf der Morgenstelle 10, 72076 Tübingen, Germany
[7] European Southern Observatory, Alonso de Córdova 3107, Casilla, 19001 Vitacura, Santiago, Chile
[8] Department of Astronomy, Stockholm University, Stockholm, Sweden
[9] Universidad de Chile, Departamento de Astronomia, Camino El Observatorio 1515, Las Condes, Santiago, Chile
[10] Institute for Particle Physics and Astrophysics, ETH Zurich, Wolfgang-Pauli-Strasse 27, 8093 Zurich, Switzerland
[11] Institute of Astronomy, University of Cambridge, Madingley Road, CB3 0HA Cambridge, UK
[12] Núcleo de Astronomía, Facultad de Ingeniería y Ciencias, Universidad Diego Portales, Av. Ejercito 441, Santiago, Chile
[13] DOTA, ONERA, Université Paris Saclay, 91123 Palaiseau, France
[14] Aix Marseille Université, CNRS, CNES, LAM, Marseille, France

Received 4 February 2020 / Accepted 17 March 2020

ABSTRACT

Context. Hydrodynamical simulations of planet-disk interactions suggest that planets may be responsible for a number of the substructures frequently observed in disks in both scattered light and dust thermal emission. Despite the ubiquity of these features, direct evidence of planets embedded in disks and of the specific interaction features like spiral arms within planetary gaps are still rare.
Aims. In this study we discuss recent observational results in the context of hydrodynamical simulations in order to infer the properties of a putative embedded planet in the cavity of a transition disk.
Methods. We imaged the transition disk SR 21 in H-band in scattered light with SPHERE/IRDIS and in thermal dust emission with ALMA band 3 (3 mm) observations at a spatial resolution of 0.1″. We combine these datasets with existing Band 9 (430 μm) and Band 7 (870 μm) ALMA continuum data.
Results. The Band 3 continuum data reveals a large cavity and a bright ring peaking at 53 au strongly suggestive of dust trapping. The ring shows a pronounced azimuthal asymmetry, with a bright region in the northwest that we interpret as a dust overdensity. A similarly asymmetric ring is revealed at the same location in polarized scattered light, in addition to a set of bright spirals inside the millimeter cavity and a fainter spiral bridging the gap to the outer ring. These features are consistent with a number of previous hydrodynamical models of planet-disk interactions, and suggest the presence of a ~1 M_{Jup} planet at 44 au and PA = 11 deg. This makes SR21 the first disk showing spiral arms inside the millimeter cavity, and the first disk for which the location of a putative planet can be precisely inferred.
Conclusions. The main features of SR 21 in both scattered light and thermal emission are consistent with hydrodynamical predictions of planet-disk interactions. With the location of a possible planet being well constrained by observations, it is an ideal candidate for follow-up observations to search for direct evidence of a planetary companion still embedded in its disk.

Key words. protoplanetary disks – techniques: polarimetric – scattering

1. Introduction

Protoplanetary disks are the places where planet formation takes place, yet the associated timescales and evolutionary processes are not well constrained by observations. Planet formation is thought to induce morphological features in their parent disk, such as rings and gaps, spiral arms, or vortices. Such structures were indeed detected in a growing sample of disks in millimeter emission and in optical and near-infrared scattered light (see, e.g., Andrews et al. 2018; Avenhaus et al. 2018 for recent examples). If indeed caused by embedded planets, this suggests that planet formation occurs early in the lifetime of the disk. Of particular interest in that respect have been the so-called transition disks. These are disks that show a lack of flux in the 10 μm wavelength range, suggestive of large cavities.

It has been proposed that these cavities are carved out by the emerging protoplanets, yet so far only one such system is known where planets are indeed detected (PDS 70,

---

[⋆] Based on observations performed with SPHERE/VLT under program ID 1100.C-0481(Q).

A&A 635, A121 (2020)
https://doi.org/10.1051/0004-6361/201936509

Astronomy & Astrophysics

Shadowing and multiple rings in the protoplanetary disk of HD 139614[⋆,⋆⋆]

G. A. Muro-Arena[1], M. Benisty[2,3], C. Ginski[1], C. Dominik[1], S. Facchini[4], M. Villenave[2,5], R. van Boekel[6], G. Chauvin[2,3], A. Garufi[7], T. Henning[6], M. Janson[8], M. Keppler[6], A. Matter[9], F. Ménard[2], T. Stolker[10], A. Zurlo[11,12,13], P. Blanchard[13], D. Maurel[2], O. Moeller-Nilsson[6], C. Petit[14], A. Roux[2], A. Sevin[15], and F. Wildi[16]

[1] Anton Pannekoek Institute for Astronomy, University of Amsterdam, Science Park 904, 1098XH Amsterdam, The Netherlands
e-mail: `g.a.muroarena@uva.nl`
[2] Univ. Grenoble Alpes, CNRS, IPAG, 38000 Grenoble, France
[3] Unidad Mixta Internacional Franco-Chilena de Astronomía (CNRS, UMI 3386), Departamento de Astronomía, Universidad de Chile, Camino El Observatorio 1515, Las Condes, Santiago, Chile
[4] European Southern Observatory, Karl-Schwarzschild-Str. 2, 85748 Garching, Germany
[5] European Southern Observatory, Alonso de Córdova 3107, Vitacura, Casilla 19001, Santiago, Chile
[6] Max Planck Institute for Astronomy, Königstuhl 17, 69117 Heidelberg, Germany
[7] INAF, Osservatorio Astrofisico di Arcetri, Largo Enrico Fermi 5, 50125 Firenze, Italy
[8] Department of Astronomy, Stockholm University, Stockholm, Sweden
[9] Laboratoire Lagrange, Université Côte d'Azur, Observatoire de la Côte d'Azur, CNRS, Boulevard de l'Observatoire, CS 34229, 06304 Nice Cedex 4, France
[10] Institute for Particle Physics and Astrophysics, ETH Zurich, Wolfgang-Pauli-Strasse 27, 8093 Zurich, Switzerland
[11] Núcleo de Astronomía, Facultad de Ingeniería y Ciencias, Universidad Diego Portales, Av. Ejercito 441, Santiago, Chile
[12] Escuela de Ingeniería Industrial, Facultad de Ingeniería y Ciencias, Universidad Diego Portales, Av. Ejercito 441, Santiago, Chile
[13] Aix-Marseille Université, CNRS, LAM – Laboratoire d'Astrophysique de Marseille, UMR 7326, 13388 Marseille, France
[14] DOTA, ONERA, Université Paris Saclay, 91123 Palaiseau France
[15] LESIA, Observatoire de Paris, Université PSL, CNRS, Sorbonne Université, Univ. Paris Diderot, Sorbonne Paris Cité, 5 place Jules Janssen, 92195 Meudon, France
[16] Geneva Observatory, University of Geneva, Chemin des Mailettes 51, 1290 Versoix, Switzerland

Received 14 August 2019 / Accepted 25 November 2019

ABSTRACT

Context. Shadows in scattered light images of protoplanetary disks are a common feature and support the presence of warps or misalignments between disk regions. These warps are possibly caused by an inclined (sub-)stellar companion embedded in the disk.
Aims. We aim to study the morphology of the protoplanetary disk around the Herbig Ae star HD 139614 based on the first scattered light observations of this disk, which we model with the radiative transfer code `MCMax3D`.
Methods. We obtained J- and H-band observations that show strong azimuthal asymmetries in polarized scattered light with VLT/SPHERE. In the outer disk, beyond ~30 au, a broad shadow spans a range of ~240 deg in position angle, in the east. A bright ring at ~16 au also shows an azimuthally asymmetric brightness, with the faintest side roughly coincidental with the brightest region of the outer disk. Additionally, two arcs are detected at ~34 and ~50 au. We created a simple four-zone approximation to a warped disk model of HD 139614 in order to qualitatively reproduce these features. The location and misalignment of the disk components were constrained from the shape and location of the shadows they cast.
Results. We find that the shadow on the outer disk covers a range of position angles too wide to be explained by a single inner misaligned component. Our model requires a minimum of two separate misaligned zones – or a continuously warped region – to cast this broad shadow on the outer disk. A small misalignment of ~4° between adjacent components can reproduce most of the observed shadow features.
Conclusions. Multiple misaligned disk zones, potentially mimicking a warp, can explain the observed broad shadows in the HD 139614 disk. A planetary mass companion in the disk, located on an inclined orbit, could be responsible for such a feature and for the dust-depleted gap responsible for a dip in the SED.

Key words. protoplanetary disks – techniques: polarimetric – radiative transfer – scattering

---

[⋆] The reduced images are only available at the CDS via anonymous ftp to `cdsarc.u-strasbg.fr` (`130.79.128.5`) or via `http://cdsarc.u-strasbg.fr/viz-bin/cat/J/A+A/635/A121`
[⋆⋆] Based on observations performed with SPHERE/VLT under program ID 096.C-0248(B) and 099.C-0147(B).

A&A 620, A94 (2018)
https://doi.org/10.1051/0004-6361/201833872

Astronomy & Astrophysics

Evolution of protoplanetary disks from their taxonomy in scattered light: spirals, rings, cavities, and shadows

A. Garufi[1], M. Benisty[2,3], P. Pinilla[4], M. Tazzari[5], C. Dominik[6], C. Ginski[6], Th. Henning[7], Q. Kral[8], M. Langlois[12,13], F. Ménard[3], T. Stolker[9], J. Szulagyi[10], M. Villenave[11,3], and G. van der Plas[3]

[1] INAF, Osservatorio Astrofisico di Arcetri, Largo Enrico Fermi 5, 50125 Firenze, Italy
e-mail: `agarufi@arcetri.astro.it`
[2] Unidad Mixta Internacional Franco-Chilena de Astronomía, CNRS/INSU UMI 3386 and Departamento de Astronomía, Universidad de Chile, Casilla 36-D, Santiago, Chile
[3] Université Grenoble Alpes, CNRS, IPAG, 38000 Grenoble, France
[4] Department of Astronomy/Steward Observatory, The University of Arizona, 933 North Cherry Avenue, Tucson, AZ 85721, USA
[5] Institute of Astronomy, Madingley Rd, Cambridge, CB3 0HA, UK
[6] Astronomical Institute Anton Pannekoek, University of Amsterdam, PO Box 94249, 1090 GE Amsterdam, The Netherlands
[7] Max Planck Institute for Astronomy, Königstuhl 17, 69117 Heidelberg, Germany
[8] LESIA, Observatoire de Paris-Meudon, CNRS, Université Pierre et Marie Curie, Université Paris Didierot, 5 Place Jules Janssen, 92195 Meudon, France
[9] Institute for Particle Physics and Astrophysics, ETH Zurich, Wolfgang-Pauli-Strasse 27, 8093 Zurich, Switzerland
[10] Institute for Computational Science, University of Zurich, Winterthurerstrasse 190, 8057 Zurich, Switzerland
[11] European Southern Observatory, Alonso de Córdova 3107, Casilla 19001 Vitacura, Santiago 19, Chile
[12] Aix-Marseille Université, CNRS, LAM, Marseille, France
[13] CRAL, UMR 5574, CNRS, Université de Lyon, Ecole Normale Supérieure de Lyon, 46 Allée d'Italie, 69364 Lyon Cedex 07, France

Received 16 July 2018 / Accepted 3 October 2018

ABSTRACT

Context. Dozens of protoplanetary disks have been imaged in scattered light during the last decade.
Aims. The variety of brightness, extension, and morphology from this census motivates a taxonomical study of protoplanetary disks in polarimetric light to constrain their evolution and establish the current framework of this type of observation.
Methods. We classified 58 disks with available polarimetric observations into six major categories (Ring, Spiral, Giant, Rim, Faint, and Small disks) based on their appearance in scattered light. We re-calculated the stellar and disk properties from the newly available *Gaia* DR2 and related these properties with the disk categories.
Results. More than half of our sample shows disk substructures. For the remaining sources, the absence of detected features is due to their faintness, their small size, or the disk geometry. Faint disks are typically found around young stars and typically host no cavity. There is a possible dichotomy in the near-infrared (NIR) excess of sources with spiral-disks (high) and ring-disks (low). Like spirals, shadows are associated with a high NIR excess. If we account for the pre-main sequence evolutionary timescale of stars with different mass, spiral arms are likely associated with old disks. We also found a loose, shallow declining trend for the disk dust mass with time.
Conclusions. Protoplanetary disks may form substructures like rings very early in their evolution but their detectability in scattered light is limited to relatively old sources ($\gtrsim$5 Myr) where the recurrently detected disk cavities cause the outer disk to be illuminate. The shallow decrease of disk mass with time might be due to a selection effect, where disks observed thus far in scattered light are typically massive, bright transition disks with longer lifetimes than most disks. Our study points toward spirals and shadows being generated by planets of a fraction of a Jupiter mass to a few Jupiter masses in size that leave their (observed) imprint on both the inner disk near the star and the outer disk cavity.

Key words. planet-disk interactions – planets and satellites: formation – protoplanetary disks

1. Introduction

The most direct observational approach to study planet formation – the direct imaging of forming planets – has thus far been unproductive, with only a handful of young planet candidates being found in the literature (e.g., Quanz et al. 2013a; Sallum et al. 2015; Keppler et al. 2018; Müller et al. 2018). On the other hand, the direct imaging of protoplanetary disks has provided several examples of disk sub-structures (e.g., cavities, annular gaps, spiral arms) that are potentially formed by an interaction with embedded (forming) planets. Currently, the paucity of planet detection and the lack of a known evolutionary trend for these substructures are hindering our understanding of planet/disk interaction processes and planet formation.

Until the advent of ALMA, optical and near-infrared (NIR) imaging of the scattered light from protoplanetary disks was the best method for detecting substructures (see pioneering work by Grady et al. 1999; Augereau et al. 2001). Observations at these wavelengths exploit the good angular resolution achieved with single telescopes but suffer from the low contrast of any circumstellar emission in comparison to the star. Much of the current focus is on Polarimetric Differential Imaging (PDI) since this

A&A 619, A171 (2018)
https://doi.org/10.1051/0004-6361/201833913

Astronomy & Astrophysics

Shadows and asymmetries in the T Tauri disk HD 143006: evidence for a misaligned inner disk*

M. Benisty[1,2], A. Juhász[3], S. Facchini[4], P. Pinilla[5], J. de Boer[6], L. M. Pérez[7], M. Keppler[8], G. Muro-Arena[9], M. Villenave[10,2], S. Andrews[11], C. Dominik[9], C. P. Dullemond[12], A. Gallenne[10], A. Garufi[13], C. Ginski[6,9], and A. Isella[14]

[1] Unidad Mixta Internacional Franco-Chilena de Astronomía (CNRS, UMI 3386), Departamento de Astronomía, Universidad de Chile, Camino El Observatorio 1515, Las Condes, Santiago, Chile
e-mail: `Myriam.Benisty@univ-grenoble-alpes.fr`
[2] Université Grenoble Alpes, CNRS, IPAG, 38000 Grenoble, France
[3] Institute of Astronomy, Madingley Road, Cambridge CB3 OHA, UK
[4] Max-Planck-Institut für Extraterrestrische Physik, Giessenbachstrasse 1, 85748 Garching, Germany
[5] Department of Astronomy/Steward Observatory, The University of Arizona, 933 North Cherry Avenue, Tucson, AZ 85721, USA
[6] Leiden Observatory, Leiden University, PO Box 9513, 2300 RA Leiden, The Netherlands
[7] Departamento de Astronoma, Universidad de Chile, Camino El Observatorio 1515, Las Condes, Santiago, Chile
[8] Max Planck Institute for Astronomy, Königstuhl 17, 69117 Heidelberg, Germany
[9] Anton Pannekoek Institute for Astronomy, University of Amsterdam, Science Park 904, 1098XH Amsterdam, The Netherlands
[10] European Southern Observatory, Alonso de Córdova 3107, Vitacura, Casilla 19001, Santiago, Chile
[11] Harvard-Smithsonian Center for Astrophysics, 60 Garden Street, Cambridge, MA 02138, USA
[12] Zentrum für Astronomie, Heidelberg University, Albert-Ueberle-Strasse 2, 69120 Heidelberg, Germany
[13] INAF, Osservatorio Astrofisico di Arcetri, Largo Enrico Fermi 5, 50125 Firenze, Italy
[14] Department of Physics and Astronomy, Rice University, 6100 Main Street, Houston, TX 77005, USA

Received 20 July 2018 / Accepted 27 August 2018

ABSTRACT

Context. While planet formation is thought to occur early in the history of a protoplanetary disk, the presence of planets embedded in disks, or of other processes driving disk evolution, might be traced from their imprints on the disk structure.

Aims. We study the morphology of the disk around the T Tauri star HD 143006, located in the ~5–11 Myr-old Upper Sco region, and we look for signatures of the mechanisms driving its evolution.

Methods. We observed HD 143006 in polarized scattered light with VLT/SPHERE at near-infrared (J-band, 1.2 μm) wavelengths, reaching an angular resolution of ~0.037″(~6 au). We obtained two datasets, one with a 145 mas diameter coronagraph, and the other without, enabling us to probe the disk structure down to an angular separation of ~0.06″(~10 au).

Results. In our observations, the disk of HD 143006 is clearly resolved up to ~0.5″ and shows a clear large-scale asymmetry with the eastern side brighter than the western side. We detect a number of additional features, including two gaps and a ring. The ring shows an overbrightness at a position angle (PA) of ~140°, extending over a range in position angle of ~60°, and two narrow dark regions. The two narrow dark lanes and the overall large-scale asymmetry are indicative of shadowing effects, likely due to a misaligned inner disk. We demonstrate the remarkable resemblance between the scattered light image of HD 143006 and a model prediction of a warped disk due to an inclined binary companion. The warped disk model, based on the hydrodynamic simulations combined with three-dimensional radiative transfer calculations, reproduces all major morphological features. However, it does not account for the observed overbrightness at PA ~ 140°.

Conclusions. Shadows have been detected in several protoplanetary disks, suggesting that misalignment in disks is not uncommon. However, the origin of the misalignment is not clear. As-yet-undetected stellar or massive planetary companions could be responsible for them, and naturally account for the presence of depleted inner cavities.

Key words. protoplanetary disks – techniques: polarimetric – radiative transfer – scattering

1. Introduction

High angular resolution observations of protoplanetary disks show a wide diversity of structures on different scales. Sub-millimeter (mm) observations show radial structure, for example, bright and dark rings (e.g., ALMA Partnership 2015; Andrews et al. 2016; Fedele et al. 2017; Dipierro et al. 2018), and azimuthal asymmetries (sometimes called "horseshoe") where the dust continuum emission is much stronger than in the surrounding background disk (e.g., van der Marel et al. 2013; Casassus et al. 2013). Atacama Large Millimeter Array (ALMA) observations at high angular resolution revealed that most, if not all, of the protoplanetary disks are not smooth, and often show ring-like features (Isella et al. 2016; Cieza et al. 2017; Fedele et al. 2018), suggesting that these features trace universal processes. One of the most interesting scenarios is that they are due to interactions between the planet-forming disk and embedded proto-planets (e.g., Dipierro et al. 2015; Rosotti et al. 2016).

---

[*] Based on observations performed with SPHERE/VLT under program ID 097.C-0902(A) and 095.C-0693(A).

A&A 614, A24 (2018)
https://doi.org/10.1051/0004-6361/201732299

Astronomy
&
Astrophysics

Dust modeling of the combined ALMA and SPHERE datasets of HD 163296

Is HD 163296 really a Meeus group II disk?

G. A. Muro-Arena[1], C. Dominik[1], L. B. F. M. Waters[1,2], M. Min[1,2], L. Klarmann[1], C. Ginski[1,3],
A. Isella[4], M. Benisty[5,6], A. Pohl[7], A. Garufi[8], J. Hagelberg[6], M. Langlois[9,10], F. Menard[6], C. Pinte[6],
E. Sezestre[6], G. van der Plas[11,12], M. Villenave[6], A. Delboulbé[6], Y. Magnard[6], O. Möller-Nilsson[7],
J. Pragt[13], P. Rabou[6], and R. Roelfsema[13]

[1] Anton Pannekoek Institute for Astronomy, University of Amsterdam, Science Park 904, 1098 XH Amsterdam, The Netherlands
e-mail: `g.a.muroarena@uva.nl`
[2] SRON Netherlands Institute for Space Research, Sorbonnelaan 2, 3584 CA Utrecht, The Netherlands
[3] Leiden Observatory, Leiden University, PO Box 9513, 2300 RA Leiden, The Netherlands
[4] Department of Physics and Astronomy, Rice University, 6100 Main Street, Houston, TX 77005, USA
[5] Unidad Mixta Internacional Franco-Chilena de Astronomía, CNRS/INSU UMI 3386 and Departamento de Astronomía, Universidad de Chile, Casilla 36-D, Santiago, Chile
[6] Université Grenoble Alpes, CNRS, IPAG, 38000 Grenoble, France
[7] Max Planck Institute for Astronomy, Königstuhl 17, 69117 Heidelberg, Germany
[8] Universidad Autónoma de Madrid, Dpto. Física Teórica, Módulo 15, Facultad de ciencia, Campus de Cantoblanco, 28049 Madrid, Spain
[9] CRAL, UMR 5574, CNRS, Université Lyon 1, 9 avenue Charles André, 69561 Saint Genis Laval Cedex, France
[10] Aix–Marseille Université, CNRS, LAM (Laboratoire d'Astrophysique de Marseille) UMR 7326, 13388 Marseille, France
[11] Departamento de Astronomía, Universidad de Chile, Casilla 36-D, Santiago, Chile
[12] Millenium Nucleus Protoplanetary Disks in ALMA Early Science, Universidad de Chile, Casilla 36-D, Santiago, Chile
[13] NOVA Optical Infrared Instrumentation Group, Oude Hoogeveensedijk 4, 7991 PD Dwingeloo, The Netherlands

Received 15 November 2017 / Accepted 6 February 2018

ABSTRACT

Context. Multiwavelength observations are indispensable in studying disk geometry and dust evolution processes in protoplanetary disks.

Aims. We aim to construct a three-dimensional model of HD 163296 that is capable of reproducing simultaneously new observations of the disk surface in scattered light with the SPHERE instrument and thermal emission continuum observations of the disk midplane with ALMA. We want to determine why the spectral energy distribution of HD 163296 is intermediary between the otherwise well-separated group I and group II Herbig stars.

Methods. The disk was modeled using the Monte Carlo radiative transfer code *MCMax3D*. The radial dust surface density profile was modeled after the ALMA observations, while the polarized scattered light observations were used to constrain the inclination of the inner disk component and turbulence and grain growth in the outer disk.

Results. While three rings are observed in the disk midplane in millimeter thermal emission at ~80, 124, and 200 AU, only the innermost of these is observed in polarized scattered light, indicating a lack of small dust grains on the surface of the outer disk. We provide two models that are capable of explaining this difference. The first model uses increased settling in the outer disk as a mechanism to bring the small dust grains on the surface of the disk closer to the midplane and into the shadow cast by the first ring. The second model uses depletion of the smallest dust grains in the outer disk as a mechanism for decreasing the optical depth at optical and near-infrared wavelengths. In the region outside the fragmentation-dominated regime, such depletion is expected from state-of-the-art dust evolution models. We studied the effect of creating an artificial inner cavity in our models, and conclude that HD 163296 might be a precursor to typical group I sources.

Key words. protoplanetary disks – scattering – techniques: polarimetric – techniques: interferometric –
stars: individual: HD 163296

1. Introduction

Protoplanetary disks are the sites of planet formation, of which the disks around Herbig Ae/Be are the best-studied examples owing to their brightness and proximity to Earth. The structure and morphology of protoplanetary disks around Herbig Ae/Be stars is as of now not well understood, although various models have been proposed over the years to link their global geometry to the characteristics of their spectral energy distributions (SEDs). The classification system initially proposed by Meeus et al. (2001) first divided Herbig Ae/Be SEDs into two groups based on the far-infrared (FIR) excess of these sources: those whose SEDs can be fitted by a single power-law component (group II), and those that require an additional broad component

The Astrophysical Journal, 850:52 (15pp), 2017 November 20 https://doi.org/10.3847/1538-4357/aa94c2

The Circumstellar Disk HD 169142: Gas, Dust, and Planets Acting in Concert?*

A. Pohl[1,2], M. Benisty[3,4], P. Pinilla[5], C. Ginski[6,7], J. de Boer[6], H. Avenhaus[8], Th. Henning[1], A. Zurlo[9,10,11], A. Boccaletti[12], J.-C. Augereau[4], T. Birnstiel[13], C. Dominik[7], S. Facchini[14], D. Fedele[15], M. Janson[1,16], M. Keppler[1], Q. Kral[12,17], M. Langlois[9,18], R. Ligi[9], A.-L. Maire[1], F. Ménard[4], M. Meyer[8], C. Pinte[4], S. P. Quanz[8], J.-F. Sauvage[19], É. Sezestre[4], T. Stolker[7], J. Szulágyi[8], R. van Boekel[1], G. van der Plas[4], M. Villenave[4], A. Baruffolo[20], P. Baudoz[12], D. Le Mignant[9], D. Maurel[4], J. Ramos[1], and L. Weber[21]

[1] Max-Planck-Institute for Astronomy, Königstuhl 17, D-69117 Heidelberg, Germany; pohl@mpia.de
[2] Heidelberg University, Institute of Theoretical Astrophysics, Albert-Ueberle-Str. 2, D-69120 Heidelberg, Germany
[3] Unidad Mixta Internacional Franco-Chilena de Astronomía, CNRS/INSU UUMI 3386 and Departamento de Astronomía, Universidad de Chile, Casilla 36-D, Santiago, Chile
[4] Univ. Grenoble Alpes, CNRS, IPAG, F-38000 Grenoble, France
[5] Department of Astronomy/Steward Observatory, University of Arizona, 933 North Cherry Avenue, Tucson, AZ 85721, USA
[6] Leiden Observatory, Leiden University, PO Box 9513, 2300 RA, Leiden, The Netherlands
[7] Anton Pannekoek Institute for Astronomy, University of Amsterdam, Science Park 904, 1098 XH Amsterdam, The Netherlands
[8] Institute for Astronomy, ETH Zurich, Wolfgang-Pauli-Strasse 27, 8093 Zurich, Switzerland
[9] Aix Marseille Université, CNRS, LAM (Laboratoire d'Astrophysique de Marseille) UMR 7326, F-13388, Marseille, France
[10] Núcleo de Astronomía, Facultad de Ingeniería, Universidad Diego Portales, Av. Ejercito 441, Santiago, Chile
[11] Departamento de Astronomía, Universidad de Chile, Casilla 36-D, Santiago, Chile
[12] LESIA, Observatoire de Paris, PSL Research University, CNRS, Sorbonne Universités, UPMC Univ. Paris 06, Univ. Paris Diderot, Sorbonne Paris Cité, 5 place Jules Janssen, F-92195 Meudon, France
[13] University Observatory, Faculty of Physics, Ludwig-Maximilians-Universität München, Scheinerstr. 1, D-81679 München, Germany
[14] Max-Planck-Institut für Extraterrestrische Physik, Giessenbachstrasse 1, D-85748 Garching, Germany
[15] INAF—Osservatorio Astrofisico di Arcetri, L.go E. Fermi 5, I-50125 Firenze, Italy
[16] Department of Astronomy, Stockholm University, AlbaNova University Center, SE-10691 Stockholm, Sweden
[17] Institute of Astronomy, University of Cambridge, Madingley Road, Cambridge CB3 0HA, UK
[18] CRAL, UMR 5574, CNRS, Université Lyon 1, 9 avenue Charles André, F-69561 Saint Genis Laval Cedex, France
[19] ONERA, Optics Department, BP 72, F-92322 Chatillon, France
[20] INAF—Osservatorio Astronomico di Padova, Vicolo dell'Osservatorio 5, I-35122 Padova, Italy
[21] Geneva Observatory, University of Geneva, Chemin des Maillettes 51, 1290 Versoix, Switzerland

Received 2017 July 27; revised 2017 October 10; accepted 2017 October 17; published 2017 November 16

Abstract

HD 169142 is an excellent target for investigating signs of planet–disk interaction due to previous evidence of gap structures. We perform *J*-band (~1.2 μm) polarized intensity imaging of HD 169142 with VLT/SPHERE. We observe polarized scattered light down to 0.″16 (~19 au) and find an inner gap with a significantly reduced scattered-light flux. We confirm the previously detected double-ring structure peaking at 0.″18 (~21 au) and 0.″56 (~66 au) and marginally detect a faint third gap at 0.″70–0.″73 (~82–85 au). We explore dust evolution models in a disk perturbed by two giant planets, as well as models with a parameterized dust size distribution. The dust evolution model is able to reproduce the ring locations and gap widths in polarized intensity but fails to reproduce their depths. However, it gives a good match with the ALMA dust continuum image at 1.3 mm. Models with a parameterized dust size distribution better reproduce the gap depth in scattered light, suggesting that dust filtration at the outer edges of the gaps is less effective. The pileup of millimeter grains in a dust trap and the continuous distribution of small grains throughout the gap likely require more efficient dust fragmentation and dust diffusion in the dust trap. Alternatively, turbulence or charging effects might lead to a reservoir of small grains at the surface layer that is not affected by the dust growth and fragmentation cycle dominating the dense disk midplane. The exploration of models shows that extracting planet properties such as mass from observed gap profiles is highly degenerate.

Key words: planet–disk interactions – protoplanetary disks – radiative transfer – scattering – techniques: polarimetric

1. Introduction

About two decades ago, our own solar system was the only available laboratory to test models of planet formation. Today, we know that planetary systems are common around other stars and that their architectures are very diverse. The initial conditions and evolution of protoplanetary disks, where planets form, must have a direct influence on most fundamental properties of their planetary systems (Mordasini et al. 2012, 2016). It is therefore essential to improve our knowledge of the structure of protoplanetary disks by observing and studying them at high spatial scales and with various tracers that enable us to characterize different disk regions. This, indirectly, can constrain the physical processes that influence the disk evolution (e.g., gap opening by a planet, dust growth and settling, photo-evaporation). Even with the advent of a new generation of extreme adaptive optics instruments, the detection of forming planets within their host disks is still challenging, but one can look for indirect

---

[*] Based on observations collected at the European Organisation for Astronomical Research in the Southern Hemisphere under ESO program 095.C-0273.

GLOSSARY

ABBREVIATIONS

ALMA	Atacama Large Millimeter Array
CASA	Common Astronomy Software Application
CMB	Cosmic Microwave Background
CO	Carbon Monoxide
Cha II	Chamaeleon II
DPI	Dual Polarization Imaging
EOD	Edge-On Disks
FWHM	Full Width Half Maximum
GAIA	Gaia Space Telescope
GTO	Garanteed Time Observations
HR diagram	Hertzsprung-Russell diagram
HST	Hubble Space Telescope
IR	Infrared wavelengths
IRDIS	Infra-Red Dual-band Imager and Spectrograph, sub instrument of SPHERE
ISM	Interstellar Medium
LTE	Local Thermodynamic Equilibrium
MCFOST	Radiative transfer code developed at IPAG
MHD	Magnetohydrodynamics
Myr	Million year
PA	Position Angle
PDI	Polarimetric differential imaging
PI	Polarized intensity
PSF	Point Spread Function
PV diagram	Position Velocity diagram
RMS	Root Mean Square
SED	Spectral Energy Distribution
SFR	Star Forming Region
SPHERE	Spectro-Polarimetic High contrast imager for Exoplanets REsearch
SPW	Spectral Window in ALMA observations
TD	Transition disk

VLT	Very Large Telescope
VSI	Vertical Shear Instability
WVR	Water Vapor Radiometer
YSO	Young Stellar object

OBSERVATIONNAL BANDS MENTIONNED IN THIS THESIS

R BAND – 0.65 μm

Y BAND – 1.02 μm

J BAND – 1.25 μm

H BAND – 1.65 μm

K BAND – 2.2 μm

Q BAND – 21 μm

BAND 7 – 890 μm — 345 GHz

BAND 6 – 1330 μm — 230 GHz

BAND 4 – 2060 μm — 145 GHz

BAND 3 – 3000 μm — 100 GHz

PHYSICAL CONSTANTS

Arcsecond	$1''$	=	1/3600 rad
Astronomical unit	1 au	=	1.5×10^{11} m
Parsec	1 pc	=	3.1×10^{16} m
Solar Mass	$1\ M_\odot$	=	2.0×10^{30} kg
Jupiter Mass	$1\ M_J$	=	$1.0 \times 10^{-3}\ M_\odot$
Earth Mass	$1\ M_\oplus$	=	$3.0 \times 10^{-6}\ M_\odot$
Jansky	1 Jy	=	$10^{-26}\,\mathrm{W\,m^{-2}\,Hz^{-1}}$

BIBLIOGRAPHY

Alcalá, J. M., C. F. Manara, A. Natta, et al., 2017, *A&A*, 600, A20, « X-shooter spectroscopy of young stellar objects in Lupus. »

Alexander, R. D., C. J. Clarke, and J. E. Pringle, 2006, *MNRAS*, 369, 1, pp. 229–239, « Photoevaporation of protoplanetary discs - II. Evolutionary models and observable properties. »

Alexander, R., I. Pascucci, S. Andrews, et al., 2014, *Protostars and Protoplanets VI*, 475, « The Dispersal of Protoplanetary Disks. »

Alibert, Y., C. Mordasini, W. Benz, et al., 2005, *A&A*, 434, 1, pp. 343–353, « Models of giant planet formation with migration and disc evolution. »

Amard, L. and S. P. Matt, 2020, *ApJ*, 889, 2, p. 108, « The Impact of Metallicity on the Evolution of the Rotation and Magnetic Activity of Sun-like Stars. »

André, P., 2002, *EAS Publications Series*, vol. 3, pp. 1–38, « The Initial Conditions for Protostellar Collapse: Observational Constraints. »

Andre, P., D. Ward-Thompson, and M. Barsony, 1993, *ApJ*, 406, p. 122, « Submillimeter Continuum Observations of rho Ophiuchi A: The Candidate Protostar VLA 1623 and Prestellar Clumps. »

Andrews, S. M., 2020, *arXiv e-prints*, arXiv:2001.05007, « Observations of Protoplanetary Disk Structures. »

Andrews, S. M. and J. P. Williams, 2005, *ApJ*, 631, pp. 1134–1160, « Circumstellar Dust Disks in Taurus-Auriga: The Submillimeter Perspective. »

Andrews, S. M. and J. P. Williams, 2007, *ApJ*, 659, 1, pp. 705–728, « High-Resolution Submillimeter Constraints on Circumstellar Disk Structure. »

Andrews, S. M., M. C. Liu, J. P. Williams, et al., 2008, *ApJ*, 685, pp. 1039–1045, « Submillimeter Observations of the Young Low-Mass Object IRAS 04158+2805. »

Andrews, S. M., K. A. Rosenfeld, D. J. Wilner, et al., 2011, *ApJ*, 742, p. L5, « A Closer Look at the LkCa 15 Protoplanetary Disk. »

Andrews, S. M., K. A. Rosenfeld, A. L. Kraus, et al., 2013, *ApJ*, 771, p. 129, « The Mass Dependence between Protoplanetary Disks and their Stellar Hosts. »

Andrews, S. M., M. Terrell, A. Tripathi, et al., 2018, *ApJ*, 865, 2, p. 157, « Scaling Relations Associated with Millimeter Continuum Sizes in Protoplanetary Disks. »

Andrews, S. M., J. Huang, L. M. Pérez, et al., 2018, *ApJ*, 869, 2, p. L41, « The Disk Substructures at High Angular Resolution Project (DSHARP). I. Motivation, Sample, Calibration, and Overview. »

Ansdell, M., J. P. Williams, N. van der Marel, et al., 2016, *ApJ*, 828, 1, p. 46, « ALMA Survey of Lupus Protoplanetary Disks. I. Dust and Gas Masses. »

Ansdell, M., J. P. Williams, L. Trapman, et al., 2018, *ApJ*, 859, 1, p. 21, « ALMA Survey of Lupus Protoplanetary Disks. II. Gas Disk Radii. »

Ansdell, M., J. P. Williams, C. F. Manara, et al., 2017, *AJ*, 153, 5, « An ALMA Survey of Protoplanetary Disks in the σ Orionis Cluster. »

Antoniucci, S., R. García López, B. Nisini, et al., 2014, *A&A*, 572, A62, « POISSON project. III. Investigating the evolution of the mass accretion rate. »

Appenzeller, I., C. Bertout, and O. Stahl, 2005, *A&A*, 434, 3, pp. 1005–1019, « Edge-on T Tauri stars. »

Armitage, P. J., 2011, *ARA&A*, 49, 1, pp. 195–236, « Dynamics of Protoplanetary Disks. »

Avenhaus, H., S. P. Quanz, H. M. Schmid, et al., 2014, *ApJ*, 781, p. 87, « Structures in the Protoplanetary Disk of HD142527 Seen in Polarized Scattered Light. »

Avenhaus, H., S. P. Quanz, A. Garufi, et al., 2018, *ApJ*, 863, p. 44, « Disks around T Tauri Stars with SPHERE (DARTTS-S). I. SPHERE/IRDIS Polarimetric Imaging of Eight Prominent T Tauri Disks. »

Bae, J., Z. Zhu, and L. Hartmann, 2016, *ApJ*, 819, 2, p. 134, « Planetary Signatures in the SAO 206462 (HD 135344B) Disk: A Spiral Arm Passing through Vortex? »

Bae, J., P. Pinilla, and T. Birnstiel, 2018, *ApJ*, 864, 2, p. L26, « Diverse Protoplanetary Disk Morphology Produced by a Jupiter-mass Planet. »

Baraffe, I., D. Homeier, F. Allard, et al., 2015, *A&A*, 577, A42, « New evolutionary models for pre-main sequence and main sequence low-mass stars down to the hydrogen-burning limit. »

Barenfeld, S. A., J. M. Carpenter, L. Ricci, et al., 2016, *AJ*, 827, 2, « ALMA Observations of Circumstellar Disks in the Upper Scorpius OB Association. »

Baron, F., D. Lafrenière, É. Artigau, et al., 2019, *AJ*, 158, 5, p. 187, « Constraints on the Occurrence and Distribution of 1-20 M $_{Jup}$ Companions to Stars at Separations of 5-5000 au from a Compilation of Direct Imaging Surveys. »

Baruteau, C., M. Barraza, S. Pérez, et al., 2019, *MNRAS*, 486, 1, pp. 304–319, « Dust traps in the protoplanetary disc MWC 758: two vortices produced by two giant planets? »

Bayo, A., C. Rodrigo, D. Barrado Y Navascués, et al., 2008, *A&A*, 492, pp. 277–287, « VOSA: virtual observatory SED analyzer. An application to the Collinder 69 open cluster. »

Beckwith, S., A. I. Sargent, R. Chini, et al., 1990, *ApJ*, 99, 3, « A survey for circumstellar disks around young stellar objects. »

Benisty, M., A. Juhasz, A. Boccaletti, et al., 2015, *A&A*, 578, p. L6, « Asymmetric features in the protoplanetary disk MWC 758. »

Benisty, M., T. Stolker, A. Pohl, et al., 2017, *A&A*, 597, A42, « Shadows and spirals in the protoplanetary disk HD 100453. »

Benisty, M., A. Juhász, S. Facchini, et al., 2018, *A&A*, 619, A171, « Shadows and asymmetries in the T Tauri disk HD 143006: evidence for a misaligned inner disk. »

Bergin, E. A. and J. P. Williams, 2018, *arXiv e-prints*, arXiv:1807.09631, « The determination of protoplanetary disk masses. »

Bergin, E. A., F. Du, L. I. Cleeves, et al., 2016, *ApJ*, 831, 1, p. 101, « Hydrocarbon Emission Rings in Protoplanetary Disks Induced by Dust Evolution. »

Bertrang, G. H. M., H. Avenhaus, S. Casassus, et al., 2018, *MNRAS*, 474, pp. 5105–5113, « HD 169142 in the eyes of ZIMPOL/SPHERE. »

Beuzit, J. L., A. Vigan, D. Mouillet, et al., 2019, *A&A*, 631, A155, « SPHERE: the exoplanet imager for the Very Large Telescope. »

Beuzit, J.-L., M. Feldt, K. Dohlen, et al., 2008, *Ground-based and Airborne Instrumentation for Astronomy II*, vol. 7014, p. 701418, « SPHERE: a 'Planet Finder' instrument for the VLT. »

Biller, B. A., J. Males, T. Rodigas, et al., 2014, *ApJ*, 792, p. L22, « An Enigmatic Point-like Feature within the HD 169142 Transitional Disk. »

Birnstiel, T., S. M. Andrews, and B. Ercolano, 2012, *A&A*, 544, A79, « Can grain growth explain transition disks? »

Birnstiel, T. and S. M. Andrews, 2014, *ApJ*, 780, p. 153, « On the Outer Edges of Protoplanetary Dust Disks. »

Bjorkman, J. E. and K. Wood, 2001, *ApJ*, 554, 1, pp. 615–623, « Radiative Equilibrium and Temperature Correction in Monte Carlo Radiation Transfer. »

Blum, J. and G. Wurm, 2008, *ARA&A*, 46, pp. 21–56, « The growth mechanisms of macroscopic bodies in protoplanetary disks. »

Boehler, Y., E. Weaver, A. Isella, et al., 2017, *ApJ*, 840, p. 60, « A Close-up View of the Young Circumbinary Disk HD 142527. »

Boss, A. P., 1997, *Science*, 276, pp. 1836–1839, « Giant planet formation by gravitational instability. »

Bouvier, J., S. Cabrit, M. Fernandez, et al., 1993, *A&A*, 272, pp. 176–206, « COYOTES I : the photometric variability and rotational evolution of T Tauri stars. »

Brauer, F., C. P. Dullemond, A. Johansen, et al., 2007, *A&A*, 469, 3, pp. 1169–1182, « Survival of the mm-cm size grain population observed in protoplanetary disks. »

Bruderer, S., N. van der Marel, E. F. van Dishoeck, et al., 2014, *A&A*, 562, A26, « Gas structure inside dust cavities of transition disks: Ophiuchus IRS 48 observed by ALMA. »

Burrows, C. J., K. R. Stapelfeldt, A. M. Watson, et al., 1996, *ApJ*, 473, p. 437, « Hubble Space Telescope Observations of the Disk and Jet of HH 30. »

Calvet, N., A. Patino, G. C. Magris, et al., 1991, *ApJ*, 380, p. 617, « Irradiation of Accretion Disks around Young Objects. I. Near-Infrared CO Bands. »

Canovas, H., F. Ménard, J. de Boer, et al., 2015, *A&A*, 582, p. L7, « Nonazimuthal linear polarization in protoplanetary disks. »

Canovas, H., C. Caceres, M. R. Schreiber, et al., 2016, *MNRAS*, 458, pp. L29–L33, « A ring-like concentration of mm-sized particles in Sz 91. »

Cánovas, H., C. Cantero, L. Cieza, et al., 2019, *A&A*, 626, A80, « Census of ρ Ophiuchi candidate members from Gaia Data Release 2. »

Carbillet, M., P. Bendjoya, L. Abe, et al., 2011, *Experimental Astronomy*, 30, pp. 39–58, « Apodized Lyot coronagraph for SPHERE/VLT. I. Detailed numerical study. »

Carrasco-González, C., A. Sierra, M. Flock, et al., 2019, *ApJ*, 883, 1, p. 71, « The Radial Distribution of Dust Particles in the HL Tau Disk from ALMA and VLA Observations. »

Casassus, S., G. van der Plas, S. P. M, et al., 2013, *Nature*, 493, pp. 191–194, « Flows of gas through a protoplanetary gap. »

Casassus, S., H. Avenhaus, S. Pérez, et al., 2018, *MNRAS*, 477, pp. 5104–5114, « An inner warp in the DoAr 44 T Tauri transition disc. »

Cazzoletti, P., E. F. van Dishoeck, R. Visser, et al., 2018, *A&A*, 609, A93, « CN rings in full protoplanetary disks around young stars as probes of disk structure. »

Cazzoletti, P., E. F. van Dishoeck, P. Pinilla, et al., 2018, *A&A*, 619, A161, « Evidence for a massive dust-trapping vortex connected to spirals. Multi-wavelength analysis of the HD 135344B protoplanetary disk. »

Cazzoletti, P., C. F. Manara, H. Baobab Liu, et al., 2019, *A&A*, 626, A11, « ALMA survey of Class II protoplanetary disks in Corona Australis: a young region with low disk masses. »

Chandler, C. J., D. W. Koerner, A. I. Sargent, et al., 1995, *ApJ*, 449, p. L139, « Dust Emission from Protostars: The Disk and Envelope of HH 24 MMS. »

Cieza, L. A., D. L. Padgett, L. E. Allen, et al., 2009, *ApJ*, 696, 1, pp. L84–L88, « Primordial Circumstellar Disks in Binary Systems: Evidence for Reduced Lifetimes. »

Cieza, L. A., D. Ruíz-Rodríguez, A. Hales, et al., 2018, *MNRAS*, p. 2538, « The Ophiuchus DIsc Survey Employing ALMA (ODISEA) - I : project description and continuum images at 28 au resolution. »

Clanton, C. and B. S. Gaudi, 2016, *ApJ*, 819, 2, p. 125, « Synthesizing Exoplanet Demographics: A Single Population of Long-period Planetary Companions to M Dwarfs Consistent with Microlensing, Radial Velocity, and Direct Imaging Surveys. »

Cox, E. G., R. J. Harris, L. W. Looney, et al., 2017, *ApJ*, 851, 2, p. 83, « Protoplanetary Disks in ρ Ophiuchus as Seen from ALMA. »

Crida, A. and A. Morbidelli, 2007, *MNRAS*, 377, pp. 1324–1336, « Cavity opening by a giant planet in a protoplanetary disc and effects on planetary migration. »

Crida, A., A. Morbidelli, and F. Masset, 2006, *Icarus*, 181, 2, pp. 587–604, « On the width and shape of gaps in protoplanetary disks. »

Currie, T. and A. Sicilia-Aguilar, 2011, *ApJ*, 732, 1, p. 24, « The Transitional Protoplanetary Disk Frequency as a Function of Age: Disk Evolution In the Coronet Cluster, Taurus, and Other 1-8 Myr Old Regions. »

Currie, T., T. Muto, T. Kudo, et al., 2014, *ApJ*, 796, p. L30, « Recovery of the Candidate Protoplanet HD 100546 b with Gemini/NICI and Detection of Additional (Planet-induced?) Disk Structure at Small Separations. »

D'Alessio, P., J. Cantö, N. Calvet, et al., 1998, *ApJ*, 500, 1, pp. 411–427, « Accretion Disks around Young Objects. I. The Detailed Vertical Structure. »

D'Orazi, V., R. Gratton, S. Desidera, et al., 2018, *Nature Astronomy*, p. 172, « Mapping of shadows cast on a protoplanetary disk by a close binary system. »

Dartois, E., A. Dutrey, and S. Guilloteau, 2003, *A&A*, 399, pp. 773–787, « Structure of the DM Tau Outer Disk: Probing the vertical kinetic temperature gradient. »

Dent, W. R. F., C. Pinte, P. C. Cortes, et al., 2019, *MNRAS*, 482, 1, pp. L29–L33, « Submillimetre dust polarization and opacity in the HD163296 protoplanetary ring system. »

Dipierro, G. and G. Laibe, 2017, *MNRAS*, 469, pp. 1932–1948, « An opening criterion for dust gaps in protoplanetary discs. »

Dohlen, K., M. Langlois, M. Saisse, et al., 2008, *Ground-based and Airborne Instrumentation for Astronomy II*, vol. 7014, p. 70143L, « The infra-red dual imaging and spectrograph for SPHERE: design and performance. »

Dong, R. and J. Fung, 2017, *ApJ*, 835, p. 146, « What is the Mass of a Gap-opening Planet? »

Dong, R., Z. Zhu, and B. Whitney, 2015, *ApJ*, 809, p. 93, « Observational Signatures of Planets in Protoplanetary Disks I. Gaps Opened by Single and Multiple Young Planets in Disks. »

Dong, R., Z. Zhu, R. R. Rafikov, et al., 2015, *ApJ*, 809, 1, p. L5, « Observational Signatures of Planets in Protoplanetary Disks: Spiral Arms Observed in Scattered Light Imaging Can be Induced by Planets. »

Dorschner, J., B. Begemann, T. Henning, et al., 1995, *A&A*, 300, p. 503, « Steps toward interstellar silicate mineralogy. II. Study of Mg-Fe- silicate glasses of variable composition. »

Draine, B. T., 2006, *ApJ*, 636, pp. 1114–1120, « On the Submillimeter Opacity of Protoplanetary Disks. »

Draine, B. T. and H. M. Lee, 1984, *ApJ*, 285, p. 89, « Optical Properties of Interstellar Graphite and Silicate Grains. »

Dubrulle, B., G. Morfill, and M. Sterzik, 1995, *Icarus*, 114, 2, pp. 237–246, « The dust subdisk in the protoplanetary nebula. »

Duchêne, G., F. Ménard, K. Stapelfeldt, et al., 2003, *A&A*, 400, pp. 559–565, « A layered edge-on circumstellar disk around HK Tau B. »

Duchêne, G., C. McCabe, C. Pinte, et al., 2010, *ApJ*, 712, pp. 112–129, « Panchromatic Observations and Modeling of the HV Tau C Edge-on Disk. »

Duchêne, G., K. Stapelfeldt, A. Isella, et al., 2014, *Exploring the Formation and Evolution of Planetary Systems*, vol. 299, pp. 111–112, « Panchromatic imaging and modeling of SSTtau J042021+281349: A new prototypical edge-on protoplanetary disk. »

Dullemond, C. P. and C. Dominik, 2004, *A&A*, 421, pp. 1075–1086, « The effect of dust settling on the appearance of protoplanetary disks. »

Dullemond, C. P. and C. Dominik, 2005, *A&A*, 434, pp. 971–986, « Dust coagulation in protoplanetary disks: A rapid depletion of small grains. »

Dutrey, A., S. Guilloteau, G. Duvert, et al., 1996, *A&A*, 309, pp. 493–504, « Dust and gas distribution around T Tauri stars in Taurus-Auriga. I. Interferometric 2.7mm continuum and 13CO J=1-0 observations. »

Dutrey, A., S. Guilloteau, L. Prato, et al., 1998, *A&A*, 338, pp. L63–L66, « CO study of the GM Aurigae Keplerian disk. »

Dutrey, A., S. Guilloteau, V. Piétu, et al., 2017, *A&A*, 607, A130, « The Flying Saucer: Tomography of the thermal and density gas structure of an edge-on protoplanetary disk. »

Dzib, S. A., L. Loinard, G. N. Ortiz-León, et al., 2018, *ApJ*, 867, 2, p. 151, « Distances and Kinematics of Gould Belt Star-forming Regions with Gaia DR2 Results. »

Evans Neal J., I., M. M. Dunham, J. K. Jørgensen, et al., 2009, *ApJS*, 181, 2, pp. 321–350, « The Spitzer c2d Legacy Results: Star-Formation Rates and Efficiencies; Evolution and Lifetimes. »

Facchini, S., T. Birnstiel, S. Bruderer, et al., 2017, *A&A*, 605, A16, « Different dust and gas radial extents in protoplanetary disks: consistent models of grain growth and CO emission. »

Facchini, S., E. F. van Dishoeck, C. F. Manara, et al., 2019, *A&A*, 626, p. L2, « High gas-to-dust size ratio indicating efficient radial drift in the mm-faint CX Tauri disk. »

Facchini, S., G. Lodato, and D. J. Price, 2013, *MNRAS*, 433, pp. 2142–2156, « Wave-like warp propagation in circumbinary discs - I. Analytic theory and numerical simulations. »

Fedele, D., M. E. van den Ancker, T. Henning, et al., 2010, *A&A*, 510, A72, « Timescale of mass accretion in pre-main-sequence stars. »

Fedele, D., M. Carney, M. R. Hogerheijde, et al., 2017, *A&A*, 600, A72, « ALMA unveils rings and gaps in the protoplanetary system HD169142: signatures of two giant protoplanets. »

Fernandes, R. B., G. D. Mulders, I. Pascucci, et al., 2019, *ApJ*, 874, 1, p. 81, « Hints for a Turnover at the Snow Line in the Giant Planet Occurrence Rate. »

Flaherty, K. M., A. M. Hughes, R. Teague, et al., 2018, *ApJ*, 856, 2, p. 117, « Turbulence in the TW Hya Disk. »

Flaherty, K., A. M. Hughes, J. B. Simon, et al., 2020, *ApJ*, 895, 2, p. 109, « Measuring Turbulent Motion in Planet-forming Disks with ALMA: A Detection around DM Tau and Nondetections around MWC 480 and V4046 Sgr. »

Flock, M., J. P. Ruge, N. Dzyurkevich, et al., 2015, *A&A*, 574, A68, « Gaps, rings, and non-axisymmetric structures in protoplanetary disks. From simulations to ALMA observations. »

Flock, M., R. P. Nelson, N. J. Turner, et al., 2017, *ApJ*, 850, 2, p. 131, « Radiation Hydrodynamical Turbulence in Protoplanetary Disks: Numerical Models and Observational Constraints. »

Francis, L. and N. van der Marel, 2020, *ApJ*, 892, 2, p. 111, « Dust-depleted Inner Disks in a Large Sample of Transition Disks through Long-baseline ALMA Observations. »

Fromang, S. and R. P. Nelson, 2009, *A&A*, 496, pp. 597–608, « Global MHD simulations of stratified and turbulent protoplanetary discs. II. Dust settling. »

Fromang, S. and J. Papaloizou, 2006, *A&A*, 452, pp. 751–762, « Dust settling in local simulations of turbulent protoplanetary disks. »

Gaia Collaboration, A. G. A. Brown, A. Vallenari, et al., 2018, *A&A*, « Gaia Data Release 2. Summary of the contents and survey properties. »

Galli, P. A. B., H. Bouy, J. Olivares, et al., 2020, *A&A*, 634, A98, « Corona-Australis DANCe. I. Revisiting the census of stars with Gaia-DR2 data. »

Galván-Madrid, R., H. B. Liu, A. F. Izquierdo, et al., 2018, *ApJ*, 868, 1, p. 39, « On the Effects of Self-obscuration in the (Sub)Millimeter Spectral Indices and the Appearance of Protostellar Disks. »

Gammie, C. F., 1996, *ApJ*, 457, p. 355, « Layered Accretion in T Tauri Disks. »

Gammie, C. F., 2001, *ApJ*, 553, 1, pp. 174–183, « Nonlinear Outcome of Gravitational Instability in Cooling, Gaseous Disks. »

Garcia, A. J. L. and J.-F. Gonzalez, 2020, *MNRAS*, 493, 2, pp. 1788–1800, « Evolution of porous dust grains in protoplanetary discs - I. Growing grains. »

Garufi, A., S. P. Quanz, H. M. Schmid, et al., 2016, *A&A*, 588, A8, « The SPHERE view of the planet-forming disk around HD 100546. »

Garufi, A., M. Benisty, P. Pinilla, et al., 2018, *A&A*, 620, A94, « Evolution of protoplanetary disks from their taxonomy in scattered light: spirals, rings, cavities, and shadows. »

Geers, V. C., K. M. Pontoppidan, E. F. van Dishoeck, et al., 2007, *A&A*, 469, pp. L35–L38, « Spatial separation of small and large grains in the transitional disk around the young star IRS 48. »

Geoffray, H. and J.-L. Monin, 2001, *A&A*, 369, « Circumstellar medium around close southern PMS binaries. »

Ginski, C., T. Stolker, P. Pinilla, et al., 2016, *A&A*, 595, A112, « Direct detection of scattered light gaps in the transitional disk around HD 97048 with VLT/SPHERE. »

Glauser, A. M., F. Ménard, C. Pinte, et al., 2008, *A&A*, 485, pp. 531–540, « Multiwavelength studies of the gas and dust disc of IRAS 04158+2805. »

Gonzalez, J. F., G. Laibe, and S. T. Maddison, 2017, *MNRAS*, 467, 2, pp. 1984–1996, « Self-induced dust traps: overcoming planet formation barriers. »

Gorti, U. and D. Hollenbach, 2009, *ApJ*, 690, 2, pp. 1539–1552, « Photoevaporation of Circumstellar Disks By Far-Ultraviolet, Extreme-Ultraviolet and X-Ray Radiation from the Central Star. »

Gräfe, C., S. Wolf, S. Guilloteau, et al., 2013, *A&A*, 553, A69, « Vertical settling and radial segregation of large dust grains in the circumstellar disk of the Butterfly Star. »

Guilloteau, S., A. Dutrey, J. Pety, et al., 2008, *A&A*, 478, 2, pp. L31–L34, « Resolving the circumbinary dust disk surrounding HH 30. »

Guilloteau, S., E. D. Folco, A. Dutrey, et al., 2013, *A&A*, 549, A92, « A sensitive survey for 13CO, CN, H2CO and SO in the disks of T Tauri and Herbig Ae stars. »

Haffert, S. Y., A. J. Bohn, J. de Boer, et al., 2019, *Nature Astronomy*, 3, pp. 749–754, « Two accreting protoplanets around the young star PDS 70. »

Haisch Karl E., J., T. P. Greene, M. Barsony, et al., 2004, *AJ*, 127, 3, pp. 1747–1754, « A Near-Infrared Multiplicity Survey of Class I/Flat-Spectrum Systems in Six Nearby Molecular Clouds. »

Hartmann, L., N. Calvet, E. Gullbring, et al., 1998, *ApJ*, 495, 1, pp. 385–400, « Accretion and the Evolution of T Tauri Disks. »

Hendler, N. P., P. Pinilla, I. Pascucci, et al., 2018, *MNRAS*, 475, pp. L62–L66, « A likely planet-induced gap in the disc around T Cha. »

Hendler, N., I. Pascucci, P. Pinilla, et al., 2020, *arXiv e-prints*, arXiv:2001.02666, « The evolution of dust-disk sizes from a homogeneous analysis of 1-10 Myr-old stars. »

Herbst, W., D. K. Herbst, E. J. Grossman, et al., 1994, *AJ*, 108, p. 1906, « Catalogue of UBVRI Photometry of T Tauri Stars and Analysis of the Causes of Their Variability. »

Herczeg, G. J. and L. A. Hillenbrand, 2015, *ApJ*, 808, 1, p. 23, « Empirical Isochrones for Low Mass Stars in Nearby Young Associations. »

Hildebrand, R. H., 1983, *QJRAS*, « The Determination of Cloud Masses and Dust Characteristics from Submillimetre Thermal Emission. »

Howard, C. D., G. Sandell, W. D.Vacca, et al., 2013, *AJ*, 776, 1, « Herschel/PACS Survey of protoplanetary disks in Taurus/Auriga – Observations of [OI] and [CII], and far infrared continuum. »

Huang, J., S. M. Andrews, L. I. Cleeves, et al., 2018, *ApJ*, 852, 2, p. 122, « CO and Dust Properties in the TW Hya Disk from High-resolution ALMA Observations. »

Huang, J., S. M. Andrews, C. P. Dullemond, et al., 2018, *ApJ*, 869, 2, p. L42, « The Disk Substructures at High Angular Resolution Project (DSHARP). II. Characteristics of Annular Substructures. »

Huang, J., S. M. Andrews, L. M. Pérez, et al., 2018, *ApJ*, 869, 2, p. L43, « The Disk Substructures at High Angular Resolution Project (DSHARP). III. Spiral Structures in the Millimeter Continuum of the Elias 27, IM Lup, and WaOph 6 Disks. »

Hughes, A. M., D. J. Wilner, C. Qi, et al., 2008, *ApJ*, 678, 2, pp. 1119–1126, « Gas and Dust Emission at the Outer Edge of Protoplanetary Disks. »

Hughes, A. M., S. M. Andrews, D. J. Wilner, et al., 2010, *ApJ*, 140, 3, pp. 887–896, « Structure and Composition of Two Transitional Circumstellar Disks in Corona Australis. »

Hull, C. L. H., H. Yang, Z.-Y. Li, et al., 2018, *ApJ*, 860, 1, p. 82, « ALMA Observations of Polarization from Dust Scattering in the IM Lup Protoplanetary Disk. »

Isella, A., L. Testi, A. Natta, et al., 2007, *A&A*, 469, 1, pp. 213–222, « Millimeter imaging of HD 163296: probing the disk structure and kinematics. »

Jayawardhana, R., J. Coffey, A. Scholz, et al., 2006, *ApJ*, 648, 2, pp. 1206–1218, « Accretion Disks around Young Stars: Lifetimes, Disk Locking, and Variability. »

Johansen, A., J. Blum, H. Tanaka, et al., 2014, *Protostars and Planets VI*, p. 547, « The Multifaceted Planetesimal Formation Process. »

Jørgensen, J. K., T. L. Bourke, P. C. Myers, et al., 2007, *ApJ*, 659, 1, pp. 479–498, « PROSAC: A Submillimeter Array Survey of Low-Mass Protostars. I. Overview of Program: Envelopes, Disks, Outflows, and Hot Cores. »

Joy, A. H., 1945, *ApJ*, 102, p. 168, « T Tauri Variable Stars. »

Kamp, I., P. Woitke, C. Pinte, et al., 2011, *A&A*, 532, A85, « Continuum and line modelling of discs around young stars. »

Kaplan, E. L. and P. Meier, 1958, *Journal of the American Statistical Association*, 53, 282, pp. 457–481, « Nonparametric Estimation from Incomplete Observations. »

Kataoka, A., T. Muto, M. Momose, et al., 2016, *ApJ*, 820, 1, p. 54, « Grain Size Constraints on HL Tau with Polarization Signature. »

Kenyon, S. J. and L. Hartmann, 1987, *ApJ*, 323, p. 714, « Spectral Energy Distributions of T Tauri Stars: Disk Flaring and Limits on Accretion. »

Kenyon, S. J., M. Gómez, and B. A. Whitney, 2008, *Low Mass Star Formation in the Taurus-Auriga Clouds*

Keppler, M., M. Benisty, A. Müller, et al., 2018, *A&A*, 617, A44, « Discovery of a planetary-mass companion within the gap of the transition disk around PDS 70. »

Kraus, A. L. and M. J. Ireland, 2012, *ApJ*, 745, p. 5, « LkCa 15: A Young Exoplanet Caught at Formation? »

Krist, J. E., K. R. Stapelfeldt, C. J. Burrows, et al., 1998, *ApJ*, 501, 2, pp. 841–852, « Hubble Space Telescope WFPC2 Imaging of FS Tauri and Haro 6-5B. »

Kruskal, W. H. and W. A. Wallis, 1952, *Journal of the American Statistical Association*, 47, 260, pp. 583–621, « Use of Ranks in One-Criterion Variance Analysis. »

Lada, C. J., 1987, *Star Forming Regions*, vol. 115, p. 1, « Star formation: from OB associations to protostars. »

Lambrechts, M. and A. Johansen, 2012, *A&A*, 544, A32, « Rapid growth of gas-giant cores by pebble accretion. »

Langlois, M., K. Dohlen, A. Vigan, et al., 2014, *Ground-based and Airborne Instrumentation for Astronomy V*, vol. 9147, 91471R, « High contrast polarimetry in the infrared with SPHERE on the VLT. »

Langlois, M., A. Pohl, A. M. Lagrange, et al., 2018, *A&A*, 614, A88, « First scattered light detection of a nearly edge-on transition disk around the T Tauri star RY Lupi. »

Laor, A. and B. T. Draine, 1993, *ApJ*, 402, p. 441, « Spectroscopic Constraints on the Properties of Dust in Active Galactic Nuclei. »

Law, C. J., L. Ricci, S. M. Andrews, et al., 2017, *AJ*, « An SMA Continuum Survey of Circumstellar Disks in the Serpens Star-Forming Region. »

Lebouteiller, V., D. J. Barry, H. W. W. Spoon, et al., 2011, *ApJS*, 196, p. 8, « CASSIS: The Cornell Atlas of Spitzer/Infrared Spectrograph Sources. »

Lee, C.-F., Z.-Y. Li, P. T. P. Ho, et al., 2017, *ApJ*, 843, 1, p. 27, « Formation and Atmosphere of Complex Organic Molecules of the HH 212 Protostellar Disk. »

Li, A. and B. T. Draine, 2001, *ApJ*, 554, 2, pp. 778–802, « Infrared Emission from Interstellar Dust. II. The Diffuse Interstellar Medium. »

Liu, H. B., 2019, *ApJ*, 877, 2, p. L22, « The Anomalously Low (Sub)Millimeter Spectral Indices of Some Protoplanetary Disks May Be Explained By Dust Self-scattering. »

Lodato, G., G. Dipierro, E. Ragusa, et al., 2019, *MNRAS*, 486, 1, pp. 453–461, « The newborn planet population emerging from ring-like structures in discs. »

Long, F., G. J. Herczeg, I. Pascucci, et al., 2017, *ApJ*, 844, 2, p. 99, « An ALMA Survey of CO isotopologue emission from Protoplanetary Disks in Chamaeleon I. »

Long, F., P. Pinilla, G. J. Herczeg, et al., 2018, *ApJ*, 869, 1, p. 17, « Gaps and Rings in an ALMA Survey of Disks in the Taurus Star-forming Region. »

Louvet, F., C. Dougados, S. Cabrit, et al., 2018, *A&A*, 618, A120, « The HH30 edge-on T Tauri star. A rotating and precessing monopolar outflow scrutinized by ALMA. »

Lucy, L. B., 1999, *A&A*, 345, pp. 211–220, « Improved Monte Carlo techniques for the spectral synthesis of supernovae. »

Luhman, K. L., 2007, *The Astrophysical Journal Supplement Series*, 173, 1, pp. 104–136, « The Stellar Population of the Chamaeleon I Star-forming Region. »

Luhman, K. L., P. R. Allen, C. Espaillat, et al., 2010, *The Astrophysical Journal Supplement Series*, 186, pp. 111–174, « The Disk Population of the Taurus Star-Forming Region. »

Lynden-Bell, D. and J. E. Pringle, 1974, *MNRAS*, 168, pp. 603–637, « The evolution of viscous discs and the origin of the nebular variables. »

Mamajek, E. E., 2009, *American Institute of Physics Conference Series*, vol. 1158, pp. 3–10, « Initial Conditions of Planet Formation: Lifetimes of Primordial Disks. »

Manara, C. F., L. Testi, A. Natta, et al., 2014, *A&A*, 568, A18, « On the gas content of transitional disks: a VLT/X-Shooter study of accretion and winds. »

Manara, C. F., D. Fedele, G. J. Herczeg, et al., 2016, *A&A*, 585, A136, « X-Shooter study of accretion in Chamaeleon I. »

Manara, C. F., L. Testi, G. J. Herczeg, et al., 2017, *A&A*, 604, A127, « X-Shooter study of accretion in Chamaeleon I: II. A steeper increase of accretion with stellar mass for very low mass stars? »

Marino, S., S. Casassus, S. Perez, et al., 2015, *ApJ*, 813, p. 76, « Compact Dust Concentration in the MWC 758 Protoplanetary Disk. »

Martinez, P., C. Dorrer, M. Kasper, et al., 2009, *A&A*, 500, pp. 1281–1285, « Design, analysis, and testing of a microdot apodizer for the apodized pupil Lyot coronagraph. II. Impact of the dot size. »

Mathews, G. S., C. Pinte, G. Duchene, et al., 2013, *A&A*, 558, A66, « A Herschel PACS survey of the dust and gas in Upper Scorpius disks. »

Mathis, J. S., W. Rumpl, and K. H. Nordsieck, 1977, *ApJ*, 217, pp. 425–433, « The size distribution of interstellar grains. »

Maury, A. J., P. André, L. Testi, et al., 2019, *A&A*, 621, A76, « Characterizing young protostellar disks with the CALYPSO IRAM-PdBI survey: large Class 0 disks are rare. »

Mayor, M. and D. Queloz, 1995, *Nature*, 378, 6555, pp. 355–359, « A Jupiter-mass companion to a solar-type star. »

McKee, C. F. and E. C. Ostriker, 2007, *ARA&A*, 45, 1, pp. 565–687, « Theory of Star Formation. »

McMullin, J. P., B. Waters, D. Schiebel, et al., 2007, *CASA Architecture and Applications*

Menard, F., 1991, *Graduate Workshop on Star Formation*, p. 161, « Montecarlo Radiative Transfer Models of Circumstellar Disks. »

Menard, F., N. Cuello, C. Ginski, et al., 2020, *arXiv e-prints*, arXiv:2006.02439, « Ongoing flyby in the young multiple system UX Tauri. »

Miotello, A., E. F. van Dishoeck, J. P. Williams, et al., 2017, *A&A*, 599, A113, « Lupus disks with faint CO isotopologues: low gas/dust or large carbon depletion? »

Mizuno, A., R. Yamaguchi, K. Tachihara, et al., 2001, *PASJ*, 53, « A Large Scale 12CO (J= 1-0) Survey toward the Chamaeleon Region with NANTEN. »

Moriarty-Schieven, G. H., P. G. Wannier, J. Keene, et al., 1994, *ApJ*, 436, p. 800, « Circumprotostellar Environments. II. Envelopes, Activity, and Evolution. »

Motte, F. and P. André, 2001, *A&A*, 365, pp. 440–464, « The circumstellar environment of low-mass protostars: A millimeter continuum mapping survey. »

Movshovitz, N., P. Bodenheimer, M. Podolak, et al., 2010, *Icarus*, 209, 2, pp. 616–624, « Formation of Jupiter using opacities based on detailed grain physics. »

Mulders, G. D. and C. Dominik, 2012, *A&A*, 539, A9, « Probing the turbulent mixing strength in protoplanetary disks across the stellar mass range: no significant variations. »

Müller, A., M. Keppler, T. Henning, et al., 2018, *A&A*, 617, p. L2, « Orbital and atmospheric characterization of the planet within the gap of the PDS 70 transition disk. »

Muro-Arena, G. A., C. Dominik, L. B. F. M. Waters, et al., 2018, *A&A*, 614, A24, « Dust modeling of the combined ALMA and SPHERE datasets of HD 163296. Is HD 163296 really a Meeus group II disk? »

Muro-Arena, G. A., M. Benisty, C. Ginski, et al., 2020, *A&A*, 635, A121, « Shadowing and multiple rings in the protoplanetary disk of HD 139614? »

Nakagawa, Y., M. Sekiya, and C. Hayashi, 1986, *Icarus*, 67, 3, pp. 375–390, « Settling and growth of dust particles in a laminar phase of a low-mass solar nebula. »

Nielsen, E. L., R. J. De Rosa, B. Macintosh, et al., 2019, *AJ*, 158, 1, p. 13, « The Gemini Planet Imager Exoplanet Survey: Giant Planet and Brown Dwarf Demographics from 10 to 100 au. »

Ohashi, S., A. Kataoka, H. Nagai, et al., 2018, *ApJ*, 864, 1, p. 81, « Two Different Grain Size Distributions within the Protoplanetary Disk around HD 142527 Revealed by ALMA Polarization Observation. »

Okuzumi, S., M. Momose, S.-i. Sirono, et al., 2016, *ApJ*, 821, p. 82, « Sintering-induced Dust Ring Formation in Protoplanetary Disks: Application to the HL Tau Disk. »

Ormel, C. W. and H. H. Klahr, 2010, *A&A*, 520, A43, « The effect of gas drag on the growth of protoplanets. Analytical expressions for the accretion of small bodies in laminar disks. »

Ortiz-León, G. N., L. Loinard, S. A. Dzib, et al., 2018, *ApJ*, 869, 2, p. L33, « Gaia-DR2 Confirms VLBA Parallaxes in Ophiuchus, Serpens, and Aquila. »

Owen, J. E., B. Ercolano, and C. J. Clarke, 2011, *MNRAS*, 412, pp. 13–25, « Protoplanetary disc evolution and dispersal: the implications of X-ray photoevaporation. »

Padgett, D. L., W. Brandner, K. R. Stapelfeldt, et al., 1999, *AJ*, 117, pp. 1490–1504, « HUBBLE SPACE TELESCOPE/NICMOS Imaging of Disks and Envelopes around Very Young Stars. »

Pascucci, I. and M. Sterzik, 2009, *ApJ*, 702, 1, pp. 724–732, « Evidence for Disk Photoevaporation Driven by the Central Star. »

Pascucci, I., L. Testi, G. J. Herczeg, et al., 2016, *ApJ*, 831, 2, p. 125, « A Steeper than Linear Disk Mass-Stellar Mass Scaling Relation. »

Pavlyuchenkov, Y., V. Akimkin, D. Wiebe, et al., 2019, *MNRAS*, 486, 3, pp. 3907–3914, « Revealing dust segregation in protoplanetary discs with the help of multifrequency spectral index maps. »

Pecaut, M. J., E. E. Mamajek, and E. J. Bubar, 2012, *ApJ*, 746, 2, « A revised age for Upper Scorpius and the star formation history among the F-type members of the Scorpius-Centaurus OB association. »

Pérez, L. M., J. M. Carpenter, C. J. Chandler, et al., 2012, *ApJ*, 760, p. L17, « Constraints on the Radial Variation of Grain Growth in the AS 209 Circumstellar Disk. »

Pérez, L. M., M. Benisty, S. M. Andrews, et al., 2018, *ApJ*, 869, p. L50, « The Disk Substructures at High Angular Resolution Project (DSHARP). X. Multiple Rings, a Misaligned Inner Disk, and a Bright Arc in the Disk around the T Tauri star HD 143006. »

Pérez, S., A. Dunhill, S. Casassus, et al., 2015, *ApJ*, 811, p. L5, « Planet Formation Signposts: Observability of Circumplanetary Disks via Gas Kinematics. »

Pérez, S., S. Casassus, and P. Benítez-Llambay, 2018, *MNRAS*, 480, pp. L12–L17, « Observability of planet-disc interactions in CO kinematics. »

Pinilla, P., M. Benisty, and T. Birnstiel, 2012, *A&A*, 545, A81, « Ring shaped dust accumulation in transition disks. »

Pinilla, P., T. Birnstiel, L. Ricci, et al., 2012, *A&A*, 538, A114, « Trapping dust particles in the outer regions of protoplanetary disks. »

Pinilla, P., N. van der Marel, L. M. Pérez, et al., 2015, *A&A*, 584, A16, « Testing particle trapping in transition disks with ALMA. »

Pinilla, P., M. Tazzari, I. Pascucci, et al., 2018, *ApJ*, 859, p. 32, « Homogeneous Analysis of the Dust Morphology of Transition Disks Observed with ALMA: Investigating Dust Trapping and the Origin of the Cavities. »

Pinilla, P., M. Benisty, J. de Boer, et al., 2018, *ApJ*, 868, p. 85, « Variable Outer Disk Shadowing around the Dipper Star RXJ1604.3-2130. »

Pinilla, P., M. Flock, M. d. J. Ovelar, et al., 2016, *A&A*, 596, A81, « Can dead zones create structures like a transition disk? »

Pinte, C. and G. Laibe, 2014, *A&A*, 565, A129, « Diversity in the outcome of dust radial drift in protoplanetary discs. »

Pinte, C., F. Ménard, G. Duchêne, et al., 2006, *A&A*, 459, 3, pp. 797–804, « Monte Carlo radiative transfer in protoplanetary disks. »

Pinte, C., L. Fouchet, F. Ménard, et al., 2007, *A&A*, 469, pp. 963–971, « On the stratified dust distribution of the GG Tauri circumbinary ring. »

Pinte, C., T. J. Harries, M. Min, et al., 2009, *A&A*, 498, 3, pp. 967–980, « Benchmark problems for continuum radiative transfer. High optical depths, anisotropic scattering, and polarisation. »

Pinte, C., W. R. F. Dent, F. Ménard, et al., 2016, *ApJ*, 816, p. 25, « Dust and Gas in the Disk of HL Tauri: Surface Density, Dust Settling, and Dust-to-gas Ratio. »

Pinte, C., F. Ménard, G. Duchêne, et al., 2018, *A&A*, 609, A47, « Direct mapping of the temperature and velocity gradients in discs. Imaging the vertical CO snow line around IM Lupi. »

Pinte, C., D. J. Price, F. Ménard, et al., 2020, *ApJ*, 890, 1, p. L9, « Nine Localized Deviations from Keplerian Rotation in the DSHARP Circumstellar Disks: Kinematic Evidence for Protoplanets Carving the Gaps. »

Pohl, A., E. Sissa, M. Langlois, et al., 2017, *A&A*, 605, A34, « New constraints on the disk characteristics and companion candidates around T Chamaeleontis with VLT/SPHERE. »

Pohl, A., M. Benisty, P. Pinilla, et al., 2017, *ApJ*, 850, p. 52, « The Circumstellar Disk HD 169142: Gas, Dust, and Planets Acting in Concert? »

Pollack, J. B., O. Hubickyj, P. Bodenheimer, et al., 1996, *Icarus*, 124, 1, pp. 62–85, « Formation of the Giant Planets by Concurrent Accretion of Solids and Gas. »

Powell, D., R. Murray-Clay, L. M. Pérez, et al., 2019, *ApJ*, 878, 2, p. 116, « New Constraints From Dust Lines on the Surface Densities of Protoplanetary Disks. »

Price, D. J., N. Cuello, C. Pinte, et al., 2018, *MNRAS*, 477, pp. 1270–1284, « Circumbinary, not transitional: on the spiral arms, cavity, shadows, fast radial flows, streamers, and horseshoe in the HD 142527 disc. »

Price, D. J., J. Wurster, T. S. Tricco, et al., 2018, *PASA*, 35, e031, « Phantom: A Smoothed Particle Hydrodynamics and Magnetohydrodynamics Code for Astrophysics. »

Quanz, S. P., A. Amara, M. R. Meyer, et al., 2015, *ApJ*, 807, p. 64, « Confirmation and Characterization of the Protoplanet HD 100546 b—Direct Evidence for Gas Giant Planet Formation at 50 AU. »

Quast, G. R., C. A. O. Torres, R. de La Reza, et al., 2000, *IAU Symposium*, vol. 200, p. 28, « V4046 Sgr, a key young binary system. »

Reggiani, M., V. Christiaens, O. Absil, et al., 2018, *A&A*, 611, A74, « Discovery of a point-like source and a third spiral arm in the transition disk around the Herbig Ae star MWC 758. »

Reggiani, M., S. P. Quanz, M. R. Meyer, et al., 2014, *ApJ*, 792, p. L23, « Discovery of a Companion Candidate in the HD 169142 Transition Disk and the Possibility of Multiple Planet Formation. »

Ribas, Á., B. Merín, H. Bouy, et al., 2014, *A&A*, 561, A54, « Disk evolution in the solar neighborhood. I. Disk frequencies from 1 to 100 Myr. »

Ribas, A., H. Bouy, and B. Merín, 2015, *A&A*, 576, A52, « Protoplanetary disk lifetimes vs stellar mass and possible implications for giant planet populations. »

Ribas, Á., C. C. Espaillat, E. Macías, et al., 2017, *ApJ*, 849, 1, p. 63, « Far-infrared to Millimeter Data of Protoplanetary Disks: Dust Growth in the Taurus, Ophiuchus, and Chamaeleon I Star-forming Regions. »

Ricci, L., L. Testi, A. Natta, et al., 2010, *A&A*, 521, A66, « Dust grain growth in ρ-Ophiuchi protoplanetary disks. »

Rice, W. K. M. and P. J. Armitage, 2003, *ApJ*, 598, 1, pp. L55–L58, « On the Formation Timescale and Core Masses of Gas Giant Planets. »

Rice, W. K. M., P. J. Armitage, M. R. Bate, et al., 2003, *MNRAS*, 339, 4, pp. 1025–1030, « The effect of cooling on the global stability of self-gravitating protoplanetary discs. »

Riols, A. and G. Lesur, 2018, *A&A*, 617, A117, « Dust settling and rings in the outer regions of protoplanetary discs subject to ambipolar diffusion. »

Riols, A., B. Roux, H. Latter, et al., 2020, *MNRAS*, 493, 4, pp. 4631–4642, « Dust dynamics and vertical settling in gravitoturbulent protoplanetary discs. »

Riols, A., G. Lesur, and F. Menard, 2020, *arXiv e-prints*, arXiv:2006.01194, « Ring formation and dust dynamics in wind-driven protoplanetary discs: global simulations. »

Riviere-Marichalar, P., A. Bayo, I. Kamp, et al., 2015, *A&A*, 575, A19, « Herschel -PACS observations of $[OI]$ and H2O in Cha II. »

Rosenfeld, K. A., S. M. Andrews, D. J. Wilner, et al., 2013, *ApJ*, 775, p. 136, « The Structure of the Evolved Circumbinary Disk around V4046 Sgr. »

Rosotti, G. P., A. Juhasz, R. A. Booth, et al., 2016, *MNRAS*, 459, pp. 2790–2805, « The minimum mass of detectable planets in protoplanetary discs and the derivation of planetary masses from high-resolution observations. »

Ruíz-Rodríguez, D., L. A. Cieza, J. P. Williams, et al., 2018, *MNRAS*, 478, pp. 3674–3692, « ALMA survey of circumstellar discs in the young stellar cluster IC 348. »

Sallum, S., K. B. Follette, J. A. Eisner, et al., 2015, *Nature*, 527, pp. 342–344, « Accreting protoplanets in the LkCa 15 transition disk. »

Schmid, H. M., F. Joos, and D. Tschan, 2006, *A&A*, 452, pp. 657–668, « Limb polarization of Uranus and Neptune. I. Imaging polarimetry and comparison with analytic models. »

Shakura, N. I. and R. A. Sunyaev, 1973, *A&A*, 500, pp. 33–51, « Black holes in binary systems. Observational appearance. »

Sheehan, P. D. and J. A. Eisner, 2017, *ApJ*, 851, 1, p. 45, « Disk Masses for Embedded Class I Protostars in the Taurus Molecular Cloud. »

Sierra, A. and S. Lizano, 2020, *ApJ*, 892, 2, p. 136, « Effects of Scattering, Temperature Gradients, and Settling on the Derived Dust Properties of Observed Protoplanetary Disks. »

Siess, L., E. Dufour, and M. Forestini, 2000, *A&A*, 358, pp. 593–599, « An internet server for pre-main sequence tracks of low- and intermediate-mass stars. »

Silverstone, M. D., M. R. Meyer, E. E. Mamajek, et al., 2006, *ApJ*, 639, pp. 1138–1146, « Formation and Evolution of Planetary Systems (FEPS): Primordial Warm Dust Evolution from 3 to 30 Myr around Sun-like Stars. »

Simon, M., S. Guilloteau, T. L. Beck, et al., 2019, *ApJ*, 884, 1, p. 42, « Masses and Implications for Ages of Low-mass Pre-main-sequence Stars in Taurus and Ophiuchus. »

Spezzi, L., J. M. Alcalá, E. Covino, et al., 2008, *AJ*, 2, « The Young Population of the Chamaeleon II Dark Cloud. »

Spezzi, L., N. Cox, T. Prusti, et al., 2013, *A&A*, A71, « The Herschel Gould Belt Survey in Chamaeleon II. »

Stahler, S. W., 1983, *ApJ*, 274, pp. 822–829, « The birthline for low-mass stars. »

Stapelfeldt, K. R., G. Duchêne, M. Perrin, et al., 2014, *Exploring the Formation and Evolution of Planetary Systems*, vol. 299, pp. 99–103, « HST Imaging of New Edge-on Circumstellar Disks in Nearby Star-forming Regions. »

Stapelfeldt, K. R., J. E. Krist, F. Ménard, et al., 1998, *ApJ*, 502, pp. L65–L69, « An Edge-On Circumstellar Disk in the Young Binary System HK Tauri. »

Stapelfeldt, K. R., A. M. Watson, J. E. Krist, et al., 1999, *ApJ*, 516, 2, pp. L95–L98, « A Variable Asymmetry in the Circumstellar Disk of HH 30. »

Stapelfeldt, K. R., F. Ménard, A. M. Watson, et al., 2003, *ApJ*, 589, pp. 410–418, « Hubble Space Telescope WFPC2 Imaging of the Disk and Jet of HV Tauri C. »

Stokes, G. G., 1851, *Transactions of the Cambridge Philosophical Society*, 9, p. 399, « On the Composition and Resolution of Streams of Polarized Light from different Sources. »

Stolker, T., C. Dominik, H. Avenhaus, et al., 2016, *A&A*, 595, A113, « Shadows cast on the transition disk of HD 135344B. Multiwavelength VLT/SPHERE polarimetric differential imaging. »

Strom, K. M., S. E. Strom, S. Edwards, et al., 1989, *AJ*, 97, p. 1451, « Circumstellar Material Associated with Solar-Type Pre-Main-Sequence Stars: A Possible Constraint on the Timescale for Planet Building. »

Suzuki, T. K., M. Ogihara, A. r. Morbidelli, et al., 2016, *A&A*, 596, A74, « Evolution of protoplanetary discs with magnetically driven disc winds. »

Tatulli, E., M. Benisty, F. Ménard, et al., 2011, *A&A*, 531, A1, « Constraining the structure of the planet-forming region in the disk of the Herbig Be star HD 100546. »

Teague, R., J. Bae, E. A. Bergin, et al., 2018, *ApJ*, 860, p. L12, « A Kinematical Detection of Two Embedded Jupiter-mass Planets in HD 163296. »

Teague, R., J. Bae, and E. A. Bergin, 2019, *Nature*, 574, 7778, pp. 378–381, « Meridional flows in the disk around a young star. »

Teague, R., M. R. Jankovic, T. J. Haworth, et al., 2020, *MNRAS*, 495, 1, pp. 451–459, « A three-dimensional view of Gomez's hamburger. »

Terebey, S., F. H. Shu, and P. Cassen, 1984, *ApJ*, 286, pp. 529–551, « The collapse of the cores of slowly rotating isothermal clouds. »

Testi, L., T. Birnstiel, L. Ricci, et al., 2014, *Protostars and Planets VI*, p. 339, « Dust Evolution in Protoplanetary Disks. »

Thalmann, C., G. D. Mulders, M. Janson, et al., 2015, *ApJ*, 808, p. L41, « Optical Imaging Polarimetry of the LkCa 15 Protoplanetary Disk with SPHERE ZIMPOL. »

Thalmann, C., M. Janson, A. Garufi, et al., 2016, *ApJ*, 828, p. L17, « Resolving the Planet-hosting Inner Regions of the LkCa 15 Disk. »

Tobin, J. J., P. D. Sheehan, S. T. Megeath, et al., 2020, *ApJ*, 890, 2, p. 130, « The VLA/ALMA Nascent Disk and Multiplicity (VANDAM) Survey of Orion Protostars. II. A Statistical Characterization of Class 0 and Class I Protostellar Disks. »

Tout, C. A., M. Livio, and I. A. Bonnell, 1999, *MNRAS*, 310, 2, pp. 360–376, « The ages of pre-main-sequence stars. »

Trapman, L., S. Facchini, M. R. Hogerheijde, et al., 2019, *A&A*, 629, A79, « Gas versus dust sizes of protoplanetary discs: effects of dust evolution. »

Tripathi, A., S. M. Andrews, T. Birnstiel, et al., 2017, *ApJ*, 845, 1, p. 44, « A millimeter Continuum Size-Luminosity Relationship for Protoplanetary Disks. »

Tripathi, A., S. M. Andrews, T. Birnstiel, et al., 2018, *ApJ*, 861, 1, p. 64, « The Millimeter Continuum Size-Frequency Relationship in the UZ Tau E Disk. »

Tsukagoshi, T., M. Momose, J. Hashimoto, et al., 2014, *ApJ*, 783, p. 90, « High-resolution Submillimeter and Near-infrared Studies of the Transition Disk around Sz 91. »

Uyama, T., J. Hashimoto, M. Kuzuhara, et al., 2017, *AJ*, 153, 3, p. 106, « The SEEDS High Contrast Imaging Survey of Exoplanets around Young Stellar Objects. »

Vigan, A., C. Fontanive, M. Meyer, et al., 2020, *arXiv e-prints*, arXiv:2007.06573, « The SPHERE infrared survey for exoplanets (SHINE). III. The demographics of young giant exoplanets below 300 au with SPHERE. »

Villenave, M., M. Benisty, W. R. F. Dent, et al., 2019, *A&A*, 624, A7, « Spatial segregation of dust grains in transition disks. SPHERE observations of 2MASS J16083070-3828268 and RXJ1852.3-3700. »

Villenave, M., F. Menard, W. R. F. Dent, et al., 2020, *arXiv e-prints*, arXiv:2008.06518, « Observations of edge-on protoplanetary disks with ALMA I. Results from continuum data. »

Voirin, J., C. F. Manara, and T. Prusti, 2018, *A&A*, 610, A64, « A revised estimate of the distance to the clouds in the Chamaeleon complex using the Tycho-Gaia Astrometric Solution. »

Wada, K., H. Tanaka, T. Suyama, et al., 2009, *ApJ*, 702, 2, pp. 1490–1501, « Collisional Growth Conditions for Dust Aggregates. »

Wagner, K., K. B. Follete, L. M. Close, et al., 2018, *ApJ*, 863, 1, p. L8, « Magellan Adaptive Optics Imaging of PDS 70: Measuring the Mass Accretion Rate of a Young Giant Planet within a Gapped Disk. »

Watson, A. M. and K. R. Stapelfeldt, 2004, *ApJ*, 602, 2, pp. 860–874, « The Visible and Near-Infrared Dust Opacity Law in the HH 30 Circumstellar Disk. »

Weber, P., S. Pérez, P. Benítez-Llambay, et al., 2019, *ApJ*, 884, 2, p. 178, « Predicting the Observational Signature of Migrating Neptune-sized Planets in Low-viscosity Disks. »

Weidenschilling, S. J., 1977, *MNRAS*, 180, pp. 57–70, « Aerodynamics of solid bodies in the solar nebula. »

Whittet, D., T. Prusti, G. Franco, et al., 1997, *A&A*, 327, « On the distance to the Chamaeleon I and II associations. »

Williams, J. P. and W. M. J. Best, 2014, *ApJ*, 788, 1, p. 59, « A Parametric Modeling Approach to Measuring the Gas Masses of Circumstellar Disks. »

Williams, J. P. and L. A. Cieza, 2011, *ARA&A*, 49, 1, pp. 67–117, « Protoplanetary Disks and Their Evolution. »

Wilner, D. J., P. T. P. Ho, J. H. Kastner, et al., 2000, *ApJ*, 534, 1, pp. L101–L104, « VLA Imaging of the Disk Surrounding the Nearby Young Star TW Hydrae. »

Wilson, T. L., K. Rohlfs, and S. Hüttemeister, 2009, *Tools of Radio Astronomy*

Windmark, F., T. Birnstiel, C. Güttler, et al., 2012, *A&A*, 540, A73, « Planetesimal formation by sweep-up: how the bouncing barrier can be beneficial to growth. »

Winn, J. N. and D. C. Fabrycky, 2015, *ARA&A*, 53, pp. 409–447, « The Occurrence and Architecture of Exoplanetary Systems. »

Woitke, P., M. Min, C. Pinte, et al., 2016, *A&A*, 586, A103, « Consistent dust and gas models for protoplanetary disks. I. Disk shape, dust settling, opacities, and PAHs. »

Wolf, S., D. L. Padgett, and K. R. Stapelfeldt, 2003, *ApJ*, 588, 1, pp. 373–386, « The Circumstellar Disk of the Butterfly Star in Taurus. »

Wolff, S. G., M. D. Perrin, K. Stapelfeldt, et al., 2017, *ApJ*, 851, p. 56, « Hubble Space Telescope Scattered-light Imaging and Modeling of the Edge- on Protoplanetary Disk ESO-Hα 569. »

Yang, H., Z.-Y. Li, L. Looney, et al., 2016, *MNRAS*, 456, 3, pp. 2794–2805, « Inclination-induced polarization of scattered millimetre radiation from protoplanetary discs: the case of HL Tau. »

Youdin, A. N. and J. Goodman, 2005, *ApJ*, 620, 1, pp. 459–469, « Streaming Instabilities in Protoplanetary Disks. »

Zernike, F., 1938, *Physica*, 5, 8, pp. 785–795, « The concept of degree of coherence and its application to optical problems. »

Zhang, K., A. Isella, J. M. Carpenter, et al., 2014, *ApJ*, 791, p. 42, « Comparison of the Dust and Gas Radial Structure in the Transition Disk [PZ99] J160421.7-213028. »

Zhang, S., Z. Zhu, J. Huang, et al., 2018, *ApJ*, 869, 2, p. L47, « The Disk Substructures at High Angular Resolution Project (DSHARP). VII. The Planet-Disk Interactions Interpretation. »

Zhu, Z., R. P. Nelson, R. Dong, et al., 2012, *ApJ*, 755, 1, p. 6, « Dust Filtration by Planet-induced Gap Edges: Implications for Transitional Disks. »

Zhu, Z., S. Zhang, Y.-F. Jiang, et al., 2019, *ApJ*, 877, 2, p. L18, « One Solution to the Mass Budget Problem for Planet Formation: Optically Thick Disks with Dust Scattering. »

Zucker, C., J. S. Speagle, E. F. Schlafly, et al., 2019, *ApJ*, 879, 2, p. 125, « A Large Catalog of Accurate Distances to Local Molecular Clouds: The Gaia DR2 Edition. »

de Boer, J., G. Salter, M. Benisty, et al., 2016, *A&A*, 595, A114, « Multiple rings in the transition disk and companion candidates around RX J1615.3-3255. High contrast imaging with VLT/SPHERE. »

de Boer, J., M. Langlois, R. G. van Holstein, et al., 2020, *A&A*, 633, A63, « Polarimetric imaging mode of VLT/SPHERE/IRDIS. I. Description, data reduction, and observing strategy. »

de Gregorio-Monsalvo, I., F. Ménard, W. Dent, et al., 2013, *A&A*, 557, A133, « Unveiling the gas-and-dust disk structure in HD 163296 using ALMA observations. »

de Juan Ovelar, M., M. Min, C. Dominik, et al., 2013, *A&A*, 560, A111, « Imaging diagnostics for transitional discs. »

de Zeeuw, P. T., R. Hoogerwerf, J. H. J. de Bruijne, et al., 1999, *AJ*, 117, 1, « A Hipparcos Census of the Nearby OB Associations. »

van Cittert, P. H., 1934, *Physica*, 1, 1, pp. 201–210, « Die Wahrscheinliche Schwingungsverteilung in Einer von Einer Lichtquelle Direkt Oder Mittels Einer Linse Beleuchteten Ebene. »

van Holstein, R. G., J. H. Girard, J. de Boer, et al., 2020, *A&A*, 633, A64, « Polarimetric imaging mode of VLT/SPHERE/IRDIS. II. Characterization and correction of instrumental polarization effects. »

van Terwisga, S. E., A. Hacar, and E. F. van Dishoeck, 2019, *A&A*, 628, A85, « Disk masses in the Orion Molecular Cloud-2: distinguishing time and environment. »

van der Marel, N., E. F. van Dishoeck, S. Bruderer, et al., 2013, *Science*, 340, pp. 1199–1202, « A Major Asymmetric Dust Trap in a Transition Disk. »

van der Marel, N., J. P. Williams, M. Ansdell, et al., 2018, *ApJ*, 854, 2, p. 177, « New Insights into the Nature of Transition Disks from a Complete Disk Survey of the Lupus Star-forming Region. »

van der Plas, G., F. Ménard, K. Ward-Duong, et al., 2016, *ApJ*, 819, 2, p. 102, « Dust Masses of Disks around 8 Brown Dwarfs and Very Low-mass Stars in Upper Sco OB1 and Ophiuchus. »

van der Plas, G., F. Ménard, H. Canovas, et al., 2017, *A&A*, 607, A55, « An 80 au cavity in the disk around HD 34282. »

van der Plas, G., C. M. Wright, F. Ménard, et al., 2017, *A&A*, 597, A32, « Cavity and other radial substructures in the disk around HD 97048. »

van der Plas, G., F. Ménard, J. F. Gonzalez, et al., 2019, *A&A*, 624, A33, « ALMA study of the HD 100453 AB system and the tidal interaction of the companion with the disk. »